IntechOpen

Mass Transfer

Advances in Sustainable Energy and Environment Oriented Numerical Modeling

Edited by Hironori Nakajima

MASS TRANSFER - ADVANCES IN SUSTAINABLE ENERGY AND ENVIRONMENT ORIENTED NUMERICAL MODELING

Edited by **Hironori Nakajima**

Mass Transfer - Advances in Sustainable Energy and Environment Oriented Numerical Modeling
http://dx.doi.org/10.5772/3372
Edited by Hironori Nakajima

Contributors

Stanford Shateyi, Sandile Motsa, Rafał Rakoczy, Maria Angelica Simões Dornellas Barros, Pedro Augusto Arroyo, Edson Antonio da Silva, Tigran Vartanyan, Nikita Leonov, Sergey Przhibel'skii, Nikita A. Toropov, Guillaume Polidori, Marek Solecki, Leôncio Diógenes Tavares Câmara, Antônio Jose Da Silva Neto, Jader Lugon Junior, Flávio De Matos Silva, Guilherme Pereira De De Oliveira, Lídice Camps Echeverria, Orestes Llanes Santiago, Huu Doan, Amira Abdelrasoul, Ali Lohi, Michail Ivanovich Shilyaev, Helen Khromova, Eleazar Máximo Escamilla Silva, Ana Maria Mendoza-Martínez, Krzysztof Górnicki, Ali Haghighi Asl, Maryam Khajenoori, Anatoly Tsirlin, Achim A. Beylich, Precious Sibanda, Ahmed Khidir, Chiedu Owabor, Pavel Nikonovich Mikhaylov, Aleksey Mikhaylov, Alexander Filippov, Hironori Nakajima

Notice

First published in Croatia, 2013 by INTECH d.o.o.
eBook (PDF) Published by IN TECH d.o.o.
Place and year of publication of eBook (PDF): Rijeka, 2019.
IntechOpen is the global imprint of IN TECH d.o.o.
Printed in Croatia

Legal deposit, Croatia: National and University Library in Zagreb

Additional hard and PDF copies can be obtained from orders@intechopen.com

Mass Transfer - Advances in Sustainable Energy and Environment Oriented Numerical Modeling
Edited by Hironori Nakajima

p. cm.

ISBN 978-953-51-1170-2

eBook (PDF) ISBN 978-953-51-6356-5

Meet the editor

Hironori Nakajima received his B.S. degree in Engineering Science, and M.S. and Ph.D. degrees in Energy Science from Kyoto University. He has been an assistant professor in the Department of Mechanical Engineering at Kyushu University since 2006. He was a visiting scholar in the Department of Mechanical Engineering at the University of California, Berkeley in 2011. He was a visiting scientist in the Department of Mechanical and Process Engineering at the Swiss Federal Institute of Technology, Zürich in 2012. His research interests include heat and mass transfers, electrochemical analyses, and diagnosis of fuel cells and batteries. Dr. Nakajima is a member of the Electrochemical Society, the Japan Society of Mechanical Engineers, and the Electrochemical Society of Japan. Dr. Nakajima also serves as a reviewer for several peer-reviewed journals, including Journal of Power Sources and International Journal of Hydrogen Energy.

Contents

Preface

Our knowledge of mass transfer processes has been extended and applied to various fields of science and engineering including industrial and manufacturing processes in recent years. Since mass transfer is primordial phenomenon, it plays a key role in the scientific researches and fields of mechanical, energy, environmental, materials, bio, and chemical engineering. The present book contains the selected advanced topics in numerical modeling and analysis of mass transfer processes aspiring for sustainable energy and environment. This book covers both fundamentals and applications of mass transfer in various developing science and technologies.

The 19 chapters of this book are divided into two parts. The first part deals with advanced topics in numerical modeling of mass transfer. The second part is devoted to the advanced topics in numerical analysis of mass transfer on the basis of measurement.

In this book, the authors provide advances in scientific findings and technologies, and develop new theoretical models concerning mass transfer. The editor would like to express his sincere gratitude to all the authors for their contributions. This book brings valuable references for research engineers working in the variety of mass transfer sciences and related fields in mechanical, energy, environmental, materials, bio, and chemical engineering. Since the constitutive topics cover the advances in broad research areas, the topics will be mutually stimulus and informative not only to research engineers, but also to university professors and students in different areas.

Hironori Nakajima
Department of Mechanical Engineering
Kyushu University, Fukuoka, Japan

Section 1

Advanced Numerical Modelings

Chapter 1

The Theory of Random Transformation of Dispersed Matter

Marek Solecki

Additional information is available at the end of the chapter

http://dx.doi.org/10.5772/52369

1. Introduction

The development of civilization, with regard to its consequences, requires appropriate research tools. This is the reason of significant progress in different fields in mathematical modelling of processes involving mass transfer. For their description there are often used widely known models which can be written in a general form of nonlinear differential equations. Woltera [1], who conducted the research of oscillation level of selected fish species in the Adriatic, described the interaction system in the population of predator-victim type. It is compatible with the obtained by Lotka [2] description of the reaction with the expected oscillations in the concentrations of chemical compounds. The process of destruction of organisms during disinfection is included in the model of Chick [3] developed by Watson [4]. The kinetics of the course of simple enzymatic reactions was described by Michaelis and Menten [5]. Mathematical description of the process of microorganisms disintegration in high-pressure homogenizer was developed on the basis of experimental data by Hetherington et al. [6]. After over twenty years since revealing the effect of the position of enzymes in a cell on their release rate [7], Melendres et al. [8] proposed a nonlinear description of the process as a consequence of the following events: cell disruption and release of intracellular compounds. The results of pioneering protease inhibitor therapy in HIV infection were the basis for the development by Ho et al. [9] of a simple model of treatment and solving the mystery associated with the quasi-stationary phase of infection. These models are still used to describe the processes or are often the basis for future studies of more complex mathematical problems.

The essence of all the above processes is random transformation of material objects dispersed in a limited space. Their relationships may help to increase the pace of knowledge development. A uniform theory of the presented issues was developed by Solecki [10]. The common general concept based on the knowledge and understanding of important factors shaping the

specified sphere of events will facilitate particularistic analysis as well as transfer of knowledge and experience. The aim of the presented study was to develop a unified theory of the presented issues, allowing for phenomenal and mathematical modeling of various processes based on mass transfer.

2. Paradigm

This section presents a coherent conceptual system of uniform theory which includes various processes of random transformation of dispersed matter in a limited space.

2.1. Space and material objects

Let there be a set N consisting of n elements that are material objects. We assume that n is a natural number.

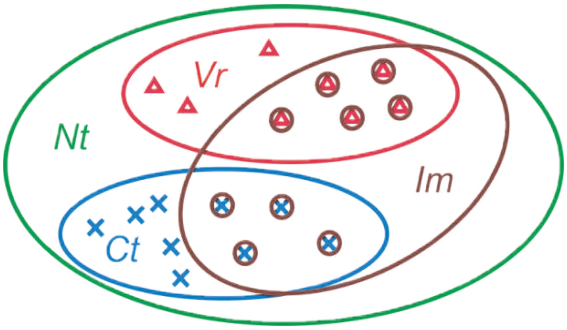

Figure 1. The set of identified properties of a material object belonging to set *N*.

Identified properties of material objects belonging to set N are the elements of set Nt (*notum*) (Fig. 1). The property of an object is the feature which characterizes it. Objects can have χ same properties ($ct_1, \ldots, ct_\chi$) belonging to set Ct (*constans*) which is a subset of set Nt. Objects from set N can differ with ξ properties ($vr_1, \ldots, vr_\xi$). They belong to set Vr (*variabilis*) which is a subset of identified features of object Nt. We assume that the ψ- th property $vr_{\psi i}$ of any i-th object belonging to set N is included within the range described by the relationship

$$vr_{\psi \min} \leq vr_{\psi i} \leq vr_{\psi \max}. \tag{1}$$

Changing the feature of an object belonging to set Vr involves a change of the parameter $vr_{\psi i}$ described by the relationship (1). An object from set N may lose some features from set Vr or Ct. Any element belonging to set N must have all the φ features belonging to set Im (*inamissibilem*). They are the basic features of any object from set N and satisfy the relationship

http://dx.doi.org/10.5772/52369

$$0<\varphi\leq\chi+\xi. \tag{2}$$

Set *Im* is a subset of set *Nt*. We assume that after the loss of at least one basic feature of set *Im* the object is no longer what it was, that is it no longer belongs to set *N*.

Objects from set *N* have limited duration after which they lose at least one basic feature from set *Im* and they do not belong to set *N* anymore.

It is assumed that the fact of existing of objects in set *N* results in a possibility of generating new elements which are objects of set *N*.

Let there be a limited medium of volume *V* described by the relationship according to the equation

$$V=f_1(t). \tag{3}$$

In his medium there is set *N* consisting of *n* dispersed material objects described by the relationship

$$n=f_2(t). \tag{4}$$

We assume that the volume of material object *V* is incomparably greater than volume V_{ni} of any *i*-th object of set *N*, according to the formula

$$V_{ni}<<V. \tag{5}$$

At the initial moment $t_0=0$ the number of objects from set *N* dispersed in space *V* amounts n_0, where n_0 is large natural number. We assume that after time Δt the number of objects belonging to set *N* may be changed. Changes may be caused by:

- addition of new objects from the outside to volume *V* – introduction,
- exclusion of some objects from volume *V* to the outside – removal,
- generating new objects resulting from the fact of existing of material objects from set *N* in volume *V* – multiplication,
- natural exclusion of objects from set *N*, resulting from its duration appropriate for the elements of this set, caused by the loss of at least one feature from set *Im* – exclusion.

Change in number of objects belonging to set *N*, resulting from introduction, removal, multiplication and exclusion, described by functions respectively $f_{31}(t)$, $f_{32}(n, t)$, $f_{33}(n, t)$ and $f_{34}(n, t)$, at the moment *t* is described by the relationship consistent with the formula

$$\Delta n_A = f_{31}(t) - f_{32}(n,t) + f_{33}(n,t) - f_{34}(n,t). \tag{6}$$

2.2. Converting of objects

The conditions of the existence of objects in the environment are determined by the interaction of physical, chemical, biological and psychical factors. We assume that for each material object from set N there exists such set of environmental conditions in which there is a loss of ς object properties (ς>0) belonging to set Nt. If at least one of ς lost features belongs to set Im we are dealing with the transformation of an element from set N. In this case the object from set N after the loss of at least one feature from set Im does not belong to set N. A set of environment conditions which may influence the transformation of an object from set N is called transformation conditions. Their intensity, at which the object is transformed, is called transformation intensity and is denoted as Γ_t. Locally occurring environmental conditions of transformation intensity were designated γ_t. The features of an object from subset Ct have no effect on the variation of transformation intensity of material objects. We assume, however, that the combination of ξ features of set Vr affects the value of the smallest transformation intensity γ_{ti} of the i-th object from set N, according to the formula

$$\gamma_{ti} = f_4(vr_1, \ldots, vr_\xi). \tag{7}$$

If none of ς lost properties by the i-th element belongs to set Im we are dealing with the formation of object from set N. After the loss of features not belonging to set Im an object from set N still belongs to set N. A set of environment conditions which may influence the formation of an object from set N is called formation conditions. Their intensity, at which the object is formed, is called formation intensity and is denoted as T_t. Locally occurring environmental conditions of formation intensity were denoted by τ_t. The features of an object from subset Ct have no effect on the variation of formation intensity of material objects. However, the combination of ξ features of set Vr affects the value of the smallest transformation intensity τ_{ti} of the i-th object from set N, according to the formula

$$\tau_{ti} = f_5(vr_1, \ldots, vr_\xi). \tag{8}$$

Later in this paper the theory of transforming objects is described. The formation of material objects is an important issue because of the possibility of changing their susceptibility to transformation. The theory of random formation of matter is analogous to the described theory.

2.3. Types of volume

The main parts of space V are volumes V_{ai}. Environmental conditions occurring in them are safe for the individual objects from set N. Thus volume V_{ai} is safe for the i-th object from the

http://dx.doi.org/10.5772/52369

set N. We assume that this volume there is intensive mixing. Its purpose is to homogenise the concentration of objects present in the volume $V_{\alpha i}$.

Volume $V_{\alpha i}$ consists of two parts:

a. $V_{\alpha ci}$ is a part of volume $V_{\alpha i}$, whose subsets are never transformed to other types of volumes,

b. $V_{\alpha ti}$ is a part of volume $V_{\alpha i}$, in which subsets can be transformed to other types of volumes ($V_{\gamma ji}$ and $V_{\beta ji}$).

Between the components of volume $V_{\alpha i}$ for the i-th object there are relationships which are described by the following formula

$$V_{\alpha i} = V_{\alpha ti} \cup V_{\alpha ci} \tag{9}$$

and

$$V_{\alpha ti} \cap V_{\alpha ci} = \emptyset. \tag{10}$$

In the space $V_{\alpha ti}$ there are generated transformation volumes $V_{\gamma ji}$. Possible cases of generating transformation volumes are shown in Figure 2. Volume $V_{\gamma ji}$ is the j-th transformation volume of the i-th material object from set N. We assume that transformation volumes generated for the i-th element are uniformly dispersed in space $V_{\alpha ti}$. Space $V_{\alpha ti}$ is incomparably greater than any j-th volume $V_{\gamma ji}$, which is described by the formula

$$V_{\gamma ji} \ll V_{\alpha ti}. \tag{11}$$

Volume $V_{\gamma ji}$ is limited from the outside with surface $F_{\gamma \alpha ji}$ and from the inside with surface $F_{\gamma \beta ji}$ (Fig. 2). Both surfaces belong to volume $V_{\gamma ji}$ according to the formula

$$F_{\gamma \alpha ji} \in V_{\gamma ji}, \tag{12}$$

and

$$F_{\gamma \beta ji} \in V_{\gamma ji}. \tag{13}$$

Component factors of transformation conditions of the i-th material object can affect it locally or even pointwise. Component factors of transformation conditions of the i-th material object can affect it locally or even pointwise. However, the effects of their action affect the whole object. We assume that the smallest transformation volume of the i-th object is equal to its volume at the moment of transformation and amounts $(V_{\gamma ji})_{min}$ (Fig. 3). Occurring in his volume

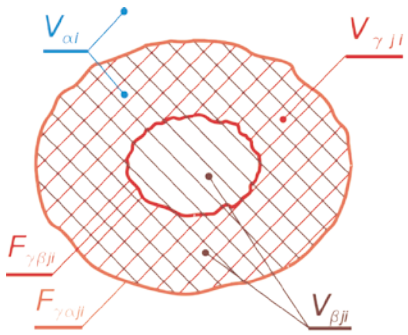

Figure 2. Schematic of formed transformation volume $V_{\gamma ji}$ mach larger then $(V_{\gamma ji})_{min}$: general case.

set of transformation conditions of intensity at least γ_{ti} ensures transformation of the i-th object from set N. Volume $(V_{\gamma ji})_{min}$ is a value characterizing the i-th material object from set N.

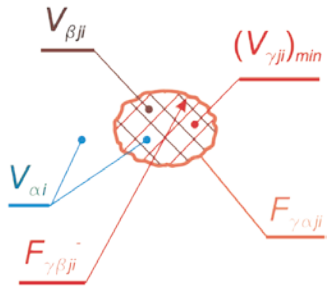

Figure 3. Schematic of formed transformation volume $V_{\gamma ji} = (V_{\gamma ji})_{min}$: special case.

The range of variation of generated in space V transformation volume $V_{\gamma ji}$ by the size of the volume is described by the following formula

$$\left(V_{\gamma ji}\right)_{\min} \le V_{\gamma ji} \le \left(V_{\gamma ji}\right)_{\max}, \tag{14}$$

and by the intensity of transformation conditions by a formula

$$V_{\gamma ji(\gamma_t=\gamma_{t\min})} \le V_{\gamma ji(\gamma_t)} \le V_{\gamma ji(\gamma_t=\gamma_{t\max})}. \tag{15}$$

By γ_{tmin} and γ_{tmax} denoted accordingly minimum and maximum intensity of transformation conditions which can be generated in space $V_{\gamma ji}$.

Transformation volume $V_{\gamma ji}$ is generated at time t ($t > t_0$) of process transformation duration. It can exist in any time interval $\Delta t > 0$. In this time interval $V_{\gamma ji}$ can increase; if it is greater than

http://dx.doi.org/10.5772/52369

$(V_{\gamma ji})_{min}$ it can decrease or stay unchanged. It can also be displaced randomly to any available place of volume V_{ati}. In general form $V_{\gamma ji}$ is described by the relationship in the following formula

$$V_{\gamma ji} = \iint_{D_1} \left[f_{61ji}(x,y,\gamma,t) - f_{62ji}(x,y,\gamma,t) \right] dxdy - \iint_{D_2} \left[f_{71ji}(x,y,\gamma,t) - f_{72ji}(x,y,\gamma,t) \right] dxdy \tag{16}$$

of course at the assumptions described by the relationships

$$f_{61ji}(x,y,\gamma,t) \geq 0 \tag{17}$$

and

$$f_{71ji}(x,y,\gamma,t) \geq 0. \tag{18}$$

Flat areas D_1 and D_2 describe relationships defined by formulas respectively

$$y = f_{63ji}(x,\gamma,t) \tag{19}$$

and

$$y = f_{73ji}(x,\gamma,t), \tag{20}$$

the range of changes in x value is described by the relationships defined in the formulas respectively

$$x_{6ji\min} \leq x \leq x_{6ji\max} \tag{21}$$

and

$$x_{7ji\min} \leq x \leq x_{7ji\max}. \tag{22}$$

Inside volume $V_{\gamma ji}$ volume $V_{\beta ji}$ is generated. It is not available for non-transformed i-th object from set N.

Axiom 1.

If linear dimensions of volume $V_{\gamma ji}$ are smaller than doubled linear dimensions of the i-th object belonging to set N, then the area of $F_{\gamma\beta ji}$ reached by the i-th object from the inside does not belong to volume $V_{\alpha i}$ according to

$$F_{\gamma\beta ji}^{-} \notin V_{\alpha i}. \tag{23}$$

Since for limit case $(V_{\gamma ji})_{min}$ there is

$$V_{\beta ji} \equiv \left(V_{\gamma ji}\right)_{\min}, \tag{24}$$

that is

$$F_{\gamma\beta ji} \equiv F_{\gamma\alpha ji} \tag{25}$$

then

$$F_{\gamma\alpha ji}^{-} \notin V_{\alpha i}. \tag{26}$$

and

$$F_{\gamma\alpha ji}^{-} \in V_{\beta ji}. \tag{27}$$

Axiom 2.

If the linear dimensions of the volume $V_{\gamma ji}$ are greater than doubled linear dimensions of the i-th object belonging to N then area $F_{\gamma\beta ji}$ does not belong to $V_{\alpha i}$ volume according to the formula

$$F_{\gamma\beta ji} \notin V_{\alpha i}. \tag{28}$$

For the case for which occurs a relationship described by a formula (28), volumes closed by area $F_{\gamma\beta ji}$ do not belong to space $V_{\alpha i}$.

Volume $V_{\beta ji}$ is closed by external surface $F_{\gamma\alpha ji}$.

http://dx.doi.org/10.5772/52369

Axiom 3.

If the linear dimensions of the volume $V_{\gamma ji}$ are smaller than doubled linear dimensions of the i-th object belonging to N then area $F_{\gamma\beta ji}$ reached by the i-th object from the inside belongs to $V_{\beta ji}$ volume according to the formula

$$F_{\gamma\beta ji}^{-} \in V_{\beta ji}. \tag{29}$$

Axiom 4.

If the linear dimensions of the volume $V_{\gamma ji}$ are greater than doubled linear dimensions of the i-th object belonging to N then area $F_{\gamma\beta ji}$ does not belong to $V_{\beta ji}$ according to the formula

$$F_{\gamma\beta ji} \in V_{\beta ji}. \tag{30}$$

For the case for which occurs relationship described by the formula

$$V_{\gamma ji} > \left(V_{\gamma ji}\right)_{\min}, \tag{31}$$

volumes closed by area $F_{\gamma\alpha ji}$ do not belong to $V_{\beta ji}$ volume according to formula

$$F_{\gamma\alpha ji} \notin V_{\beta ji}. \tag{32}$$

If the linear dimensions of the volume $V_{\gamma ji}$ are equal to the doubled linear dimensions of the i-th object belonging to N then area $F_{\gamma\beta ji}$ may be replaced by a segment (for example for cylindrical surfaces) or even a point (for example for spherical surfaces). They will belong to volume $V_{\beta ji}$ and they will not belong to volume $V_{\alpha i}$.

Volume component of the space V, apart from the above mentioned kinds of volumes, is $V_{\delta i}$. This volume meets the following conditions:

1. is safe for the i-th object from set N,

2. there is not mixing in it,

3. there is a possibility of object migration from volume $V_{\alpha i}$ to $V_{\delta i}$ and vice versa,

4. subsets of this volume are not transformed to other volumes.

We assume that there is a relationship

$$V_{\delta i} < V_{\alpha i}. \tag{33}$$

Volumes $V_{\delta i}$ may be dispersed in space V as volumes $V_{\gamma ji}$.

2.4. Transformation process

We assume that the above described events: introduction, removal, multiplication, and exclusion are not the events of the investigated process of random transformation of dispersed material objects.

In a given material medium V occurs process of random transformation of objects belonging to set N. It runs as follows:

At any moment t ($t > 0$) for the i-th object in space $V_{\alpha ti}$ there are generated randomly p transformation volumes $V_{\gamma ji}$, where p is a natural number. The i-th object belonging to set N is in the space safe volume $V_{\alpha i}$ described by a relationship

$$V_{\alpha i} = \bigcap_{j=1}^{p} V_{\alpha ji}. \tag{34}$$

We assume that random transformation of objects is independent events.

It is assumed that during transformation process the number of produced volumes $V_{\gamma ji}$ is large and may change over time, according to the formula

$$p = f_8(t). \tag{35}$$

Due to relative displacement the i-th material object is introduced for time t_{ti} to appropriate volume for its transformation $V_{\gamma ji}$. This is done by the surface $F_{\gamma \alpha ji}$ which limits volume $V_{\gamma ji}$ (Fig. 2 and 3). The considered element of set N remains unconverted if at least its one point is beyond volume $V_{\gamma ji}$. Transformation of the i-th object occurs simultaneously with its complete introduction to transformation volume $V_{\gamma ji}$. According to the conditions given in Section 2.2 transformation occurs when at least one of the ς features belonging to set Ba is lost. Only transformed in volume $V_{\gamma ji}$ i-th object may be dislocated to volume $V_{\beta ji}$.

Theorem about transformation of dispersed matter:

For each material object n_i from set N there exist such local conditions of transformation γ_{ti} belonging to set Γ_t, that if there is time t_{ti}, in which object n_i is included in volume $V_{\gamma ji}$ of transformation properties γ_{ti} then starting from time t_{ti} object n_i does not belong to set N.

This theorem recorded by means of quantifiers has the following form:

$$\left(\forall n_i \in N\right)\left(\exists \gamma_{ti} \in \Gamma_t\right)\left(\left(\exists t_t\right) n_i \subset V_{\gamma ji} \Rightarrow \left(\forall t \geq t_t\right) n_i \notin N\right), \tag{36}$$

and its falsification is included in the record

$$\left(\forall n_i \in N\right)\left(\exists \gamma_{ti} \in \Gamma_t\right)\left(\left(\exists t_t\right) n_i \subset V_{\gamma ji} \Rightarrow \left(\forall t \geq t_t\right) n_i \in N\right). \tag{37}$$

http://dx.doi.org/10.5772/52369

Proof of the theorem

The properties of an object from set N belonging to set Ba (Fig.1) are marked by ba. The relationship is introduced

$$Z_1(n;ba) \tag{38}$$

which expresses the statement that object n has the property ba. We can record the following observations:

object n_i has all the properties ba from set Ba

$$\left(\forall ba \in Ba\right)\left(Z_1\left(n_i;ba\right)\right), \tag{39}$$

and there is a property ba, which object n_i does not have

$$\left(\exists ba \in Ba\right)\left(\neg Z_1\left(ba;n_i\right)\right). \tag{40}$$

Let N be the set of all elements fulfilling condition $W(n)$ described by a logical statement (39)

$$\{n_i \in N : ((\forall\, ba \in Ba)(Z_1(n_i;ba)))\}. \tag{41}$$

The relationship is introduced

$$Z_2(V_\gamma;\gamma_t) \tag{42}$$

expressing the statement that volume V_γ has the property γ_t of object transformation n. We can write the following observation:

object $V_{\gamma ji}$ has got a property γ_{ti} of object transformation n_i

$$\left(\exists \gamma_{ti} \in \Gamma_t\right)\left(Z_2\left(V_{\gamma ji};\gamma_{ti}\right)\right). \tag{43}$$

Let P be the set of all elements fulfilling the condition $W_2(V_{\gamma ji})$ described by a logical statement (39)

$$\{V_{\gamma ji} \in P : ((\forall\, ba \in Ba)(Z_1(n_i;ba)))\}. \tag{44}$$

Let t_{ti} denotes time in which object n_i was introduced to volume $V_{\gamma ji}$. From the moment t_{ti} is true the statement about object n_i

$$\left(\forall t \geq t_{ti}\right)\left(\exists ba \in Ba\right)\left(\neg Z_1\left(ba; n_i\right)\right). \tag{45}$$

It is contrary to the assumption (31) so that from the moment t_{ti} the object n_i cannot be the element of set N according to

$$n_i \notin N \blacksquare. \tag{46}$$

Theorem about creating families of transformation volumes

If at any point 2 belonging to space $V_{\alpha ti}$ environmental conditions of the transformation would function γ_{t2} and in set N there would be r objects of the transformation conditions γ_{ti} fulfilling the relations

$$\gamma_{t2} \geq \gamma_{ti} \tag{47}$$

Then in point 2 there will be generated family consisting of r transformation volumes for r objects from set N.

Conclusions:

1. If set N consists of n elements and conditions of transformation γ_{ti} of any element from set N satisfy the relation

$$\gamma_{tmin} \leq \gamma_{ti} \leq \gamma_{tmax} \tag{48}$$

then the family can include from 1 to n transformation volumes.

2. If in any point 2 belonging to space $V_{\alpha ti}$ would function conditions of transformation γ_{t2} fulfilling the relationship

$$\gamma_{t2} < \gamma_{tmax} \tag{49}$$

and in set N there would exist s objects of transformation conditions greater then γ_{t2} then in space V there are s objects from set N which are not subjected to transformation in point 2.

Volume $V_{\gamma ji}$ is a transformation volume of the i-th material object which belongs to j-th family.

3. General phenomenological model

Figure 4 shows the general set of possibilities for generating volumes associated with the transformation of objects from set N distributed in space $V(t)$. Each vertical segment with the opposite ends located on segments AB and CD denotes space $V(t)$. On each subsequent vertical

http://dx.doi.org/10.5772/52369

section there are marked up divisions of volume V in result of generated one transformation volume. The whole rectangle ABCD includes a set of all possible divisions of space V according to one defined system.

For any i-th object from set N rectangle ABCD is divided into five parts with four segments. The first part, contained between segments LM (marked with blue dashed line) and IJ (marked with red dashed line) is a set of possible volumes $V_{\alpha ji}$. From the bottom a single volume $V_{\alpha i}$ is limited by surface $F_{\gamma\beta ji}$. Depending on the size of generated volume $V_{\gamma ji}$ this surface according to formula (23) conditionally does not belong or according to formula (28) at all does not belong to volume $V_{\alpha i}$. Space $V_{\alpha i}$ is safe for both the i-th object and other objects from set N of the smallest transformation volume not greater than that which is appropriate for the i-th object. In volume $V_{\alpha ji}$ takes place intensive mixing. Its purpose is to homogenize the dispersion of objects present in it.

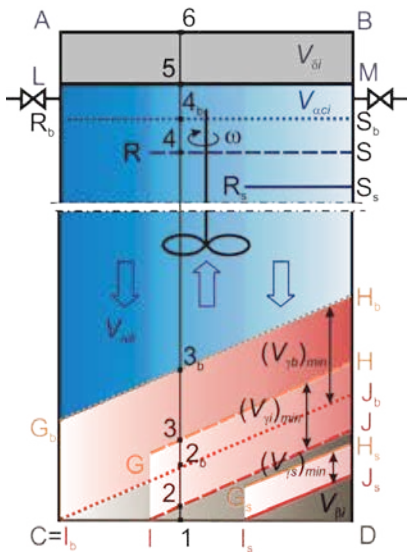

Figure 4. General set of space divisions $V(t)$ resulting from generating volume $V_{\gamma ji}$ for one hypothetical generating system.

In Figure 4 the area included between segments GH (marked with orange dashed line) and IJ (marked with red dashed line) is a set transformation volumes that can be generated. Single volume $V_{\gamma ji}$ is limited by surfaces: $F_{\gamma\alpha ji}$ from the top and $F_{\gamma\beta ji}$ from the bottom. Both these surfaces belong to volume $V_{\gamma ji}$, which is the result of assumptions accepted in formulas (12) and (13). In volume $V_{\gamma ji}$ occurs a transformation if the i-th object and other objects from set N of minimal transformation volume in accordance with that which is appropriate for the i-th object i.e. $(V_{\gamma i})_{min}$. During the process at time t there are p transformations volumes of the i-th object according to relationship (34) are they are uniformly dispersed in space $V_{\alpha ti}$. The size of the volume $V_{\gamma ji}$ in Figure 4 is defined by two parameters: $(V_{\gamma ji})_{min}$ and red colour intensity. The parameter – red colour intensity is a visualization of functional dependence.

Another area in Figure 4, contained between segments GH (marked with orange dashed line) and CD (marked with brown solid line) is a set of volumes $V_{\beta ji}$. Such single volume is limited by surface $F_{\gamma aji}$. Depending on the size of generated volume $V_{\gamma ji}$ this surface according to (27) conditionally belongs to $V_{\beta ji}$ or according to formula (32) does not belong to $V_{\beta ji}$. During the process at time t volume $V_{\beta ji}$ is no more than p. They are linked to appropriate volumes $V_{\gamma ji}$ and dispersed in space $V_{\alpha ti}$. In volume $V_{\beta ji}$ the existence of unconverted objects from set N is impossible, for which minimal transformation volume is not smaller than minimal transformation volume appropriate for the i-th object. The size of the volume $V_{\beta ji}$ in Figure 4 is defined by two parameters: vertical segment with ends located on segments GH and CD and brown colour intensity. The consequence of increasing volume $V_{\gamma ji}$ is increased volume $V_{\beta ji}$ and decreased volume $V_{\alpha ti}$. The size of volume $V_{\alpha ti}$ in Figure 4 is defined by two parameters: vertical segment with ends located on segments RS and IJ and blue colour intensity.

Between segment AB and segment LM there is volume $V_{\delta i}$.

Division of vertical segment 16 reflects the division of space V which appears after generation of the j-th volume for the i-th object n_i:

- segment $\langle 1, 3)$corresponds to volume $V_{\beta ji}$,
- segment $\langle 2, 3\rangle$ corresponds to volume $V_{\gamma ji}$,
- segment $(2, 4\rangle$ corresponds to volume $V_{\alpha tji}$,
- segment $(4, 5\rangle$ corresponds to volume $V_{\alpha cji}$,
- segment $(5, 6\rangle$ corresponds to volume $V_{\delta i}$.

In Figure 4, as for the i-th object, it is possible to determine components of space volume V for the objects of the highest and smallest transformation volume marked $(V_{\gamma b})_{min}$ and $(V_{\gamma s})_{min}$ respectively.

Between segments AC and BD it is possible to lead infinite number of vertical lines. Their division into sections, presented above, describes the field of possibilities of generation, in space V, the transformation volume $V_{\gamma ji}$ and connected with them volumes $V_{\beta ji}$. For segment AC transformation volumes are generated according to Figure 3. The divisions are on the right side of Figure 4 together with the segment BD is the general case shown in Figure 2.

At any moment of the transformation process in volume V a finite number transformation volume is generated.

Phenomenological model of random transformation of dispersed matter is constructed as follows:

1. The possibilities of generating transformation volumes in space V are shown on the system map appropriate for the given transformation process which is analogous to that presented in Figure 4. In space V transformation volumes according to many system maps can be generated simultaneously.

http://dx.doi.org/10.5772/52369

2. Phenomenological model consists of p layers formed by p transformation volumes generated at a given moment in volume V according to system maps.

3. The model is constructed in such a way that the sum of sets of all volumes is equal to V. The sum of all volumes safe for the i-th objects located above the generated in a given moment its transformation volume is equal to $V_{\alpha i}$, according to the equation (33).

4. Material objects belonging to set N, in space $V(t)$, were reduced to a point. One of their features is volume V_{ni}. On system maps (Fig. 4) and in the phenomenological model the size of volume is defined by vertical segments, so the i-th object will be a vertical segment of the length corresponding to volume $(V_{\gamma ji})_{min}$. This object can be displaced in space $V_{\alpha i}$ and $V_{\delta i}$ till the transformation moment in volume $V_{\gamma ji}$.

4. General mathematical model

In general, the concentration of elements of set N in volume $V(t)$ is determined by the number of not transformed objects n per volume V according to the formula

$$S(t) = \frac{n(t)}{V(t)}. \tag{50}$$

At the initial moment $t_0 = 0$ it will amount

$$S_0 = \frac{n_0}{V_0}. \tag{51}$$

We assume that for the process duration moment $t_0 = 0$ in space V volumes $V_{\gamma ji}$, $V_{\beta ji}$, $V_{\alpha i}$ and $V_{\delta i}$ are generated. Not transformed i-th object can occur only in the appropriate volumes $V_{\alpha i}$ and $V_{\delta i}$. From formulas (1) and (7) results the relationship between the volumes for the individual objects from set N (Fig. 4) given in the formula

$$V_{\alpha b} \subset \ldots \subset V_{\alpha i} \subset \ldots \subset V_{\alpha s}. \tag{52}$$

For relationship (52) equivalence

$$\left(V_{\gamma s}\right)_{\min} = \left(V_{\gamma b}\right)_{\min} \Leftrightarrow V_{\alpha s} = V_{\alpha b} \tag{53}$$

or

$$\left(V_{\gamma s}\right)_{\min} \langle \left(V_{\gamma b}\right)_{\min} \Leftrightarrow V_{\alpha b} \langle V_{\alpha s} \tag{54}$$

can be true. In the case included in formula (53) in the whole volume V_α defined by formula

$$V_\alpha = \bigcup_{i=1}^{n} \bigcap_{j=1}^{p} V_{\alpha ji} \tag{55}$$

occurs uniform dispersion of the elements of homogeneous set N. However, from the given in formula (54) alternative equivalence result the uneven dispersion of inhomogeneous objects from set N in volume V_α. Each object n_i characterized by feature vr_i which distinguishes it from other objects from set N results in introduction of the additional area $F_{\gamma\beta i}$ (Fig. 2 and 3). Each additional area $F_{\gamma\beta i}$ introduced in space V divides volume set V_α (Fig. 4). The resulting parts can differ with the concentration of the objects contained in them. The process of ideal mixing ensures homogeneity of the dispersion only within a volume limited by neighboring areas e.g. $F_{\gamma\beta(i-1)}$ and $F_{\gamma\beta i}$, $F_{\gamma\beta i}$ and $F_{\gamma\beta(i+1)}$. In the case covered by formula (54) due to the relationships given in formulas (5) and (11) as well as uniform dispersion of volume V_γ in space $V_{\alpha t}$ we can use average concentration of dispersed material objects. Thus, after starting the process, to the generated volumes $V_{\gamma ji}$ there will be introduced randomly appropriate objects n_i of set N dispersed in volume V_α. Elements from set N being in volumes $V_{\delta i}$ do not participate directly in the transformation process. In moment $t_0 = 0$ of process duration the number of unconverted objects $n(t)$ in volume V_α is defined by the equation

$$n_{\alpha 0} = n_0 - n_{\delta 0} \tag{56}$$

Average concentration of untransformed objects in volumes occupied by them volume V_α is described by formula

$$\left(\overline{S_\alpha}\right)_{t_0=0} = \frac{n_{0\alpha}}{V_\alpha} \tag{57}$$

where $n_{\delta 0}$ denotes initial number of elements from set N in volumes $V_{\delta i}$. Number of objects which were transformed n_{d0} for time t_0 is defined by the formula

$$n_{d0} = 0 \tag{58}$$

The degree of objects transformation $X(t)$ determined by the quotient of the number of transformed objects n_d to the initial number of unconverted objects n_0 for $t = 0$ equals 0, according to the formula

http://dx.doi.org/10.5772/52369

$$X = \frac{n_{d0}}{n_0} = 0. \tag{59}$$

At any moment of process duration t the number of transformed objects amounts $n_d(t)$. Converted objects may be located in any place of volume V. The number of unconverted objects, being exclusively in volume V_α, is defined by the difference of the initial number of objects $n_{\alpha 0}$ and converted objects n_d after time t of process duration corrected by a number of objects transferred between volumes $V_{\alpha i}$ and $V_{\delta i}$ and the number of objects described by the formula (6), which is described by equality

$$n_\alpha = n_{0\alpha} - n_d + n_{\delta\alpha} - n_{\alpha\delta} + \Delta n_A, \tag{60}$$

where:$n_{\delta\alpha}$ – means number elements of set N transferred from volume $V_{\delta i}$ to $V_{\alpha i}$,

$n_{\alpha\delta}$ – means number of elements of set N transferred from volume $V_{\alpha i}$ do $V_{\delta i}$.

After time t of process duration, to transformation volumes $V_{\gamma ji}$ there are introduced untransformed objects of average concentration $\left(\overline{S_\alpha}\right)_t$ defined by the number of unconverted n_α, per volume V_α. This is shown in formula

$$\left(\overline{S_\alpha}\right)_t = \frac{n_\alpha}{V_\alpha}. \tag{61}$$

Of course general concentration of unconverted objects in volume V will be defined by the relationship

$$S = \frac{n}{V}, \tag{62}$$

where

$$n = n_\alpha + n_\delta. \tag{63}$$

It will be shown, for example, after stopping the process. The degree of transformation of objects after time t of the transformation process is described by the formula

$$X = \frac{n_d}{n_0 + \Delta n_A}. \tag{64}$$

The increase of transformed objects dn_d in all transformation volumes $V_{\gamma ji}$ after the lapse of any small time interval dt is defined by the formula

$$dn_d = \left(\overline{S_\alpha}\right)_t dV. \tag{65}$$

The external area limiting the generated for the i-th object the j-th volume $V_{\gamma ji}$, consists of active and inactive part. Through the active part there can be introduced or removed the i-th element of set N while the inactive part is not available for such transfer. The active part of the surface is divided into surface $F_{\gamma\alpha\rightarrow}$, through which the i-th object can be introduced to $V_{\gamma ji}$ and surface $F_{\gamma\alpha\leftarrow}$, through which the transformed or not transformed i-th object can be introduced from $V_{\gamma ji}$ according to the formula

$$F_{\gamma\alpha ji} = F_{\gamma\alpha ji\rightarrow} + F_{\gamma\alpha ji\leftarrow}. \tag{66}$$

The sum of surfaces limiting the transformation volumes $V_{\gamma ji}$ generated in space V for the i-th object is described by the formula

$$F_{\gamma\alpha i} = \sum_{j=1}^{p} F_{\gamma\alpha ji}. \tag{67}$$

The sum of surfaces limiting the volumes $V_{\gamma ji}$ generated in space V for all objects form set N is described by the formula

$$F_{\gamma\alpha} = \sum_{i=1}^{n}\sum_{j=1}^{p} F_{\gamma\alpha ji}. \tag{68}$$

Volume dV displaced from space $V_{\alpha ji}$ to volume $V_{\gamma ji}$ in time increase dt depends on the size of limit area $F_{\gamma\alpha\rightarrow}$, through which dV is displaced from volume $V_{\alpha ji}$ to volume $V_{\gamma ji}$ and on the average speed of its displacement u, according to the formula

$$dV = uF_{\gamma\alpha\rightarrow}dt. \tag{69}$$

After substituting equations (61) and (69) to equation (65) we get the equation

$$dn_d = k\left(n_\alpha\right)dt \tag{70}$$

http://dx.doi.org/10.5772/52369

describing the increase of objects transformed in generated volumes $V_{\gamma j}$. Process rate constant k is described by the relationship

$$k = \frac{F_{\gamma\alpha\rightarrow}}{V_\alpha} u. \tag{71}$$

According to formulas (16), (19) and (20) parameters $F_{\gamma\alpha\rightarrow}$ and V_α depend on time t. Dislocation rate u can also be a function of process duration

$$u = f_9(t). \tag{72}$$

On the basis of formula (70) the loss of unconverted objects in set N can be expressed by the equation

$$dn = -k\left(n_\alpha\right)dt. \tag{73}$$

After substituting (60) to the relationship (73) we get

$$dn = -k\left(n_{0\alpha} - n_d + n_{\delta\alpha} - n_{\alpha\delta} + \Delta n_A\right)dt. \tag{74}$$

The total balance of the loss of objects dn_d in time interval dt will be equal on the right side of the formula (74) with the opposite sign

$$dn_d = k\left(n_0 - n_d + n_{\delta\alpha} + n_{\alpha\delta} + \Delta n_A\right)dt. \tag{75}$$

In case

$$\Delta n_A = 0 \tag{76}$$

the relationship (76) will be simplified to

$$dn_d = k\left(n_0 - n_d\right)dt. \tag{77}$$

After separation of variables in equation (77) and integration of both sides we get the relationship

$$\ln\left(\frac{n_0}{n_0 - n_d}\right) = kt, \tag{78}$$

often used to describe the kinetics of the course of transformation of various material objects. In case of homogeneity of set N (Vr is an empty subset) relationship (78) is a final description of the transformation process. Let's consider the case when the object of set N differ with only one feature vr_1, which has a considerable effect on the course of the process. In order to analyse it, the whole range of changes should be divided into m such intervals in which changes in features have no significant effect on the course of the process. Then the course of transforming objects from any interval ζ - th such that

$$\zeta \in \langle 1, m \rangle, \tag{79}$$

describes the relationship

$$\frac{n_{0\zeta}}{n_0} dn_{d\zeta} = \frac{n_{0\zeta}}{n_0} k_\zeta \left(n_{0\zeta} - n_{d\zeta}\right) dt \tag{80}$$

taking into account the existence of a whole set N.

Description of the transformation of the entire set of objects including the division of set N into intervals is described by the relationship

$$\sum_{\zeta=1}^{m} \frac{n_{0\zeta}}{n_0} dn_{d\zeta} = \sum_{\zeta=1}^{m} \frac{n_{0\zeta}}{n_0} k_\zeta \left(n_{0\zeta} - n_{d\zeta}\right) dt. \tag{81}$$

After the separation of variables (80) and integration of both sides we get

$$\sum_{\zeta=1}^{m} \frac{n_{0\zeta}}{n_0} \ln \frac{n_{0\zeta}}{n_{0\zeta} - n_{d\zeta}} = \sum_{\zeta=1}^{m} \frac{n_{0\zeta}}{n_0} k_\zeta t. \tag{82}$$

Relationship between speed constants in equations (77) and (80) is defined by a formula

$$\Phi \sum_{\zeta=1}^{m} \frac{n_{0\zeta}}{n_0} k_\zeta = k. \tag{83}$$

Coefficient Φ describes the relationship

http://dx.doi.org/10.5772/52369

$$\Phi = \ln \frac{n_0}{n_0 - n_d} \left(\sum_{\zeta=1}^{m} \frac{n_{0\zeta}}{n_0} \ln \frac{n_{0\zeta}}{n_{0\zeta} - n_{d\zeta}} \right)^{-1}. \tag{84}$$

5. Examples of application

The technological process based on the theory of random transformation of dispersed matter is the disintegration of microbial cells. At present many compounds coming from the inside of the microorganism cells have commercial application. They are used among others in the food, pharmaceutical, cosmetic, chemical industry as well as medicine and agriculture. In order to isolate the desired compounds it is usually necessary to destroy the cell walls and cytoplasmic membranes. The process of disintegration of microorganisms is carried out by different methods: physical, chemical and biological.

The technical means used to implement the process on an industrial scale are bead mills and high pressure homogenizers. On a laboratory scale there are often used vibrating mixers, ultrasonic homogenizers and enzymatic methods. All the listed methods of the process involve the random effects of the factor which destroys the cell walls of microorganisms dispersed in the liquid. The difference between them depends mainly on the method of generating the transformation volume of dispersed matter.

During the disintegration of microorganisms the suspension occupies volume V. It is constant in time. The process is carried out usually for the optimal initial concentration of biomass. The initial number of microorganisms is determined n_0. We consider the case of batch operation (constant charge). During the process microorganism cells are not added from the outside (we assume the sterility of conditions of disintegration) nor are they removed outside. The process duration compared to the lifetime of microorganisms and the time needed to form new cells is very short. So it can be assumed that the change in the number of objects described by the formula (6) satisfies the relationship (76).

In the case of disintegration of microorganisms in of bead mills the transformation consists in the disruption of microbial cell walls. Destruction volumes $V_{\gamma ji}$ are generated by circulating filling beads. To carry out the process in the bead mill, high degree of filling the working chamber with beads and high rotational speed of the agitator are applied. It can be assumed that at any time during the process for fixed working conditions number p (Eq. (35)) is constant in time and its value is high. Thus the relations given in the formulas

$$\sum_{j=1}^{p} V_{\gamma ji} = const, \tag{85}$$

$$\sum_{j=1}^{p} V_{\beta ji} = const \tag{86}$$

are fulfilled.

General diagram of cell disruption between the spherical surfaces is shown in Figure 5. It concerns the range of the distribution of suspension volume V to $V_{\alpha ji}$, $V_{\gamma ji}$ and $V_{\beta ji}$ shown on the right in Figure 4 in the area adjacent to the segment BD. Volumes $V_{\alpha c}$ occur close to the inside surface of the mill chamber in the case when filler elements have a diameter substantially greater than the dimensions of the cells of microorganisms. In a bead mill volumes $V_{\alpha c}$ occur at all surfaces of the working chamber and agitator. They are distant by a distance similar to the size of the largest cells and the thickness of their layer is slightly smaller than the radius of the smallest filling beads. In these volumes cells are never disrupted.

For a properly constructed mill chamber volumes V_δ (may be slots at the interface between two structural elements) are negligibly small and insignificant in terms of technology, especially when conducting sterilization of equipment between the processes. In the analyzed case it was assumed that disintegrated microorganisms have an ellipsoidal shape. After the limit deformation of the *i*-th cell, its walls are disrupted. (Fig. 5). The generated transformation volume $V_{\gamma ji}$ is limited by surfaces: active $F_{\gamma\alpha ji}$ (orange dashed line), $F_{\gamma\beta ji}$ (red dashed line) and two inactive spherical of filling elements. Limiting surfaces $F_{\gamma\alpha ji}$ and $F_{\gamma\beta ji}$ belong to volume $V_{\gamma ji}$. Its axis of symmetry is axis OO. To the presented in Figure 5 volume $V_{\alpha i}$, in which *i*-th living cell can be present, does not belong the volume limited by two spherical surfaces and surface $F_{\gamma\beta ji}$. Straight line OO is a symmetry axis of this volume. Surfaces limiting volume $V_{\alpha ji}$ do not belong to it. The volume unavailable for the living *i*-th cell $V_{\beta ji}$ is limited by two spherical surfaces and surface $F_{\gamma\alpha ji}$. Limiting surfaces do not belong to $V_{\beta ji}$. The axis of symmetry of volume $V_{\beta ji}$ is also straight line OO. In the special case the line dividing volume V in an AC position (Fig. 4), there is generated volume $(V_{\gamma ji})_{min}$ shown in Figure 6. It is limited by two spherical surfaces and active surface $F_{\gamma\alpha ji}$ (orange dashed line). Volume symmetry axis $(V_{\gamma ji})_{min}$ passes through points O and O. Surface $F_{\gamma\alpha ji}$ does not belong to generated volume $V_{\beta ji.}$ If all points of the *i*-th object are not introduced to $(V_{\gamma ji})_{min}$ it will not be transformed.

For monogenic set N (Vr is an empty subset) cell disintegration process, taking into account the above assumptions, is described by differential equation (77). The case when the objects of set N differ with only one feature vr_1 that has a significant impact on the course of cell disruption is included in equation (80) and (81). The process of release of intracellular compounds, using the theory of transformation of dispersed matter, has been widely described by Heim at all [12], Heim and Solecki [13] as well as Solecki [10 and 14]. These works included more complex cases of the course of the process, causes of nonlinearity of kinetics were given, and the effect of concentration of microorganism suspension was explained as well as disappearance of the largest size fraction during the process for very low concentrations of the suspension.

There are many devices implementing the process of disintegration of microorganisms due to critical stresses in the cell walls caused by stress in the liquid. Best known are: high pressure homogenizers [6, 15-18], French press [19], Ribie press [20], Chaikoff press [21]. The technical method of process realization in the above mentioned equipment is similar and consists in disruption of microorganisms during pumping suspension through a valve under high pressure. High performance in continuous operation and fairly wide range of diversity of disintegrated microorganisms made that high pressure homogenizers are widely used on a

http://dx.doi.org/10.5772/52369

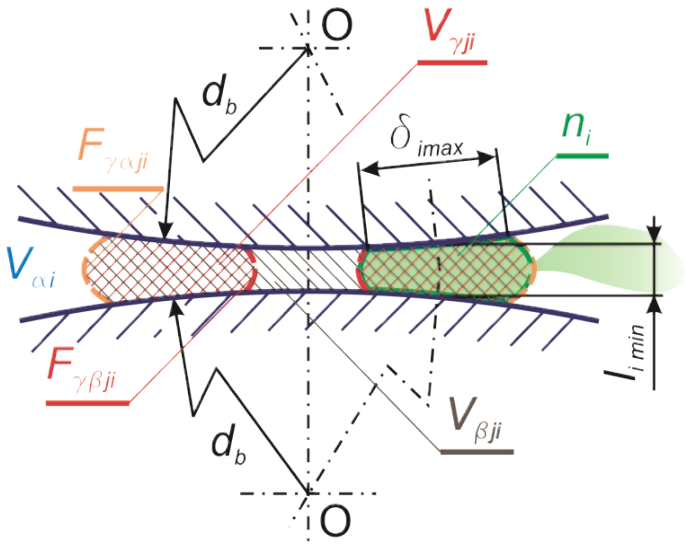

Figure 5. Model of cell disruption during non-axial hitting with spherical elements – general case [10].

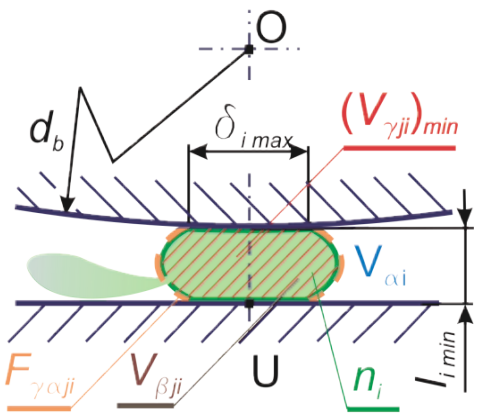

Figure 6. Model of cell disruption during axial hitting with spherical element and plane – special case [14].

technical scale. The general model of disintegration of mechanisms, developed by Hetherington et al. [6], and then modified by Sauer et al. [15] is included in a formula

$$\ln\left(\frac{R_m}{R_m - R}\right) = k N^{b_2} P^{b_1}, \tag{87}$$

where: R concentration of released proteins [mg/g],

R_m - maximum concentration of released proteins; [mg/g],

k - process rate constant; [1/s],

N - number of suspension passage cycles through homogenizer; [-],

P - suspension pumping pressure, [MPa].

b_1 - exponent depending on the type of microorganisms and their growth conditions; [-],

b_2 - exponent including the effect of suspension concentration on the course of the process; [-].

Pumping pressure of the suspension of microorganisms is within the range from 50 to 120 MPa. Transformation volumes $V_{\gamma ji}$ are generated, according to the results of research conducted by Keshavarz Moore at al. [16] and Engler [17] on the cell disruption mechanism, in homogenization zone within the valve unit and with the impingement in the exit zone. The results of research conducted by Lander at al. [18] showed that disruption of cells is mainly due to shearing of the liquid in the valve unit and as a result of cavitation occurring in the impingement section, where the stream of suspension hits the impact ring and follows an implosion of bubbles caused by the increased pressure.

High-frequency ultrasounds (in the supersonic wavelength range 15 - 25 kHz) are used for disruption of dispersed in a liquid microbial cells and releasing contained in them intracellular compounds [22-25]. The mechanism of microorganisms disintegration is associated with the occurrence of cavitation induced by ultrasound and hypothetically runs as follows:

1. Passing sound wave causes the thickening and thinning of the liquid.
2. During the thinning of the liquid occurs nucleation and growth of gas and vapor bubbles.
3. During the thickening of the liquid bubble implosion occurs at a rate not less than the speed of sound (hence the loud roar accompanying cavitation).
4. Bubbles which are not adhering to the cells of microorganisms are sinking evenly in all directions. Bubbles adhering to cells are sinking from the free side so that the surface of the liquid with a powerful force strikes the cell wall breaking it and releasing intracellular compounds. The striking force may be so powerful that the released compounds are often destroyed and free radicals are formed.

Daulah [22], using the theory of local isotropic turbulence Kolmogorov [26 and 27], presented a description of the process of ultrasonic disintegration of cells of baker's yeast as a model

$$1 - S_p = \exp(k \cdot t), \tag{88}$$

where: S_p – concentration of released proteins, [g/kg]

t – duration of the process; [min],

k – process rate constant; [1/min].

Dependence of constant k on energy dissipation P_d is described by the relationship

http://dx.doi.org/10.5772/52369

$$k = \zeta \cdot \left(P_d - P_c \right)^{0,9} \tag{89}$$

where: ζ - constant; [kg/J],

P_c - threshold energy dissipation ensuring occurrence of cavitation; [J/kgs].

Confirming the above results experimentally for brewing yeast showed no effect of suspension concentration on constant k and its proportionality to the energy dissipation level [25].

The process of disinfection consists in an impact of physical or chemical agents in a limited gas, liquid or solid medium on biological contaminants. They may be it viruses, bacteria and their spores, protozoa and their cysts and eggs of parasites. The purpose of disinfection is to destroy the above mentioned objects and to prevent in a required, limited period of time their re-growth. The disinfectants selected according to pathogens cause: an irreversible destruction of cells, disruption of metabolic processes, disruption of biosynthesis and growth. An example of such process is chemical disinfection of water [28]. Its kinetics is often described by Chick's model [3] in form of equation (77). The dependence of the rate constant

$$k = AC^s t \tag{90}$$

taking into account the disinfecting power coefficient A and the concentration of disinfectant C was given by Watson [4]. Exponent s is dependent on the type of disinfectant and medium's pH.

The developed theory can be used to model the impact of population of predator-prey or competition type. If we assume that:

- change objects from the set of N (f_{31} from Eq. (6)) in equation (75) is described under the law of Malthus by the formula

$$f_{31} = a_1 N \tag{91}$$

- rate constant from equation (75) will be marked as k_γ and is written in the form

$$k_\gamma = a_2 P, \tag{92}$$

directly dependent on the generated families of transformation volume (see formula (71)),

- unconverted objects N cause an increase in the families of transformation volume of families in the form of $a_3 NP$,

in the absence of objects N (N is an empty set), there is an exponential decrease in the number of families of transformation volume – $a_4 P$,

the received equations in the form

$$dN = N\left(a_1 - a_2 P\right)dt \tag{93}$$

and

$$dP = P\left(a_3 N - a_4\right)dt \tag{94}$$

are a model for predator-prey for the Lotka-Volterra system [1 and 2]. The coefficients a_1, a_2, a_3 and a_4 are constants with positive values.

On the basis of the presented theory it is possible to build other more realistic models of predator-prey system taking into account e.g. natural selection, nutrient profile, the effect of age on the activity of predators and many other factors. It is also possible to model chemical reactions, and assuming the generation in space V of different types of transformation volume, including reversible transformation, enzymatic reactions can be modeled [5].

The theory can be used to study and model the action of immune system [10]. It can also be employed in constructing artificial immunology and controlling the support of various therapies. Simple applications cover responses of the immune system to viral, bacterial, fungal and parasitic infections. The immune response depends on the type, properties, portal of entry and severity of infection and the state of organism. Application of the theory is illustrated by viral infection. Virus replication in the host cells in space V is represented by the function in Eq. (6). The aim of an immune response is to inhibit virus replication in the cell and its spread to other cells. Next goals include the elimination of transformed objects from the organism and development of long-lasting immunity. Initially, transformation volumes $V_{\gamma ji}$ are formed as a result of action of the complement system, interferon (IFN) and natural killer cells (NK) within non-specific anti-viral response. At the next stage, neutralizing antibodies, mainly of class IgG (immunoglobulin G), prevent infection of other cells. Their fragment Fab (fragment antygen binding) binds to antigens of the virus, while fragment Fc (fragment crystallizable) to relevant receptors on NK cells, macrophages and others. This enables phagocytosis and cellular cytotoxicity dependent on antibodies, but probably also immediate destruction with the use of the complement system. In the case of infections through mucous membranes of the intestinal tract and respiratory system the same role is played by IgA (immunoglobulin A) antibodies. In development of humoral immune response the active role is played by $CD4^+$ lymphocytes. In this case antigen proteolysis occurs in endosome. Cytotoxic $CD8^+$ lymphocytes play the crucial role in the response to viral infections. They function inside the cells. They recognize a viral antigen on cells transformed by the infection in association with MHC (major histocompatibility complex) class I molecules. In the infected cells, cytotoxic lymphocytes can induce a synthesis of nucleases destroying genetic material of the virus and enhance IFN synthesis. Responses of the immune system occurring at subsequent stages of antigen

http://dx.doi.org/10.5772/52369

destruction according to different mechanisms can be described by the relation analogous to Eq. (81).

Many pathogens developed such properties which allow them to avoid non-specific and specific immune response. High variability of a pathogen caused by differences in the gene sequence region leads to a delay of specific immune response. This is so in the case of influenza, hepatitis C and HIV (human immunodeficiency virus) viruses. Ho et al. [9] studied the effects of HIV treatment with inhibitors. A linear model based on experimental data in the form concordant with Eq. (77) well described the healing process at the first stage of the therapy. At the final stage, however, control over the virus population was lost due to multiplication of drug-resistant strains. A result of genetic modifications is the formation of virus mutations in transformation conditions γ_{lb} resulting from their properties which belong to set *Pr*. In volumes $V_{\gamma ji(\gamma<\gamma_{lb})}$ formed by the drug, the concentration of transformation conditions γ is smaller than that required for the transformation of so mutated viruses. Similar effects are observed in presently used, much more efficient highly active antiretroviral therapy (HAART). It includes the interactions of protease inhibitors combined with reverse transcriptase inhibitors. A mathematical model of the combined therapy was developed by Perelson et al. [29]. The same relations can be generated from Eq. (81). Objects from set *N* according to their properties may be vulnerable to any of the means used in combination therapy (usually five) or to none. In the case of AIDS (acquired immunodeficiency syndrome), HAART does not result in patient's recovery despite a decrease of virus concentration below the detectability threshold. One of the reasons can be hiding of the virus in the milieu of limited immune response, such as brain and testes. They are unreachable for therapy just like memory lymphocytes and dendritic cells which are also a target of HIV attack. In the phenomenological model (Fig. 3), regions inaccessible for transformations are volumes V_δ (brain, testes) and $V_{\alpha c}$ (dendritic cells, memory lymphocytes). Objects can remain in them until producing mutation which is resistant to the applied drug combination, capable of regaining the whole space V.

Now, to model an artificial immune system, the shape space concept proposed by Perelson and Ostera [30] is often used. Antigen and antibody were determined as a point in the L-dimensional space of complementary traits. The notion of threshold ε determines the level of imperfectness of fitting of the antigen-antibody activation.

The idea of the transformation process preceded by a process of forming objects from a set *N* (Section 2.2) can be used to model the epidemic taking into account such factors as vaccinations or immunization. The solution achieve for the simple SIR model (division of the individuals: susceptible, infecting and convalescents with acquired resistance) is consistent with a simple epidemic model developed by Kermack and McKendrick [31].

6. Summary

The presented theory relates to the physical, chemical and biological processes of random transformation of dispersed matter. It has the interdisciplinary significance allowing the phenomenological and mathematical modeling of mass transfer processes in many areas.

These include among others: industrial technology, ecology and environment protection, medicine, veterinary medicine, immunology, oncology, epidemiology, hygiene and agriculture. Specific descriptions of the processes create the possibility of linking phenomena, mechanisms and factors determining the process. Obtaining a correct modeling effect must be preceded by knowledge and deep understanding of the nature of the problem. However, full success depends on the proper, conducted on the basis of areas considered process, final interpretation of the results. The presented general concept of transformation of matter can be used both to study and describe the processes as well as for their management and control. It systematizes a range of knowledge concerning the transformation of dispersed matter whose nature has not previously been combined into unity. Together with the given methodology of building phenomenological and mathematical models it makes a platform on which it seems possible to achieve significant scientific development among others through analogies, critical comparisons and transfer of knowledge.

Acknowledgements

The study was carried out within the frames of the grant W-10/1/2012/Dz. St.

Author details

Marek Solecki*

Address all correspondence to: solecki@wipos.p.lodz.pl, msolecki@toya.net.pl

Department of Process Equipment, Faculty of Process and Environmental Engineering, Lodz University of Technology, Poland

References

[1] Volterra V. Variazioni e fluttuazioni del numero d'individui in specie animal conviventi. Mem Acad Lincei Roma (1926) 2, 31-113; Volterra V. Variation and fluctuations of the number of individuals in animal species living together, in R.N. Chapman (Ed.), Animal Ecology, McGraw-Hill, New York (1931) 409-448.

[2] Lotka A.J. Undamped oscillations derived from the law of mass action. Journal of the American Chemical Society (1920) 42, 1595-1599.

[3] Chick H. An investigation of the laws of disinfection. Journal of Hygiene (1908) 8, 92-158.

[4] Watson H.E. A note on the variation of rate of disinfection with the change in the concentration of disinfectant. Journal of Hygiene (1908) 8, 536-542.

[5] Michaelis L., Menten M.I. Die Kinetik der Invertinwirkung. Biochemische Zeitschrift (1913) 49, 333-369.

[6] Hetherington P.J., Follows M., Dunnill P., Lilly M.D. Release of protein from baker's yeast (Saccharomyces cerevisiae) by disruption in an industrial homogeniser. Transactions of the Institution of Chemical Engineers (1971) 49, 142-148.

[7] Follows M., Hetherington P.J., Dunnill P., Lilly M.D. Release of enzymes from bakers' yeast by disruption in an industrial homogenizer. Biotechnology and Bioengineering (1971) 13, 549-560.

[8] Melendres A.V., Honda H., Shiragami N., Unno H. Enzyme release kinetics in a cell disruption chamber of a bead mill. Journal of Chemical Engineering of Japan (1993) 26(2), 148-152.

[9] Ho D.D., Neumann A.U., Perelson A.S., Chen W., Leonard J.M., Markowitz M., Rapid turnover of plasma virions and CD4 lymphocytes in HIV-1 infection. Nature (1995) 373, 123-126.

[10] Solecki, M. Mechaniczna dezintegracja komórek mikroorganizmów. Zeszyty naukowe Politechniki Łódzkiej (2012) 1114(421), 1-95.

[11] histi, Y, & Moo-Young, M. Disruption of microbial cells for intracellular products. Enzyme and Microbial Technology (1986) 8, 194-204.

[12] Heim A., Kamionowska U., Solecki M., The effect of microorganism concentration on yeast cell disruption in a bead mill. Journal of Food Engineering (2007) 83, 121-128.

[13] Heim A., Solecki M., Disintegration of microorganisms in a circulating bed of balls. Proceedings of the 3rd World Congress on Particle Technology, CD-ROM, ISBN 0-85295-401-8Brighton UK, 6-9 July (1998) 1-10.

[14] Solecki M. The release of compounds from microbial cells, in Nakajima H. (Ed.), Mass Transfer - Advanced Aspects, ISBN 978-953-307-636-2, InTech, Rijeka, 26 (2011) 595-618. Available from: http://www.intechopen.com/articles/show/title/the-release-of-compounds- from-microbial-cells, 26(2011) 595-618.

[15] Sauer T., Robinson C. W. and Glick B. R. Disruption of native and recombinant *Escherichia coli* in a high-pressure homogenizer. Biotechnology and Bioengineering (1989) 33, 1330-1342.

[16] Keshavarz Moore, E, Hoare, M, & Dunnill, P. Disruption of baker's yeast in a high-pressure homogenizer: new evidence on mechanism. Enzyme and Microbial Technology (1990) 12, 764-770.

[17] Engler, C. R. Cell disruption by homogenizer. In: Separation Processes in Biotechnology (Asenjo J.A., Ed.), Marcel Dekker, New York (1990) 95-105.

[18] Lander R., Manger W., Scouloudis M., Ku A., Davis C., Lee A. Gaulin homogenization; a mechanistic study. Biotechnology Progress (2000) 16, 80-85.

[19] Milner H.W., Lavrence N. S. and French G. S. Colloidal dispersion of chloroplast material. Science (1950) 111, 633-634.

[20] Wimpenny W.T. Breakage of micro-organizm, Process Biochemistry (1967) July 2(7), 41-44.

[21] Emanuel C.F. and Chaikoff J.L. An hydraulic homogenizer for the controlled release of cellular components from various tissues. Biochimica biophysica Acta (1957) May, 24, 254-261.

[22] Daulah M.S. Mechanism o disintegration of biological cells in ultrasonic cavitation. Biotechnology and Bioengineering (1977) 19, 649-660.

[23] James C.J., Coakley W.T., Hughes D.E., Kinetics of protein release from yeast sonicated in batch and flow systems at. 20 kHz. Biotechnology and Bioengineering (1972) 14, 33-42.

[24] Esche R., Untersuchung der Schwingungskavitation in Flüssigkeiten. Acoustica(Akustische Beihefte), (1952) 2, 208-219.

[25] Wang D.I.C., Cooney C.L., Demain A.L., Dunnill P., Humphrey A.E., Lilly M.D., Fermentation and Enzyme Technology, in Wiley J. (Ed.), New York, (1979).

[26] олмогоров, А. Н. *Локальная структура турбулентности в несжимаемой вязкой жидкости при очень больших числах Рейнольдса. Доклады АН СССР* (1941) 30 299-303.

[27] Колмогоров, А. Н. Рассеяние энергии при локально изотропной турбулентности. *Доклады АН СССР* (1941) 32, 19-21.

[28] Hunt N.K., Mariañas B.J. Inactivation of Escherichia coli with ozone: chemical and inactivation kinetics. Water Research (1999) 33(11), 2633-2641.

[29] Perelson A.S., Neumann A.U., Markowicz M., Leonard J.M., Ho D.D. HIV-1 dynamics in vivo: Virionclearance rate, infected life-span, and viral generation time. Science (1996) 271, 1582-1586.

[30] Perelson A.S., Ostera G.F. Theoretical studies of clonal selection: Minimal antibody repertoire size and reliability of self-non-self discrimination. Journal of Theoretical Biology (1979) 81, 645-670.

[31] Kermack W.O., McKendrick A.G. Contributions to the mathematical theory of epidemics. Proceedings of the Royal Society Lond. A (1927) 115, 700-721.

Chapter 2

Minimum Dissipation Conditions of the Mass Transfer and Optimal Separation Sequence Selection for Multicomponent Mixtures I

A.M. Tsirlin and I.N. Grigorevsky

Additional information is available at the end of the chapter

http://dx.doi.org/10.5772/54546

1. Introduction

1.1. The mass transfer process with minimum irreversibility

In many processes, heat and mass transfer are distributed in time or space. The problem of thermodynamically perfect organization lies in the choice of such concentration and temperature change, in space or time, laws to minimize the entropy production σ. Below we consider stationary processes and a spatial distribution, for definiteness.

1.1.1. Optimal organization of an irreversible mass transfer process

Consider the irreversible process of mass transfer, in which from one flow to another one substance is transmitted. The problem of minimal irreversibility of this process at a given average intensity of mass transfer takes the form:

$$\sigma = \int_0^L \frac{g(c_1, c_2)}{T}(\mu_1(c_1) - \mu_2(c_2))dl \to \min \tag{1}$$

under conditions

$$\int_0^L g(c_1, c_2)dl = \overline{g}; \tag{2}$$

$$\frac{d(G_1 c_1)}{dl} = \frac{dN_1}{dl} = -g(c_1, c_2); \quad N_1(0) - N_1^0. \tag{3}$$

The minimum is searched by selecting the concentration $c_2(l)$. change law. (In the equation (1) $\mu_i(c_i)$ denotes the chemical potential of the i-th flow dependence on the concentration of the redistributed substance in it). Here G_1 and c_1 is an amount and molarity of the redistributed substance respectively, N_1-number of moles of that component.

Minimal irreversibility conditions of mass transfer arise from the solution of (1) — (3). They can be described as follows [24]: *In the mass transfer process with minimum irreversibility the ratio of flow g and chemical potential μ_2 derivatives with respect to the concentration c_2 is proportional to the ratio of relative flow g square to the temperature, in any cross-section of l.*

$$\frac{\partial g / \partial c_2}{\partial \mu_2 / \partial c_2} = \xi \frac{g^2}{T} \tag{4}$$

Indeed, the entropy production after transition from dt to dN is:

$$\sigma = \int_{N_1^0}^{N_1^L} -\frac{1}{T}(\mu_1(c_1) - \mu_2(c_2))dN_1 \to \min \tag{5}$$

under the condition

$$\int_{N_1^0}^{N_1^L} -\frac{1}{g(c_1, c_2)} dN_1 = L. \tag{6}$$

The Lagrange function of problem (5), (6) takes the form

$$R = \frac{1}{T}(\mu_1(c_1) - \mu_2(c_2)) + \lambda \frac{1}{g(c_1, c_2)}, \tag{7}$$

stationarity conditions with respect to c_2:

$$\frac{\partial R}{\partial c_2} = 0 \to \frac{1}{T}\frac{\partial \mu_2}{\partial c_2} + \lambda \frac{1}{g^2(c_1, c_2)}\frac{\partial g}{\partial c_2} = 0 \tag{8}$$

http://dx.doi.org/10.5772/54546

lead to the equation (4). The proportionality coefficient ξ in (4) is defined from the initial data of the current problem.

For a specific task $g(c_1, c_2)$ condition (4) allows us to find a relation between the c_1 and c_2 for the optimal mass transfer organization. For example, if

$$g = k\left(\frac{\mu_1(c_1)}{T} - \frac{\mu_2(c_2)}{T}\right), \tag{9}$$

we'll get the following equation from (4) :

$$\mu_1(c_1) - \mu_2(c_2) = const. \tag{10}$$

At the constant temperature and pressure, this condition leads to the equation

$$c_1(l)/c_2(l) = const \tag{11}$$

and the constancy of flow $g(c_1, c_2)$ for any l.

For the mass transfer law of the form

$$g = k(c_1(l) - c_2(l)) \tag{12}$$

Derivatives are

$$\partial g / \partial c_2 = -K; \quad \frac{\partial \mu_2}{\partial c_2} = \frac{RT}{c_2}. \tag{13}$$

After their substitution into (4), we obtain

$$(c_1(l) - c_2(l))^2 / c_2(l) = const. \tag{14}$$

During the mass transfer between phases the driving force of the process is expressed as the difference between the concentration of a redistributed component in one phase c_1 and the equilibrium concentration $c_1^p(c_2)$ linearly independent of c_2 (concentration of the same component in another phase). In this case, $c_1^p$is substituted in (11) or (14) instead of concentration c_2.

1.1.2. Example

Let optimality conditions of irreversible mass transfer have the form (11). From the view of flow $g = \bar{g} / L$ constancy from (3) follows:

$$c_1^*(l) = c_1^0 - \frac{\bar{g}}{rL}; \quad c_1^{p*}(l) = c_1^0 - \frac{c_1^*(l)}{M}, \tag{15}$$

where M denotes the right side of (11). Substituting c_1^* and c_1^{p*} in the expression for the mass flux and taking the constancy of this flux into account, we obtain

$$\frac{k}{T}(\mu_1(c_1^*) - \mu_1(c_1^{p*})) = \frac{\bar{g}}{L}, \tag{16}$$

Or $kR\ln M = \bar{g} / L$, from which $M = e^{\bar{g}/kLR}$.

Assuming a linear dependence

$$c_1^p(c_2) = ac_2 + b, \tag{17}$$

where a, b — are some constants determined by processing experimental data of the equilibrium. Then, find the optimum profile

$$c_2^*(l) = \frac{c_1^0 rL - \bar{g}l}{arL} e^{-\bar{g}/kRL} - \frac{b}{a}. \tag{18}$$

2. Irreversible work of separation and heat-driven separation

2.1. Introduction

The minimal amount of energy needed for separation a mixture with a given composition can be estimated using reversible thermodynamics. These estimates turn out to be very loose and unrealistic. They also do not take into account kinetic factors (laws and coefficients of heat and mass transfer, productivity of the system, etc.). In this paper we derive irreversible estimates of the work of separation that take into account all these factors.

The majority of separation systems are open systems that exchange mass and energy with the environment. If mass and heat transfer coefficients (determined by the size and construction of the apparatus) are finite and if the productivity of the system is finite then the processes in such systems are reversible. The energy flows, the compositions of the mass flows, and the

http://dx.doi.org/10.5772/54546

productivity of the system are linked via the balance equations of energy, mass, and entropy. The latter also includes entropy production in the system. Minimal energy used for separation corresponds to minimal entropy production in the system subject to various constraints. This allows us to estimate this minimal energy.

There is a qualitative as well as a quantitative difference between the reversible and irreversible estimates obtained in this paper. For example, the irreversible estimate of the work of separation for poor mixtures (where the concentration of one of the components is close to one) tends to a finite nonzero limit, which depends on the kinetics factors. The reversible work of separation for such mixtures tends to zero. The reversible estimate differs from the amount of energy needed in practice for separation of poor mixtures by a factor of 10^5.

For heat-driven separation processes the novel results obtained in this paper include the estimate of the minimal heat consumption as a function of kinetic factors and the thermodynamic limit on the productivity of a heat-driven separation.

2.2. Thermodynamic balances of Separation Processes and the Link between Energy Consumption and Entropy Production

Consider the system, shown in Figure 1, where the flow of mixture with rate g_0, composition x_0, temperature T_0, and pressure P_0 is separated into two flows with the corresponding parameters g_i, x_i, T_i,P_i(i=1, 2). The flow of heat q_+ with the temperature T_+ can be supplied, and the flow of heat q_- with the temperature T_- can be removed. The mechanical work with the rate (power) $p$can be supplied.

In centrifuging, membrane separation, and adsorption–desorption cycles that are driven by pressure variations, no heat is supplied/removed and only mechanical work is spent. In absorption–desorption cycles, distillation, and so forth, no mechanical work is spent, only heat is consumed (heat-driven separation). In some cases the number of input and output flows can be larger. As a rule one can still represent the system as an assembly of separate blocks, whose structure is shown in Figure 1.

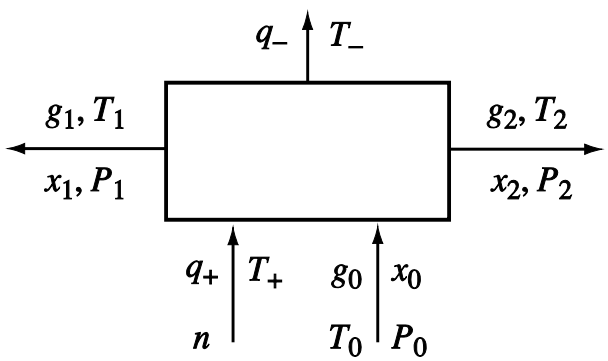

Figure 1. Simplified schematic of thermodynamic balances for separation processes.

2.2.1. Heat-driven separation

Consider a heat-driven separation (p=0) and assume that each of the vectors x_i=(x_{i1}, ..., x_{ij}, ..., x_{ik}) i=0, 1, 2 consists of k components which denote the molar fraction of the j-th substance in the i-th flow. The thermodynamic balance equations of mass, energy, and entropy here take the following form

$$g_0 x_{0j} - g_1 x_{1j} - g_2 x_{2j} = 0, \quad j = 1,...,k \tag{19}$$

$$\sum_{j=1}^{k} x_{ij} = 1, \quad i = 0,1,2 \tag{20}$$

$$q_+ - q_- + g_0 h_0 - g_1 h_1 - g_2 h_2 = 0 \tag{21}$$

where h_i is the enthalpy of the i-th flow;

$$\frac{q_+}{T_+} - \frac{q_-}{T_-} + g_0 s_0 - g_1 s_1 - g_2 s_2 + \sigma = 0 \tag{22}$$

σ denotes entropy production. From eq (19), eq (20) follows that g_0=g_1 + g_2. After elimination of g_0 from eqs (21) and (22) and introduction of enthalpy increments Δh and entropy increment Δs we get

$$q_+ - q_- + g_1 \Delta h_{01} + g_2 \Delta h_{02} = 0 \tag{23}$$

$$g_2 \Delta s_{02} + g_1 \Delta s_{01} + \frac{q_+}{T_+} - \frac{q_-}{T_-} + \sigma = 0 \tag{24}$$

Here, Δh_{0i}=h_0−h_i, Δs_{0i}=s_0−s_i (i=1, 2).

Elimination of q_- using eq (23) and its substitution into eq (24) yields

$$\sum_{i=1}^{2} g_i \left(\Delta s_{0i} - \frac{\Delta h_{0i}}{T_-} \right) + q_+ \left(\frac{1}{T_+} - \frac{1}{T_-} \right) + \sigma = 0$$

and the flow of used heat for heat-driven separation is

$$q_+ = \frac{T_+}{T_+ - T_-} \left[\sum_{i=1}^{2} g_i (\Delta s_{oi} T_- - \Delta h_{oi}) + \sigma T_- \right] \tag{25}$$

http://dx.doi.org/10.5772/54546

The first term in the square brackets depends only on the parameters of the input and output flows and represents the reversible work of separation per unit of time (reversible power of separation). The second term there represents the process kinetics and corresponding energy dissipation.

For mixtures that are close to ideal gases and ideal solutions, molar enthalpies and entropies h_i and s_i in the eqs (21) and (22) can be expressed in terms of compositions and specific enthalpies and entropies of the pure substances. We obtain for each of the flows

$$\begin{aligned} \Delta h_{0i} &= \sum_{j=1}^{k}\left[x_{0j}h_j(T_0,P_0) - x_{ij}h_j(T_i,P_i)\right] \\ \Delta s_{0i} &= \sum_{j=1}^{k}\left[x_{0j}s_j^0(T_0,P_0) - x_{ij}s_j^0(T_i,P_i) - R(x_{0j}\ln x_{0j} - x_{ij}\ln x_{ij})\right], \quad i=1,2 \end{aligned} \tag{26}$$

where R is the universal gas constant. The reversible energy consumption here is

$$q_+^0 = \frac{1}{\eta_k}\sum_{i=1}^{2} g_i \sum_{j=1}^{k}\left[[x_{0j}s_j^0(T_0,P_0) - x_{ij}s_j^0(T_i,P_i) - R(x_{0j}\ln x_{0j} - x_{ij}\ln x_{ij})]T_- + x_{ij}h_j(T_i,P_i) - x_{0j}h_j(T_0,P_0)\right] \tag{27}$$

We denote here the Carnot efficiency of the ideal cycle of the heat engine as

$$\eta_C = \frac{T_+ - T_-}{T_+}$$

Condition (25) can be rewritten as

$$q_+ = \frac{1}{\eta_C}(p^0 + \sigma T_-) \tag{28}$$

Here, $p_0$is the reversible power of separation that is equal to the reversible flow of heat given by eq (27) multiplied by the Carnot efficiency. When eq (28) was derived we took into account only the irreversibility σ of the separation process (the irreversibility of the heat transfer was not taken into account). In reality heat can be supplied/removed with a finite rate only irreversibly. Any transformation of heat into work with finite heat transfer coefficients and finite power is irreversible. This leads to a lower efficiency than the Carnot efficiency. The closed form expression for this efficiency was obtained in ref [16]. It depends on the power p and on heat transfer coefficients for heat supply and heat removal α_+ and α_-. For the Newton (linear) law of heat transfer it has the form

$$\eta_p = \max\frac{p}{q_+} = 1 - \frac{1}{2T_+}\left(T_+ + T_- - \frac{4p}{\alpha} - \sqrt{(T_+ - T_-)^2 + \left(\frac{4p}{\alpha}\right)^2 - 8\frac{p}{\alpha}(T_+ + T_-)}\right) \tag{29}$$

where it is assumed that there is constant contact of the working body with the heat reservoirs and

$$\alpha = \frac{4\alpha_+\alpha_-}{\alpha_+ + \alpha_-} \tag{30}$$

It is easy to show that if $p \to 0$ then η_p tends to the Carnot efficiency.

Substitution of η_p instead of η_C in eq (28) allows us to derive a tighter estimate for the heat consumption in heat-driven separation processes by finding the minimal possible entropy production σ subject to various constraints

$$q_+ \geq q_+^{\min} = \frac{p^{\min}}{\eta_p(p^{\min}, \alpha, T_+, T_-)} \tag{31}$$

where

$$p^{\min} = p^0 + \sigma^{\min} T_- \tag{32}$$

Conditions (29-31) single out the area of thermodynamically feasible heat-driven separation systems.

Expressions (27) and (28) and eq (25) can be further specified by assuming the constancy of heat capacities, that the mixture is binary, and so forth.

2.2.2. Mechanical separation

Consider a separation system that uses mechanical work with rate p. Assume that no heat is supplied/removed ($q_+ = q_- = 0$) and that input and output flows have the same temperature T and the same pressure. Multiplication of eq (24) by T and subtraction of the result from the energy balance eq (23), where $(q_+ - q_-)$ is replaced with the supplied power p, yields

$$p = T\sigma + g_0 \sum_{i=1}^{2} \gamma_i (T\Delta s_{0i} - \Delta h_{0i}) \tag{33}$$

here $\gamma_i = g_i / g_0$

After taking into account eq (27) that the enthalpy increment Δh_{0i} in a mechanical separation is zero, we get

http://dx.doi.org/10.5772/54546

$$p = g_0 RT\left[\sum_{i=1}^{2}\gamma_i\sum_{j=1}^{k}x_{ij}\ln x_{ij} - \sum_{j=1}^{k}x_{0j}\ln x_{0j}\right] + T\sigma = p^0 + T\sigma \tag{34}$$

The first term in this expression represents the minimal power for separation that corresponds to the reversible process ($\sigma=0$). This power p^0 is equal to the difference between the reversible power for complete separation of the input flow $p_0^0 = -g_0 RT\sum_j x_{0j}\ln x_{0j}$ and the combined reversible power of separation of the output flows p_1^0 and p_2^0.

Here

$$p_i^0(x_i) = -RTg_0\gamma_i\sum_{j=1}^{k}x_{ij}\ln x_{ij}, \quad i=0,1,2 \tag{35}$$

is the reversible power of separation of the *i*-th flow into pure substances.

2.3. Minimal work of separation in irreversible processes

2.3.1. Assumptions and problem formulation

Assume that the components of the input mixture are close to ideal gases or ideal solutions. The chemical potential of the *i*-th component can then be written in the following form

$$\mu_i(T,P) = \mu_0(T,P) + RT\ln x_i, \quad i=1,\ldots,k \tag{36}$$

where x_i is the concentration of the *i*-th component.

First we consider a system that includes three elements, a reservoir with the time independent temperature *T*, pressure *P*, and vector of concentrations $x_0=\{x_{01}, \ldots, x_{0k}\}$ (therefore its chemical potential μ_0 is also time independent), the finite capacity output subsystem with chemical potential μ_1 that depends on the current compositions of the mixture and of the working body that has controllable values of chemical potential μ_o^w and μ_1^w, at the points of contact with reservoir and output subsystem. At the time the intensive variables of the output subsystem coincide with the values of the reservoir's intensive variables, and the number of moles in it is given and equal to N_0. At time τ the number of moles $N(\tau)$ and the composition $x(\tau)$ in the output subsystem are given. The mass transfer coefficients between the reservoir and the working body and the working body and the output subsystem are finite and fixed. The minimal necessary work required for the separation is sought.

We do not consider here how to implement the derived optimal dependence of the chemical potential of the working body because of two reasons. First, our main objective is to derive a

lower bound on the work of separation. However, imposing constraints on feasible variations of chemical potential would lead to an increase in energy consumption. Second, we will demonstrate that for the majority of mass transfer laws the optimal mass transfer flow is time independent, and its implementation is straightforward.

The work of separation in an isothermal process for an adiabatically insulated system can be found using the Stodola formula in terms of the reversible work A_0 and the entropy increment ΔS

$$A = A_0 + T\Delta S \tag{37}$$

The reversible work is equal to the increment of the system's internal energy. Since as a result of the process $(N(\tau)-N(0))$ moles of mixture with the composition x_0 is removed from the reservoir, and the energy of the output subsystem rises because of the increase of the amount of moles in it from $N(0)$ to $N(\tau)$ and its composition from x_0 to x_τ, the total change of the system's internal energy is

$$A_0 = N(\tau)\sum_{i=1}^{k}\Delta\mu_i = N(\tau)RT\sum_{i=1}^{k}[x_i(\tau)\ln x_i(\tau) - x_{i0}\ln x_{i0}] \tag{38}$$

and it is independent of $N(0)$. Because A_0 is determined by N, $x(\tau)$, $x(0)$, the minimum of A corresponds to the minimum of the entropy increment

$$\begin{aligned}\Delta S &= \frac{1}{T}\int_0^\tau \sum_{i=1}^{k}[g_{0i}(\mu_{0i}-\mu_i^w) + g_{1i}(\mu_i^w - \mu_{1i})]dt \\ &= \frac{1}{T}\int_0^\tau \sum_{i=1}^{k}(g_{0i}\Delta\mu_{0i} + g_{1i}\Delta\mu_{1i})dt\end{aligned} \tag{39}$$

Because the working body's parameters have the same values at the beginning and at the end of a cycle

$$\begin{aligned}\int_0^\tau g_{i0}dt &= \int_0^\tau g_{i1}dt \\ N(\tau)x_i(\tau) - N(0)x_i(0) &= \Delta(Nx_i), \quad i = 1,2,...,k\end{aligned} \tag{40}$$

2.3.2. Optimal solution

The problem of minimization of ΔS subject to constraints eq (40) on $g_{0i}\geq 0$, $g_{1i}\geq 0$ becomes simpler in a common case where the chemical potentials' increments $\Delta\mu_{0i}$, $\Delta\mu_{1i}$ are unique

http://dx.doi.org/10.5772/54546

functions of flows g_{0i} and g_{1i}, correspondingly. If processes are close to equilibrium then this dependence is linear.

Assume

$\Delta\mu_{0i}=\phi_{0i}(g_{0i}), \quad \Delta\mu_{1i}=\phi_{1i}(g_{1i})$

then the problems (39) and (40) can be decomposed into 2k problems

$$\Delta S_{ji}=\int_0^\tau \sigma_{ji}(g_{ji})dt \to \min \Big/ \int_0^\tau g_{ji}dt=\Delta(Nx_i) \quad j=0,1, \quad i=1,2,...,k \tag{41}$$

where $\sigma_{ji}=g_{ji}\phi_{ji}(g_{ji})$ is the function that determines dissipation.

Problems eq (41) are averaged nonlinear programming problems. Their optimal solutions g_{ji}^* are either constants and equal to

$$g_{ji}^*=g_{1i}^*=\frac{\Delta(Nx_i)}{\tau} \tag{42}$$

or switches between two so-called basic values on the interval (0, τ), the solution eq (42) corresponding to the case where the convex envelope of the function $\sigma_{ji}(g_{ji})$ is lower than the value of this function at g_{ji}^*. Characteristic forms of the function $\sigma_{ji}(g_{ji})$ for the constant and switching regimes are shown in Figure 2.

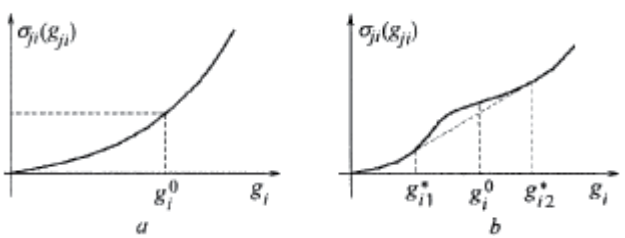

Figure 2. Dependence of the entropy production on the rate for the constant (a) and switching (b) solutions (g_{1i}^* and g_{2i}^* are the basic values of the rate).

If the function σ_{ji} is concave then the optimal rate g_{ji} is always constant. Let us calculate the second derivative of σ on g (we omit subscripts for simplicity). If it is positive then the constancy of the rate in the optimal process is guaranteed.

$$\sigma''(g)=2\phi'(g)+g\phi''(g)\geq 0 \tag{43}$$

The first term in this expression is always positive because the chemical potentials' difference is the driving force of mass transfer and monotonically depends on the flow. For the majority of laws of mass transfer the inequality eq (43) holds. In particular, it holds if the flow of mass transfer is proportional to the difference of chemical potentials in any positive degree.

Consider mass transfer flow that depends linearly on the chemical potential difference for all *i, j.* Then

$$g_{ji} = \alpha_{ji}\Delta\mu_{ji} \to \phi_{ji} = \frac{g_{ji}}{\alpha_{ji}} \tag{44}$$

It is clear that the conditions eq (43) hold and the optimal rates of flows obey equalities (42).

Equalities (42) hold for any nonswitching solution. The minimal increment of the entropy production for such solution is

$$\Delta S^{\min} = \sum_{ij} \Delta S_{ji}^{\min} = \tau \sum_{ij} \sigma_{ji} \left(\frac{\Delta(Nx_i)}{\tau} \right) \tag{45}$$

and the minimal work of separation is

$$A_{\min} = A_0 + \tau T \sum_{ij} \sigma_{ji} \left(\frac{\Delta(Nx_i)}{\tau} \right) \tag{46}$$

The optimal rates are determined by the initial and final states which allows us to specify the estimate eq (46).

Near equilibrium the flows obey Onsanger's kinetics eq (44), and from eq (46) it follows that

$$A_{\min} = A_0 + \tau \sum_{i=1}^{k} g_i^2 \left(\frac{1}{\alpha_{0i}} + \frac{1}{\alpha_{1i}} \right) = A_0 + \frac{1}{\tau} \sum_{i=1}^{k} \frac{\Delta^2(Nx_i)}{\bar{\alpha}_i} \tag{47}$$

$$\bar{\alpha}_i = \frac{\alpha_{0i}\alpha_{1i}}{\alpha_{0i} + \alpha_{1i}} \tag{48}$$

is the equivalent mass transfer coefficient on the i-th component and the minimal entropy production is

http://dx.doi.org/10.5772/54546

$$\sigma_{\min} = \frac{1}{T\tau^2}\sum_{i=1}^{k}\frac{\Delta^2(Nx_i)}{\bar{\alpha}_i} \tag{49}$$

The lower bound for the average power of separation is

$$p_{\min} = \frac{A_{\min}}{\tau} = \frac{A_0}{\tau} + \frac{1}{\tau^2}\sum_{i=1}^{k}\frac{\Delta^2(Nx_i)}{\bar{\alpha}_i} \tag{50}$$

$p_0 = A_0/\tau$ is the reversible power of separation.

If

$N(0)=0, \quad \Delta(N x_i) = N x_i(\tau)$

then expressions (47) and (50) take the form

$$A_{\min} = A_0 + \frac{N^2}{\tau}\sum_{i=1}^{k}\frac{x_i^2(\tau)}{\bar{\alpha}_i} \tag{51}$$

$$p_{\min} = p_0 + g^2\sum_{i=1}^{k}\frac{x_i^2(\tau)}{\bar{\alpha}_i} \tag{52}$$

Where

$$A_0 = NRT\sum_{i=1}^{k}[x_i(\tau)\ln x_i(\tau) - x_i \ln x_i] \tag{53}$$

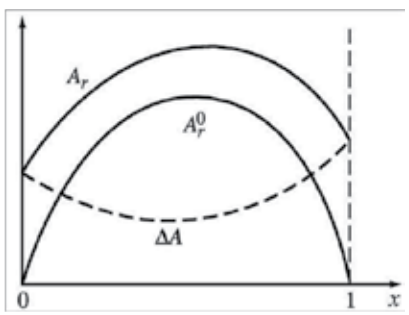

Figure 3. Reversible (A_0) and irreversible (A_r) estimates of the minimal work of separation of binary mixture as functions of key component's concentrations.

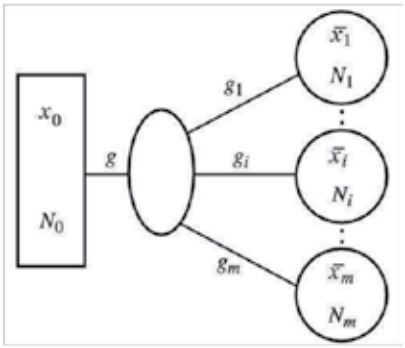

Figure 4. Separation of the system with finite capacity on m subsystems.

Note that the irreversible estimate of the work of separation eq (51) does not tend to zero for poor mixtures when the concentration of one of the components tends to one (Figure 3).

If system includes not one but a number of output subsystems then it is clear that the estimate for the minimal work of separation is equal to the sum of the estimates for each subsystem.

$$A_{\min} = \sum_{j=1} A^j_{\min}, \quad p_{\min} = \sum_{j=1} p^j_{\min} \tag{54}$$

The superscript j here denotes the subsystems.

2.3.3. Separation of a System with finite capacity into m subsystems

Consider a system that is shown in Figure 4. Its initial state is described by the vector of concentrations x_0, the number of moles of the mixture N_0, and its final state by the number of moles N_j, $j=1, \ldots, m$ in each of the subsystems and their concentrations, x_j. The mass balances yields

$$\begin{gathered} \sum_{j=1}^{m} \bar{N}_j = N_0 \\ \sum_{j=1}^{m} \bar{N}_j \bar{x}_{ji} = N_0 x_{0i}, \quad i = 1,2,\ldots,k \end{gathered} \tag{55}$$

The work in the reversible separation process here is

$$A^0_r(x_0, \bar{x}) = RT\left[\sum_{j=1}^{m} \bar{N}_j \sum_i \bar{x}_{ji} \ln \bar{x}_{ji} - N_0 \sum_i x_{0i} \ln x_{0i}\right] = A^0_{r0}(x_0, N_0) - \sum_{j=1}^{m} A^0_{rj}(\bar{x}_j, \bar{N}_j) \tag{56}$$

http://dx.doi.org/10.5772/54546

The reversible work of separation is equal to the difference of the reversible work of separation of the initial mixture into pure components and the reversible work of separation for mixtures in each of the subsystems.

We again assume that flows g_j have components g_{ji} proportional to the difference of the chemical potential of the subsystem and the working body with the coefficient α_{ji}. Here, the condition of minimal work of separation corresponds to the condition of flow constancy

$$g_{ji} = \frac{\bar{N}_j \bar{x}_{ji}}{\tau}, \quad i = 1,2,...,k, \quad j = 1,...,m \tag{57}$$

$$\Delta\mu_{ji} = \frac{g_{ji}}{\bar{\alpha}_{ji}}, \quad j = 0,1,...,m \tag{58}$$

Here, $\bar{\alpha}_{ji}$ is the equivalent mass transfer coefficient calculated using eq (48) for the flow into the j-th output subsystem of the i-th component. Similarly as was done above for the system with the reservoir and one finite capacity output subsystem and flows proportional to the final concentrations eq (57), these concentrations in the output subsystems are time independent and equal to $\bar{x}_j$, correspondingly, and the number of moles $\overline{N}_j(t)$ depends linearly on time. The power p here is constant

$$p = \frac{RT}{\tau}\sum_{j=1}^{m}\bar{N}_j\sum_i \bar{x}_{ji}\ln\frac{\bar{x}_{ji}}{x_{0i}} + \frac{1}{\tau^2}\sum_{j=1}^{m}N_j^2\sum_i \bar{x}_{ji}^2 \Big/ \bar{\alpha}_{ji} \tag{59}$$

The minimal work of separation for the mixture with concentrations x_0 into m subsystems with concentrations $\bar{x}_i$ over the time τ is

$$A_r = RTN_0\sum_{j=1}^{m}\gamma_j\sum_i \bar{x}_{ji}\ln\frac{\bar{x}_{ji}}{x_{0i}} + \frac{N_0^2}{\tau}\sum_{j=1}^{m}\gamma_j^2\sum_i \bar{x}_{ji}^2 \Big/ \bar{\alpha}_{ji} \tag{60}$$

Here, $\gamma_j = N_j / N_0$, $\bar{\alpha}_{ji} = \alpha_{ji}\alpha_{0i} / (\alpha_{0i} + \alpha_{ji})$

The first term here coincides with the reversible work of separation A_r^0 of the mixture of N_0 moles with concentration x_0 into subsystems with number of moles $\overline{N}_j$ and concentrations $\bar{x}_j$. The second term takes into account irreversibility of the process. A_r decreases monotonically and tends to A_r^0 when process duration τ and mass transfer coefficient $\bar{\alpha}_{ji}$ increases.

2.3.4. Example

Consider separation of the binary mixture into pure components in time τ. In this case $N_1 = x_0 N_0$, $N_2 = (1 - x_0) N_0$, where x_0 is the concentration of the key component, $\bar{x}_{11} = \bar{x}_{22} = 1$. From the formula (60) we get

$$A_r = -RTN_0(x_0 \ln x_0 + (1 - x_0)\ln(1 - x_0)) + \frac{N_0^2}{\tau}\left(\frac{x_0^2}{\bar{\alpha}_{11}} + \frac{(1 - x_0)^2}{\bar{\alpha}_{22}}\right) = A_r^0(x_0) + \frac{N_0^2}{\tau}\left(\frac{x_0^2}{\bar{\alpha}_{11}} + \frac{(1 - x_0)^2}{\bar{\alpha}_{22}}\right) \tag{61}$$

The estimate eq (61) was derived in ref [1] by solving the problem of optimal separation of the binary mixture in the given time τ in Van't Hoff's thought experiment with movable pistons and semitransparent membrane where $\bar{\alpha}_{11}$ and $\bar{\alpha}_{22}$ are the permeability coefficients on the first and second component. If flows do not depend explicitly on the chemical potentials' differentials, for example, are proportional to the concentrations' differential, then an estimate similar to the one obtained above can be constructed by solving the following auxiliary nonlinear programming problem

$$\Delta\mu_i(P_0^i, P_i) \to \min_{P_0^i, P_i} / \; g_i(P_0^i, P_i) = g_i, \quad i = 1, 2, \ldots \tag{62}$$

Here, (P_0^i, P_i)are partial pressures of the components in contacting subsystems that depend on the chemical potentials' differentials $\Delta\mu_i$. The flow g_i depends on the same differentials. Minimums in these problems are sought for different values of constant $g_i > 0$ and nonpositive P_0^i and P_i We denote the minimal values of the objective in each of these problems $\Delta\mu_i^{\min}(g_i)$ as $\Delta\mu_i^*(g_i)$. This dependence can be used in the estimate eq (41) of the irreversible work of separation.

2.3.5. Example

Assume $\Delta\mu = RT\ln(P_0 / P)$, $g(P_0, P) = (P_0 - P)/\alpha$, and $0 < P < P_{\max}$. Let us express P_0 in terms of g and P:

$P_{0i} = \alpha_i g_i + P_i, \quad i = 1, 2$

$\Delta\mu = RT\ln(\alpha g / P + 1)$ attains its minimum at $P = P_{\max} \forall\, g$.

Therefore, $\Delta\mu_i^*(g_i) = RT\ln(\alpha_i g_i / P_{\max} + 1)$.

2.4. Potential application of obtained estimates

We will illustrate the possibilities of the application of the derived estimates.

http://dx.doi.org/10.5772/54546

2.4.1. Estimate of the power of separation in a continuous separation system

Consider a continuous separation system with the input flow g_0 with concentration x_0 and m output flows g_j (j=1, ..., m) with concentrations x_j={x_{j0}, x_{j1}, ..., x_{jk}}. Here, the temperatures on the input and output flows are close to each other.

Equation (59) allows us to estimate the minimal power required for continuous separation in such system

$$p_{\min} = \sum_{j=1}^{m} p_{0j} + g_0^2 \sum_{j=1}^{m} \gamma_j^2 \sum_{i=1}^{k} \frac{x_{ji}^2}{\alpha_{ji}} \tag{63}$$

Where

$$\gamma_j = \frac{g_j}{g_0} \geq 0, \quad \sum_{j=1}^{m} \gamma_j = 1 \tag{64}$$

$$p_{0j} = g_0 \gamma_j RT \sum_{i=1}^{k} [x_{ji} \ln x_{ji} - x_{0i} \ln x_{0i}] p_{0j} = \gamma_j M_j(g_0, x_j) \tag{65}$$

Mass balance equations yield

$$\begin{aligned} &\sum_{j=1}^{m} \gamma_j x_{ji} = x_{0i}, \quad i = 1, ..., k-1, \\ &\sum_{i=1}^{k} x_{ji} = 1, \quad j = 0, ..., m \end{aligned} \tag{66}$$

The number of conditions eq (66) is $k-1$, because the concentration of one of the components is determined by the conditions eq (64).

If the number of flows $m>k$, and their compositions are given, then the removal fractions can be chosen in such a way that the power of separation is minimal subject to constraints eqs (64) and (66). The Lagrange function of this problem is

$$L = \sum_{j=1}^{m} \left\{ \gamma_j M_j + \gamma_j^2 r_j - \lambda_0 \gamma_j - \sum_{i=1}^{k} \lambda_i \gamma_j x_{ji} \right\} \tag{67}$$

here

$r_j(g_0, x_j)=g_0^2\sum_{i=1}^{k}\frac{x_{ji}}{\alpha_{ji}}$

L is the concave function on γ_j, and its conditions of stationarity determine the flows that minimize the power for separation for a given flow's compositions

$$\gamma_j^* = \frac{\lambda_0 - M_j + \sum_{i=1}^{k-1}\lambda_i x_{ji}}{2r_j}, \quad j=1,...,m \tag{68}$$

We have k linear equations for λ_0 and λ_i

$$\frac{1}{2}\left[\sum_{j=1}^{m}\frac{\lambda_0 - M_j}{r_j} + \sum_{i=1}^{k-1}\lambda_i\sum_{j=1}^{m}\frac{x_{ji}}{r_j}\right]=1 \tag{69}$$

$$\frac{1}{2}\left[\sum_{j=1}^{m}x_{ji}\left(\frac{\lambda_0 - M_j}{r_j} + \frac{1}{r_j}\sum_{i=1}^{k-1}\lambda_i x_{ji}\right)\right]=x_{0i}, \quad i=1,...,k-1 \tag{70}$$

2.4.2. Example

Assume m=3, k=2, g_0=1 mol/s, T=300K, and the compositions and transfer coefficients are

$x_{01}=x_{02}=0.5$

$x_{11}=0.9;\quad x_{12}=0.1;\quad \bar{\alpha}_{11}=\bar{\alpha}_{12}=0.004\ mol^2/(J\ s)$

$x_{21}=0.3;\quad x_{22}=0.7;\quad \bar{\alpha}_{21}=\bar{\alpha}_{22}=0.01\ mol^2/(J\ s)$

$x_{31}=0.1;\quad x_{32}=0.9;\quad \bar{\alpha}_{31}=\bar{\alpha}_{32}=0.06\ mol^2/(J\ s)$

From eq (65) we obtain M_1=910, M_2=197, M_3=910, and r_1=205, r_2=580, r_3=137.

Equations (69) and (70) for λ-multipliers take the form

$$\frac{1}{2}\left[\frac{\lambda_0-M_1}{r_1}+\frac{\lambda_0-M_2}{r_2}+\frac{\lambda_0-M_3}{r_3}+\lambda\left(\frac{x_{11}}{r_1}+\frac{x_{21}}{r_2}+\frac{x_{31}}{r_3}\right)\right]=1$$

$$\frac{1}{2}\left[x_{11}\left(\frac{\lambda_0-M_1}{r_1}+\frac{\lambda_1 x_{11}}{r_1}\right)+x_{21}\left(\frac{\lambda_0-M_2}{r_2}+\frac{\lambda_1 x_{21}}{r_2}\right)+x_{31}\left(\frac{\lambda_0-M_3}{r_3}+\frac{\lambda_1 x_{31}}{r_3}\right)\right]=x_{01}$$

We obtain λ_0=894,λ_1=183. Their substitution in eq (68) yields γ_1^*=0.36, γ_2^*=0.64, γ_3^*=0and the corresponding estimate for the minimal irreversible power of separation eq (63) is

http://dx.doi.org/10.5772/54546

$p_{\min}$=718 wt

2.4.3. The selection of the separation sequence for a multicomponent mixture

In practice, separation of multicomponent mixtures is often realized via a sequence of binary separations. So, a three-component mixture is first separated into two flows, one of which does not contain one of the components. The second flow is then separated into two unicomponent flows. The reversible work of separation (that corresponds to the power p_0) does not depend on the sequence of separation, because p_0 is determined by the rates and compositions of the input and output flows of the system as a whole. The irreversible component of the power Δp in eq (63) depends on the sequence of separation and can be used to find the optimal one.

Consider a three-component mixture with concentration x_0=(x_{01}, x_{02}, x_{03}), and rate g_0 we set to one. We denote the mass transfer coefficients at the first and second stages of separation as α_1 and α_2. They depend on the construction of the apparatus. First, we assume for simplicity that these coefficients do not depend on the mixture's composition (in the general case they do depend on it). We consider irreversible power consumption for two cases:

a. The first component is first separated, then the second and the third are separated.

b. The second component is separated, and then the first and the third are separated.

We assume that the separation at each stage is complete. We get up to the constant multiplier

$$\Delta p_a = \Delta p_{a1} + \Delta p_{a2} = x_{01}^2 / \alpha_1 + \frac{(x_{02} + x_{03})^2}{\alpha_1} + (x_{02} + x_{03})^2 + (x_{02}^2 / \alpha_2 + x_{03}^2 / \alpha_3) \tag{71}$$

The first two terms in this sum represent the loss of irreversibility during the first stage of separation. For g_0=1 and complete separation the output rates of this stage g_1 and g_2 are x_{01} and (x_{02} + x_{03}), correspondingly.

Consider the first stage of case a for g_0=1 and complete separation and view the second and third component as the same substance with the output rate x_{02} + x_{03}=1−x_{01}. The irreversible expenses eq (63) are

$$\Delta p_{a1} = \frac{x_{01}^2}{\alpha_1} + \frac{(1 - x_{01})^2}{\alpha_1} = \frac{2x_{01}^2 + 1 - 2x_{01}}{\alpha_1} \tag{72}$$

When the second flow is separated into two flows their rates are

$$g_{22} = \frac{x_{02}}{(1 - x_{01})}, \quad g_{23} = \frac{x_{03}}{(1 - x_{01})}$$

and the irreversible power is

$$\Delta p_{a2} = \frac{1}{\alpha_2 (1 - x_{01})^2} (x_{02}^2 + x_{03}^2)$$

The combined irreversible power is

$$\Delta p_a(x_{01},\ x_{02}) = \frac{2x_{01}^2 - 2x_{01} + 1}{\alpha_1} + \frac{x_{02}^2 + (1 - x_{01} - x_{02})^2}{\alpha_2 (1 - x_{01})^2}$$

Similarly in case b we get

$$\Delta p_b(x_{01},\ x_{02}) = \frac{2x_{02}^2 - 2x_{02} + 1}{\alpha_1} + \frac{x_{01}^2 + (1 - x_{01} - x_{02})^2}{\alpha_2 (1 - x_{02})^2}$$

The differential between these two values is

$$\Delta p_{ab} = \Delta p_a + \Delta p_b = \frac{2}{\alpha_1}\left[(x_{01}^2 - x_{02}^2) - (x_{01} - x_{02})\right] + \frac{1}{\alpha_2 (1 - x_{01})(1 - x_{02})}\left[(1 - x_{02})^2 (x_{02}^2 + x_{03}^2) - (1 - x_{01})^2 (x_{01}^2 + x_{03}^2)\right] \quad (73)$$

If $\Delta p_{ab} > 0$, then sequence b is preferable.

Note that it is not possible to formulate the general rule to choose the optimal separation sequence for a multicomponent mixture, in particular, on the basis of the reversible work of separation. It is necessary here to compare irreversible losses for each sequence.

2.4.4. Example

Assume that the composition of the input three component mixture is $x_{01}=0.6$, $x_{02}=0.3$, $x_{03}=1-x_{01}-x_{02}$; the mass transfer coefficients are $\alpha_1=0.01\text{mol}^2/(\text{J s})$, $\alpha_2=0.02\text{mol}^2/(\text{J s})$. From (eq 73) we find that the difference in power between sequences *a* and *b* is

$$\Delta p_{ab} = \Delta p_a - \Delta p_b = -7.82 \text{ J}$$

The comparison of the combined minimal irreversible power for the same initial data shows that the power for separation of a mixture using sequence *b* is higher than the power used for sequence *a*, that is, $\Delta p_{ab} < 0$.

Thus, sequence *a* is preferable, and it is better to perform the complete separation by separating the first component.

2.5. Limiting productivity and minimal heat consumption for a heat-driven separation

In many separation processes a heat engine is used to create the differential of the chemical potential between the working body and the reservoirs (the driving force of mass transfer). Here, the working body is heated during contact with one reservoir and is cooled during contact with the other reservoir. One can represent the heat-driven separation system as a transformer of heat into the work of separation that generates power p, consumes heat flow

http://dx.doi.org/10.5772/54546

from hot reservoir g_+, and rejects flow g_- to the cold reservoir. Heat transfer coefficients for contacts with the hot and cold reservoir α_+ and α_- are fixed.

It was shown in refs [12] and [6] that the potential of the direct transformation of heat to work is limited and the maximal generated power for the working body with the distributed parameters is

$$p_{\max} = \bar{\alpha}(\sqrt{T_+} - \sqrt{T_-})^2 \tag{74}$$

In this expression $\bar{\alpha} = (\alpha_+\alpha_-)/(\alpha_+ + \alpha_-)$ is the equivalent heat transfer coefficient for continuous contact with the reservoirs; $\bar{\alpha} = (\alpha_+\alpha_-)/(\sqrt{\alpha_+} + \sqrt{\alpha_-})^2$ is the equivalent heat transfer coefficient for sequential contact.

The maximal power determines the heat flow consumed from the hot reservoir. Further increase of heat consumption for given values of heat transfer coefficients requires an increase of the temperature differential between the reservoirs and the working body and reduces the power.

The dependence of the used power on the productivity of irreversible separation processes is monotonic eq (63). Therefore, the limiting productivity of heat-driven separation processes corresponds to the maximal possible power produced by transformation of heat into work. Further increase of heat consumption q_+ reduces power and therefore reduces the productivity of separation process.

For the Newton (linear) law of mass transfer and heat–work transformer the dependence of the power on the heat used is

$$q^+(p) = \frac{p}{\eta_p} = \frac{2p}{\left(\frac{p}{\bar{\alpha}T_+} + \eta_C\right) + \sqrt{\left(\frac{p}{\bar{\alpha}T_+} + \eta_C\right)^2 - \frac{4p}{\bar{\alpha}T_+}}} \tag{75}$$

Here, $\eta_C = (T_+ - T_-)/T_+$ is the Carnot efficiency, T_+ and T_- are the hot and cold reservoir's temperatures, and $\bar{\alpha} = (\alpha_+\alpha_-)/(\alpha_+ + \alpha_-)$ is the equivalent heat transfer coefficient.

The minimal heat consumption q_+ as a function of productivity g_0 for a heat-driven separation can be obtained by substituting expression (75) instead of p in the right-hand side of eq (63). The result holds for $p \le p_{\max}$ and therefore for $g_0 \le g_{0\max}$. The duration here must not exceed the maximal possible duration.

Substitution of the right-hand side of eq (74) instead of p in eq (63) yields the maximal possible productivity of the system (where $\bar{\alpha}$ is chosen according to the type of contact between the transformer and reservoir). We denote

$$B = RT\sum_j \gamma_j^2 \sum_i x_{ji} \ln\frac{x_{ji}}{x_{0i}}, \quad D = T\sum_j \gamma_j^2 \sum_i \ln\frac{x_{ji}^2}{\alpha_{ji}} \tag{76}$$

We obtain

$p_{\max} = \bar{\alpha}(\sqrt{T_+} - \sqrt{T_-})^2 = Bg_{\max} + Dg_{0\max}^2$

and the limiting productivity is

$$g_{0\max} = \frac{-B + \sqrt{B^2 + 4\bar{\alpha}D(\sqrt{T_+} - \sqrt{T_-})^2}}{2D} \tag{77}$$

Formulas (76) and (77) allow us to estimate the limiting productivity of a heat-driven separation process for Newton's laws of heat transfer between the working body and reservoirs and mass transfer proportional to the differentials in chemical potentials (mass transfer is close to isothermal with the temperature T).

2.5.1. Example

Consider heat-driven monoethanamide gas cleansing. One of the components is absorbed by the cold solution from the input gas mixture. This solution is then heated and this component is vaporized. The input mixture's parameters are $\bar{T}$=350 K, the key component's molar concentration x=0.5, the rate of mixture g_0=5 mol/s. The temperatures of heat supplied/removed are correspondingly T_h=400 K, T_c=300K, and the heat transfer coefficients are α_+=8.368 kJ/(s K) and α_-=16.736 kJ/(s K). The concentrations of the key components in the output flows are x_1=0.9, x_1=0.1; the mass transfer coefficients for each of the components (integral values over the whole contact surface) for the hot and cold reservoir's contacts are α_1=0.07 mol^2/(kg s), α_2=0.03 mol^2/(kg s).

Because the solution circulates and is heated and cooled in turns, the limiting power for transformation of heat into work is given by the expression (74) with the corresponding $\bar{\alpha}$

$p_{\max}$=20.711 kJ/s

The power for separation is given by eq (63).

We have

$$p^0 = RTg_0\sum_{j=1}^{m}\gamma_j\sum_i x_{ji}\ln\frac{x_{ji}}{x_{0i}} = 5.397 \text{ kJ/s}$$

The minimal work required for a system with Onsanger's equations are (see eq (63))

$$\Delta p = g_0^2\sum_{j=1}^{m}\gamma_j^2\sum_i\frac{x_{ji}^2}{\alpha_{ji}} = 7.238 \text{ kJ/s}$$

http://dx.doi.org/10.5772/54546

Thus, $p = p^0 + \Delta p = 12.636 \text{kJ/s} < p_{\max}$. The work needed for separation does not exceed the maximal possible value for given heat transfer coefficients.

Let us estimate the minimal heat consumption. From eq (75) we get

$q_+ = 32.426$ kJ/s

If the temperatures of the input and output flows are not the same then the minimal energy required for separation can be estimated using the thermodynamic balance equations (31) and (32) and the expression for $\sigma^{\min}$ eq (49).

2.6. Conclusion

New irreversible estimates of the in-principle limiting possibilities of separation processes are derived in this paper. They take into account the unavoidable irreversibility caused by the finite rate of flows and heat and mass transfer coefficients. They also allow us to estimate the limiting productivity of a heat-driven separation and to find the most energy efficient separation sequence/regime of separation for a multicomponent mixture.

3. Optimization of membrane separations

3.1. Introduction

As the properties of membranes improve, the membrane separation of liquids and gases is more widely used in chemical engineering [8,10,11,20]. Since the mathematical modeling of membrane separations is simpler than that for most of the other separation processes, they could be controlled by varying the pressure, contact surface area, and the like during the separation process.

The minimal work needed to separate mixtures into pure components or into mixtures of given compositions can be minorized using well-known relationships of reversible thermodynamics [15]. However, this estimate is not accurate because it ignores the mass transfer laws and the properties of membranes, process productivity, possible intermediate processes of mixing, and so on. The estimates based on reversible thermodynamics are not suitable for determining the optimal sequence of operations in the separation of multicomponent systems, because they depend only on the compositions of feeds and end products and do not reflect the sequence of operations in which the end product was obtained. The work needed for separation consists of its reversible work and irreversible energy losses. The losses are equal to ΔST, where ΔS is the increment of the system entropy due to the irreversibility of the process. Below, the minimum possible production of entropy (that is, the minimal additional separation work) will be found for the separation of one component at a specified production rate and transport coefficients. Also, we will determine the dependence of this minimum on the input data for one or another process flowsheet at a fixed production rate.

3.2. Batch membrane separation

We will first consider a batch separation of a mixture in a system consisting of two chambers separated by a membrane permeable to only one active (to be separated) component of the mixture (Fig. 5). Let and $G_i(t)$, $C_i(t)$, $\mu_i(C_i$, and $P_i)$ denote the amount, the concentration of the active component, and its chemical potential in chamber *I*, respectively. These parameters can be varied during the process. At the initial moment of time ($t=0$), the parameters that are specified include the mixture amount $G_1(0)=G_{10}$ in chamber *1* and the concentration $C_1(0)=C_{10}$ of the active component passing through membrane *3* at a mass transfer rate *g*, which depends on its chemical potentials on both membrane sides, μ_1 and μ_2. In turn, the potentials depend on the variation of the pressure and mixture composition in the first and second chambers. The pressure in the first chamber can be varied using piston *4*. The process is isothermal, and the temperature T is specified and remains unchanged.

The intensive variables in the second chamber are the pressure $P_2(t)$ and the chemical potential $\mu_2(t)$, which varies with time due to the accumulation of the active component in the chamber and the variation of the external conditions. Assume that the laws of this variation are known. The specification of the initial composition of the mixture C_{10}, the number of moles G of the component that passed through the membrane in time τ, and the initial number of moles G_{10} determines the final composition in the first chamber,

$$C_1(\tau)=\frac{G_{10}C_{10}-G}{G_{10}-G},$$

and, hence, the reversible work of separation, which is equal to the increment of the free energy of the system:

$$A^0=-G_{10}RT[C_{10}\ln C_{10}+(1-C_{10})\ln(1-C_{10})]+(G_{10}-G)RT\{C_1(\tau)\ln C_1(\tau)+[1-C_1(\tau)]\ln[1-C_1(\tau)]\}. \quad (78)$$

Consequently, the minimum of the produced work corresponds to the minimum of the irreversible losses of energy, which is proportional to ΔS.

The increment of entropy in the system, the minimum of which should be determined for a separation process of duration τ, is equal to the product of the flux and driving force:

$$\Delta S=\frac{1}{T}\int_0^\tau g(\mu_1,\mu_2)(\mu_1-\mu_2)dt\to\min. \quad (79)$$

The amount of the active component that passed through the membrane is written as

$$G=\int_0^\tau g(\mu_1,\mu_2)dt. \quad (80)$$

http://dx.doi.org/10.5772/54546

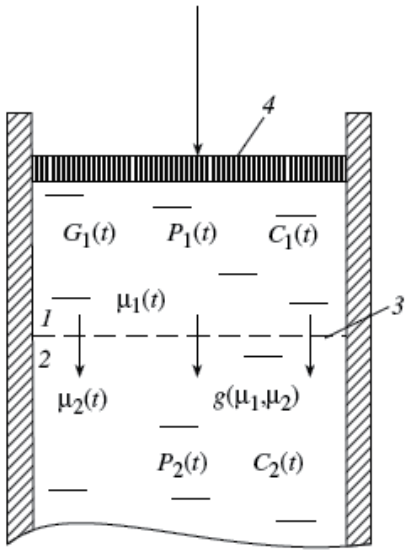

Figure 5. Batch separation of a mixture: *1*, chamber with the mixture to be separated; *2*, chamber to which the active component passes; *3*, membrane; *4*, piston.

The process duration τ will be fixed.

The variation of G_1 and concentration C_1 are determined by the equation:

$$\frac{d(G_1C_1)}{dt}=\frac{dG_1}{dt}=-g(\mu_1,\mu_2). \tag{81}$$

It follows from Eq. (81) that $\frac{d[G_1(1-C_1)]}{dt}=0$, implying that $G_1(t)(1-C_1(t))=const$ for any moment of time. The latter is equal to the amount of the "inert" component of the mixture in the first chamber. It will be denoted as $\widetilde{G}=G_1(0)[1-C_1(0)]$.

The solution of Eq. (81) determines the dependence of the mixture amount in the first chamber on the active component concentration $G_1(C_1)$:

$$G_1(t)=\frac{\tilde{G}}{1-C_1(t)}. \tag{82}$$

After expression (82) is substituted into Eq. (81), the latter takes the form

$$\frac{dC_1}{dt}=-\frac{1}{\tilde{G}_1}(1-C_1)^2 g(\mu_1,\mu_2),\quad C_1(10)=C_{10}. \tag{83}$$

First, we will find such time variation of, chemical potential $\mu_1(t)$ that the increment of entropy takes the minimum value at a specified value of G. Then, for a specific form of chemical potential, we will find the time variation of pressure $P_1(t)$ corresponding to the found optimal variation of the chemical potential.

We will write the Lagrangian function F for the problem given by Eqs. (79) and (80) in view of the fact that the constant factor 1/T does not affect the optimality condition:

$$F = g(\mu_1,\ \mu_2)(\mu_1 - \mu_2 - \lambda).$$

The mass transfer rate g is equal to zero when $\mu_1 = \mu_2$ and increases monotonically with increasing μ_1. As a result, the function F is, as a rule, convex with respect to μ_1. Consequently, this dictates the stationary of F in the solution of the problem and this solution is unique:

$$\frac{\partial F}{\partial \mu_1} = 0 \rightarrow \frac{\partial g}{\partial \mu_1}(\mu_1 - \mu_2 - \lambda) = -g(\mu_1,\ \mu_2).$$

To cancel out λ, we integrate the both sides of this equality from zero to τ in view of Eq. (80) to obtain

$$\lambda = \frac{G + \int_0^\tau \frac{\partial g}{\partial \mu_1}(\mu_1 - \mu_2)dt}{\int_0^\tau \frac{\partial g}{\partial \mu_1}dt}.$$

Consequently, to determine $\mu_1(t)$ with a convex function F, we have the equation determining the optimal variation of $\mu_2(t)$ in the function $g(\mu_1,\ \mu_2)$ for any $\mu_1(t)$ and mass transfer law $\mu_2(t)$:

$$g(\mu_1, \mu_2) = \frac{\partial g}{\partial \mu_1}\left[\frac{G + \int_0^\tau \frac{\partial g}{\partial \mu_1}(\mu_1 - \mu_2)dt}{\int_0^\tau \frac{\partial g}{\partial \mu_1}dt} - (\mu_1 - \mu_2)\right]. \tag{84}$$

If the flux is proportional to the difference of chemical potentials,

$$g = \alpha(\mu_1 - \mu_2), \tag{85}$$

it follows from optimality condition (84) that

http://dx.doi.org/10.5772/54546

$$\mu_1^*(t) = \mu_2(t) + \frac{G}{\tau\alpha}, \quad g^* = \frac{G}{\tau} = const. \tag{86}$$

The variation of $P_1(t)$ corresponding to $\mu_1^*(t)$ depends on the form of the chemical potential.

For mixtures close in properties to ideal gases, the chemical potential (molar Gibbs energy) of the active component of the mixture is written as

$$\mu_1 = \mu_{11}(T, P_1) + RT \ln C_1 = \mu_{01}(T) + RT \ln P_1 + RT \ln C_1, \tag{87}$$

where μ_{01} is the standard chemical potential for $P_1 = C_1 = 1$.

The variation of $C_1^*(t)$ (t) is determined by Eq. (83) with known mass transfer rate g. After $C_1^*(t)$ and $\mu_1^*(t)$ are substituted into Eq. (87), we obtain an expression for the pressure in the first chamber:

$$P_1^*(t) = \frac{1}{C_1^*(t)} \exp\left[\frac{\mu_1^*(t) - \mu_{01}(T)}{RT}\right]. \tag{88}$$

For the flux defined by Eq. (85) and defined by Eq. (86), Eq. (83) takes the form:

$$\frac{dC_1}{dt} = -\frac{G(1-C_1)^2}{\tau G_1} = \frac{G(1-C_1)^2}{G_{10}(1-C_{10})\tau}, \; C_1(0) = C_{10}.$$

The solution to this equation is written as

$$C_1^*(t) = \frac{G_{10}C_{10} - \frac{G}{\tau}t}{G_{10} - \frac{G}{\tau}t}. \tag{89}$$

Substituting the latter into Eq. (88) gives the time variation of the pressure:

$$P_1^*(t) = \frac{G_{10} - \frac{G}{\tau}t}{G_{10}C_1(0) - \frac{G}{\tau}t} \exp\left(\frac{\mu_2 + \frac{G}{\alpha\tau} - \mu_{10}(T)}{RT}\right).$$

After the optimal variation of $\mu_1^*(t)$, or optimal value of this chemical potential, is found, we can determine $\Delta S_{\min}$ by substituting μ_1^* and μ_2 into Eq. (79). Using the flux defined by Eq. (85) and relationship (79), we obtain

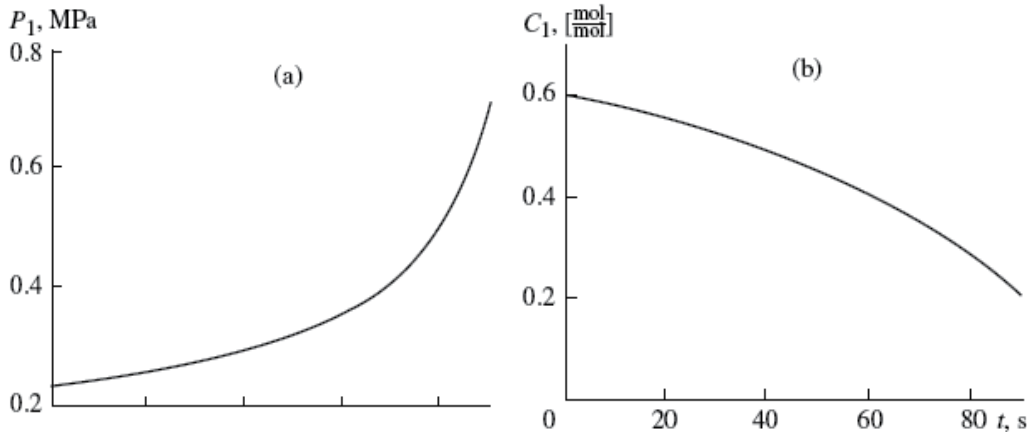

Figure 6. Optimal time variation of (a) pressure and (b) mole fraction of the active component in the first chamber for a gas mixture.

$$\Delta S_{\min} = \frac{G^2}{T\alpha\tau}.$$

The optimal variation of the pressure and mole fraction of oxygen in the first chamber is shown in Fig. 6. It corresponds to the separation of a gas mixture composed of carbon dioxide, 120 moles of CO_2, and oxygen, 180 moles of O_2 (active component), when G_{10}=300 moles, C_{10}=0.6, G=150moles, τ=90s, α=2.13×10^{-3}mol^2/(s J), P_2=101330Pa, C_2=1.0, and T=283 K. At the moment when the process is terminated, $C(\tau)$=0.2. The production of entropy is $\Delta S = \Delta S_{\min}$=415 J/K.

The produced work is $A = A^0 + T\Delta S$=415730 J, where according to Eq. (78) A_0=298300J.

Although the chemical potential for ideal solutions is written like Eq. (87), the function $\mu_{11}(T, P_1)$ for them takes a different form. This is caused by the fact that the chemical potential $\mu_1(T, P_1, x_1)$ is the molar Gibbs energy of the active component and the derivative of the chemical potential with respect to pressure is the molar volume of this component v_1 [15]. In contrast to gases, the molar volume of liquids is virtually independent of pressure and varies vary little with temperature. As

$$\frac{\partial \mu_1}{\partial P_1} = \frac{\partial \mu_{11}}{\partial P_1} = v,$$

we obtain

$$\mu_1(T, P_1, x_1) = \mu_{01}(T) + vP_1 + RT\ln C_1. \tag{90}$$

http://dx.doi.org/10.5772/54546

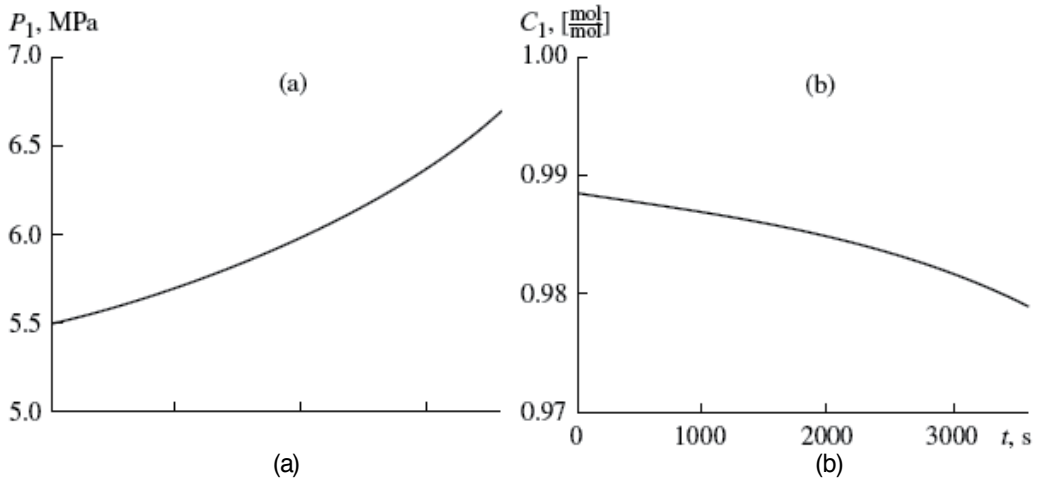

Figure 7. Optimal time variation of (a) pressure and (b) the mole fraction of the active component in the first chamber for a near-ideal solution.

For the flux defined by Eq. (85) and μ_1^* defined by Eq. (86), the variation of $C_1^*(t)$ for liquids can be written in the same way as for gases in Eq. (89). After $\mu_1^*(t)$ and $C_1^*(t)$ are substituted into Eq. (90), we obtain an equation for the optimal variation of pressure in the first chamber:

$$P_1^*(t)=\frac{1}{v_1}\left[\mu_2+\frac{G}{\tau\alpha}-\mu_{01}(T)-RT\ln\left(\frac{G_{10}C_1(0)-\frac{G}{\tau}t}{G_{10}-\frac{G}{\tau}t}\right)\right].$$

For illustration, we considered the separation of water with a high salt concentration. Like ocean water, it contained 36 g/l of salt (inert component). The other process parameters were G_{10}=552.3 moles, C_{10}=0.989, G=250moles, τ=3600s, $\alpha=9.92\times10^{-4}$mol²/(s J), P_2=101330Pa, C_2=1.0, and T=283 K. The time variation of the optimal pressure of the liquid and the mole fraction of water in the first chamber are illustrated in Fig. 7. At the moment when the process is terminated, $C(\tau)$=0.979. The production of entropy is $\Delta S=\Delta S_{\min}$=61.8 J/K. The produced work is $A=A^0+T\Delta S$=26470 J, where according to Eq. (78) A_0=8973J.

3.3. Membrane separation process distributed along the filter

The parameters of the system can vary with length rather than with time, as in the previous system. The flow diagram of this system is shown in Fig. 8. The mixture to be separated, which is characterized by a molar flux $g_1(0)=g_{10}$ and concentration $C_1(0)=C_{10}$, is continuously supplied to the first chamber, the overall length of which is L. As the mixture travels over the length l, the active component passes across the membrane into the second chamber. The concentration of the active component in the mixture to be separated at the outlet of the first chamber is $C_1(L)=C_{1L}$. The chemical potential of this component in the second chamber,

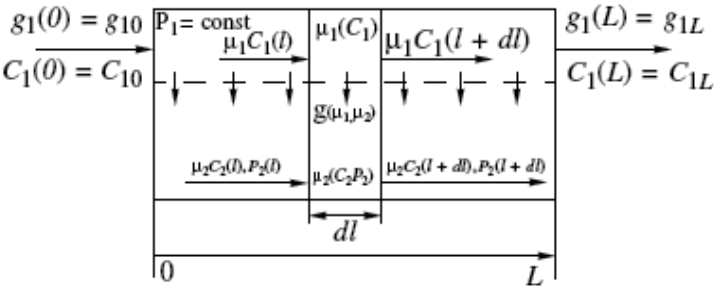

Figure 8. Continuous separation of a mixture.

$\mu_2(l)$, should be chosen so that in the isothermal process the increment of entropy in the system should be a minimum for the specified values of production rate $\bar{g}$ and total membrane surface area *s(L)*. In irreversible continuous separation, the power p expended for separation is the sum of the reversible component

$$p^0 = -g_1(0)RT[C_{10}\ln C_{10} + (1-C_{10})\ln(1-C_{10})] + (g_1(0)-\bar{g})RT[C_1(L)\ln C_1(L) + (1-C_1(L))\ln(1-C_1(L))], \tag{91}$$

which is determined at the given conditions, and the irreversible losses $p_H = T\sigma$. Consequently, the minimal production of entropy σ corresponds to the minimal separation work p.

The flux of the component to be distributed at section l is equal to $g[\mu_1(l),\ \mu_2(l)]$. The production rate is specified as

$$\int_0^L g(\mu_1,\mu_2)dl = \bar{g}. \tag{92}$$

The production of entropy is determined by the expression

$$\sigma = \frac{1}{T}\int_0^L g(\mu_1,\mu_2)(\mu_1-\mu_2)dl \to \min_{\mu_2(l)}. \tag{93}$$

Assume that $\mu_2(l)$ is the control parameter.

If the operating regime in the first chamber is close to plug flow, the material balance equations for section l give equations analogous to Eqs. (81).

$$\frac{d}{dl}(C_1 g_1) = \frac{d}{dl}g_1 = -g(\mu_1,\mu_2). \tag{94}$$

The above equation can be used to obtain a relationship analogous to Eq. (83):

http://dx.doi.org/10.5772/54546

$$\frac{dC_1}{dl} = -\frac{(1-C_1)^2}{\tilde{g}_1} g(\mu_1, \mu_2),$$
$$C_1(0) = C_{10}, \quad g_1(l) = \frac{\tilde{g}_1}{1-C_1(l)}, \tag{95}$$

where $\tilde{g}_1 = g_1(0)(1-C_{10})$ is the molar flux of the inert component through the first chamber.

Equations (92), (93), and (95) represent an optimal control problem in which C_1 is the state coordinate and the potential μ_2 is the control action. This problem can be simplified using the fact that for optimal processes the right-hand side of Eq. (95) never change the sign and C_1 monotonically varies with time. The independent variable l can be replaced by C_1. It follows from Eq. (95) that

$$dl = -\frac{\tilde{g}_1 dC_1}{(1-C_1)^2 g(\mu_1, \mu_2)}.$$

In view of this replacement, the problem given by Eqs. (92), (93), and (95) can be written as

$$\sigma = \frac{\tilde{g}_1}{T} \int_{C_{1L}}^{C_{10}} (\mu_1 - \mu_2) \frac{dC_1}{(1-C_1)^2} \to \min_{\mu_2} \tag{96}$$

with the constraints

$$\int_{C_{1L}}^{C_{10}} \frac{dC_1}{(1-C_1)^2} = \frac{\bar{g}}{\tilde{g}_1}, \tag{97}$$

$$\int_{C_{1L}}^{C_{10}} \frac{dC_1}{(1-C_1)^2 g(\mu_1, \mu_2)} = \frac{L}{\tilde{g}_1}. \tag{98}$$

The concentration C_{1L} is determined by the initial concentration C_{10} and production rate $\bar{g}$ in constraint (97) or (94). Using constraint (94), we obtain

$$C_{1L}\, g_1(L) = C_{10} g_1(0) - \bar{g}, \quad g_1(L) = g_1(0) - \bar{g}$$

and, hence,

$$C_{1L} = \frac{C_{10} g_1(0) - \bar{g}}{g_1(0) - \bar{g}}. \tag{99}$$

The same follows from constraint (97) with $\tilde{g}_1[C_{10}, g_1(0)]$. Consequently, after C_{1L} is found using constraint (99), constraint (97) can be ignored.

In distinction to batch membrane processes, the control action in a continuous membrane separation can be additionally represented by the coefficient of heat transfer $\alpha(l)$, because the membrane surface area can be varied from section to section, which corresponds to the variation of heat transfer coefficient α. Let α be a function of C_1. After $\alpha(C_1)$ and $C_1(l)$ are found, we can pass to $\alpha(l)$. The mass transfer equation can be written as

$$g(\mu_1, \mu_2) = \alpha g_0(\mu_1, \mu_2) \tag{100}$$

where g_0 is called the specific mass transfer rate. In this case, the total surface area of the membrane and, hence, the overall value of the heat transfer coefficient will be bounded:

$$\int_{C_{1L}}^{C_{10}} \alpha(C_1) dC_1 = \bar{\alpha}. \tag{101}$$

In constraint (98), the mass transfer rate can be written as Eq. (100), and equality (101) can be added to the constraints of the problem. The resulting problem, given by Eqs. (96), (98), and (101), is an isoperimetric variation problem. The necessary condition for the optimality of its solution is the requirement that the Lagrangian function should be stationary with respect to μ_2 and α:

$$F = \frac{1}{(1-C_1)^2}\left[\mu_1(C_1) - \mu_2 - \frac{\lambda_1}{\alpha g_0(\mu_1, \mu_2)}\right] - \lambda_2 \alpha,$$

where the multipliers λ_1 and λ_2 correspond to constraints (98) and (101). The conditions for the stationary of F with respect to the desired variables are written as

$$\frac{\partial F}{\partial \mu_2} = 0 \rightarrow \frac{\lambda_1 \partial g_0 / \partial \mu_2}{\alpha g_0^2(\mu_1, \mu_2)} = 1,$$

$$\frac{\partial F}{\partial \alpha} = 0 \rightarrow \frac{1}{(1-C_1)^2} \frac{\lambda_1}{\alpha^2 g_0(\mu_1, \mu_2)} = \lambda_2.$$

The above equations give the process optimality conditions:

$$\frac{\lambda_1 \partial g_0 / \partial \mu_2}{\alpha(C_1) g_0^2(\mu_1, \mu_2)} = const = \frac{1}{\lambda_1}, \tag{102}$$

http://dx.doi.org/10.5772/54546

$$\alpha^2(C_1)(1-C_1)^2 g_0(\mu_1,\mu_2) = const = \frac{\lambda_1}{\lambda_2}. \tag{103}$$

From constraints (98) and (103) we obtain

$$\frac{\lambda_1}{\lambda_2} = \frac{\tilde{g}_1 \int_{C_{1L}}^{C_{10}} \alpha(C_1) dC_1}{L} = \frac{\tilde{g}_1 \bar{\alpha}}{L}. \tag{104}$$

It follows from (101) and (102) that

$$\frac{1}{\lambda_1} = \frac{1}{\bar{\alpha}} \int_{C_{1L}}^{C_{10}} \frac{\partial g_0 / \partial \mu_2}{g_0^2(\mu_1,\mu_2)} dC_1. \tag{105}$$

After expressions (105) and (104) are substituted into conditions (102) and (103), respectively, we can use the known function $\mu_1(C_1)$ to find the functions $\mu_2^*(C_1)$ and $\alpha^*(C_1)$ that are optimal in terms of minimal irreversibility, which with the help of Eq. (95) determine $C_1^*(l)$ and, hence, $\mu_2^*(l)$ and $\alpha^*(l)$.

Let us write the above relationships specifically for the function g written as a linear function of the difference of chemical potentials, Eq. (85), and chosen functions $\mu_i(C_i)$. Assume that the specific mass transfer rate takes the form:

$g_0(\mu_1, \mu_2) = \mu_1 - \mu_2$.

Constraints (102)–(105) lead to the equations

$$\frac{1}{\alpha(C_1)(\mu_1(C_1)-\mu_2(C_1))^2} = \frac{1}{\bar{\alpha}} \int_{C_{1L}}^{C_{10}} \frac{dC_1}{(\mu_1(C_1)-\mu_2(C_1))^2}, \tag{106}$$

$$\alpha(C_1)(1-C_1)^2[\mu_1(C_1)-\mu_2(C_1)] = \frac{\tilde{g}_1 \bar{\alpha}}{L}. \tag{107}$$

For brevity, we will introduce the notation $\mu_1 - \mu_2 = \Delta\mu$ and the right-hand sides in constraints (106) and (107) will be denoted as R_1 and R_2. In this case, the above equations can be written as

$$\frac{1}{\alpha \Delta \mu^2} = R_1, \quad \alpha^2 (1 - C_1) \Delta \mu = R_2,$$

and we obtain

$$\Delta \mu^*(C_1) = \frac{(1 - C_1)^{2/3}}{R_2^{1/3} R_1^{2/3}}, \quad \alpha^*(C_1) = \frac{R_1^{1/3} R_2^{2/3}}{(1 - C_1)^{4/3}}. \tag{108}$$

The concentration of the active component in the first chamber declines with increasing l. Therefore, under optimal operating conditions, $\Delta \mu^*(l) = \Delta \mu^*[C_1(l)]$ increases while the surface area of the membrane, which is proportional to $\alpha^*(l) = \alpha^*[C_1(l)]$, decreases.

To find R_1, we will substitute Eq. (108) into Eq. (106) to obtain the equation

$$\frac{R_1^{4/3} R_2^{2/3}}{\bar{\alpha}} \int_{C_{1L}}^{C_{10}} \frac{dC_1}{(1 - C_1)^{4/3}} = R_1.$$

The evaluation of the integral gives us the desired formula:

$$R_1 = \frac{\bar{\alpha} L^2}{B^3 \tilde{g}_1^2}, \tag{109}$$

where

$$B = \left(\frac{3}{\sqrt[3]{1 - C_1(0)}} - \frac{3}{\sqrt[3]{1 - C_1(L)}} \right).$$

Equation (108) in view of Eq. (109) yields the optimal dependence of the difference of chemical potentials on the concentration C_1:

$$\Delta \mu^*(C_1) = \frac{(1 - C_1)^{2/3} B^2 \tilde{g}_1}{\bar{\alpha} L}, \tag{110}$$

$$\alpha^*(C_1) = \frac{\bar{\alpha}}{B(\sqrt[3]{1 - C_1})^4}. \tag{111}$$

Consequently, Eq. (95) takes the form:

http://dx.doi.org/10.5772/54546

$$\frac{dC_1}{dl} = -\frac{(1-C_1)^2}{\tilde{g}_1}\alpha^*(C_1)\Delta\mu^*(C_1) = -\frac{(1-C_1)^{4/3}B}{L}.$$

Integrating this equation with specified initial conditions, we can find the variation of the concentration of the active component over the length of the first chamber under optimal operating conditions:

$$C_1^*(l) = 1 - \frac{27L^3}{\left(\frac{3L}{\sqrt[3]{1-C_1(0)}} - Bl\right)^3}. \tag{112}$$

Substituting this expression into Eqs. (110) and (111) yields the variation of the desired variables over the length:

$$\Delta\mu^*(l) = \frac{9LB^2\tilde{g}_1}{\bar{\alpha}\left(\frac{3L}{\sqrt[3]{1-C_1(0)}} - Bl\right)^2}, \tag{113}$$

$$\alpha^*(l) = \frac{\bar{\alpha}\left(\frac{3L}{\sqrt[3]{1-C_1(0)}} - Bl\right)^4}{3^4 BL^4}. \tag{114}$$

The minimal value of the production of entropy corresponding to the above solution is written as

$$\bar{\sigma}_{\min} = \frac{\tilde{g}}{T}\int_{C_{1L}}^{C_{10}} \Delta\mu^*(C_1)\frac{dC_1}{(1-C_1)^2} = \frac{\tilde{g}_1^2}{LT\bar{\alpha}}B^3. \tag{115}$$

We will introduce α, the mass transfer coefficient per unit area of the membrane surface, and ds(l), the elementary membrane surface area. If $\alpha = const$, then

$$\bar{\alpha} = \alpha\int_0^L ds(l) = \alpha s(L),$$

where *s(L)* is the total contact surface area.

If the specific mass transfer coefficient of the membrane material α and the total contact surface area $s(L)$ are known, we can find the optimal distribution of the membrane surface area over the length of the filter:

$ds^*(l) = \frac{\alpha^*(l)}{\bar{\alpha}}$.

For near-ideal gas mixtures, we can write

$\mu_1(C_1) = \mu_{10}(P_1, T) + RT\ln C_1$,

where P_1 and T are assumed to be specified, and

$$\mu_2(P_2, T, C_2) = \mu_{20}(T) + RT\ln P_2 + RT\ln C_2. \tag{116}$$

When $\Delta\mu^*(C_1)$ is known, expression (116) can be used to find the pressure function in the second chamber for which $\sigma_{\min}$ is achieved:

$$P_2^*(C_1, C_2) = \frac{1}{C_2}\exp\left\{\frac{1}{RT}[\mu_1(C_1) - \mu_{20}(R) - \Delta\mu^*(C_1)]\right\}. \tag{117}$$

The optimal curves for the pressure and mass transfer coefficient are plotted in Fig. 9, in which the data refer to the separation of a gas mixture composed of carbon dioxide CO_2 and oxygen O_2 (active component) when $C_{10} = 0.6$, $g_1(0) = 3.33$ mol/s, $\bar{g} = 1.66$ mol/s, $P_1 = 2\times10^6$ Pa, $\bar{\alpha} = 3.18\times10^{-4}$ mol^2/(s J), $\alpha = 0.013$ mol^2/(s J), $L = 2.5$ m, and $T = 283$ K.

At the filter outlet, $C_1(L) = 0.2$. The production of entropy is $\sigma = \sigma_{\min} = 4.6$ J/(s K).

The consumed power is $p = p_0 + T\sigma = 4600$ J/s, where according to Eq. (91) $p_0 = 3292$ J/s.

For ideal solutions, the calculation is almost the same except for the form in which the chemical potentials are written. For the first chamber,

$\mu_1(C_1) = \mu_{10}(T) = vP_1 + RT\ln C_1$,

where v is the molar volume of the active component.

For the second chamber,

$\mu_2(P_2, T, C_2) = \mu_{20}(T) + vP_2 + RT\ln C_2$.

The dependence of the solution pressure in the second chamber on the concentration is written as

$P_2^*(C_1, C_2) = \frac{1}{v}[\mu_1(C_1) - \mu_{20}(T) - \Delta\mu^*(C_1) - RT\ln C_2]$.

http://dx.doi.org/10.5772/54546

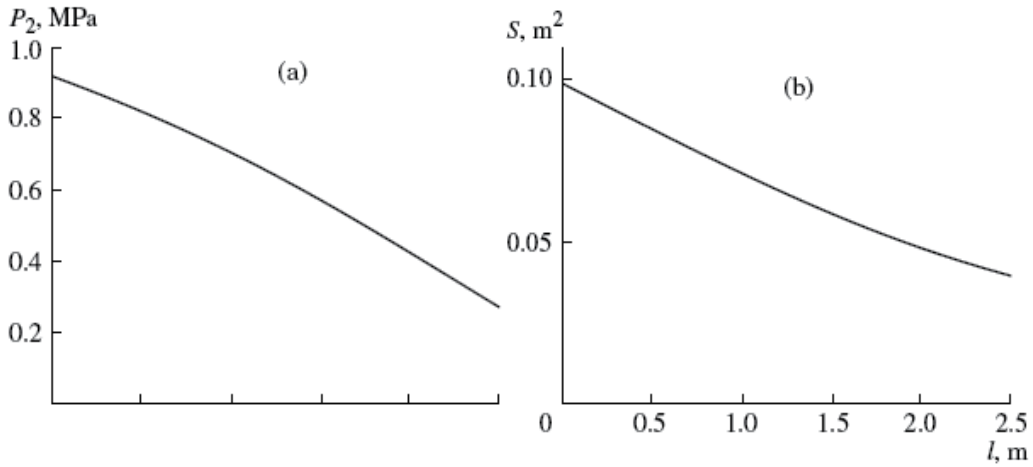

Figure 9. Optimal variation of (a) pressure and (b) the membrane surface area over the filter length for a near-ideal gas mixture.

For illustration, we considered the separation of water with a high salt concentration. Like ocean water, it contained 36 g/l of salt (inert component). The other process parameters were $g_1(0)=0.153$ mol/s, $C_{10}=0.989$, $\bar{g}=1.66$mol/s, $\bar{\alpha}=2.92\times10^{-6}$mol^2/(s J), $\alpha=0.011$mol^2/(s J), $P_1=7.7\times10^6$Pa, $L=3$m, and $T=283$ K. The profile of optimal pressure in the first chamber and the variation of the mass transfer coefficient over the filter length are illustrated in Fig. 10. At the filter outlet, $C_1(L)=0.979$. The production of entropy is $\sigma=\sigma_{\min}=0.017$ J/(s K).

The consumed power is $p=p_0+T\sigma=7.35$ J/s, where according to Eq. (91) $p_0=2.47$J/s.

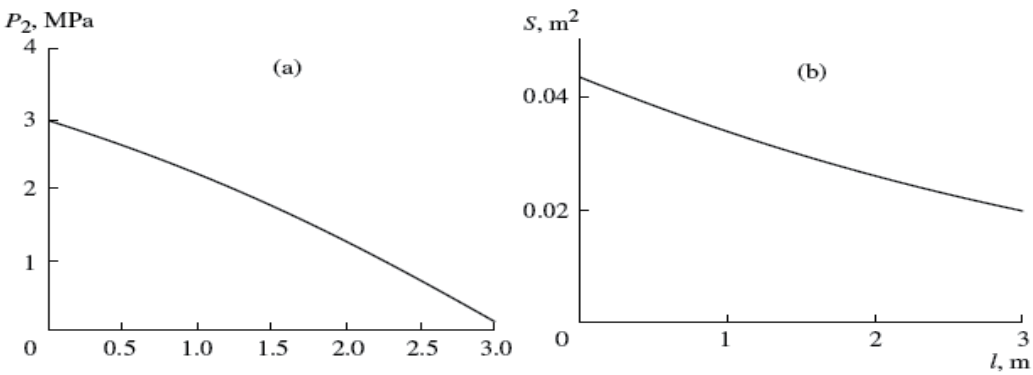

Figure 10. Optimal variation of (a) pressure and (b) membrane surface area over the filter length for a near-ideal solution.

3.4. Conclusion

The minimal losses of energy for irreversible membrane separations with specified production rates are estimated. The variation of the driving force (difference of chemical potentials) and the distribution of the membrane surface area over the filter length corresponding to the process with minimal energy losses are found.

The obtained estimates can be used for assessing the deviation of the actual membrane separation from the optimal process and for comparing the thermodynamic efficiency of membrane separation processes with different flow diagrams, as well as for formulating and solving problems regarding the optimal sequence of operations in the separation of multicomponent mixtures.

4. Optimization of diffusion systems

4.1. Introduction

The problem of deriving work from a irreversible thermodynamic system and the inverse problem of maintaining its irreversible state by consuming energy are central in thermodynamics. For systems that are not in equilibrium with respect to temperature, the first (direct) of the above problems is solved using heat engines and the second one (inverse) is solved using heat pumps. For systems that are not in equilibrium with respect to composition, the second problem is solved using separation systems and the first one is solved using diffusion engines. As a rule, separation systems and diffusion engines are based on membranes.

There is a lot of studies of membrane separation systems and diffusion engines in the literature [5,7]. In the present paper, these systems will be considered using the theory of finite-time thermodynamics. The finite-time thermodynamics, which evolved in the past years, studies the limiting performance of irreversible thermodynamic systems when the duration of the processes is finite and the average rate of the streams is specified [14, 17]. For example, some problems for heat engines, such as maximizing the power at given heat transfer coefficients and maximizing the efficiency at given power for different conditions of contact between the working body and surroundings, are already solved. In this case, the irreversible processes of the interaction of subsystems each of which is in internal equilibrium are considered.

For systems that are not uniform in concentration, it is most important to study the limiting performance of separation systems. In this case, however, the inverse problem of studying the performance of diffusion engines is of definite interest as well. The simplest variant of this problem was first formulated by Rozonoer [17]. The review of the literature shows that this problem was discussed rather superficially.

In the present paper, we will study the limiting performance of membrane systems in the separation processes with fixed rates, focusing on the following problems:

1. Minimizing the amount of energy necessary for the separation of a feed mixture with a given composition into separation products with given compositions at a given average production rate.

http://dx.doi.org/10.5772/54546

2. Maximizing the power and efficiency of diffusion engines.

The solution of these problems depends strongly on whether the feed mixture used by the engine is gaseous or liquid because this determines the form of the chemical potentials of components and, hence, the driving forces of the process. For near-ideal gas mixtures, the chemical potential of component *I* of the mixture takes the form [15]:

$$\mu_i(T,\ P_i)=\mu_0(T)+RT\ln P_i,\quad i=1,\ 2,\ \ldots,$$

where P_i is the partial pressure of component *I* and $\mu_0(T)$ is the chemical potential of the pure component. Assuming that the ratio of the partial pressure to the total pressure is equal to x_i,

$$P_i=P\,x_i=P\frac{N_i}{N},\quad i=1,\ 2,\ \ldots,$$

we can rewrite the expression for the chemical potential in the form:

$$\mu_i(T,P,x_i)=\mu_1(T,P)+RT\ln x_i, \tag{118}$$

where $\mu_1(T,\ P)=\mu_0(T)+RT\ln P$.

Although the chemical potential for liquids has the same form as Eq. (118), the form of the function $\mu_1(T,\ P)$ is different. This is caused by the fact that the chemical potential $\mu_i(T,\ P,\ x_i)$ represents the molar Gibbs energy of component I and its derivative with respect to pressure is equal to the molar volume of this component v_i [15]. In contrast to gases, the molar volume of liquids is virtually independent of pressure and weakly dependent on temperature. As

$$\frac{\partial\mu_i}{\partial P}=\frac{\partial\mu_1}{\partial P}=v_i,$$

we obtain

$$\mu_i(T,P,x_i)=\mu_1(T)+RT\ln x_i. \tag{119}$$

It is assumed that the processes are isothermal and the temperatures of all subsystems are equal to T. The problems listed above will be considered for gaseous mixtures and then for liquid solutions.

4.2. Limiting performance of diffusion systems for gaseous mixtures

4.2.1. Maximum work in a membrane process

Consider a system consisting of a thermodynamic reservoir, the intensive variables of which are fixed and are independent of mass transfer fluxes, and a working body, the intensive variables of which can be varied with time by one or another way. The system can consume

external energy or generate work. In the first case, the work will be negative; in the second, positive.

The reservoir and the working body interact through a membrane that is permeable only to one (active) component of the mixture. The mass transfer rate g depends on the chemical potentials of the active component in the reservoir μ_0 and in the working body $\mu(t)$. When these chemical potentials are equal to each other, the flux is equal to zero. In the particular case under consideration,

$$g(\mu_0, \mu) = \alpha(\mu_0 - \mu), \tag{120}$$

where α is the mass transfer coefficient. The working-body temperature T is maintained constant and equal to the reservoir temperature.

When the process duration τ and the total amount of the component G_0 transferred from the reservoir to the working body and in the reverse direction are fixed in the process characterized by a finite mass transfer coefficient, the chemical potentials μ_0 and $\mu(t)$ should differ from each other at every moment of time and the mass transfer process should be irreversible. For definiteness, we assume that $\mu_0 > \mu(0)$ and that the component is transferred from the reservoir to the working body.

The variation of the system entropy will be caused by the decrease in the reservoir entropy, the increase in the entropy of the working body, and the production of entropy due to the irreversible mass transfer σ. For a given initial state of the system (that is, the compositions of mixtures at the initial moment of time, the total amount of the substance in the working body) and a given constant value of the quantity

$$G_0 = \int_0^\tau g[\mu_0, \mu(t)]dt \tag{121}$$

the variation of the entropies of the reservoir and working body with time τ are completely determined and the minimal increase in the system entropy corresponds to the minimum of the entropy production:

$$\bar{\sigma} = \frac{1}{T}\int_0^\tau [\mu_0 - \mu(t)]g[\mu_0, \mu(t)]dt \to \min. \tag{122}$$

In this case, the function $\mu(t)$ should be chosen.

Let us find the quantitative relationship between the work A, which can be extracted (consumed) in this process, and the value of $\bar{\sigma}$. For simplicity, we assume that the mixture in the reservoir and working body consists of two components (a more general case can similarly be

http://dx.doi.org/10.5772/54546

considered by introducing an equivalent component). If the concentrations of the active component in the reservoir and working body are x_0 and $x(t)$, the concentrations of the second component will be equal to $1-x_0$ and $1-x(t)$, respectively. The variation of the substance amount G and the concentration $x(t)$ of the active component in the working body are determined by the differential equations:

$$\begin{aligned} &\frac{d}{dt}(Gx)=\frac{dG}{dt}=g(\mu_0,\mu), \quad G(0)\to fix, \\ &x(0)\to fix. \end{aligned} \tag{123}$$

As the amount of the second component is maintained constant, we obtain

$$G(0)[1-x(0)]=[G(0)+G_0][1-x(\tau)]. \tag{124}$$

It follows from (123) and (124) that

$$\begin{aligned} &\frac{dx}{dt}=\frac{1}{G(0)[1-x(0)]}(1-x)^2\,g(\mu_0,\mu), \\ &x(0)\to fix. \end{aligned} \tag{125}$$

The equations for the material, energy, and entropy balances around the system take the form:

$$G_0x_0=G(\tau)x(\tau)-G(0)x(0), \tag{126}$$

$$G_0h_0-[G(\tau)h(\tau)-G(0)h(0)]=A, \tag{127}$$

$$G_0s_0=[G(\tau)s(\tau)-G(0)s(0)]+\bar{\sigma}=0, \tag{128}$$

where h_0 and h, $s_0$and s are the molar enthalpies and entropies of the mixture in the working body and reservoir, respectively. They are related by the equation [15]:

$$s=\frac{1}{T}\left(h-\sum_{i=1}^{2}\mu_i x_i\right), \tag{129}$$

$$s_0=\frac{1}{T}\left(h_0-\sum_{i=1}^{2}\mu_{i0}x_{i0}\right). \tag{130}$$

The pressure in the working body can vary with time, provided that $P(0)=P(\tau)$. For the chemical potentials defined by Eq. (118), the equation of entropy balance (128) in view of (127), (129), and (130) can be rewritten as

$$\begin{aligned} A/T = &-\bar{\sigma} + R\{G_0[x_0 \ln x_0 + (1-x_0)\ln(1-x_0)] \\ &+G(0)[x(0)\ln x(0) + (1-x(0))\ln(1-x(0))] \\ &-G(\tau)[x(\tau)\ln x(\tau) + (1-x(\tau))\ln(1-x(\tau))]\}. \end{aligned} \tag{131}$$

The second term in the right-hand side of this equality can be calculated using G_0, x_0, $G(0)$, and $x(0)$. The latter ones are related through (124) and (126) to the values of $G(\tau)$ and $x(\tau)$. Let us denote the second term as $B[G_0,\ x_0,\ G(0),\ x(0)]$. It can be either positive or negative. It follows from equality (131) that

$$A_{\max} = T(B - \bar{\sigma}_{\min}). \tag{132}$$

The maximum of the produced (minimum of the spent) work corresponds to the minimum of entropy production in the mass transfer process.

The problem of finding the minimum of $\bar{\sigma}$ when constraint (121) is valid (or the equivalent problem for the maximum of G_0 at a given constant value of $\bar{\sigma}$) is an averaged nonlinear programming problem [22]. Unlike the problem for the constrained maximum of a function, its optimal solution can vary with time. This solution is a piecewise constant function that can take not more than two values. We will not calculate these values and the fraction of the whole process time during which $\mu^*(t)$ takes each of these values because in the most common case, where the Lagrangian function for the unaveraged problem

$$L = g[\mu_0,\ \mu(t)][\mu_0 - \mu(t) - \lambda]$$

is convex with respect to μ (second derivative of L with respect to μ is positive), the solution to the formulated problem is constant. Consequently, the constancy condition depends on the validity of the inequality:

$$\frac{\partial^2 g}{\partial \mu^2}(\mu_0 - \mu(t) - \lambda) - 2\frac{\partial g}{\partial \mu} \geq 0. \tag{133}$$

The multiplier λ, which is equal to the derivative of the minimum value of $\bar{\sigma}$ with respect to G_0, should be positive due to the physical nature of the problem. The second derivative of L with respect to μ for the mass transfer rate in the form of (120) is equal to $2\lambda\alpha$ and is known to be positive. In all cases where inequality (133) holds, the optimal value of the chemical potential of the active component for the working body is constant and determined by the equation:

http://dx.doi.org/10.5772/54546

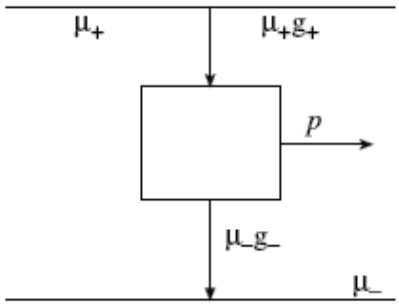

Figure 11. Schematic diagram of a diffusion engine with a constant contact between the working body and sources.

$$g(\mu_0, \mu^*) = \frac{G_0}{\tau}. \tag{134}$$

Consequently, the chemical potential of the active component of the working body for any rate satisfying (133) should be controlled so that the mass transfer rate should be constant.

The law of variation of the control variable, such as the working-body pressure, corresponding to this solution will not be constant in time because the mixture composition is varied during the process according to Eq. (125), in which the flux is determined by Eq. (134).

For mass transfer law (120), the minimal entropy produced is $\bar{\sigma}_{\min} = G_0^2 / \alpha\tau$. It follows from equality (132) that positive work can be extracted from the system under study only when $\tau > \tau_{\min} = G_0^2 / \alpha B$. It is easy to see that the process duration τ^*, for which the average extraction rate of work $A^*(\tau)/\tau$ is maximal, is twice larger than $\tau_{\min}$.

In the case where the system contains a source of a finite capacity at constant temperature and pressure instead of the reservoir (source of an infinite capacity), the fraction of the active component varies according to an equation similar to (125). As a result, the chemical potential μ_0 is changed. However, here also, the minimum of the entropy production for mass transfer law (120) corresponds to such variation of $\mu(t)$ that the mass transfer rate is maintained constant.

Instead of the calendar time, the problem can be studied using the time of contact, when the working body moves and its parameters at every point of the loop remain constant. This can be used to determine the optimal laws of pressure variation for the zones of contact between the working body and source.

4.2.2. Diffusion-mechanical cycle for maximum power

Let us consider the direct cycle of work extraction in a system consisting of a working body and two reservoirs with different chemical potentials. In the first reservoir, the chemical potential of the key element is equal to μ_+; in the second, μ_-; for definiteness, $\mu_+ > \mu_-$ (Fig. 11).

The process is cyclic: the increase in entropy, internal energy, and mass of the key component of the working body around the cycle is equal to zero. The temperatures are the same for all subsystems.

Alternating contact with reservoirs. Consider the case where the working body alternately contacts the first and second reservoirs and its parameters are cyclically varied with time. Let τ stand for the cycle duration and $\mu_0(t)$ stand for the source chemical potential, which can take the values of μ_+ and μ_-. The formulation of the problem dealing with the production of maximum work A in a given time τ takes the form:

$$A = \int_0^\tau \mu g(\mu_0, \mu) dt \to \max_{\mu_0, \mu} \tag{135}$$

with the constraints placed on the increment in the amount of the working-body:

$$\Delta G = \int_0^\tau g(\mu_0, \mu) dt = 0. \tag{136}$$

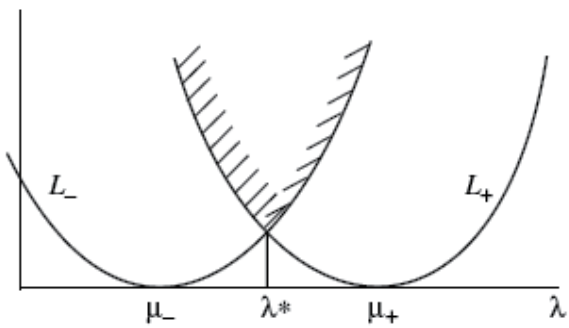

Figure 12. Dependence of the maximum of the Lagrangian function with respect to μ onλ.

To calculate the basic values of μ and μ_0 in the problem given by (135) and (136), we can write the Lagrangian function and find its maximum with respect to μ_0 and μ and its minimum with respect to λ:

$$L = \left\{ g(\mu_0, \mu)(\mu - \lambda) \right\} \to \max_{\mu_0, \mu} \min_{\lambda}.$$

The number of basic values of μ_0 is equal to two: one of them corresponds to $\mu_0 = \mu_+$ and the other to $\mu_0 = \mu_-$. For the Lagrangian function L that is strictly convex with respect to μ, the basic values of μ satisfy the conditions:

http://dx.doi.org/10.5772/54546

$$\frac{\partial L}{\partial \mu} = \frac{\partial g}{\partial \mu}(\mu - \lambda) + g(\mu_0, \mu) = 0$$

or

$$\frac{g(\mu_0, \mu)}{(\mu - \lambda)} = -\frac{\partial g(\mu_0, \mu)}{\partial \mu}.$$

The roots for this equation for $\mu_0 = \mu_+$ and $\mu_0 = \mu_-$ will be denoted by μ_1 and μ_2, respectively. As L is maximal at the basic points, we can write

$$L(\mu_+, \mu_1, \lambda) = L(\mu_-, \mu_1, \lambda), \tag{137}$$

which determines the value of λ.

Let us specify the obtained relations for

$g(\mu_0, \mu) = \alpha(\mu_0)(\mu_0 - \mu)$.

It follows from (137) that

$$\mu_1 = \frac{\mu_+ + \lambda}{2}, \quad \mu_2 = \frac{\mu_- + \lambda}{2}. \tag{138}$$

Substituting μ_1 and μ_2 into the function L for each basic value gives its dependence on λ:

$$L_+ = L(\mu_+, \mu_1) = \frac{\alpha_+}{4}(\mu_+ - \lambda)^2,$$

$$L_- = L(\mu_-, \mu_2) = \frac{\alpha_-}{4}(\mu_- - \lambda)^2.$$

The maximum of L with respect to μ_0 and μ reaches its minimal value with respect to λ (Fig. 12) when

$$L_+(\lambda) = L_-(\lambda) \to \lambda^* = \frac{\sqrt{\alpha_+}\mu_+ + \sqrt{\alpha_-}\mu_-}{\sqrt{\alpha_+} + \sqrt{\alpha_-}}. \tag{139}$$

The fractions of time τ of contact with reservoirs are determined by Eq. (136) and can be written as

$$\gamma_+ = \frac{\alpha_-\sqrt{\alpha_+}}{\alpha_-\sqrt{\alpha_+} + \alpha_+\sqrt{\alpha_-}},$$

$$\gamma_- = \frac{\alpha_+\sqrt{\alpha_-}}{\alpha_-\sqrt{\alpha_+} + \alpha_+\sqrt{\alpha_-}}.$$

The maximal work in time τ takes the form:

$$A^*(\tau)=\tau[\gamma_+\mu_1\alpha_+(\mu_+-\mu_1)+\gamma_-\mu_2\alpha_-(\mu_2-\mu_-)],$$

where μ_1 and μ_2 can be determined from (138) after the value of λ from (139) is substituted into this expression. The maximal power is equal to

$$\frac{A^*(\tau)}{\tau}=[\gamma_+\mu_1\alpha_+(\mu_+-\mu_1)+\gamma_-\mu_2\alpha_-(\mu_2-\mu_-)].$$

Constant contact with sources. In heat engines, there can be either alternate or constant contact between the working body and sources. In the latter case, the parameters of the working body are distributed and the process in it can be regarded close to reversible if the distribution of the parameters is caused by the conductive flux. Likewise, a constant contact with sources is possible in systems that are not homogeneous in concentration, such as separation systems and diffusion engines.

In this case, the maximal power takes the form of a nonlinear programming problem:

$$p=[g_1(\mu_+,\ \mu_1)\mu_1-g_2(\mu_2,\ \mu_-)\mu_2]\to\max_{\mu_1,\mu_2}$$

with the constraint

$$g_1(\mu_+,\mu_1)-g_2(\mu_2,\mu_-)=0. \tag{140}$$

The optimality constraint for this problem leads to the relation:

$$\mu_1-\mu_2=\frac{g_2(\mu_2,\mu_-)}{\partial g_2/\partial\mu_2}-\frac{g_1(\mu_+,\mu_1)}{\partial g_1/\partial\mu_1}, \tag{141}$$

which together with equality (140) determines the desired variables.
Let g_1 and g_2 are proportional to the difference between the chemical potentials:

$$g_1=\alpha_1(\mu_+-\mu_1),\quad g_2=\alpha_2(\mu_2-\mu_-).$$

Equality (141) can be written in the form:

$$\mu_1-\mu_2=\frac{\mu_+-\mu_-}{2}. \tag{142}$$

The constraint $g_1=g_2$ results in

$$\alpha_1\mu_1+\alpha_2\mu_2=\alpha_1\mu_++\alpha_2\mu_-. \tag{143}$$

The solution to Eqs. (142) and (143) can be written as

http://dx.doi.org/10.5772/54546

$$\mu_2^* = \frac{1}{2(\alpha_1 + \alpha_2)}[\mu_+\alpha_1 + \mu_-(\alpha_1 + 2\alpha_2)],$$

$$\mu_1^* = \frac{1}{2(\alpha_1 + \alpha_2)}[\mu_+(\alpha_2 + 2\alpha_1) + \mu_-\alpha_2].$$

The value of maximal power corresponding to this choice is

$$p_{\max} = \frac{\bar{\alpha}}{4}(\mu_+ - \mu_-)^2,$$

where the equivalent mass transfer coefficient is defined as

$$\bar{\alpha} = \frac{\alpha_1\alpha_2}{\alpha_1 + \alpha_2}.$$

4.3. Limiting performance of diffusion systems for liquid mixtures

The result obtained above for the membrane systems consisting of a working body and a source of finite or infinite capacity using gaseous mixtures can be translated in the same form to liquid solutions with allowance for the different form of the chemical potential. Diffusion engines are most often designed for the treatment of saline water. Let us consider two flow-sheets of liquid diffusion engines.

4.3.1. Diffusion engine with a constant contact between the working body and the sources

Let the system consist of two liquids with the same temperature separated by a semipermeable membrane. One of the liquids is a pure solvent and the other is a solution in which some substance of concentration *C* is dissolved. The membrane is permeable only to the solvent. The equilibrium in the system is reached as soon as the chemical potentials calculated by formula (119) become equal to each other:

$$v_0 P_0 - v_r P_r = -RT \ln x_r.$$

Let the difference of pressure across the membrane be denoted as π. Also, we will keep in mind that the molar volumes v_0 and v_r for low concentrations are equal to each other. The mole fraction of the dissolved component will be denoted as x_1. If its value is low, then $\ln x_r = \ln(1 - x_1) \approx -x_1$. In this case,

$$\pi = RT\frac{x_1}{v_0} = -RTC. \tag{144}$$

Equation (144) is called the Van't Hoff equation for osmotic pressure.

Consider the system shown in Fig. 13. The chamber to the left of the membrane contains a pure solvent at an environmental pressure equal to P_0. The chamber of volume V to the right of the membrane contains a continuously replenished solution in which the concentration of the

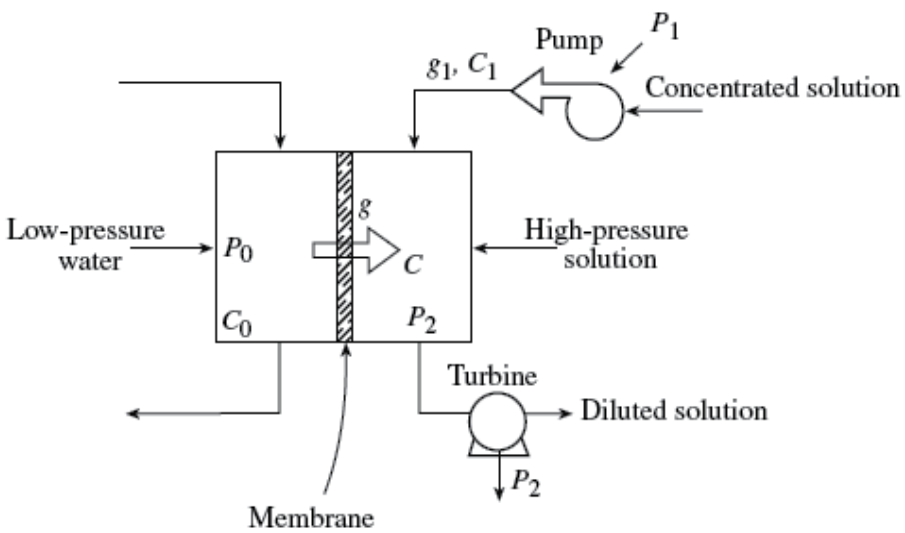

Figure 13. Schematic diagram of a diffusion engine with a constant contact between the working body and sources.

dissolved component is C. The pressure in the right chamber is P_2 and the solution is assumed to be ideal. When an equilibrium is reached in the right chamber (that is, the flux through it is equal to zero), the pressure established in it will exceed P_0 by the value of osmotic pressure π. The osmotic pressure value is related to the concentration and temperature in the chamber by the Van't Hoff equation. When the solution in the chamber is replenished, the pressure $P_2 < P_0 + \pi$, giving rise to a solvent flux g across the semipermeable membrane. Conventionally, the diffusion flux is taken to be equal to the difference between the actual and equilibrium pressures:

$$g = \alpha(P_0 + \pi - P_2) = \alpha(\pi - \Delta P), \tag{145}$$

where $\Delta P = P_2 - P_0$

Let p_1 stand for the power of the pump supplying the concentrated solution, g_1 stand for the flow rate of this solution, and C_1 stand for the solution concentration. Assuming that the pump efficiency is 100%, we obtain

$p_1 = \Delta P g_1$.

The additional flux across the membrane increases the volume of the solution, which drives a turbine and generates power p_2:

$p_2 = (g_1 + g)\Delta P$.

Consequently, the power r and efficiency η of the saline diffusion engine can be written as

http://dx.doi.org/10.5772/54546

$$p = p_2 - p_1 = g\Delta P = \alpha(\pi - \Delta P)\Delta P,$$
$$\eta = \frac{P}{g_1} = \frac{\alpha(\pi - \Delta P)\Delta P}{g_1}.$$

where the diffusion engine efficiency is the work extracted from 1 m^3 of the concentrated solution. From here on, according to the accepted system of units, the units of power and efficiency referred to a unit membrane surface area are J/(m^2 s) and J/m^3, respectively. If the relationship between π and ΔP is ignored, the power reaches a maximum when $\Delta P = \pi / 2$ and its upper limit is written as

$$\bar{p} = \alpha\pi^2 / 4 = \alpha / 4(CRT)^2.$$

As$C < C_1$, the value of the power is always less than

$$\bar{p}^* = \alpha / 4(C_1 RT)^2. \tag{146}$$

which is the upper bound for the maximal power.

The estimate produced by Eq. (146) can be refined if we take into consideration that g, ΔP, and C are related to each other by Eq. (145) and the equation of material balance on the dissolved component

$$(g_1 + g)C = g_1 C_1. \tag{147}$$

Expressing C and ΔP in terms of g from Eqs. (145) and (147) and substituting them into p and η, we obtain

$$C = \frac{g_1 C_1}{g_1 + g}, \quad \Delta P = CRT - \frac{g}{\alpha}, \tag{148}$$

$$p = g\Delta P = \frac{RTC_1 g_1 g}{g_1 + g} - \frac{g^2}{\alpha}, \tag{149}$$

$$\eta = \frac{\alpha(\pi - \Delta P)\Delta P}{g_1} = \frac{RTC_1 g}{g_1 + g} - \frac{g^2}{\alpha g_1}. \tag{150}$$

The points of maximum with respect to g for two concave functions (149) and (150) coincide. Consequently, to find the optimal value of g^*, we will use one of the functions, specifically the expression for p. The condition for the maximum with respect to g leads to the inequality:

$$g(g_1 + g)^2 = \frac{\alpha RT g_1^2 C_1}{2}. \tag{151}$$

Equation (151) can be rewritten as

$$\frac{g^3}{g_1^2} + 2\frac{g^2}{g_1} + g = \frac{\alpha RTC_1}{2} \tag{152}$$

and its right-hand side can be denoted for brevity as M. Its solution will be denoted as g^*. It is obvious that it satisfies the inequality:

$0 < g < M$.

Numerical solution of Eq. (152) makes it possible to refine the value of the limiting power of the diffusion engine and find the corresponding operating conditions. Equation (151) determines g^* for the chosen values of g_1 and C_1; Eq. (148), for C^* and ΔP^*.

It should be noted that the ideal solution bounds the value of the concentration of the working solution:

$$C = C_1 \frac{g_1}{g_1 + g}.$$

The concentration should not be very high: otherwise, the molecules of the dissolved component will interact with each other and relation (144) is upset.

Diffusion Engine with an Alternate Contact between the Working Body and Sources. In the schematic diagram of the diffusion engine discussed in the preceding section, the working body was an open system working in constant contact with two sources under steady-state conditions. One of them supplied a concentrated solution and the other supplied a solvent.

Figure 14 shows the schematic diagram for a diffusion engine in which the working body alternately contacts each of the sources, receiving a solvent through one membrane and giving it up to a concentrated solution through another membrane. In this case, the pressure and flow rate of the working body are periodically varied: pressure increases for a lower flow rate (power p_1 is consumed) and decreases for a higher flow rate (power p_2 is generated).

We will write the balance equations for this diagram and study its limiting performance, ignoring the energy losses for driving the flow of the concentrated solution through the bottom chamber and assuming that the concentration of the dissolved component in the g_2 flow is equal to unity and that the pressure of the surrounding medium is equal to P_0. For simplicity, flow rates will be used instead of mole fluxes

The engine power is

$p = p_2 - p_1 = (g_1 + g)\Delta P_{21} - g_1 \Delta P_{21} = g\Delta P_{21}$,

http://dx.doi.org/10.5772/54546

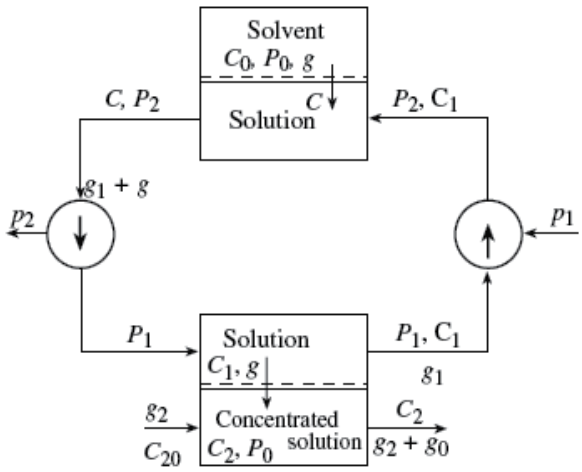

Figure 14. Schematic diagram of a diffusion engine with an alternate contact between the working body and sources.

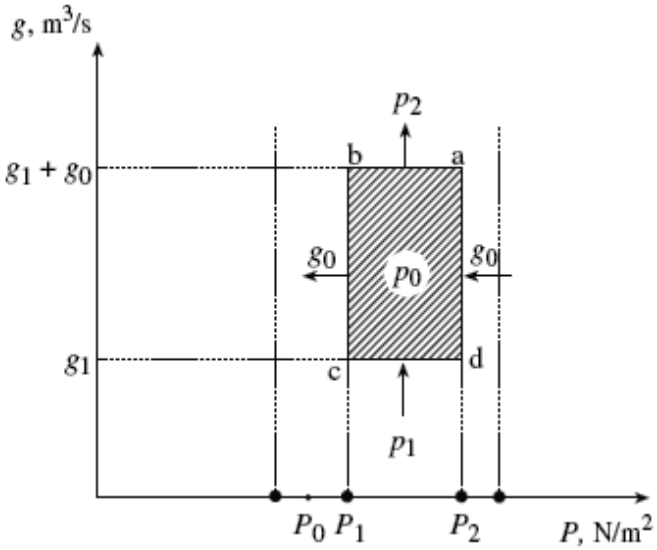

Figure 15. Variation cycle for the parameters of the working body in a diffusion engine.

where

The efficiency will be defined as the ratio of power p to the flow rate g_2 of the dissolved component:

$$h = \frac{p}{g_2} = \frac{g}{g_2} \Delta P_{21}.$$

The rate of mass transfer is determined by the relations:

$$g = \alpha_1(P_0 + \pi - P_2) = \alpha_1(\pi - \Delta P_{20}) \\ = \alpha_2[(P_1 + \pi_2) - (P_0 + \pi_1)] = \alpha_2(\Delta\pi_{21} + \Delta P_{10}), \tag{153}$$

where $\Delta P_{20} = P_2 - P_0$, $\Delta\pi_{21} = \pi_2 - \pi_1$, $\Delta P_{10} = P_1 - P_0$. Equation (153) corresponds to the condition that the mass of the working body averaged over the cycle is constant.

Figure 15 demonstrates the cycle of the working body of this diffusion engine. The power p_1 is equal to the area of the rectangular P_2dcP_1, and the power p_2 to the area of P_2abP_1. The engine power p is equal to the area of the hatched rectangular *abcd*.

The power of the diffusion engine will be determined when the relationship between the osmotic pressures in the chambers and the flow rates is ignored. To do it, we will solve the problem of constrained optimization:

$p = (P_2 - P_1)g \to \max\limits_{P_1, P_2}$

with the constraints:

$$\alpha_1(P_0 + \pi - P_2) = \alpha_2(P_1 - P_0 + \pi_2 - \pi_1) = g. \tag{154}$$

It follows from Eq. (154) that

$P_1 = \frac{g}{\alpha_2} + P_0 + \pi_1 - \pi_2$, $P_2 = P_0 + \pi - \frac{g}{\alpha_1}$.

Let us introduce the equivalent permeability:

$\bar{\alpha} = \frac{\alpha_1\alpha_2}{\alpha_1 + \alpha_2}$

and write the equation:

$P_2 - P_1 = \pi - \pi_1 + \pi_2 - \frac{g}{\alpha}$.

Then

$$p = g(\pi - \pi_1 + \pi_2 - \frac{g}{\alpha}) = g(\pi + \Delta\pi_{21} - \frac{g}{\alpha}) \to \max_g. \tag{155}$$

The maximum of this expression, which is equal to

$p^* = \frac{\bar{\alpha}(\pi - \pi_1 + \pi_2)^2}{4} = \frac{\alpha(\pi + \Delta\pi_{21})^2}{4}$,

is reached at

http://dx.doi.org/10.5772/54546

$$g^* = \frac{\bar{\alpha}(\pi - \pi_1 + \pi_2)}{2} = \frac{\alpha(\pi + \Delta\pi_{21})}{2}.$$

Keeping in mind that the osmotic pressures in the chambers are related to the concentrations by Van't Hoff equation (144) and the concentrations are related to the flow rates g_1, g_2, and g, we obtain

$$\pi = CRT = C_1 \frac{g_1 RT}{g_1 + g},$$

$$\Delta\pi_{21} = (C_2 - C_1)RT = \left(\frac{g_2 C_{20} + g C_1}{g_2 + g} - C_1 \right) RT.$$

In view of these relations, expression (155) for the engine power takes the form:

$$\begin{aligned} p &= g\left[RT\left(\frac{C_1 g_1}{g_1 + g} + \frac{g_2 C_{20} + g C_1}{g_2 + g} - C_1 \right) - \frac{g}{\alpha} \right] \\ &= g\left[RT\left(\frac{g_2 C_{20} + g C_1}{g_2 + g} - \frac{C_1 g}{g_1 + g} \right) - \frac{g}{\alpha} \right] \to \max_g. \end{aligned} \tag{156}$$

The expression for the efficiency is written as

$$\eta = \frac{g}{g_2}\left[RT\left(\frac{g_2 C_{20} + g C_1}{g_2 + g} - \frac{C_1 g}{g_1 + g} \right) - \frac{g}{\alpha} \right] \to \max_g. \tag{157}$$

The points of maximum with respect to g for the criteria (156) and (157) coincide. Therefore, we can use either of them in the conditions of optimality to find g^*. The stationarity condition of p with respect to g leads to an equation for the optimal flow rate:

$$g = \frac{\bar{\alpha} RT}{2}\left[\left(\frac{g_2^2 C_{20} + 2 g g_2 C_1 + g^2 C_1}{(g_2 + g)^2} \right) - C_1 \frac{g(g + 2g_1)}{(g_1 + g)^2} \right]. \tag{158}$$

The solution to Eq. (158) will be g^*: it is the optimal value of flow rate g at which the efficiency η and power p take their maximal values. The values of flow rate g^* depends on the values of g_1, g_2, and C_1. Its substitution into the equations for p and η determines the maximal power $p^*(g_1, g_2, C_1)$ and efficiency $\eta^*(g_1, g_2, C_1)$. The nonnegative nature of p^* and η^* imposes

constraints on the possible values of g_1, g_2, and C_1. For example, increasing g_1 and g_2 or decreasing C_1 causes an increase in p^*.

4.4. Conclusion

The estimates obtained in the present paper for the limiting performance of diffusion engines can be used to make their reversible-thermodynamics analysis more accurate and consider the influence of the kinetic factors (mass transfer relations, membrane permeabilities) and production flow rate. These estimates can also be used for the optimization of more complex membrane systems. The capacity of membrane systems increases in proportion to the membrane permeability. In this case, the performance of membranes is decreased by the nonuniformity of concentrations in the solution, polarization phenomena, and the other factors ignored in obtaining the above estimates.

Author details

A.M. Tsirlin* and I.N. Grigorevsky

*Address all correspondence to: tsirlin@sarc.botik.ru; ivan_ger@mail.ru

The Program Systems Institute of RAS, Pereslavl – Zalessky, Russia

References

[1] Amelkin, S. A, Burtcler, I. M, Hoffman, K. H, & Tsirlin, A. M. *Estimates of Limiting Possibilities of Separation Process;.* Theor. Found. Chem. Tech. (1983).

[2] Andresen, B. *Finite-Time Thermodynamics.* Copenhagen: Univers, (1983).

[3] Berry, R. S, Kazakov, V, Sieniutycz, S, Szwast, Z, & Tsirlin, A. M. *Thermodynamic Optimization of Finite Time Processes,* Wiley: Chichester, U.K., (1999).

[4] Bosnajakovic, F. *Technical Thermodynamics;* Holt, Rinehart and Winston: New York, (1965). , 2

[5] (Brock, T.D. Membrane Filtration. A User's Guide and Reference Manual, Heidelberg: Seiten-Springer, 1983. Translated under the title Membrannaya fil'tratsiya, Moscow: Mir, 1987).

[6] Curzon, F. L, & Ahlborn, B. *Efficiency of a Carnot Engine at Maximum Power Output.* Am. J. Phys. (1975). , 1975(43), 22-24.

http://dx.doi.org/10.5772/54546

[7] Dubyaga, V. P, Perepechkin, L. P, & Katalevskii, E. E. *Polymer Membranes*, Moscow: Khimiya, (1981).

[8] DytnerskiiYu.I., Brykov, V.P., and Kagramanov, G.G., *Membrannoe razdelenie gazov (Membrane Separation of Gases)*, Moscow: Khimiya, (1991).

[9] Hwang, S, & Kammermeyer, T. K., *Membranes in Separations,* New York: John Wiley & Sons, (1975).

[10] Kesting, R. E. *Synthetic Polymeric Membranes,* New York: Wiley, (1985).

[11] KirshYu.E., *Water Soluble Poly-N-Vinylamides. Synthesis and Physicochemical Properties,* Chichester: Wiley, (1998).

[12] Novikov, I. I. *The Efficiency of Atomic Power Stations.* J. Nucl. Energy II (USSR) (1958). , 1958(7), 125-128.

[13] Orlov, V. N, & Rozonoer, L. I. *Estimates of Efficiency of Controlled Thermodynamic Processes Based on the Balance Equations of Mass, Energy and Entropy.* Abstracts of the 10th All-Union Conference on Control Problems, Moscow, AN SSSR, IPU, (1986). , 75-76.

[14] Orlov, V. N, & Rudenko, A. V. *Optimal Control in Problems of the Limiting Performance of Irreversible Thermodynamic Processes*, Avtom. Telemekh., (1985). (5), 27-41.

[15] Prigogine, I, & Defay, R. *Chemical Thermodynamics,* London: Longmans Green, (1954).

[16] Rozonoer, L. I, & Tsirlin, A. M. *Optimal Control of Thermodynamic Processes.* Autom. Remote Control (1983).

[17] Rozonoer, L. I. *Optimal Thermodynamic Processes with Chemical Reaction and Diffusion, in Thermodynamics and Regulation of Biological processe;* Moscow: Nauka, (1984).

[18] Salamon, P, & Nitzan, A. *Finite Time Optimizations of a Newton's Law Carnot Cycle*, J. Chem. Phys., (1981). , 20(1), 51.

[19] Shambadal, P. *Development and Application of the Concept of Entropy;* Nauka: Moscow, (1967).

[20] Timashev, S. F. *Physical Chemistry of Membrane Processes,* Chichester: Ellis Horwood, (1991).

[21] Tsirlin, A. M. *Irreversible-Thermodynamics Estimates of the Limiting Performance of Thermodynamic and Microeconomic System;* Moscow: Nauka, (2003).

[22] Tsirlin, A. M. *Methods of Averaged Optimization and Their Applications;* Moscow: Fizmatlit, (1997).

[23] Tsirlin, A. M. *Optimal Processes in Thermodynamics and Microeconomics;* Nauka: Moscow, (2003).

[24] Tsirlin, A. M, Mironova, V. A, Amelkin, S. A, & Kazakov, V. A. *Finite-Time Thermodynamics: Conditions of Minimal Dissipation for Thermodynamic Process with Given Rate.* Phys. ReV. E (1998).

[25] Tsirlin, A. M. *Separation of Ideal Mixtures in Multistage Systems: An Algorithm for Selecting a Separation Sequence*; Theoretical Foundations of Chemical Engineering, (2012). , 46(2), 128-134.

[26] Tsirlin, A. M, & Grigorevsky, I. N. *Thermodynamical estimation of the limit potentialiies of irreversible binary distillation*. J. Non-Equilib. Thermodyn. 35 (2010). , 213-233.

Chapter 3

Successive Linearization of Heat and Mass Transfer over an Unsteady Stretching Permeable Surface in the Presence of Thermal Radiation and a Variable Chemical Reaction

Stanford Shateyi and Sandile S. Motsa

Additional information is available at the end of the chapter

http://dx.doi.org/10.5772/51228

1. Introduction

Theoretical studies of viscous incompressible flows over continuous stretching surfaces through a quiescent fluid have their origins in the pioneering work of Crane 1970. These types of flows occur in many industrial processes, such as in glass fibre production, food stuff processing reactor fluidization, and transpiration cooling. The prime aim in almost every extrusion is to maintain the surface quality of the extrudate. The pioneering works of Crane have been extended by many researchers to explore various aspects of the flow and heat and mass transfer occurring in infinite domains of the fluid surrounding the stretching sheet, [Liu and Andersson 2008; Abd EL-Aziz 2009; Abel and Mahesha 2008; Shateyi and Motsa 2009; Ziabakhsh et al. 2010; Motsa and Sibanda 2011], among others.

Many practical diffusive processes involve molecular diffusion of species in the presence of chemical reaction within and/or at the boundary. Chemical reaction can tremendously alter diffusion rates in convective heat and mass transfer processes. The effect of a chemical reaction depends on whether the reaction is heterogenous or homogeneous, as well as whether it occurs at an interface or a single phase volume reaction. We call a reaction of order n, if the reaction rate is proportional to the nth power of the concentration. The study of chemical reaction processes is useful for improving a number of chemical technologies such as polymer production and food processing. Various aspects of this problem have been studied by some researchers (Alam et al. 2009; Shateyi et al. 2010; Cortel 2007; Alam and Ahammad 2011; Afify and Elgazery 2012).

There has been much interest in the study of radiative heat transfer flows due to the effect of radiation on performance of many engineering systems applying electrically conducting fluids. Many engineering processes such as nuclear plants, gas turbines, satellites and space vehicles, take place at high temperatures and thus the effect of thermal radiation cannot be

ignored. Recently, flow, heat and/or mass transfer with thermal radiation have been studied by (Abd El-Aziz 2008; Shateyi and Motsa 2009; Pal and Mondal 2011).

In this chapter, we explore the semi analytic solution of the non linear heat and mass transfer over an unsteady stretching permeable surface with prescribed wall conditions in the presence of thermal radiation and a non-uniform chemical reaction. The proposed method of solution employed in this work is based on an extension of the quasilinearization method (QLM) that was initially proposed in Bellman and Kalaba (1965). This method employs Taylor series linearization to convert a nonlinear two-point boundary value problem into an iterative scheme of solution which can be integrated using various numerical techniques. Mandelzweig and his co-workers (see for example, Krivec et al. 1991; Mandelzweig 2005; Krivec and Mandelzweig 2008, among others) have recently extended the application of the QLM to a wide variety of nonlinear BVPs and established that the method converges quadratically. The integration of the QLM iteration scheme is performed using the Chebyshev spectral collocation method Canuto et al. 1988. Several studies (see for example, Awad et al.2011; Makukula et al. 2010a; Makukula et al. 2010b; Makukula et al. 2010c; Makukula et al. 2010d; Motsa 2011; Motsa and Shateyi 2010; Motsa 2011 and Shateyi Motsa 2011) have shown that blending the Chebyshev spectral method with iteration schemes like the QLM results in a highly accurate method which can be used to solve a wide variety of nonlinear boundary value problems.

In this work we present new iteration schemes which are based on systematically extending the QLM. The objective of this work is to demonstrate that the convergence rate of the QLM can be significantly improved by using the proposed iterations schemes.

2. Mathematical formulation

The study investigates the unsteady laminar boundary layer in a quiescent viscous incompressible fluid on a horizontal sheet which comes through a slot at the origin. At $t = 0$, the sheet is stretched with velocity $U_w(x,t)$ along the x-axis, keeping the origin in the fluid of ambient temperature T_∞ and concentration C_∞. The RosseLand approximation is used to describe the radiative heat flux in the energy equation. We also assume a variable chemical reaction.

The velocity, temperature and concentration fields in the boundary layer are governed by the two dimensional boundary layer equations for mass, and chemical species given by

$$\frac{\partial u}{\partial x} + \frac{\partial v}{\partial y} = 0, \tag{1}$$

$$\frac{\partial u}{\partial t} + u\frac{\partial u}{\partial x} + v\frac{\partial u}{\partial y} = \nu\frac{\partial^2 u}{\partial y^2}, \tag{2}$$

$$\frac{\partial T}{\partial t} + u\frac{\partial T}{\partial x} + v\frac{\partial T}{\partial y} = \alpha_0\frac{\partial^2 T}{\partial y^2} - \frac{1}{\rho cp}\frac{\partial q_r}{\partial y}, \tag{3}$$

$$\frac{\partial C}{\partial t} + u\frac{\partial C}{\partial x} + v\frac{\partial C}{\partial y} = D_m\frac{\partial^2 C}{\partial y^2} - K_l(C - C_\infty)^n, \tag{4}$$

Where u, v are the velocity components in the x and y directions,respectively, ν is the kinematic viscosity,g is the acceleration due to gravity, ρ is the density of the fluid, T and T_∞

http://dx.doi.org/10.5772/51228

are the temperature of the fluid inside the thermal boundary layer and of the fluid in the free stream, respectively while C and C_∞ are the corresponding concentrations, α_0 is the thermal diffusivity, c_p is the specific heat at constant pressure, D_m is the mass diffusivity and q_r is the radiative heat flux.

The boundary conditions are given as follows:

$$u = U_w, \;\; v = V_w, \;\; T = T_w, \;\; C = C_w \quad \text{at} \;\; y = 0, \tag{5}$$

$$u \to 0, \;\; T \to T_\infty, \;\; C = C_\infty, \;\; \text{as} \;\; y \to \infty. \tag{6}$$

The stretching velocity $U_w(x,t)$, the surface temperature $T_w(x,t)$ and the surface concentration are assumed to be of the form: $U_w(x,t) = a/(1-ct)$, $T_w(x,t) = T_\infty + bx/(1-ct)$, $C_w(x,t) = C_\infty + bx/(1-ct)$, where a, b and c are positive constants with (ct<1), and both a and c have dimension reciprocal time.

The radiative heat flux q_r is described by the Rosseland approximation such that

$$q_r = -\frac{4\sigma^*}{3K}\frac{\partial T^4}{\partial y}, \tag{7}$$

where σ^* and K are the Stefan-Boltzman constant and the mean absorption coefficient, respectively. Following Chamkha (1997), we assume that the temperature differences within the flow are sufficiently small so that the T^4 can be expressed as a linear function after using Taylor series to expand T^4 about the free stream temperature T_∞ and neglecting higher order terms. This results in the following approximation

$$T^4 \approx 4T_\infty^3 T - 3T_\infty^4 \tag{8}$$

Using equations (7) and (8) in equation (3) we obtain

$$\frac{\partial q_r}{\partial y} = -\frac{16\sigma^* T_\infty^3}{3K}\frac{\partial^2 T}{\partial y^2}.$$

2.1. Similarity solutions

Now we introduce the following dimensionless functions of f, θ and ϕ and similarity variable η (Ishak et al., 2009).

$$\eta = \left(\frac{U_w}{\nu x}\right)^{\frac{1}{2}} y, \;\; \psi = (\nu x U_w)^{\frac{1}{2}} f(n), \;\; \theta(n) = \frac{T - T_\infty}{T_w - T_\infty}, \;\; \phi = \frac{C - C_\infty}{C_w - C_\infty}, \tag{9}$$

where

$\psi(x,y,t)$ is a stream function defined as $u = \frac{\partial \psi}{\partial y}$ and $v = -\frac{\partial \psi}{\partial x}$

The governing equations are then transformed into a set of ordinary equations and associated boundary conditions as given below:

$$f''' + ff'' - (f')^2 - A(f' + \frac{\eta}{2}f'') = 0, \tag{10}$$

$$(3R+4)\theta'' + 3RPr[f\theta' - 2f'\theta - \frac{A}{2}(3\theta + \eta\theta')] = 0, \tag{11}$$

$$\phi'' + Sc[f\phi' - 2f'\phi - \frac{A}{2}(3\phi + \eta\phi')] - ScK\phi^n = 0, \tag{12}$$

where A=c/a is the component that measures the unsteadiness, $Pr = \nu/\alpha$ is the Prandtl number, $R = 16\sigma T_\infty^3/3Kk$ is the radiation parameter, $Sc = \nu/D_m$ is the Schmidt number and $K = K_l(C_w - C_\infty)^{n-1}x/U_w(x,t)$ is the local chemical reaction parameter.

The boundary conditions are:

$$f(0) = f_w,\ f'(0) = 1,\ \phi(0) = 1,\ \theta(0) = 1, \tag{13}$$

$$f'(\infty) = 0,\ \theta(\infty) = 0,\ \phi(\infty) = 0, \tag{14}$$

with $f_w < 0$ and $f_w > 0$ corresponding to injection and suction, respectively.

3. Method of solution

To solve the governing system of equations (12 - 14) we observe that equation (10) depends on $f(\eta)$ only. Thus, it can be solved independently of the other equations in the system. The solution for $f(\eta)$ is then substituted in equations (11) and (12) which can also be solved for θ and ϕ separately. We begin by obtaining the solution for $f(\eta)$. We assume that an estimate of the the solution of (10) is f_γ. For convenience, we introduce the following notation

$$f_0 = f, \quad f_1 = f', \quad f_2 = f'', \quad f_3 = f'''. \tag{15}$$

In terms of the new variables (15), equation (10) can be written as

$$L[f_0, f_1, f_2, f_3] + N[f_0, f_1, f_2, f_3] = 0, \tag{16}$$

where

$$L[f_0, f_1, f_2, f_3] = f_3 - A(f_1 + \frac{\eta}{2}f_2), \quad N[f_0, f_1, f_2, f_3] = f_0 f_2 - f_1^2 \tag{17}$$

We introduce the following coupled system,

$$L[f_0, \ldots, f_3] + N(f_{0,\gamma}, \ldots, f_{3,\gamma}) + \sum_{s=0}^{3}(f_s - f_{s,\gamma})\frac{\partial N}{\partial f_s}(f_{0,\gamma}, \ldots, f_{3,\gamma}) + G(f_0, \ldots, f_3) = 0, \tag{18}$$

$$G(f_0, \ldots, f_3) = N(f_0, \ldots, f_3) - N(f_{0,\gamma}, \ldots, f_{3,\gamma}) - \sum_{s=0}^{3}(f_s - f_{s,\gamma})\frac{\partial N}{\partial f_s}(f_{0,\gamma}, \ldots, f_{3,\gamma}). \tag{19}$$

http://dx.doi.org/10.5772/51228

Note that when equations (18) and (19) are added, we obtain equation (16). Separating the known and unknown variables, equation (18) can be written as

$$L[f_0,\ldots,f_3]+\sum_{s=0}^{3} f_s\frac{\partial N}{\partial f_s}(f_{0,\gamma},\ldots,f_{3,\gamma})+G(f_0,\ldots,f_3)=0 \tag{20}$$

where

$$H(f_{0,\gamma},\ldots,f_{3,\gamma})=\sum_{s=0}^{3} f_{s,\gamma}\frac{\partial N}{\partial f_s}(f_{0,\gamma},\ldots,f_{3,\gamma})-N(f_{0,\gamma},\ldots,f_{3,\gamma}) \tag{21}$$

We use the quasilinearization method (QLM) of Bellman and Kalaba (1965) to solve equation (20). The QLM determines the $(i+1)$th iterative approximation $f_{s,i+1}$ as the solution of the differential equation

$$\begin{aligned} &L[f_{0,i+1},\ldots,f_{3,i+1}]+\sum_{s=0}^{3} f_{s,i+1}\frac{\partial N}{\partial f_s}(f_{0,\gamma},\ldots,f_{3,\gamma})+G(f_{0,i},\ldots,f_{3,i}) \\ &+\sum_{s=0}^{3}(f_{s,i+1}-f_{s,i})\frac{\partial G}{\partial f_s}(f_{0,i},\ldots,f_{3,i})=H(f_{0,\gamma},\ldots,f_{3,\gamma}). \end{aligned} \tag{22}$$

Separating the unknowns $f_{s,i+1}$ from the known functions $f_{s,i}$ yields

$$\begin{aligned} L[f_{0,i+1},\ldots,f_{3,i+1}]+\sum_{s=0}^{3}\left[\frac{\partial N}{\partial f_s}(f_{0,\gamma},\ldots,f_{3,\gamma})+\frac{\partial G}{\partial f_s}(f_{0,i},\ldots,f_{3,i})\right]f_{s,i+1}= \\ \sum_{s=0}^{3} f_{s,i}\frac{\partial G}{\partial f_s}(f_{0,i},\ldots,f_{3,i})-G(f_{0,i},\ldots,f_{3,i})+H(f_{0,\gamma},\ldots,f_{3,\gamma}), \end{aligned} \tag{23}$$

subject to

$$f_{0,i+1}(0)=0,\quad f_{1,i+1}(0)=1,\quad f_{1,i+1}(\infty)=0, \tag{24}$$

We assume that $f_{s,0}$ is obtained as a solution of the linear part of equation (20) given by

$$L[f_{1,0},\ldots,f_{3,0}]+\sum_{s=0}^{3} f_{s,0}\frac{\partial N}{\partial f_s}(f_{0,\gamma},\ldots,f_{3,\gamma})=H(f_{0,\gamma},\ldots,f_{3,\gamma}), \tag{25}$$

which yields the iteration scheme

$$L[f_{0,r+1},\ldots,f_{3,r+1}]+\sum_{s=0}^{3} f_{s,r+1}\frac{\partial N}{\partial f_s}(f_{0,r},\ldots,f_{3,r})=H(f_{0,r},\ldots,f_{3,r}). \tag{26}$$

It can easily be shown that equation (26) is the standard QLM iteration scheme for solving (16).

When $i = 0$ in (23) we can approximate f_s as

$$f_s \approx f_{s,1}. \tag{27}$$

Thus, setting $i = 0$ in (23) we obtain

$$L[f_{0,1}, \ldots, f_{3,1}] + \sum_{s=0}^{3} \left[\frac{\partial N}{\partial f_s}(f_{0,\gamma}, \ldots, f_{3,\gamma}) + \frac{\partial G}{\partial f_s}(f_{0,0}, \ldots, f_{3,0}) \right] f_{s,1} =$$
$$\sum_{s=0}^{3} f_{s,0} \frac{\partial G}{\partial f_s}(f_{0,0}, \ldots, f_{3,0}) - G(f_{0,0}, \ldots, f_{3,0}) + H(f_{0,\gamma}, \ldots, f_{3,\gamma}), \tag{28}$$

which yields the iteration scheme

$$L[f_{0,r+1}, \ldots, f_{3,r+1}] + \sum_{s=0}^{3} \left[\frac{\partial N}{\partial f_s}(f_{0,r}, \ldots, f_{3,r}) + \frac{\partial G}{\partial f_s}(f_{0,r+1}^{(0)}, \ldots, f_{3,r+1}^{(0)}) \right] f_{s,r+1} =$$
$$\sum_{s=0}^{3} f_{s,r+1}^{(0)} \frac{\partial G}{\partial f_s}(f_{0,r+1}^{(0)}, \ldots, f_{3,r+1}^{(0)}) - G(f_{0,r+1}^{(0)}, \ldots, f_{3,r+1}^{(0)}) + H(f_{0,r}, \ldots, f_{3,r}) \tag{29}$$

where $f_{s,r+1}^{(0)}$ is the solution of

$$L[f_{0,r+1}^{(0)}, \ldots, f_{3,r+1}^{(0)}] + \sum_{s=0}^{3} f_{s,r+1}^{(0)} \frac{\partial N}{\partial f_s}(f_{0,r}, \ldots, f_{3,r}) = H(f_{0,r}, \ldots, f_{3,r}). \tag{30}$$

The general iteration scheme obtained by setting $i = m$ ($m \geq 2$) in equation (23), hereinafter referred to as scheme-m is

$$L[f_{0,r+1}, \ldots, f_{3,r+1}] + \sum_{s=0}^{3} \left[\frac{\partial N}{\partial f_s}(f_{0,r}, \ldots, f_{3,r}) + \frac{\partial G}{\partial f_s}(f_{0,r+1}^{(m-1)}, \ldots, f_{3,r+1}^{(m-1)}) \right] f_{s,r+1} =$$
$$\sum_{s=0}^{3} f_{s,r+1}^{(m-1)} \frac{\partial G}{\partial f_s}(f_{0,r+1}^{(m-1)}, \ldots, f_{3,r+1}^{(m-1)}) - G(f_{0,r+1}^{(m-1)}, \ldots, f_{3,r+1}^{(m-1)}) + H(f_{0,r}, \ldots, f_{3,r}) \tag{31}$$

http://dx.doi.org/10.5772/51228

where $f_{s,r+1}^{(m-1)}$ is obtained as the solution of

$$L[f_{0,r+1}^{(m-1)},\ldots,f_{3,r+1}^{(m-1)}]+\sum_{s=0}^{3}\left[\frac{\partial N}{\partial f_s}(f_{0,r},\ldots,f_{3,r})+\frac{\partial G}{\partial f_s}(f_{0,r+1}^{(m-2)},\ldots,f_{3,r+1}^{(m-2)})\right]f_{s,r+1}^{(m-1)}=$$
$$\sum_{s=0}^{3}f_{s,r+1}^{(m-2)}\frac{\partial G}{\partial f_s}(f_{0,r+1}^{(m-2)},\ldots,f_{3,r+1}^{(m-2)})-G(f_{0,r+1}^{(m-2)},\ldots,f_{3,r+1}^{(m-2)})+H(f_{0,r},\ldots,f_{3,r}) \tag{32}$$

The iterative schemes (26) and (31) can easily be solved using numerical methods such as finite differences, finite elements, Runge-Kutta based shooting methods or collocation methods. Several studies, (see for example, Awad et al.2011; Makukula et al. 2010a; Makukula et al. 2010b; Makukula et al. 2010c; Makukula et al. 2010d; Motsa 2011; Motsa and Shateyi 2010; Motsa 2011 and Shateyi Motsa 2011), have shown that the Chebyshev spectral collocation (CSC) method is very robust in solving iterations schemes of the type discussed in this work. The CSC method is based on approximating the unknown functions by the Chebyshev interpolating polynomials in such a way that they are collocated at the Gauss-Lobatto points defined as

$$z_j=\cos\frac{\pi j}{M},\quad j=0,1,\ldots,M. \tag{33}$$

where M is the number of collocation points used (see for example Canuto et al. 1988, Trefethen 2000). For the convenience of numerical implementation, the domain $[0,\infty)$ is truncated as $[0,L_e]$ where L_e is chosen to be a sufficiently large real number. In order to implement the method, the physical region $[0,L_e]$ is transformed into the region $[-1,1]$ using the mapping

$$\eta=L_e\frac{z+1}{2},\quad -1\le z\le 1 \tag{34}$$

The derivatives of f at the collocation points are represented as

$$\frac{d^nf}{d\eta^n}=\sum_{k=0}^{M}\mathbf{D}_{kj}^2f(z_k),\quad j=0,1,\ldots,M \tag{35}$$

where $\mathbf{D}=2D/Le$, with D being the Chebyshev spectral differentiation matrix (see for example, Canuto et al. 1988, Trefethen 2000). Thus, applying the CSC on the functions f_s we obtain

$$f_s=\mathbf{D}^s\mathbf{F} \tag{36}$$

where $\mathbf{F}=[f_0(z_0),f_0(z_1),\ldots,f_0(z_{M-1}),f_0(z_M)]^T$.

Thus, applying the spectral method, with derivative matrices on equation (26) and the corresponding boundary conditions gives the following matrix system

$$\mathbf{C}_r\mathbf{F}_{r+1}=\mathbf{H}_r \tag{37}$$

with the boundary conditions

$$f_{0,r+1}(z_M) = 0, \quad \sum_{k=0}^{M} \mathbf{D}_{Mk} f_{0,r+1}(z_k) = 0, \quad \sum_{k=0}^{M} \mathbf{D}_{0k} f_{0,r+1}(z_k) = 1, \tag{38}$$

where

$$\mathbf{C}_r = \mathbf{D}^3 + \left(\mathbf{a}_{2,r} - \frac{A}{2}\eta_d\right)\mathbf{D}^2 + (\mathbf{a}_{1,r} - A)\mathbf{D} + \mathbf{a}_{0,r}. \tag{39}$$

The vector $\mathbf{H}_r$ corresponds to the function H when evaluated at the collocation points and $\mathbf{a}_{s,r}$ $(s = 0, 1, 2)$ is a diagonal matrix corresponding to the vector of $a_{i,r}$ which is defined as

$$a_{s,r} = \frac{\partial N}{\partial f_s} \tag{40}$$

and η_d is an $(M+1) \times (M+1)$ diagonal matrix of η. The boundary conditions (38) are imposed on the first, Mth and $(M+1)$th rows of C_r and $\mathbf{H}_r$ to obtain

$$\begin{pmatrix} \mathbf{D}_{0,0} & \mathbf{D}_{0,1} & \cdots & \mathbf{D}_{0,M-1} & \mathbf{D}_{0,M} \\ & & \mathbf{C_r} & & \\ \mathbf{D}_{M,0} & \mathbf{D}_{M,1} & \cdots & \mathbf{D}_{M,M-1} & \mathbf{D}_{M,M} \\ 0 & 0 & \cdots & 0 & 1 \end{pmatrix} \begin{pmatrix} f_{0,r+1}(z_0) \\ f_{0,r+1}(z_1) \\ \vdots \\ f_{0,r+1}(z_{M-2}) \\ f_{0,r+1}(z_{M-1}) \\ f_{0,r+1}(z_M) \end{pmatrix} = \begin{pmatrix} 1 \\ H_r(z_1) \\ \vdots \\ H_r(z_{N-2}) \\ 0 \\ 0 \end{pmatrix} \tag{41}$$

Starting from a suitable initial guess $f_{0,0}(\eta)$, the iteration scheme (41) can be used to iteratively give approximate solutions of the governing equation (10). The application of the CSC on the general iteration schemes (31) and (32) can be done in a similar manner for any value of m.

4. Results and discussion

In this section we present the results for the governing physical parameters of interest. In applying the Chebyshev spectral method described in the previous section $M = 100$ collocation points were used. The value of L_e for numerically approximating infinity was chosen to be $Le = 20$. In order to assess the accuracy of the proposed iteration methods, the present numerical results were compared against results generated using the MATLAB routine `bvp4c`. For illustration purposes, results are presented for the first three iterations schemes obtained by setting $m = 0, 1, 2$.

In Table 1 we give a comparison between the results of scheme-0 against results generated using `bvp4c`. We observe that the QLM results converge very rapidly to the `bvp4c` results. It takes only three or four iterations to achieve an exact match that is accurate to order 10^{-8} for the selected parameters of A. We also observe in this table that stretching increases the absolute values of the skin friction.

http://dx.doi.org/10.5772/51228

iter.	$A = 0$	$A = 0.5$	$A = 1$	$A = 1.5$	$A = 2$
1	-1.000000000	-1.166255146	-1.317872855	-1.455413216	-1.581765234
2	-1.000000000	-1.167211134	-1.320520326	-1.459662889	-1.587362322
3	-1.000000000	-1.167211513	-1.320522065	-1.459665895	-1.587366111
4	-1.000000000	-1.167211515	-1.320522065	-1.459665895	-1.587366111
5	-1.000000000	-1.167211517	-1.320522065	-1.459665895	-1.587366111
bvp4c	-1.000000000	-1.167211517	-1.320522065	-1.459665895	-1.587366111

Table 1. Comparison of the bvp4c values of $f''(0)$ at different values of A for Scheme-0 (QLM)

iter.	$A = 1$	$A = 2$	$A = 3$	$A = 4$
		Scheme-0		
1	-1.215913833273934	-1.508012270141307	-1.750647835613831	-1.963118416905635
2	-1.315711765474042	-1.586229425552791	-1.816415412229436	-2.022058898487201
3	-1.320495400678920	-1.587365641569519	-1.816850675892770	-2.020976536521761
4	-1.320522063086358	-1.587366111631070	-1.816849325533777	-2.020950025633773
5	-1.320522064602713	-1.587366111619306	-1.816849325468859	-2.020950025517386
6	-1.320522064602713	-1.587366111619306	-1.816849325468859	-2.020950025517386
		Scheme-1		
1	-1.315711765474042	-1.586229425552791	-1.816415412229436	-2.022058898487201
2	-1.320522063086358	-1.587366111631070	-1.816849325533777	-2.020950025633773
3	-1.320522064602713	-1.587366111619306	-1.816849325468859	-2.020950025517386
4	-1.320522064602713	-1.587366111619306	-1.816849325468859	-2.020950025517386
5	-1.320522064602713	-1.587366111619306	-1.816849325468859	-2.020950025517386
6	-1.320522064602713	-1.587366111619306	-1.816849325468859	-2.020950025517386
		Scheme-2		
1	-1.315240928788073	-1.585906261457893	-1.816236653612290	-2.021499891062478
2	-1.320522059975388	-1.587366111619187	-1.816849325470411	-2.020950025519239
3	-1.320522064602713	-1.587366111619306	-1.816849325468859	-2.020950025517386
4	-1.320522064602713	-1.587366111619306	-1.816849325468859	-2.020950025517386
5	-1.320522064602713	-1.587366111619306	-1.816849325468859	-2.020950025517386
6	-1.320522064602713	-1.587366111619306	-1.816849325468859	-2.020950025517386

Table 2. $f''(0)$ at different values of A for scheme-0,1,2

iter.	$A = 1$	$A = 2$	$A = 3$	$A = 4$
		Scheme-0		
1	0.104608231328780	0.079353841477999	0.066201489855027	0.057831608611751
2	0.004810299128671	0.001136686066515	0.000433913239423	0.001108872969816
3	0.000026663923793	0.000000470049787	0.000001350423911	0.000026511004376
4	0.000000001516355	0.000000000011764	0.000000000064918	0.000000000116388
5	0.000000000000000	0.000000000000000	0.000000000000000	0.000000000000000
6	0.000000000000000	0.000000000000000	0.000000000000000	0.000000000000000
		Scheme-1		
1	0.004810299128671	0.001136686066515	0.000433913239423	0.001108872969816
2	0.000000001516355	0.000000000011764	0.000000000064918	0.000000000116388
3	0.000000000000000	0.000000000000000	0.000000000000000	0.000000000000000
4	0.000000000000000	0.000000000000000	0.000000000000000	0.000000000000000
5	0.000000000000000	0.000000000000000	0.000000000000000	0.000000000000000
6	0.000000000000000	0.000000000000000	0.000000000000000	0.000000000000000
		Scheme-2		
1	0.005281135814640	0.001459850161413	0.000612671856568	0.000549865545092
2	0.000000004627325	0.000000000000119	0.000000000001552	0.000000000001853
3	0.000000000000000	0.000000000000000	0.000000000000000	0.000000000000000
4	0.000000000000000	0.000000000000000	0.000000000000000	0.000000000000000
5	0.000000000000000	0.000000000000000	0.000000000000000	0.000000000000000
6	0.000000000000000	0.000000000000000	0.000000000000000	0.000000000000000

Table 3. $f''(0)$ at different values of A

Tables 2 and 3 give the results of the comparison of the values of $f''(0)$ between three levels of the iteration schemes and their corresponding errors. In computing the errors it was assumed that the result corresponding to the 6th iteration is the converged solution. From numerical experimentation it was found that all the iteration schemes would have completely converged to a fixed value by the time the 5th or 6th iteration is used. The results from Table 2 and 3 clearly indicate that the the convergence to the solution progressively improves when you use the higher level iteration schemes. For instance, from Table 3 we note that it takes only 2 iterations to achieve full convergence in scheme-1 and scheme-2 compare to four iterations in scheme-0. This results demonstrates the improvement offered by the proposed new iteration scheme on the original quasilinearization method which corresponds to scheme-0.

In Figs. 1 - 7 we give illustrations showing the effect of the governing parameters on the flow properties. Unless otherwise specified, the sample illustrations were generated using $R = 1$, $Pr = 0.7$, $Sc = 1$, $K = 1$, $A = 1$. In Figs. 1 - 3 we show the velocity, temperature and concentration profiles for different values of A. In Fig. 1 we observe that the velocity $f'(\eta)$ is a monotonically decreasing function of the stretching parameter A. From Figs. 2 and 3, we observe that both the temperature and concentration distributions are reduced as values of the stretching parameter increase. The velocity, thermal and solutal boundary layer thicknesses all decrease as the values of A increase. As a consequence the transition from

http://dx.doi.org/10.5772/51228

laminar flow to turbulent flow is delayed. This shows that stretching of surfaces can be used as a flow stabilizing mechanism.

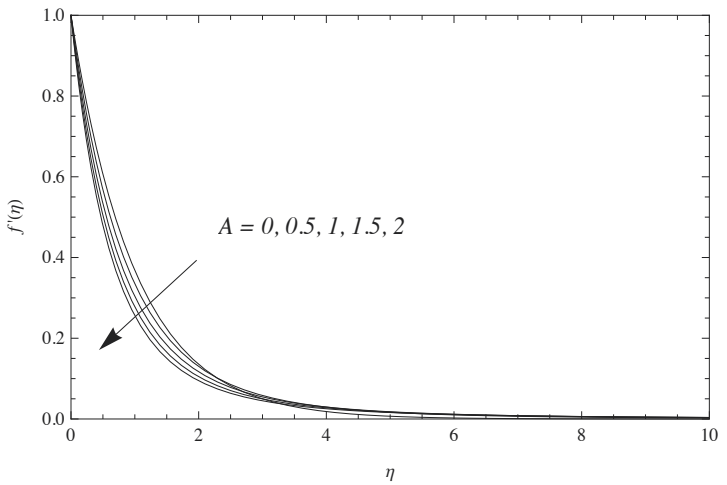

Figure 1. The variation of A on the flow velocity, $f'(\eta)$

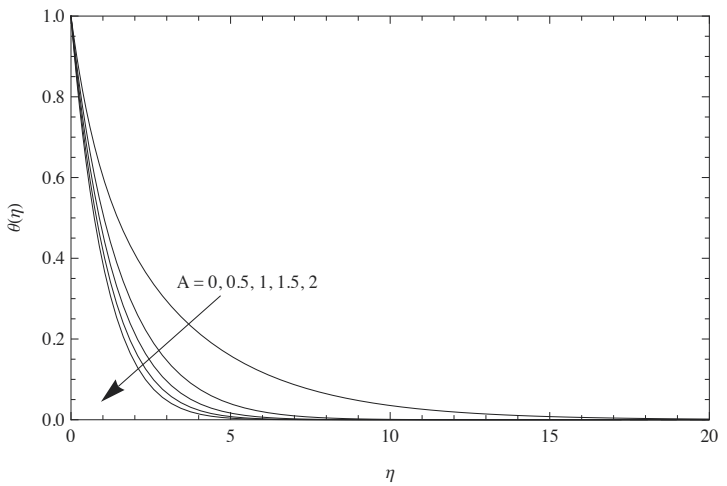

Figure 2. Effect of A on the fluid temperature, $\theta(\eta)$

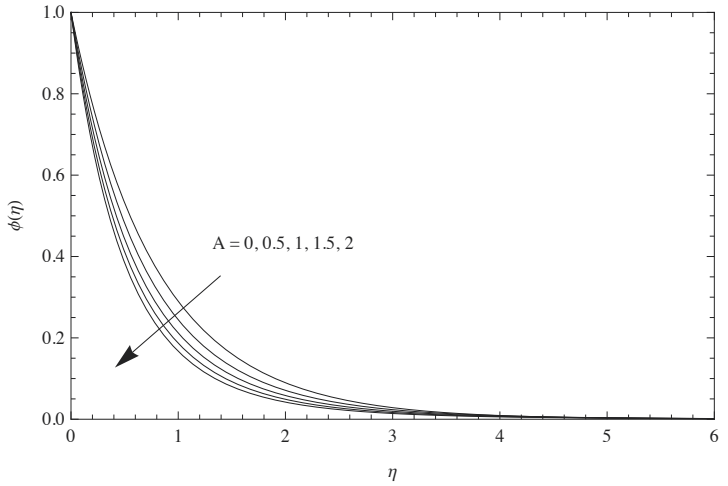

Figure 3. Effect of A on the fluid concentration, $\phi(\eta)$

Fig. 4 depicts the effects of the Prandtl number on the temperature distributions. We observe that as Pr increases, the temperature profiles and the thermal boundary layer thickness become smaller. This is because when Pr increases, the thermal diffusivity decreases, leading to the decrease of the energy transfer ability that decreases the thermal boundary layer. The effect of thermal radiation R on the temperature field is shown in Fig. 5. From this figure we see that the effect of increasing the thermal radiation parameter R is to reduce the temperature profiles.

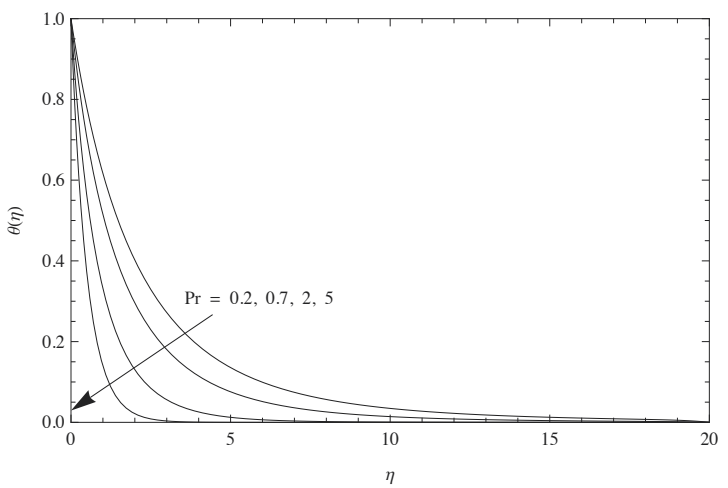

Figure 4. Temperature profiles for various values of Pr

Fig. 6 shows the dimensionless concentration profiles for different values of the Schmidt number Sc. We clearly see from this figure that the concentration boundary layer thickness

http://dx.doi.org/10.5772/51228

decreases as the Schmidt number Sc increases. This phenomenon occurs because when Sc, the mass diffusivity decreases and the fluid becomes heavier. The effects of chemical reaction K on the concentration distributions is displayed in Fig. 7. It should be noted here that physically positive values of K implies the destructive reaction. We observe in this figure that an increase in the chemical reaction leads to the decrease in the concentration can profiles. This shows that diffusion rate can be tremendously altered by chemical reaction.

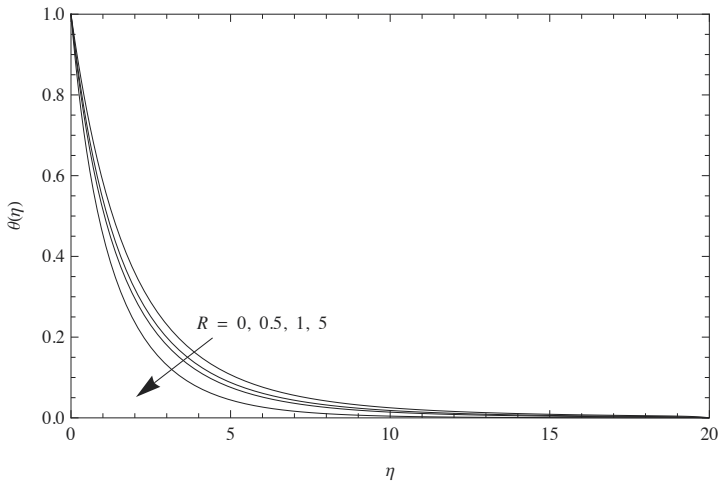

Figure 5. Effect of R on the fluid temperature, $\theta(\eta)$

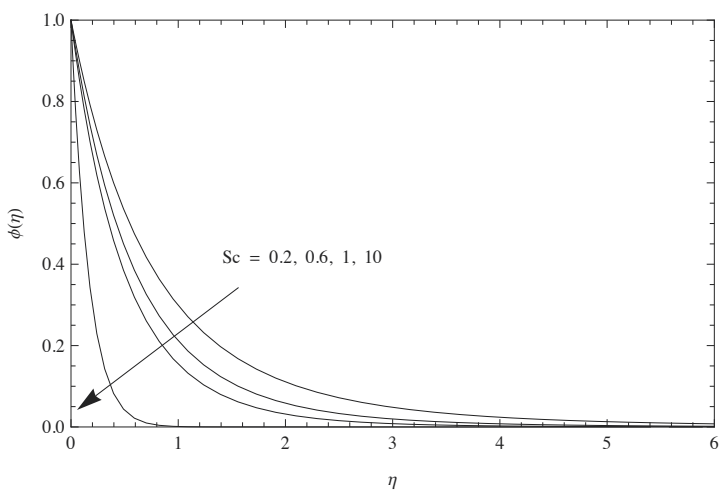

Figure 6. Effect of Sc on the solute concentration, $\phi(\eta)$

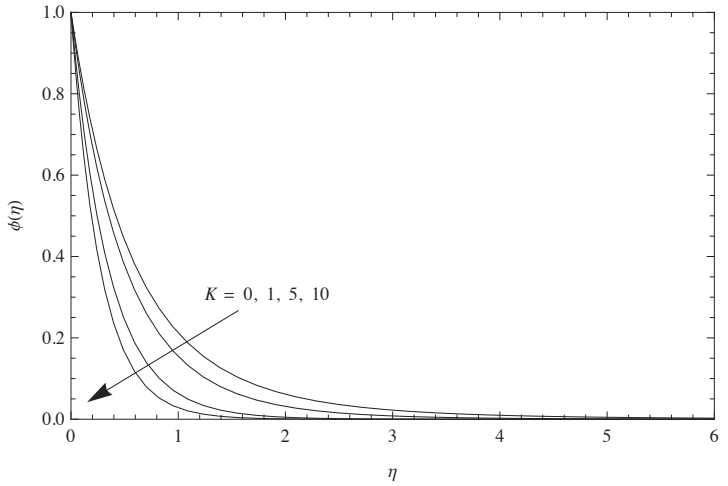

Figure 7. The solute concentration profiles for various values of K.

5. Conclusion

In this chapter we explored the semi-analytic solution of the non linear heat and mass transfer flow over an unsteady stretching permeable surface with prescribed wall conditions in the presence of thermal radiation and non-uniform chemical reaction. From the present investigation we may conclude the following:

1. Blending the QLM scheme with Chebyshev spectral collocation method leads to more accurate and faster convergence scheme.
2. Radiation significantly affect the fluid flow properties.
3. The diffusion rate is significantly altered by chemical radiation.
4. The velocity, temperature and concentration profiles decrease with increasing values of the stretching parameter A.

Author details

Stanford Shateyi[1] and Sandile S. Motsa[2]

[1]University of Venda, South Africa
[2]University of KwaZulu-Natal, South Africa

6. References

[1] Abd El-Aziz, M. (2008). Thermal-diffusion and diffusion-thermo effects on combined heat and mass transfer by hydromagnetic three-dimensional free convection over a permeable stretching surface with radiation. *Physics Letters A*. 372, 263-372.

http://dx.doi.org/10.5772/51228

[2] Abd El-Aziz, M. (2009). Radiation effect on the flow and heat transfer over an unsteady stretching sheet, *Int. Commun. Heat Mass Transf,* doi:10.1016/j.icheatmasstransfer.2009.01.016.

[3] Abel, M.S. & Mahesha, N. (2009). Heat transfer in MHD viscoelastic fluid over a stretching sheet with variable thermal conductivity, non-uniform heat source and radiation. *Appl. Math. Modell.* 32, 1965-1983.

[4] Alam, M.S., Rahman, M.M., & Sattar, M.A. (2009). Transient Magnetohydrodynamic Free Convective Heat and Mass Transfer Flow with Thermophoresis past a Radiative Inclined Permeable Plate in the Presence of Variable Chemical Reaction and Temperature Dependent Viscosity. *Nonlinear Analysis: Modelling and Control.* 14., 1., pp 3-20.

[5] Alam, M.S., & Ahammad, M.U.(2011). Effects of variable chemical reaction and variable electric conductivity on free convective heat and mass transfer flow along an inclined stretching sheet with variable heat and mass fluxes under the influence of Dufour and Soret effects. *Nonlinear Analysis: Modelling and Control*. 16.1., pp 1-16.

[6] Afify, A.A., & Elgazery, N.S. (2012). Lie group analysis for the effects of chemical reaction on MHD stagnation-point flow of heat and mass transfer towards a heated porous stretching sheet with suction or injection. *Nonlinear Analysis: Modelling and Control*. 17.1. pp 1-15.

[7] Awad, F.G. Sibanda, P. Motsa, S.S. & Makinde, O.D. (2011). Convection from an inverted cone in a porous medium with cross-diffusion effects, *Computers and Mathematics with Applications,* 61, pp 1431–1441.

[8] Bellman. R.E., & R.E. Kalaba, (1965), Quasilinearization and Nonlinear Boundary-Value Problems, *Elsevier, New York.*

[9] Canuto, C, Hussaini, M.L, Quarteroni, A. & Zang, T.A. (1988). Spectral Methods in Fluid Dynamics. *Springer-Verlag, Berlin.*

[10] Chamkha, A. J., (1997). Hydromagnetic natural convetion from an isothermal inclined surface adjacent to a thermally stratified porous medium, *Int. J. Eng. Sci.,* 37, 10.11, pp 975 - 986.

[11] Crane, L. J. (1970). Flow past a stretching plate, *Z. Angew. Math. Physc.* 12, pp 645-647.

[12] Cortell, R. (2007). MHD flow and mass transfer of an electrically conducting fluid of second grade in a porous medium over a stretching sheet with chemically reactive species. *Chemical Engineering and Processing*. 46, pp 721-728.

[13] Ishak, A., Nazar, R., and Pop, I. (2009). Heat Transfer over an Unsteady Stretching Permeable Surface with Prescribed Temperature, *Nonlinear Analysis: Real World Applications*, 10, pp 2909-2913.

[14] Krivec, R.; Haftel, M.I. & Mandelzweig, V.B. (1991). Precisse nonvariational calculation of excited states of helium with the correction-function hyperspherical-harmonic method. *Physical Review A.* Vol. 44. No. 11. pp 7159-7164. December 1991.

[15] Krivec, R. & Mandelzweig, V.B. (2008). Quasilinearization approach to computations to computations with singular potentials. *Computer Physics Communications.* Vol. 179. pp 865-867.

[16] Chung Liu I & Andersson, H.L. (2008).Heat transfer in a liquid film on an unsteady stretching sheet, *International Journal of Thermal Sciences,* 47, pp 766-772.

[17] Makukula, Z.G. Sibanda, P.& Motsa, S.S. (2010a). A novel numerical technique for two-dimensional laminar flow between two moving porous walls, *Mathematical Problems in Engineering* Article ID 528956, pp 1-15; doi:10.1155/2010/528956.

[18] Makukula, Z.G. Sibanda, P.& Motsa, S.S. (2010b) A note on the solution of the von KÃąrmÃąn equations using series and Chebyshev spectral methods. *Boundary Value Problems,* Vol. 2010, Article ID 471793, pp 1-17 ; doi:10.1155/2010/471793.

[19] Makukula, Z.G., Sibanda, P., & Motsa, (2010c). On new solutions for heat transfer in a visco-elastic fluid between parallel plates. *International Journal of Mathematical Models and Methods in Applied Sciences*. 4, (4), pp 221 - 230.

[20] Makukula, Z.G., Motsa, S.S., & P. Sibanda. (2010). On a new solution for the viscoelastic squeezing flow between two parallel plates, *Journal of Advanced Research in Applied Mathematics.* 2, pp 31 - 38.

[21] Mandelzweig, V.B. (2005). Quasilinearization Method: Nonperturbative Approach to Physical Problems. *Physics of Atomic Nuclei.* Vol. 68. No. 7. pp 1228-1257.

[22] Motsa, S.S.& Shateyi,S. (2010). A New Approach for the Solution of Three-Dimensional Magnetohydrodynamic Rotating Flow over a Shrinking Sheet, *Mathematical Problems in Engineering,* vol. 2010, Article ID 586340, pp 1-15. doi:10.1155/2010/586340

[23] Motsa, S.S., & Sibanda, P., (2011). On the solution of MHD flow over a nonlinear stretching sheet by an efficient semi-analytical technique, *Int.J Numer.fluids*, pp 1-13.

[24] Motsa, S.S. (2011). New algorithm for solving non-linear BVPs in heat transfer, *International Journal of Modeling, Simulation & Scientific Computing*, 2(3), pp 355–373.

[25] Motsa, S.S. & Shateyi,S. (2011). Successive Linearisation Solution of Free Convection Non-Darcy Flow with Heat and Mass Transfer, *Advanced Topics in Mass Transfer*, Mohamed El-Amin (Ed.), pp 425-438, InTech Open Access Publishers.

[26] Pal, D., & Mondal, H., (2011). Hydromagnetic non-Darcy flow and heat transfer iver a stretching sheet in the presence of thermal radiation and Ohmic dissipation. *Commun Nonlinear Sci Numer Simulat*. 15. 1197-1209.

http://dx.doi.org/10.5772/51228

[27] Shateyi, S. Motsa, S.S., (2009). Thermal radiation effects on heat and mass transfer over an unsteady stretching surface, *Mathematical Problems in Engineering,* Vol. 2009, doi:10.1155/2009/965603.

[28] Shateyi, S., Motsa, S.S., & Sibanda, P. (2010). Homotopy analysis of heat and mass transfer boundary layer flow through a non-porous channel with chemical reaction and heat generation. *The Canadian Journal of Chemical Engineering*. 88. pp 975-982.

[29] Shateyi, S., Motsa, S.S., (2010). Variable viscosity on magnetohydrodynamic fluid flow and heat transfer over an unsteady stretching surface with Hall effect, *Boundary Value Problems,* Vol. 2010, Article ID 257568, pp 1-20, doi:10.1155/2010/257568

[30] Trefethen, L.N., Spectral Methods in MATLAB, SIAM, 2000

[31] Zibakhsh, Z., Domairry, G., Mozaffari, M., & Mahbobifar, M. (2010). Analytical solution of heat transfer over an unsteady stretching permeable surface with prescribed wall temperature. *Journal of the Taiwan Institute of Chemical Engineers*. 41, pp 169-177.

Chapter 4

Continuous Chromatography Modelling with 2D and 3D Networks and Stochastic Methods – Effects of Porous Structure and Solute Population

Leôncio Diógenes T. Câmara, Jader Lugon Junior, Flávio de Matos Silva, Guilherme Pereira de Oliveira, Lídice Camps Echevarria, Orestes Llanes Santiago and Antônio J. Silva Neto

Additional information is available at the end of the chapter

http://dx.doi.org/10.5772/51957

1. Introduction

The modelling of separation chromatographic processes reported in the literature is, in general, related to macroscopic approaches for the phenomenological representation of the mass transfer mechanisms involved. In such models the microscopic aspects of the porous medium structure, related to the separation mechanisms, are incorporated implicitly, limiting the quality of the representation of the separation systems, which are strongly influenced by the micro porous adsorbent.

The modelling of fluid flow in porous media through the application of interconnected networks, which considers the global result from a system of interconnected microscopic elements, is related to the concepts of percolation theory.

The classical macroscopic models of chromatography have limitations in representing the structural parameters of the solid adsorbents, such as topology and morphology, as well as population effects of the molecules in the liquid phase, i.e. multi-molecules movement. Such important microscopic properties can be represented applying interconnected network models which can lead to a better understanding of the phenomenological aspects that contribute to the separation mechanisms in micro-porous media.

In the simulation of the molecules flow through the column porous medium, a stochastic approach is utilized to represent the adsorption, diffusion and convection phenomena.

The molecules can move freely in the network structure, from one neighbor site to another, being respected the requirement that the final position is not occupied by another molecule. Therefore, two molecules cannot occupy the same network site.

This chapter is dedicated to the modelling of continuous chromatography with a network approach combined with Monte Carlo like random walk stochastic methods. The porous structure of the solid adsorbent phase of the chromatographic column is represented by two and three dimensional networks, respectively square and cubic lattices (Oliveira *et al.*, 2008; Biasse *et al.* 2010), in which population effects are taken into account, being related to the movement of multi-molecules modeled by stochastic phenomena of adsorption, desorption, diffusion and advection.

The use of network models to study chromatographic separation processes has been observed in the literature with different techniques and applications (Loh & Wang, 1995; Kier *et al.*, 2000; Loh & Geng, 2003; Geng & Loh, 2004; Bryntensson, 2002; Oliveira et al., 2008, Biasse et al., 2010). In the work of Kier *et al*. (2000), a square network model was applied in the representation of the chromatographic column utilizing a cellular automata approach. The authors assumed arbitrarily pre-defined probabilities for the particles motion and interactions among them. Loh & Geng (2003) applied a cubic network model of interconnected cylindrical pores in the study of chromatographic systems of perfusion. Topological and morphological aspects, such as connectivity and pore size distribution, were analyzed, being observed a great influence of such porous adsorbent media characteristics on the mass transfer of the phenomena studied. In Geng & Loh (2004), the porous structure of the column was modeled considering three different Gaussian distributions of pore size, in order to represent the macro-pores, the micro-pores and the interstitial pores.

In this chapter, the fluid advection is assumed to be the main factor contributing to the molecules movement in the network structure. Such assumption is reasonable since the fluid movement in the chromatographic column comes from the external driving force provided by the pumping system. Two pore dimensions are assumed in the porous structure of adsorbent, the small and large cavities, which leads to steric and non-steric effects, respectively, due to the required space for the molecules movement.

The application of interconnected network models combined with stochastic phenomena of adsorption, diffusion and advection represents the main dynamical behaviors of the chromatographic processes of separation. The multi-molecules population effects allow the study of the dynamics of percolation through the chromatographic column, being therefore possible to evaluate the influence of molecules concentration on the mass transport phenomena along the chromatographic column.

2. Phenomenological and structural modelling

In the adsorption phenomenon, the molecule arriving at a new site can be adsorbed according to a probability of adsorption (p_{ads}). In this case, the system generates a random

http://dx.doi.org/10.5772/51957

number R, from a uniform distribution between 0 and 1, being it compared to a predefined adsorption probability (p_{ads}). The molecule is then adsorbed at the new site if the random number R is smaller than the adsorption probability ($R < p_{ads}$). The same procedure is applied in the desorption of a previously adsorbed molecule, with a desorption probability (p_{des}). The relation between the adsorption and desorption probabilities considered in the simulations is

$$p_{ads} + p_{des} = 1, \quad (0 \le p_{ads} \le 1) \tag{1}$$

The adsorption and desorption phenomena are represented by

$$A + s \underset{k_2}{\overset{k_1}{\rightleftharpoons}} A.s \tag{2}$$

in which a molecule of solute A can be adsorbed at or desorbed from a site s according to a kinetic constant of adsorption (k_1) or desorption (k_2), respectively. From Eq. (2) it can be observed that the adsorption rate is proportional to the concentration of both solute A and vacant sites s.

The simulation of the dynamic process of chromatographic separation in adsorption columns was performed combining the network modelling of the column porous structure with the stochastic modelling of molecules movement and interactions percolating the system.

In the schematic representation of the adsorption column shown in Fig. 1, the symbols C_0 and C represent the solute concentrations at the entrance and at the exit of the column, respectively.

A square network was used to model surface phenomenon (studying equilibrium isotherms) and a cubic one to model the diffusion phenomenon. The porous medium of the chromatography column was represented by a two or three-dimensional cubic network model of interconnected sites (Vide Fig. 2). In such structure the connectivity, i.e. the number of neighbors connected to each site, is equal to four (2D) or six (3D). Each intersection node or site in the network corresponds to a potential adsorption location, in which the solute molecule may be adsorbed, being permitted only one adsorbed molecule per intersection.

In Fig. 2 one can see the graphical representation of both models used with the percolation threshold values (p_{cs}) considered over the site approach. The percolation threshold is the minimum probability of site occupation that represents the percolation through the whole system, becoming a cluster that goes from one extreme of the network to the other.

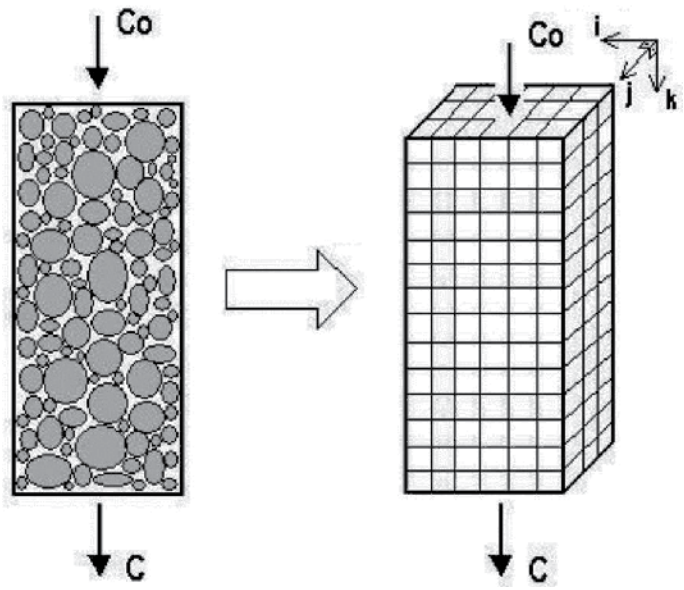

Figure 1. Chromatographic column represented by a three-dimensional cubic network.

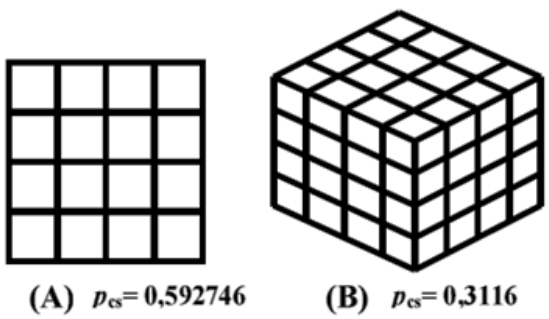

Figure 2. Graphical representation of two-dimension square network (A) and cubic network (B) with respective percolation threshold values (p_{cs})

2.1. Adsorption isotherm model

In this stage, molecules adsorption in stirred tanks was modeled, so that the adsorption surface was represented as a two-dimensional network. In Fig. 3 the process is represented, the liquid phase molecule can be adsorbed at the adsorbent surface material, being the latter represented as the network at the tank bottom.

http://dx.doi.org/10.5772/51957

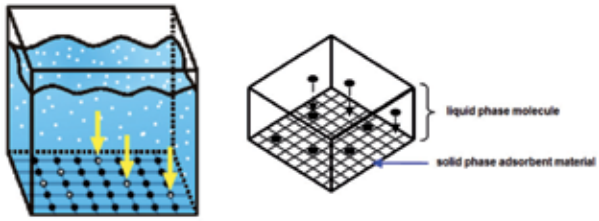

Figure 3. Stirred tank represented by a two-dimensional square network.

In this model it is assumed that the liquid phase molecules can be adsorbed at the network according to an adsorption probability (p_{ads}), defined as

$$p_{ads} = \frac{C_{i_t}}{C_{i_0}} \tag{3}$$

where C_{i_t} and C_{i_0} represent the liquid phase molecules concentration at adsorption times previously prescribed as t and $t=0$ respectively. It is known that at time $t=0$, the concentration is $C_{i_t}=C_{i_0}$. The network used was a 100 x 100 sites, so that it takes to a number of 10.000 adsorbent sites that can be occupied, or not, by the molecules in the system. For each time step (t) a liquid phase molecule can adsorb to the surface according to a previously prescribed adsorption probability (p_{ads}). The adsorption takes place if the random number (R), taken by a uniform random number generator, is lower than (p_{ads}), that is, $R<p_{ads}$. Another condition is that the random chosen position is not occupied by another molecule. The adsorbed molecules are subtracted from the liquid phase. It is considered a final time equal to 10^6, so that a infinite adsorption time, or equilibrium, is represented. It is not considered the interaction between adsorbed molecules, i.e. the superficial diffusion processes are not taken into account.

2.2. Diffusion phenomenon modelling

The diffusion phenomenon model was preformed through the "random walks" technique both for the two-dimensional and three-dimensional percolation at the square network and at the cubic network, respectively. Using this procedure one can use diffusion parameters for chromatography porous media and topological properties from network models, and obtain a fundamental universal correlation for these complex phenomena. Two different diffusion phenomena were studied at this stage: the first assumes that a certain molecule may follow any direction at the network; and the second that assumes that a molecule is only able to diffuse in the axial direction. The second case establishes diffusion relations for the axial dispersion for a chromatographic column, which is a important phenomenon that draws a lot of attention in separation chromatographic processes. In general, on the macroscopic models, only dispersion at the axial direction is taken into account, neglecting the transversal dispersion, that makes the numerical solutions to be simpler. In the present

modelling, both axial and transversal dispersion are implicit on the stochastic "random walk" model, since the molecule is able to diffuse on both directions.

Equation 4 represents the diffusion mechanism, in which the molecule can diffuse in (n) directions with equal diffusion probability (p_i) for each direction. In general, for the square and cubic network, with axial dispersion, (n) corresponds respectively to 4 and 6, but when axial dispersion is considered (n) corresponds to 3 and 5, respectively, being neglected the backward diffusion along the axial direction. In all cases, the moving probability for each direction (i) is considered to be equal.

$$\sum_{i=1}^{n} p_i = 1 \tag{4}$$

At first, a probability of occupation for network elements (p_{oc}) in each direction i is considered to be equal. Simulations for $p_{oc}<1$ were also done, in such a way to represent the porosity (ε) of the porous adsorbent media. A porosity represents the empty space fraction in the chromatographic column, being proportional to the occupation probability ($p_{oc} \propto \varepsilon$). In the case that $p_{oc}=1$, it is considered that the column is completely empty, and therefore ($\varepsilon=1$). Networks with $p_{oc}<1$ were built randomly, being the existence of a certain site conditioned to the generation of a random number R, and the satisfaction of $R < p_{oc}$ condition.

Simulations for different time ranges were made (10, 25, 50 and 75), being monitored the distance (d_p) by the "random walk" and also the area (A_p), the latter counted in site units. In the case of 3D, the latter has a relationship with the volume (V_d), also counted in site units. For each time-step, a different molecule direction was randomly chosen, in a such way that the destination site was forced to exist; A random number of events $N=10^6$ was performed in order to obtain a distance (d_p) by the "random walk" with smaller dispersion.

In the case of smaller molecular diffusion (D_m), it was observed a certain proportion $D_m \propto d_p$ with the distance, obeying to the power law (Stauffer and Aharony, 1992, Biasse et al., 2010).

$$d_p \propto c.t^k \tag{5}$$

where c and k are constants and t represents time.

2.3. Movement rules and steric effect

In the simulation of the molecules movements, four rules (MR – movement rules) are considered to be representative of the diffusion and advection mechanisms. Such rules are schematically represented in Fig. 4.

From Fig. 4 it can be observed that the movement rules are determined by the directions considered in each situation. In the movement rules (I) and (II), the molecules can move in all directions of the structure while in the movement rules (III) and (IV) the molecules can-

http://dx.doi.org/10.5772/51957

not move in the direction 6, which corresponds to the movement against the longitudinal main stream flow direction, i.e. the upstream movement is not allowed. The MR-(II) and (IV) are similar to MR-(I) and (III), respectively, with a higher chance of movement in the direction 5 (longitudinal or axial direction).

The MR-(I) is considered to be representative of the diffusion mechanism of solute molecules through the porous structure.

This assumption is coherent as there is not a driving mechanism forcing the flow in any particular direction of the network. In this case, according to the first law of Fick (Bird et al., 2002), the solute flow is determined by the concentration gradient of molecules, without significant effects of external forces. The diffusion mechanism of MR-(I) is governed by

$$p_i = \frac{1}{6}, \quad i = 1,2, \ \ldots, 6 \tag{6}$$

in which P_i represents the probability of the solute molecule to move in the i-th direction of the network. According to Eq. (6), the chance of the molecules to follow any direction (six directions) in the network is the same.

The MR-(II), (III) and (IV) are considered to be representative of the advective mechanism as these configurations favor the flow in the axial downstream direction of the column.

The advective mechanism MR-(II) is governed by

$$p_i = \frac{1 - p_5}{5}, \ i = 1,2, \ \ldots, 6 (i \neq i_5), \ \ p_5 > \frac{1}{6} \tag{7}$$

in which p_5 represents the probability of the solute molecule to move in the axial downward direction of the column. In this case, the chance of the solute molecule to move in the axial downward direction is greater than the other directions, and the probabilities related to the movements in the remaining directions are the same.

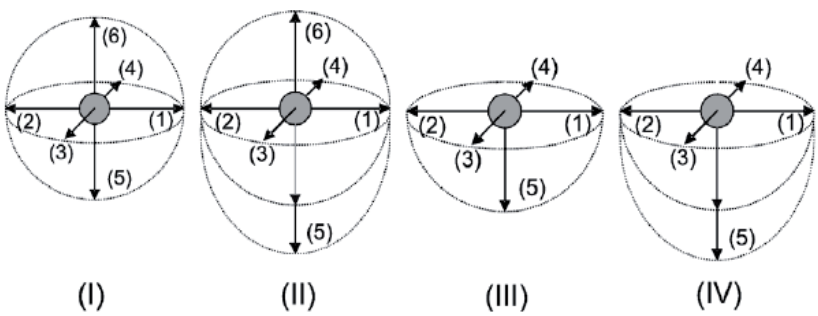

Figure 4. Movement rules (MR) for the solute molecules with the corresponding directions.

The advective mechanisms MR-(III) and (IV) are determined, respectively, by

$$p_i = \frac{1}{5}, \quad i = 1,2, \ \ldots, 5 \tag{8}$$

$$p_i = \frac{1 - p_5}{4}, \quad i = 1,2, \ \ldots, 4, \quad p_5 > \frac{1}{5} \tag{9}$$

From Eq. (8) it can be observed that the solute movement in the direction 6 is prohibited, having the same probability for the moves in the other directions. In Eq. (9) as in Eq. (7), the probability of moving in the direction 5 is greater than in the other directions.

The simulation of the flow of solute molecules was carried out according to the procedure described next. The molecules were introduced randomly at the column entrance (at the nodes with k = 1), maintaining the concentration constant at this section (C_0). The molecules concentration (C) at the column exit (k = 30) was calculated as the ratio of the number of molecules occupying the network intersections (sites) and the total number of intersections. In each step of the simulation, corresponding to a discrete time (t^*), all the network sites occupied by molecules were checked, being assumed for each molecule a direction of movement according to the MR to be followed. A molecule was kept at its original location if the new site, it was supposed to be move to, was occupied by another molecule or was located outside the lateral limits of the network domain. The molecules at the entrance could move only in the axial downward direction, being kept for every discrete time t^*, a constant value for the concentration at this section (C_0, k = 1). At the column exit (k = 30) the concentration (C) was monitored as a function of the discrete time (t^*).

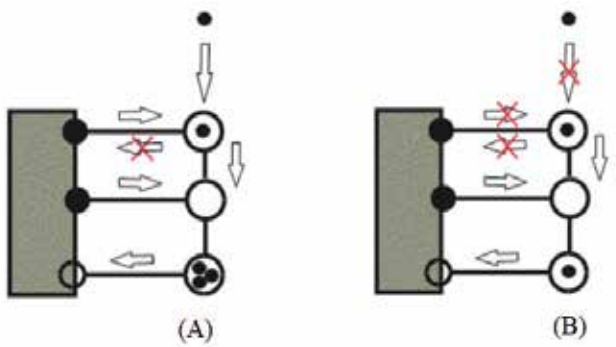

Figure 5. Representation of molecule movement along the column: (A) the non-steric model and (B) with steric model. Obs.: The arrows represent the allowed movement that the molecule can do, and crossed arrows represent movement that can´t be done.

http://dx.doi.org/10.5772/51957

An important parameter to be taken into account in the stochastic modelling is the number of simulations (N), which indicates the number of times that the same procedure of the simulation is performed using the same control parameters. The increase in the number of simulations (N) leads to a decrease in the dispersion of the calculated value.

The steric effects were also investigated, that is, while the solid phase is able to adsorb one molecule at each site, one possibility is that the liquid phase site is able to contain one molecule and another possibility is that it is able to contain a unlimited number of molecules. In Fig. 5 are represented those two possibilities, being (A) for the case without the steric limitation and (B) representing the steric restriction.

3. Results and discussions

3.1. Langmuir isotherm model for surface adsorption

In Fig. 6 are represented the adsorption isotherms: in (A) are the results obtained for the simulations using a square network and in (B) are the experimental and deterministic model adapted from Silva (2004). One can observe that the results obtained using the stochastic adsorption method are representative for the studied phenomenon with the classic Langmuir isotherm.

These results show that the stochastic phenomenology is determinant to the behavior of equilibrium systems with multimolecules, and the overall result is governed by the individual actions of each component.

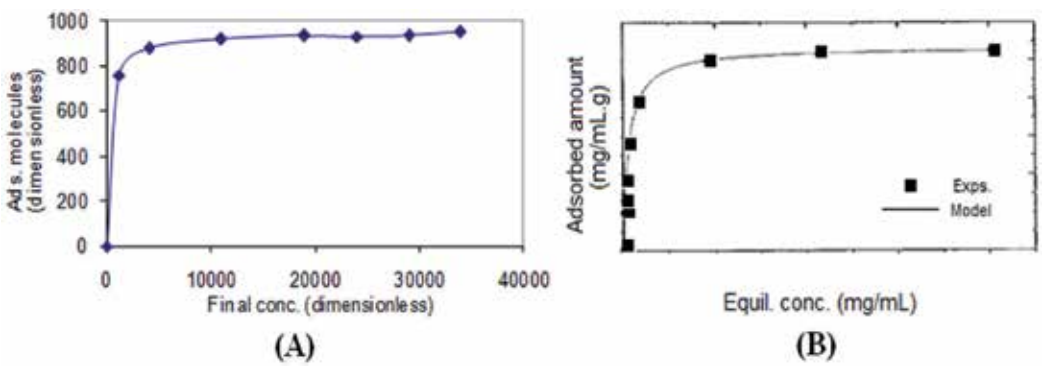

Figure 6. Results obtained with the stochastic simulation (A) and the experimental and classical modelling (B) by Silva (2004).

3.2. Results for the diffusion phenomenon (2D and 3D modelling)

In Figs. 7, 8 and 9 are represented the percolation evolution both in the square and cubic networks using different moving mechanisms. In Fig. 7 are represented the percolation using a square network of 50x50 nodes, for a time equal to 2000 steps, for four directions, and occupation probability $p_{oc}=1$ (Fig. 7 A) and $p_{oc}=0.7$ (Fig. 7 B).

In Fig. 8 are represented results for the same conditions considered before, but allowing only 3 directions for the dispersion mechanism. One can observe a greater tendency towards the axial diffusion.

A evolution percolation method for 3D is presented in Fig. 9 for two movement mechanisms.

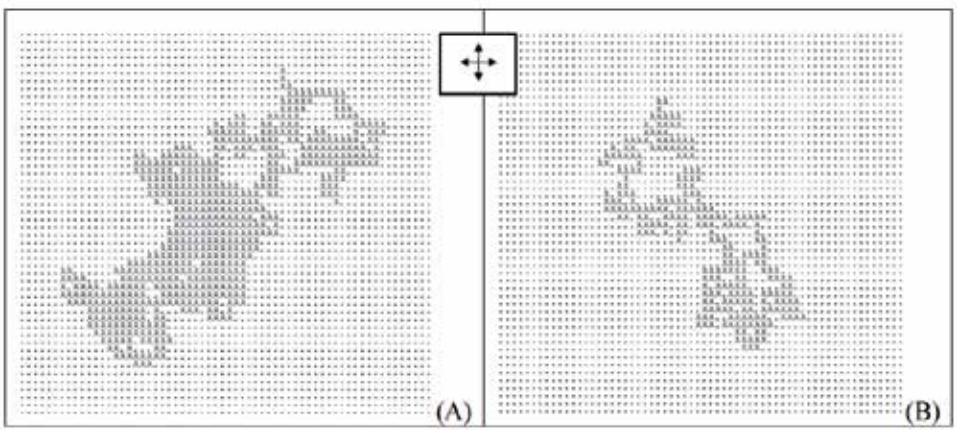

Figure 7. Diffusion through the square network for four directions with $p_{oc}=1$ (A) and $p_{oc}=0.7$ (B).

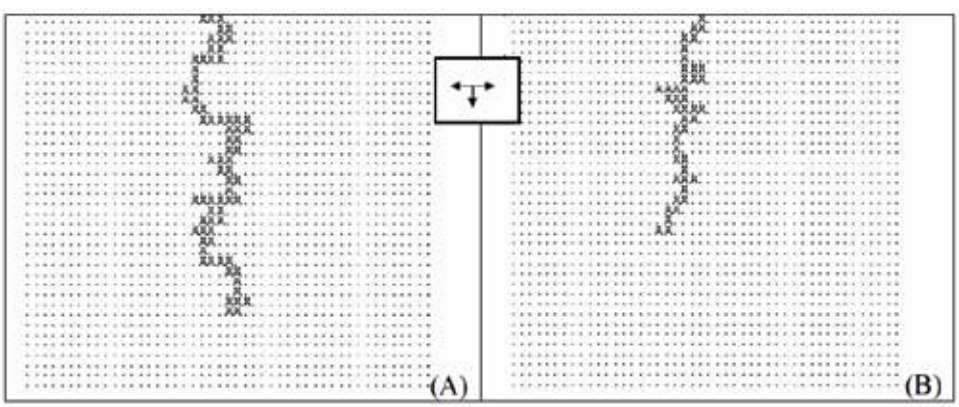

Figure 8. Diffusion through the square network for three directions with $p_{oc}=1$ (A) and $p_{oc}=0.7$ (B).

http://dx.doi.org/10.5772/51957

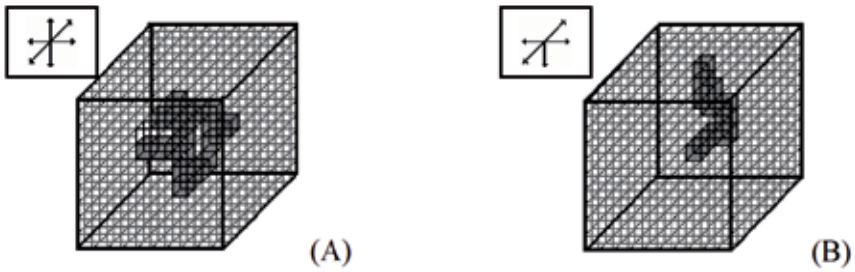

Figure 9. Representation for cubic percolation considering six directions (A) and five directions (B).

In Figs. 10 and 11 are presented the distance (d_p) with time in log scale. Using this scale, the power law (Biasse et al., 2010) represented by Eq. (5) becomes

$$\log(d_p) = \log(c) + k.\log(t) \tag{10}$$

We can obtain the expoent k, that corresponds to the angular coefficient of the expression above. The k exponent is important because of its relation to the molecular diffusivity and time, being this a fundamental parameter for this relation and sensitive to those values.

From the analysis of Figs. 10 and 11 we are able to observe that diffusivity, which presents a relation with d_p, has a direct link to the power law established by Eq. (5), once the model leads to a good correlation with the simulated data for the percolation both for the square (2D) and cubic (3D) networks. The results presented high correlation coefficients, which indicates a good agreement to the power law. Both situations for the regular network with p_{oc}=1, for the 2D (Fig. 10A) and 3D (Fig. 11A) networks, presented ideal percolation with universal exponents equal to 0.5014 and 0.4987, respectively. In those cases, because both are regular, with p_{oc}=1 and movement in all directions, the correlation coefficient was very closed to 1 (R^2=1).

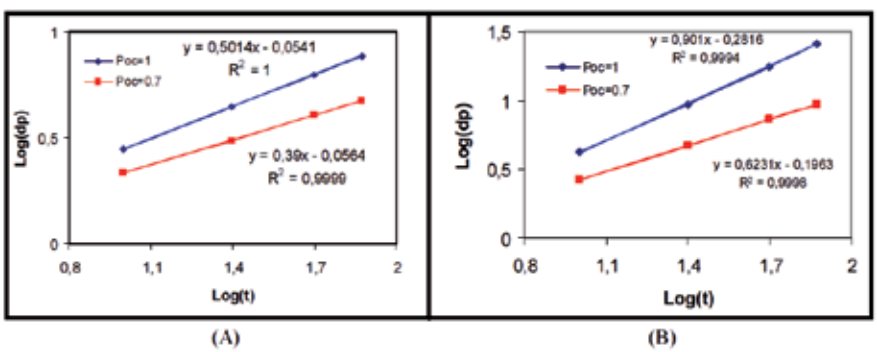

Figure 10. Results for 2D networks for four (A) and three (B) moving directions

It is observed, in axial and radial dispersion situations, represented by Figs. 10B and 11B, a significant increase in the value of k exponent when compared to the conditions with diffusion in all directions, demonstrating that diffusion was higher in those cases. For example, we can point out the difference between Figs. 10A and 10B (with p_{oc}=1), where the k exponent was increased by 79,7%. With respect to the porosity ε effect, that has a relation to the p_{oc} was observed that the reduction of p_{oc} from 1 to 0.7 had a more significant effect over the k exponent on 2D networks than on 3D ones. This effect can be observed by the greater slope in Fig. 10. Therefore the porosity reduction leads to a more significant slope on the diffusion for the 2D network represented by lower k exponents. The 3D network, has a lower percolation threshold when compared to the 2D network, presenting a structure with a larger number of possible percolation ways, that with the possibility for the "random walk" to go over larger distances, leading therefore to the larger values of k exponents when compared to 2D networks with the same value of p_{oc}<1.

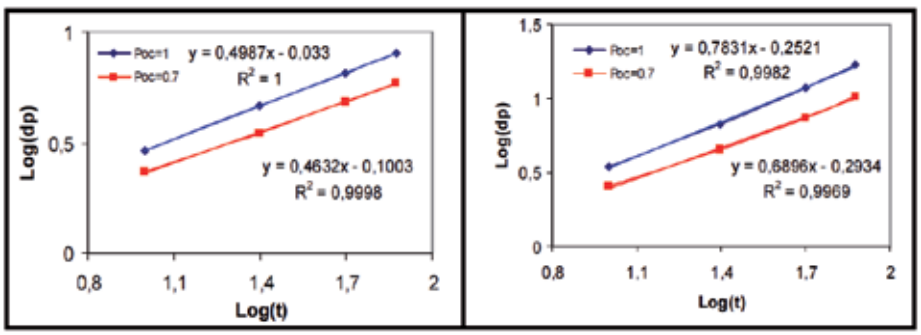

Figure 11. Results for 3D network for six (A) and five (B) movement directions.

The analysis of the power law Eq. 5 (Biasse et al., 2010), not only related to the distance (d_p) but mainly in terms of (A_p) and (V_p), took to equivalent results to those previously reported, showing a good agreement of the experimental data with the power law model assumed. Table 1 presents the values of k exponents and the corresponding correlation coefficients. The values for A_p and V_p were obtained in percolated site units, being these units respectively related to 2D and 3D. Such as in the previous cases reported, related to d_p, it was observed a reduction of exponent k for the axial and radial dispersion (three and five directions) situations. It was also observed a more significant reduction of k with the porosity reduction in 2D networks.

3.3. Results of 3D network column with advective phenomenon

All results presented in this section were obtained for 5000 simulations. In Figs. 12 and 13 the test results varying p_{ads} are presented. One can observe that for p_{ads}=0 there is a concen-

http://dx.doi.org/10.5772/51957

tration step, because since no molecule is retained at each time, all of them are allowed to move to the next column section until they reach the exit section. Another observation is that when p_{ads} is increased there is a delay in the variation of the concentration at the column exit, because the chances for the molecule to be adsorbed are higher.

	2D		3D	
	4 directions	3 directions	6 directions	5 directions
$p_{ac}=1$	0.7706 (R^2=0.9986)	0.929 (R^2=0.9997)	0.8951 (R^2=0.9997)	0.9304 (R^2=0.9997)
$p_{ac}=0.7$	0.636 (R^2=0.9996)	0.6413 (R^2=0.9998)	0.8201 (R^2=0.9993)	0.8449 (R^2=0.9991)

Table 1. Exponents (k) from power law related to the area A_p (2D) and volume V_d (3D).

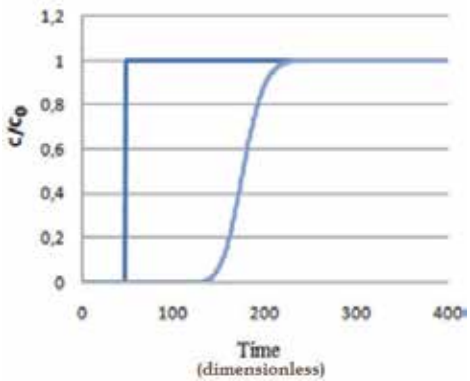

Figure 12. Chromatography column exit for $p_{ads}=0$ and $p_{ads}=1$.

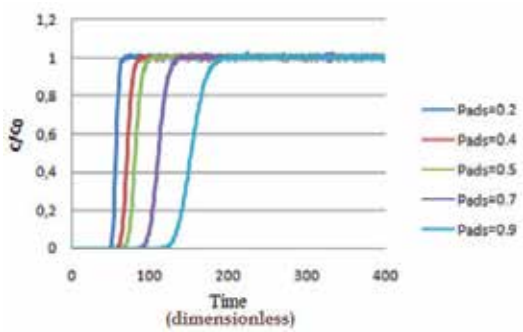

Figure 13. Chromatography column exit for different values of p_{ads}.

In Fig. 14 it is presented a comparison of the simulation results, without considering axial dispersion, with the experimental data acquired by Cruz (1997). One can observe the good results obtained by the network simulations, despite the breakthrough curve too sharp when equilibrium is reached (C/C_0 =1), in which the curve does not fit well, probably because of the effects of axial dispersion.

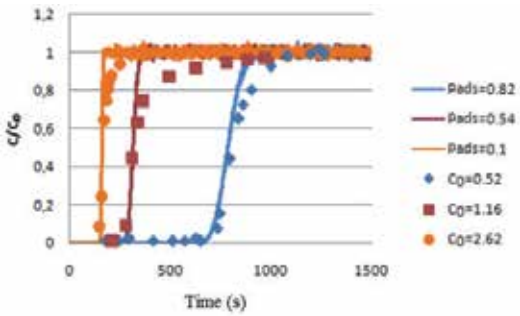

Figure 14. Dimensionless concentration at the column exit as a function of time. A comparison between the experimental data of Cruz (1997) and network simulations without axial dispersion

Another important parameter to be considered here is the equilibrium fraction (k_{eq}), i.e. the fraction between adsorption and desorption. Another way to find the value for that ratio is comparing the amount of particles adsorbed and the amount of particles in the liquid phase (q_e/c_e). Using this model one can confirm that there is a direct relationship between the concentration fraction and the p_{ads}/p_{des}. See Table 2.

Concentration (Simulation)	k_{eq}	p_{ads}/p_{des}
$C_0 = 0.52$	4.455	4.555
$C_0 = 1.16$	1.222	1.173
$C_0 = 1.76$	0.466	0.470
$C_0 = 2.06$	0.353	0.369
$C_0 = 2.62$	0.160	0.111

Table 2. Relationship between k_{eq} and p_{ads}/p_{des}

In Fig. 15 the same network, as the one used to obtain the results shown in Fig. 14 and Table 2, was considered assuming also the axial dispersion phenomenon.

Finally, in Fig. 16 are presented the simulation results (3D network model) for the discrete relative concentration (C/C_0) as a function of the adsorption probability (C/C_0) taking into

http://dx.doi.org/10.5772/51957

account the steric and non-steric effects. The relative concentration indicates a measure of the porous medium resistance to the molecules percolating through the system.

The resistance to the percolation through the chromatographic column decreases as the relative concentration (p_{ads}) increases and vice-versa. Therefore, values close to one show a structure without any resistance to the molecules to percolate the column structure.

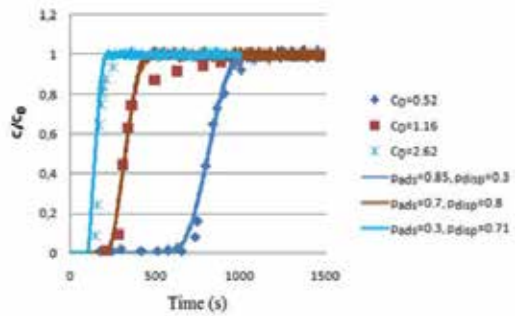

Figure 15. Dimensionless Concentration at the column exit as a function of time. Comparison of experimental data acquisition by Cruz (1997) and network simulation considering axial dispersion.

The highest medium resistance corresponds to an adsorption probability near 0.68 which is the minimum point of the curve. At this point the number of molecules percolating the system is reduced to the lowest level.

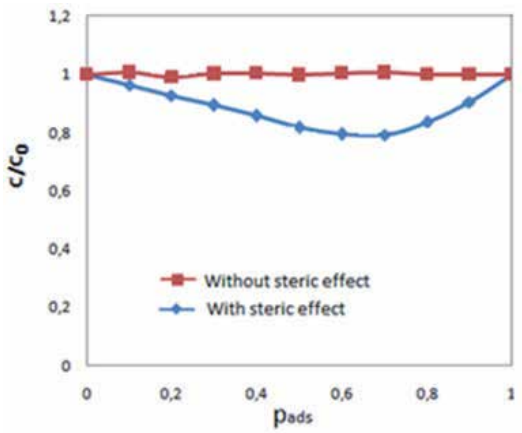

Figure 16. Relative concentration as a function of the adsorption probability considering steric and non-steric effects.

It must be noted that the medium resistance disappears at adsorption probability equal to 1 as at this point the adsorption is irreversible (no desorption is observed), and no molecule

already adsorbed goes back to the liquid phase of the cavity, and therefore there is no interference in the movement of the other molecules.

4. Conclusions

The network stochastic surface multimolecular modelling was able to represent the behavior of Langmuir type adsorption isotherms. Such computational tool can be used to better understand the adsorption mechanisms to surfaces, resulting in the improvement of adsorbent materials.

The diffusion modelling through the 2D and 3D network "random walks" presented results obeying the power law with universal exponents well defined, being the latter related to the diffusive coefficients.

The effects of the power law were observed through the distance C/C_0, the area d_p and the volume A_p, being these values related to the diffusion phenomenon. Axial and radial dispersion mechanisms were also represented with a power law modelling, being that behavior related the variations of porosity V_d and probability of occupation ε.

A final important result is the observation of the existence of a direct relationship between the adsorption and desorption probabilities ratio with the equilibrium constant p_{oc}.

Acknowledgements

The authors acknowledge the financial support provided by CNPq, Conselho Nacional de Desenvolvimento Científico e Tecnológico, FAPERJ, Fundação Carlos Chagas Filho de Amparo à Pesquisa do Estado do Rio de Janeiro, and CAPES, Coordenação de Aperfeiçoamento de Pessoal de Nível Superior.

Author details

Leôncio Diógenes T. Câmara[1], Jader Lugon Junior[2], Flávio de Matos Silva[1], Guilherme Pereira de Oliveira[1], Lídice Camps Echevarria[3], Orestes Llanes Santiago[3] and Antônio J. Silva Neto[1]

1 Instituto Politécnico, Universidade do Estado do Rio de Janeiro, Brazil

2 Instituto Federal de Educação, Ciência e Tecnologia Fluminense, Brazil

3 Facultad de Ingeniería Eléctrica - Instituto Superior Politécnico José Antonio Echeverría, Cuba

http://dx.doi.org/10.5772/51957

References

[1] Biasse, A. D., Fonseca, E. X., Silva, Neto. A. J., & Câmara, L. D. T. (2010). Power-Laws of Diffusion Phenomena In Chromatographic Columns, Advances and Applications in Mathematical Sciences , 2(2), 313-320.

[2] Bird, R. B., Stewart, W. E., & Lightfoot, E. N. (2002). Transport Phenomena, second ed., Wiley.

[3] Bryntesson, L. M. (2002). Pore Network Modelling of the Behaviour of a Solute in Chromatography Media: Transient and Steady-State Diffusion Properties,. J. Chromatogr. A, 945, , 103-115.

[4] Cruz, J. M. (1997). Insulin Adsorption in Ion Exchanger Resins using Fix and Fluidzed Beds, M.Sc. Dissertation, Chemical Engineering Faculty, UNICAMP. (In Portuguese).

[5] Geng, A., & Loh, K. C. (2004). Effects of Adsorption Kinetics and Surface Heterogeneity on Band Spreading in Perfusion Chromatography- A Network Model Analysi. s, Chem. Eng. Sci. 59, , 2447-2456.

[6] Kier, L. B., Cheng, C. K., & Karnes, H. T. (2000). A Cellular Automata Model of Chromatography,. Biomed. Chromatogr. 14, , 530-534.

[7] Loh, K. C., & Geng, A. (2003). Hydrodynamic Dispersion in Perfusion Chromatography- A Network Model Analysis, Chem. Eng. Sci. 58, , 3439-3451.

[8] Loh, K. C., & Wang, D. I. C. (1995). Characterization of Pore Size Distribution of Packing Materials Used in Perfusion Chromatography Using Network Model,. J. Chromatogr. A, 718, , 239-255.

[9] Oliveira, G. P., Câmara, L. D. T., & Silva, Neto. A. J. (2008). Modelling of the Separation Mechanisms in Chromatographic Columns through Adsorption and Advection in Two Dimensional Networks, XI Computational Modelling Meeting, Volta Redonda, Brazil. (In Portuguese)

[10] Silva,(2000). Study of Insulin Adsorption in Ion Exclange Resin Columns: Experimental Parameters and Modelling, D.Sc. Thesis, Chemical Engineering Faculty, UNICAMP. (in Portuguese)

[11] Stauffer, D., & Aharony, A. (1992). Introduction to Percolation Theory. Second Edition.

Chapter 5

Cross-Diffusion, Viscous Dissipation and Radiation Effects on an Exponentially Stretching Surface in Porous Media

Ahmed A. Khidir and Precious Sibanda

Additional information is available at the end of the chapter

http://dx.doi.org/10.5772/55320

1. Introduction

In the last few decades, fluid flow with heat and mass transfer on a continuously stretching surface has attracted considerable attention because of its many applications in industrial and manufacturing processes. Examples of these applications include the drawing of plastic films, glass-fibre and paper production, hot rolling and continuous casting of metals and spinning of fibers. The kinematics of stretching and the simultaneous heating or cooling during such processes play an important role on the structure and quality of the final product.

Sakiadis [30, 31] was the first to study the boundary layer flow due to a continuous moving solid surface. Subsequently, a huge number of studies dealing with different types of fluids, different forms of stretching velocity and temperature distributions have appeared in the literature. Ali [2] investigated similarity solutions of laminar boundary-layer equations in a quiescent fluid driven by a stretched sheet subject to fluid suction or injection. Elbashbeshy [13] extended this problem to a three dimensional exponentially continuous stretching surface. The problem of an exponentially stretching surface with an exponential temperature distribution has been discussed by Magyari and Keller [19]. The problem of mixed convection from an exponentially stretching surface was studied by Partha et al. [24]. They considered the effect of buoyancy and viscous dissipation in the porous medium. They observed that these had a significant effect on the skin friction and the rate of heat transfer. This problem has been extended by Sajid and Hayat [28] who investigated heat transfer over an exponentially stretching sheet in the presence of heat radiation. The same problem was solved numerically by Bidin and Nazar [6] using the Keller-box method. Flow and heat transfer along an exponentially stretching continuous surface with an exponential temperature distribution and an applied magnetic field has been investigated numerically by

Al-Odat et al. [1] while Khan [17] and Sanjayanand and Khan [29] investigated heat transfer due to an exponentially stretching sheet in a viscous-elastic fluid.

Thermal-diffusion and diffusion-thermo effects in boundary layer flow due to a vertical stretching surface have been studied by, *inter alia*, Dursunkaya and Worek [10] while MHD effects, injection/suction, heat radiation, Soret and Dufour effects on the heat and mass transfer on a continuously stretching permeable surface was investigated by El-Aziz [12]. He showed that the Soret and Dufour numbers have a significant influence on the velocity, temperature and concentration distributions.

Srinivasacharya and RamReddy [33] analyzed the problem of mixed convection in a viscous fluid over an exponentially stretching vertical surface subject to Soret and Dufour effects. Ishak [15] investigated the effect of radiation on magnetohydrodynamic boundary layer flow of a viscous fluid over an exponentially stretching sheet. Pal [9] analyzed the effects of magnetic field, viscous dissipation and internal heat generation/absorption on mixed convection heat transfer in the boundary layers on an exponentially stretching continuous surface with an exponential temperature distribution. Loganathan et al. [18] investigated the effect of a chemical reaction on unsteady free convection flow past a semi-infinite vertical plate with variable viscosity and thermal conductivity. They assumed that the viscosity of the fluid was an exponential function and that the thermal conductivity was a linear function of the temperature. They noted that in the case of variable fluid properties, the results obtained differed significantly from those of constant fluid properties. Javed et al. [16] investigated the non-similar boundary layer flow over an exponentially stretching continuous in rotating flow. They observed a reduction in the boundary layer thickness and an enhanced drag force at the surface with increasing fluid rotation.

The aim of the present study is to investigate the effects of cross-diffusion, chemical reaction, heat radiation and viscous dissipation on an exponentially stretching surface subject to an external magnetic field. The wall temperature, solute concentration and stretching velocity are assumed to be exponentially increasing functions. The successive linearisation method (SLM) which has been used in a limited number of studies (see [3, 5, 20–22, 32]) is used to solve the governing coupled non-linear system of equations. Recent studies such as [4, 22, 23] have suggested that the successive linearisation method is accurate and converges rapidly to the numerical results when compared to other semi-analytical methods such as the Adomian decomposition method, the variational iteration method and the homotopy perturbation method. The SLM method can be used in place of traditional numerical methods such as finite differences, Runge-Kutta shooting methods, finite elements in solving non-linear boundary value problems. We compared the results with the Matlab `bvp4c` numerical routine.

2. Governing equations

Consider a quiescent incompressible conducting fluid of constant ambient temperature T_∞ and concentration C_∞ in a porous medium through which an impermeable vertical sheet is stretched with velocity $u_w(x) = u_0 e^{x/\ell}$, temperature distribution $T_w(x) = T_\infty + T_0 e^{2x/\ell}$ and concentration distribution $C_w(x) = C_\infty + C_0 e^{2x/\ell}$ where C_0, T_0, u_0 and ℓ are positive constants. The x-axis is directed along the continuous stretching surface and the y-axis is normal to the surface. A variable magnetic field $B(x)$ is applied in the y-direction. In

http://dx.doi.org/10.5772/55320

addition, heat radiation and cross-diffusion effects are considered to be significant. The governing boundary-layer equations subject to the Boussinesq approximations are

$$\frac{\partial u}{\partial x}+\frac{\partial v}{\partial y}=0, \tag{1}$$

$$u\frac{\partial u}{\partial x}+v\frac{\partial u}{\partial y}=\nu\frac{\partial^2 u}{\partial y^2}+g\beta_T(T-T_\infty)+g\beta_C(C-C_\infty)-\left(\frac{\nu}{K}+\frac{\sigma B^2}{\rho}\right)u, \tag{2}$$

$$u\frac{\partial T}{\partial x}+v\frac{\partial T}{\partial y}=\frac{k}{\rho c_p}\frac{\partial^2 T}{\partial y^2}+\frac{\nu}{c_p}\left(\frac{\partial u}{\partial y}\right)^2+\frac{D_m K_T}{c_s c_p}\frac{\partial^2 C}{\partial y^2}-\frac{1}{\rho c_p}\frac{\partial q_r}{\partial y}, \tag{3}$$

$$u\frac{\partial C}{\partial x}+v\frac{\partial C}{\partial y}=D_m\frac{\partial^2 C}{\partial y^2}+\frac{D_m K_T}{T_m}\frac{\partial^2 T}{\partial y^2}-\gamma(C-C_\infty), \tag{4}$$

The boundary conditions are given by

$$\left.\begin{array}{l} u=u_w(x), v=0, T=T_w(x), C=C_w(x) \quad \text{at} \quad y=0, \\ u\to 0, T\to T_\infty, C\to C_\infty \quad \text{as} \quad y\to\infty. \end{array}\right\} \tag{5}$$

where u and v are the velocity components along the x and y axis, respectively, T and C denote the temperature and concentration, respectively, K is the permeability of the porous medium, ν is the kinematic viscosity, g is the acceleration due to gravity, β_T is the coefficient of thermal expansion, β_C is the coefficient of concentration expansion, B is the uniform magnetic field, ρ is the liquid density, σ is the electrical conductivity, D_m is the mass diffusivity, c_s is the concentration susceptibility, c_p is the specific heat capacity, T_m is the mean fluid temperature, K_T is the thermal diffusion ratio and γ is the rate of chemical reaction.

The radiative heat flux term q_r is given by the Rosseland approximation (see Raptis [26] and Sparrow [27]);

$$q_r=-\frac{4\sigma^*}{3k^*}\frac{\partial T^4}{\partial y}, \tag{6}$$

where σ^* and k^* are the Stefan-Boltzman constant and the mean absorption coefficient, respectively. We assume that the term T^4 may be expanded in a Taylor series about T_∞ and neglecting higher-order terms to get

$$T^4\cong 4T_\infty^3 T-3T_\infty^4, \tag{7}$$

Substituting equations (6) and (7) in equation (3) gives

$$u\frac{\partial T}{\partial x}+v\frac{\partial T}{\partial y}=\left(\frac{k}{\rho c_p}+\frac{16\sigma^* T_\infty^3}{3\rho c_p k^*}\right)\frac{\partial^2 T}{\partial y^2}+\frac{\nu}{c_p}\left(\frac{\partial u}{\partial y}\right)^2+\frac{D_m K_T}{c_s c_p}\frac{\partial^2 C}{\partial y^2}, \tag{8}$$

A similarity solutions may be obtained by assuming that the magnetic field term $B(x)$ has the form

$$B(x) = B_0 e^{x/2\ell} \tag{9}$$

where B_0 is the constant magnetic field. The system of partial differential equations (1) - (4) and (8) can be simplified further by introducing the stream function ψ where

$$u = \frac{\partial \psi}{\partial y} \quad \text{and} \quad v = -\frac{\partial \psi}{\partial x}, \tag{10}$$

together with transformations

$$\left.\begin{array}{l} \eta = \dfrac{y}{L}\sqrt{\dfrac{Re}{2}}\, e^{x/2\ell}, \psi = \sqrt{2Re}\nu\, e^{x/2\ell} f(\eta), \\ T = T_\infty + T_0 e^{2x/\ell}\theta(\eta), C = C_\infty + C_0 e^{2x/\ell}\phi(\eta) \end{array}\right\}. \tag{11}$$

Substituting (11) into the governing partial differential equations gives

$$f''' + ff'' - 2f'^2 - \left(M + \frac{1}{Re_D}\right) f' + 2\frac{Gr_x}{Re^2}\left(\theta + N_1\phi\right) = 0, \tag{12}$$

$$\frac{1}{Pr}\left(1 + \frac{4}{3}R_d\right)\theta'' + f\theta' - 4f'\theta + Gb(f'')^2 + D_f\phi'' = 0, \tag{13}$$

$$\frac{1}{Sc}\phi'' + f\phi' - 4f'\phi + Sr\theta'' - 2R\phi = 0. \tag{14}$$

The corresponding dimensionless boundary conditions take the form

$$\left.\begin{array}{l} f(\eta) = 0,\ f'(\eta) = 1,\ \theta(\eta) = 1,\ \phi(\eta) = 1 \quad \text{at} \quad \eta = 0 \\ f'(\eta) \to 0,\ \theta(\eta) \to 0,\ \phi(\eta) \to 0 \quad \text{as} \quad \eta \to \infty \end{array}\right\} \tag{15}$$

where M is the magnetic parameter, Gr_x is the Grashof number Re is the Reynolds number, N_1 is the buoyancy ratio, Re_D is the Darcy-Reynolds number, Da is the Darcy number, Pr is the Prandtl number, R_d is the thermal radiation parameter, Gb is the viscous dissipation parameter or Gebhart number, D_f is the Dufour number, Sc is the Schmidt number, S_r is the Soret number and R is the chemical reaction rate parameter. These parameters are defined as

$$M = \frac{2\sigma B_0^2 \ell}{\rho u_0}, \quad Gr_x = \frac{g\beta_T T_0 \ell^3 e^{2x/\ell}}{\nu^2}, \quad Re = \frac{u_w \ell}{\nu}, \quad N_1 = \frac{\beta_c C_0}{\beta_T T_0}, \tag{16}$$

$$Re_D = \frac{2}{ReDa}, \quad Da = \frac{K}{\ell^2}, \quad Pr = \frac{\nu}{\alpha}, \quad R_d = \frac{4\sigma^* T_\infty^3}{kk^*}, \quad Gb = \frac{u_0^2}{c_p\, T_0}, \tag{17}$$

$$D_f = \frac{D_m K_T C_0}{c_s c_p \nu T_0}, \quad Sc = \frac{\nu}{D_m}, \quad S_r = \frac{D_m K_T T_0}{T_m \nu C_0}, \quad R = \frac{\alpha \ell}{u_0}. \tag{18}$$

http://dx.doi.org/10.5772/55320

The ratio Gr_x/Re^2 in equation (12) is the mixed convection parameter which represents aiding buoyancy if $Gr_x/Re^2 > 0$ and opposing buoyancy if $Gr_x/Re^2 < 0$. The skin friction coefficient C_{fx}, the Nusselt number Nu_x and the Sherwood Sh_x number are given by

$$C_{fx} = \frac{2\mu}{\rho u_w^2} \left.\frac{\partial u}{\partial y}\right|_{y=0} = \sqrt{\frac{2x}{\ell\, Re_x}}\, f''(0), \tag{19}$$

$$Nu_x = -\frac{x}{T_w - T_\infty} \left.\frac{\partial T}{\partial y}\right|_{y=0} = -\sqrt{\frac{xRe_x}{2\ell}}\, \theta'(0) \tag{20}$$

$$Sh_x = -\frac{x}{C_w - C_\infty} \left.\frac{\partial C}{\partial y}\right|_{y=0} = -\sqrt{\frac{xRe_x}{2\ell}}\, \phi'(0) \tag{21}$$

where $Re_x = xu_w(x)/\nu$ is the local Reynolds number.

3. Method of solution

The system of equations (12)-(14) together with the boundary conditions (15) were solved using a successive linearisation method (SLM) (see [22, 32]). The SLM is based on the assumption that the unknown functions $f(\eta)$, $\theta(\eta)$ and $\phi(\eta)$ can be expanded as

$$f(\eta) = f_i(\eta) + \sum_{m=0}^{i-1} F_m(\eta), \theta(\eta) = \theta_i(\eta) + \sum_{m=0}^{i-1} \Theta_m(\eta), \phi(\eta) = \phi_i(\eta) + \sum_{m=0}^{i-1} \Phi_m(\eta), \tag{22}$$

where f_i, θ_i and ϕ_i are unknown functions and F_m, Θ_m and Φ_m $(m \geq 1)$ are successive approximations which are obtained by recursively solving the linear part of the equation system that results from substituting firstly expansions in the governing equations. The initial guesses $F_0(\eta)$, $\Theta_0(\eta)$ and $\Phi_0(\eta)$ are chosen to satisfy the boundary condition

$$\left.\begin{array}{l} F_0(\eta) = 0,\ F_0'(\eta) = 1,\ \Theta_0(\eta) = 1,\ \Phi_0(\eta) = 1 \quad \text{at} \quad \eta = 0 \\ F_0'(\eta) \to 0,\ \Theta_0(\eta) \to 0,\ \Phi_0(\eta) \to 0 \quad \text{as} \quad \eta \to \infty \end{array}\right\}. \tag{23}$$

Suitable choices in this problem are

$$F_0(\eta) = 1 - e^{-\eta},\ \Theta_0(\eta) = e^{-\eta} \quad \text{and} \quad \Phi_0(\eta) = e^{-\eta}. \tag{24}$$

Starting from the initial guesses, the subsequent solutions F_i, Θ_i and Φ_i $(i \geq 1)$ are obtained by successively solving the linearised form of the equations which are obtained by substituting equation (22) in the governing equations. The linearised equations to be solved are

$$a_{1,i-1}F_i''' + a_{2,i-1}F_i'' + a_{3,i-1}F_i' + a_{4,i-1}F_i + a_{5,i-1}\Theta_i + a_{6,i-1}\Phi_i = r_{1,i-1}, \tag{25}$$

$$b_{1,i-1}\Theta_i'' + b_{2,i-1}\Theta_i' + b_{3,i-1}\Theta_i + b_{4,i-1}F_i'' + b_{5,i-1}F_i' + b_{6,i-1}F_i + b_{7,i-1}\Phi_i = r_{2,i-1}, \tag{26}$$

$$c_{1,i-1}\Phi_i'' + c_{2,i-1}\Phi_i' + c_{3,i-1}\Phi_i + c_{4,i-1}F_i' + c_{5,i-1}F_i + c_{6,i-1}\Theta_i'' = r_{3,i-1}. \tag{27}$$

subject to the boundary conditions

$$F_i(0) = F_i'(0) = F_i'(\infty) = \Theta_i(0) = \Theta_i(\infty) = \Phi_i(0) = \Phi_i(\infty) = 0, \tag{28}$$

where the coefficient parameters are

$$a_{1,i-1} = -1, \quad a_{2,i-1} = \sum_{m=0}^{i-1} f_m', \quad a_{3,i-1} = -4\sum_{m=0}^{i-1} f_m' - M - \frac{1}{Re_D}, a_{4,i-1} = \sum_{m=0}^{i-1} f_m''$$

$$a_{5,i-1} = 2\frac{Gr_x}{Re^2},\ a_{6,i-1} = 2N_1\frac{Gr_x}{Re^2},\ b_{1,i-1} = \sum_{m=0}^{i-1} f_m,\ b_{2,i-1} = -4\sum_{m=0}^{i-1} \theta_m, b_{3,i-1} = \sum_{m=0}^{i-1} \theta_m',$$

$$b_{4,i-1} = \frac{3+4R_d}{3Pr},\ b_{5,i-1} = \sum_{m=0}^{i-1} f_m,\ b_{6,i-1} = -4\sum_{m=0}^{i-1} f_m',\ b_{7,i-1} = D_f,\ c_{1,i-1} = -4\sum_{m=0}^{i-1} \phi_m$$

$$c_{2,i-1} = \sum_{m=0}^{i-1} \phi_m',\ c_{3,i-1} = Sr,\ c_{4,i-1} = \frac{1}{Sc},\ c_{5,i-1} = \sum_{m=0}^{i-1} f_m,\ c_{6,i-1} = -2R - 4\sum_{m=0}^{i-1} f_m',$$

$$r_{1,i-1} = -\sum_{m=0}^{i-1} f_m''' - \sum_{m=0}^{i-1} f_m \sum_{m=0}^{i-1} f_m'' + 2\sum_{m=0}^{i-1} f_m'^2 + \left(M + \frac{1}{Re_D}\right)\sum_{m=0}^{i-1} f_m'$$
$$-\frac{2Gr_x}{Re^2}\sum_{m=0}^{i-1}(\theta_m + N_1\phi_m)$$

$$r_{2,i-1} = -\sum_{m=0}^{i-1}\frac{1}{Pr}(\phi_m'' + \frac{4R_d}{3Pr}\theta_m'') - \sum_{m=0}^{i-1} f_m \sum_{m=0}^{i-1}\theta_m' + 4\sum_{m=0}^{i-1} f_m' \sum_{m=0}^{i-1}\theta_m - Gb\sum_{m=0}^{i-1} f_m''^2 -$$
$$D_f\sum_{m=0}^{i-1}\phi_m''$$

$$r_{3,i-1} = -\frac{1}{Sc}\sum_{m=0}^{i-1}\phi_m'' \sum_{m=0}^{i-1} f_m \sum_{m=0}^{i-1}\phi_m' + 4\sum_{m=0}^{i-1} f_m \sum_{m=0}^{i-1}\theta_m - Sr\sum_{m=0}^{i-1}\phi_m'' + 2R\sum_{m=0}^{i-1}\phi_m$$

The solutions F_i, Θ_i and Φ_i for $i \geq 1$ are found by iteratively solving equations (25)-(27). Finally, after M iterations, the solutions $f(\eta)$, $\theta(\eta)$ and $\phi(\eta)$ may be written as

$$f(\eta) \approx \sum_{m=0}^{M} F_m(\eta), \theta(\eta) \approx \sum_{m=0}^{M} \Theta_m(\eta), \Phi(\eta) \approx \sum_{m=0}^{M} \Phi_m(\eta). \tag{29}$$

where M is termed the order of SLM approximation. Equations (25)-(27) are solved using the Chebyshev spectral collocation method. We first transform the domain of solution $[0, \infty)$ into the domain $[-1, 1]$ using the domain truncation technique where the problem is solved

http://dx.doi.org/10.5772/55320

in the interval $[0, L]$ where L is a scaling parameter used to invoke the boundary condition at infinity. This is achieved by using the mapping

$$\frac{\eta}{L} = \frac{\xi + 1}{2}, -1 \leq \xi \leq 1, \tag{30}$$

We discretize the domain $[-1, 1]$ using the Gauss-Lobatto collocation points given by

$$\xi = \cos\frac{\pi j}{N}, j = 0, 1, 2, \ldots, N, \tag{31}$$

where N is the number of collocation points used. The functions F_i, Θ_i and Φ_i for $i \geq 1$ are approximated at the collocation points as follows

$$F_i(\xi) \approx \sum_{k=0}^{N} F_i(\xi_k)T_k(\xi_j), \Theta_i(\xi) \approx \sum_{k=0}^{N} \Theta_i(\xi_k)T_k(\xi_j), \Phi_i(\xi) \approx \sum_{k=0}^{N} \Phi_i(\xi_k)T_k(\xi_j) j = 0, 1, \ldots, N, \tag{32}$$

where T_k is the k^{th} Chebyshev polynomial given by

$$T_k(\xi) = \cos\left[k\cos^{-1}(\xi)\right]. \tag{33}$$

The derivatives of the variables at the collocation points are represented as

$$\frac{d^r F_i}{d\eta^r} = \sum_{k=0}^{N} \mathbf{D}_{kj}^r F_i(\xi_k), \frac{d^r \Theta_i}{d\eta^r} = \sum_{k=0}^{N} \mathbf{D}_{kj}^r \Theta_i(\xi_k), \frac{d^r \Phi_i}{d\eta^r} = \sum_{k=0}^{N} \mathbf{D}_{kj}^r \Phi_i(\xi_k) j = 0, 1, \ldots, N, \tag{34}$$

where r is the order of differentiation and $\mathbf{D} = \frac{2}{L}\mathcal{D}$ with $\mathcal{D}$ being the Chebyshev spectral differentiation matrix (see, for example [7, 8]), whose entries are defined as

$$\left.\begin{aligned} \mathcal{D}_{00} &= \frac{2N^2+1}{6}, \\ \mathcal{D}_{jk} &= \frac{c_j}{c_k}\frac{(-1)^{j+k}}{\xi_j - \xi_k}, j \neq k; j, k = 0, 1, \ldots, N, \\ \mathcal{D}_{kk} &= -\frac{\xi_k}{2(1-\xi_k^2)}, k = 1, 2, \ldots, N-1, \\ \mathcal{D}_{NN} &= -\frac{2N^2+1}{6}. \end{aligned}\right\} \tag{35}$$

Substituting equations (30)-(34) into equations (25)-(27) leads to the matrix equation

$$\mathbf{A}_{i-1}\mathbf{X}_i = \mathbf{R}_{i-1}, \tag{36}$$

In equation (36), $\mathbf{A}_{i-1}$ is a $(3N+3)\times(3N+3)$ square matrix and $\mathbf{X}_i$ and $\mathbf{R}_{i-1}$ are $(3N+3)\times 1$ column vectors defined by

$$\mathbf{A}_{i-1}=\begin{bmatrix} A_{11} & A_{12} & A_{13} \\ A_{21} & A_{22} & A_{23} \\ A_{31} & A_{32} & A_{33} \end{bmatrix}, \mathbf{X}_i=\begin{bmatrix} F_i \\ \Theta_i \\ \Phi_i \end{bmatrix}, \mathbf{R}_{i-1}=\begin{bmatrix} \mathbf{r}_{1,i-1} \\ \mathbf{r}_{2,i-1} \\ \mathbf{r}_{3,i-1} \end{bmatrix}, \tag{37}$$

where

$$\begin{aligned}
&F_i=[f_i(\xi_0),f_i(\xi_1),...,f_i(\xi_{N-1}),f_i(\xi_N)]^T,\\
&\Theta_i=[\theta_i(\xi_0),\theta_i(\xi_1),...,\theta_i(\xi_{N-1}),\theta_i(\xi_N)]^T,\\
&\Phi_i=[\phi_i(\xi_0),\phi_i(\xi_1),...,\phi_i(\xi_{N-1}),\phi_i(\xi_N)]^T,\\
&\mathbf{r}_{1,i-1}=\left[r_{1,i-1}(\xi_0),r_{1,i-1}(\xi_1),...,r_{1,i-1}(\xi_{N-1}),r_{1,i-1}(\xi_N)\right]^T,\\
&\mathbf{r}_{2,i-1}=\left[r_{2,i-1}(\xi_0),r_{2,i-1}(\xi_1),...,r_{2,i-1}(\xi_{N-1}),r_{2,i-1}(\xi_N)\right]^T,\\
&\mathbf{r}_{3,i-1}=\left[r_{3,i-1}(\xi_0),r_{3,i-1}(\xi_1),...,r_{3,i-1}(\xi_{N-1}),r_{3,i-1}(\xi_N)\right]^T,\\
&A_{11}=\mathbf{a}_{1,i-1}\mathbf{D}^3+\mathbf{a}_{2,i-1}\mathbf{D}^2+\mathbf{a}_{3,i-1}\mathbf{D}+\mathbf{a}_{4,i-1}\mathbf{I}, A_{12}=\mathbf{a}_{5,i-1}\mathbf{I}+\mathbf{a}_{6,i-1}\mathbf{I}, A_{13}=\mathbf{I},\\
&A_{21}=\mathbf{b}_{1,i-1}\mathbf{D}^2+\mathbf{b}_{2,i-1}\mathbf{D}+\mathbf{b}_{3,i-1}\mathbf{I}, A_{22}=\mathbf{b}_{4,i-1}\mathbf{D}^2+\mathbf{b}_{5,i-1}\mathbf{D}+\mathbf{b}_{6,i-1}\mathbf{I}, A_{23}=\mathbf{b}_{7,i-1}\mathbf{D}^2,\\
&A_{31}=\mathbf{c}_{1,i-1}\mathbf{D}^2+\mathbf{c}_{2,i-1}\mathbf{D}+\mathbf{c}_{3,i-1}\mathbf{I}, A_{32}=\mathbf{c}_{4,i-1}\mathbf{D}+\mathbf{c}_{5,i-1}\mathbf{I}, A_{33}=\mathbf{c}_{6,i-1}\mathbf{D}^2.
\end{aligned}$$

In the above definitions T stands for transpose, $\mathbf{a}_{k,i-1}$ $(k=1,\ldots,6)$, $\mathbf{b}_{k,i-1}$ $(k=1,\ldots,7)$, $\mathbf{c}_{k,i-1}$ $(k=1,\ldots,6)$, and $\mathbf{r}_{k,i-1}$ $(k=1,2,3)$ are diagonal matrices of order $(N+1)\times(N+1)$, $\mathbf{I}$ is an identity matrix of order $(N+1)\times(N+1)$. Finally the solution is obtained as

$$\mathbf{X}_i=\mathbf{A}_{i-1}^{-1}\mathbf{R}_{i-1}. \tag{38}$$

4. Results and discussion

In generating the results presented here it was determined through numerical experimentation that $L=15$ and $N=60$ gave sufficient accuracy for the linearisation method. In addition, the results in this work were obtained for $Pr=0.71$ which physically corresponds to air and the Schmidt number $Sc=0.22$ for hydrogen at approximately 25° and one atmospheric pressure. The Darcy-Reynolds number was fixed at $Re_D=100$.

Tables 1 - 7 show, firstly the effects of various parameters on the skin-friction, the local heat and the mass transfer coefficients for different physical parameters values. Secondly, to confirm the accuracy of the linearisation method, these results are compared to those obtained using the Matlab `bvp4c` solver. The results from the two methods are in excellent agreement with the linearisation method converging at the four order with accuracy of up to six decimal places.

The effect of increasing the magnetic filed parameter M on the skin-friction coefficient $f''(0)$, the Nusselt number $-\theta'(0)$ and the Sherwood number $-\phi'(0)$ are given in Table 1. Here

http://dx.doi.org/10.5772/55320

we find that increasing the magnetic filed parameter leads to reduces Nusselt number and Sherwood number as well as skin friction coefficient in case of aiding buoyancy. These results are to be expected, and are, in fact, similar to those obtained previously by, among others (Ishak [15] and Ibrahim and Makinde [14]).

		SLM results				
	M	1st order	2nd order	3rd order	4th order	**bvp4c**
$f''(0)$	0.0	-0.130330	-0.137803	-0.138236	-0.138242	-0.138242
	0.1	-0.172947	-0.179731	-0.179950	-0.179952	-0.179952
	0.5	-0.334846	-0.339272	-0.339242	-0.339242	-0.339242
	1.0	-0.521003	-0.523599	-0.523568	-0.523568	-0.523568
$-\theta'(0)$	0.0	1.422819	1.354658	1.354263	1.354252	1.354252
	0.1	1.407222	1.345231	1.345006	1.345004	1.345003
	0.5	1.349392	1.308530	1.308480	1.308480	1.308480
	1.0	1.286198	1.264064	1.264037	1.264037	1.264037
$-\phi'(0)$	0.0	1.297706	1.288178	1.288065	1.288063	1.288063
	0.1	1.294285	1.285273	1.285212	1.285212	1.285212
	0.5	1.281653	1.274574	1.274572	1.274572	1.274572
	1.0	1.267871	1.262761	1.262760	1.262760	1.262760

Table 1. The effect of various values of M on skin-friction, heat and mass transfer coefficients when $Gr_x/Re^2 = 1.5$, $Gb = 0.5$, $R_d = 0.2$, $D_f = 0.3$, $Sr = 0.2$, $R = 2$ and $N_1 = 0.1$

In Table 2 an increase in the mixed convection parameter Gr_x/Re^2 (that is, aiding buoyancy) enhances the skin friction coefficient. This is explained by the fact that an increase in the fluid buoyancy leads to an acceleration of the fluid flow, thus increasing the skin friction coefficient. Similar results were obtained in the past by Srinivasacharya and RamReddy [33] and Partha et al. [24]. Also, the non-dimensional heat and mass transfer coefficients increase when Gr_x/Re^2 increases. This is because an increasing in mixed convection parameter, increases the momentum transport in the boundary layer this is leads to carried out more heat and mass species out of the surface, then reducing the thermal and concentration boundary layers thickness and hence increasing the heat and mass transfer rates.

Tables 3 and 4 show the effects of increasing the radiation parameter R_d and the chemical reaction parameter R on the skin-friction, and the heat and mass transfer rates respectively. The skin-friction coefficient is enhanced by the radiation parameter. It is however reduced by the chemical reaction parameter (Loganathan et. al[18]). Increasing the radiation parameter R_d and chemical reaction parameter R have the same effect on heat and mass transfer rates, that is, $-\theta'(0)$ decreases while $-\phi'(0)$ is increases. Large values of R_d and R lead to a decrease in the buoyancy force and, consequently, a decrease in the thicknesses of both the thermal and the momentum boundary layers (see Sajid [28]).

		SLM results				
	Gr_x/Re^2	1st order	2nd order	3rd order	4th order	**bvp4c**
$f''(0)$	0.0	-1.459148	-1.469821	-1.469885	-1.469885	-1.469885
	0.5	-1.042194	-1.044162	-1.044208	-1.044208	-1.044208
	1.0	-0.674522	-0.678490	-0.678447	-0.678447	-0.678447
	1.5	-0.334846	-0.339272	-0.339242	-0.339242	-0.339242
$-\theta'(0)$	0.0	0.973213	0.934517	0.933372	0.933372	0.933372
	0.5	1.135051	1.134112	1.134083	1.134083	1.134083
	1.0	1.253215	1.236804	1.236738	1.236738	1.236738
	1.5	1.349392	1.308530	1.308480	1.308480	1.308480
$-\phi'(0)$	0.0	1.200469	1.201715	1.201709	1.201709	1.201709
	0.5	1.234639	1.233314	1.233299	1.233299	1.233299
	1.0	1.260335	1.255659	1.255655	1.255655	1.255655
	1.5	1.281653	1.274574	1.274572	1.274572	1.274572

Table 2. The effect of various values of Gr_x/Re^2 on skin-friction, heat and mass transfer coefficients when $M = 0.5,\ Gb = 0.5,\ R_d = 0.2,\ D_f = 0.3,\ Sr = 0.2,\ R = 2$ and $N_1 = 0.1$

		SLM results				
	R_d	1st order	2nd order	3rd order	4th order	**bvp4c**
$f''(0)$	0.0	-0.390151	-0.384799	-0.385087	-0.385088	-0.385088
	0.2	-0.334846	-0.339272	-0.339242	-0.339242	-0.339242
	0.5	-0.267055	-0.286928	-0.286715	-0.286715	-0.286715
	1.0	-0.178534	-0.223773	-0.224247	-0.224239	-0.224239
$-\theta'(0)$	0.0	1.508929	1.466549	1.466541	1.466540	1.466540
	0.2	1.349392	1.308530	1.308480	1.308480	1.308480
	0.5	1.184709	1.146728	1.146321	1.146321	1.146321
	1.0	1.008715	0.976294	0.974693	0.974674	0.974674
$-\phi'(0)$	0.0	1.267312	1.263619	1.263567	1.263567	1.263567
	0.2	1.281653	1.274574	1.274572	1.274572	1.274572
	0.5	1.298805	1.286546	1.286483	1.286483	1.286483
	1.0	1.320928	1.300398	1.299833	1.299832	1.299832

Table 3. The effect of R_d on skin-friction, heat and mass transfer coefficients when $M = 0.5,\ Gr_x/Re^2 = 1.5,\ Gb = 0.5,\ D_f = 0.3,\ Sr = 0.2,\ R = 2$ and $N_1 = 0.1$

http://dx.doi.org/10.5772/55320

		SLM results				
	R	1st order	2nd order	3rd order	4th order	**bvp4c**
$f''(0)$	0.0	-0.332793	-0.334754	-0.334629	-0.334629	-0.334629
	0.5	-0.333949	-0.336858	-0.336797	-0.336797	-0.336797
	1.0	-0.334431	-0.337995	-0.337952	-0.337952	-0.337952
	3.0	-0.334965	-0.339959	-0.339936	-0.339936	-0.339936
$-\theta'(0)$	0.0	1.413844	1.364409	1.364235	1.364232	1.364232
	0.5	1.392460	1.347513	1.347472	1.347472	1.347472
	1.0	1.376336	1.333290	1.333247	1.333247	1.333247
	3.0	1.326247	1.286737	1.286682	1.286682	1.286682
$-\phi'(0)$	0.0	0.773109	0.807913	0.809416	0.809448	0.809448
	0.5	0.950211	0.956980	0.957025	0.957025	0.957025
	1.0	1.076976	1.076044	1.076055	1.076055	1.076055
	3.0	1.452263	1.442740	1.442734	1.442734	1.442734

Table 4. The effect of R on skin-friction, heat and mass transfer coefficients when $M = 0.5$, $Gr_x/Re^2 = 1.5$, $Gb = 0.5$, $R_d = 0.2$, $D_f = 0.3$, $Sr = 0.2$ and $N_1 = 0.1$

Table 5 shows the influence of the viscous dissipation parameter Gb. The skin-friction coefficient and the Sherwood number increase as Gb increases. However, the heat transfer rate is reduced when Gb is increased.

The effect of the Soret parameter on the skin-friction, the heat and the mass transfer coefficients is presented in Table 6. Clearly, increasing this parameter leads to increase in the heat transfer rate and a decrease in both the skin friction coefficient and the mass transfer rate. Similar findings were reported by Partha et al. [25].

Table 7 shows the effect of the Dufour number on the skin-friction, the heat and the mass transfer coefficients. It seen that as the Dufour parameter increases, the skin-friction coefficient and mass transfer rate are enhanced while the mass transfer rate is reduced. The Soret and Dufour numbers have opposite effects on Nusselt and Sherwood numbers.

		SLM results				
	Gb	1st order	2nd order	3rd order	4th order	**bvp4c**
$f''(0)$	0.0	-0.351301	-0.354490	-0.354558	-0.354558	-0.354558
	0.5	-0.334846	-0.339272	-0.339242	-0.339242	-0.339242
	1.0	-0.320079	-0.325029	-0.324930	-0.324930	-0.324930
	2.0	-0.295309	-0.299203	-0.298988	-0.298988	-0.298988
$-\theta'(0)$	0.0	1.364554	1.341183	1.341179	1.341179	1.341179
	0.5	1.349392	1.308530	1.308480	1.308480	1.308480
	1.0	1.340317	1.278965	1.278884	1.278884	1.278883
	2.0	1.337606	1.227792	1.227640	1.227640	1.227640
$-\phi'(0)$	0.0	1.278392	1.271621	1.271607	1.271607	1.271607
	0.5	1.281653	1.274574	1.274572	1.274572	1.274572
	1.0	1.284491	1.277309	1.277310	1.277310	1.277310
	2.0	1.289013	1.282196	1.282194	1.282194	1.282194

Table 5. The effect of Gb on skin-friction, heat and mass transfer coefficients when $M = 0.5,\ Gr_x/Re^2 = 1.5,\ R_d = 0.2,\ D_f = 0.3,\ Sr = 0.2,\ R = 2$ and $N_1 = 0.1$

		SLM results				
	Sr	1st order	2nd order	3rd order	4th order	**bvp4c**
$f''(0)$	0.1	-0.271640	-0.289773	-0.289559	-0.289559	-0.289559
	0.5	-0.332574	-0.337635	-0.337603	-0.337603	-0.337603
	1.0	-0.338023	-0.341848	-0.341863	-0.341863	-0.341863
	1.5	-0.338296	-0.341846	-0.341878	-0.341878	-0.341878
$-\theta'(0)$	0.1	1.192649	1.151536	1.151190	1.151190	1.151190
	0.5	1.343705	1.304565	1.304512	1.304512	1.304512
	1.0	1.363632	1.324409	1.324369	1.324369	1.324369
	1.5	1.371163	1.331565	1.331527	1.331527	1.331527
$-\phi'(0)$	0.1	1.311432	1.298783	1.298733	1.298733	1.298733
	0.5	1.233004	1.228589	1.228590	1.228590	1.228590
	1.0	1.146766	1.147516	1.147516	1.147516	1.147516
	1.5	1.061229	1.066875	1.066878	1.066878	1.066878

Table 6. The effect of Sr on skin-friction, heat and mass transfer coefficients when $M = 0.5,\ Gr_x/Re^2 = 1.5,\ Gb = 0.5,\ R_d = 0.3,\ R = 2$ and $N_1 = 0.1$

http://dx.doi.org/10.5772/55320

		SLM results				
	D_f	1st order	2nd order	3rd order	4th order	**bvp4c**
$f''(0)$	0.1	-0.2897226	-0.3041903	-0.3039915	-0.3039916	-0.3039916
	0.3	-0.2670553	-0.2869281	-0.2867154	-0.2867154	-0.2867154
	0.7	-0.2181199	-0.2504226	-0.2503761	-0.2503747	-0.2503747
	1.5	-0.1168316	-0.1785689	-0.1797718	-0.1797642	-0.1797642
$-\theta'(0)$	0.1	1.2407545	1.2030266	1.2027860	1.2027860	1.2027860
	0.3	1.1847094	1.1467282	1.1463211	1.1463211	1.1463211
	0.7	1.0731585	1.0350043	1.0341356	1.0341344	1.0341344
	1.5	0.8462011	0.8114925	0.8093554	0.8093376	0.8093375
$-\phi'(0)$	0.1	1.2343382	1.2276842	1.2276800	1.2276800	1.2276800
	0.3	1.2988048	1.2865458	1.2864829	1.2864829	1.2864829
	0.7	1.3245499	1.3072132	1.3069707	1.3069708	1.3069708
	1.5	1.3489087	1.3224155	1.3214809	1.3214790	1.3214790

Table 7. The effect of D_f on skin-friction, heat and mass transfer coefficients when $M = 0.5$, $Gr_x/Re^2 = 1.5$, $Gb = 0.5$, $R_d = 0.5$, $R = 2$ and $N_1 = 0.1$

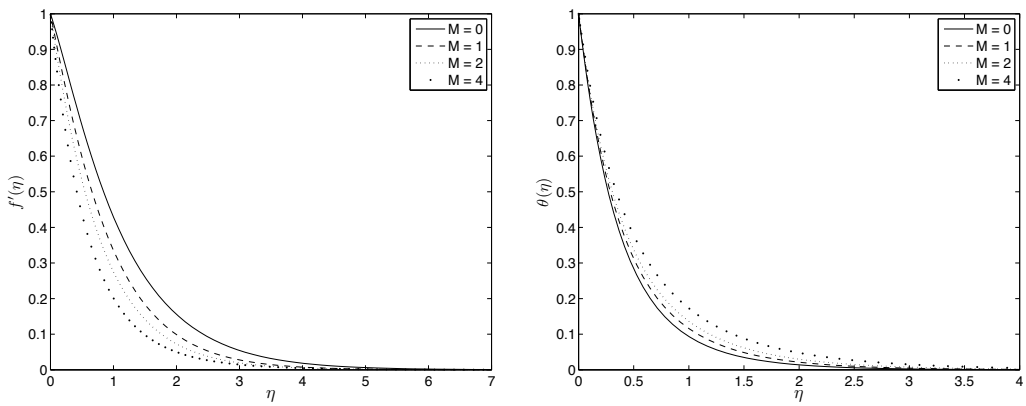

Figure 1. Effect of magnetic parameter M on the (a) velocity and, (b) temperature when $Gr_x/Re^2 = 1.5$, $Gb = 0.5$, $R_d = 1$, $D_f = 0.3$, $Sr = 0.2$, $R = 0.1$ and $N_1 = 0.1$

The effects of the various fluid and physical parameters on the fluid properties are displayed qualitatively in Figures 1 - 7. Figure 1 illustrates the effect of the magnetic parameter M on the boundary layer velocity and the temperature within the thermal boundary layer. As expected, we observe that increasing the magnetic filed parameter reduces the velocity due to an increase in the Lorentz force which acts against the flow if the magnetic field is applied in the normal direction. This naturally leads to an increase in the temperature (and concentration) within the boundary layer as less heat is conducted away.

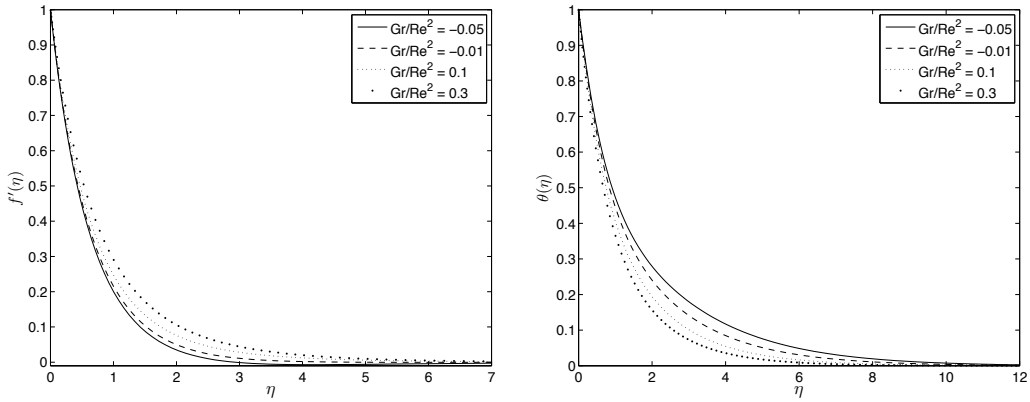

Figure 2. Effect of the mixed convection parameter Gr_x/Re^2 on the (a) velocity and (b) temperature when $M = 0.1$, $Gb = 0.1$, $R_d = 0.01$, $D_f = 0.3$, $Sr = 0.2$, $R = 0.2$ and $N_1 = 0.1$

Figure 2 shows the dimensionless velocity and temperature for various values of the mixed convection parameter Gr_x/Re^2 in the case of both aiding and opposing flow. We note that when the convection parameter increases, the velocity increases (the velocity is higher for aiding flow and less for opposing flow). The temperature (and solute concentration although not shown here) reduces as the convection parameter increases. Similar results were reported by Srinivasacharya and RamReddy [33].

Figure 3 shows the influence of the thermal radiation parameter R_d and the viscous dissipation Gb on the fluid velocity. The velocity increase with increasing thermal radiation parameter

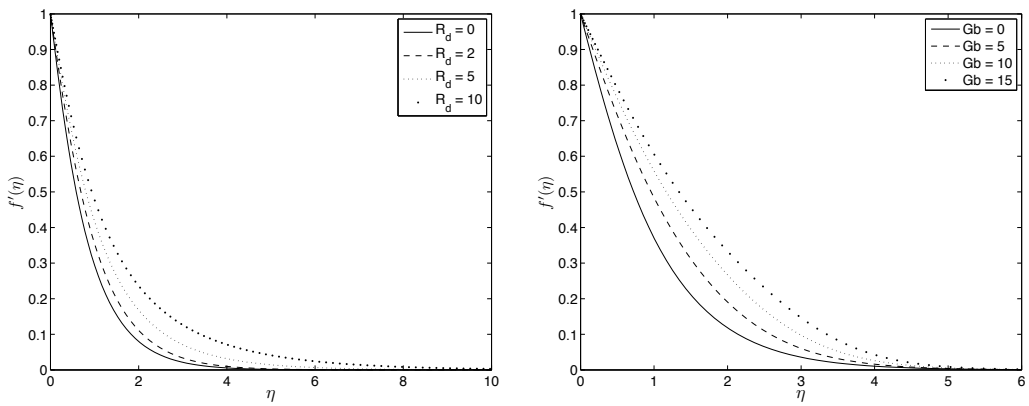

Figure 3. Effect of (a) the thermal radiation parameter R_d, and (b) viscous dissipation parameter Gb on the fluid velocity when $M = 0.5$, $Gr_x/Re^2 = 1.5$, $Gb = 0.5$, $D_f = 0.3$, $Sr = 0.2$, $R = 0.1$ and $N_1 = 0.1$

Figure 4 shows the influence of the thermal radiation parameter R_d and the viscous dissipation Gb on the temperature within the thermal boundary layer. Naturally, the temperature increases with an increase in the thermal radiation and viscous dissipation parameters.

http://dx.doi.org/10.5772/55320

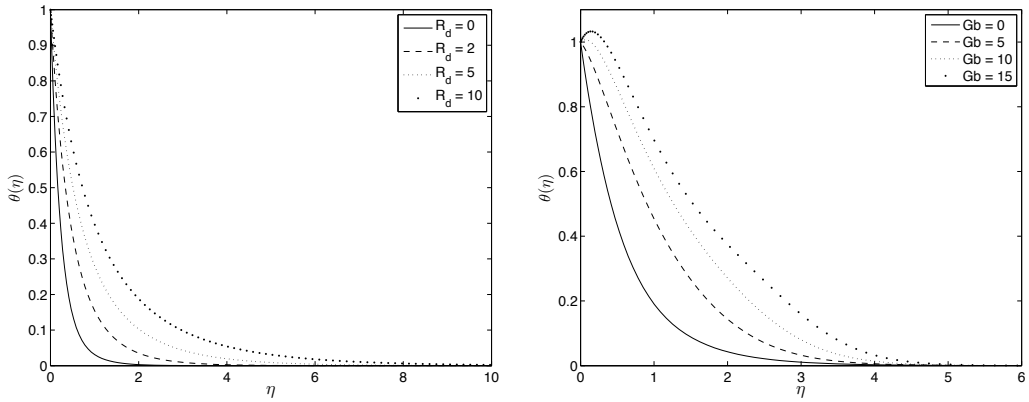

Figure 4. Effect of (a) the thermal radiation parameter R_d, and (b) viscous dissipation parameter Gb on the temperature within the thermal boundary layer when $M = 0.5,\ Gr_x/Re^2 = 1.5,\ Gb = 0.5,\ D_f = 0.3,\ Sr = 0.2,\ R = 0.1$ and $N_1 = 0.1$

The effect of the viscous dissipation parameter Gb on the solute concentration is shown in Figure 5. The solute concentration decreases with increasing viscous dissipation.

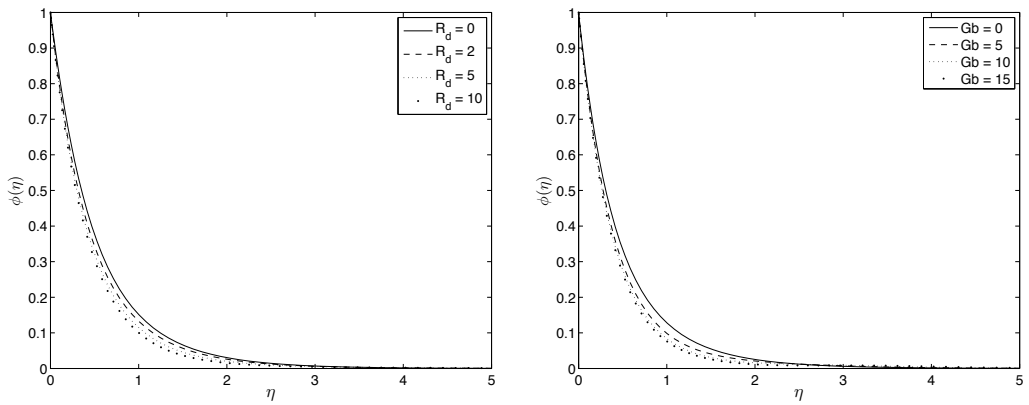

Figure 5. Effect of (a) the thermal radiation parameter R_d, and (b) the viscous dissipation parameter Gb on the solute concentration when $M = 0.5,\ Gr_x/Re^2 = 1.5,\ R_d = 1,\ D_f = 0.3,\ Sr = 0.2,\ R = 0.1$ and $N_1 = 0.1$

In Figure 6 we show the effect of increasing the Dufour D_f (that is, reducing the Soret Sr) parameter on the fluid velocity, temperature and solute concentration, respectively. The fluid velocity is found to increase with both parameters. An increase in D_f enhances the temperature within the thermal boundary layer.

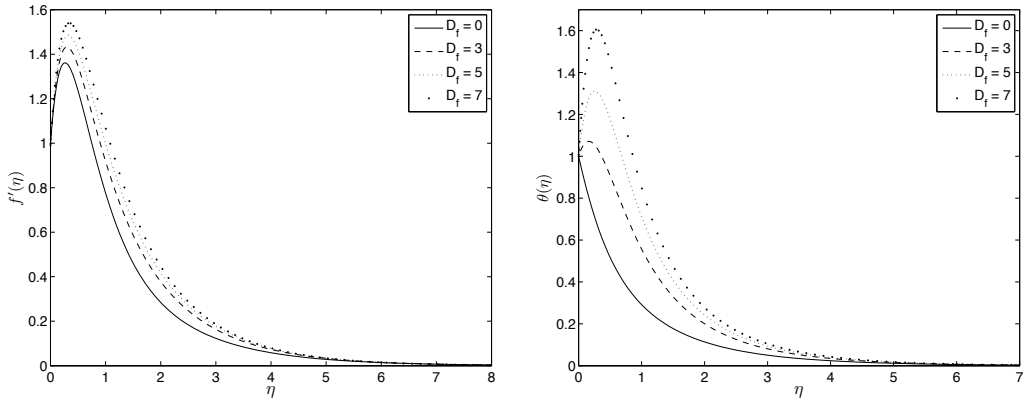

Figure 6. Effect of the Dufour number D_f on the (a) velocity, and (b) temperature when $M = 0.5$, $Gr_x/Re^2 = 1.5$, $Gb = 0.5$, $R_d = 0.2$, $R = 0.1$ and $N_1 = 2$

The effect of the chemical reaction parameter R on the fluid properties is shown in Figure 7. We note that the velocity reduces as the chemical reaction parameter R increases. However, the solute concentration within boundary layer naturally decreases with an increase in the chemical reaction.

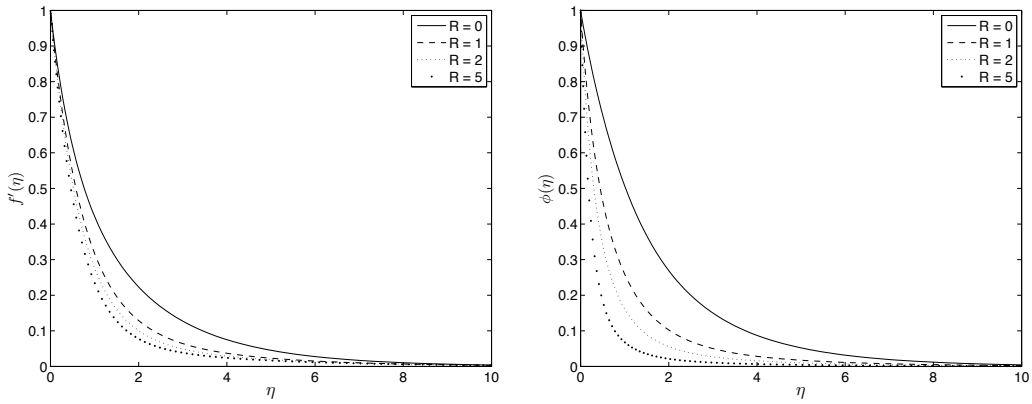

Figure 7. Effect of the chemical reaction parameter R on the (a) velocity, and (b) concentration distributions when $M = 2$, $Gr_x/Re^2 = 1.5$, $Gb = 0.5$, $R_d = 1$, $R = 0.1$, $D_f = 0.3$, $Sr = 0.2$ and $N_1 = 5$

5. Conclusion

In this chapter we have studied the effects of cross-diffusion and viscous dissipation on heat and mass transfer from an exponentially stretching surface in porous media. We further considered the effects of thermal radiation and a chemical reaction. The governing equations were solved using the successive linearisation method. This has been shown to give accurate results. The effects of various physical parameters on the fluid properties, the skin-friction coefficient and the heat and the mass transfer rates have been determined. It was found, inter alia, that the velocity increase with the mixed convection parameter while the temperature and concentration profiles decrease. An increase in both viscous dissipation and radiation

http://dx.doi.org/10.5772/55320

parameters reduced the concentration distribution while the temperature was enhanced by viscous dissipation and radiation parameters. The skin-friction, heat and mass transfer coefficients decreased with an increase in the magnetic field strength. The skin-friction and mass transfer coefficients decreased whereas the heat transfer coefficient increased with increasing Soret numbers.

Author details

Ahmed A. Khidir and Precious Sibanda

School of Mathematics, Statistics and Computer Science, University of KwaZulu-Natal, South Africa

References

[1] Al-Odat, M.Q.; Damseh, R.A. & Al-Azab, T.A. (2006). Thermal boundary layer on an exponentially stretching continuous surface in the presence of magnetic field effect. *Int. J. Appl. Mech. Eng*. 11, pp. 289-299.

[2] Ali, M. E. (1995). On thermal boundary layer on a power law stretched surface with suction or injection. *International Journal of Heat and Fluid Flow*, 16, pp. 280-290.

[3] Awad, F. G.; Sibanda, P.; Motsa, S. S. & Makinde, O. D. (2011). Convection from an inverted cone in a porous medium with cross-diffusion effects. *Computers & Mathematics with Applications*, 61, pp. 1431-1441.

[4] Awad, F. G.; Sibanda, P.; Narayana, M. & Motsa, S. S. (2011). Convection from a semi-finite plate in a fluid saturated porous medium with cross-diffusion and radiative heat transfer. *Int. J Physical Sciences*, 6, pp. 4910-4923.

[5] Awad, F.G.; Sibanda, P. & Narayana, M. (2011). *Heat and mass transfer from an inverted cone in a porous medium with cross-diffusion effects*. Mass Transfer-Advanced Aspects. pp. 81-106. InTech Open Access Publisher, Croatia.

[6] Bidin, B. & Nazar, R. (2009). Numerical solution of the boundary layer flow over an exponentially stretching sheet with thermal radiation. *Euro J. Sci. Res*, 33(4), pp. 710-717.

[7] Canuto, C.; Hussaini, M. Y.; Quarteroni, A. & Zang, T. A. (1988). *Spectral Methods in Fluid Dy- namics*. Springer-Verlag, Berlin.

[8] Don, W. S. & Solomonoff, A. (1995). Accuracy and speed in computing the Chebyshev collocation derivative. *SIAM J. Sci. Comput*, 16, pp. 1253-1268.

[9] Dulal, P. (2010). Mixed convection heat transfer in the boundary layers on an exponentially stretching surface with magnetic field. *App. Math. and Com*, 217, pp. 2356-2369.

[10] Dursunkaya, Z. & Worek, W. M. (1992). Diffusion-thermo and thermal diffusion effects in transient and steady natural convection from a vertical surface. *Int. J. Heat Mass Transfer*, 35, pp. 2060 -2065.

[11] Eckeret, E. R. G. & Drake, R. M. (1972). *Analysis of heat and mass transfer*. McGraw-Hill, New York.

[12] El-Aziz, M. A. (2008). Thermal-diffusion and diffusion-thermo effects on combined heat mass transfer by hydromagnetic three-dimensional free convection over a permeable stretching surface with radiation. *Physics Letter A*, 372, pp. 263-272.

[13] Elbashbeshy, E. M. A. (2001). Heat transfer over an exponentially stretching continuous surface with suction. *Archive of Mechanics*, 53, pp. 643-651.

[14] Ibrahim, S. Y. & Makinde, O. D. (2010). Chemically reacting MHD boundary layer flow of heat and mass transfer past a moving vertical plate with suction. *Scientific Research and Essay*, 5, pp. 2875-2882.

[15] Ishak, A. (2011). MHD boundary layer flow due to an exponentially stretching sheet with radiation effect. *Sains Malaysiana*, 40, pp. 391-395.

[16] Javed, T.; Sajid, M.; Abbas, Z. & Ali, N. (2011). Non-similar solution for rotating flow over an exponentially stretching surface. *Int. J. Numerical Methods for Heat and Fluid Flow*, 21, pp. 903-908.

[17] Khan, S. K. (2006). Boundary layer viscoelastic fluid flow over an exponentially stretching sheet. *International Journal of Applied Mechanics and Engineering*, 11, pp. 321-335.

[18] Loganathan, P.; Iranian, D. & Ganesan, P. (2011). Effects of chemical reaction on unsteady free convection and mass transfer flow past a vertical plate with variable viscosity and thermal conductivity. *European J. of Sc. Research*, 59, pp. 403-416.

[19] Magyari, E. & Keller, B. (1999). Heat and mass transfer in the boundary layers on an exponentially stretching continuous surface. *J Phys D: Appl Phy*, 32, pp. 577-585.

[20] Makukula, Z. G.; Sibanda, P. & Motsa, S. S. (2010). A note on the solution of the Von Kármán equations using series and chebyshev spectral methods. *Boundary Value Problems*, ID 471793 (2010).

[21] Makukula, Z.G.; Sibanda, P. & Motsa, S. S. (2010). On new solutions for heat transfer in a visco-elastic fluid between parallel plates. *Internationl Journal of Mathematical Models and Method in Applied Sciences*, 4, pp. 221-230.

[22] Makukula, Z.G.; Sibanda, P. & Motsa, S. S. (2010). A novel numerical technique for two-dimensional laminar flow between two moving porous walls. *Mathematical Problems in Engineering*, 2010, Article ID 528956. doi:10.1155/2010/528956.

http://dx.doi.org/10.5772/55320

[23] Motsa, S. S.; Sibanda, P. & Shateyi, S. (2011). On a new quasi-linearization method for systems of nonlinear boundary value problems. *Mathematical Methods in the Applied Sciences*, 34, pp. 1406-1413.

[24] Partha, M. K.; Murthy, P. V. S. N. & Rajasekhar, G. P. (2005). Effect of viscous dissipation on the mixed convection heat transfer from an exponentially stretching surface. *Heat Mass Transfer*, 41, pp. 360-366.

[25] Partha, M. K.; Murthy, P. V. S. N. & Rajasekhar, G. P. (2006). Soret and Dufour effects in a non-Darcy porous medium. *J. Heat Transfer*, 128, pp. 605-610.

[26] Raptis, A. (1998). Radiation and free convection flow through a porous medium. *International Communications in Heat and Mass Transfer*, 25, pp. 289-295.

[27] Sparrow, E.M. & Cess, R.D. (1978). *Radiation Heat Transfer*. Hemisphere, Washington.

[28] Sajid, M. & Hayat, T. (2009). Influence of thermal radiation on the boundary layer flow due to an exponentially stretching sheet. *Int. Comm. Heat Mass Transfer*, 35, pp. 347-356.

[29] Sanjayanand, E. & Khan, S. K. (2006). On heat and mass transfer in a viscoelastic boundary layer flow over an exponentially stretching sheet. *International Journal of Thermal Sciences*, 45, pp. 819-828.

[30] Sakiadis, B.C. (1961). Boundary layer behavior on continuous solid surfaces I: Boundary layer equations for two dimensional and axi-symmetric flow. *AIChE J*, 7, pp. 26-28.

[31] Sakiadis, B.C. (1976). Boundary layer behavior on continuous solid surfaces II. The boundary layer on a continuous flat surfaces. *AIChE J*, 7, pp. 221-225.

[32] Shateyi, S. & Motsa, S.S. (2010). Variable viscosity on magnetohydrodynamic fluid flow and heat transfer over an unsteady stretching surface with hall effect. *Boundary Value Problems*, 2010, Article ID 257568. doi:10.1155/2010/257568.

[33] Srinivasacharya, D. & RamReddy, Ch. (2011). Soret and Dufour Effects on Mixed Convection from an Exponentially Stretching Surface. *Int. J of Nonlinear Science*, 12, pp. 60-68.

Chapter 6

Numerical Analysis of Mixed Convection Magnetohydrodynamic Heat and Mass Transfer past a Stretching Surface in a Micro-Polar Fluid-Saturated Porous Medium Under the Influence of Ohmic Heating

Sandile S. Motsa and Stanford Shateyi

Additional information is available at the end of the chapter

http://dx.doi.org/10.5772/52785

1. Introduction

Coupled head and mass transfer by mixed convection in a micro-polar fluid-saturated porous medium due to a stretching sheet has numerous applications in geophysics and energy related engineering problems that engineering problems that includes both metal and polymer sheets. The micro rotation of each particle about its centroid as well as the translatory motion of each particle are taken into account in the study of micro polar fluids.

Past studies on micro polar fluids include, among others, the boundary layer flow of a micro polar fluid over a plate (Rees and Bassom 1996), the flow of a micro polar fluid over a stretching sheet (Raptis,1998) and the flow of a micro polar of fluid in a porons medium (Rawat et al.2007; Motsa et al. 2010; Pal and Chatterjec 2011) .

In many engineering areas processes occur at high temperature so knowledge of radiation heat transfer plays very significant roles and cannot be neglected. Thermal radiation effects become important when the difference between the surface and the ambient temperature is large. Numerous studies have been made to analyze the effect of radiation boundary layer flows under different geometry, (Pal 2009, Pal and Mondal 2010; Shateyi and Motsa 2009; Shateyi and Motsa 2011; Pal and Chatterjec 2011), among others.

In view of the above discussions, we envisage to investigate the steady two-dimensional mixed convection and mass transfer flow past a semi infinite vertical porous plate embedded in a micro polar fluid-saturated porous medium in the presence of thermal radiation, Ohmic dissipation, inertia effects and dispersion effects as these parameters have significant contribution to convective transport process. The problem considered in this chapter has many practical situations such as polymer extrusion processes and the combined effects of the physical parameters will have a large impact on heat and mass transfer characteristics. In this chapter we also aim to solve the current problem using the successive linearization method (Motsa 2011; Motsa and Sibanda 2012) .

2. Mathematical formulation

We consider a steady two-dimensional magnetohydrodynamic laminar mixed convection heat and mass transfer flow of a viscous incompressible fluid over a vertical sheet in a micro polar fluid-saturated porous medium. A uniform transverse magnetic field B_0 is applied normal to the flow. In this chapter, we assume that the applied magnetic field is taken being weak so that Hall and ion-slip effects maybe neglected. The radiative heat flux in the x-direction is considered negligible in comparison to the y-direction. Under the usual boundary layer approximation, along with Boussinesq's approximations the governing equations describing the conservation of mass, momentum, energy and concentration in the presence of thermal radiation and ohmic heating are governed by the following equations:

$$\frac{\partial u}{\partial x}+\frac{\partial v}{\partial y}=0, \tag{1}$$

$$u\frac{\partial u}{\partial x}+v\frac{\partial u}{\partial y}=\left(\nu+\frac{k_1^*}{\rho}\right)\frac{\partial^2 u}{\partial y^2}+\frac{k_1^*}{\rho}\frac{\partial N}{\partial y}-\left(\frac{\nu\varphi}{k}+\frac{\sigma B_0^2}{\rho}\right)u-\frac{C_b}{\sqrt{k}}\varphi u^2+g\beta_t(T-T_\infty)$$
$$+g\beta_c(C-C_\infty), \tag{2}$$

$$\rho j\left(u\frac{\partial N}{\partial x}+v\frac{\partial N}{\partial y}\right)=\gamma\frac{\partial^2 N}{\partial y^2}-k_1^*(2N+\frac{\partial u}{\partial y}), \tag{3}$$

$$u\frac{\partial T}{\partial x}+v\frac{\partial T}{\partial y}=\frac{1}{\rho c_p}\frac{\partial}{\partial y}\left(\kappa\frac{\partial T}{\partial y}\right)-\frac{1}{\rho c_p}\frac{\partial q_r}{\partial y}+\frac{\delta B_0^2}{\rho c_p}u^2+\frac{\mu}{\rho c_p}\left(\frac{\partial u}{\partial y}\right)^2, \tag{4}$$

$$u\frac{\partial C}{\partial x}+v\frac{\partial C}{\partial y}=D\frac{\partial^2 C}{\partial y^2}. \tag{5}$$

Where u, v are the velocity components along the x- and y - direction, ρ is the density of the fluid, T and C are the temperature and concentration, respectively, C_b is the form of drag coefficient which is independent of viscosity and other properties of the fluid but is dependent on the geometry of the medium, k is the permeability of the porous medium, β_t and β_c are the coefficients of thermal and concentration expansions, respectively, γ is the spin gradient and k_1^* is the vortex viscosity, c_p is the specific heat constant pressure, ν is the kinematic viscosity, σ is the electrical conductivity of the fluid,B_0 is externally imposed magnetic field strength, D is the molecular diffusivity , j is the micro inertia per unit mass, N is the component of microrotation or angular velocity whose rotation is in the $x-y$ plane direction. The spin gradient viscosity γ, defines the relationship between the coefficient of viscosity and micro-inertia as follows (Kim 1999):

$$\gamma=\mu\left(1+\frac{K}{2}\right)j, \tag{6}$$

with $K=k_1^*/\nu$ being the material parameter. We take $j=\nu/b$ as a reference length. The thermal conductivity κ is assumed to vary linearly with temperature and is of the form:

http://dx.doi.org/10.5772/52785

$$\kappa = \kappa_\infty[1 + \epsilon\theta(\eta)], \tag{7}$$

where ϵ is a small parameter, and following the Rosseland approximation, the radiative heat flux q_r is modeled as,

$$q_r = -\frac{4\sigma^*}{3k^*}\frac{\partial T^4}{\partial y}, \tag{8}$$

where σ^* is the Stefan-Boltzmann constant and k^* is the mean absorption coefficient. We assume that the difference in temperature within the flow are such T^4 can be expressed as linear combination of the temperature and then T^4 can be expanded in Taylor's series about T_∞ as follows:

$$T^4 = T_\infty^4 + 4T_\infty^3(T - T_\infty) + 6T_\infty^2(T - T_\infty)^2 + ... \tag{9}$$

Now neglecting higher order terms beyond the first degree in $(T - T_\infty)$ gives

$$T^4 \cong -3T_\infty^4 + 4T_\infty^4 T. \tag{10}$$

Using equations (8) and (10) we obtain

$$\frac{\partial q_r}{\partial y} = -\frac{16T_\infty^3\sigma^*}{3k^*}\frac{\partial^2 T}{\partial y^2}, \tag{11}$$

Using equation (11) in equation (4) gives

$$u\frac{\partial T}{\partial x} + v\frac{\partial T}{\partial y} = \frac{1}{\rho c_p}\frac{\partial}{\partial y}\left(\kappa\frac{\partial T}{\partial y}\right) + \frac{16T_\infty^3\sigma^*}{3k^*}\frac{\partial^2 T}{\partial y^2} + \frac{\delta B_0^2}{\rho c_p}u^2 + \frac{\mu}{\rho c_p}\left(\frac{\partial u}{\partial y}\right)^2, \tag{12}$$

The appropriate boundary conditions for the problem under study are given by:

$$u = u_w = bx, \;\; v = 0, \; N = -n\frac{\partial u}{\partial y} \;\text{ at }\; y = 0, \;\; u \to 0, \; N \to 0 \;\; \text{as} \;\; y \to \infty, \tag{13}$$

$$T = T_w = \; T_\infty + A_0\left(\frac{x}{l}\right)^2, \;\; C = C_w = C_\infty + A_1\left(\frac{x}{l}\right)^2, \;\text{ at }\; y = 0, \tag{14}$$

where A_0, A_1 are constants, l being the characteristics length, T_w is the wall temperature of the fluid and T_∞ is the ambient fluid temperature, C_w is the wall concentration of the solute and C_∞ is the concentration of the solute far away from the sheet, n is a constant taken as $0 \leq n \leq 1$.

2.1. Similarity solutions

In order to reduce the governing equations into a convenient system of ordinary differential equations. We introduce the following self-similar solution of the form:

$$u = bxf'(\eta),\ \ v = -\sqrt{b\nu}f(\eta),\ \ \eta = \sqrt{\frac{b}{\nu}}y, \tag{15}$$

$$N = bx(b/\nu)^{\frac{1}{2}}g(\eta),\ \ \theta(n) = \frac{T - T_\infty}{T_w - T_\infty},\ \ \phi(\eta) = \frac{C - C_\infty}{C_w - C_\infty}, \tag{16}$$

where f is the dimensionless stream function and η is the similarity variable. Substituting these into the governing equations, we obtain the following nonlinear ordinary differential equations:

$$(1+K)f''' + ff'' - (1+\alpha)f'^2 - \left(M^2 + \frac{1}{Da}\right)f' + Kg' + Gr_t\theta + Gr_m\phi = 0, \tag{17}$$

$$\left(1 + \frac{K}{2}\right)g'' + fg' - f'g - 2Kg - Kf'' = 0, \tag{18}$$

$$\frac{1}{Pr}(1 + R + \epsilon\theta)\theta'' + f\theta' + \frac{\epsilon}{Pr}(\theta')^2 - 2f'\theta + M^2E_c(f')^2 + Ec(f'')^2 = 0, \tag{19}$$

$$\frac{1}{Sc}\phi'' + f\phi' - 2\phi f' = 0, \tag{20}$$

where $\alpha = \frac{C_b}{\sqrt{k}}\varphi x$ is the local inertia coefficient parameter, $\frac{1}{Da} = \frac{\varphi r}{Kb}$ is inverse Darcy number, $M = \sqrt{\frac{\delta}{\rho b}}B_0$ is the Hartmann number, $Gr_t = \frac{g\beta_t(T-T_\infty)}{b^2l}$ is the local Grashof number, $Gr_c = \frac{g\beta_c(C-C_\infty)}{b^2l}$ local concentration Grashof number and $K = k^*/\nu$ is the material parameter, $Pr = \frac{\mu c_p}{k_\infty}$ is the Prandtl number, $E_c = \frac{b^2l^2}{Ac_p}$ is Ekert number, $R = \frac{16\delta^* T_\infty^3}{3k_\infty k^*}$ is the thermal radiation parameter, $S_c = \frac{\nu}{D}$ is the Schmidt number. The appropriate boundary conditions 12 and 13 now become:

$$f(\eta) = 0,\ f'(\eta) = 1,\ g(\eta) = -nf''(\eta),\ \theta(\eta) = 1,\ \phi(\eta) = 1,\ \text{at } \eta = 0, \tag{21}$$

$$f'(\eta) \to 0,\ \ g(\eta) \to 0,\ \theta(\eta) \to 0\ \phi(\eta) \to 0\ \ \text{as} \to \infty. \tag{22}$$

3. Method of solution

The governing nonlinear problem (16 - 19) is solved using the successive linearization method (SLM). In its basic form, the SLM ([4, 5]) seeks to linearize the governing nonlinear differential equations to a system of linear differential equations which, in most cases, cannot be solved analytically. The Chebyshev pseudospectral method (or any other collocation method or numerical scheme) is then used to transform the iterative sequence of linearized differential equations into a system of linear algebraic equations.

http://dx.doi.org/10.5772/52785

To solve the system of nonlinear equations (16 - 19), we introduce the following notation,

$$(z_1, z_2, z_3, z_4) = (f, g, \theta, \phi) \tag{23}$$

to represent the governing independent variables. In terms of the variables (23), we define the following vector of derivatives of z_j $(j = 1, 2, 3, 4)$, with respect to η

$$Z_1 = [f, f', f'', f'''] = [z_1^{(0)}, z_1^{(1)}, z_1^{(2)}, z_1^{(3)}], \tag{24}$$

$$Z_2 = [g, g', g''] = [z_2^{(0)}, z_2^{(1)}, z_2^{(2)}], \tag{25}$$

$$Z_3 = [\theta, \theta', \theta''] = [z_3^{(0)}, z_3^{(1)}, z_3^{(2)}], \tag{26}$$

$$Z_4 = [\phi, \phi', \phi''] = [z_4^{(0)}, z_4^{(1)}, z_4^{(2)}]. \tag{27}$$

In general we have

$$Z_i = [z_i^{(0)}, z_i^{(1)}, \ldots, z_i^{(n_i)}], \tag{28}$$

where $z_i^{(0)} = z_i$, $z_i^{(p)}$ is the pth derivative of z_i with respect to η and n_i $(i = 1, 2, \ldots m)$ is the highest derivative order of the variable z_i appearing in the system of equations. The system (16 - 19) can be written as a sum of it's linear $\mathcal{L}$ and nonlinear components N as

$$\mathcal{L}[z_1(\eta), z_2(\eta), z_3(\eta), z_4(\eta)] + \mathcal{N}[z_1(\eta), z_2(\eta), z_3(\eta), z_4(\eta)] = 0 \tag{29}$$

subject to the boundary conditions

$$A_i[z_1(0), z_2(0), z_3(0), z_m(0)] = K_{a,i}, \qquad B_b[z_1(\infty), z_2(\infty), z_3(\infty), z_4(\infty)] = K_{b,i}, \tag{30}$$

where A_i and B_i are linear operators and $K_{a,i}$ and $K_{b,i}$ are constants for $i = 1, 2, \ldots, 4$. In addition, we define L_i and N_i to be the linear and nonlinear operators, respectively, that operate on the Z_i for $i = 1, 2, 3, 4$ With these definitions, equation (29) and (30) can be written as

$$L_i[Z_1, Z_2, Z_3, Z_4] + N_i[Z_1, Z_2, Z_3, Z_4] = \sum_{j=1}^{4} \sum_{p=0}^{n_j} \alpha_{i,j}^{[p]} z_j^{(p)} + N_i[Z_1, Z_2, Z_3, Z_4] = 0 \tag{31}$$

where $\alpha_{i,j}^{[p]}$ are the constant coefficient of $z_j^{(p)}$, the derivative of z_j $(j = 1, 2, 3, 4)$ that appears in the ith equation for $i = 1, 2, 3, 4$

The boundary conditions (30) can be written as

$$\sum_{j=1}^{4}\sum_{p=0}^{n_j-1}\beta_{\nu,j}^{[p]}z_j^{(p)}(0)=K_{a,\nu},\qquad \nu=1,2,\ldots,m_a \tag{32}$$

$$\sum_{j=1}^{4}\sum_{p=0}^{n_j-1}\gamma_{\sigma,j}^{[p]}z_j^{(p)}(\infty)=K_{b,\sigma},\qquad \sigma=1,2,\ldots,m_b \tag{33}$$

where $\beta_{\nu,j}^{[p]}$ ($\gamma_{\sigma,j}^{[p]}$) are the constant coefficients of $z_j^{(p)}$ in the boundary conditions, and m_a, m_b are the total number of prescribed boundary conditions at $\eta=0$ and $\eta=\infty$ respectively. We remark that the sum m_a+m_b is equal to the sum of the highest orders of the derivatives corresponding to the dependent variables z_i, that is

$$m_a+m_b=\sum_{i=1}^{m}n_i. \tag{34}$$

The SLM assumes that the solution of (29) can be obtained as the convergent series

$$z_i(x)=\sum_{r=0}^{+\infty}z_{i,r}, \tag{35}$$

which, for numerical implementation is truncated at $r=s$ and written as

$$z_i(x)=z_{i,s}+\sum_{r=0}^{s-1}z_{i,r}. \tag{36}$$

A recursive iteration scheme is obtained by substituting (36) into the governing equation (29) and linearizing by neglecting nonlinear terms in $z_{i,s}$ and all it's derivatives. Substituting (36) in (29 - 30) and linearizing gives

$$L_i[Z_{1,s},Z_{2,s},Z_{3,s},Z_{4,s}]+\sum_{j=0}^{4}\sum_{p=0}^{n_j}z_{j,s}^{(p)}\frac{\partial N_i}{\partial z_j^{(p)}}[....]=-L_i[....]-N_i[....], \tag{37}$$

subject to

$$\sum_{j=1}^{4}\sum_{p=0}^{n_j-1}\beta_{\nu,j}^{[p]}z_{j,s}^{(p)}(0)=0,\qquad \nu=1,2,\ldots,m_a \tag{38}$$

$$\sum_{j=1}^{4}\sum_{p=0}^{n_j-1}\gamma_{\sigma,j}^{[p]}z_{j,s}^{(p)}(\infty)=0,\qquad \sigma=1,2,\ldots,m_b \tag{39}$$

http://dx.doi.org/10.5772/52785

where

$$[....] = \left[\sum_{r=0}^{s-1} Z_{1,r}, \sum_{r=0}^{s-1} Z_{2,r}, \sum_{r=0}^{s-1} Z_{3,r}, \sum_{r=0}^{s-1} Z_{4,r},\right] \tag{40}$$

The initial approximation ,$z_{j,0}(\eta)$, required to start the iteration scheme (37) is chosen to be a function that satisfies the boundary conditions (30). As a guide, the initial guess can be obtained as a solution of the linear part of (29) subject to the boundary conditions (30), that is, we solve

$$\sum_{j=1}^{m}\sum_{p=0}^{n_j} \alpha_{i,j}^{[p]} z_{j,0}^{(p)} = 0 \tag{41}$$

subject to

$$\sum_{j=1}^{4}\sum_{p=0}^{n_j-1} \beta_{\nu,j}^{[p]} z_{j,0}^{(p)}(0) = K_{a,\nu}, \qquad \nu = 1,2,\ldots,m_a \tag{42}$$

$$\sum_{j=1}^{4}\sum_{p=0}^{n_j-1} \gamma_{\sigma,j}^{[p]} z_{j,0}^{(p)}(\infty) = K_{b,\sigma}, \qquad \sigma = 1,2,\ldots,m_b \tag{43}$$

To solve the iteration scheme (37), it is convenient to use the Chebyshev spectral collocation method. For brevity, we omit the details of the spectral methods, and refer interested readers to [[12, 13])]. Before applying the spectral method, it is convenient to transform the domain on which the governing equation is defined to the interval [-1,1] on which the spectral method can be implemented. We use the transformation $\eta = \eta_e(\tau+1)/2$ to map the interval $[0, \eta_e]$ to [-1,1]. Here, it is assumed that η_e is a finite real number which is chosen to be large enough to numerically approximate infinity. The basic idea behind the spectral collocation method is the introduction of a differentiation matrix D which is used to approximate the derivatives of the unknown variables $z_i(\eta)$ at the collocation points as the matrix vector product

$$\frac{dz_i}{d\eta} = \sum_{k=0}^{\bar{N}} \mathbf{D}_{lk} z_i(\tau_k) = \mathbf{D}\mathbf{Z}_i, \qquad l = 0,1,\ldots,\bar{N} \tag{44}$$

where $\bar{N}+1$ is the number of collocation points (grid points), $\mathbf{D} = 2D/\eta_e$, and $\mathbf{Z} = [z(\tau_0), z(\tau_1), \ldots, z(\tau_N)]^T$ is the vector function at the collocation points. Higher order derivatives are obtained as powers of $\mathbf{D}$, that is

$$z_j^{(p)} = \mathbf{D}^p \mathbf{Z}_j. \tag{45}$$

Applying the Chebyshev spectral collocation on the recursive iteration scheme (37) gives

$$\sum_{j=1}^{m}\left[\Lambda_{i,j}+\Pi_{i,j}\right]\mathbf{Z}_{j,s}=\Phi_{i,s-1},\quad i,j=1,2,3,4 \tag{46}$$

where $\mathbf{Z}_{i,s}=[z_{i,s}(\tau_0),z_{i,s}(\tau_1),\ldots,z_{i,s}(\tau_N)]^T$, $\Lambda_{i,j}$, $\Pi_{i,j}$ and Φ_i are given by

$$\Lambda_{i,j}=\sum_{p=0}^{n_j}\alpha_{i,j}^{p}\mathbf{D}^{p},\qquad \Pi_{i,j}=\sum_{p=0}^{n_j}\frac{\partial N_i}{\partial z_j^{(p)}}\mathbf{D}^{p},\quad i,j=1,2,3,4. \tag{47}$$

and

$$\Phi_{i,s-1}=-L_i[....]-N_i[....], \tag{48}$$

respectively.

Defining $\Delta=\Lambda+\Pi$, we can write equation (46) in matrix form as

$$\begin{bmatrix}\Delta_{1,1} & \Delta_{1,2} & \cdots & \Delta_{1,m}\\ \Delta_{2,1} & \Delta_{2,2} & \cdots & \Delta_{2,m}\\ \vdots & \vdots & & \vdots\\ \Delta_{m,1} & \Delta_{m,2} & \cdots & \Lambda_{m,m}\end{bmatrix}\begin{bmatrix}\mathbf{Z}_{1,s}\\ \mathbf{Z}_{2,s}\\ \mathbf{Z}_{3,s}\\ \mathbf{Z}_{4,s}\end{bmatrix}=\begin{bmatrix}\mathbf{\Phi}_{1,s-1}\\ \mathbf{\Phi}_{2,s-1}\\ \mathbf{\Phi}_{3,s-1}\\ \mathbf{\Phi}_{4,s-1}\end{bmatrix} \tag{49}$$

where $\mathbf{Z}_{i,s}$, $\mathbf{\Phi}_{i,s-1}$ are vectors of size $(\bar{N}+1)\times 1$ and $\Delta_{i,j}$ are $(\bar{N}+1)\times(\bar{N}+1)$ matrices . After imposing the boundary conditions on the matrix system (49), and starting from $Z_{i,0}$, the recursive sequence (49) is solved iteratively for $s=1,2,3\ldots$ and the approximate solution for each $z_i(\eta)$ is obtained from the series

$$z_i(\eta)=z_{i,0}(\eta)+z_{i,1}(\eta)+z_{i,2}(\eta)+z_{i,3}(\eta)+\ldots \tag{50}$$

4. Results and discussion

This section presents the effects of various parameters on the velocity, temperature, microrotation and concentration profiles. We remark that the, unless otherwise specified, the SLM results presented in this analysis where obtained using $N=100$ collocation points and $\eta_e=20$ was used as a numerical approximation infinity. In order to get physical insight into the problem, the effects of these parameters encountered in the governing equations of the problem are analyzed with the help of figures. Figures 1 to 3 depicts effects of the local inertia coefficient parameter α, on the velocity, concentration and microrotation distributions. From Figure 1 it is observed that the horizontal velocity profiles decrease with the increasing values of α due to the fact that the second-order quadratic drag is offered by the porous medium to the fluid motion. This drag force results in decreased fluid in the boundary layer. In turn the reduced fluid flow causes the concentration $\phi(\eta)$ to increase as depicted in Figure 2. As expected the increasing values of the local inertia coefficient parameter α, causes the gyration component $g(\eta)$ as shown in Figure 3.

http://dx.doi.org/10.5772/52785

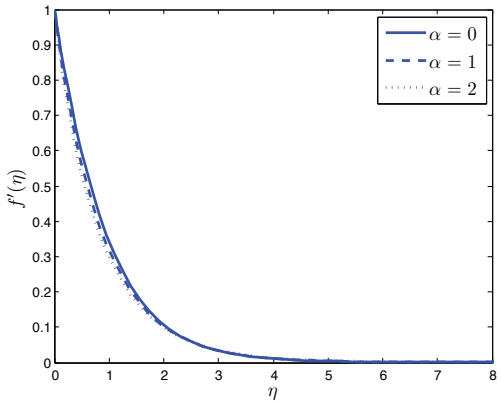

Figure 1. Variation of $f'(\eta)$ for different values of α with $K = 0.2; Da = 1; Grt = 1; M = 1; Grm = 1;\ Pr = 0.71; R = 1; \epsilon = 0.01; Ec = 1; Sc = 1; n = 0.5$.

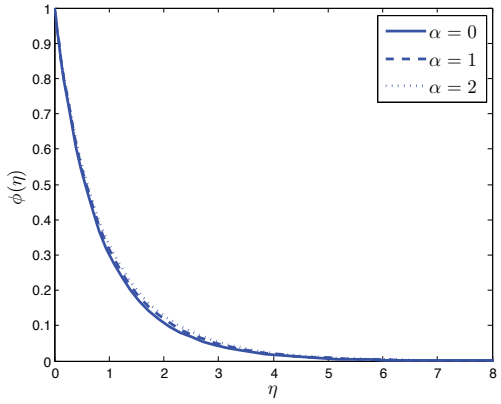

Figure 2. Plot of $\phi(\eta)$ for different values of α with $K = 0.2; Da = 1; Grt = 1; M = 1; Grm = 1;\ Pr = 0.71; R = 1; \epsilon = 0.01; Ec = 1; Sc = 1; n = 0.5$.

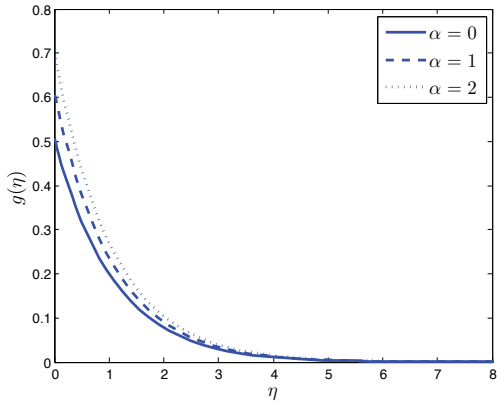

Figure 3. Variation of $g(\eta)$ for different values of α with $K = 0.2; Da = 1; Grt = 1; M = 1; Grm = 1;\ Pr = 0.71; R = 1; \epsilon = 0.01; Ec = 1; Sc = 1; n = 0.5$.

The effects of thermal Grashof number Gr_t on the velocity, temperature, concentration and microrotation distributions are displayed in Figure 4 through Figure 7. From Figure 4 we observe that the horizontal velocity profiles increase with increasing values of the thermal Grashof number Gr_t. Buoyancy force acts like a favourable pressure gradient which in turn accelerates the fluid flow within the boundary layer. This accelerated fluid flow leads to the reduction of both the fluid temperature and concentration as can be seen from Figure 5 and Figure 6, respectively. The microrotation profiles are significantly affected by the thermal buoyancy parameter as shown in Figure 7. The increasing values of Gr_t causes the microrotation significantly decrease.

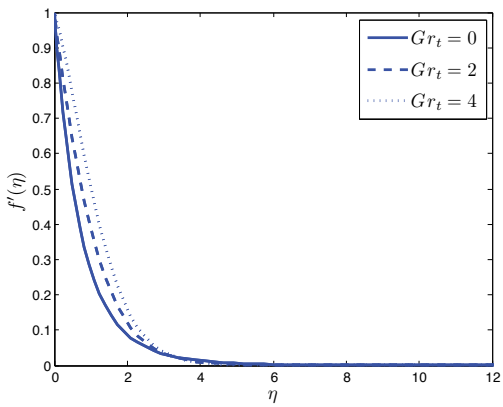

Figure 4. The influence of Gr_t on $f'(\eta)$ with $K = 0.2; \alpha = 0.5; Da = 1; Mm = 1; Grm = 1; Pr = 0.71; R = 1; \epsilon = 0.01; Ec = 1; Sc = 1; n = 0.5$.

http://dx.doi.org/10.5772/52785

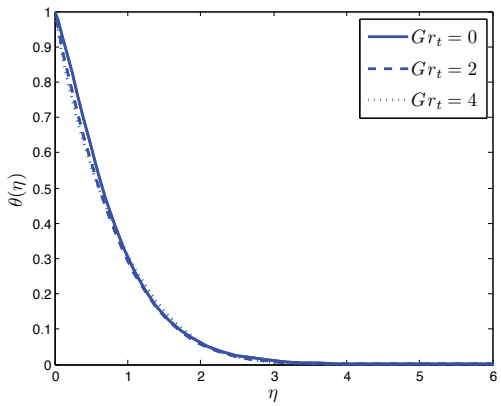

Figure 5. Variation of Gr_t on $\theta(\eta)$ when $K = 0.2; \alpha = 0.5; Da = 1; Mm = 1; Grm = 1; Pr = 0.71; R = 1; \epsilon = 0.01; Ec = 1; Sc = 1; n = 0.5$.

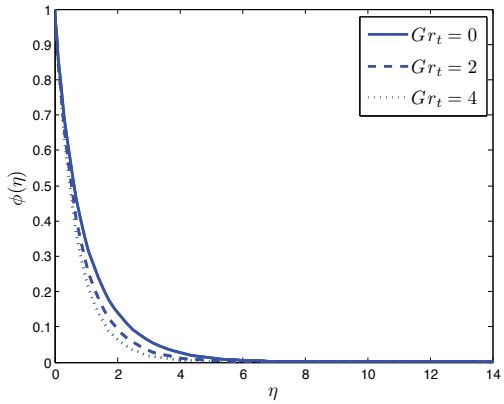

Figure 6. $Plot of \phi(\eta)$ for various values of Gr_t when $K = 0.2; \alpha = 0.5; Da = 1; Mm = 1; Grm = 1; Pr = 0.71; R = 1; \epsilon = 0.01; Ec = 1; Sc = 1; n = 0.5$.

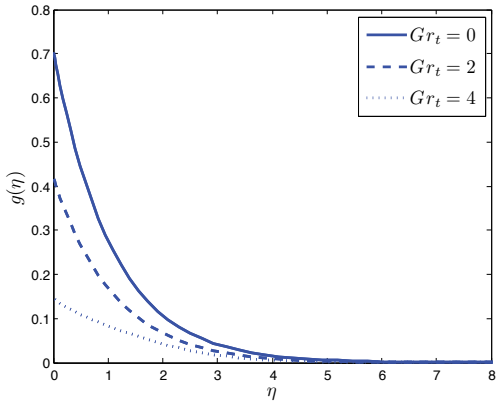

Figure 7. Plot of $g(\eta)$ when varying Gr_t with $K = 0.2; \alpha = 0.5; Da = 1; Mm = 1; Grm = 1; Pr = 0.71; R = 1; \epsilon = 0.01; Ec = 1; Sc = 1; n = 0.5$.

Figures 8-11 display results of velocity, temperature, concentration and microrotation distribution for various values of the magnetic parameter M. As expected, the existence of the magnetic field is to decrease the velocity in the boundary layer because the application of the transverse magnetic field results in a drag type of force known as Lorentz force. The drag force resists the fluid flow which results in reducing the velocity of the fluid in the boundary layer. The temperature in the boundary layer increases with increasing values of M, as shown in Figure 9. From Figure 10, we also observe that the concentration distributions increase as the magnetic parameter M increases. As the magnetic field is applied in the direction of the gyration component, the increasing values of M cause the microrotation distribution to increase as depicted in Figure 11.

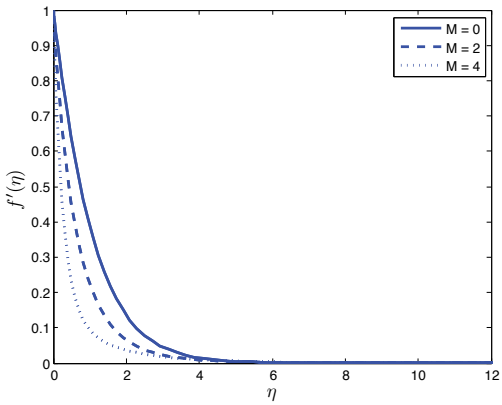

Figure 8. The influence of M on $f'(\eta)$ with $K = 0.2; \alpha = 0.5; Da = 1; Grt = 1; Grm = 1; Pr = 5; R = 1; \epsilon = 0.01; Ec = 1; Sc = 1; n = 0.5$.

http://dx.doi.org/10.5772/52785

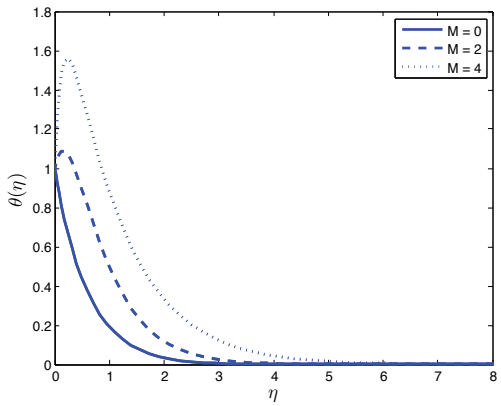

Figure 9. Plot of $\theta(\eta)$ for various values of M with $K = 0.2; \alpha = 0.5; Da = 1; Grt = 1; Grm = 1; Pr = 5; R = 1; \epsilon = 0.01; Ec = 1; Sc = 1; n = 0.5$.

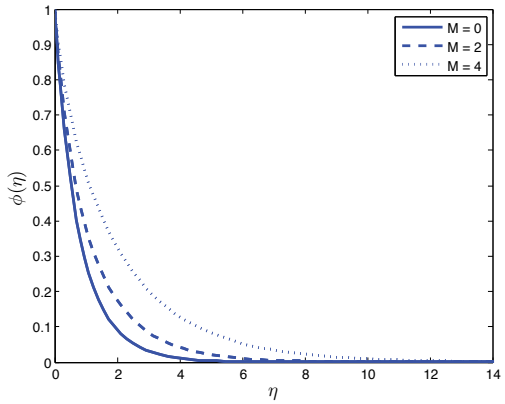

Figure 10. Variation of $\phi(\eta)$ for different values of M with $K = 0.2; \alpha = 0.5; Da = 1; Grt = 1; Grm = 1; Pr = 5; R = 1; \epsilon = 0.01; Ec = 1; Sc = 1; n = 0.5$.

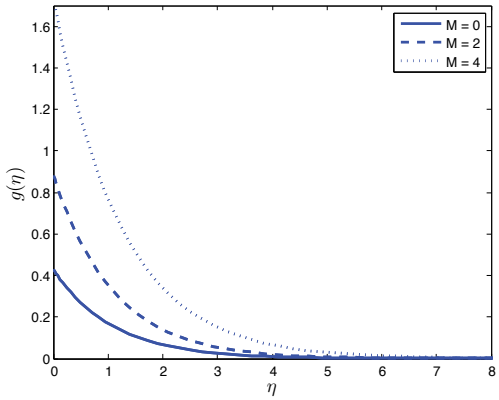

Figure 11. Plot of $g(\eta)$ when varying M when $K = 0.2; \alpha = 0.5; Da = 1; Grt = 1; Grm = 1; Pr = 5; R = 1; \epsilon = 0.01; Ec = 1; Sc = 1; n = 0.5$.

The influence of the Darcy number Da on the velocity, temperature, concentration and microrotation profiles is depicted in Figure 12-15. It is clearly observed from these figures that the velocity distribution $f'(\eta)$ increasing with increasing values of the Darcy number Da, whereas revers trend is seen on the temperature, concentration and microrotation distributions. This is because the presence of porous medium is to increase the resistance to the flow which causes the fluid flow to decrease.

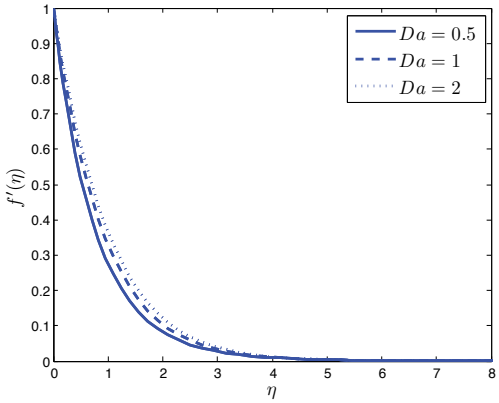

Figure 12. Variation of $f'(\eta)$ for different values of Da with $K = 0.2; \alpha = 0.5; Grt = 1; Mm = 1; Grm = 1; Pr = 5; R = 1; e = 0.01; Ec = 1; Sc = 1; n = 0.5$.

http://dx.doi.org/10.5772/52785

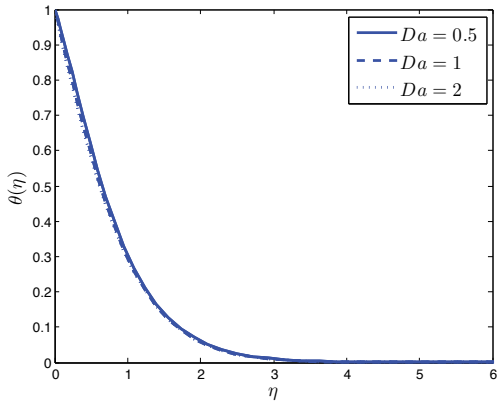

Figure 13. Plot of $\theta(\eta)$ for different values of Da $K = 0.2; \alpha = 0.5; Grt = 1; Mm = 1; Grm = 1; Pr = 5; R = 1; e = 0.01; Ec = 1; Sc = 1; n = 0.5$.

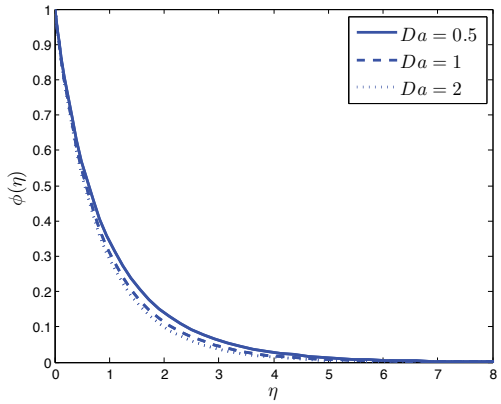

Figure 14. Influence of Da on $\phi(\eta)$ when $K = 0.2; \alpha = 0.5; Grt = 1; Mm = 1; Grm = 1; Pr = 5; R = 1; e = 0.01; Ec = 1; Sc = 1; n = 0.5$.

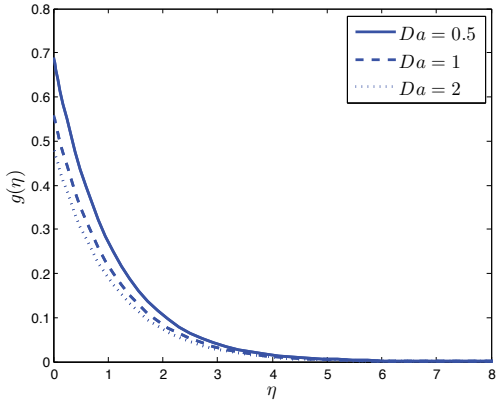

Figure 15. The effect of Da on $g(\eta)$ when $K = 0.2; \alpha = 0.5; Grt = 1; Mm = 1; Grm = 1; Pr = 5; R = 1; e = 0.01; Ec = 1; Sc = 1; n = 0.5$.

5. Conclusion

Numerical analysis has been carried out in this chapter to study mixed convection heat and mass transfer in MHD flow past a stretching sheet in a micropolar fluid saturated medium under the influence of Ohmic heating. The governing partial differential equations which describe the problem are transformed in a system of ordinary differential equations by using suitable similarity transformations. A recently developed iterative technique together with Chebyshev spectral collocation method is used to solve the highly non-linear and coupled ordinary differential equations. The effects of various physical parameters on the velocity, microrotation, temperature and concentration are obtained. The following main conclusions can be drawn from the present study:

1. The fluid velocity increases with increase in the Grashof numbers, but decreases with increasing values of the Hartman number, local inertia coefficient parameter and inverse Darcy number.
2. The microrotation profiles decrease with thermal/solutal buoyancy force, and the Darcy number, whereas opposite trends are seen by enhancing values of the magnetic field and inertia coefficient parameter.
3. The fluid temperature increases with increasing values of magnetic field, inertia coefficient parameter, while opposite effects are seen by enhancing buoyancy forces and Darcy number.
4. Concentration decreases with increasing values of buoyancy forces and the Darcy number, whereas reverse trends are seen with increasing values of magnetic field, inertia coefficient parameter.

Acknowledgement

The authors wish to acknowledge financial support from the National Research Foundation (NRF).

http://dx.doi.org/10.5772/52785

Author details

Sandile S. Motsa[1] and Stanford Shateyi[2]

1 University of KwaZulu-Natal, South Africa
2 University of Venda, South Africa

References

[1] D. A. S. Rees, and A. P. Bassom, The Blasius Boundary Layer Flow of a Micropolar Fluid, Int. J. Eng. Sci. 34, 113-124 (1996).

[2] A. Raptis, Flow of a Micropolar Fluid Past a Continuously Moving Plate by the Presence of Radiation, Int. J. Heat Mass Transf. 41, 2865–2866 (1998).

[3] S. Rawat, R. Bhargava and O. A. Bt'eg, A Finite Element Study of the Transport Phenomena in MHD Micropolar Flow in a Darcy-Forchheimer Porous Medium, Proc. WCECS, San Francisco, CA (2007).

[4] S.S. Motsa, New algorithm for solving non-linear BVPs in heat transfer, International Journal of Modeling, Simulation & Scientific Computing, 2:3, 355–373, (2011)

[5] Motsa,S.S.,Sibanda,P. (2012). A linearisation method for non-linear singular boundary value problems, Computers and Mathematics with Applications, 63,1197–1203 (2012)

[6] S.S Motsa,S. Shateyi and P. Sibanda, A Model of Steady Viscous Flow of a Micropolar Fluid Driven by Injection or Suction Between a Porous Disk and a Non-Porous Disk Using a Novel Numerical Technique, Can. J. Chem. Eng. 88:991–1002, (2010).

[7] D. Pal and S. Chatterjee, Mixed convection magnetohydrodynamic heat and mass transfer past a stretching surface in a micropolar fluid-saturated porous medium under the influence of Ohmic heating, Soret and Dufour, Comm. Nonlinear Sci. Numer. Simul. 16, 1329-1346, (2011).

[8] D. Pal, Heat and mass transfer in stagnation-point flow towards in a stretching surface in the presence of buoyancy force and thermal radiation, Meccanica, 44,145-158, (2009).

[9] Pal, D., and Mondal, H, The influence of thermal radiation on hydromagnetic Darcy-Forchheimer mixed convection flow past a stretching sheet embedded in a porous medium, Meccanica, 45(2), doi 10.1007/s11012- 010-9334-8, (2010).

[10] S. Shateyi , Motsa S.S,Thermal Radiation Effects on Heat and Mass Transfer over an Unsteady Stretching Surface, Mathematical Problems in Engineering Volume 2009, Article ID 965603, 13 pages doi:10.1155/2009/965603.

[11] S. Shateyi, and Motsa, S. S. Hydromagnetic non-Darcy flow, heat and mass transfer over a stretching sheet in the presence of thermal radiation and Ohmic dissipation. The Canadian Journal of Chemical Engineering, 89: n/a. doi: 10.1002/cjce.20499,(2011).

[12] C. Canuto, M.Y. Hussaini, A. Quarteroni, and T.A. Zang, Spectral Methods in fluid dynamics, Springer-Verlag, Berlin, 1988.

[13] L. N. Trefethen, Spectral Methods in MATLAB, SIAM, 2000.

Chapter 7

Modeling of Heat and Mass Transfer and Absorption-Condensation Dust and Gas Cleaning in Jet Scrubbers

M. I. Shilyaev and E. M. Khromova

Additional information is available at the end of the chapter

http://dx.doi.org/10.5772/53094

1. Introduction

The process of complex cleaning of gases, injected into the atmosphere, for instance, by thermal power plants, metallurgical, chemical or other industrial enterprises, from dust and harmful gaseous admixtures by means of their irrigation by wash liquids (water or specially selected water solutions) is considered. This process can be implemented in gas pipes or gas-cleaning apparatuses (direct flow or counter flow jet scrubbers) [1]. The process of gas cleaning from dust and gas admixtures is carried out in the following manner. The fluid dispersed by jets is introduced into the dust-vapor-gas flow in the form of droplets, interacts with it, and under nonisothermal conditions the increased moisture content leads to intensive condensation of liquid vapors on particles, their significant enlargement and efficient absorption of liquid droplets due to collisions of the latter with particles [2]. Simultaneously, the liquid droplets and condensate on particles absorb harmful gas components, dissolving them and removing from the vapor-gas flow.

The authors failed to find the mathematical description of this complex process in literature. From the engineering point of view the importance of development of generalized mathematical models, which reflect properly the interaction of heat and mass transfer with the effects of gas components removal and dust capture by the droplets of irrigating liquid in jet scrubbers and reactors, is undisputable, and it is determined by significant opportunities for optimization of operation conditions and constructions of energy-intensive and large-scale equipment in various industries both in terms of reducing of material and energy costs.

2. Problem statement, main equations and assumptions

In the current work we suggest the model for mathematical description of the above process with the following assumptions:

1. droplets and particles are considered monodispersed with equivalent sizes, equal to mass-median by distributions;

2. concentrations of droplets of irrigating liquid, dust particles and harmful gas components are low, what allows us to use the Henry's law for equilibrium of gas components in liquid and gas phases at the interface and assume that the solution in droplet is ideal;

3. the mean-mass temperature of droplets and temperature of their surfaces are equal because of their small sizes [3];

4. the typical time of gas component dissolution in droplet is significantly less than the typical time of mass transfer processes, commonly occurring in the apparatus;

5. the motion velocities of particles with condensate on their surface ("formations") and vapor-gas flow are equal;

6. the moisture content in the flow can be high, what requires consideration of the Stefan correction in mass transfer equations for evaporation-condensation process on droplets and "formations";

7. we do not take into account the evaporation-condensation correction for the resistance and heat transfer coefficients of droplets and "formations", it is insignificant and becomes obvious only at the initial stages of the process at high moisture contents [4];

8. in equation of droplet motion we take into account variability of its mass;

9. the radiant component in the process of heat transfer is neglected because of low temperatures of droplet, "formations" and flow;

10. mutual coalescence of droplets and "formations" is not taken into account, and merging of droplets and "formations" due to collision is the basis of condensation-inertial mechanism of dust capture in jet scrubbers [2].

Under the above conditions equations of model system will take the following form:

Motion equation of a mass-median droplet with variable mass

$$\frac{\mathbf{d}\vec{V}_d}{\mathbf{d}\tau} = \vec{R}_d + \vec{g} - \frac{\vec{V}_d}{m_d}\frac{\mathbf{d}m_{\mathrm{d}}}{\mathbf{d}\tau}; \tag{1}$$

equation of heat transfer between droplet and vapor-gas flow

http://dx.doi.org/10.5772/53094

$$c_f m_d \frac{d\mathrm{T}_d}{d\tau} = -\alpha_d \pi \delta_d^2 (T_d - T) + \sum r_i \frac{d m_{id}}{d\tau} + c_\delta \rho_\delta V_c \frac{\pi \delta_d^2}{4} \eta_{Stk} (T_\delta - T_0); \quad (2)$$

equation of mass transfer between droplet and the i-th component of vapor-gas flow

$$\frac{\mathbf{d} m_{i\delta}}{\mathbf{d}\tau} = -\beta_{id} \pi \delta_d^2 \left(\rho_{id} - \rho_i\right); \quad (3)$$

equation of mass transfer between "formation" and the i-th component of vapor-gas flow

$$\frac{\mathbf{d} m_{i\delta}}{\mathbf{d}\tau} = -\beta_{i\delta} \pi \delta^2 \left(\rho_{i\delta} - \rho_i\right); \quad (4)$$

continuity equation for i-th reacting components, including vapor of liquid

$$\frac{\partial \rho_i}{\partial \tau} + div\left(\rho_i \vec{\mathrm{U}}\right) = -\frac{\mathbf{d} m_{id}}{\mathbf{d}\tau} n_d - \frac{\mathbf{d} m_{i\delta}}{\mathbf{d}\tau} n_\delta; \quad (5)$$

continuity equation for (mass concentration) of non-reacting component of the vapor-gas mixture

$$\frac{\partial \rho_g}{\partial \tau} + div\left(\rho_g \vec{U}\right) = 0; \quad (6)$$

continuity equation for (mass concentration) of "formations"

$$\frac{\partial \rho_\delta}{\partial \tau} + div\left(\rho_\delta \vec{U}\right) = \sum \frac{\mathbf{d} m_{i\delta}}{\mathbf{d}\tau} n_\delta - \rho_\delta V_c \frac{\pi \delta_d^2}{4} \eta_{\mathrm{Stk}} n_d; \quad (7)$$

continuity equation for (mass concentration) of droplets

$$\frac{\partial \rho_d}{\partial \tau} + div\left(\rho_d \vec{V}_d\right) = \frac{\mathbf{d} m_d}{\mathbf{d}\tau} n_d; \quad (8)$$

equation of heat transfer between "formation" and vapor-gas flow

$$\tilde{n}_\delta m_\delta \frac{\mathbf{d}T_\delta}{\mathbf{d}\tau} = -\alpha_\delta \pi \delta^2 \left(T_\delta - T\right) + \sum r_i \frac{\mathbf{d}m_{i\delta}}{\mathbf{d}\tau}; \tag{9}$$

equation of convective heat transfer between vapor-gas flow and droplets and "formations"

$$\rho \frac{\mathbf{d}\tilde{n}\left(T - T_0\right)}{\mathbf{d}\tau} = \alpha_d \pi \delta_d^2 \left(T_d - T\right) n_d + \alpha_\delta \pi \delta^2 \left(T_\delta - T\right) n_\delta; \tag{10}$$

general rate of droplet mass change due to evaporation-condensation and absorption of removed gas components (droplet collision is assumed unlikely) and "formation" absorption

$$\frac{\mathbf{d}m_d}{\mathbf{d}\tau} = \sum \frac{\mathbf{d}m_{id}}{\mathbf{d}\tau} + \rho_\delta V_c \frac{\pi \delta_d^2}{4} \eta_{\text{Stk}} \tag{11}$$

general rate of "formation" mass change ("formation" collision is assumed unlikely)

$$\frac{\mathbf{d}m_\delta}{\mathbf{d}\tau} = \sum \frac{\mathbf{d}m_{i\delta}}{\mathbf{d}\tau}; \tag{12}$$

continuity equation for (mass concentration) of dry particles

$$\frac{\partial \rho_{\text{p}}}{\partial \tau} + div\left(\rho_p \vec{U}\right) = -\rho_p V_c \frac{\pi \delta_d^2}{4} \eta_{\text{Stk}} n_d. \tag{13}$$

The following closure relationships shall be added to equations (1-13):

for the force of droplet aerodynamic resistance per a unit of droplet mass,

$$\vec{R}_{\text{d}} = -\xi \frac{\left(\vec{V}_d - \vec{U}\right)}{\tau_d}; \tag{14}$$

where relative coefficient of droplet resistance is $\tilde{\xi} = \xi / \xi_c$, $\xi_c = 24 / \text{Re}_d$,

$$\tilde{\xi} = 1 + 0{,}197\,\text{Re}_d^{0{,}63} + 2{,}6 \cdot 10^{-4}\,\text{Re}_d^{1{,}38} \quad (0{,}1 \le \text{Re}_d \le 3 \cdot 10^5)\ \left[5\right], \tag{15}$$

$$\tau_d = \frac{\rho_f \delta_d^2}{18\mu}, \text{Re}_d = \frac{V_c \delta_d \rho}{\mu}, V_{\text{c}} = \left|\vec{V}_{\text{d}} - \vec{U}\right|; \tag{16}$$

http://dx.doi.org/10.5772/53094

coefficient of "formation" entrainment according to the empirical formula of Langmuir–Blodgett with Fuchs correction on engagement effect [1]

$$\eta_{\text{Stk}} = \left(\frac{\text{Stk}}{\text{Stk} + 0,5} \right)^2 + 2,5 \frac{\delta}{\delta_d}, \tag{17}$$

$$\text{Stk} = \tau_\delta \frac{V_\text{c}}{\delta_\text{d}}, \tau_\delta = \frac{\rho_{\text{f}\delta} \delta^2}{18\mu} \left(\rho_{f\delta} \approx \rho_f \right), \tag{18}$$

where $\rho_{f\delta}$ is efficient density of "formation';

mass transfer coefficient of the i-th component with droplets both via evaporation-condensation and absorption-desorption [2]

$$\text{Nu}_{id} = \frac{\beta_{id} \delta_d}{D_i} = 2\left(1 + 0,\ 276 \text{Re}_d^{0,5} Sc_i^{0,33}\right) K_{ci},\ Sc_\text{i} = \frac{\mu}{\rho D_i}; \tag{19}$$

Stefan correction on increased moisture content

$$K_{\tilde{n}\tilde{i}} = 1 + \frac{P_{id} + P_i}{2B}; \tag{20}$$

barometric (total) pressure

$$B = P_g + \sum P_i; \tag{21}$$

density of vapor-gas mixture

$$\rho = \rho_g + \sum \rho_i; \tag{22}$$

state equation for gas components and vapor of liquid

$$\rho_g = \frac{M_g P_g}{RT},\ \ \rho_i = \frac{M_i P_i}{RT},\ \ \rho_{id} = \frac{M_i P_{id}}{RT_d},\ \ \rho_{i\delta} = \frac{M_i P_{i\delta}}{RT_\delta}; \tag{23}$$

diffusion coefficient of the i-th component in non-reacting component of the vapor-gas flow (we assume that its fraction in the flow is predominant)

$$D_i = D_{i0}\frac{B_0}{B}\left(\frac{T}{T_0}\right)^{1,75},\ B_0 = 0.1\ MPa,\ T_0 = 273\ \text{K};\tag{24}$$

coefficient of droplet heat transfer according to Drake's formula

$$\text{Nu}_d = \frac{\alpha_d \delta_d}{\lambda} = 2 + 0,459\,\text{Re}_d^{0,5}\,\text{Pr}^{0,3}, \text{Pr} = \frac{\mu c}{\lambda};\tag{25}$$

countable concentrations of droplets and "formations"

$$n_d = \frac{\rho_d}{m_d},\tag{26}$$

$$n_\delta = \frac{\rho_\delta}{m_\delta};\tag{27}$$

heat and mass transfer coefficients of "formations"

$$\alpha_\delta = 2\frac{\lambda}{\delta}\ \ \left(\text{Nu}_\delta = 2\right),\ \ \beta_{i\delta} = 2\frac{D_i}{\delta}\ \ \left(\text{Nu}'_{i\delta} = 2\right),\tag{28}$$

heat capacity of the vapor-gas mixture

$$c = \frac{\sum \rho_i c_i}{\rho};\tag{29}$$

specific heat of gas absorption with the made assumptions [6]

$$r_i = M_i^{-1} R T^2 \frac{\mathbf{d}\ln m_{px,i}}{\mathbf{d}T},\tag{30}$$

it can be assumed for water vapors that $r_d \approx 2500$ kJ/kg [2-4];

http://dx.doi.org/10.5772/53094

according to Henry's law for partial saturation pressure at the interface between i-th gas components, the equilibrium condition is [6]

$$P_{id} = m_{px,i} x_{id}, \quad P_{i\delta} = m_{px,i} x_{i\delta}; \tag{31}$$

$$x_{id,\delta} = \frac{\frac{c_{mid,\delta}}{M_i}}{\frac{c_{mid,\delta}}{M_i} + \frac{1}{M_{dis}}}, \tag{32}$$

where $x_{id,\delta}$ is a molar part, equal to the number of moles of dissolved gas per the total number of moles in solution, M_{dis} is the molar mass of dissolvent.

The equation for mass concentration of dissolved i-th gas component in the kilogram per 1 kg of dissolvent in the droplet and "formation" is written as

$$\frac{\mathbf{d}c_{mid,\delta}}{\mathbf{d}\tau} = \frac{\mathbf{d}m_{id,\delta}}{\mathbf{d}\tau} \frac{6}{\pi \delta_{d,f}^3 \rho_f}. \tag{33}$$

Diameters of specific spherical volume of dissolvent for "formation" δ_f and droplet δ_d are calculated by equations:

$$\frac{\mathbf{d}\delta_f^3}{\mathbf{d}\tau} = \frac{6}{\pi} \frac{1}{\rho_f} \frac{\mathbf{d}m_{v\delta}}{\mathbf{d}\tau}, \delta_d = \sqrt[3]{\frac{6m_d}{\pi \rho_f}}; \tag{34}$$

"formation" diameter is

$$\delta = \sqrt[3]{\frac{6m_\delta}{\pi \rho_s} + \delta_0^3}, \left(\rho_s \approx \rho_f\right), \tag{35}$$

where ϱ_s is solution density, kg/m^3.

The reactive force in equation (1) is neglected because of evaporation-condensation and absorption [2]. In equation (2) specific heat capacity c_f is taken constant and equal to specific heat capacity of dissolvent because of low concentrations of absorbed dust and absorbed gases. For small particles and significant amount of condensate on them [2] we will take c_δ equal to specific heat capacity of dissolvent c_f. In this equation the first summand in the right determines convective heat transfer between the droplet and flow, the second summand de-

termines the total heat of phase transitions due to evaporation-condensation and absorption-desorption of gas components, and the third summand determines heat introduced by "formations" into the droplet due to their absorption at collision. In equations (3) and (4) $dm_{id}/d\tau$, $dm_{i\delta}/d\tau$ are the rates of droplet and "formation" mass change due to the processes of evaporation-condensation or absorption-desorption of the i-th gas component. In relationships (16) dynamic viscosity of the vapor-gas flow μ is calculated by generalized Wilkey's formulas, in our case on the basis of research performed in [2] and [4] with consideration of low concentrations of reacting gas components we will determine μ by Sutherland formulas [2, 4] for a non-reacting component of the vapor-gas mixture. The coefficient of mixture heat conductivity λ will be calculated similarly by Sutherland formula [2, 4] in formulas (25) and (28). The diffusion components of the vapor-gas flow will be determined by their dependences on temperature in the non-reacting component by formula (24). The correction for Stefan flow of gas components is not taken into account because of their low concentrations (K_{ci}=1). In the current study we will consider water as the absorbent and $m_{px,i}$ will be taken from tables depending on temperature [6]. If there are no data for some gases in [6], for instance, for SO_2, we suggest to recalculate volumetric 1 and weight q_s solubility [7] as the limit ones by $m_{px,i}$, this will be described in detail in this work.

3. Numerical implementation of the model, comparison of calculation results with experimental data

As it is shown in [2], in most technically implemented situations it is possible to use a single-dimensional model for calculation of heat and mass transfer in irrigation chambers, what is determined by the vertical position of apparatuses (hollow jet scrubbers HJC); at their horizontal position it is determined by high velocities of cleaned gases, dust particles and droplets (Venturi scrubber VS), when the gravity force, influencing the flow components and causing its 2D character, is low in comparison with the inertia forces.

The calculation scheme of the problem for the vertical construction of apparatus is shown in Fig. 1a). The scheme of interaction between a droplet of washing liquid dispersed by the jets with vapor-gas flow and dust particles is shown in Fig. 1b).

The hollow jet scrubber HJS can have direct-flow and counter-flow construction. In the direct-flow scheme the initial parameters of the vapor-gas flow, irrigating liquid and dust are set on one side (inlet) of apparatus, and the resulting parameters are achieved at the apparatus outlet. In the counter-flow scheme the parameters of vapor-gas flow and dust are set on one side of apparatus, the parameters of irrigating liquid are set on the opposite side (at apparatus outlet). Scheme 1a) is attributed to the counter-flow. From the point of numerical implementation the direct-flow scheme is the Cauchy problem, and the counter-flow scheme is the boundary problem. Let's perform calculations for the direct-flow scheme according to the known experimental data for generalized volumetric mass transfer coefficients, shown in [6, p. 562], for different gases absorbed on dispersed water. The calculation scheme is shown in Fig. 2 (it is conditional, the construction can differ).

http://dx.doi.org/10.5772/53094

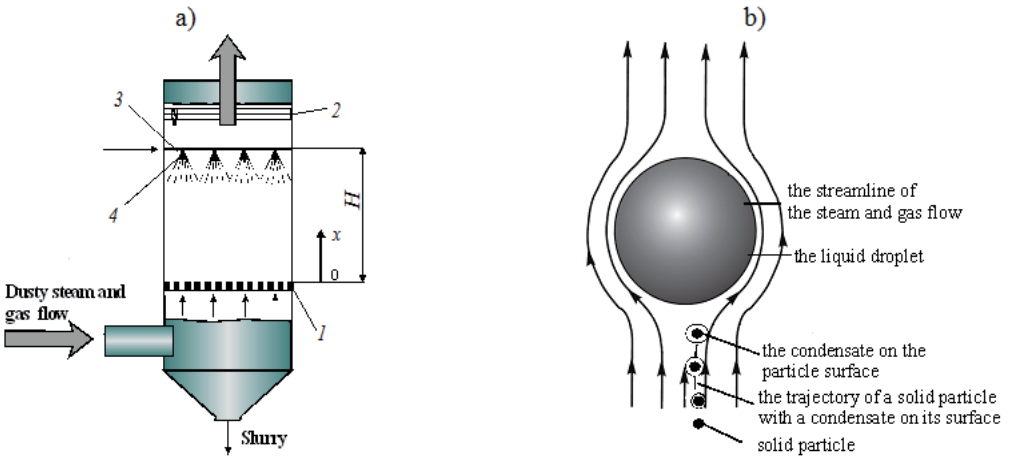

Figure 1. The HJS scheme: *1* – gas-distributing grate, *2* – droplet catcher, *3* – water collector, *4* – jets, *H* – scrubber operation height; b) the scheme of droplet interaction with the flow and dust particle

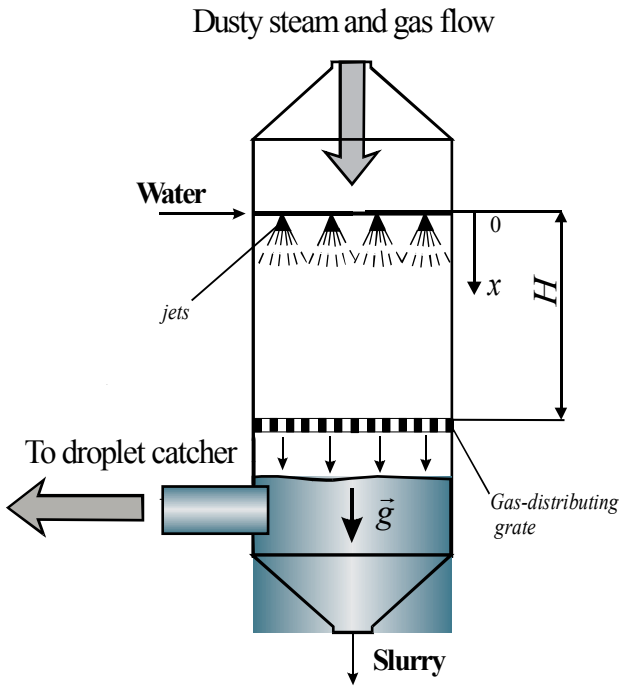

Figure 2. The scheme of direct-flow HJS

The problem will be solved in the stationary statement. The boundary conditions are set at x=0 (τ=0) in the following manner:

$$\left.\begin{array}{ll} \text{for the vapor-gas flow} & U=U_0,\ d=d_0,\ d_i=d_{i0},\ T=T_{00}; \\ \text{for dispersed liquid} & V_d=V_{d0},\ \delta_d=\delta_{d0},\ q=q_0,\ T_d=T_{d0}; \\ \text{for dust} & \rho_p=\rho_{p0},\ \delta=\delta_0. \end{array}\right\} \tag{36}$$

Continuity equations (6) and (8) in stationary single-dimensional case can be reduced to the following, as in [2], analytical dependences:

$$U=U_0\frac{T}{T_{00}}\frac{B-\sum P_{j0}}{B-\sum P_j}\approx U_0\frac{T}{T_{00}}\frac{K_{ave}+d_\Sigma}{K_{ave}+d_{\Sigma 0}}; \tag{37}$$

$$\rho_d=\rho_{d0}\frac{V_{d0}}{V_{dx}}\frac{m_d}{m_{d0}},\ \rho_{d0}=q\rho_f\frac{U_0}{V_{d0}},m_d=\rho_f\frac{\pi\delta_d^3}{6},\ m_{d0}=\rho_f\frac{\pi\delta_{d0}^3}{6}, \tag{38}$$

where

$$K_{ave}=\frac{\sum_1^k K_i}{k},K_i=\frac{M_i}{M_g}, \tag{39}$$

k is the number of reacting components, including liquid vapors, M_g is molecular mass of a non-reacting component of gas;

$$d_\Sigma=\frac{\sum_1^k K_iP_i}{B-\sum_1^k P_i}\approx K_{ave}\frac{\sum_1^k P_i}{B-\sum_1^k P_i}, \tag{40}$$

efficiency of dust capture and gas component removal is determined by relationships:

$$\eta_p=1-\frac{\left(\rho_pU\right)_H}{\rho_{p0}U_0}, \tag{41}$$

$$\eta_i=1-\frac{\left(\rho_{d.a}d_iU\right)_H}{\rho_{d.a.0}d_{i0}U_0}. \tag{42}$$

http://dx.doi.org/10.5772/53094

3.1. Calculation with the use of m_{px} [6] or Henry's coefficient E [7]

Calculation results on absorption of CO_2 by water droplets in the direct-low hollow jet scrubber are shown in Fig. 3. There are no any restrictions for calculations by solubility limit (concentration of gas dissolving in the droplet). However, the solubility limits exists as the experimental fact for gases, presented in tables of Hand-books as absorption coefficient α, in volumetric fractions reduced to 0 °C and pressure of 0.1 MPa or in the form of solubility coefficient q_p in mass fractions to solution or dissolvent [8, 9]. Thus, in [9] for $\alpha(T)$, m^3 of gas/ m^3 of water, for CO_2 and CH_4 the following data are shown (Table 1).

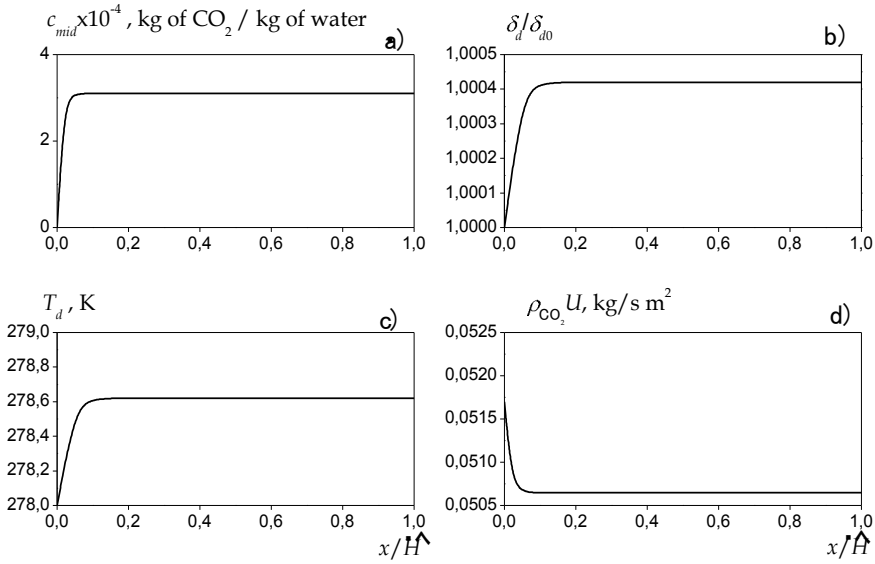

Figure 3. Calculation of CO_2 absorption in direct-flow jet scrubber: H =12.75 m; q =0.015 m^3/m^3; δ_{d0} =700 μm; V_{d0} =24.5 m/s; U_0 =0.25 m/s; T_{d0} =278 K; T_{00} =293 K; d_0 =0.02 kg/kg of dry air; d_{CO_2} =0.2 kg of CO_2/kg of dry air; η_{CO_2} =0.022262

T, K	273	283	293	303	313	323	333	353	373
α_{CO_2}	1.713	1.194	0.878	0.665	0.530	0.436	0.359	…	…
$\alpha_{CH_4} \cdot 10^3$	55.6	41.8	33.6	27.6	23.7	21.3	19.5	17.7	17.0

Table 1. Absorption coefficients for CO_2 and CH_4 α, m^3/m^3 of water at B=0.1 MPa and T_0=273 K

It follows from this table that the limit value of CO_2 concentration in a water droplet is

$$c_{mco_2,\lim} = \alpha_{co_2}\rho_{co_2}(T_0,\ B_0) = \alpha_{co_2}(T)\frac{M_{co_2}B_0}{RT_0} = \alpha_{co_2}\frac{44\cdot 101325}{8,\ 314\cdot 10^3\cdot 273} = \\ = 1,\ 964\cdot 10^{-3}\cdot \alpha_{co_2}(T),\ \ \frac{\kappa g\, CO_2}{\kappa g\,\text{water}}, \tag{43}$$

where $\alpha_{co_2}(T)$ is the table value of absorption coefficient for CO_2 (Table 1).

This value shall limit concentration of CO_2 dissolved in the droplet. It can be seen in Fig. 3a) that according to Table 1 calculated value of c_{mid} does not reach the solubility limit and it is one order lower. Thus, $c_{mid,\lim}$ ($T_d = 278,\ 63\,K$, see Fig. 3c)) =2.81•10^{-3} kg of CO_2/kg of water. It can be seen in Fig. 3b) that as a result of water vapor condensation and CO_2 absorption the size of droplet increases insignificantly, less than by 0.05 %, i.e., a small amount of water vapors condenses on the droplet and a small amount of CO_2 is absorbed by the droplet, Fig. 3a). The calculated amount of the mass of gas component absorbed by liquid droplets in the scrubber is determined by formula, kg/h•m^2,

$$W_{i,th} = \rho_{d.a.,0} d_{i0} U_0 \eta_i 3600. \tag{44}$$

For calculated situation with consideration of partial density of dry air at the inlet $\rho_{d.a.,0}$ =1.0363 kg/m^3, gas content $d_{CO_2,0}$=0.2 kg/kg of dry air, U_0=0.25 m/s and η_{CO_2}=0.022262 according to formula (44) we will obtain

$$W_{i,th} = 1,0363\cdot 0,2\cdot 0,25\cdot 0,022262\cdot 3600 = 4,153\ \ kg/h\cdot m^2. \tag{45}$$

Let's compare the obtained result with the value achieved via the empirical volumetric mass transfer coefficient, shown in [6, p. 562] (in our nomenclature):

$$\beta_{iv} = 720 U_0^{0,9} Q^{0,45} H^{-0,65} \left(\frac{D_{i,0}}{D_{\mathrm{NH_3},0}}\right)^{0,67}, \text{ 1/h.} \tag{46}$$

Here Q is irrigation density, m/h, $D_{\mathrm{NH_3},0}$=0,198 10^{-4} m^2/s is coefficient of methane diffusion in air at B_0=0.1 MPa and T_0=273 K, H is calculated scrubber height, m.

Let's write down the value of obtained coefficient per an area unit of apparatus cross-section via coefficient β_{iv} in the following form, kg/h•m^2:

$$W_{i,e} = \beta_{iv}\Delta\rho_i l, \tag{47}$$

http://dx.doi.org/10.5772/53094

where $\Delta\rho_i$ is calculated concentration pressure on the way of gas component obtaining x=0, x=l, where l corresponds to the coordinate, where thermodynamic equilibrium is achieved for the i-th component in the flow.

Substituting (46) into (47) and assuming l=H, as it was made at treatment of experimental data in [6], we get

$$W_{i,e} = 720U_0^{0,9}\left(3600U_0 q\right)^{0,45} H^{0,35}\Delta\rho_i\left(\frac{D_{i,0}}{D_{\mathrm{NH}_3,0}}\right)^{0,67}, \mathrm{kg/h\cdot m^2}, \tag{48}$$

where q is irrigation coefficient, m^3 of water/ $м^3$ of vapor-gas flow at apparatus inlet.

Let's transform formula (48), and finally for calculation we obtain dependence

$$W_{i,e} = 28685,9U_0^{1,35}q^{0,45}H^{0,35}\Delta\rho_i\left(\frac{D_{i,0}}{D_{\mathrm{NH}_3,0}}\right)^{0,67}. \tag{49}$$

For the considered situation $D_{i,0}$=$D_{CO_2,0}$=0, 138 · $10^{-4}$$m^2$/s [6].

Let's take the average experimental data of [6] as the calculation working height of absorber H_{ave}=(H_{min} H_{max})$^{1/2}$=(4.3 12)$^{1/2}$≈7 m, then for calculated value $\Delta\rho_{CO_2}$=$\rho_{d.a.,0}d_{CO_2,0}\eta_i$=1, 0363 · 0, 2 · 0, 022262=0, 004614 kg/m^3

$$W_{i,e} = 28685,9\cdot\left(0,25\right)^{1,35}\left(0,015\right)^{0,45}\left(7\right)^{0,35}0,004614\left(\frac{0,138}{0,198}\right)^{0,67} \approx 4,772\ \mathrm{kg/h\cdot m^2} \tag{50}$$

since D_i=$D_{i,0}\frac{B_0}{B}\left(\frac{T}{T_0}\right)^{1,75}$ and total multiplier $\frac{B_0}{B}\left(\frac{T}{T_0}\right)^{1,75}$ in (50) is reduced.

Calculated (45) and experimental (50) results differ by Δ≈13 %. If we take H=4.3 m, then $W_{i,e}$=4, 024 kg/h m^2 and Δ≈3 %. At H=12 m, $W_{i,e}$=5, 76 kg/h m^2 and Δ=28 %.

It follows from formula (42) for calculated concentration difference at apparatus inlet and outlet that

$$\Delta\rho_{i,cal}=\left(\frac{U_{out}}{U_0}-1\right)\rho_{iin}+\Delta\rho_i,$$

where calculated value is $\Delta\rho_{i,cal}=\eta_i\rho_{i,in}$. Thus, for U_{out}= U_0 $\Delta\rho_{i,cal}=\eta_i\rho_{i,in}=\Delta\rho_i$, i.e., the calculated value of concentration difference coincides with real value $\Delta\rho_i$. Therefore, we can make a conclusion that efficiency of dust capture and mass transfer shall be calculated not

by the measured difference of dust concentrations and extracted gas components at the inlet and outlet, but by difference of their mass fluxes in accordance with the law of mass conservation, and if velocities at the inlet and outlet are equal or close efficiencies can be calculated by real concentration difference. Distribution of mass flux of CO_2 along the scrubber height is shown in Fig. 3d). It is obvious from Figs. 3c) and 3d) that the process of absorption completes long before the flow escape from the scrubber, for the given version of calculation at $x/H \approx 0.1$ (≈1.3 m). Hence, the residual height of the scrubber is excessive, and it can not be determined experimentally.

Previous comparison can be made in the relative form, what will prove the validity of calculation of mass transfer coefficient as a measure determining process intensity, on the basis of model in comparison with its experimental expression [6]:

$$\frac{W_{i,th}}{W_{i,e}} = \frac{\rho_{d.a.,0} d_{i0} U_0 \eta_i 3600}{28685,9 U_0^{1,35} q^{0,45} H^{0,35} \Delta\rho_i \left(\frac{D_{i,0}}{D_{\mathrm{NH_3},0}} \right)^{0,67}} = \frac{0,1255}{q^{0,45} \left(H U_0 \right)^{0,35} \left(\frac{D_{i,0}}{D_{\mathrm{NH_3},0}} \right)^{0,67}}, \tag{51}$$

where it is assumed that $\Delta\rho_i = \eta_i \rho_{d.a.,0} d_{i0}$. Thus, for our case $\frac{W_{i,th}}{W_{i,e}} = \frac{0,1255}{0,616 \cdot 0,151 \cdot H^{0,35} \cdot 0,785} = \frac{1,72}{H^{0,35}} = 0,87$ at H=7 m and $\frac{W_{i,th}}{W_{i,e}} = 1,03$ at H=4.3 m.

Here $\Delta\rho_i$ has the meaning of efficient drop of gas concentration, not real, but corresponding to extraction of the gas component due to absorption on a liquid droplet. Real drop of CO_2 concentrations at the inlet and outlet at the example of Fig. 4 is even negative: $\Delta\rho_{CO_2} = \rho_{CO_2,in} - \rho_{CO_2,out} = 0,1245 - 0,2099 = -0,0854$ kg/m^3, here $U_{in} = U_0 = 0.25$ m/s, $U_{out} = 0.1439$ m/s.

Extractions per a total volume of apparatus can be presented as, kg/h,

$$\Delta G_{i,th} = \beta_{iv,th} \Delta\rho_i \pi D^2 H; \tag{52}$$

$$\Delta G_{i,e} = \beta_{iv,e} \Delta\rho_i \pi D^2 H. \tag{53}$$

On the other hand

$$\beta_{iv,th} = \frac{\Delta G_{i,th}}{\Delta\rho_i \pi D^2 H} = \frac{\rho_{d.a.,i0} d_{i0} U_0 \eta_i 3600 \pi D^2}{\Delta\rho_i \pi D^2 H}.$$

Hence, with consideration of formulas (46) and (53) we will obtain the relationship for volumetric mass transfer coefficients (theoretical and experimental ones)

http://dx.doi.org/10.5772/53094

$$\frac{\beta_{iv,th}}{\beta_{iv,e}} = \frac{3600 U_0 \Delta\rho_i \pi D^2}{28685,\ 9 U_0^{1,35} q^{0,45} H^{-0,65} \Delta\rho_i \left(\frac{D_{i,0}}{D_{NH_3,0}}\right)^{0,67} \pi D^2 H},$$

after elementary reductions in numerator and denominator this corresponds to formula (51). Here D is apparatus diameter.

Calculations results for the same situation as in Fig. 3 are shown in Fig. 4, but for the increased moisture content d_0=0.5 kg/kg of dry air. The theoretical value of absorbed CO_2 is:

$W_{i,th}$ =0, 6226 · 0, 2 · 0, 25 · 0, 029136 · 3600=3, 265 kg/h•m^2.

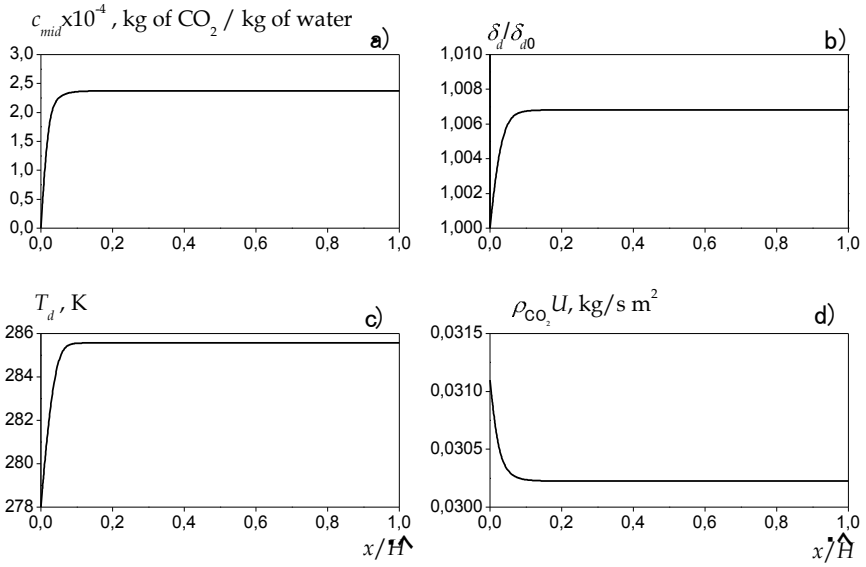

Figure 4. Fig. 4. Calculation of CO_2 absorption in the direct-flow jet scrubber: H =12.75 m; q =0.015 m^3/m^3; δ_{d0} =700 μm; V_{d0} =24.5 m/s; U_0 =0.25 m/s; T_{d0} =278 K; T_{00} =293 K; d_0 =0.5 kg/kg of dry air; d_{CO_2} =0.2 kg of CO_2/kg of dry air; η_{CO_2} =0.029136

Calculation by formula (48) for height H=4.3 m gives the following

$W_{i,e}$=28685, 9 · (0, 25)^{1,35}(0, 15)^{0,45}(4, 3)^{0,35}0, 00363 · 0, 785=3, 165 кg/h•m^2,

what differs from the theoretical value by 3 %. Here $\Delta\rho_{CO_2}$=0, 00363 kg/m^3 by calculation ($\Delta\rho_{CO_2}$=0, 62226 · 0, 2 · 0, 029136). We should note that even for the increased moisture contents the size of droplets increases slightly due to condensation and absorption (less than by 1 %) (Fig. 4b). For calculated scrubber height H_{ave}=7 m $W_{i,e}$=3, 75 kg/h•m^2 (Δ=15.6 %).

According to comparison, the model agrees well with the experimental data.

In calculations tabular data m_{px} for water solution of CO_2 [6] were approximated by temperature dependence T,

$$m_{px} = \left(2,389T^2 - 994,6T + 100765\right) 10^4, \text{Pa}. \tag{54}$$

Partial pressures of saturated water vapors on droplet and "formation" surfaces were calculated by formula [2] (the partial pressure of saturated vapors of gas components were not taken into account)

$$P_{sd,\delta} = P_{\text{cr}} \exp\left(A_1 \ln \frac{T_{d,\delta}}{T_{\text{cr}}} + A_2 f_2 \right), \tag{55}$$

where

$$f_2 = \frac{4\left(\frac{T_{d,\delta}}{T_{cr}} - 1\right)}{\frac{T}{T_{cr}}} + f_1 - 5,\ 3 \ln \frac{T_{d,\delta}}{T_{cr}},$$

$$f_1 = \left(\frac{T_{d,\delta}}{T_{cr}} - 1\right)\left[\frac{\left(\frac{T_{d,d}}{T_{cr}} + 1\right)^2}{5} + 0,\ 5\right],$$

P_{cr} = 221.29 10^5 Па; t_{cr} = 374.1 °C; A_1 = 7.5480; A_2 = 2.7870.

For hydrogen sulfide m_{px} for water solution [6] was approximated by dependence:

$$m_{px} = \left(-0,0251T^2 + 148,73T - 36374\right) 10^4, \text{ Pa}. \tag{56}$$

Calculation results on absorption of hydrogen sulfide on a water droplet from the vapor-gas flow are shown in Fig. 5.

Theoretical value of $W_{i,th}$ for H_2S ($\rho_{d.a.,0}$=1, 0029kg/m^3) is

$$W_{i,th} = 1,0029 \cdot 0,2 \cdot 0,25 \cdot 0,062478 \cdot 3600 = 11,28 \text{ kg/h m}^2. \tag{57}$$

Calculation by formula (48) with experimental mass transfer coefficient gives for H=4.3 m

http://dx.doi.org/10.5772/53094

$$W_{i,e} = 28685,9 \cdot 0,1539 \cdot 0,151 \cdot 1,66615 \cdot 0,01253 \cdot 0,7426 = 10,335 \text{ kg/h m}^2, \quad (58)$$

where $\left(\frac{D_{H_2S}}{D_{NH_3}}\right)^{0,67} = \left(\frac{0,127}{0,198}\right)^{0,67} = 0,7426, \quad \Delta\rho_{H_2S} \approx \eta\rho_{SO_2,0} \approx 0,22031 \cdot 1,0029 \cdot 0,2 = 0,01253$ kg/m^3. Difference between results of (57) and (58) is $\Delta \approx 8$ %. For calculated height H=7 m $W_{i,e}$=12, 257 kg/h m^2 and $\Delta \approx 8$ % on the other hand. In calculations for H_2S the limit of concentration (solubility) in water is not exceeded (solubility for 20 °C is about 3.85 10^{-3} kg of H_2S/kg of water) (see Fig. 5a)). According to the diagrams, here absorption is completed at 1.3 – 1.5 m from the scrubber inlet.

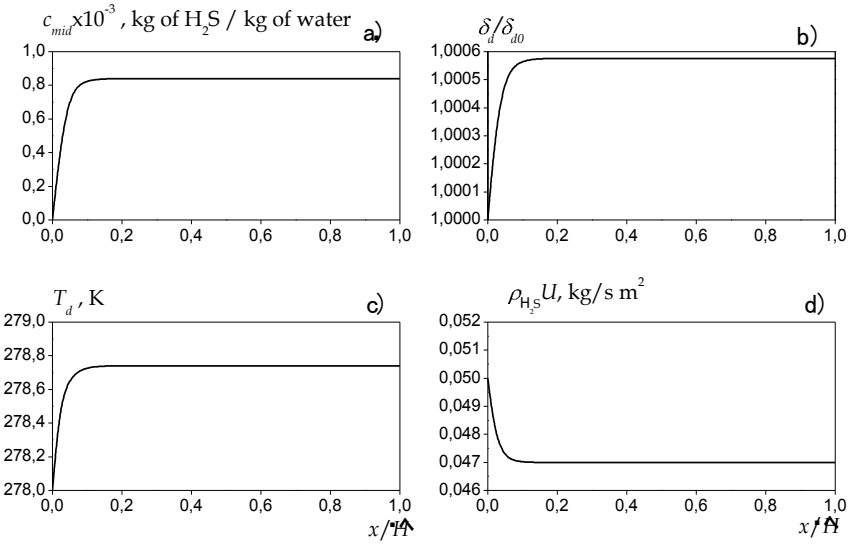

Figure 5. Calculation of hydrogen sulfide absorption: H =12.75 m; q =0.015 m^3/m^3; δ_{d0} =700 μm; V_{d0} =24.5 m/s; U_0 =0.25 m/s; T_{d0} =278 K; T_{00} =293 K; d_0 =0.02 kg/kg of dry air; $d_{H_2S,0}$ =0.2 kg of H_2S/kg of dry air; η_{H_2S}=0.062478

3.2. Calculation of absorption by solubility of l and q_s

If there are no tabular data for m_{px} (or E) of any gas, and solubility information is available in the hand-book, for instance, for l, m^3 of gas/m^3 of water and for q_s, g of gas/100 g of water, we can relate l and q_s to the limit density of saturated gas on the droplet surface $\rho_{id,lim.}$, kg/m^3, taking into account that the process of its dissolution occurs in droplet volume fast, i.e., the typical time of gas dissolution is significantly less than the typical time of droplet stay in the working volume of scrubber. Then,

$$\rho_{id,\lim} = 10\frac{q_s}{l}. \tag{59}$$

Thus, in [8, p. 260-261] there are tabular data for SO_2 for l and q_s, where we have shown re-calculation of $\rho_{SO_2 d,\lim}$ by formula (59) in the last line of Table 2:

t, °C	0	10	20	30	40
l	79.8	56.7	39.4	27.2	18.8
q_s	22.8	16.2	11.3	7.8	5.41
$\rho_{SO_2 d,\lim} = 10\frac{q_s}{l}$	2.8571	2.8571	2.8680	2.8676	2.8777

Table 2. Volumetric l and weight q_s solubility coefficients for SO

According to this Table, $\rho_{SO_2 d,\lim}$=2.8655≈2.9 kg/m^3 and it is almost constant value.

First, for this case we calculate m_{px}:

$$P_{id,\lim} = P_{SO_2 d,\lim} = \rho_{SO_2 d,\lim}\frac{RT_d}{M_{SO_2}} = 2,\ 8655\frac{8,\ 314\cdot 10^3}{64}T_d; \tag{60}$$

$$\left(m_{px}\right)_{SO_2} = \frac{P_{SO_2 d,\lim}}{x_{SO_2 d,\lim}}; \tag{61}$$

$$x_{SO_2 d,\lim} = \frac{\frac{q_s 10^{-2}}{M_{SO_2}}}{\frac{q_s 10^{-2}}{M_{SO_2}} + \frac{1}{M_{water}}}. \tag{62}$$

As a result, the following approximation was obtained by formula (61) for SO_2

$$\left(m_{px}\right)_{SO_2} = 2976,\ 58T^2 - 1594158T + 215090898, \quad \text{Pa.}, \tag{63}$$

Knowing $\left(m_{px}\right)_{SO_2}$, we determine specific heat of SO_2 absorption by water:

http://dx.doi.org/10.5772/53094

$$RTM_{SO_2}^{-1}\frac{\mathbf{d}\ln\left(m_{px}\right)_{SO_2}}{\mathbf{d}t}=r_{SO_2}\left(T_d\right),\ \text{J/kg}. \tag{64}$$

Following calculation is performed by the general scheme (formulas (31)–(35)).

Results of calculation are shown in Fig. 6 at ventilation of air humidity d_0=0.02 kg/kg of dry air, $d_{SO_2,0}$=0.2 kg/kg of dry air, $d_{CH_4,0}$=0.2 kg/kg of dry air. Other parameters are shown in captions to the figure. It was obtained for this calculation version that η_{SO_2}=51.1 %, η_{CH_4}=0.08 %. The limit value of SO_2 concentration in a droplet is not achieved even for CH_4. According to tabular data on absorption coefficient α, m^3/m^3 of water (see Table 1):

$c_{mid,\lim}=0,\ 717\cdot 10^{-6}\alpha$, kg of CH_4/ kg of water.

According to calculation of extracted SO_2 for the given case ($\rho_{d.a.,0}$=0, 8121kg/m^3):

$W_{i,th}=0,\ 8121\cdot 0,\ 2\cdot 900\cdot 0,\ 51072=74,\ 656$ kg/h•m^2,

$W_{i,e}=28685,\ 9\cdot 0,\ 1539\cdot 0,\ 151\cdot (12)^{0,35}\cdot 0,\ 8121\cdot 0,\ 2\cdot 0,\ 51072\cdot 0,\ 715=94,\ 34$ kg/h•m^2

for H=12 m,

$W_{i,e}=28685,\ 9\cdot 0,\ 1539\cdot 0,\ 151\cdot (7)^{0,35}\cdot 0,\ 8121\cdot 0,\ 2\cdot 0,\ 51072\cdot 0,\ 715=78,\ 13$ kg/h•m^2

at H_{ave}=7 m ($H_{ave}=\sqrt{4,\ 3\cdot 12}\approx 7$m). Here $\left(\frac{D_{SO_2,0}}{D_{NH_3,0}}\right)^{0,67}=0,\ 715$.

Comparison of $W_{i,th}$ and $W_{i,e}$ for SO_2 proves good agreement between theory and experiment.

According to calculation, Fig. 6c), methane is not absorbed by water. However, even for methane comparison of calculation with experiment yields satisfactory agreement:

$W_{i,th}=0,\ 1624\cdot 900\cdot 0,\ 00079541=0,\ 11626$ kg/h•m^2;

$W_{i,e}=28685,\ 9\cdot 0,\ 1539\cdot 0,\ 151\cdot 0,\ 1624\cdot 0,\ 00079541\cdot 0,\ 715=0,\ 1026$ kg/ h•m^2

at H=4.3 m, Δ=11.75 %. At H=7 m, $W_{i,e}=0,\ 1217$ kg/ h•m^2 and Δ=4.5 %.

We should note that absorber height H in experimental dependence for β_{iv} is taken improperly. The optimal and calculated height of setup should equal path l, where the process of component extraction is completed. In most cases of calculations, it completed earlier at the height less than the accepted height of absorber H=12.75 m. Therefore, at comparison of calculation and experimental data in experimental dependence for mass transfer coefficient we have varied the calculated height in the range of the heights of tested setups from 4.3 to 12 m [6].

For CH_4 m_{px} is approximated by dependence

$$m_{px} = \left(-47,\ 154T^2 + 35490T - 5962310\right)\ 10^4, \quad \text{Pa.} \tag{65}$$

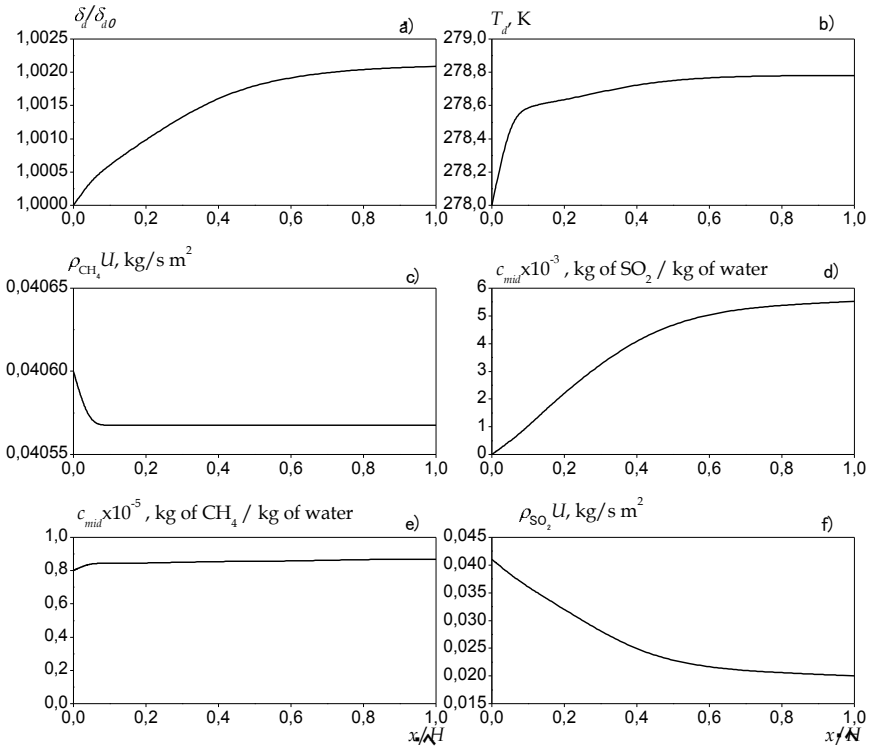

Figure 6. Calculation of SO_2 and CH_4 absorption in direct-flow jet scrubber: H =12.75 m; q =0.015 m^3/m^3; δ_{d0} =700 μm; V_{d0} =24.5 m/s; U_0 =0.25 m/s; T_{d0} =278 K; T_{00} =293 K; d_0 =0.02 kg/kg of dry air; $d_{SO_2,0}$ =0.2 kg/kg of dry air; $d_{CH_4,0}$ =0.2 kg/kg of dry air; η_{SO_2}=0.51064; η_{CH_4}=0.00079541

3.3. Calculation of combined absorption-condensation dust-gas cleaning

Calculations of combined condensation dust capture and absorption extraction of hydrogen sulfide from the vapor-air flow in direct-flow hollow scrubber are shown in Fig. 7. Calculated parameters are shown below the figure. According to Fig. 7a), even at increased moisture content the size of droplets increases weak due to condensation. Therefore, for similar processes the equation of droplet motion can be calculated with a constant mass.

An increase in the size of "formations" is more significant due to condensation of water vapors on them: for δ_0=0.01 μm it is 2.1, for δ_0=0.1 μm it is 2.3, and for δ_0=1 μ it is 32 and more for the same total concentration of dust at the inlet of 1.72 g/m^3. In the first case, particles are not caught, in the second case, about 5.76 % of particles are caught, and in the third case, 100 % of particles are caught at the inlet to the apparatus. For this version of calculation the stable state by concentrations of H_2S dissolved in droplets and in condensate on "formations"

http://dx.doi.org/10.5772/53094

occurs far from the flow escape from the scrubber. For particles water vapor condensation at flow escape from the scrubber has been also competed already (see Fig. 7g). Therefore, in this case the height of absorber above 1.5 m is excessive, and in construction it can be limited by 2 m. According to Figs. 7d) and 7e), concentration of H_2S dissolved in condensate on the particle and in droplets increases, but it does not exceed the solubility limit (in this case it is about $3.85 \bullet 10^{-3}$ kg of H_2S/kg of water).

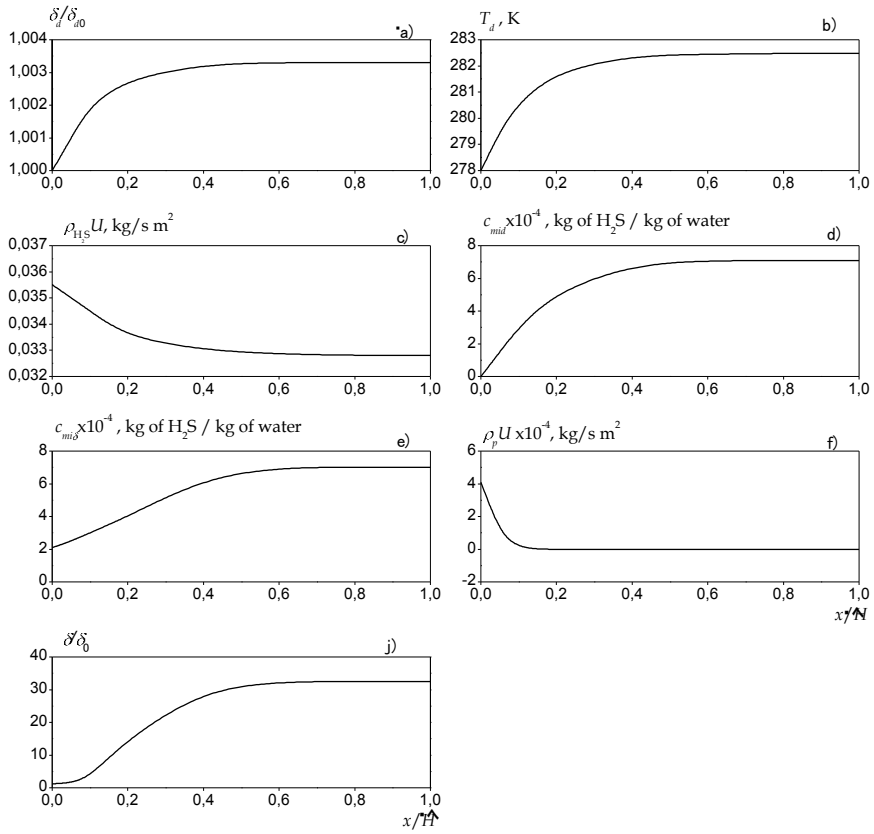

Figure 7. Calculation of combined air cleaning from submicron dust and hydrogen sulfide in direct-flow scrubber: H =2 m; q =0.015 m^3/m^3; δ_{d0} =700 μm; V_{d0} =24.5 m/s; U_0 =0.25 m/s; T_{d0} =278 K; T_{00} =333 K; d_0 =0.2 kg/kg of dry air; $d_{H_2S,0}$ =0.2 kg/kg of dry air; ρ_{p0} =1.72 g/m^3; δ_0=1 μm; η_{H_2S}=0.075411; η_p=1.0

3.4. Calculation of absorption and condensation dust capture in Venturi scrubber

Calculation results on H_2S absorption and condensation capture of dust with different sizes in Venturi scrubber are shown in Fig. 8. As an example the Venturi scrubber with following parameters was chosen for calculations: diameter of Venturi tube mouth d_m=0.02 m, diffuser

length l=0.2 m, diffuser opening angle α=6° (α=6–7°, l/d_m=10–15 are recommended for normalized Venturi tube [6, 10]), vapor-gas flow velocity in the tube mouth U_0=80 m/s, initial velocity of droplets in the tube mouth V_{d0}=4 m/s, irrigation coefficient q=0.015 m^3/m^3, temperature of the vapor-gas flow and droplets in the tube mouth T_{00}=333 K and T_{d0}=278 K, respectively, concentration of dust particles at the inlet ρ_{p0}=1.72 g/m^3, size of dust particles δ_0=0.1 μm, moisture content in water vapor at the inlet was set d_0=0.2 kg/kg of dry air, gas content $d_{H_2S,0}$ =0.1 kg/kg of dry air. Efficient of H_2S extraction and dust capture were determined η_{H_2S}=0.072959 and η_p=0.52904, respectively.

The mean-mass size of droplets in the tube mouth was calculated by Nukiyama-Tanasava formula [1]:

$$\delta_{d0} = \frac{0,585}{U_0 - V_{d0}} \sqrt{\frac{\sigma_f}{\rho_f}} + 53,4 \left(\frac{\mu_f}{\sqrt{\rho_f \sigma_f}} \right)^{0,45} q^{1,5}, \text{ m}, \tag{66}$$

where ρ_f (kg/m^3), μ_f (Pa•s), σ_f (N/m) and q (m^3/m^3) are density, dynamic viscosity, surface tension coefficient of pneumatically atomized liquid, and irrigation coefficient.

Velocity U was calculated with consideration of diffuser expansion angle [2, 11].

Dependences of droplet size along the diffuser length are presented in Fig. 8a). It can be seen that firstly condensation of water vapors occurs intensively, then this process stops at the length of x/l≈0.2, and the size of droplets stays constant up to the scrubber outlet. At this, the quantitative droplet size changes slightly along the diffuser length (it stays almost constant: the maximal increase is a little bit higher than 0.3 %).

A change in droplet temperature due to convective heat transfer between droplets and vapor-gas flow, thermal effects of water vapor condensation on droplets, and gas dissolution is shown in Fig. 8d). A change in mass concentration of H_2S dissolved in a droplet is shown in Fig. 8c). It is obvious that absorption is almost completed at the length of tube diffuser 1 for this version of calculation. The same circumstance is illustrated by mass concentration of H_2S in "formation" condensate along the diffuser in Fig. 8c). According to the figure, the solubility limit on "formations" and droplets is not achieved as in the hollow jet scrubbers. A change in "formation" size due to water vapor condensate on their surfaces is illustrated in Fig. 8f). It can be seen that firstly water vapors condense very intensively, then at the distance of about x/l≈0.1 this process completes, the size increases more than twice and stays constant until the leaving from the scrubber. Efficiency of dust capture in this version is up to 53 %. Calculation at the same parameters of the vapor-gas flow and dust at the scrubber inlet with mouth d_c=0.1 m and constrictor length l=1 m gives η_p=0.77729, η_{H_2S}=0.074965. It follows from the diagrams in this figure that for the calculated version it is practically reasonable to be limited by diffuser length x/l≈0.4 (x=0.08 m), where the processes of dust capture (Fig. 8g)) and absorption are completed (Fig. 8b)). Therefore, the residual length of 0.12 m is

http://dx.doi.org/10.5772/53094

excessive. Figs. 8b) and 8g) illustrate distributions of dust and H_2S mass fluxes along the diffuser of Venturi tube.

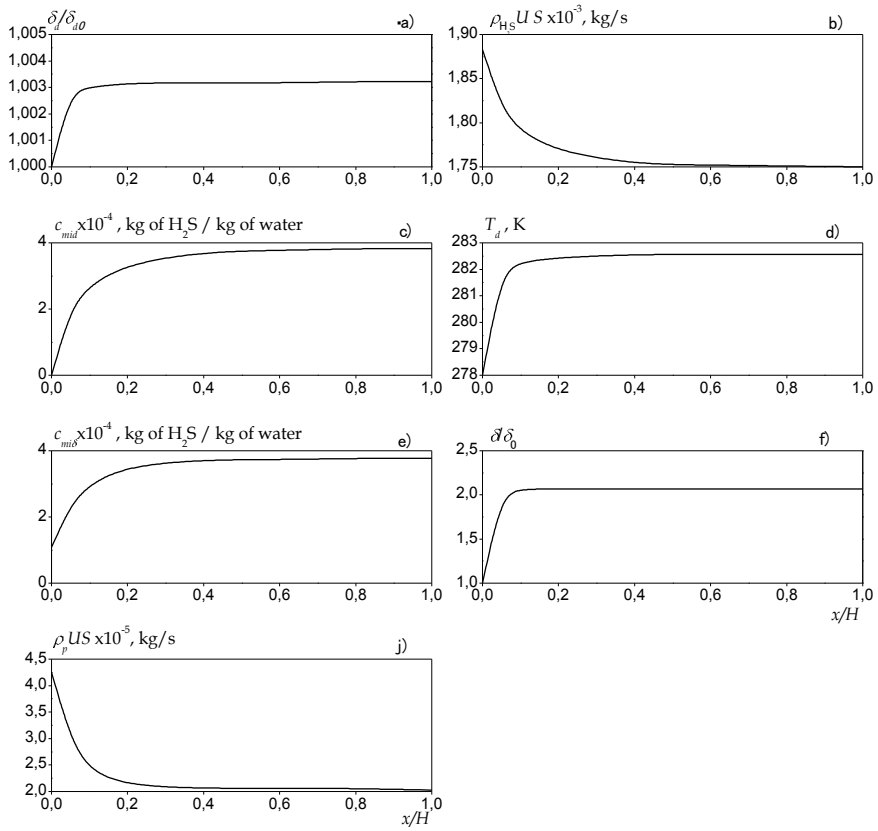

Figure 8. Calculation of H_2S absorption and dust capture in Venturi scrubber (calculated parameters are presented in the text)

It is necessary to note that these calculation versions do not meet the conditions of optimal scrubber operation; they only illustrate the character of complex gas cleaning. To determine the optimal regimes, a series of calculation on the basis of suggested model should be carried out and analyzed for the specific industrial conditions.

Let's turn to comparison of calculation results with the known experimental data. The experimental volumetric mass transfer coefficient is shown in [6] for NH_3 absorption in the Venturi tube with mouth diameter d_m=0.02 m. There no geometrical and other parameters. This coefficient is presented as

$$\beta_{iv,e}^{NH_3} = 260 U_0^{1,56} q_l^{0,57}, \tag{67}$$

where q_l is irrigation coefficient in l/m^3, U_0 is in m/s, and β_{iv} is in 1/h.

The experimental value of H_2S absorbed in Venturi tube is expressed by formula, kg/h,

$$\Delta G_{i,e} = \beta_{iv,e}^{H_2S} \Delta\rho_{i,e} V_{dif}, \tag{68}$$

where V_{dif} is diffuser volume, $\Delta\rho_i$ is calculated drop of gas concentration along the diffuser length, kg/m^3, corresponding to experimental data.

The theoretical value of mass of absorbed gas, kg/h, is

$$\Delta G_{i,th} = \beta_{iv,th}^{H_2S} \Delta\rho_{i,th} V_{dif} \approx \Delta\rho_{i,th} U_0 \frac{\pi d_m^2}{4} 3600. \tag{69}$$

Then

$$\frac{\Delta G_{i,th}}{\Delta G_{i,e}} = \frac{U_0 \frac{\pi d_m^2}{4} 3600 \Delta\rho_{i,th}}{\beta_{iv,e}^{NH_3} V_{dif} \left(\frac{D_{i,0}}{D_{NH_3,0}} \right)^{0,67} \Delta\rho_{i,e}}, \tag{70}$$

where (see Fig. 9) the volume of truncated cone is

$$V_{dif} = \frac{\pi}{24} \frac{d_m^3}{\operatorname{tg}\frac{\alpha}{2}} \left[\left(\frac{2l}{d_m} \operatorname{tg}\frac{\alpha}{2} + 1 \right)^3 - 1 \right]. \tag{71}$$

Substituting (67), (71) into (70), at α=6°, l=0.2 m, d_m=0.02 m, U_0=80 m/s, q_l=15 l/m^3 we get the following, assuming that $\Delta\rho_{i,th} \approx \Delta\rho_{i,e}$,

$$\frac{\Delta G_{i,th}}{\Delta G_{i,e}} = 0,9457, \tag{72}$$

where for H_2S $\left(\frac{D_{i,0}}{D_{NH_3,0}} \right)^{0,67}$=0.7426, i.e., the difference between the theory and experiment is less than 6 %, what is a good agreement, considering the assumed parameters for normalized Venturi tube.

http://dx.doi.org/10.5772/53094

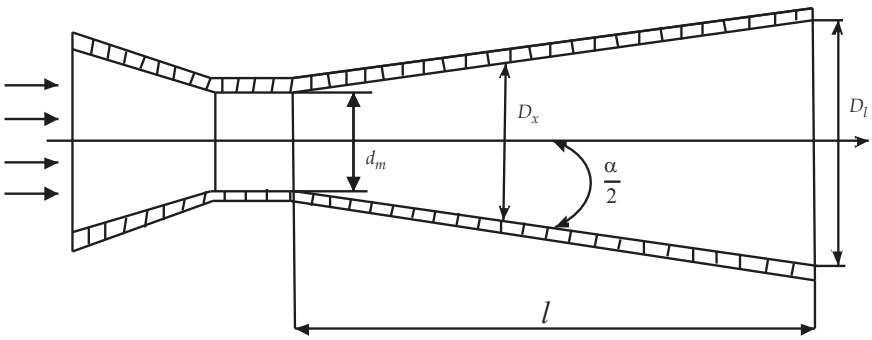

Figure 9. The scheme of Venturi tube

The amount of absorbed H_2S for the version of calculation in Fig. 8 (η_{H_2S}=0.072959, $\rho_{d.a.,0}$ =0.7541 kg/m^3) is

$$W_{i,th} = 0,\ 7541 \cdot 0,\ 1 \cdot 0,\ 072959 \cdot 80 \frac{3,\ 14(0,\ 02)^2}{4} 3600 = 0,\ 5 \ \text{kg/h}.$$

For the scrubber with d_m=0.1 m, l=1 m at the same dust and gas parameters at the inlet $W_{i,e}$=12, 78 kg/h.

The experimental values of efficiency of condensation capture of submicron dust are compared with results of model calculation inn [2, 11, 12] at the example of deposition of ash particles from cracking gases under the industrial conditions in hollow jet scrubbers [13]; good agreement is achieved.

4. The choice of the value of calculated concentration difference for the absorbed gas component

Let's consider this important question in detail as an addition to iss. 2 at the example of water absorption of SO_2, comparing calculation and experimental data [6] on volumetric mass transfer coefficient.

It follows from equation (3) that

$$W_{i,th} = -\int_0^H \beta_{id} \pi \delta_{d0}^2 \left(\rho_{id} - \rho_i\right) n_d \mathbf{d}x,\ kg/s \cdot m^2, \tag{73}$$

where, according to formulas (26) and (38)

$$n_d = 6q\frac{U_0}{V_{dx}}\frac{1}{\pi\delta_{d0}^3}. \tag{74}$$

In (73) and (74), according to calculation results, it is assumed that $\delta_d = \delta_{d0}$.

Let's put β_{id} from (19) to (73) at $K_{ci}=1$ and n_d from (74), we obtain, proved by estimates,

0, 276$\mathrm{Re}_d^{0,55}\mathrm{Sc}_i^{0,33}$>>1, V_{dx}>>U,

$$W_{i,th} \approx -3,312\frac{qU_0}{\delta_{d0}}\int_0^H \frac{(\rho_{id}-\rho_i)\mathbf{d}x}{\mathrm{Re}_d^{0,45}\,\mathrm{Sc}_i^{0,67}}, \tag{75}$$

where

$$\mathrm{Re}_d \approx \frac{V_{dx}\delta_{d0}\rho}{\mu}. \tag{76}$$

Lets' turn dependence (74) to the following form using the theorem about an average for integral:

$$W_{i,th} \approx 3,312qU_0\frac{\left(\bar{D}_{\mathrm{NH_3}}\right)^{0,67}}{\delta_{d0}^{1,45}\bar{V}_d^{0,45}}\left(\bar{\nu}\right)^{-0,22}\left(\int_0^H \Delta\rho_{id}\mathbf{d}x\right)\left(\frac{D_{i,0}}{D_{\mathrm{NH_3},0}}\right)^{0,67},\ kg/s\cdot m^2, \tag{77}$$

where $\bar{\nu}=(\bar{\mu}/\bar{\rho})$ is the average value of kinematic viscosity of the vapor-gas flow in the scrubber volume, m²/s, $\bar{D}_{\mathrm{NH_3}}$ is the average value of diffusion coefficient of methane NH_3, $\bar{V}_{dx}$ is average velocity of droplets on the 0–H way at motion from scrubber inlet to the outlet, m/s, $\Delta\rho_{id} = |\rho_{id}-\rho_i|$.

Expressing velocity U_0 and V_{dx} in m/h, and assuming $\delta_{d0}=7\cdot10^{-4}$m (700 μm), $\bar{D}_{\mathrm{NH_3}}(T_{d,ave}\approx 278,\ 5\,K)=0,\ 198\cdot10^{-4}\left(\frac{285}{273}\right)^{1,75}=0,\ 205\cdot10^{-4}$m²/s (see Fig. 10 b)), $\bar{\nu}=(285\,K)\approx 1,\ 5\cdot10^{-6}$ m²/s, $\bar{V}_{dx}\approx 5,\ 25$ m/s (see Fig. 10 e)), $\left(D_{\mathrm{SO_2},0}/D_{\mathrm{NH_3},0}\right)^{0,67}=0,\ 715$, we obtain for calculation parameters of Fig. 10 $W_{i,th}\approx 83$ kg/h•m², where $\int_0^H \Delta\rho_{id}\mathbf{d}x = 0,\ 6437$ kg/m² is obtained via model calculation (see Fig. 11).

http://dx.doi.org/10.5772/53094

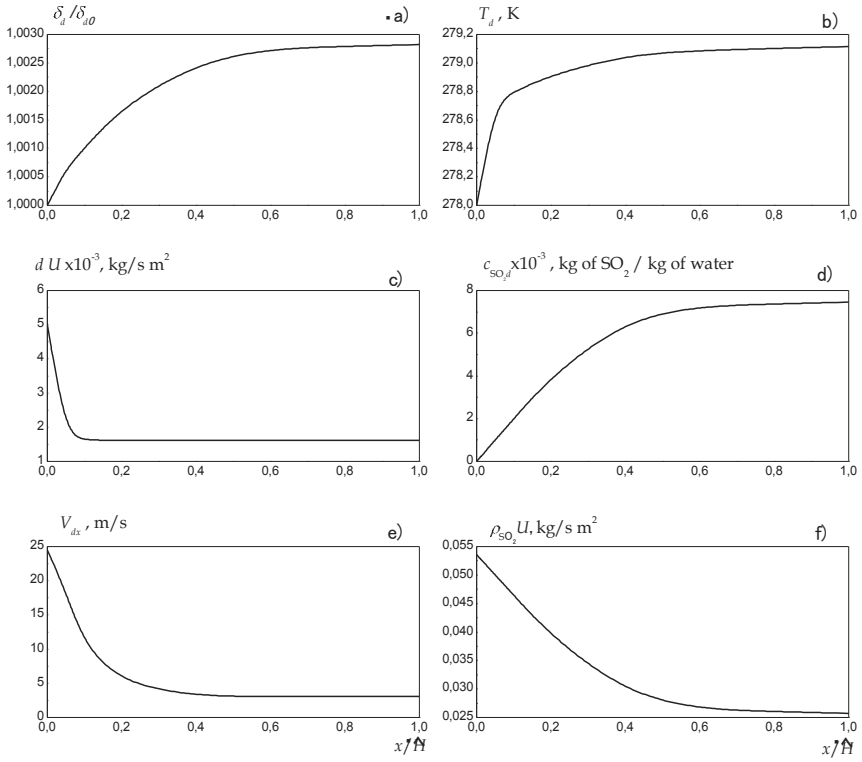

Figure 10. Calculation of SO_2 absorption in direct-flow jet scrubber: H =12.75 m; q =0.015 m³/m³; δ_{d0} =700 μm; V_{d0} =24.5 m/s; U_0 =0.25 m/s; T_{d0} =278 K; T_{00} =293 K; d_0 =0.02 kg/kg of dry air; $d_{SO_2,0}$ =0.2 kg/kg of dry air; η_{SO_2}=0.51722

We should note that multiplier $\left(D_{i,0}/D_{NH_3,0}\right)^{0,67}$ was included into formula (76) as a correction like to was dome for empirical dependence (46).

Numerical calculation by the model give the value of SO_2 extraction

$$W_{i,th} = \rho_{d.a.,0} d_{SO_2,0} U_0 \eta_{SO_2} 3600 = 1,0743 \cdot 0,2 \cdot \cdot 0,25 \cdot 0,51722 \cdot 3600 = 100 \ \text{kg/h} \cdot \text{m}^2. \quad (78)$$

The difference is 17 %, what is a sequence of simplifications and averaging in dependence (76).

If we assume average concentration difference in accordance to average experimental height H=7 m $\Delta\rho_i$=0, 6437/7=0, 092kg/m³, then

$$W_{i,e}=28685,\ 9U_0^{1,35}q^{0,45}H^{0,35}\Delta\rho_i\left(\frac{D_{i,0}}{D_{NH_3,0}}\right)^{0,67}=28685,\ 9\cdot 0,\ 1539\cdot 0,\ 151\cdot 1,\ 976\cdot 0,\ 092\cdot 0,\ 715=86,\ 6\,kg/h\cdot m^2.$$

The difference with $W_{i,e}$=83 kg/h•m² is 4.2 %.

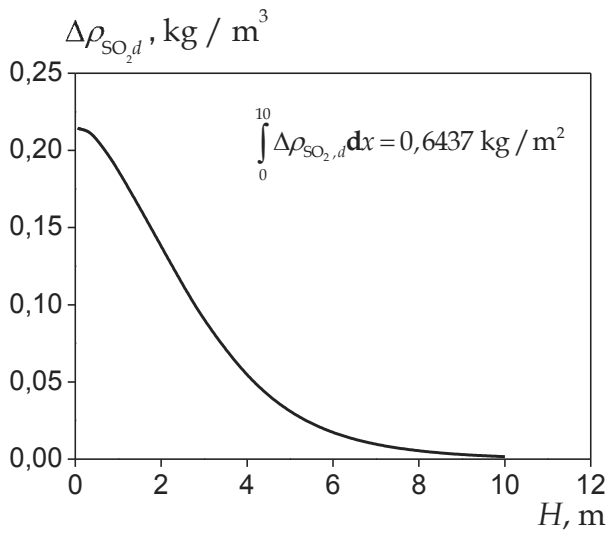

Figure 11. Distribution of $\Delta\rho_{SO_2 d}$ along the scrubber height for calculation parameters of Fig. 10.

If we take $\Delta\rho_i = \rho_{d.a.,0} d_{SO_2,0} \eta_{SO_2}$=0, 111 kg/m^3, then $W_{i,e}$=104.5 kg/h•m^2, what differs from result of (77) by similar 4.3 % with accuracy of estimation error. This proves the fact that calculated volumetric mass transfer coefficient agrees empirical dependence (46) of [6].

On the basis of analysis performed the calculated concentration difference should be recommended for practical application as the most appropriate

$$\Delta\rho_i = \rho_{i,0} - \rho_{i,H} \frac{U_H}{U_0} \tag{79}$$

at determination of the value of extracted gas component by formula (49), thus, it is necessary to measure $\rho_{i,0}$, $\rho_{i,H}$ and U_0, U_H at apparatus inlet and outlet. Calculation of moisture content is shown in Fig. 10 c), at this, it was obtained that U_H=0, 2234 m/s, $\rho_{d.a.,0}$=1, 0743 kg/m^3.

5. Conclusions

The suggested physical-mathematical model of complex heat and mass transfer and condensation-absorption gas cleaning from dust and harmful gaseous components is confirmed by the known experimental data and can be used for engineering calculations and optimization of construction and operation parameters of hollow jet scrubbers of direct and counter flow types. This was proved by its numerical implementation for the specific conditions. Calcula-

http://dx.doi.org/10.5772/53094

tions on absorption of some gases (CO_2, H_2S, SO_2, CH_4) on water droplets, dispersed by coarse centrifugal nozzles in hollow direct-flow jet scrubber and pneumatic Venturi scrubber from wet air is shown in the current paper together with calculation of combined absorption-condensation air cleaning from H_2S and various-sized fine dust in these apparatuses at an increased moisture content. The system of model equations is written at some certain conditions for the multicomponent vapor-gas mixture with particle. This makes it possible to use this system for calculation of complex gas cleaning from several harmful gas components and several fractions of dust particles and investigate regularities of this process.

Nomenclature

$\vec{V}_d$ vector of droplet velocity

$\vec{U}$ nvector of vapor-gas low velocity

$\vec{g}$ vector of gravity acceleration

m_d droplet mass (variable value due to evaporation-condensation and absorption), kg

c_f specific heat capacity of liquid, J/ kg•K

T_d mean mass temperature of droplets, K

α_d heat transfer coefficient of droplet, W/m^2•K

δ_d mass-median size of droplet, m

T temperature of vapor-gas flow, K

r_i specific heat of absorption, evaporation-condensation, J/kg

c_δ specific heat capacity of "formation", J/kg•K

ρ_δ mass concentration of "formations' in the vapor-gas flow, kg/m^3

$V_c = |\vec{V}_d - \vec{U}|$ module of relative droplet velocity, m/s

η_{Stk} coefficient of "formation" capture by droplets

T_δ mean mass temperature of "formations", K

β_{id} coefficient of droplet mass transfer with the i-th component of vapor-gas flow by concentration difference, m/s

ρ_{id} and ρ_i partial densities (mass concentrations) of saturated vapors of dissolvent and gas components near droplet surface and far from it (in the flow), kg/m^3

n_d and n_δ calculated concentrations of droplets and "formations" in the flow, $1/m^3$

ρ_g partial density of non-reacting gas component, kg/m^3

ρ_d mass concentration of droplets, kg/m^3

α_δ heat transfer coefficient of "formation", $W/m^2 \bullet K$

δ size of "formation", m

ρ density of vapor-gas flow, kg/m^3

c specific heat capacity of vapor-gas flow, J/ kg•K

ρ_p mass concentration of dry dust particles in the flow, kg/m^3

ρ_f density of liquid (droplets), kg/m^3

μ dynamic viscosity of vapor-gas flow, Pa•s

M_i molar masses of components of the vapor-gas mixture, kg/kmole

R =8, 314 kJ/kmole•K universal gas constant

D_i diffusion coefficient of mixture component, m^2/s

P_i partial pressure of the i-th component of the vapor-gas mixture, Pa

$P_{id,\delta}$ partial saturation pressures of mixture components, calculated by droplet and "formation" temperature, Pa

$m_{px,i}$ constants of phase equilibrium of solutions of i-^{ths} components of extracted gases, Pa

$x_{id,\delta}$ mole fractions of gas components dissolved in a droplet and "formation" condensate

$c_{mid,\delta}$ mass fractions of gas components in droplet and "formation" dissolvent, kg/kg of dissolvent

M_{dis} molar mass of dissolvent, kg/kmole

$\boldsymbol{d}m_{v\delta}/\boldsymbol{d}\tau$ rate of "formation" mass change due to evaporation-condensation of liquid, kg/s

δ_0 initial size of dust particles, m

ρ_s density of solution on "formation" due to condensation of liquid vapors and absorp-tion of gas components, kg/m^3

d moisture content, kg of vapors/kg of dry non-reacting component of vapor-gas mixture

d_i gas content, kg of reacting gas component/ kg of dry non-reacting component of vapor-gas mixture

$q = Q_f / Q_{sg0}$ irrigation coefficient

Q_f volumetric flow rate of liquid, m^3/s

Q_{sg0} volumetric flow rate of vapor-gas mixture at apparatus inlet, m^3/s

Author details

M. I. Shilyaev and E. M. Khromova

*Address all correspondence to: helenka24@rambler.ru

Department of heating and ventilation, Tomsk State University of Architecture and Building, Tomsk, Russia

References

[1] Shilyaev M.I., Shilyaev A.M., Grischenko E.P. Calculation Methods for Dust Catchers. Tomsk: Tomsk State University of Architecture and Building; 2006.

[2] Shilyaev M.I., Khromova E.M., Bogomolov A.R. Intensification of heat and mass transfer in dispersed media at condensation and evaporation. Tomsk: Tomsk State University of Architecture and Building; 2010.

[3] Shilyaev M.I., Khromova E.M. Simulation of heat and mass transfer in spray chambers. Theoretical Foundations of Chemical Engineering 2008; 42(4) 404-414.

[4] Tumasheva A.V. Modeling of heat and mass transfer processes in jet irrigation chambers: abstract of the thesis of candidate dissertation: 01.04.14: defended on 17.06.2011. Novosibirsk; 2011.

[5] Shilyaev M.I., Shilyaev A.M. Aerodynamics and heat and mass transfer of gas-dispersed flows. Tomsk: Tomsk State University of Architecture and Building; 2003.

[6] Ramm V.M. Absorption of Gases. Moscow: Khimiya; 1976.

[7] Pavlov K.F., Romankov P.G., Noskov A.A. Sums and Problems in the Course of Processes and Apparatuses of Chemical Technology. The 8th edition, revised and added. Leningrad: Khimiya; 1976.

[8] Perelman V.I. Brief Hand-Book of a Chemist. Edit. by Corr. Member of AS of USSR B.V. Nekrasov. The 3rd edition, revised and added. Moscow: State Scientific-Technical Publishing House of Chemical Literature; 1954.

[9] Goronovsly I.T., Nazarenko Yu.P., Nekryach E.F. Brief Chemistry Guide. Edit. by Academician of AS of USSR A.T. Pilipenko. Kiev: Naukova Dumka; 1987.

[10] Hand-Book on Dust and Ash Capture. Edit by A.A. Rusanov. Moscow: Energia; 1975.

[11] Shilyaev M.I., Khromova E.M. Capture of Fine Dust in Jet Scrubbers. In: Mohamed El-Amin (ed.) Mass Transfer in Multiphase Systems and its Applications. Vienna: In Tech4; 2011. 311-335.

[12] Shilyaev M.I., Khromova E.M., Grigoriev A.V., Tumashova A.V. Physical-mathematical model of condensation process of the sub-micron dust capture in sprayer scrubber. Thermophysics and Aeromechanics 2011; 18(3) 409-422.

[13] Uzhov V.N., Valdberg A.Yu. Gas Cleaning by Wet Filters. Moscow: Khimiya; 1972.

Chapter 8

Fouling in Membrane Filtration and Remediation Methods

A. Abdelrasoul, H. Doan and A. Lohi

Additional information is available at the end of the chapter

http://dx.doi.org/10.5772/52370

1. Introduction

The growth of the membrane technologies has fell far behind the initial anticipation, one of the major obstacles, which hinders more widespread of its application, is that the filtration performance inevitably decreases with filtration time. This phenomenon is commonly termed as membrane fouling, which refers to the blockage of membrane pores during filtration by the combination of sieving and adsorption of particulates and compounds onto the membrane surface or within the membrane pores. Pore blockage reduces the permeate production rate and increases the complexity of the membrane filtration operation. This is the most challenging issue for further membrane development and applications.

Permeate flux and transmembrane pressure (TMP) are the best indicators of membrane fouling. Membrane fouling leads to a significant increase in hydraulic resistance, manifested as permeate flux decline or TMP increase when the process is operated under constant-TMP or constant-flux conditions. In a system where the permeate flux is maintained by increasing TMP, the energy required to achieve filtration increases. Over a long period of operation, membrane fouling is not totally reversible by backwashing. As the number of filtration cycles increases, the irreversible fraction of membrane fouling also increases. In order to obtain the desired production rate, chemical cleaning is required for membrane to regain most of its permeability. The resultant elevated cost makes membranes economically less feasible for many separation processes. There are also concerns that repeated chemical cleaning might affect the membrane life.

Fouling can be broadly classified into backwashable or non-backwashable, and reversible or irreversible based on the attachment strength of particles to the membrane surface. Backwashable fouling can be removed by reversing the direction of permeate flow through the pores of the membrane at the end of each filtration cycle. Non-backwashable

fouling is the fouling that cannot be removed by normal hydraulic backwashing in between filtration cycles. However, non-backwashable fouling of the membrane can be handled by chemical cleaning. On the other hand, irreversible fouling cannot be removed with flushing, backwashing, chemical cleaning, or any other means, and the membrane cannot be restored to its original flux. Fouling also can be classified, based on the type of fouling material, into four categories: inorganic fouling/scaling, particle/colloidal fouling, microbial/biological fouling, and organic fouling. Inorganic fouling or scaling is caused by the accumulation of particles when the concentration of the chemical species exceeds its saturation concentration. Several studies have shown that increased concentration of Ca^{2+} and Mg^{2+} caused more fouling [1-3]. On the other hand, organic fouling occurs due to the clogging of the membrane by organic substances, and organic carbons generally concentrate on the internal surface of the membrane [4]. Based on the analysis of the extracted solution during chemical cleaning, it was found that most soluble organic foulants were of low molecular weights, and calcium was the major inorganic foulant [5].

Natural organic matter (NOM) is the organic material present in surface or ground water and contains various high molecular weight organic compounds. NOM includes both humic and non-humic fractions. The humic fraction consists of high molecular weight organic molecules. Common non-humic NOM foulants are proteins, amino sugars, polysaccharides, and polyoxyaromatics [6]. Several studies have shown that NOM is the major ultrafiltration membrane foulant, and different components of NOM cause different forms of fouling [7-9]. According to Makdissy *et al.*, the organic colloidal fraction causes significant fouling [10]. However, polysaccharides are identified as the dominant foulant [11]. Other studies reported that most fouling was caused by hydrophobic NOM components [12]. Nevertheless, neutral hydrophilic NOM components were found the major foulants by some researchers [13]. The NOM components, as the major foulants, can be ranked in the order neutral hydrophilics > hydrophobic acids > transphilic acids > charged hydrophilics. Due to conflicting results from different researchers and many facets of membrane fouling, there would be no universal solution for membrane fouling remediation, but it has to be dealt with and designed specifically for a certain type of foulant and membrane in use, as presented later in this paper.

2. Membrane fouling mechanism

A typical flux-time curve of ultrafiltration (UF), as shown in Figure 1, starts with (I) a rapid initial drop of the permeate flux, (II) followed by a long period of gradual flux decrease, and (III) ended with a steady-state flux.

Flux decline in membrane filtration is a result of the increase in the membrane resistance by the membrane pore blockage and the formation of a cake layer on the membrane surface. The pore blocking increases the membrane resistance while the cake formation creates an additional layer of resistance to the permeate flow. Pore blocking and cake formation can be considered as two essential mechanisms for membrane fouling.

http://dx.doi.org/10.5772/52370

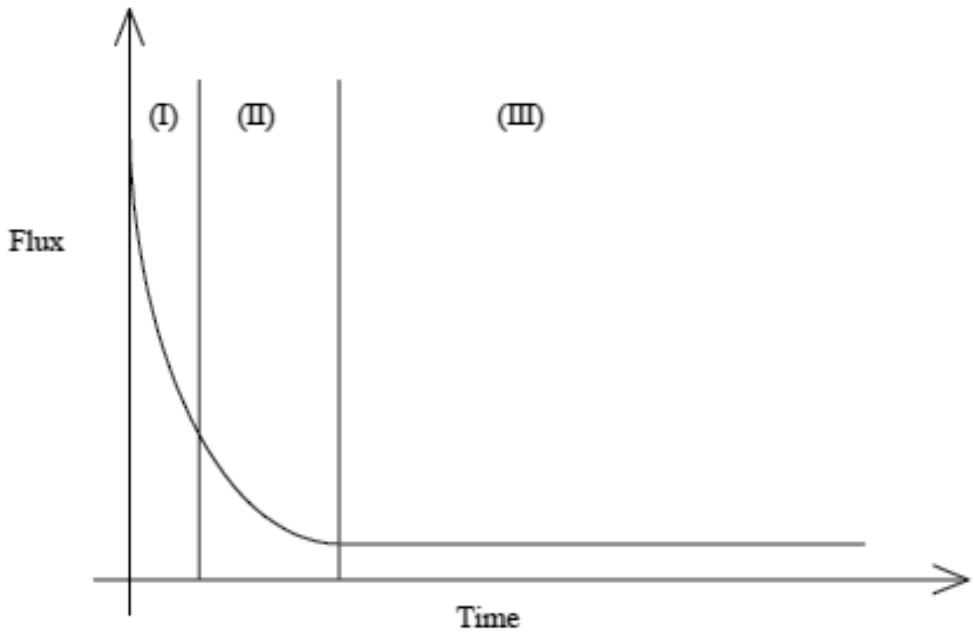

Figure 1. A Schematic presentation of the three stages in flux decline [14]

The rapid initial drop of the permeate flux can be attributed to quick blocking of membrane pores. The maximal permeate flux always occurs at the beginning of filtration because membrane pores are clean and opened at that moment. Flux declines as membrane pores are being blocked by retained particles. Pores are more likely to be blocked partially and the degree of pore blockage depends on the shape and relative size of particles and pores. The blockage is generally more complete when the particles and pores are similar in both shape and size [15-17]. Pore blocking is a quick process compared with cake formation since less than one layer of particles is sufficient to achieve the full blocking [16, 18].

Further flux decline after pore blockage is due to the formation and growth of a cake layer on the membrane surface. The cake layer is formed on the membrane surface as the amount of retained particles increases. The cake layer creates an additional resistance to the permeate flow and the resistance of the cake layer increases with the growth of cake layer thickness. Consequently, the permeate flux continues decreasing with time.

3. Mathematical models for membrane fouling

Pursuant to the understanding of different roles of aquatic components in membrane fouling, different mathematical models have been developed to describe the membrane fouling. The

most widely used empirical model is the cake filtration model that focuses on the role of particles larger than membrane pore sizes. In this model, the hydrodynamic resistance of cake layer [Rc, m^{-1}] is defined as:

$$R_c = \hat{R}_c.m_d \tag{1}$$

where $\hat{R}_c$ [m/kg] is the specific cake resistance of the cake layer on the membrane surface and *md* [kg/m^2] is the mass of deposit per unit surface area of membrane. The corresponding permeate flux (J, m^3/m^2.s) is expressed using Darcy's law and a resistance-in-series model (RIS) as below:

$$J = \frac{\Delta P}{\mu\ (R_m + R_c)} \tag{2}$$

where ΔP (Pa) is transmembrane pressure, μ (Pa-s) is the solution viscosity and *Rm* (1/m) is the hydrodynamic resistance of clean membrane. Additional work has been done to relate $\hat{R}_c$ to the structure of the cake layer formed by particles or aggregates [19, 20]. The cake filtration model has been used to fit filtration data and reasonable results have been obtained [21]. However, the model does not explain the mechanisms of fouling, but only indicates the proportionality between the increase in hydrodynamic resistance and the mass of deposit on the membrane as filtration proceeds under some conditions. The values of $\hat{R}_c$ vary from 10^{10} to 10^{16} m/kg for different aquatic substances [22]. Babel *et al.* [23] found that $\hat{R}_c$ for a *Chlorella* algae culture changed from 10^{11} to 10^{12} m/kg when the growth condition became inhibitive. Foley [24] reviewed different factors affecting the permeability of the cake layer formed in dead-end microfiltration of microbial suspensions. It was found that $\hat{R}_c$ is dependent on cell morphology, surface properties, operating pressure, and time. The resistance-in-series model has been used frequently to analyze membrane fouling phenomenon. Although it is easy to apply, one should be cautious in the use of this model as it doesn't consider pore blocking mechanism.

Kosvintsev et al. [25] developed another model to describe fouling by physical sieving of low pressure membranes by particles larger than membrane pore sizes. According to their analysis, membrane fouling by cake filtration does not start right after the onset of filtration, and the fouling is rather dominated by pore blocking until the membrane surface is covered by particles. This model describes the permeate volume as a function of permeate time, dominated by pore blocking at constant pressure as follows:

$$V = \frac{1}{\gamma n \beta} ln\ (1\ + \beta t^*) \tag{3}$$

http://dx.doi.org/10.5772/52370

where V is the permeate volume (cm^3), βit is the ratio of the membrane area fouled with particles to the area of clean pores. This constant must be identified from experimental measurement for a given membrane and it should be slightly greater than unity. n the number of particles per unit volume of the feed, γ is the ratio of the pores area to the total membrane area and t^* *is* the dimensionless filtration time = γ n $\int_0^t \frac{dV}{dt}$. More details of the model are presented in the authors' recent work [26]. This model was limited to pore blocking fouling and the effect of cake layer on the permeate volume was not considered.

Zydney *et al.* combined two fouling mechanisms, pore blockage and cake formation, to describe fouling of low pressure membranes by proteins and humic acids [27, 28]. Again, this model is established by assuming that the fouling is caused primarily by large particles, aggregates of proteins and humic acids. The mathematical development is based on constant pressure operation and varying flux, and it can be written as below:

$$\frac{J}{J_o} = \exp\left(-\frac{K_b \Delta P C_b}{\mu R_m} t\right) + \frac{R_m}{R_m + R_c}\left[1 - \exp\left(-\frac{K_b \Delta P C_b}{\mu R_m} t\right)\right] \tag{4}$$

where J and J_0 (m^3/s) are the permeate flux at a given time and the initial flux through the unfouled membrane respectively, K_b (m^2/kg), a pore blockage parameter, is equal to the blocked membrane area per unit mass of aggregates convected to the membrane. This parameter can be measured experimentally. C_b (kg/m^3) is the bulk concentration of large aggregates, R_m (1/m) is the clean membrane resistance, Rc is cake layer resistance (1/m), μ is the solution viscosity and ΔP is the transmembrane pressure (Pa). Both resistances can be measured experimentally. The right-hand side of the equation has two terms that are related to pore blocking and cake formation, respectively. The first term (pore blocking) dominates the early stage of fouling, and the second term (cake filtration) governs fouling at longer times. The impact of solution chemistry on membrane fouling is, however, not included in the model, but was rather considered as a prerequisite for the aggregation of proteins or humic acids.

In comparison to the aforementioned models, adsorptive fouling of membranes by particles smaller than membrane pore sizes is incorporated in the following model. The impact of the adsorption layer on the permeability of membranes can be estimated using a modified form of Hagen-Poiseulle capillary filtration model [29] as below:

$$\frac{J}{J_o} = [1 - \frac{\delta'}{r_p}]^4 \tag{5}$$

where J and J_0 ($m^3/m^2.s$) are the permeate flux after the formation of the adsorptive fouling layer and the initial flux, respectively, under a given transmembrane pressure, δ'(m) is the thickness of the adsorption layer that can be measured experimentally and r_p (m) is the membrane pore radius. The major difficulty in applying the adsorptive fouling model to

filtration of natural surface waters lies in the complex nature of aquatic NOM. In other words, the value of δ' is not easy to obtain either theoretically or experimentally. This problem is further complicated by the heterogeneity of membrane surface properties.

4. Chemical attachment of foulants on membrane surfaces

An underlying question on membrane fouling is the origin of the attachment of foulants on the membrane surface. The major forces contribute to attachment are dispersion interaction force and polar interactions force [30]. These forces apply to material entities at different scales.

4.1. Chemical attachment by dispersion interaction

Foulants stay together on membrane surfaces most likely due to the presence of physiochemical interactions, such as the dispersion interaction between aqueous entities. This dispersion interaction is due to Van der Waals attractive force between molecules across water and is balanced by the electrostatic repulsion between particles and the membrane surface due to the presence of surface charges. As shown in energy curve figure (2) the height of the energy barrier depends not only on how strong the attractive interaction is, but also on the magnitude of the repulsive electrostatic interaction. Therefore, it is usually considered beneficial to increase the charge density of the similarly charged interacting entities to reduce attachment.

To represent the dispersion interaction, the Hamaker constant can be used. It is the property of a material, which represents the strength of van der Waals interactions forces between macroscopic bodies through a third medium as shown in Figure (3). Typical values of the Hamaker constant are in the range of 10^{-19} - 10^{-21} Joules. It can be estimated using the Lifshitz theory of macroscopic van der Waals interactions forces, which ignores the atomic structures of the interacting molecules, and calculates the forces between them in terms of their dielectric constants (ε) and refractive indices (n) [31, 32].The Hamaker constant, A, for two macroscopic phases 1 and 2 interacting across a medium 3 is approximated as:

$$A \approx \frac{3}{4}KT\frac{\varepsilon_1-\varepsilon_3}{\varepsilon_1+\varepsilon_3}\cdot\frac{\varepsilon_2-\varepsilon_3}{\varepsilon_2+\varepsilon_3}\cdot\frac{3h\nu_e}{8\sqrt{2}}\cdot\frac{\left(n_1^2-n_3^2\right)(n_2^2-n_3^2)}{\left(n_1^2+n_3^2\right)^{1/2}\left(n_2^2+n_3^2\right)^{1/2}\left\{\left(n_1^2+n_3^2\right)^{1/2}+\left(n_2^2+n_3^2\right)^{1/2}\right\}} \quad (6)$$

where "1" and "2" denote two interacting bodies inside medium "3", A is the Hamaker constant, *ve* is the medium absorption frequency (for H_2O, *ve* = 3 x 10^{15} s^{-1}), ε is the dielectric constant that indicates the extent to which a material concentrates electric flux, n is the refractive index, K is the Boltzamnn constant, h is the Plank constant and T is the absolute temperature [33].

http://dx.doi.org/10.5772/52370

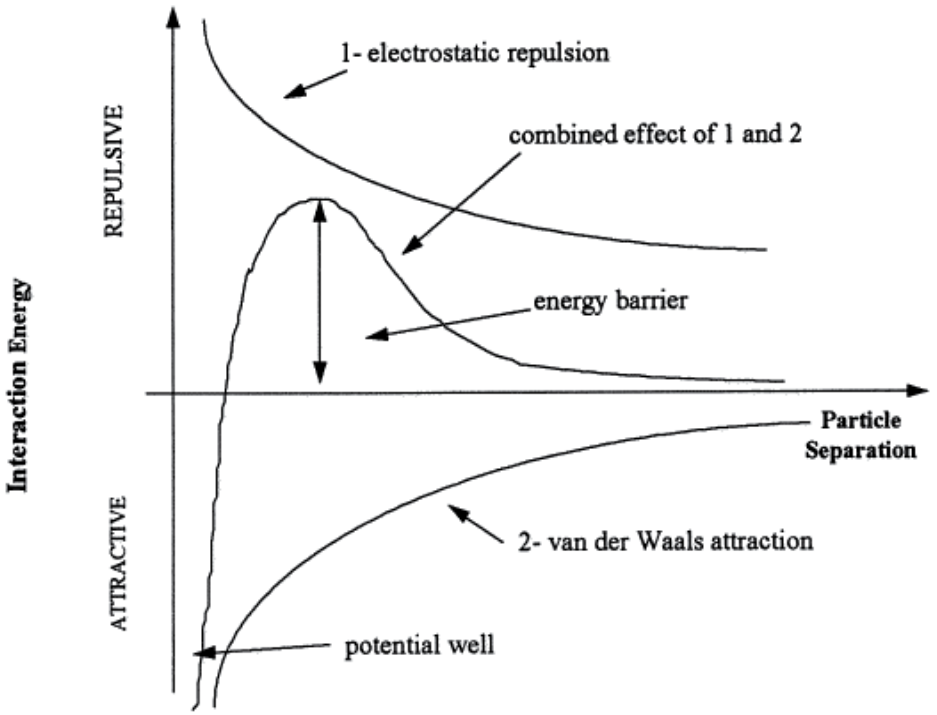

Figure 2. Energy curve of interaction forces [33]

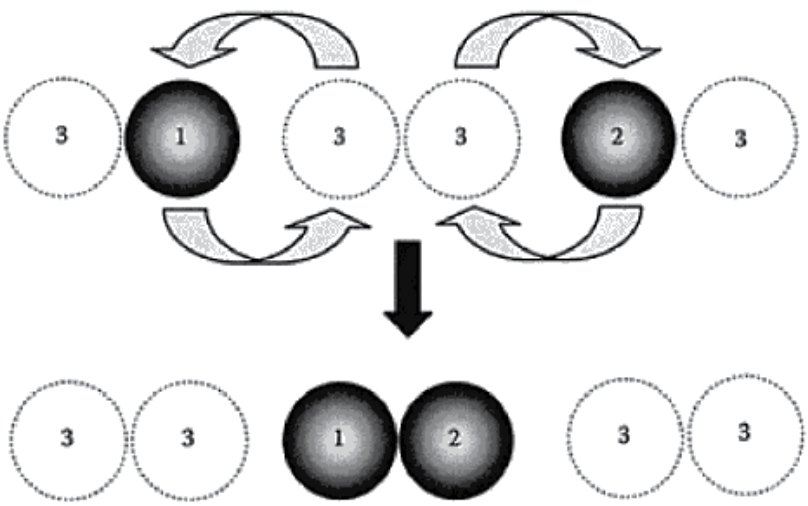

Figure 3. Interaction between 2 microscopic bodies 1 and 2 through medium 3 [33]

Table 1 lists the Hamaker constants representing the van der Waals interaction between polystyrene latex particles and different membrane materials across water, calculated using the macroscopic approach [30]. The Hamaker constant at zero frequency, Aν=0, represents the static interaction and this term is always less than or closed to ¾ KT. The Hamaker constant at zero frequency is less than the total strength of van der Waals interactions forces. Hamaker constants at frequencies above zero, Aν>0, is related to the three refractive indices, or fundamentally, the dispersion interaction between these surfaces. As shown in Table 1, the minimum and the maximum interaction force are observed in PTFE and alumina membranes with latex particles, respectively. The dispersion interaction between latex and PVDF is slightly less than half of that between two latex particles which indicates less irreversible fouling. [33]

Interaction System [1] (1-3-2)	Dielectric Constant (kHz) [2]			Refractive Index [3]		Hamaker Constant x 10^{21} (J)			
ε1	ε3	ε2	n1	n3	n2	$A_{v=0}$	$A_{v>0}$	A_{tot}	
Latex -Water- PTFE	2.55	80	2.1	1.557	1.333	1.359	2.75	1.55	4.3
Latex -Water- PVDF	2.55	80	6.4	1.557	1.333	1.42	2.47	5.12	7.59
Latex -Water- CA	2.55	80	4.5	1.557	1.333	1.475	2.59	8.27	10.9
Latex -Water- PP	2.55	80	1.5	1.557	1.333	1.49	2.79	9.12	11.9
Latex -Water- Cellulose nitrate	2.55	80	6.4	1.557	1.333	1.51	2.47	10.2	12.7
Latex -Water- PES	2.55	80	3.5	1.557	1.333	1.55	2.65	12.5	15.1
Latex -Water- Latex	2.55	80	2.55	1.557	1.333	1.557	2.72	12.8	15.6
Latex -Water- PC	2.55	80	2.95	1.557	1.333	1.586	2.69	14.4	17.1
Latex -Water- Alumina	2.55	80	11.6	1.557	1.333	1.75	2.16	22.9	25.1
Latex -Water- fused quartz	2.55	80	3.8	1.557	1.333	1.448	2.63	6.74	9.37

Note: 1 PTFE: Polytetrafluoroethylene, PVDF: Polyvinylidene fluoride, CA: Cellulose acetate, PP: Polypropylene, PES: Polyethersulfone, PC: Polycarbonate; dielectric constant [31], Refractive index [32]; $A_{tot} = A_{v>0} + A_{v=0}$

Table 1. Hamaker constants calculated using the Lifshitz equation for representative particle-membrane interaction systems [30]

4.2. Physiochemical attachment by "polar" interactions

The Derjaguin and Landau, Verwey and Overbeek (DLVO) theory has been extended, including different types of interactions, to applications with aqueous phase. Van Oss postulated the concepts of apolar and polar interactions to classify and predict these interactions [30]. The apolar interaction mainly consists of dispersion interaction. On the other hand, the polar (or Lewis acid-base) interaction is comprised of the interactions between Lewis acid-base pairs in the system, including the two interacting entities and surrounding water molecules. These interactions are useful in explaining the advantage of hydrophilizing the membrane surface to reduce the irreversible attachment of particles and other fouling materials

http://dx.doi.org/10.5772/52370

on membrane surface. According to the concept of apolar/polar interactions, the strength of chemical attachment depends not only on the dispersion interaction (apolar), but also, or even more dominantly, on the polar interactions. The latter can be either attractive or repulsive based on the hydrophilicity of the two interacting surfaces.

For two hydrophilic surfaces, the polar interaction is repulsive and counteracts the attractive dispersion interaction. Therefore, the total interaction becomes either weakly attractive or repulsive even in the absence of electrostatic repulsion which leads to reduce fouling. In comparison, the polar interactions would be fairly attractive between hydrophobic surfaces, which are additive to the attractive dispersion interactions. Consequently, electrostatic repulsion becomes the dominant factor in balancing the attractive and repulsive interaction which enhances fouling. Therefore, there are in principle at least two possible approaches to make the membrane less vulnerable to the attachment of aquatic contaminants: hydrophilization of membrane surfaces (to enhance thermodynamic stability) and ionization of membrane surfaces (to achieve kinetic stability). Both approaches have been investigated by several researchers [34, 35-39]. The presence of polar interaction has also been used to explain different affinities of silica and latex particles on hydrophilic membranes [40]. Hydrophobic polystyrene latex particles showed less affinity to three commercial hydrophilic membranes than silica particles, as measured using atomic force microscopy (AFM). The hydrogen bonding attraction between silica particles and membrane surfaces was speculated to be the primary reason for the greater attachment. Regardless of the true mechanisms, such results suggest that the molecular structure of membranes and aquatic particles can be important to their interactions. Another complicated problem is the presence of NOM in natural water. The sorption or deposition of NOM moieties on particle and membrane surfaces can form an additional polymeric layer at solid/water interfaces.

4.3. Chemical attachments between heterogeneous surfaces

All previous chemical attachment mechanisms are based on the assumption that the interacting surfaces have homogeneous surface properties, and thus can be characterized using some global parameters, such as: charge density, hydrophobicity, and the Hamaker constant. However, this may not be realistic because particles could have heterogeneous surfaces. Different parts of the surface have different affinities to the membrane. In addition, the membrane surface, especially that modified, also likely has heterogeneous surface properties relevant to foulant attachment. This heterogeneity can be attributed to different physical and/or chemical origins. For instance, the attachment of particles to membrane pores of various shapes was investigated. It was found that membrane pores with round corners are the least affinitive to colloidal fouling compared to those with sharp and spiky corners due to enhanced electrostatic repulsion [41]. In another investigation, the surface heterogeneity of nanofiltration and reverse osmosis membranes was studied using chemical force microscopy, a modified technique based on AFM to obtain the lateral distribution of surface energies/stickiness. It was found that the surfaces of the two membranes used were chemically heterogeneous, and that the heterogeneity became more significant below micron-sized dimensions [42]. This implies

that the stickiness of membrane surfaces to foulants can be heterogeneous, rather than uniformly homogenous as considered previously.

5. Factors affecting fouling

- Membrane properties: pore size, hydrophobicity, pore size distribution and membrane material.
- Solution properties: solid (particle) concentration, particle size and nature of components.
- Operating conditions: pH, temperature, flow rate and pressure.

5.1. Membrane properties

In an aqueous environment a membrane can be attractive or repulsive to water. The composition of the membrane and its corresponding surface chemistry determine its interaction with water, thus affecting its wettability. The wettability of the membrane can be determined by measuring the contact angle between the membrane surface and a droplet of liquid, as shown in Figure (4). Hydrophilic membranes are characterized by the presence of active groups that have the ability to form hydrogen-bonds with water and so these membranes have wettability as can be seen in Figure (4.b). Hydrophobic membranes have the opposite interaction to water compared to hydrophilic membranes as they have little or no tendency to adsorb water and water tends to bead on their surfaces (i.e. discrete droplets) as shown in Figure (4.a). This tends to enhance fouling. Hydrophobic membranes possess low wettability due to the lack of active groups in their surface for the formation of hydrogen-bonds with water. Particles, which foul membranes in aqueous media, tend to be hydrophobic. They tend to cluster or group together to form colloidal particles because this process lowers the interfacial free energy. Usually, greater charge density on a membrane surface is associated with greater membrane hydrophilicity. Polysulfone, cellulose acetate, ceramic and thin-film composite membranes used for water treatment and wastewater recovery typically carry some degree of negative surface charge and hydrophilic. Thus, fouling can be reduced with use of membranes with surface chemistry which have been modified to render them hydrophilic.

Figure 4. a) Hydrophobic membrane, (b) Hydrophilic membrane [14]

Membrane morphology also has a considerable effect on fouling as pore size, pore size distribution and pore geometry especially at the surface of the membrane. These determines

http://dx.doi.org/10.5772/52370

the predominant fouling mechanisms such as pore blocking and cake formation as previously discussed in section 2.

5.2. Solution properties

The properties of the feed solution also significantly influence membrane fouling. Some of the important feed properties are solid (particle) concentration, particle properties, pH and ionic strength. Generally, an increase in the feed concentration results in a decline in the permeate flux. This is due to the increase in membrane fouling by the presence of a higher foulant concentration. Particles may be present in the feed because of the nature of the feed or through precipitation of soluble feed component(s). The particles can cause fouling by pore blocking, pore narrowing or cake formation, dependent on the particle sizes. Higher permeate fluxes and cake thicknesses are usually obtained with larger particles [43]. Large particle size is one of the factors that inhibit deposition. In a filtration process, the particle sizes in the feed often cover a wide range. The presence of fine as well as coarse particles results in a lower cake porosity as the fine particles can slide between the large ones, filling the interstices. The range of the particle size distribution plays a major role in the selective deposition at high crossflow. In addition to the particle size, the particle shape affects the porosity of the cake formed on the membrane surface. In general, the lower the particle sphericity, the greater is the porosity [43].

Some other factors, such as: pH, ionic strength, and electric charges of particles, are also important. The pH and ionic strength of the feed affect the charge on the membrane, the charge on the particles, conformation and stability of, and thereby adhesiveness of particles/molecules and the size of the cake. For example, a study of the impact of pH of the latex emulsion on membrane fouling showed that the latex emulsion pH should be high enough to prevent the coagulation of latex particles, and hence, to increase the antifouling properties of the latex emulsion. Also, it has been showed that a reduction in pH could decrease the molecular size of NOM and thus enhances adsorption onto membrane, resulting in a significant fouling.

5.3. Operating conditions

The effect of temperature on the permeate flux was investigated and found that at higher temperatures, the permeate flux increased, indicating a lower degree of fouling. Changing the feed temperature from 20°C to 40°C lead to an increase in the permeate flux up to 60% [44]. This might be due to the fact that changes in the feed water temperature resulted in changes in the permeate diffusion rate through the membrane.

The cross-flow velocity is defined as the superficial velocity of the feed stream travelling parallel to the membrane surface. The effect of the cross-flow velocity on permeate flux has been studied for a wide variety of feed solutions. It is believed that increasing the cross-flow velocity positively affects the mass transfer coefficient of the solute and the extent of mixing near the membrane surface [45]. Consequently, the permeate flux is increased with cross-flow velocity. Higher mixing experienced with larger cross-flow velocity leads to a reduction of aggregation of the feed solids in the gel layer, essentially due to increasing diffusion of these

components back towards the bulk, leading to an overall reduction in the effect of concentration polarization.

The control of the transmembrane pressure (TMP) which is the pressure difference between the feed and permeate stream is essential as it greatly affects the permeation rate. At a higher TMP, the force of the fluid flowing towards the membrane is increased, leading to a higher permeate flux. Increasing the applied pressure influence the permeate flux as illustrated in Figure (5). At very low pressure $p_{1,}$ the flux is close to pure water flux at the same pressure. As the applied pressure is increased to pressure $p_{2,}$ the higher flux causes increased concentration polarization of the retained material at the membrane surface increases. If the pressure is increased further to p_3 which considered the critical pressure, concentration polarization becomes enough for the retained solutes at the membrane surface to reach the gel concentration, c_{gel}. Once a gel layer has formed, further increase in the applied pressure does not lead to further increase in the permeate flux above this critical value. The gel layer thickness and the density of the retained material at the membrane surface layer, however, increase. This limits the permeate flux through the membrane, and hence, the flux reaches a steady state level. It was reported that no fouling was experimentally observed when the process was operated under this critical flux [14].

6. Remediation of membrane fouling

Fouling remediation can be done through pre-treatment the feed to limit its fouling propensity, improving the antifouling properties of the membrane, membrane cleaning and backwash conditions and optimization of the operating conditions already discussed previously.

6.1. Feed pre-treatment

Membranes are susceptible to fouling; therefore, pretreatment of the feed is required to control colloidal, organic, and biological fouling as well as scaling. The pretreatment scheme must be capable of controlling membrane fouling to such an extent that a practical cleaning frequency can be achieved. For low-pressure membranes, a number of pretreatment methods are currently used.

6.1.1. Coagulation

Coagulation involves the addition of chemicals coagulants, such as: $FeCl_3$, $FeSO_4$, alum, polyaluminum chloride, etc.., to increase the size of suspended and colloidal particles in the feed prior to filtration. It was found that reversible fouling was reduced with coagulation pretreatment, but the extent of irreversible fouling was unchanged. This can be attributed to the fact that large particles are formed from small particles, and hence, reversible fouling decreases with the use of coagulation. However, smaller particles, which are not coagulated, still remain in the feed and causes irreversible fouling. Factors affecting membrane fouling includes coagulant dosage, pH, nature of dissolved organic matters as well as Ca^{2+} content of the feed water [14]. Moreover it was found that following coagulation pretreatment, most membrane

http://dx.doi.org/10.5772/52370

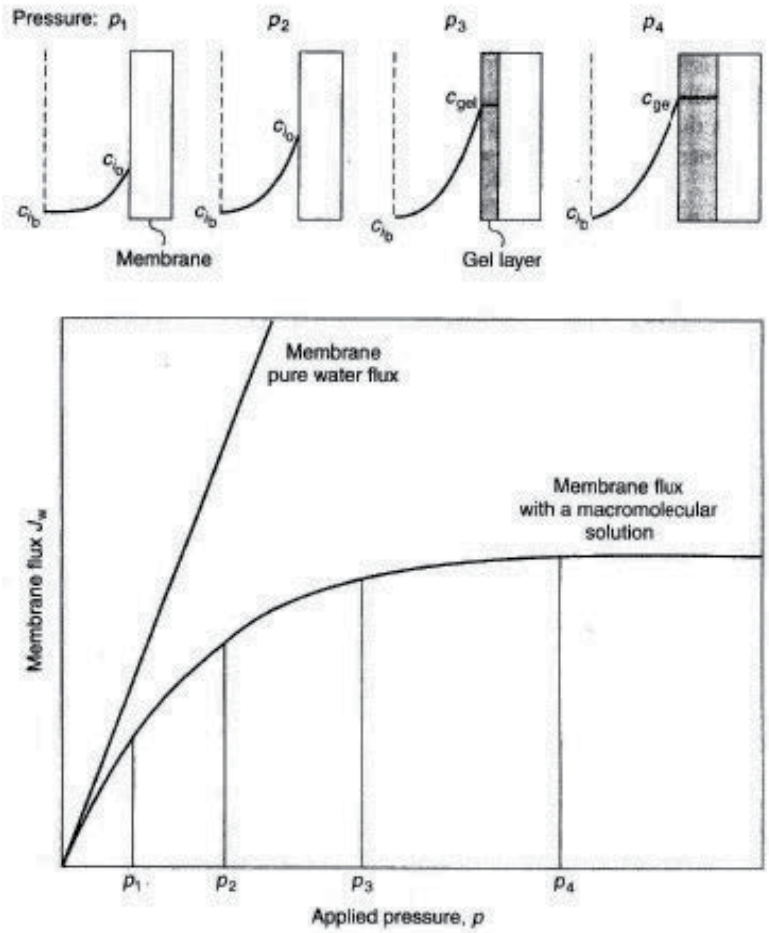

Figure 5. The effect of pressure on membrane flux [14]

fouling was due to the smaller hydrophilic NOM particles [13]. This finding is consistent with the fact that most metal-based coagulants are known to preferentially remove hydrophobic rather than hydrophilic substances. Coagulation reduced the rate of membrane fouling by minimizing pore plugging and increasing the efficiency of membrane backwashing.

Coagulation can be done by In-line coagulation process (IC), which refers to the dosing of coagulant into the feed stream. Rapid mixing in the feed stream allows the flocs to form (but not to settle) and finally enter the filtration unit (e.g., UF). Therefore, In-line coagulation doesn't require the sedimentation or prefiltration step prior to UF. Despite a larger fouling load in terms of suspended matter, IC may improve membrane performance due to the change in the fouling mechanism to cake formation rather than pore blocking. Once a cake is built up, it can be removed by backwashing easily. For in-line coagulation, the influence of membrane polymer nature and structure on fouling is alleviated. Cleaning frequency is also reduced and

cleaning aggressiveness could be lowered. Consequently, the permeate flux increases, and the effect of seasonal water quality variations on filtration can be better controlled [46].

Sedimentation process can be used following the coagulation process. In this combined pretreatment method, a coagulant is applied and the formed flocs are settled out by sedimentation. The supernatant is then fed to the membrane filtration unit. In one study at East St. Louis, when UF was used after coagulation-sedimentation (CS) for 400 h, no membrane fouling was observed [47]. The coagulation or CS pretreatment process was very effective in increasing UF membrane life because this process removed the primary foulants such as high molecular weight humics [48].

Alternative process is coagulation-adsorption, which refers to adsorption of foulants using an adsorbent such as powdered activated carbon (PAC) between the coagulation step and UF. In one study, wastewater with the initial COD of 165 mg/L and turbidity of 90 NTU was treated with 120 mg $FeCl_3$/L at pH of 5.5. The COD and turbidity of the treated water were reduced to 23 mg/L and 12 NTU, respectively. When a further treatment step by adsorption with PAC was used, the COD dropped further to 7 mg/L [49]. The use of adsorption (PAC) and coagulation (alum and polyaluminum chloride) as pretreatment steps prior to membrane filtration was also investigated to remove organics. Significant improvement in the removal of organic materials and trihalomethane precursors were obtained [50].

Flocculation is another pretreatment method that can remove particles and colloids and hence improve the permeate flux. It is used to achieve three objectives: eliminating the penetration of colloidal particles into the membrane pores, increasing the critical flux, and modifying the characteristics of the deposits. The use of flocculation prior to membrane filtration reduced clogging of the membrane by aggregating smaller particles, thereby retaining them on the surface of the membrane. The larger flocs on the membrane surface are washed off by the retentate due to the tangential force (cross-flow) of the incoming solution, thus preventing membrane clogging. Flocculation can be used in combination with coagulation. Flocculation enhances the formation of larger flocs from particle aggregates generated by coagulation. In addition, flocculants induce floc formation from smaller particles that would not form particle clusters by coagulants.

6.1.2. Magnetic ion exchange

Magnetic ion exchange (MIEX) is a chemical process in which dissolved ions and charged species in water are adsorbed to polymer beads. Once they are saturated, the beads can be recovered and regenerated using a brine solution to desorb the charged species and ions. As a large percentage of the dissolved organic carbon (DOC) is polar, so it can be removed by MIEX, by exchanging chloride ions on the resin surface for polar dissolved and colloidal organic materials. Numerous studies have shown that ion exchange preferentially removes high charge density, medium-to-low molecular weight organic materials, which can consist of hydrophobic, transphilic and hydrophilic organic fractions. Ion exchange can therefore be synergistic with coagulation in reducing DOC loading entering the membrane unit, where coagulation removes the lower charge density, higher molecular weight hydrophobic fractions. A number of DOC removal methods were compared: alum coagulation (without pH

http://dx.doi.org/10.5772/52370

control), alum coagulation (with pH controlled at 6), ion exchange using MIEX resin, and combined treatment of alum coagulation and MIEX. The relative effectiveness of those pretreatment methods for DOC removal was ranked in the order: alum/ MIEX > MIEX > alum pH 6 > alum (no pH control) [51]. Also, it was found that MIEX could remove more NOM than coagulation process could, even at very high coagulant concentrations [52]. When it is used as a pretreatment step, up to 80% of NOM can be removed prior to UF. Moreover, combining coagulation with MIEX was found to be able to remove 90 % of trihalomethane and haloacetic acid precursors from water [53].

6.1.3 Micellar-Enhanced filtration

Micellar enhanced ultrafiltration is an emerging technique that it is used to improve the performance of a filtration process by adding a surfactant to the feed in order to promote the entrapment of foulants in the micelles formed by the surfactant. Surfactants are molecules that contain a hydrophobic tail (usually long chain hydrocarbon) and a hydrophilic head. Above a specific concentration, surfactant molecules come together to form clusters or micelles. This concentration is termed the critical micelle concentration (CMC) and differs depending on the type of surfactant.

There are numerous types of surfactants used in industry today, categorized by the charge of the hydrophilic portion of the molecule: anionic (negatively charged), cationic (positively charged), non anionic (neither positively nor negatively charged), and zwitterionic (both negatively and negatively charged). The formation of micelles increases the particle size, allowing the use of membranes with larger pore sizes for the same feed. Some surfactants also interfere with hydrophobic interactions between bacteria and membranes. In addition, surfactants can disrupt functions of bacterial cell walls. Therefore, they reduce fouling dominated by the biofilm formation. The choice of a surfactant is based on its compatibility with the solid for the solid recovery and reuse and its effect on the filtration system. A study has been conducted to compare the use of dodecylbenzesulfonic acid, as an anionic surfactant, and dodecylamine, as a cationic surfactant, to improve the removal of lead and arsenic from municipal wastewater [54]. It was concluded that while both surfactants enhanced separation of the heavy metals, the cationic surfactant was more effective than the anionic one. In another study, sodium dodecyl sulphate (SDS), as an anionic surfactant, and trimethylammonium bromide (CTAB), as cationic surfactant, were used to improve ultrafiltration of latex paint wastewater [55]. With SDS at twice its CMC, a reduction of 58% of permeate flux was observed. In contrast, using CTAB at twice its CMC, the permeate flux increased up to 134%. The effectiveness of surfactant also depends on the membrane material and its surface charge. One study indicated that for hydrophilic membranes, the permeate flux was reduced when ethoxylated alkyl phenol alcohol (Triton X-100), a non-ionic surfactant, was used above its CMC. However, for hydrophobic membranes, no significant flux reduction was observed with the same surfactant [56].

6.2. Membrane properties modification

Membrane properties affect the solute-membrane interaction and, consequently, the extent of adsorption and fouling. For filtration of proteins, since proteins adsorb more strongly to hydrophobic surfaces than hydrophilic ones, the use of hydrophilic membranes (cellulose esters, aliphatic polyamides) can help reducing membrane fouling. Chemical modification of a membrane (for example, sulfonation of polysulfone) or blending a hydrophobic polymer (polyetherimide, polyvinylidenefluoride) with a hydrophilic one (polyvinylpyrrolidone) can enhance the anti-fouling property of membranes. Another way to influence the solute-membrane interaction can be achieved by the pretreatment of the membrane with hydrophilic surfactants or enzymes. Conventional ultrafiltration membranes, such as: polysulfone, polyethersulfone or polyvinylidene fluoride, can be made more hydrophilic by surface modification using various methods [57, 58]:

- Plasma treatment of the membrane surface;
- Polymerization or grafting of the membrane surface initiated by UV, heat or chemicals;
- Interfacial polymerization;
- Introduction of polar or ionic groups to the membrane surface by reaction with bromine, fluorine, strong bases and strong acids.

Hydrophilization of the membrane surface also can be done by pre-coating the membrane with a nonionic surfactant. This method is very attractive for practical application because of it is simple. With this treatment, ultrafiltration of antifoam rejection was improved significantly, and hence, the permeate flux was almost doubled [59]. Alternatively, ozone can be used to modify the membrane surface and its hydrophobicity. This treatment introduces peroxide groups to the polymer surface, which can initiate graft polymerization of monomers with hydrophilic groups, and thus improves the hydrophilicity of the polymer surface. The concentration of peroxide groups formed can be used to determine the effectiveness of the ozonation process. The effect of ozonation on the permeate flux was studied using a polysulfone UF membrane. It was found that ozonation increased the permeate flux by 10%, and membrane surface oxidation by the mixture of ozone and hydrogen peroxide was even more effective. Ozone prolonged the period required to reach appreciable fouling rather than eliminated it [57]. The applied ozone dose and ozonation time determine the amount of peroxide groups generated and thus the degree of hydrophilicity enhancement of the membrane surface.

6.3. Membrane fouling cleaning

Membrane cleaning is an integral part of a membrane system operation and has a significant impact on the process operation. Fouling materials can be removed by hydraulic means such as backwashing or by chemical means such as enhanced backwash (EBW). Cleaning operation can be classified as cleaning in-place (CIP) or off-line chemical cleaning (or soaking). In CIP the membrane module is cleaned without removing it from the installation while in off-line cleaning the module is removed from the system and soaked in a chemical.

http://dx.doi.org/10.5772/52370

Backwashing is done by reversing the flow across the membrane, using the permeate to remove foulants accumulated on the membrane surface and/or clogged the membrane pores.

In EBW a cleaning chemical is added to the backwash water and the water is recirculated for a short period of time (10-15 min). Chemical cleaning is an integral part of a membrane process operation, which has a profound impact on the performance and economics of the process. Currently, types of cleaning chemicals used are recommended by membrane manufacturers. Some of them are proprietary cleaners while others are commercial chemicals. Chemical cleaning is required for the membrane to regain most of its permeability. Chemical cleaning is performed when flushing and/ or backwashing cannot restore the permeate flux. In chemical cleaning, the chemical dose is usual higher than that for the enhanced backwashing and the frequency of chemical cleaning is usual lower (approximately 1 per week). Moreover, the enhanced backwashing can be fully automated while the chemical cleaning involves manual labor due to its off-line operation. Proper selection of chemical cleaning agents, conditions for their application and understanding their performance are important. A cleaning agent is usually selected based on the types of foulants. The effectiveness of various operating strategies for different fouling types is summarized in Table 2. As indicated in Table 2, the chemical cleaning is an effective control strategy for a majority of membrane fouling types.

Type of Fouling	Effects of Operating Strategy			
	Hydraulic Cleaning / Backwashing	Feed Chlorination	Feed Acidification	Chemical Cleaning
Inorganic	-	-	++	++
Particulate	++	-	-	++
Microbial	+	++	+*	++
Organic	-	+	-	++

Notes: "-": No effect/ negative effects; "+": some positive affects; "++": positive effects; "*": together with feed chlorination.

Table 2. Effects of operating strategies on membrane fouling [14]

Calcium, magnesium and silica scaling, often a serious problem in reverse osmosis operation, is generally not a concern in ultrafiltration because these ions permeate through the membrane. Ultrafiltration of cheese whey, in which high calcium levels can lead to calcium scaling, is an exception. Because many feed waters contain small amount of soluble ferrous salts, hydrate iron oxide scaling is a problem. In ultrafiltration, these salts are oxidized to ferric iron by entrained air. Ferric iron is insoluble in water; hence, an insoluble iron hydroxide gel forms and accumulates on the membrane surface. Such deposits are usually removed with citric or hydrochloric acid wash. Chemicals commonly used for cleaning UF and MF membranes in water industry fall into five categories, as summarized in Table 3

Category	Major Functions	Typical Chemicals
Caustic	Hydrolysis, solubilisation	NaOH
Oxidants / disinfectants	Oxidation, disinfection	NaOCl, H_2O_2, peroxyacetic acid
Acids	Solubilization	Citric, nitric, hydrochloric acid
Chelating agents	Chelation	Citric acid, EDTA
Surfactants	Emulsifying, dispersion, surface conditioning	Surfactants, detergents

Table 3. Major categories of membrane cleaning chemicals [14]

Regardless of the membrane system used, chemical cleaning is cumbersome and requires shutdown of the unit. This results in a reduction of the overall plant capacity and produces a waste that may be difficult to dispose of. There are also concerns that repeated chemical cleaning might affect the membrane life. Chemical cleaning should thus be limited. Because membrane cleaning is essentially conducted through chemical reactions between cleaning chemicals and fouling materials, factors that affect the cleaning efficiency are concentration, temperature, length of the cleaning period and hydrodynamic conditions. The cleaning chemical concentration can affect both the equilibrium and the rate of the reaction. The cleaning chemical concentration plays a key role not only to maintain a reasonable reaction rate but also to overcome mass transfer barriers imposed by the fouling layer. In practice, the cleaning chemical concentration is usually high enough to ensure a desirable reaction rate. It is mass transfer, which dictates the limiting chemical concentration that is adequate for cleaning purpose.

Temperature can affect membrane cleaning by (1) changing the equilibrium of a chemical reaction, (2) changing the reaction kinetics, and (3) changing the solubility of fouling materials and/or reaction products during the cleaning. Generally, membrane cleaning is more efficient at elevated temperatures. However, compatibility of the membrane and other filter components regarding temperature should also be checked.

Membrane cleaning involves mass transfer of chemicals to the fouling layer and the reaction products back to the bulk liquid phase. Therefore, hydrodynamic conditions that promote contact between cleaning chemicals and fouling materials during cleaning are required. From a mass transfer point of view, dynamic cleaning involving circulating cleaning solutions through the system can be more effective than static cleaning such as soaking.

Moreover, mechanical cleaning can be used if chemical cleaning does not restore the permeate flux. Tubular membrane modules could be effectively cleaned by forcing sponge balls of a slightly larger diameter. The balls gently scrape the membrane surface, removing deposited materials. Sponge-ball cleaning is an effective but relatively time-consuming process, so it is performed rather infrequently.

http://dx.doi.org/10.5772/52370

7. Conclusion

Membrane fouling is a critical problem that reduces the permeate flux, requires periodic cleanings, and limits further membrane development due to the hindrance of wider application to various processes by fouling. Fouling is caused by the deposition of suspended or dissolved solids in the feed on the external membrane surface, on the membrane pores, or within the membrane pores. One of the two main factors, which has a significant effect on membrane fouling, is the membrane properties, such as: pore size and distribution, hydrophobicity and membrane material. Membranee fouling is a phenomenon involving the interaction between the membrane and the solution. Therefore, another important factor governing fouling is the solution properties, such as: concentration and nature of components and the particle size distribution. In addition, operational conditions such as pH, temperature, flow rate and pressure also greatly affect fouling.

Even though membrane fouling is inevitable during the filtration process, it can be controlled and alleviated. Current approaches to deal with membrane fouling include mathematical model prediction of membrane fouling and membrane fouling reduction using different techniques such as pre-treatment of the feed water, membrane modification, improving the operational conditions and cleaning. In order to determine the proper pre-treatment, a complete and accurate analysis of the feedwater should be made. In addition, the interaction of a particular membrane and a specific foulant needs be understood so that an appropriate method can be selected. Finally the fouling behaviour and autopsy protocol for membrane fouling can be concluded in four basic aspects: identification of fouling components, development of conceptual or phenomenological models for membrane fouling, establishment of mathematical models to describe or predict fouling, and development of fouling control strategies.

Nomenclature

Symbol	Unit	Physical Meaning
β	dimensionless	Ratio of membrane area influenced with the particles suspension to open area of the membrane pores
C_b	kg/m^3	Bulk concentration of large aggregates
J	m^3/m^2.s	Permeate flux at any time
J_0	m^3/m^2.s	Initial permeate flux
K_b	m^2/kg	Pore blockage parameter
m_d	kg/m^2	Mass of deposits accumulated on unit surface area of membranes
m_p	kg	Total mass of aggregates retained by the membrane
μ	Pa-s	Solution viscosity

Symbol	Unit	Physical Meaning
n	dimensionless	Number of particles per unit volume
ΔP	Pa	Transmembrane pressure (TMP)
r_p	m	Pore radius of membranes
R_c	m^{-1}	Hydrodynamic resistance of cake layers
$\hat{R}_c$	m/kg	Specific resistance of cake layer on the membrane surface
R_m	m^{-1}	Hydrodynamic resistance of clean membranes
t^*	dimensionless	Filtration time
V	cm^3	Permeate volume
δ'	m	Thickness of the adsorption layer
γ	dimensionless	Ratio of the pores area to the total membrane area
ε	dimensionless	Dielectric Constant

Author details

A. Abdelrasoul, H. Doan and A. Lohi

Department of Chemical Engineering, Ryerson University, Victoria Street, Toronto, Ontario, Canada

References

[1] Hong, S., & Elimelech, M. (1997). Chemical and physical aspects of natural organic matter (NOM) fouling of NF membranes. *Journal of Membrane Science*, 132, 159-181.

[2] Quintanilla, V. A. Y., (2005). Colloidal and non-colloidal NOM fouling of ultrafiltration membranes: analysis of membrane fouling and cleaning. M. Sc. Thesis, UNESCO-IHE.

[3] Lee, S., Cho, J. and Elimelech, M. (2005). Combined influence of natural organic matter (NOM) and colloidal particles on nanofiltration membrane fouling. *Journal of Membrane Science*, 262, 27-41.

[4] Schafer, A.I. (2001). Natural organic matter removal using membranes, Ph.D. Thesis, UNESCO-IHE, UNSW, Australia.

[5] Mo, L., & Huanga, X. (2003). Fouling characteristics and cleaning strategies in a coagulation micro filtration combination process for water purification. *Desalination*, 159, 1-9.

[6] Weisner, M. R., Clarke, M. M., Jacanglo, J.G., Lykins, B.W., Marinas, B. J., O'Mellia, C.R., Ritmann, B.E., and Semmens, M.J. (1992). Committee report: Membrane processes in portable water treatment. *Journal of the American Water Works Association*, 84(1), 59-67.

[7] Aoustin, E., Schafer, A.I., Fane, A. G. and Waite, T. D. (2001). Ultrafiltration of natural organic matter. *Separation and Purification Technology*, 22-23, 63-78.

[8] Makdissy, G., Croue , J.P., Buisson, H., Amy, G., and Legube, B. ,(2003). Organic matter fouling of ultrafiltration membranes. *Water Science and Technology Water Supply*, 3(5-6), 175-182.

[9] Jucker, C., & Clark, M. M. (1994). Adsorption of aquatic humic substances on hydrophobic ultrafiltration membranes. *Journal of Membrane Science*, 97, 37-52.

[10] Makdissy, G., Croue, J.P., Buisson, H., Amy, G., and Legube, B. (2003). Organic matter fouling of ultrafiltration membrane. *Water Science and Technology Water Supply*, 3(5-6), 175-182.

[11] Kimura, K., Hane,Y., Watanabe , Y., Amy, G., and Ohkuma, N. (2004). Irreversible membrane fouling during ultrafiltration of surface water. *Water Research Journal*, 38, 3431-3441

[12] Nilson, J., and Digiano, F. A. (1996). Influence of NOM composition on nanofiltration. *American Water Works Association*, 88, 53-66.

[13] Carroll, T., King, S., Gray, S.R., Bolto, B. A., and Booker, N.A., (2000). The fouling of microfiltration membranes by NOM after coagulation treatment. *Water Research Journal*, 34, 2861-2868

[14] Li, N.N., Fane, A.G., Winston, W. S. H., and Matsuura, T., (2008).Advanced membrane technology and applications, John Wiley& sons Inc.

[15] Belfort, G.R.H., & Zydney, A.L.,(1994). The behavior of suspensions and macromolecular solutions in crossflow microfiltration. *Journal of Membrane Science*, 96, 1-58.

[16] Javacek, M. H., & Bouchet, F. (1993) Constant flowrate blocking laws and an example of their application to dead-end microfiltration of protein solutions. *Journal of Membrane Science*, 82, 285-295.

[17] Hermia, J. (1982). Constant pressure blocking filtration laws, application to power-law non-Newtonian fluids. *Transactions of the American Institute of Chemical Engineers*, 60, 183-187.

[18] Granger, J., Leclerc, D., and Dodds, J.A. (1985). Filtration of dilute suspensions of latexes. *Filtration and Separation*, 22, 58-60.

[19] Kim, A.S., & Hoek, E.M.V. (2002).Cake structure in dead-end membrane filtration: Monte Carlo simulations. *Environmental Engineering Science*, 19(6), 373-386.

[20] Zhang, M. & Song, L. (2000) .Mechanisms and parameters affecting flux decline in cross-flow microfiltration and ultrafiltration of colloids. *Environmental Science & Technology*, 34(17), 3767-3773.

[21] Chellam, S., Jacangelo, J.G., and Bonacquisti, T.P. (1998). Modeling and experimental verification of pilot-scale hollow fiber, direct flow microfiltration with periodic backwashing. *Environmental Science & Technology*, 32(1), 75-81.

[22] Endo, Y., & Alonso, M., (2001). Physical meaning of specific cake resistance and effects of cake properties in compressible cake filtration. *Filtration and Separation*, (9), 43-46.

[23] Babel, S., Takizawa, S., and Ozaki, H., (2002) .Factors affecting seasonal variation of membrane filtration resistance caused by Chlorella algae. *Water Research*, 36(5), 1193-1202.

[24] Foley, G., (2006). A review of factors affecting filter cake properties in dead-end microfiltration of microbial suspensions. *Journal of Membrane Science*, 274, 38-46.

[25] Kosvintsev, S., Holdich, R.G., Cumming, I.W., and Starov, V.M., (2002). Modelling of dead-end microfiltration with pore blocking and cake formation. *Journal of Membrane Science*, 208, 181-192.

[26] Kosvintsev, S., Cumming, I.W., Holdich, R.G., Lloyd, D., and Starov, V.M., (2004). Mechanism of microfiltration separation colloids and surfaces. *Physicochemical and Engineering Aspects*, 230, 167-182.

[27] Yuan, W., Kocic, A., and Zydney, A.L., (2002) .Analysis of humic acid fouling during microfiltration using a pore blockage-cake filtration model. *Journal of Membrane Science*, 198(1), 51-62.

[28] Ho, C.C., & Zydney, A.L., (2002) .Transmembrane pressure profiles during constant flux microfiltration of bovine serum albumin. *Journal of Membrane Science*, 209(2), 363-377.

[29] Srebnik, S., (2003). Polymer adsorption on multi component surfaces with relevance to membrane fouling. *Chemical Engineering Science*, 58(23-24), 5291-5298.

[30] Israelachvili, J., (1992). Intermolecular & surface forces. 2nd ed., San Diego, CA 92101, USA: Academic Press Inc. 450.

[31] Dielectric Constants of Materials ,http://www.clippercontrols.com/info/dielectric_constants.html

[32] Refractive index , http://www.texloc.com/closet/cl_refractiveindex.html

[33] John Gregory (2005), Particles in Water: Properties and Processes,Chapter 4

[34] Carroll, T., Booker, N.A., and Meier-Haack, J., (2002). Polyelectrolyte-grafted microfiltration membranes to control fouling by natural organic matter in drinking water. *Journal of Membrane Science*, 203(1-2), 3-13.

[35] Taniguchi, M., Kilduff, J.E., and Belfort, G., (2003) Low fouling synthetic membranes by UV-assisted graft polymerization: monomer selection to mitigate fouling by natural organic matter. *Journal of Membrane Science*, 222, 59-70.

[36] Hester, J.F., & Mayes, A.M., (2002). Design and performance of foul-resistant poly (vinylidene fluoride) membranes prepared in a single-step by surface segregation. *Journal of Membrane Science*, 202(1-2), 119-135.

[37] Wavhal, D.S., & Fisher, E.R., (2003) Membrane surface modification by plasma induced polymerization of acrylamide for improved surface properties and reduced protein fouling. *Langmuir,* 19(1), 79-85.

[38] Liu, Z.M., Xu, Z.K., Wang, J.Q., Yang, Q., Wu, J., and Seta, P. , (2003).Surface modification of microporous polypropylene membranes by the grafting of poly(gamma-stearyl- L-glutamate). *European Polymer Journal*, 39(12), 2291-2299.

[39] Yu, H.Y., Xie, Y.J., Hu, M.X., Wang, J.L., Wang, S.Y., and Xu, Z.-K. , (2005). Surface modification of polypropylene microporous membranes to improve its antifouling property in MBR: CO_2 plasma treatment. *Journal of Membrane Science*,254(1-2), 219-227.

[40] Brant, J.A., & Childress, A.E., (2004).Colloidal adhesion to hydrophilic membrane surfaces. *Journal of Membrane Science*, 241(2), 235-248.

[41] Bowen, W.R., & Sharif, A.O., (2002). Prediction of optimum membrane design: pore entrance shape and surface potential. colloids and surfaces. *Physicochemical and Engineering Aspects*, 201, 207-217.

[42] Brant, J.A., Johnson, K.M., and Childress, A.E., (2006). Characterizing NF and RO membrane surface heterogeneity using chemical force microscopy. colloids and surfaces. *Physicochemical and Engineering Aspects*, 280(1-3), 45-57.

[43] Vyas, H.K., Bennett, R.J., and Marshall, A.D., (2000). Influence of feed properties on membrane fouling in crossflow microfiltration of particulate suspension. *International Dairy Journal,* 10 ,855-861

[44] Salahi, A., Abbasi, M., and Mohammedi, T., (2010). Permeate flux decline during UF of oily wastewater. *Desalination*, 251,153-160.

[45] Salahi, A., Mohammedi, T., Pour, A., Rekabdar, F., (2000). Oily wastewater treatment using ultrafiltration. *Desalination*, 6,289-298.

[46] Doyen, W., (2003). Latest developments in ultrafiltration for large-scale drinking water. *Desalination, 113*, 165-177.

[47] Kruithof, J. C., Nederlof, M. M., Hoffman, J. A. M. H., and Taylor, J. S., (2004). Integrated membrane systems. *Research Foundation and American Water Works Association*, Elbert, Colorado.

[48] Minegishi, S., Jang, N.Y., Watanabe, Y., Hirata, S., and Ozawa, G., (2001). Fouling mechanism of hollow fibre ultrafiltration membrane with pre-treatment by coagulation/sedimentation process. *Water Science and Technology Water Supply*, 1(4), 49-56.

[49] Abdessemed, D., & Nezzal, G., (2002). Treatment of primary effluent by coagulation-adsorption-ultrafiltrationn for reuse. *Desalination*, 152, 367-373.

[50] Berube, P. R., Mavinic, D. S., Hall, E. R., Kenway, S.E., and Roett, K., (2002). Evaluation of adsorption and coagulation as membrane pretreatment steps for the removal of organic material and disinfection by product precursors. *Journal of Environmental Engineering and Science*, 1, 465-476.

[51] Drikas, M., Christopher, W., Chow, K., and Cook, D., (2003). The impact of recalcitrant on disinfection stability, trihalomethane formation and bacterial regrowth: A magnetic ion exchange resin (MIEX) and alum coagulation. *Journal Water Supply Research*, 52(7), 475-487.

[52] Slunjski, M., Bourke, M., and O'Leary, B., (2000). MIEX DOC process for removal of humics in water treatment. In Proceeding of IHSS – Australian Branch Symposium: Humic Substances Science and Commercial Applications. Monash University, Melbourne, 22-27.

[53] Singer,P.C., & Bilyk,K. (2002). Enhanced coagulation using a magnetic ion exchange resin, *Water Research* 36, 4009–4022.

[54] Ferella,F., Prisciandaro, M., Michelis, I., and Veglio, F., (2007). Removal of heavy metals by surfactant-enhanced ultrafiltration from wastewaters. *Desilination*, 207, 125-133.

[55] Bedasie,R., (2010).An investigation into the fouling phenomena of polycarbonate membranes used in the treatment of latex paint wastewater. M. Sc. Thesis.

[56] Byhlin, H. A., & Jonsson, A. S., (2002). Influence of adsorption and concentration polarisation on membrane performance during ultrafiltration of a non-ionic surfactant. *Desalination*,151 , 21-31

[57] Park, Y. G., (2002). Effect of ozonation for reducing membrane fouling in the UF membrane. *Desalination*, 147, 43-48.

[58] Mulder, M.H.V., (1993). Membranes in Bioprocessing, theory and application. Chapman and Hall, London, P.13.

[59] Noble, R.D., & Stern, S. A., (1995). Membrane separation technology principles and applications, Elsevier Science B.V., 46-83.

Chapter 9

Filtration of Radioactive Solutions in Jointy Layers

Mikhaylov Pavel Nikonovich,
Filippov Alexander Ivanovich and
Mikhaylov Aleksey Pavlovich

Additional information is available at the end of the chapter

http://dx.doi.org/10.5772/56042

1. Introduction

The solution of global energy problems of mankind, first and foremost associated with the development of nuclear energy. Already by 2030 the share of nuclear power generation in total electricity production should be about 25-30% (today - 16%). Currently, the total amount of radioactive waste in Russia is estimated at 5 10^8 m^3, the total β-activity of which is estimated at 7.3 10^{19} Bq. At the same time on the liquid radioactive waste (LRW) accounts for about 85% of total activity, and their treatment and disposal become the most important task of nuclear energy.

One of the safest ways of disposal of waste of nuclear and chemical production is injection of them into deep-seated subterranean formations. Therefore, an important issue is to study the processes of the joint heat and mass transfer during the injection of waste into a porous collector layer to predict and control the state of the areas covered by the influence of radioactive impurities. The above forecast is carried out mainly by calculations, since the possibility of experimentally sizing of deep zones of contamination is very limited.

The processes of mass transfer in porous media have long been the object of study for many researchers. Have become classics of the G.I. Barenblatt [1], Bear J. [2, 3, 4], Bachmat Y. [5], A. A. Ilyushin [6], V. M. Keyes [7], L. D. Landau [8], R. I. Nigmatullin [9], V. N. Nikolayevsky [10, 11], L. I. Sedov [12]. In the works of Prakash A. [13], A. A. Barmin [14], E. A. Bondarev [15], M. L. Zhemzhurov [16, 17], E. V. Venetsianov, R. N. Rubinstein [18] the problems of the filtration of solutions, taking into account the phenomenon of adsorption, are regarded. Fluid flow through porous materials [19-24] are coincided to be well studied. Study of models of multi-component flows is devoted to the work of R. E. Swing [25].

Problems of disposal of radioactive waste in geological formations and the resulting ecological problems discussed in works of A. S. Belitsky, E. Orlova [26], A. Rybalchenko, M. K. Pimenov [27]. Modeling of temperature and radiation fields examined in works of D. M. Noskov, A. D. Istomin, A. G. Kessler, A. Zhiganov [28-29] (Seversk Technological Institute), I. Kosareva, and E. V. Zakharova [30-31] (Institute of Physical Chemistry RAS), and other researchers. In the works of A. Lehova, Y. Shvarova studied the rate of radionuclides in groundwater, the behavior of radioactive waste in the earth's crust after the injection. At the same time remain relevant problem of determining the concentration dependence of the fields on the parameters of injection of radioactive impurities, injection technology on the parameters of layers, etc.

The study of filtration processes in multilayer formations, as well as any thermodynamic problems of contacts of the bodies and environments, leads to the necessity of solving the problems of conjugation. To solve these problems are widely used numerical methods. The analytical solutions are constructed only for simple cases, such as linear flow in mass-isolated formation [32, 33]. And as the disposal at the request of the IAEA carried out on the timing of the order of tens thousand years, in these circumstances, the porous layer, can hardly be considered mass-isolated.

In this paper, in example of study of the filtration process of radioactive solutions, represented a modification of the asymptotic method, allowing successfully construct approximated solutions to conjugacy problems.

2. The mathematical formulation of the problem of heat and mass transfer in fluid flow with radioactive contaminant in the deep layers

Let us consider problem of heat and mass transfer, which describe the interrelated fields of concentration and temperature of the radioactive contaminant in the porous layer, through which flows a liquid with impurities, and the covering and the underlying layers are water-proof.

Typically, in deep horizons an aqueous solution is injected. This solution consist of a different soluble chemical compounds formed during the acid treatment process of structural elements of reactors and other parts of the design (process waste), or in the decontamination of buildings, cars, clothing and so on (non-technological waste) and includes a mixture of various radioactive nuclides [34]. Quite naturally the initial density of the solution divided into two factions

$$\rho_{tot} = \sum_{k=0}^{Nch} \rho_k + \sum_{i=1}^{Nrc} \rho_i, \tag{1}$$

where ρ_k is the density of the dissolved non-radioactive components (for $k = 0$, we obtain the density of the solvent) ρ_i is the concentration of radioactive i-th nuclide, N_{ch}, N_{rc} - the number of different non-radioactive and radioactive components in the solution, respectively.

http://dx.doi.org/10.5772/56042

Consider an arbitrary reaction volume dV in a porous layer containing a multi-component mixture (1). Mass flow passing through the surface of dS reaction volume dV can be represented as the sum of four terms

$$\frac{\partial}{\partial \tau}\int \rho_j dV = \int_S \vec{j}_j \vec{n} dS + \Delta_j^{ch} + \Delta_j^{reac} + \Delta_j^{ex}, \tag{2}$$

where the first term takes into account the mass exchange with the environment through the diffusion and convection currents, the second term describes the rate of change of mass in chemical reactions, the third term takes into account the change in mass due to radioactive decay of radionuclides and the fourth term describes the mass transfer processes between the components of the solution and formation.

Denote by p the number of chemical reactions involving a j-component, and ω_i is the reaction rate per unit reactor volume, while the second term on the right side of (2) can be written as

$$\Delta_j^{ch} = \sum_{i=1}^{p} k_{ji} \int \omega_i dV, \tag{3}$$

where k_{ji} - the stoichiometric coefficients of chemical reactions of j-component.

The third term can be represented as

$$\Delta_j^{reac} = -\delta \int (\alpha \rho)_j dV, \tag{4}$$

where α_j - the radioactive decay constant of j -th radionuclide, δ - Kronecker delta function, equal to either one if the of j-component of the radionuclide, or zero if otherwise.

We assume that the transition of the impurity molecules of the liquid in the skeleton and its transition from a skeleton into a liquid are determined by the chemical potentials μ_s, μ_w. The fourth term is of the form

$$\Delta_j^{ex} = \int g(\mu_w, \mu_s) dV - \int g(\mu_j, \mu_s) dV, \tag{5}$$

where $g(\mu_j, \mu_s)$ - a function of mass transfer between the of j-component of the solution and the skeleton of rock, $g(\mu_w, \mu_s)$ - mass transfer function corresponding to the transition of matter from the rock matrix in the solution.

Substituting (3) - (5) into (2) and transforming the surface integral into a volume integral, we obtain

$$\frac{\partial}{\partial \tau}\int \rho_j dV = -\int \mathrm{div}\left(\vec{j}_j\right)dV + \sum_{i=1}^{p} k_{ji}\int \omega_i dV - \delta\int\left(\alpha\rho\right)_j dV + \int g\left(\mu_w,\mu_s\right)dV - \int g\left(\mu_j,\mu_s\right)dV\ . \tag{6}$$

By the arbitrariness of the reaction volume dV and the continuity of the functions under the integral, we obtain

$$\frac{\partial \rho_j}{\partial \tau} = -\mathrm{div}\left(\vec{j}_j\right) + \sum_{i=1}^{p} k_{ji}\omega_i - \delta\left(\alpha\rho\right)_j + g\left(\mu_w,\mu_s\right) - g\left(\mu_j,\mu_s\right). \tag{7}$$

The resulting equation is nonlinear, even in simple cases the values ω_i are polynomial functions of concentration. Therefore, in general, equation (7) forms a system of nonlinear partial differential equations. The solution of this system is quite complicated both mathematically, and in terms of its applicability to the description of particular phenomena.

Let us estimate in (7) the contribution of the second term. Obviously, the maximum change of mass in chemical reactions, while other things being equal, will be observed in the following two cases:

$A + B \rightarrow C\uparrow$ (evaporation),
$A + B \rightarrow C\downarrow$ (precipitation).

In both reactions the dissolved substances are excluded from consideration, which entails a decrease in the concentrations of the components of the solution. But this type of unpredictable chemical reactions creates the conditions for dangerous situations and in the deep burial of radioactive waste should be excluded. The chemical reaction scheme (acid-base and redox)

$$A + B + \ldots \rightarrow A' + B' + \ldots\left(\pm\Delta H^0\right). \tag{8}$$

are valid and give a slight variation in the concentration of the solution, because typical of enthalpy ΔH^0 change is of the order of several hundred kilojoules per mole of interacting substances and the corresponding change in mass $10^{-7} \div 10^{-12}$ kg, which is negligible in comparison with the mass of dissolved chemical components. Therefore, the change in mass due to chemical reactions will be neglected.

As shown in [35], the time of mass transfer between the fluid and the skeleton of the order of 0.1 s. Thus, the mass transfer, which is characterized by a concentration gradient, is almost instantaneous compared to the time of injection of pollutant that may be from several months to several years. Let us also neglect the processes of chemical compounds leaching from the porous rock to the solution, i.e. assume the condition $g(\mu_w,\mu_s) - g(\mu_j,\ \mu_s) \approx 0$.

Based on the above, equation (7) takes the form

http://dx.doi.org/10.5772/56042

$$\frac{\partial \rho_j}{\partial \tau} = -\mathrm{div}\left(\vec{j}_j\right) - \delta\left(\alpha\rho\right)_j. \tag{9}$$

Divide the resulting equation into two components: non-radioactive and radioactive fractions

$$\frac{\partial \rho_k}{\partial \tau} + \mathrm{div}\left(\vec{j}_k\right) = 0,\ \frac{\partial \rho_i}{\partial \tau} + \mathrm{div}\left(\vec{j}_i\right) = -\left(\alpha\rho\right)_i, \tag{10}$$

where the index k takes values $\overline{1,\ N_{ch}}$, and the index i takes value $\overline{1,\ N_{rc}}$.

Because of the neglected mass changes in the course of chemical reactions and mass transfer processes in the equilibrium case, it follows that the concentration of impurities non-radioactive fraction with high accuracy can be taken as constant, i. e. ρ_k=const. Then the system of equations (10) can be written as

$$\mathrm{div}\left(\vec{w}\right) = 0, \frac{\partial \rho_i}{\partial \tau} + \mathrm{div}\left(\vec{j}_i\right) = -\left(\alpha\rho\right)_i, \tag{11}$$

where - a vector velocity of the fluid.

Write out the flow $\vec{j}_i$ as the sum of two terms $\vec{j}_i = \vec{j}_{Di} + \rho_i\vec{v}$, where $\vec{j}_{Di}$ - the diffusion flux, $\rho_i\vec{w}$- the convective flow, and, taking into account the first equation (11), the second equation takes form

$$\frac{\partial \rho_i}{\partial \tau} + \mathrm{div}\left(\vec{j}_{Di}\right) + \vec{w}\cdot\nabla\rho_i = -\left(\alpha\rho\right)_i. \tag{12}$$

According to the Onsager linear theory, the flow for a multicomponent mixture can be written as follows

$$\vec{j}_{Di} = -\frac{L_{ij}}{T}\sum_k\left(\frac{\partial \mu_j}{\partial \rho_k}\right)\nabla\rho_k, \tag{13}$$

where L_{ij} - the Onsager kinetic coefficients, μ_j - the chemical potential of j-th radionuclide.

The real radioactive solutions, arriving at the burial in a deep-seated formations, depending on the half-life have a total volumetric activity of about 10^{-6} ~10^{1} Ci/l. Let us estimate the mass of radionuclides in solution. Strontium-90 from the volumetric activity 1 Ci/l has a mass of about 7.57 10^{-6} kg, and Ruthenium-106 is the same volumetric activity of the mass of the order of 0.3 10^{-6} kg. These estimates of the mass of radionuclides provide a basis for considering

solution under investigation to be a very dilute solution (with respect to radionuclide fractions). Therefore, the correlation between the diffusion fluxes of components j and k will be negligible.

Thus, the assumption of a very dilute solution leads to the following representation of (13)

$$\vec{j}_{Di} = -\frac{L_{ii}}{T}\left(\frac{\partial \mu_i}{\partial \rho_i}\right)\nabla \rho_i, \tag{14}$$

Introducing the notation $D_{ii} = \frac{L_{ii}}{T}\left(\frac{\partial \mu_i}{\partial \rho_i}\right)$, we obtain

$$\vec{j}_{Di} = -D_{ii}\nabla \rho_i. \tag{15}$$

Relation (15) is known as Fick's first law, where D_{ii} is the diffusion coefficient of *i*-th - radionuclide.

In many cases, the diffusion coefficient D_{ii} can be considered to be constant, then using (15) in equation (12), we obtain a system of equations for evolution of radionuclides in a porous layer

$$\frac{\partial \rho_i}{\partial \tau} - D_{ii}\Delta \rho_i + \vec{w}\cdot\nabla \rho_i = -\left(\alpha \rho\right)_i. \tag{16}$$

Equation (16) is written for the porous layer, but it does not take into account the presence of porosity and sorption of radionuclides in the skeleton of the formation. To account for these effects, we introduce an auxiliary space-time function $m = m(t, x, y, z)$, such that $\int m(t, x, y, z)dV = V_{por}$, where V_{por} - the volume of pore space. Obviously, the $V_s = V - V_{por}$ - the volume occupied by the formation. Integrating each term of the of equation (16) by volume

$$\int \frac{\partial \rho_i}{\partial \tau}dV - D_{ii}\int \Delta \rho_i dV + \vec{w}\cdot\int \nabla \rho_i dV = -\int \left(\alpha \rho\right)_i dV. \tag{17}$$

Under the integral expression $\rho_i dV$ can be represented as the sum of two terms as $\rho_i dV = \rho_{is} dV_s + \rho_{iw} dV_{por}$, because the other terms, taking into account the mass transfer between the solution and the formation, give a zero contribution due to the steady equilibrium. Therefore

http://dx.doi.org/10.5772/56042

$$\int \frac{\partial \rho_{is}}{\partial \tau} dV_s + \int \frac{\partial \rho_{iw}}{\partial \tau} dV_{por} - D_{is}^i \int \Delta \rho_{is} dV_s - D_{iw}^i \int \Delta \rho_{iw} dV_{por} + \vec{w} \cdot \int \nabla \rho_{iw} dV_{por} = \\ = -\int \left(\alpha \rho_s\right)_i dV_s - \int \left(\alpha \rho_w\right)_i dV_{por}. \tag{18}$$

Using the definition of an auxiliary function m, it is easy to obtain the following obvious relations

$$dV_{por} = m dV, dV_s = \left(1-m\right) dV. \tag{19}$$

Substituting (19) in equation (18), we obtain

$$\int (1-m) \frac{\partial \rho_{is}}{\partial \tau} dV + \int m \frac{\partial \rho_{iw}}{\partial \tau} dV - D_{is}^i \int (1-m) \Delta \rho_{is} dV - D_{iw}^i \int m \Delta \rho_{iw} dV + \\ + \vec{w} \cdot \int m \nabla \rho_i dV = -\int (1-m) \left(\alpha \rho_s\right)_i dV - \int m \left(\alpha \rho_w\right)_i dV. \tag{20}$$

Again, because of the arbitrary choice of the reaction volume dV and continuity of integrand functions, we obtain

$$(1-m) \frac{\partial \rho_{is}}{\partial \tau} + m \frac{\partial \rho_{iw}}{\partial \tau} - D_{is}^i (1-m) \Delta \rho_{is} - D_{iw}^i m \Delta \rho_{iw} + \vec{w} \cdot m \nabla \rho_{iw} = -(1-m) \left(\alpha \rho_s\right)_i - m \left(\alpha \rho_w\right)_i. \tag{21}$$

We assume that the dependence of the impurity concentration in the skeleton of its concentration in the fluid is linear (Henry's isotherm) and does not depend on the volume activity, that is a good approximation for relatively small concentrations of fraction of radionuclide

$$\rho_{is} = K_{i\Gamma}^i \rho_{i\mathrm{w}}. \tag{22}$$

Then the mass transfer equations take the form:

$$\left[\left(1-m\right) K_{i\Gamma}^i + m\right] \frac{\partial \rho_{iw}}{\partial \tau} - \left[D_{is}^i \left(1-m\right) K_{i\Gamma}^i + m D_{iw}^i\right] \Delta \rho_{iw} + \vec{w} \cdot m \nabla \rho_{iw} = \\ - \left[\left(1-m\right) K_{i\Gamma}^i + m\right] \left(\alpha \rho_w\right)_i, \tag{23}$$

where the function m- void factor, depending on lithological and mineral composition of the layer, $K_{i\Gamma}^i$ - the Henry's coefficient of i-th - radionuclide.

The final form of the equations of evolution of radionuclides in solution (liquid phase) in a porous layer, taking into account the porosity and adsorption on the skeleton, one can divide both sides of equation (23) by a factor $\left((1-m)K_{iT}^{i}+m\right)$

$$\frac{\partial \rho_{i\,\mathrm{w}}}{\partial \tau}-D_{ii}\Delta\rho_{i\,\mathrm{w}}+\vec{\mathrm{v}}'_{ii}\cdot\nabla\rho_{i\,\mathrm{w}}=-\left(\alpha\,\rho_{\mathrm{w}}\right)_{i}, \tag{24}$$

here $D_{ii}=\left(D_{is}^{i}(1-m)K_{iT}^{i}+m\,D_{iw}^{i}\right)/\left((1-m)K_{iT}^{i}+m\right)$ - the effective diffusion coefficient in the layer, $\vec{v}'_{ii}=m\vec{w}/\left((1-m)K_{iT}^{i}+m\right)$ - modified velocity of propagation of *i*-th - radionuclide in a porous layer, (the rate of convective transport of radioactive contaminants).

Note that equation (24) is derived for the case when a radionuclide decaying, forms a non-radioactive nuclide. Possible decay scheme

$A\rightarrow B\rightarrow C\,(stable)$,

i. e. when the decay product B will also be radioactive. The equation takes into account the formation of a child radionuclide

$$\frac{\partial \rho_{\mathrm{w}}^{c}}{\partial \tau}-D\Delta\rho_{\mathrm{w}}^{c}+\vec{\mathrm{v}}'\cdot\nabla\rho_{\mathrm{w}}^{c}=\alpha\,\rho_{\mathrm{w}}-\alpha^{c}\rho_{\mathrm{w}}^{c}, \tag{25}$$

where ρ_{w}^{c} - density of the child radionuclide, ρ_{w} - density of the parent radionuclide. Investigations of these cases [36], [37] in the work are not included.

The rate of filtration of snap motion of the liquid phases is determined by Darcy's law

$$\vec{v}=-\frac{k}{\mu}\mathrm{grad}\,P.$$

In most common filtration processes, the deformation of the porous skeleton, compressibility, and associated with this changes in the temperature of liquids are small. The main effects that determine the motion of the system are the non-equlibrium joint motion of several liquid phases, molecular and convective diffusion of solute in the phases of the components, the absorption of the solid phase or sorption of the components, mass transfer between phases.

Thus, the system of equations describing the mass transfer during injection of liquid radioactive wastes in deep porous horizon is as follows:

$$\begin{aligned}
&\mathrm{div}\left(\vec{\mathrm{w}}\right)=0,\\
&\frac{\partial \rho_{i\,\mathrm{w}}}{\partial \tau}-D_{i}\Delta\rho_{i\,\mathrm{w}}+\vec{\mathrm{v}}'_{i}\cdot\nabla\rho_{i\,\mathrm{w}}=-\alpha_{i}\,\rho_{i\,\mathrm{w}},\\
&\frac{\partial \rho_{\mathrm{w}}^{\tilde{n}}}{\partial \tau}-D\Delta\rho_{\mathrm{w}}^{\tilde{n}}+\vec{\mathrm{v}}'\cdot\nabla\rho_{\mathrm{w}}^{\tilde{n}}=\alpha\,\rho_{\mathrm{w}}-\alpha^{\tilde{n}}\rho_{\mathrm{w}}^{\tilde{n}}.
\end{aligned} \tag{26}$$

http://dx.doi.org/10.5772/56042

For a complete statement of the problem requires knowledge of the radiochemical composition of the solution, flow rate of the injection, diffusion parameters and the geometry of the simulated porous layer. Note that if the injection rate is known, it is easy to determine the rate of filtration. Then integrating Darcy's equation, we can describe the pressure field in the formation.

The problem under consideration has cylindrical symmetry about the axis of the well, through which the liquid wastes are ejected; it is convenient to represent the system of equations (26) in a cylindrical coordinate system.

Writing the first equation (26) in a cylindrical coordinate system and, given that the liquid is distributed in the porous layer only in the radial direction, we obtain the equation for the velocity field:

$$\frac{\partial(r\mathrm{w}_r)}{\partial r_\mathrm{d}}=0,$$

solving this equation and applying the obvious boundary condition $\mathrm{w}_r \mid_{r=r_0}=\mathrm{w}_0$, where w_0 - velocity of the fluid from the cased hole in the porous layer, we have

$$\mathrm{w}_r = \mathrm{w}_0 r_0 / r_\mathrm{d}. \tag{27}$$

Then the remaining equations of (26) using (27), and the anisotropy of diffusion coefficients and thermal conductivity in the directions r and z in a cylindrical coordinate system can be written as

$$\begin{aligned}
&\frac{\partial \rho_{i\mathrm{w}}}{\partial \tau}+\frac{\mathrm{v}_0' r_0}{r_\mathrm{d}}\frac{\partial \rho_{i\mathrm{w}}}{\partial r_\mathrm{d}}-D_{ri}\frac{1}{r_\mathrm{d}}\frac{\partial}{\partial r_\mathrm{d}}\left(r_\mathrm{d}\frac{\partial \rho_{i\mathrm{w}}}{\partial r_d}\right)-D_{zi}\frac{\partial^2 \rho_{i\mathrm{w}}}{\partial {z_\mathrm{d}}^2}=-\alpha_i \rho_{i\mathrm{w}},\\
&\frac{\partial \rho_{\mathrm{w}}^{\tilde{n}}}{\partial \tau}+\frac{\mathrm{v}_0' r_0}{r_\mathrm{d}}\frac{\partial \rho_{w}^{\tilde{n}}}{\partial r_F}-D_r\frac{1}{r_\mathrm{d}}\frac{\partial}{\partial r_\mathrm{d}}\left(r_\mathrm{d}\frac{\partial \rho_{\mathrm{w}}^{c}}{\partial r_\mathrm{d}}\right)-D_z\frac{\partial^2 \rho_{\mathrm{w}}^{c}}{\partial {z_\mathrm{d}}^2}=\alpha\rho_{\mathrm{w}}-\alpha\rho_{\mathrm{w}}^{c},
\end{aligned} \tag{28}$$

where $\mathrm{v}_0=m\mathrm{w}_0$ - the rate of fluid filtration, D_{ri}, D_{zi} - an effective diffusion coefficient in the direction r_d and z_d, respectively, and the multiplier $\gamma_i=[(1-m)K_{i\Gamma}+m]$.

It is assumed that the real porous layer is represented by a multiphase system, where each phase consists of a sufficiently large number of randomly distributed small particles. Particle size, small in comparison with the basic physical quantities are assumed to be so large that within each particle condition of "local equilibrium" [38] and all the conservation laws are satisfied [9]. All contact surfaces of particles of different nature are surfaces of discontinuity of some physical fields. However, the above assumptions allow us in physically small volumes to define the space of continuous functions, carrying out the description of the fields of each phase. This determination is carried out by a predetermined method of averaging, from which, in general, depend on the results obtained in [9]. As with most occurring filtration processes,

the deformation of the porous skeleton, compressibility and associated changes in temperature fluids rely small.

Given that the determining factor in the process of mass transfer is the concentration of the parent nuclide, confine ourselves to the problem for a single pollutant, which is radioactive and chemically active. The first equation (28) is represented as

$$\frac{\partial \rho_{\mathrm{w}}}{\partial \tau}+\frac{\vec{\mathrm{v}}\nabla \rho_{\mathrm{w}}}{\left(1-m\right)K_{\Gamma}+m}-D\Delta \rho_{\mathrm{w}}=-\alpha\,\rho_{\mathrm{w}}. \tag{29}$$

Here we have introduced the notation

$$D=\frac{D_s(1-m)K_{\mathrm{r}}+D_w m}{(1-m)K_{\mathrm{r}}+m} \tag{30}$$

D is the effective diffusion coefficient in the layer. From (29) that in the equation describing the migration of contaminants, it is necessary to take into account the convective transport of pollutants, "complicated by" the presence of porosity in the skeleton and mass transfer processes occurring between the pollutant and the skeleton. Equation (29) to determine the rate of convective transport of pollutants in porous layer $\vec{v}'$, by analogy with the rate of convective heat transfer and flow rate $\vec{v}$

$$\vec{\mathrm{v}}'=\frac{\vec{\mathrm{v}}}{\left(1-m\right)K_{\Gamma}+m}. \tag{31}$$

The rate of convective transport of the impurity $\vec{v}'$ determines the position of the front of pollution R_{d}, just as the filtration rate $\vec{v}$ determines the position of the front of injected fluid R_{w}. The position of the injected fluid front is determined from the mass balance of the injected fluid and, for the case of injection at a constant speed v_0 into the layer through a cased hole of radius r_0, the corresponding expression is given by

$$R_{\mathrm{w}}=\sqrt{\frac{2\mathrm{v}_0 r_0\tau}{m}+r_0^2}=\sqrt{2\,\mathrm{w}_0 r_0\tau+r_0^2}=\sqrt{\frac{Q\tau}{\pi m H}+r_0^2}. \tag{32}$$

3. The mathematical formulation of the problem of mass transfer

Fig. 1 shows the geometry of the problem in a cylindrical coordinate system whose axis coincides with the axis of the borehole. The environment is presented by three areas with flat boundaries. Injection of impurities into the area is out of the hole radius, covering and

http://dx.doi.org/10.5772/56042

underlying layers are impermeable, middle area is a the porous region, all layers are considered homogeneous and anisotropic on the diffusion properties. Observation is carried out at a distance from the axis of the borehole

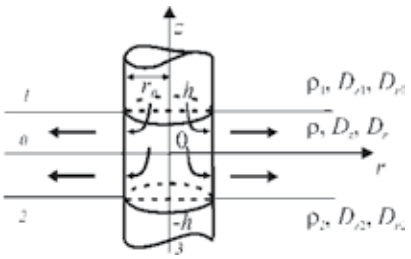

Figure 1. The geometry of the problem: *0, 1, 2* - porous, covering and underlying layers, respectively, *3* – borehole

Through a hole of small (compared to the distance to the observation point) radius r_0 in an infinite horizontal layer of thickness $-h < z_d < h$ water with a radioactive contaminant are injected. In arriving liquid at $r \le r_0$ the concentration of impurities kept constant and equal to ρ_0. The concentration of pollutants in the layer changes due to convective transport along the direction r, the diffusion along r, z and the concentration of sources. As such sources of radioactive decay of pollutant are considered. Field of densities during the filtration of radioactive solutions was investigated in [36, 39-50].

The mathematical formulation of the problem of mass transfer for all areas involves the diffusion equation with taking into account the radioactive decay in the covering

$$\frac{\partial \rho_{1d}}{\partial \tau} - D_{z1}\frac{\partial^2 \rho_{1d}}{\partial z_d^2} - D_{r1}\frac{1}{r_d}\frac{\partial}{\partial r_d}\left(r_d \frac{\partial \rho_{1d}}{\partial r_d}\right) = -\alpha \rho_{1d}, \ \tau > 0, \ r_d > 0, \ z_d > h \tag{33}$$

and the underlying

$$\frac{\partial \rho_{2d}}{\partial \tau} - D_{z2}\frac{\partial^2 \rho_{2d}}{\partial z_d^2} - D_{r2}\frac{1}{r_d}\frac{\partial}{\partial r_d}\left(r_d \frac{\partial \rho_{2d}}{\partial r_d}\right) = -\alpha \rho_{2d}, \ \tau > 0, \ r_d > 0, \ z_d < -h \tag{34}$$

layers, as well as the equation of convective diffusion, taking into account the radioactive decay in the porous layer

$$\frac{\partial \rho_d}{\partial \tau} - D_z\frac{\partial^2 \rho_d}{\partial z_d^2} - D_r\frac{1}{r_d}\frac{\partial}{\partial r_d}\left(r_d \frac{\partial \rho_d}{\partial r_d}\right) + \frac{v_0' r_0}{r_d}\frac{\partial \rho_d}{\partial r_d} = -\alpha \rho_d, \ \tau > 0, \ r_d > 0, \ |z_d| < h. \tag{35}$$

The conditions of conjugation represent the equality of densities and fluxes of dissolved substances at the interface of the layers

$$\rho_{\mathrm{d}}\big|_{z_{\mathrm{d}}=h}=\rho_{\mathrm{d}1}\big|_{z_{\mathrm{d}}=h},\ \rho_{\mathrm{d}}\big|_{z_{\mathrm{d}}=-h}=\rho_{\mathrm{d}2}\big|_{z_{\mathrm{d}}=-h}, \tag{36}$$

$$D_z\frac{\partial\rho_{\mathrm{d}}}{\partial z_{\mathrm{d}}}\bigg|_{z_{\mathrm{d}}=h}=D_{z1}\frac{\partial\rho_{1\mathrm{d}}}{\partial z_{\mathrm{d}}}\bigg|_{z_{\mathrm{d}}=h},\ D_z\frac{\partial\rho_{\mathrm{d}}}{\partial z_{\mathrm{d}}}\bigg|_{z_{\mathrm{d}}=-h}=D_{z2}\frac{\partial\rho_{2\mathrm{d}}}{\partial z_{\mathrm{d}}}\bigg|_{z_{\mathrm{d}}=-h}. \tag{37}$$

The density of pollutant at the entrance of porous layer assumed to be constant

$$\rho_{\mathrm{d}}\big|_{r_{\mathrm{d}}=0}=\left[m+K\left(1-m\right)\right]\rho_0. \tag{38}$$

Assuming that at the initial time the density of the of pollutant is equal to zero

$$\rho_{\mathrm{d}}\big|_{\tau=0}=\rho_{1\mathrm{d}}\big|_{\tau=0}=\rho_{2\mathrm{d}}\big|_{\tau=0}=0. \tag{39}$$

In addition, at infinity the conditions of regularity

$$\rho_{\mathrm{d}}\big|_{r_{\mathrm{d}}\to+\infty}=0,\ \rho_{1\mathrm{d}}\big|_{r_{\mathrm{d}}+z_{\mathrm{d}}\to+\infty}=0,\ \rho_{2\mathrm{d}}\big|_{r_{\mathrm{d}}+|z_{\mathrm{d}}|\to+\infty}=0. \tag{40}$$

Let us turn then to the dimensionless quantities

$$\rho=\frac{\rho_d}{\rho_0},\quad r=\frac{r_d}{h},\quad z=\frac{z_d}{h},\quad t=\frac{\lambda_{z1}\tau}{c_1\rho_{n1}h^2},\quad \mathrm{At}=\frac{c_1\rho_{n1}}{\lambda_{z1}}\alpha h^2,\quad {}_1^2D=\frac{D_{z2}}{D_{z1}},$$

$${}_1^0D=\frac{D_z}{D_{z1}},\quad {}_2^0D=\frac{D_z}{D_{z2}},\ a_{z1}=\frac{\lambda_{z1}}{c_1\rho_{n1}},\quad \gamma=\frac{1}{m+K(1-m)}.$$

We also introduce the analogue of the Péclet number

$$\mathrm{Pd}=v_0'r_0/D_{z1},$$

where v_0' is the rate of convective transport of the pollutant at a distance r_0 from the axis of the borehole. With this notation equations (33) - (40) take the form

$$\frac{\partial\rho_1}{\partial t}-\frac{\partial^2\rho_1}{\partial z^2}-\frac{D_{r1}}{D_{z1}}\frac{1}{r}\frac{\partial}{\partial r}\left(r\frac{\partial\rho_1}{\partial r}\right)=-\mathrm{At}\ \rho_1,\quad t>0,\quad r>0,\quad z>1, \tag{41}$$

http://dx.doi.org/10.5772/56042

$$\frac{\partial \rho_2}{\partial t} - {}_1^2D\frac{\partial^2 \rho_2}{\partial z^2} - \frac{D_{r2}}{D_{z1}}\frac{1}{r}\frac{\partial}{\partial r}\left(r\frac{\partial \rho_2}{\partial r}\right) = -\mathrm{At}\ \rho_2,\ \ t>0,\quad r>0,\quad z<-1, \tag{42}$$

$$\frac{\partial \rho}{\partial t} - {}_1^0D\frac{\partial^2 \rho}{\partial z^2} - \frac{D_r}{D_{z1}}\frac{1}{r}\frac{\partial}{\partial r}\left(r\frac{\partial \rho}{\partial r}\right) + \frac{\mathrm{Pd}}{r}\frac{\partial \rho}{\partial r} = -\mathrm{At}\ \rho,\ t>0, r>0, |z|<1. \tag{43}$$

Let us estimate the ratio of the third and fourth terms in equation (43)

$$\frac{\frac{D_r}{D_{z1}}\frac{1}{r}\frac{\partial}{\partial r}\left(r\frac{\partial \rho}{\partial r}\right)}{\frac{\mathrm{Pd}}{r}\frac{\partial \rho}{\partial r}} \approx \frac{D_r\frac{\rho_0}{R^2}}{D_{z1}\mathrm{Pd}\frac{\rho_0}{R^2}} = \frac{D_r}{D_{z1}\mathrm{Pd}} \approx \frac{1}{\mathrm{Pd}} << 1,$$

Boundary, initial conditions and conjugation conditions are not changed

$$\rho\big|_{t=0} = \rho_1\big|_{t=0} = \rho_2\big|_{t=0} = 0\ , \tag{44}$$

$$\rho\big|_{r=0} = 1/\gamma,\quad \rho\big|_{z=1} = \rho_1\big|_{z=1},\quad \rho\big|_{z=-1} = \rho_2\big|_{z=-1}\ , \tag{45}$$

$$\left.\frac{\partial \rho}{\partial z}\right|_{z=1} = {}_0^1D\left.\frac{\partial \rho_1}{\partial z}\right|_{z=1},\quad \left.\frac{\partial \rho}{\partial z}\right|_{z=-1} = {}_0^2D\left.\frac{\partial \rho_2}{\partial z}\right|_{z=-1}\ , \tag{46}$$

$$\rho\big|_{r\to\infty} = 0,\quad \rho_1\big|_{r+z\to\infty} = 0,\quad \rho_2\big|_{r+|z|\to\infty} = 0\ . \tag{47}$$

The system of equations (44) - (50) defines a mathematical formulation of the problem of mass transfer.

4. Expansion of the solution to the problem of mass transfer on the asymptotic parameter

Let us consider the more general problem, which is obtained by introducing into the equations and boundary conditions of arbitrary asymptotic parameter ε of formal substitution in the diffusion coefficient D_z for D_z/ε. In accordance with the designations this performed by replacing ${}_0^1D$ for $\varepsilon\,{}_0^1D$ and ${}_0^2D = {}_1^2D\,{}_0^1D$ for $\varepsilon\,{}_0^2D$. Note that the original problem can be obtained from the solution of a parameterized the problem when $\varepsilon = 1$. The problem (44) - (50) is thus a

particular case of the more general parameterized problem, containing a parameter of the asymptotic expansion both in the equation for the layer and in the conditions of conjugation

$$\frac{\partial \rho_1}{\partial t} - \frac{\partial^2 \rho_1}{\partial z^2} = -\mathrm{At}\ \ \rho_1, \quad t > 0, \quad r > 0, \quad z > 1, \tag{51}$$

$$\varepsilon \frac{\partial \rho}{\partial t} - {}_1^0 D \frac{\partial^2 \rho}{\partial z^2} + \varepsilon \frac{\mathrm{Pd}}{r} \frac{\partial \rho}{\partial r} = -\varepsilon\, \mathrm{At}\, \rho, \quad t > 0, \quad r > 0, \quad |z| < 1, \tag{52}$$

$$\frac{\partial \rho_2}{\partial t} - {}_1^2 D \frac{\partial^2 \rho_2}{\partial z^2} = -\mathrm{At}\, \rho_2, \quad t > 0, \quad r > 0, \quad z < -1 \tag{53}$$

with boundary conditions

$$\left.\frac{\partial \rho}{\partial z}\right|_{z=1} = {}_0^1 D \varepsilon \left.\frac{\partial \rho_1}{\partial z}\right|_{z=1}, \left.\frac{\partial \rho}{\partial z}\right|_{z=-1} = {}_0^2 D\, \varepsilon \left.\frac{\partial \rho_2}{\partial z}\right|_{z=-1}, \tag{54}$$

$$\rho\big|_{r=0} = 1/\gamma, \rho\big|_{z=1} = \rho_1\big|_{z=1}, \quad \rho\big|_{z=-1} = \rho_2\big|_{z=-1}, \tag{55}$$

$$\rho\big|_{t=0} = \rho_1\big|_{t=0} = \rho_2\big|_{t=0} = 0, \tag{56}$$

$$\rho\big|_{r\to+\infty} = 0, \rho_1\big|_{r+z\to+\infty} = 0, \rho_2\big|_{r+|z|\to+\infty} = 0\,. \tag{57}$$

To find the solution to (51) - (57), one can represent the density function ρ of each region by the asymptotic formula of the parameter ε

$$\rho = \rho^{(0)} + \varepsilon\rho^{(1)} + \ldots + \varepsilon^n \rho^{(n)} + \theta^{(n)}, \rho_i = \rho_i^{(0)} + \varepsilon\rho_i^{(1)} + \ldots + \varepsilon^n \rho_i^{(n)} + \theta_i^{(n)}, \ i = 1,2. \tag{58}$$

Substituting expression (58) in (51) - (57) and grouping terms in powers of the expansion parameter ε, one can easily obtain

$$\left(\frac{\partial \rho_1^{(0)}}{\partial t} - \frac{\partial^2 \rho_1^{(0)}}{\partial z^2} + \mathrm{At}\, \rho_1^{(0)}\right) + \varepsilon\left(\frac{\partial \rho_1^{(1)}}{\partial t} - \frac{\partial^2 \rho_1^{(1)}}{\partial z^2} + \mathrm{At}\, \rho_1^{(1)}\right) + \ldots = 0, \ t > 0, \quad r > 0, \quad z > 1, \tag{59}$$

http://dx.doi.org/10.5772/56042

$$\left(\frac{\partial \rho_2^{(0)}}{\partial t} - {}_1^2 D\frac{\partial^2 \rho_2^{(0)}}{\partial z^2} + \mathrm{At}\,\rho_2^{(0)}\right) + \varepsilon\left(\frac{\partial \rho_2^{(1)}}{\partial t} - {}_1^2 D\frac{\partial^2 \rho_2^{(1)}}{\partial z^2} + \mathrm{At}\,\rho_2^{(1)}\right) + \ldots = 0,\ t > 0,\ r > 0,\ z < -1, \tag{60}$$

$$\begin{aligned} &-{}_1^0 D\frac{\partial^2 \rho^{(0)}}{\partial z^2} + \varepsilon\left(\frac{\partial \rho^{(0)}}{\partial t} - {}_1^0 D\frac{\partial^2 \rho^{(1)}}{\partial z^2} + \frac{Pd}{r}\frac{\partial \rho^{(0)}}{\partial r} + \mathrm{At}\,\rho^{(0)}\right) + \\ &+\varepsilon^2\left(\frac{\partial \rho^{(1)}}{\partial t} - {}_1^0 D\frac{\partial^2 \rho^{(2)}}{\partial z^2} + \frac{Pd}{r}\frac{\partial \rho^{(1)}}{\partial r} + \mathrm{At}\,\rho^{(1)}\right) + \ldots = 0,\ \ t > 0,\ r > 0,\ |z| < 1, \end{aligned} \tag{61}$$

$$\left.\frac{\partial \rho^{(0)}}{\partial z}\right|_{z=1} + \varepsilon\left(\left.\frac{\partial \rho^{(1)}}{\partial z}\right|_{z=1} - {}_0^1 D\left.\frac{\partial \rho_1^{(0)}}{\partial z}\right|_{z=1}\right) + \ldots = 0, \left.\frac{\partial \rho^{(0)}}{\partial z}\right|_{z=-1} + \varepsilon\left(\left.\frac{\partial \rho^{(1)}}{\partial z}\right|_{z=-1} - {}_0^2 D\left.\frac{\partial \rho_2^{(0)}}{\partial z}\right|_{z=-1}\right) + \ldots = 0, \tag{62}$$

$$\left(\rho^{(0)} + \varepsilon\rho^{(1)} + \ldots\right)\Big|_{z=1} = \left(\rho_1^{(0)} + \varepsilon\rho_1^{(1)} + \ldots\right)\Big|_{z=1}, \left(\rho^{(0)} + \varepsilon\rho^{(1)} + \ldots\right)\Big|_{z=-1} = \left(\rho_2^{(0)} + \varepsilon\rho_2^{(1)} + \ldots\right)\Big|_{z=-1}, \tag{63}$$

$$\left(\rho^{(0)} + \varepsilon\rho^{(1)} + \ldots\right)\Big|_{t=0} = \left(\rho_1^{(0)} + \varepsilon\rho_1^{(1)} + \ldots\right)\Big|_{t=0} = \left(\rho_2^{(0)} + \varepsilon\rho_2^{(1)} + \ldots\right)\Big|_{t=0} = 0, \tag{64}$$

$$\left(\rho^{(0)} + \varepsilon\rho^{(1)} + \ldots\right)\Big|_{r=0} = 1/\gamma, \tag{65}$$

$$\left(\rho^{(0)} + \varepsilon\rho^{(1)} + \ldots\right)\Big|_{r\to+\infty} = 0, \left(\rho_1^{(0)} + \varepsilon\rho_1^{(1)} + \ldots\right)\Big|_{r+z\to+\infty} = 0, \left(\rho_2^{(0)} + \varepsilon\rho_2^{(1)} + \ldots\right)\Big|_{r+|z|\to+\infty} = 0\ . \tag{66}$$

Analysis of the formulation of the problem shows that the factors of powers of ε in (61) contain the neighboring coefficients of the expansion, and in this sense, are linked. To solve the corresponding equations implemented decoupling procedure.

4.1. The mathematical formulation of the problem of mass transfer in a zero approximation

If we formally consider ε in equation (61) to be infinitely small, we obtain ${}_1^0 D\partial^2 \rho^{(0)} / \partial z^2 = 0$. The result of integration $\partial \rho^{(0)} / \partial z = A(r, t)$ with the boundary conditions (62) allows us to establish that $A(r, t) = 0$. Thus, in the zero approximation, the density of the pollutant $\rho^{(0)} = \rho^{(0)}(r, t)$ is a function only of r and t. Consequently, in the zero approximation the density

of the pollutant in each cylindrical cross section with the axis z is the same in height of the carrier layer. Next, equating to zero coefficients near ε in equation (61), we obtain

$$\frac{\partial \rho^{(0)}}{\partial t} - {}_1^0 D \frac{\partial^2 \rho^{(1)}}{\partial z^2} + \frac{Pd}{r} \frac{\partial \rho^{(0)}}{\partial r} + \mathrm{At}\, \rho^{(0)} = 0. \tag{67}$$

Since $\rho^{(0)}(r,\ t)$ does not depend on z, the auxiliary function $E(r,\ t)$, composed of the terms of the equation (67) containing $\varrho^{(0)}$

$$E(r,t) = \frac{\partial \rho^{(0)}}{\partial t} + \frac{Pd}{r} \frac{\partial \rho^{(0)}}{\partial r} + \mathrm{At}\, \rho^{(0)}, \tag{68}$$

is also independent of z. Then (1) can be written as

$${}_1^0 D \frac{\partial^2 \rho^{(1)}}{\partial z^2} = E(r,t). \tag{69}$$

Integrating successively, one can find the expression for the first derivative of the first coefficient $\rho^{(1)}$ of the variable z

$$\frac{\partial \rho^{(1)}}{\partial z} = {}_0^1 D \left[z E(r,t) + F(r,t) \right], \tag{70}$$

and the first coefficient of expansion in the form of a quadratic trinomial

$$\rho^{(1)} = {}_0^1 D \left(\frac{z^2}{2} E(r,t) + z F(r,t) + Q(r,t) \right), \tag{71}$$

with the functional coefficients to be determined. From the boundary conditions (62) with the cofactor ε we have

$${}_1^2 D \frac{\partial \rho_1^{(0)}}{\partial z}\bigg|_{z=1} = E(r,t) + F(r,t), \; {}_1^2 D \frac{\partial \rho_2^{(0)}}{\partial z}\bigg|_{z=-1} = -E(r,t) + F(r,t). \tag{72}$$

http://dx.doi.org/10.5772/56042

Hence, one can obtain an expression for the functional coefficients and through the traces of derivatives of the outer regions

$$E(r,t)=\frac{1}{2}\left(\left.\frac{\partial\rho_1^{(0)}}{\partial z}\right|_{z=1}-{}_l^2D\left.\frac{\partial\rho_2^{(0)}}{\partial z}\right|_{z=-1}\right), \tag{73}$$

$$F(r,t)=\frac{1}{2}\left(\left.\frac{\partial\rho_1^{(0)}}{\partial z}\right|_{z=1}+{}_l^2D\left.\frac{\partial\rho_2^{(0)}}{\partial z}\right|_{z=-1}\right). \tag{74}$$

Substituting (73) in (74), one can obtain the desired equation for the zero approximation of the density of impurities in the layer

$$\frac{\partial\rho^{(0)}}{\partial t}+\frac{\mathrm{Pd}}{r}\frac{\partial\rho^{(0)}}{\partial t}+\mathrm{At}\,\rho^{(0)}=\frac{1}{2}\left(\left.\frac{\partial\rho_1^{(0)}}{\partial z}\right|_{z=1}-{}_1^2D\left.\frac{\partial\rho_2^{(0)}}{\partial z}\right|_{z=-1}\right). \tag{75}$$

The final statement of the problem in the zero approximation also includes the equations in the covering and underlying formations

$$\frac{\partial\rho_1^{(0)}}{\partial t}-\frac{\partial^2\rho_1^{(0)}}{\partial z^2}=-\mathrm{At}\,\rho_1^{(0)},\quad t>0,\ r>0,\ z>1, \tag{76}$$

$$\frac{\partial\rho_2^{(0)}}{\partial t}-{}_l^2D\frac{\partial^2\rho_2^{(0)}}{\partial z^2}=-\mathrm{At}\,\rho_2^{(0)},\quad t>0,\ r>0,\ z<-1, \tag{77}$$

$$\frac{\partial\rho^{(0)}}{\partial t}+\frac{\mathrm{Pd}}{r}\frac{\partial\rho^{(0)}}{\partial r}+\mathrm{At}\,\rho^{(0)}=\frac{1}{2}\left(\left.\frac{\partial\rho_1^{(0)}}{\partial z}\right|_{z=1}-{}_1^2D\left.\frac{\partial\rho_2^{(0)}}{\partial z}\right|_{z=-1}\right),\ t>0,\ r>0,\ |z|<1, \tag{78}$$

and the appropriate initial and boundary conditions

$$\left.\rho^{(0)}\right|_{t=0}=\left.\rho_1^{(0)}\right|_{t=0}=\left.\rho_2^{(0)}\right|_{t=0}=0, \tag{79}$$

$$\rho^{(0)} = \rho_1^{(0)}\Big|_{z=1} = \rho_2^{(0)}\Big|_{z=-1}, \tag{80}$$

$$\rho^{(0)}\Big|_{r=0} = 1/\gamma, \tag{81}$$

$$\rho^{(0)}\Big|_{r\to+\infty} = 0, \rho_1^{(0)}\Big|_{r+z\to+\infty} = 0, \rho_2^{(0)}\Big|_{r+|z|\to+\infty} = 0. \tag{82}$$

Expressions (76) - (82) represent the boundary value problem for zero expansion coefficient $\rho^{(0)}$ or zero approximation. Note that in contrast to the original, which is the problem of conjugation for parabolic equations, it is mixed, since the equation contains traces of derivatives from the outer regions.

Finding the zero approximation of the density of the radioactive contaminant is important because just that approach arises in the zero approximation of the temperature problem.

4.2. The zero approximation of the problem of mass transport as the solution of the averaged problem

Let us average a parameterized problem (51) - (57) over z within the carrier layer according to

$$\langle\rho\rangle = \frac{1}{2}\int_{-1}^{1} \rho\, dz.$$

Successively averaging each term of equation (34)

$$\left\langle \frac{\partial \rho}{\partial t} \right\rangle = \frac{1}{2}\int_{-1}^{1} \frac{\partial \rho}{\partial t}\, dz = \frac{\partial \langle\rho\rangle}{\partial t},\ \mathrm{Pd}\frac{1}{r}\left\langle \frac{\partial \rho}{\partial r} \right\rangle = \mathrm{Pd}\frac{1}{r}\frac{\partial \langle\rho\rangle}{\partial r}$$

$$\frac{1}{\varepsilon}\cdot {}_1^0D\left\langle \frac{\partial^2 \rho}{\partial z^2} \right\rangle = \frac{{}_1^0D}{2\varepsilon}\int_{-1}^{1} \frac{\partial^2 \rho}{\partial z^2} dz = \frac{{}_1^0D}{2\varepsilon}\left(\frac{\partial \rho}{\partial z}\Big|_{z=1} - \frac{\partial \rho}{\partial z}\Big|_{z=-1} \right) = \frac{1}{2}\left(\frac{\partial \rho_1}{\partial z}\Big|_{z=1} - {}_1^2D\frac{\partial \rho_2}{\partial z}\Big|_{z=-1} \right),$$

one can obtain the following formulation of the averaged parameterized problem:

$$\frac{\partial \rho_1}{\partial t} - \frac{\partial^2 \rho_1}{\partial z^2} + \mathrm{At}\,\rho_1 = 0, \quad t > 0, \quad r > 0, \quad z > 1, \tag{83}$$

$$\frac{\partial \langle\rho\rangle}{\partial t} - \frac{1}{2}\left(\frac{\partial \rho_1}{\partial z}\Big|_{z=1} - {}_1^2D\frac{\partial \rho_2}{\partial z}\Big|_{z=-1} \right) + \mathrm{Pd}\frac{1}{r}\frac{\partial \langle\rho\rangle}{\partial r} = -\mathrm{At}\langle\rho\rangle, \ t > 0, \quad r > 0, \quad |z| < 1, \tag{84}$$

http://dx.doi.org/10.5772/56042

$$\frac{\partial \rho_2}{\partial t} - {}^2_1 D \frac{\partial^2 \rho_2}{\partial z^2} + \mathrm{At}\,\rho_2 = 0, \quad t > 0, \quad r > 0, \quad z < -1 \tag{85}$$

$$\langle \rho \rangle = \rho_1\big|_{z=1} = \rho_2\big|_{z=-1}, \tag{86}$$

$$\langle \rho \rangle\big|_{r=0} = 1/\gamma, \tag{87}$$

$$\langle \rho \rangle\big|_{t=0} = \rho_1\big|_{t=0} = \rho_2\big|_{t=0} = 0, \tag{88}$$

$$\langle \rho \rangle\big|_{r\to+\infty} = 0, \rho_1\big|_{r+z\to+\infty} = 0, \rho_2\big|_{r+|z|\to+\infty} = 0. \tag{89}$$

The resulting problem coincides with problem (83) - (89) for the zero approximation of the density of pollutant. The uniqueness of solutions implies that $\langle \rho \rangle = \rho^{(0)}$, i. e. zero approximation describes the known way averaged solutions to the original problem. If average the original nonparameterized problem (44) - (50), it also coincides with the problem for zero approximation of the field densities of the pollutant.

4.3. The mathematical formulation of the problem of mass transfer in the first approximation

Equations (41) - (43) for the coefficients for ε take the form

$$\frac{\partial \rho_1^{(1)}}{\partial t} - \frac{\partial^2 \rho_1^{(1)}}{\partial z^2} + \mathrm{At}\,\rho_1^{(1)} = 0, \quad t > 0,\ r > 0,\ z > 1, \tag{90}$$

$$\frac{\partial \rho_2^{(1)}}{\partial t} - {}^2_1 D \frac{\partial^2 \rho_2^{(1)}}{\partial z^2} + \mathrm{At}\,\rho_2^{(1)} = 0, \quad t > 0,\ r > 0,\ z < -1, \tag{91}$$

$$\frac{\partial \rho^{(1)}}{\partial t} + \frac{\mathrm{Pd}}{r}\frac{\partial \rho^{(1)}}{\partial r} - {}^0_1 D \frac{\partial^2 \rho^{(2)}}{\partial z^2} + \mathrm{At}\,\rho^{(1)} = 0, \quad t > 0,\ r > 0,\ |z| < 1, \tag{92}$$

appropriate boundary and initial conditions are represented as

$$\left.\frac{\partial \rho^{(1)}}{\partial z}\right|_{z=1} - {}_0^1 D \left.\frac{\partial \rho_1^{(0)}}{\partial z}\right|_{z=1} = 0, \left.\frac{\partial \rho^{(1)}}{\partial z}\right|_{z=-1} - {}_0^2 D \left.\frac{\partial \rho_2^{(0)}}{\partial z}\right|_{z=-1} = 0, \tag{93}$$

$$\left.\rho^{(1)}\right|_{z=1} = \left.\rho_1^{(1)}\right|_{z=1}, \left.\rho^{(1)}\right|_{z=-1} = \left.\rho_2^{(1)}\right|_{z=-1}, \tag{94}$$

$$\left.\rho^{(1)}\right|_{t=0} = \left.\rho_1^{(1)}\right|_{t=0} = \left.\rho_2^{(1)}\right|_{t=0} = 0, \tag{95}$$

$$\left.\rho^{(1)}\right|_{r\to+\infty} = 0, \left.\rho_1^{(1)}\right|_{r+z\to+\infty} = 0, \left.\rho_2^{(1)}\right|_{r+|z|\to+\infty} = 0, \tag{96}$$

$$\left.\rho^{(1)}\right|_{r=0} = 0. \tag{97}$$

The solution to the problem is sought in the form of quadratic polynomial for z according to (71), where the auxiliary functions $E(r,\ t)$ and $F(r,\ t)$ are defined by (73) - (74), and the function $Q(r,\ t)$ is unknown. For its determination we can write (92) as

$$\frac{\partial^2 \rho^{(2)}}{\partial z^2} = \frac{{}_0^1 D}{\delta} \hat{L} \rho^{(1)}, \tag{98}$$

here $\hat{L}$ is the operator

$$\hat{L} = \frac{\partial}{\partial t} + \frac{\mathrm{Pd}}{r}\frac{\partial}{\partial r} + \mathrm{At}. \tag{99}$$

Using (71) and (98), and linearity of the operator $\hat{L}$, one can obtain

$$\frac{\partial^2 \rho^{(2)}}{\partial z^2} = \frac{{}_0^1 D^2}{\delta^2}\left(\frac{z^2}{2}\hat{L}E(r,t) + z\hat{L}F(r,t) + \hat{L}Q(r,t)\right). \tag{100}$$

Integrating the last expression over z

http://dx.doi.org/10.5772/56042

$$\frac{\partial \rho^{(2)}}{\partial z} = \frac{{}_0^1 D^2}{\delta^2}\left(\frac{z^3}{6}\hat{L}E(r,t) + \frac{z^2}{2}\hat{L}F(r,t) + z\hat{L}Q(r,t) + W(r,t) \right). \tag{101}$$

From the expression (101) and the boundary conditions (62) we have

$${}_1^0 D \frac{\partial \rho_1^{(1)}}{\partial z}\bigg|_{z=1} = \frac{1}{6}\hat{L}E(r,t) + \frac{1}{2}\hat{L}F(r,t) + \hat{L}Q(r,t) + W(r,t), \tag{102}$$

$${}_1^0 D\, {}_1^2 D \frac{\partial \rho_2^{(1)}}{\partial z}\bigg|_{z=-1} = -\frac{1}{6}\hat{L}E(r,t) + \frac{1}{2}\hat{L}F(r,t) - \hat{L}Q(r,t) + W(r,t). \tag{103}$$

From (90) and (91) one can get the equation for the definition of Q

$$\hat{L}Q(r,t) = \frac{{}_1^0 D}{2}\left(\frac{\partial \rho_1^{(1)}}{\partial z}\bigg|_{z=1} - {}_1^2 D \frac{\partial \rho_2^{(1)}}{\partial z}\bigg|_{z=-1} \right) - \frac{1}{6}\hat{L}E(r,t). \tag{104}$$

The equation for the determination of first coefficient of expansion is obtained by substituting (57), (58) and (55) in (98) with using (100)

$$\begin{aligned} \hat{L}\,\rho^{(1)} = {} & \frac{{}_0^1 D}{4}\left(z^2 - \frac{1}{3} \right)\hat{L}\left(\frac{\partial \rho_1^{(0)}}{\partial z}\bigg|_{z=1} - {}_1^2 D \frac{\partial \rho_2^{(0)}}{\partial z}\bigg|_{z=-1} \right) + \\ & \frac{{}_0^1 D}{2} z\hat{L}\left(\frac{\partial \rho_1^{(0)}}{\partial z}\bigg|_{z=1} + {}_1^2 D \frac{\partial \rho_2^{(0)}}{\partial z}\bigg|_{z=-1} \right) + \frac{1}{2}\left(\frac{\partial \rho_1^{(1)}}{\partial z}\bigg|_{z=1} - {}_1^2 D \frac{\partial \rho_2^{(1)}}{\partial z}\bigg|_{z=-1} \right). \end{aligned} \tag{105}$$

The problem to determine the first coefficient of expansion also includes equations (90), (91) for the density field in the covering and underlying layers, respectively.

It is easy to see that the problem formulated by (90), (91), (105), (93) - (96) with the condition (97) has a trivial solution, so the condition (97) is redundant and should be weakened.

4.4. The problem for the remainder — Additional boundary condition

Substituting the expansion (58) with $n = 1$ in the parameterized problem (51) - (57), we obtain a problem for the remainder term

$$\frac{\partial \theta_1}{\partial t} - \frac{\partial^2 \theta_1}{\partial z^2} = -\mathrm{At}\,\theta_1,\ t>0,\ r>0,\ z>1, \tag{106}$$

$$\varepsilon \frac{\partial \theta}{\partial t} - {}^{0}_{1}D \frac{\partial^2 \theta}{\partial z^2} + \varepsilon \frac{\mathrm{Pd}}{r} \frac{\partial \theta}{\partial r} + \varepsilon\,\mathrm{At}\,\theta = -\varepsilon^2 \hat{L}\,\rho^{(1)},\quad t>0,\ r>0,\ |z|<1, \tag{107}$$

$$\frac{\partial \theta_2}{\partial t} - {}^{2}_{l}D \frac{\partial^2 \theta_2}{\partial z^2} = -\mathrm{At}\,\theta_2,\ t>0,\ r>0,\ z<-1 \tag{108}$$

with the boundary conditions and conjugation conditions

$$\left.\frac{\partial \theta}{\partial z}\right|_{z=1} = {}^{1}_{0}D\varepsilon \left.\frac{\partial \theta_1}{\partial z}\right|_{z=1} + {}^{1}_{0}D\varepsilon^2 \left.\frac{\partial \rho_1^{(1)}}{\partial z}\right|_{z=1},\ \left.\frac{\partial \theta}{\partial z}\right|_{z=-1} = {}^{2}_{0}D\varepsilon \left.\frac{\partial \theta_2}{\partial z}\right|_{z=-1} + {}^{2}_{0}D\varepsilon^2 \left.\frac{\partial \rho_2^{(1)}}{\partial z}\right|_{z=-1}, \tag{109}$$

$$\theta\,|_{z=1} = \theta_1|_{z=1},\quad \theta\,|_{z=-1} = \theta_2|_{z=-1}, \tag{110}$$

$$\theta|_{t=0} = \theta_1|_{t=0} = \theta_2|_{t=0} = 0, \tag{111}$$

$$\theta|_{r=0} = -\varepsilon\rho^{(1)}\Big|_{r=0}, \tag{112}$$

$$\theta|_{r\to+\infty} = 0, \theta_1|_{r+z\to+\infty} = 0, \theta_2|_{r+|z|\to+\infty} = 0. \tag{113}$$

Restrict our investigation of the problem, averaged over the thickness of the layer. By averaging the second derivative over the vertical coordinate, use the conjugation conditions (109)

$$\frac{{}^{0}_{1}D}{\varepsilon}\left\langle \frac{\partial^2 \theta}{\partial z^2} \right\rangle = \frac{{}^{0}_{1}D}{2\varepsilon}\int_{-1}^{1} \frac{\partial^2 \theta}{\partial z^2} dz = \frac{{}^{0}_{1}D\delta}{2\varepsilon}\left(\frac{\partial \theta}{\partial z}\Big|_{z=1} - \frac{\partial \theta}{\partial z}\Big|_{z=-1} \right) =$$

$$\frac{1}{2}\left(\frac{\partial \theta_1}{\partial z}\Big|_{z=1} - {}^{2}_{1}D \frac{\partial \theta_2}{\partial z}\Big|_{z=-1} \right) + \frac{\varepsilon}{2}\left(\frac{\partial \rho_1^{(1)}}{\partial z}\Big|_{z=1} - {}^{2}_{1}D \frac{\partial \rho_2^{(1)}}{\partial z}\Big|_{z=-1} \right).$$

The final formulation of the averaged problem for the remainder term represented as

http://dx.doi.org/10.5772/56042

$$\frac{\partial \theta_1}{\partial t} - \frac{\partial^2 \theta_1}{\partial z^2} = -\mathrm{At}\,\theta_1, \ t > 0, \ r > 0, \ z > 1, \tag{114}$$

$$\begin{aligned} &\frac{\partial \langle \theta \rangle}{\partial t} + \frac{\mathrm{Pd}}{r}\frac{\partial \langle \theta \rangle}{\partial r} + \mathrm{At}\langle \theta \rangle - \frac{1}{2}\left(\left.\frac{\partial \theta_1}{\partial z}\right|_{z=1} - \gamma_l^2 D \left.\frac{\partial \theta_2}{\partial z}\right|_{z=-1} \right) = \\ &= -\varepsilon \left(\hat{L}\langle \rho^{(1)} \rangle - \frac{1}{2}\left(\left.\frac{\partial \rho_1^{(1)}}{\partial z}\right|_{z=1} - \gamma_l^2 D \left.\frac{\partial \rho_2^{(1)}}{\partial z}\right|_{z=-1} \right) \right), \quad t > 0, \ r > 0, \ |z| < 1, \end{aligned} \tag{115}$$

$$\frac{\partial \theta_2}{\partial t} - \gamma_l^2 D \frac{\partial^2 \theta_2}{\partial z^2} = -\mathrm{At}\,\theta_2, \ t > 0, \ r > 0, \ z < -1, \tag{116}$$

$$\langle \theta \rangle = \theta_1|_{z=1} = \theta_2|_{z=-1}, \tag{117}$$

$$\langle \theta \rangle|_{r=0} = -\varepsilon \langle \rho^{(1)} \rangle|_{r=0}, \tag{118}$$

$$\langle \theta \rangle|_{t=0} = \theta_1|_{t=0} = \theta_2|_{t=0} = 0, \tag{119}$$

$$\langle \theta \rangle|_{r\to+\infty} = 0, \theta_1|_{r+z\to+\infty} = 0, \theta_2|_{r+|z|\to+\infty} = 0 \tag{120}$$

It is easy to show that the averaged problem (110) - (116) for the remainder term has a trivial solution if and only if

$$\langle \rho^{(1)} \rangle|_{r=0} = 0, \tag{121}$$

$$\hat{L}\langle \rho^{(1)} \rangle - \frac{1}{2}\left(\left.\frac{\partial \rho_1^{(1)}}{\partial z}\right|_{z=1} - \gamma_l^2 D \left.\frac{\partial \rho_2^{(1)}}{\partial z}\right|_{z=-1} \right) = 0, \tag{122}$$

that is, when in the averaged problem for remainder term there are no sources. Averaging (107) with regard to (109), one can show that (122) is satisfied identically. Thus, in order to the averaged problem for the remainder term had a trivial solution it is sufficient for the average

condition (121) to be satisfied. Therefore, in order to get the exact on the average solution of (44) - (50) on the field of density in the layer, in the formulation of the problem for the first coefficients of the asymptotic expansion (90) (91), (105) (95) - (97) the boundary condition (97) must be replaced by non-local (121).

5. Solution to the problem of mass transfer in the zero approximation

5.1. Solution to the problem in the zero approximation

In the image space of Laplace-Carson the problem (76) - (82) in the zero approximation is represented as

$$p\,\rho_1^{(0)u} - \frac{\partial^2 \rho_1^{(0)u}}{\partial z^2} = -\mathrm{At}\,\rho_1^{(0)u}, \quad r > 0,\ z > 1, \tag{123}$$

$$p\,\rho_2^{(0)u} - {}_1^2D\frac{\partial^2 \rho_2^{(0)u}}{\partial z^2} = -\mathrm{At}\,\rho_2^{(0)u}, \quad r > 0,\ z < -1, \tag{124}$$

$$p\,\rho^{(0)u} + \frac{\mathrm{Pd}}{r}\frac{\partial \rho^{(0)u}}{\partial r} + \mathrm{At}\,\rho^{(0)u} = \frac{1}{2}\left(\left.\frac{\partial \rho_1^{(0)u}}{\partial z}\right|_{z=1} - {}_1^2D\left.\frac{\partial \rho_2^{(0)u}}{\partial z}\right|_{z=-1} \right),\ r > 0,\ |z| < 1, \tag{125}$$

$$\left.\rho_1^{(0)u}\right|_{z=1} = \rho^{(0)u} = \left.\rho_2^{(0)u}\right|_{z=-1}, \tag{126}$$

$$\left.\rho^{(0)u}\right|_{r=0} = 1/\gamma, \tag{127}$$

$$\left.\rho^{(0)u}\right|_{r\to\infty} = 0, \quad \left.\rho_1^{(0)u}\right|_{r+z\to\infty} = 0, \quad \left.\rho_2^{(0)u}\right|_{r+|z|\to\infty} = 0. \tag{128}$$

Taking into account the boundary conditions (126), as well as the fact that in the zero approximation the density of the pollutant in the porous layer is independent of z and is a function only of r and t, the solution of equations (123), (124) can be rewritten as follows:

http://dx.doi.org/10.5772/56042

$$\rho_1^{(0)u} = \rho^{(0)u} \exp\left(-\sqrt{p + \mathrm{At}}\,(z-1)\right), \tag{129}$$

$$\rho_2^{(0)u} = \rho^{(0)u} \exp\left(\sqrt{{}^1_2 D\left(p + \mathrm{At}\right)}\,(z+1)\right). \tag{130}$$

These expressions allow us to determine the values of the traces of derivatives from the outer regions included in the equation for the layer, through the density of impurities in it

$$\left.\frac{\partial \rho_1^{(0)u}}{\partial z}\right|_{z=1} = -\sqrt{p + \mathrm{At}}\,\rho^{(0)u}, \quad \left.\frac{\partial \rho_2^{(0)u}}{\partial z}\right|_{z=-1} = \sqrt{{}^1_2 D\left(p + \mathrm{At}\right)}\,\rho^{(0)u}. \tag{131}$$

Substituting (131) into equation (125), after simple transformations we obtain an ordinary differential equation for the determination of $\rho^{(0)u}$

$$\frac{\mathrm{Pd}}{r}\frac{d\rho^{(0)u}}{dr} = -\left(p + \mathrm{At} + \frac{1}{2}\sqrt{p + \mathrm{At}}\left(1 + \sqrt{{}^2_1 D}\right)\right)\rho^{(0)u}, \tag{132}$$

from which we finally get

$$\rho^{(0)u} = \gamma \exp\left[-\left(p + \mathrm{At} + \frac{1}{2}\sqrt{p + \mathrm{At}}\left(1 + \sqrt{{}^2_1 D}\right)\right)\frac{r^2}{2\mathrm{Pd}}\right]. \tag{133}$$

Translation in the original space is carried out by the reference [51]. The expression for the density of radioactive contaminants for the porous layer in the original space is represented as

$$\begin{aligned}\rho^{(0)} &= \frac{\gamma}{2}\exp\left(-\mathrm{At}r^2/2\mathrm{Pd}\right)\Phi\left(t - r^2/2\mathrm{Pd}\right)\times \\ \times\Bigg[&\exp\left(\frac{-\sqrt{\mathrm{At}}\left(1+\sqrt{{}^2_l D}\right)r^2}{4\mathrm{Pd}}\right)\mathrm{erfc}\left(\frac{\sqrt{\delta}\left(1+\sqrt{{}^2_l D}\right)r^2}{8\mathrm{Pd}\sqrt{t - r^2/2\mathrm{Pd}}} - \sqrt{\mathrm{At}\left(t - r^2/2\mathrm{Pd}\right)}\right) + \\ &+\exp\left(\frac{\sqrt{\mathrm{At}}\left(1+\sqrt{{}^2_l D}\right)r^2}{4\mathrm{Pd}}\right)\mathrm{erfc}\left(\frac{\left(1+\sqrt{{}^2_l D}\right)r^2}{8\mathrm{Pd}\sqrt{t - r^2/2\mathrm{Pd}}} + \sqrt{\mathrm{At}\left(t - r^2/2\mathrm{Pd}\right)}\right)\Bigg], \; t>0, \; r>0, \; |z|<1.\end{aligned} \tag{134}$$

Also transition is feasible in the original space for the coating (129) and underlying (130) layers

$$\begin{aligned}\rho_1^{(0)} &= \frac{\gamma}{2}\exp\left(-\mathrm{At}\,r^2/2\mathrm{Pd}\right)\Phi\left(t-r^2/2\mathrm{Pd}\right)\times\\ &\times\left\{\exp\left(-\sqrt{\mathrm{At}}\left(1+\sqrt{{}_1^2D}\right)r^2\Big/4\mathrm{Pd}-\sqrt{\mathrm{At}}\left(z-1\right)\right)\times\right.\\ &\times\mathrm{erfc}\left(\frac{\left(1+\sqrt{{}_1^2D}\right)r^2+4\mathrm{Pd}\left(z-1\right)}{8\mathrm{Pd}\sqrt{t-r^2/2\mathrm{Pd}}}-\sqrt{\mathrm{At}\left(t-\frac{r^2}{2\mathrm{Pd}}\right)}\right)+\\ &+\exp\left(\sqrt{\mathrm{At}}\left(1+\sqrt{{}_1^2D}\right)r^2\Big/4\mathrm{Pd}+\sqrt{\mathrm{At}}\left(z-1\right)\right)\times\\ &\times\left.\mathrm{erfc}\left(\frac{\left(1+\sqrt{{}_1^2D}\right)r^2+4\mathrm{Pd}\left(z-1\right)}{8\mathrm{Pd}\sqrt{t-r^2/2\mathrm{Pd}}}+\sqrt{\mathrm{At}\left(t-\frac{r^2}{2\mathrm{Pd}}\right)}\right)\right\},\quad t>0,\ \ r>0,\ \ z>1,\end{aligned} \tag{135}$$

$$\begin{aligned}\rho_2^{(0)} &= \frac{\gamma}{2}\exp\left(-\mathrm{At}\,r^2/2\mathrm{Pd}\right)\Phi\left(t-r^2/2\mathrm{Pd}\right)\times\left\{\exp\left(-\sqrt{\mathrm{At}}\left(1+\sqrt{{}_1^2D}\right)r^2\Big/4\mathrm{Pd}+\sqrt{\mathrm{At}\,{}_2^1D}\left(z+1\right)\right)\times\right.\\ &\times\mathrm{erfc}\left(\frac{\left(1+\sqrt{{}_1^2D}\right)r^2-4\mathrm{Pd}\sqrt{{}_2^1D}\left(z+1\right)}{8\mathrm{Pd}\sqrt{t-r^2/2\mathrm{Pd}}}-\sqrt{\mathrm{At}\left(t-\frac{r^2}{2\mathrm{Pd}}\right)}\right)+\\ &+\exp\left(\sqrt{\mathrm{At}}\left(1+\sqrt{{}_1^2D}\right)r^2\Big/4\mathrm{Pd}-\sqrt{\mathrm{At}\,{}_2^1D}\left(z+1\right)\right)\times\\ &\times\left.\mathrm{erfc}\left(\frac{\left(1+\sqrt{{}_1^2D}\right)r^2-4\mathrm{Pd}\sqrt{{}_2^1D}\left(z+1\right)}{8\mathrm{Pd}\sqrt{t-r^2/2\gamma Pt}}+\sqrt{\mathrm{At}\left(t-\frac{r^2}{2\mathrm{Pd}}\right)}\right)\right\},\ t>0,\ r>0,\ z<-1.\end{aligned} \tag{136}$$

The first factor in the solution (134) - (136) describes the decrease in the density of the pollutant as a result of radioactive decay, the second - the Heaviside function, determines the radius of the spread of contamination zone and the third (the expression in curly brackets) takes into account changes of the density due to the diffusion of pollutants, and radioactive decay of diffusing nuclide. Since the contribution of radioactive decay is described by the factor of $\exp\left(-\mathrm{At}\,r^2/2\mathrm{Pd}\right)$, then it can be argued that the concentration of the radioactive contaminant is reduced by a factor of e due to the decay at the distances defined by the simple relation $R_e=h\sqrt{2\mathrm{Pd}/\mathrm{At}}=\sqrt{2v_0r_0/\alpha}$. It follows that for short-lived isotopes, zone of contamination is low. On the other hand, to reduce the zone of influence of long-lived radioactive isotopes, the rate of filtration should be reduced.

The resulting solution (134) contains the Heaviside function, which vanishes for $r \geq \sqrt{2\mathrm{Pd}\,t}$, and helps to determine the radius of the zone of radioactive contamination

http://dx.doi.org/10.5772/56042

$$R_p = h\sqrt{2\mathrm{Pd}\ t} = \sqrt{2\mathrm{v}_0 r_0 \tau}. \tag{137}$$

The most important physical results are described by the zero approximation of the asymptotic expansion, the first and the following coefficients determine the "correction term". In addition, due to the smallness of the diffusion coefficient (D_z~10^{-9}÷10^{-11}), the spread of a contaminant in water-resistant layers in the vertical direction is negligible compared to the convective transport in a porous layer and has little effect on the size of the zone of contamination.

5.2. The solution to the problem of mass transfer in the first approximation

In the space transformations of Laplace-Carson, the problem (90), (91), (105), (95) - (97), (121) for the first coefficient of expansion is represented as

$$\begin{aligned}\widehat{L}^u \rho^{(1)u} = {} & \frac{{}_0^1 D}{4}\left(z^2 - \frac{1}{3}\right)\widehat{L}^u\left(\left.\frac{\partial \rho_1^{(0)u}}{\partial z}\right|_{z=1} - {}_1^2 D\left.\frac{\partial \rho_2^{(0)u}}{\partial z}\right|_{z=-1}\right) + \\ & + \frac{{}_0^1 D}{2} z\widehat{L}^u\left(\left.\frac{\partial \rho_1^{(0)u}}{\partial z}\right|_{z=1} + {}_1^2 D\left.\frac{\partial \rho_2^{(0)u}}{\partial z}\right|_{z=-1}\right) + \frac{1}{2}\left(\left.\frac{\partial \rho_1^{(1)u}}{\partial z}\right|_{z=1} - {}_1^2 D\left.\frac{\partial \rho_2^{(1)u}}{\partial z}\right|_{z=-1}\right), \quad r>0,\ |z|<1,\end{aligned} \tag{138}$$

$$p\rho_1^{(1)u} - \frac{\partial^2 \rho_1^{(1)u}}{\partial z^2} + \mathrm{At}\,\rho_1^{(1)u} = 0, \quad r>0,\ z>1, \tag{139}$$

$$p\rho_2^{(1)u} - {}_1^2 D\frac{\partial^2 \rho_2^{(1)u}}{\partial z^2} + \mathrm{At}\,\rho_2^{(1)u} = 0, \quad r>0,\ z<-1. \tag{140}$$

The initial conditions and conjugation conditions at the boundaries are represented as

$$\rho^{(1)u}\Big|_{z=1} = \rho_1^{(1)u}\Big|_{z=1}, \tag{141}$$

$$\rho^{(1)u}\Big|_{z=-1} = \rho_2^{(1)u}\Big|_{z=-1}, \tag{142}$$

$$\rho^{(1)u}\Big|_{r\to+\infty} = 0, \rho_1^{(1)u}\Big|_{r+z\to+\infty} = 0, \rho_2^{(1)u}\Big|_{r+|z|\to+\infty} = 0, \tag{143}$$

$$\left\langle \rho^{(1)u} \right\rangle \Big|_{r=0} = 0. \tag{144}$$

The operator $\hat{L}$ in the image space has the form

$$\hat{L}^{u} = p + \mathrm{At} + \gamma \frac{\mathrm{Pt}}{r} \frac{\partial}{\partial r}.$$

The action of this operator on the zero expansion in the image space is determined by the formula

$$\hat{L}^{u} \rho^{(0)u} = -\frac{\sqrt{p + \mathrm{At}}}{2} \left(1 + \sqrt{{}_{l}^{2}D} \right) \rho^{(0)u}. \tag{145}$$

The solution in the first approximation, according to (71), is sought in the form of quadratic polynomial

$$\rho^{(1)u} = {}_{0}^{1}D \left(\frac{z^2}{2} E^{u} + z F^{u} + Q^{u} \right), \tag{146}$$

in which E^{u} and F^{u} are expressed through the zero approximation according to (73), (74)

$$E^{u} = \frac{1}{2} \left(\frac{\partial \rho_1^{(0)u}}{\partial z} \Big|_{z=1} - {}_{1}^{2}D \frac{\partial \rho_2^{(0)u}}{\partial z} \Big|_{z=-1} \right), F^{u} = \frac{1}{2} \left(\frac{\partial \rho_1^{(0)u}}{\partial z} \Big|_{z=1} + {}_{1}^{2}D \frac{\partial \rho_2^{(0)u}}{\partial z} \Big|_{z=-1} \right), \tag{147}$$

and the function Q^{u}, according to (104), is defined by the equation

$$\hat{L}^{u} Q^{u} = \frac{{}_{1}^{0}D}{2} \left(\frac{\partial \rho_1^{(1)u}}{\partial z} \Big|_{z=1} - {}_{1}^{2}D \frac{\partial \rho_2^{(1)u}}{\partial z} \Big|_{z=-1} \right) - \frac{1}{6} \hat{L}^{u} E^{u}. \tag{148}$$

Solutions of equations (139), (140) shall be as follows:

$$\rho_1^{(1)u} = \rho^{(1)u} \Big|_{z=1} \exp\left(-\sqrt{p + \mathrm{At}} \left(z - 1 \right) \right), \rho_2^{(1)u} = \rho^{(1)u} \Big|_{z=-1} \exp\left(\sqrt{{}_{2}^{1}D \left(p + \mathrm{At} \right)} \left(z + 1 \right) \right). \tag{149}$$

Let us find the traces of the outer regions of the right side of equation (138)

http://dx.doi.org/10.5772/56042

$$\left.\frac{\partial \rho_1^{(1)u}}{\partial z}\right|_{z=1} = -{}_1^0 D\sqrt{p+\mathrm{At}}\left(\frac{1}{2}E^u + F^u + Q^u\right), \tag{150}$$

$$\left.{}_1^2 D\frac{\partial \rho_2^{(1)u}}{\partial z}\right|_{z=-1} = {}_0^2 D\sqrt{{}_2^1 D\left(p+\mathrm{At}\right)}\left(\frac{1}{2}E^u - F^u + Q^u\right). \tag{151}$$

Note also that the action of the operator $\hat{L}^u$ on functions

$$E^u = -\frac{\sqrt{p+\mathrm{At}}}{2}\left(1+\sqrt{{}_1^2 D}\right)\rho^{(0)u}, F^u = -\frac{\sqrt{\delta\left(p+\mathrm{At}\right)}}{2}\left(1-\sqrt{{}_1^2 D}\right)\rho^{(0)u} \tag{152}$$

according to (147), this leads to the following:

$$\hat{L}^u E^u = \frac{p+\mathrm{At}}{4}\left(1+\sqrt{{}_1^2 D}\right)^2 \rho^{(0)u}, \hat{L}^u F^u = \frac{p+\mathrm{At}}{4}\left(1-{}_1^2 D\right)^2 \rho^{(0)u}. \tag{153}$$

The final equation for determination of Q^u takes the form

$$\frac{\mathrm{Pd}}{r}\frac{dQ^u}{dr} + \left(p+\mathrm{At} + \frac{\sqrt{p+\mathrm{At}}}{2}\left(1+\sqrt{{}_1^2 D}\right)\right)Q^u = \frac{1+{}_1^2 D-\sqrt{{}_1^2 D}}{3}\left(p+\mathrm{At}\right)\rho^{(0)u}. \tag{154}$$

It's general solution is represented as

$$\begin{aligned} Q^u = {} & \frac{1+{}_1^2 D-\sqrt{{}_1^2 D}}{3\mathrm{Pd}}\delta\left(p+\mathrm{At}\right)\times\int_0^r \rho^{(0)u}\exp\left[-\left(p+\mathrm{At}+\frac{\sqrt{p+\mathrm{At}}}{2}\left(1+\sqrt{{}_1^2 D}\right)\right)\frac{r^2-r'^2}{2\mathrm{Pd}}\right]r'dr' + \\ & + C\exp\left[-\left(p+\mathrm{At}+\frac{\sqrt{p+\mathrm{At}}}{2}\left(1+\sqrt{{}_1^2 D}\right)\right)\frac{r^2}{2\mathrm{Pd}}\right]. \end{aligned} \tag{155}$$

Constant C is determined from the averaging (144)

$$Q^u\Big|_{r=0} = -\frac{1}{6}E^u\Big|_{r=0}. \tag{156}$$

Hence, one can obtain

$$Q^u = \frac{1}{6}\left[\frac{\left(1+{}_1^2D-\sqrt{{}_1^2D}\right)}{\mathrm{Pd}}\delta\left(p+\mathrm{At}\right)r^2+\frac{\sqrt{p+\mathrm{At}}}{2}\left(1+\sqrt{{}_1^2D}\right)\right]\rho^{(0)u}. \tag{157}$$

As a result, the solution for the first coefficient of expansion in the images is represented as

$$\rho^{(1)u} = \frac{{}_0^1D}{2}\sqrt{p+\mathrm{At}}\left[\left(\frac{1}{6}-\frac{z^2}{2}\right)\left(1+\sqrt{{}_1^2D}\right)-z\left(1-\sqrt{{}_1^2D}\right)\right]\rho^{(0)u}+{}_0^1D\frac{1+{}_1^2D-\sqrt{{}_1^2D}}{6\mathrm{Pd}}r^2\left(p+\mathrm{At}\right)\rho^{(0)u}, \tag{158}$$

$$\rho_1^{(1)u} = \frac{{}_0^1D}{3}\left[\frac{1+{}_1^2D-\sqrt{{}_1^2D}}{2Pd}r^2\left(p+\mathrm{At}\right)-\sqrt{p+\mathrm{At}}\left(2-\sqrt{{}_1^2D}\right)\right]\rho^{(0)u}\times\exp\left(-\left(z-1\right)\sqrt{p+\mathrm{At}}\right), \tag{159}$$

$$\rho_2^{(1)u} = \frac{{}_0^1D}{3}\left[\frac{1+{}_1^2D-\sqrt{{}_1^2D}}{2\mathrm{Pd}}r^2\left(p+\mathrm{At}\right)+\sqrt{p+\mathrm{At}}\left(1-2\sqrt{{}_1^2D}\right)\right]\rho^{(0)u}\times\exp\left(\left(z+1\right)\sqrt{{}_2^1D\left(p+\mathrm{At}\right)}\right). \tag{160}$$

Determination of the originals is carried out by help of the following correspondence:

$$\sqrt{p+\gamma}\exp\left(-\sqrt{\beta(p+\gamma)}\right)\to\frac{1}{\sqrt{\pi t}}\exp\left(-\gamma t-\frac{\beta}{4t}\right)-$$

$$-\frac{\sqrt{\gamma}}{2}\left[\exp\left(\sqrt{\beta\gamma}\right)\mathrm{erfc}\left(\frac{1}{2}\sqrt{\frac{\beta}{t}}+\sqrt{\gamma t}\right)-\exp\left(-\sqrt{\beta\gamma}\right)\mathrm{erfc}\left(\frac{1}{2}\sqrt{\frac{\beta}{t}}-\sqrt{\gamma t}\right)\right],$$

$$p\exp\left(-\sqrt{\beta(p+\gamma)}\right)\to\frac{\sqrt{\beta}}{2t\sqrt{\pi t}}\exp\left(-\frac{\beta}{4t}-\gamma t\right).$$

Finally, we obtain for the porous layer

http://dx.doi.org/10.5772/56042

$$\rho^{(1)} = \frac{{}_0^1 D}{4\gamma}\sqrt{\mathrm{At}}\exp\left(-\mathrm{At}r^2/2\mathrm{Pd}\right)\Phi\left(t-r^2/2\mathrm{Pd}\right)\times$$
$$\times\left[\frac{2\left(1+\sqrt{{}_1^2 D}\right)\sqrt{\mathrm{At}\left(t-r^2/2\mathrm{Pd}\right)}}{\sqrt{\pi}}\left(\frac{1-\sqrt{{}_1^2 D}+{}_1^2 D}{24\mathrm{Pd}^2\left(t-r^2/2\mathrm{Pd}\right)}r^4+\left(\frac{1}{6}-\frac{z^2}{2}-z\frac{1-\sqrt{{}_1^2 D}}{1+\sqrt{{}_1^2 D}}\right)\right)\times\right.$$
$$\left.\times\exp\left(-\frac{\left(1+\sqrt{{}_1^2 D}\right)^2}{64\mathrm{Pd}^2\left(t-r^2/2\mathrm{Pd}\right)}r^4-\mathrm{At}\left(t-\frac{r^2}{2\mathrm{Pd}}\right)\right)+\right.$$
$$+\left(\sqrt{\mathrm{At}}\frac{1-\sqrt{{}_1^2 D}+{}_1^2 D}{3\mathrm{Pd}}r^2-\left(1+\sqrt{{}_1^2 D}\right)\left(\frac{1}{6}-\frac{z^2}{2}-z\frac{1-\sqrt{{}_1^2 D}}{1+\sqrt{{}_1^2 D}}\right)\right)\times \tag{161}$$
$$\times\exp\left(\frac{\sqrt{\mathrm{At}}\left(1+\sqrt{{}_1^2 D}\right)}{4\mathrm{Pd}}r^2\right)\mathrm{erfc}\left(\frac{1+\sqrt{{}_1^2 D}}{8\mathrm{Pd}\sqrt{t-r^2/2\mathrm{Pd}}}r^2+\sqrt{\mathrm{At}\left(t-\frac{r^2}{2\mathrm{Pd}}\right)}\right)+$$
$$+\left(\sqrt{\mathrm{At}}\frac{1-\sqrt{{}_1^2 D}+{}_1^2 D}{3\mathrm{Pd}}r^2+\left(1+\sqrt{{}_1^2 D}\right)\left(\frac{1}{6}-\frac{z^2}{2}-z\frac{1-\sqrt{{}_1^2 D}}{1+\sqrt{{}_1^2 D}}\right)\right)\times$$
$$\left.\times\exp\left(-\frac{\sqrt{\mathrm{At}}\left(1+\sqrt{{}_1^2 D}\right)}{4\mathrm{Pd}}r^2\right)\mathrm{erfc}\left(\frac{1+\sqrt{{}_1^2 D}}{8\mathrm{Pd}\sqrt{t-r^2/2\mathrm{Pd}}}r^2-\sqrt{\mathrm{At}\left(t-\frac{r^2}{2\mathrm{Pd}}\right)}\right)\right],\quad r>0,\ t>0,\ |z|<1,$$

for the covering layer

$$\rho_1^{(1)} = {}_0^l D\frac{\sqrt{\mathrm{At}}}{6\gamma}\exp\left(-\frac{\mathrm{At}}{2\mathrm{Pd}}r^2\right)\Phi\left(t-\frac{r^2}{2\mathrm{Pd}}\right)\times$$
$$\times\left[\frac{2}{\sqrt{\pi}\sqrt{\mathrm{At}\left(t-r^2/2\mathrm{Pd}\right)}}\left(\frac{1+{}_l^2 D-\sqrt{{}_l^2 D}}{4\mathrm{Pd}\left(t-r^2/2\mathrm{Pd}\right)}r^2\left(\frac{1+\sqrt{{}_l^2 D}}{4\mathrm{Pd}}r^2+\mathrm{z}-1\right)-\left(2-\sqrt{{}_l^2 D}\right)\right)\times\right.$$
$$\left.\times\exp\left(-\frac{\left(\left(1+\sqrt{{}_l^2 D}\right)r^2+4\mathrm{Pd}(\mathrm{z}-1)\right)^2}{64\mathrm{Pd}^2\left(t-r^2/2\mathrm{Pd}\right)}-\mathrm{At}\left(t-\frac{r^2}{2\mathrm{Pd}}\right)\right)+\right.$$
$$+\left(\frac{\sqrt{\mathrm{At}}\left(1+{}_l^2 D-\sqrt{{}_l^2 D}\right)}{2\mathrm{Pd}}r^2-\left(2-\sqrt{{}_l^2 D}\right)\right)\exp\left(-\frac{\sqrt{\mathrm{At}}\left(1+\sqrt{{}_l^2 D}\right)}{4\mathrm{Pd}}r^2-\sqrt{\mathrm{At}}(\mathrm{z}-1)\right)\times \tag{162}$$
$$\times\mathrm{erfc}\left(\frac{\left(1+\sqrt{{}_l^2 D}\right)r^2}{8\mathrm{Pd}\sqrt{t-r^2/2\mathrm{Pd}}}+\frac{\mathrm{z}-1}{2\sqrt{t-r^2/2\mathrm{Pd}}}-\sqrt{\mathrm{At}\left(t-\frac{r^2}{2\mathrm{Pd}}\right)}\right)+$$
$$+\left(\frac{\sqrt{At}\left(1+{}_1^2 D-\sqrt{{}_1^2 D}\right)}{2\mathrm{Pd}}r^2+\left(2-\sqrt{{}_1^2 D}\right)\right)\exp\left(-\frac{\sqrt{\mathrm{At}}\left(1+\sqrt{{}_l^2 D}\right)}{4\mathrm{Pd}}r^2+\sqrt{\mathrm{At}}(\mathrm{z}-1)\right)\times$$
$$\times\mathrm{erfc}\left(\frac{\left(1+\sqrt{{}_l^2 D}\right)r^2}{8\mathrm{Pd}\sqrt{t-r^2/2\mathrm{Pd}}}+\frac{\mathrm{z}-1}{2\sqrt{t-r^2/2\mathrm{Pd}}}+\sqrt{\mathrm{At}\left(t-\frac{r^2}{2\mathrm{Pd}}\right)}\right).$$

and for the underlying layer

$$\rho_2^{(1)} = {}_0^1D\frac{\sqrt{\mathrm{At}}}{6\gamma}\exp\left(-\frac{\mathrm{At}}{2\mathrm{Pd}}r^2\right)\Phi\left(t-\frac{r^2}{2\mathrm{Pd}}\right)\times\times\left[\frac{2}{\sqrt{\pi}\sqrt{\mathrm{At}\left(t-r^2/2\mathrm{Pd}\right)}}\left(\frac{1+{}_1^2D-\sqrt{{}_1^2D}}{4\mathrm{Pd}\left(t-r^2/2\mathrm{Pd}\right)}r^2\left(\frac{1+\sqrt{{}_1^2D}}{4\mathrm{Pd}}r^2-\sqrt{{}_2^1D}\left(z+1\right)\right)+1-2\sqrt{{}_1^2D}\right)\times\right.$$
$$\times\exp\left(-\frac{\left(\left(1+\sqrt{{}_1^2D}\right)r^2-4\mathrm{Pd}\sqrt{{}_2^1D}\left(z+1\right)\right)^2}{64\mathrm{Pd}^2\left(t-r^2/2\mathrm{Pd}\right)}-\mathrm{At}\left(t-\frac{r^2}{2\mathrm{Pd}}\right)\right)+$$
$$+\left(\frac{\sqrt{\mathrm{At}}\left(1+{}_1^2D-\sqrt{{}_1^2D}\right)}{2\mathrm{Pd}}r^2+1-2\sqrt{{}_1^2D}\right)\exp\left(-\frac{\sqrt{\mathrm{At}}\left(1+\sqrt{{}_1^2D}\right)}{4\mathrm{Pd}}r^2+\sqrt{{}_2^1D\,\mathrm{At}}\left(z+1\right)\right)\times \tag{163}$$
$$\times\mathrm{erfc}\left(\frac{\left(1+\sqrt{{}_1^2D}\right)r^2-4\mathrm{Pd}\sqrt{{}_2^1D}\left(z+1\right)}{8\mathrm{Pd}\sqrt{t-r^2/2\mathrm{Pd}}}-\sqrt{\mathrm{At}\left(t-\frac{r^2}{2\mathrm{Pd}}\right)}\right)+$$
$$+\left(\frac{\sqrt{\mathrm{At}}\left(1+{}_1^2D-\sqrt{{}_1^2D}\right)}{2\mathrm{Pd}}r^2-1+2\sqrt{{}_1^2D}\right)\exp\left(\frac{\sqrt{\mathrm{At}}\left(1+\sqrt{{}_1^2D}\right)}{4\mathrm{Pd}}r^2-\sqrt{{}_2^1D\,\mathrm{At}}\left(z+1\right)\right)\times$$
$$\left.\times\mathrm{erfc}\left(\frac{\left(1+\sqrt{{}_1^2D}\right)r^2-4\mathrm{Pd}\sqrt{{}_2^1D}\left(z+1\right)}{8\mathrm{Pd}\sqrt{t-r^2/2\mathrm{Pd}}}+\sqrt{\mathrm{At}\left(t-\frac{r^2}{2\mathrm{Pd}}\right)}\right)\right],\quad r>0,\ t>0,\ z<-1.$$

Note that when $r = 0$ the first coefficient of expansion (158)

$$\rho^{(1)u}\big|_{r=0} = \frac{{}_0^1D}{2}\sqrt{p+\mathrm{At}}\left[\frac{1}{2}\left(\frac{1}{3}-z^2\right)\left(1+\sqrt{{}_1^2D}\right)-z\left(1-\sqrt{{}_1^2D}\right)\right] \tag{164}$$

depends on the variable z and does not vanish, that is constructed solution does not satisfy the boundary condition (48). To eliminate the marked lack, it is necessary to build a boundary-layer functions in a neighborhood of $r = 0$.

5.3. Construction of boundary-layer solutions

Let us represent the solution to (78) - (82) as

$$\rho_1 = \hat{\rho}_1 + \Pi_1, \rho = \hat{\rho} + \Pi, \rho_2 = \hat{\rho}_2 + \Pi_2 \tag{165}$$

where $\hat{\rho} = \hat{\rho}(r,\ z,\ t)$ - the regular part, $\Pi = \Pi(y,\ z,\ t)$ - boundary-layer part of the expansion by the asymptotic parameter, $y = r^2/2\varepsilon$ the stretched variable [44]. Substituting (165) to (44) - (50) and applying the transformation of Laplace-Carson over the variable t, in the image space we obtain a problem for the boundary-layer functions

$$\Pi^{\grave{e}} = \Pi^{(0)u} + \varepsilon\Pi^{(1)u} + \ldots, \Pi_1^u = \Pi_1^{(0)u} + \varepsilon\Pi_1^{(1)u} + \ldots, \Pi_2^u = \Pi_2^{(0)u} + \varepsilon\Pi_2^{(1)u} + \ldots \tag{166}$$

http://dx.doi.org/10.5772/56042

in the following way:

$$\left(\frac{\partial^2\Pi_1^{(0)u}}{\partial z^2}-\left(p+\mathrm{At}\right)\Pi_1^{(0)u}\right)+\varepsilon\left(\frac{\partial^2\Pi_1^{(1)u}}{\partial z^2}-\left(p+\mathrm{At}\right)\Pi_1^{(1)u}\right)+\ldots=0,\ y>0,\quad z>1, \tag{167}$$

$$\left(\frac{\partial^2\Pi^{(0)u}}{\partial z^2}-{}_0^1 D\,\mathrm{Pd}\frac{\partial\Pi^{(0)u}}{\partial y}\right)+\varepsilon\left(\frac{\partial^2\Pi^{(1)u}}{\partial z^2}-{}_0^1 D\,\mathrm{Pd}\frac{\partial\Pi^{(1)u}}{\partial y}-\left(p+\mathrm{At}\right)\Pi^{(0)u}\right)+\ldots=0,\ y>0,|z|<1, \tag{168}$$

$$\left(\frac{\partial^2\Pi_2^{(0)u}}{\partial z^2}-{}_2^1 D\left(p+\mathrm{At}\right)\Pi_2^{(0)u}\right)+\varepsilon\left(\frac{\partial^2\Pi_2^{(1)u}}{\partial z^2}-{}_2^1 D\left(p+\mathrm{At}\right)\Pi_2^{(1)u}\right)+\ldots=0,\ y>0,\quad z<-1, \tag{169}$$

$$\frac{\partial\Pi^{(0)u}}{\partial z}\Big|_{z=1}+\varepsilon\left(\frac{\partial\Pi^{(1)u}}{\partial z}\Big|_{z=1}-{}_0^1 D\frac{\partial\Pi_1^{(0)u}}{\partial z}\Big|_{z=1}\right)+\ldots=0,\frac{\partial\Pi^{(0)u}}{\partial z}\Big|_{z=-1}+\varepsilon\left(\frac{\partial\Pi^{(1)u}}{\partial z}\Big|_{z=-1}-{}_0^2 D\frac{\partial\Pi_2^{(0)u}}{\partial z}\Big|_{z=-1}\right)+\ldots=0, \tag{170}$$

$$\left(\Pi^{(0)\dot{e}}-\Pi_1^{(0)u}+\varepsilon\left(\Pi^{(1)u}-\Pi_1^{(1)u}\right)+\ldots\right)\Big|_{z=1}=0,\left(\Pi^{(0)u}-\Pi_2^{(0)u}+\varepsilon\left(\Pi^{(1)u}-\Pi_2^{(1)u}\right)+\ldots\right)\Big|_{z=-1}=0, \tag{171}$$

$$\Pi^{(0)u}\Big|_{y=0}+\varepsilon\left(\rho^{(1)u}+\Pi^{(1)u}\right)\Big|_{y=0}+\ldots=0, \tag{172}$$

$$\left(\Pi^{(0)u}+\varepsilon\Pi^{(1)u}+\ldots\right)\Big|_{y\to\infty}=0,\left(\Pi_1^{(0)u}+\varepsilon\Pi_1^{(1)u}+\ldots\right)\Big|_{y+z\to\infty}=0,\left(\Pi_2^{(0)u}+\varepsilon\Pi_2^{(1)u}+..\right)\Big|_{y+|z|\to\infty}=0. \tag{173}$$

The problem for the zero coefficients has only the trivial solution

$$\Pi^{(0)u}=\Pi_1^{(0)u}=\Pi_2^{(0)u}=0. \tag{174}$$

The problem for the first coefficient is divided into three independent parts. The first one is the problem for the boundary layer functions in the layer of the form

$$\frac{\partial^2 \Pi^{(1)u}}{\partial z^2} - \left(p + \mathrm{At}\right)\frac{\partial \Pi^{(1)u}}{\partial y} = 0, y > 0, \quad |z| < 1, \tag{175}$$

$$\frac{\partial \Pi^{(1)u}}{\partial z}\Big|_{z=1} = \frac{\partial \Pi^{(1)u}}{\partial z}\Big|_{z=-1} = 0, \tag{176}$$

$$\Pi^{(1)u}\Big|_{y=0} = -\rho^{(1)u}\Big|_{y=0} = -\sqrt{p + \mathrm{At}}\,\frac{{}^1_0 D}{2}\left[\left(\frac{1}{6} - \frac{z^2}{2}\right)\left(1 + \sqrt{{}^2_1 D}\right) - z\left(1 - \sqrt{{}^2_1 D}\right)\right], \tag{177}$$

$$\Pi^{(1)u}\Big|_{y\to\infty} = 0. \tag{178}$$

The solution to this problem found by the method of separation of variables and is defined by the formula

$$\begin{aligned}\Pi^{(1)u} = {} & \frac{4\sqrt{p + \mathrm{At}}\,{}^0_1 D}{\pi^2}\left(1 - \sqrt{{}^2_1 D}\right)\sin\left(\frac{\pi}{2}z\right)\exp\left(-\left(\frac{\pi}{2}\right)^2 \frac{{}^0_1 D}{\mathrm{Pd}}y\right) + \\ & + \frac{\sqrt{p + \mathrm{At}}\,{}^0_1 D}{\pi^2}\sum_{n=1}^{\infty}\left(4\frac{(-1)^n}{(1+2n)^2}\left(1 - \sqrt{{}^2_1 D}\right)\sin\left[\left(\frac{\pi}{2} + \pi n\right)z\right]\exp\left(-\left(\frac{\pi}{2} + \pi n\right)^2 \frac{{}^0_1 D}{\mathrm{Pd}}y\right) + \right. \\ & \left. + \frac{(-1)^n}{n^2}\left(1 + \sqrt{{}^2_1 D}\right)\cos(\pi n z)\exp\left(-(\pi n)^2 \frac{{}^0_1 D}{\mathrm{Pd}}y\right)\right).\end{aligned} \tag{179}$$

Returning to the original, we obtain an expression for the first coefficient of expansion of the boundary-layer functions in the layer

$$\begin{aligned}\Pi^{(1)} = {} & \frac{{}^0_1 D}{\pi^2}\left(\frac{\exp(-t\cdot \mathrm{At})}{\sqrt{\pi t}} + \sqrt{\mathrm{At}}\,erf\sqrt{t\cdot Ad}\right)\times\left\{4\left(1 - \sqrt{{}^2_1 D}\right)\sin\left(\frac{\pi}{2}z\right)\exp\left(-\left(\frac{\pi}{2}\right)^2 \frac{{}^0_1 D}{\mathrm{Pd}}y\right) + \right. \\ & + \sum_{n=1}^{\infty}\left(4\frac{(-1)^n}{(1+2n)^2}\left(1 - \sqrt{{}^2_1 D}\right)\sin\left[\left(\frac{\pi}{2} + \pi n\right)z\right]\exp\left(-\left(\frac{\pi}{2} + \pi n\right)^2 \frac{{}^0_1 D}{\mathrm{Pd}}y\right) + \right. \\ & \left.\left. + \frac{(-1)^n}{n^2}\left(1 + \sqrt{{}^2_1 D}\right)\cos(\pi n z)\exp\left(-(\pi n)^2 \frac{{}^0_1 D}{\mathrm{Pd}}y\right)\right)\right\}.\end{aligned} \tag{180}$$

http://dx.doi.org/10.5772/56042

Equation (180) allows determining the boundary values of the first boundary layer coefficients for the surrounding half-spaces, the problem to determine which are the following:

$$\frac{\partial^2 \Pi_1^{(1)u}}{\partial z^2} - \left(p + \mathrm{At}\right)\Pi_1^{(1)u} = 0, z > 1, \Pi_1^{(1)u}\Big|_{z=1} = \Pi^{(1)u}\Big|_{z=1}, \Pi_1^{(1)u}\Big|_{y+z\to\infty} = 0, \tag{181}$$

$$\frac{\partial^2 \Pi_2^{(1)u}}{\partial z^2} - {}_2^1 D\left(p + \mathrm{At}\right)\Pi_2^{(1)u} = 0, z < -1, \Pi_2^{(1)u}\Big|_{z=-1} = \Pi^{(1)u}\Big|_{z=-1}, \Pi_2^{(1)u}\Big|_{y+|z|\to+\infty} = 0\,. \tag{182}$$

Solutions to (181), (182) is represented through $\Pi^{(1)u}$ by the following form:

$$\Pi_1^{(1)u} = \Pi^{(1)u}\Big|_{z=1} \exp\left(-\sqrt{p + \mathrm{At}}\left(z-1\right)\right) \tag{183}$$

$$\Pi_2^{(1)u} = \Pi^{(1)u}\Big|_{z=-1} \exp\left(\sqrt{{}_2^I D\left(p + \mathrm{At}\right)}\left(z+1\right)\right) \tag{184}$$

which in the originals are represented as

$$\begin{aligned}
\Pi_1^{(1)} = \Bigg\{ & \frac{1}{\sqrt{\pi t}} \exp\left(-t\cdot \mathrm{At} - \frac{\left(z-1\right)^2}{4t} \right) - \frac{\sqrt{\mathrm{At}}}{2}\Bigg[\exp\Big[\left(z-1\right)\sqrt{\mathrm{At}}\Big] \operatorname{erfc}\left(\frac{z-1}{2\sqrt{t}} + \sqrt{t\cdot \mathrm{At}} \right) - \\
& - \exp\Big[-\left(z-1\right)\sqrt{\mathrm{At}}\Big] \operatorname{erfc}\left(\frac{z-1}{2\sqrt{t}} - \sqrt{t\cdot \mathrm{At}} \right)\Bigg]\Bigg\}\Bigg(\frac{4\,{}_1^0 D}{\pi^2}\left(1 - \sqrt{{}_1^2 D}\right) \exp\left[-\left(\frac{\pi}{2}\right)^2 \frac{{}_1^0 D}{\mathrm{Pd}} y \right] + \\
& + \frac{{}_1^0 D}{\pi^2} \sum_{n=1}^{\infty} \Bigg(\frac{4\left(-1\right)^{2n}}{\left(1+2n\right)^2}\left(1 - \sqrt{{}_1^2 D}\right) \exp\left[-\left(\frac{\pi}{2} + \pi n\right)^2 \frac{{}_1^0 D}{\mathrm{Pd}} y \right] + \\
& + \frac{\left(-1\right)^{2n}}{n^2}\left(1 + \sqrt{{}_1^2 D}\right) \exp\left[-\left(\pi n\right)^2 \frac{{}_1^0 D}{\mathrm{Pd}} y \right] \Bigg) \Bigg),
\end{aligned} \tag{185}$$

$$\Pi_2^{(1)} = \left\{ \frac{1}{\sqrt{\pi t}} \exp\left(-t \cdot Ad - \frac{{}_1^2 D (z+1)^2}{4t} \right) - \right.$$
$$- \frac{\sqrt{\mathrm{At}}}{2} \left[\exp\left[-(z+1)\sqrt{{}_1^2 D\,\mathrm{At}} \right] \mathrm{erfc}\left(\sqrt{t \cdot \mathrm{At}} - \frac{(z+1)\sqrt{{}_1^2 D}}{2\sqrt{t}} \right) - \right.$$
$$\left. \left. - \exp\left[(z+1)\sqrt{{}_1^2 D\,\mathrm{At}} \right] \mathrm{erfc}\left(-\frac{(z+1)\sqrt{{}_1^2 D}}{2\sqrt{t}} - \sqrt{t \cdot \mathrm{At}} \right) \right] \right\} \times$$
$$\times \left(\frac{4\,{}_1^0 D}{\pi^2} \left(\sqrt{{}_1^2 D} - 1 \right) \exp\left[-\left(\frac{\pi}{2} \right)^2 \frac{{}_1^0 D}{\mathrm{Pd}} y \right] + \right.$$
$$+ \frac{{}_1^0 D}{\pi^2} \sum_{n=1}^{\infty} \left(\frac{4(-1)^{2n+1}}{(1+2n)^2} \left(1 - \sqrt{{}_1^2 D} \right) \exp\left[-\left(\frac{\pi}{2} + \pi n \right)^2 \frac{{}_1^0 D}{\mathrm{Pd}} y \right] + \right.$$
$$\left. \left. + \frac{(-1)^{2n}}{n^2} \left(1 + \sqrt{{}_1^2 D} \right) \exp\left[-(\pi n)^2 \frac{{}_1^0 D}{\mathrm{Pd}} y \right] \right) \right). \tag{186}$$

The solution to the nonstationary problem (44) - (50) in the asymptotic approximation, taking into account the boundary-layer functions, represented as the sum of (134), (161) and (180) in the layer and, relevantly, for the surrounding area

$$\rho = \rho^{(0)} + \varepsilon\left(\rho^{(1)} + \Pi^{(1)} \right), \rho_1 = \rho_1^{(0)} + \varepsilon\left(\rho_1^{(1)} + \Pi_1^{(1)} \right), \rho_2 = \rho_2^{(0)} + \varepsilon\left(\rho_2^{(1)} + \Pi_2^{(1)} \right). \tag{187}$$

6. Conclusion

Figure 2 shows the dependence (134), the density of radioactive contaminants on the radial coordinate in the zero approximation for different times of injection with (curves 1, 2, 3) and without (curve 4), radioactive decay, as well as in diffusional approximation (curve 5). In many technological and non-technological liquid wastes of atomic industry, as one of the component contains a radioactive isotope of strontium Sr_{90}^{38} with a half-life $T_{1/2}$=28years, which is a very dangerous chemical element for the biological structures due to its ability to replace atoms of calcium. Calculated options: half-thickness of the layer h = 1m, the diffusion coefficients D_{1z}= D_{2z} =10^{-11}m^2/c, D_z=10^{-9} m^2/c; borehall radius of 0.1 m, the polluter - Strontium 90; activity of the solution - 1 Ci / l (high level waste), the initial density of radioactive substances in the solution 7.34 g/m^3; injection volume 100 m^3/day (At = 75.8, Pe =1.84 10^7)

http://dx.doi.org/10.5772/56042

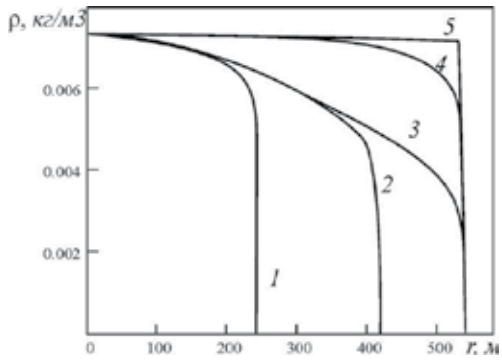

Figure 2. Plots of density on distance for different times of observation: Given the radioactive decay of *1* - 5 years, *2* - 15 years old, *3* - 25 years, *4* - 25 years (in the absence of decay At = 0), *5* - 25 years (in the absence of decay in non-diffusive approximation)

Figure 2 allows carrying out estimate of the contribution of diffusion and radioactive decay. The figure shows that the account of the radioactive decay (see curves 3 and 4) is the priority in comparison with the account of the mass transfer of the layer (curves 4 and 5) with the surrounding formations by diffusion. The figure also implies that the contribution of diffusion is essential in the front zone of radioactive contamination, where it is comparable with the magnitude of the density of matter in solution. With the zero approximation the size of the zone of contamination are determined.

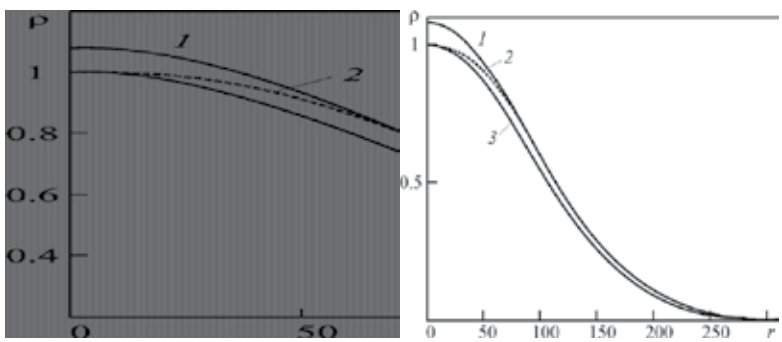

Figure 3. The dependence of the density of radioactive contaminants on the radial coordinate for the dimensionless time $t = 0.01$ (a), $t = 0.001$ (b): *1.2* - without and with taking into account the boundary-layer correction, respectively, *3* - zero approximation at $z = 0$

On the fig. 3 a, b it is shown that taking into account the boundary layer solution eliminates the disadvantage of the first approximation, which consists in the fact that the density of radioactive contaminants exceeds one (curve 1). In the calculations agreed: $\mathrm{Pd}=2\cdot 10^7$, ${}_1^0D=0.01$, ${}_1^2D=1$, $\varepsilon=0.05$, Ad = 2200, which corresponds to the half-life $T_{1/2}=1$ year. Boundary layer correction results in the behavior of the curve in accordance with the conditions of the problem (see curves 1, 2) and at the same time clarifies the first approximation. Note that for

short times accounting of the first expansion coefficient leads to refinements of the design parameters up to 20% (curves 1 and 3 in Fig.3 b). At the same time the importance of taking into account the boundary-layer functions in the near-well zone is illustrated (r <70).

As the figure 3 b shows, on the border of the front distribution of contaminants occurs a sharp jump of density, indicating the presence of internal moving boundary layer, the patterns of which have not been investigated, and mathematical methods of eliminating it - not developed.

Appendix: Note on the stationary solution to the problem

It is extremely important to find a stationary solution to set the maximum size of the zone of contamination. The equations describing the stationary regime are obtained from (44) - (50) if we consider the first term $(\partial \rho_i / \partial t)$ to be zero. The solution to this problem is given in [39, 40, 43]. Here we note that the solution to the stationary problem can be obtained from the first asymptotic approximation for $t \to \infty$.

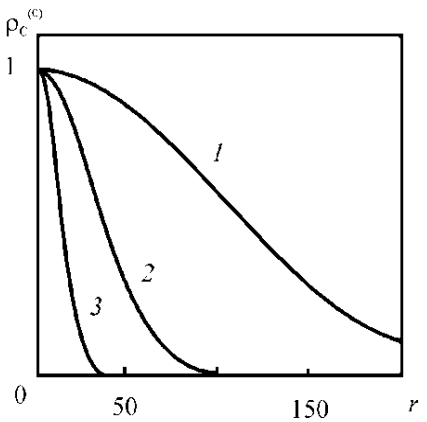

Figure 4. The dependence of the densities of radioactive contaminants in the porous layer for the stationary case (zero approximation) on the distance from the borehole at different decay constants: *1* - Ad = 0.01, *2* - 0.1, *3* - 1. Other parameters: Pd = 10^2, $\delta = 10^{-4}$, $D_1^2 = 1$

Fig. 4 shows the dependence of the density of radioactive contaminants on the radial coordinate at the center of layer for various radioactive contaminants: curve *1* - ^{239}Pu ($T_{1/2}$ = 2,24 10^4 years), curve *2* – ^{226}Ra ($T_{1/2}$ = 1590 years), curve *3* – ^{90}Sr ($T_{1/2}$ = 28 years).

The zero approximation in this case is the most important; it determines the general form of the dependence. The value of the density of the pollutant decreases exponentially, and as follows from the graphs, even for the middle half-life and most dangerous radionuclides (^{90}Sr, ^{137}Cs) at distances of 200 h (200 m) of the order of percent of maximum, observed in the area of injection.

http://dx.doi.org/10.5772/56042

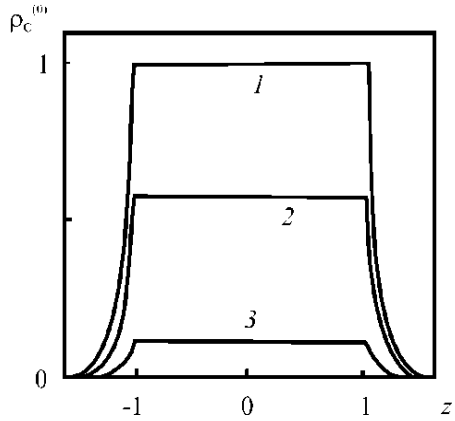

Figure 5. The dependence of the density radioactive contaminants in the stationary case (zero approximation) on the *z* coordinate at different distances from the borehole: *1* - $r = 0$, *2* – 100, *3* - 200. Other parameters: Ad = 0.01, Pd = 10^2, $\delta = 10^{-4}$, $D_1^2 = 1$

Figure 5 shows a picture of the field distribution of the radioactive contaminant in the stationary case along the vertical coordinate (zero approximation). "Slices" are given for distances 0, 100*h* and 200*h* from the axis of borehall. We see that for the middle half-life nuclides ($T_{1/2}$ ~ 30 years) in the covering and underlying layers pollutant density decreases rapidly, and even at distances of 0,5*h* are negligible.

In general, the increase in the parameter Pd (rate of the injection of the solutions) leads to the "elongation" of the graphic along the radial direction, reducing the At (which corresponds to an increase in the average lifetime of the nuclide) - to "enhance" the graph along the axes *r* and *z*. The field of pollutant remains limited.

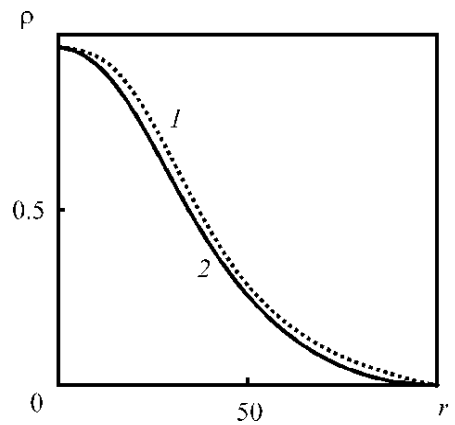

Figure 6. The dependence of the density of radioactive contaminant on the distance to the borehole axis Graphs are constructed (for the dimensionless time t = 100): the grid method - *1* and the method of asymptotic expansion - *2*. Other parameters: At = 0.1, Pd = 102, $\delta = 10^{-3}$, $D_1^2 = 1$

Fig. 6 shows the results obtained using a modified method of asymptotic expansions and the numerical solution to the problem of mass transfer by the grid method. Numerically was solved the problem (67) - (74), neglecting the radial diffusion.

Comparisons of the curves shown in Fig. 6 allow to conclude that the results obtained by numerical and asymptotic methods are in a good agreement.

So, based on the asymptotic method, approximated analytical solution to the problem of subterranean waste disposal is obtained, and accounting the boundary layer correction allows to provide the calculation of the areas of radioactive contaminants in the subterranean horizons with high accuracy at all distances from the injection borehall, and thus to clarify the forecast of the areas of radioactive contamination to ensure the environmental safety.

In conclusion, note that the above modification of the asymptotic method is quite general and provides the construction of "exact on the average" analytical solutions as to the nonstationary problem of the underground waste disposal as well as to the other problems of underground thermo- and hydrodynamics. The zero approximation of the asymptotic solution is of the particular importance, because it describes the average value of the variables, which is important for many practical problems.

List of designations

A, B, C, E, F,M	–	auxiliary functions;
α, Ad, At	–	dimensional and dimensionless constants for radioactive decay for the diffusion and the temperature problem, respectively, 1/c;
λ_{z1}, λ_z, λ_{z2}, λ_{r1}, λ_r, λ_{r2}		coefficients of thermal conduction for the covering, porous, and the underlying layers in the vertical and radial directions, respectively, W/(m·K);
ρ_n, ρ_{n1}, ρ_{n2}	–	density of the porous, covering and underlying layers, kg/m^3;
ρ_d, ρ_{1d}, ρ_{2d}	–	dimensional concentration of the impurity in a porous, covering and underlying layers, kg/m^3;
ρ_f , ρ_s		dimensionless densities of the impurity in the carrier, the skeleton;
D_r,D_{1r}, D_2 , D_z,D_{1z}, D_{2z}	–	coefficients of diffusion of the layers in the radial and vertical directions, m^2/s;
$\delta_{i,j}$	–	the Kronecker delta,
μ_s, μ_w	–	chemical potentials of the skeleton and water, respectively
$g(\mu_s, \mu_w)$	–	function of the mass transfer between the skeleton and the fluid;
H, h	–	power and half-thickness of the porous layer, m;
K_r	–	Henry's coefficient;
$\bar{L}$	–	differential operator;

http://dx.doi.org/10.5772/56042

Pd	–	analog of the parameter Peclet;
R_p	–	radiuses of the radionuclide contamination;
p, s	–	parameters of the Laplace-Carson,;
r_0	–	radius of the bonehole, m;
r_d, z_d, r, z	–	dimensional and dimensionless cylindrical coordinates, m;
τ, t	–	dimensional and dimensionless time, s;
m, m_0 , m_1	–	effective, initial and maximum porosity;
v	–	filtration rate, m/s;
	–	rate of convective transport of contaminant in the porous layer, m/s;
w	–	the true velocity of the fluid, m/s;
q_d, q	–	dimensional and dimensionless source function (mass, kg/(s·m^3);)
k, k_1, k_2	–	stoichiometric coefficients;
$\theta, \theta_1, \theta_2$	–	the remainder term of the asymptotic expansion in a porous, covering and underlying layers.

Author details

Mikhaylov Pavel Nikonovich[1], Filippov Alexander Ivanovich[1] and
Mikhaylov Aleksey Pavlovich[2*]

*Address all correspondence to: a.p.mikhaylov@gmail.com

1 Institute of Applied Researches, Sterlitamak, Bashkortostan, Russia

2 Department of General and Applied Physics, Moscow Institute of Physics and Technology, Dolgoprudny, Russia

References

[1] Barenblatt G. I., Entov V. M. Ryzhik V. M. The movement of liquids and gases in natural reservoirs // - Moscow: Nedra. 1984. 211 p.

[2] Bear J. Dynamics of fluids in porous media. New York: American Elsevier publ. 1967. – 764 p.

[3] Bear J. Hydraulics of groundwater. New York etc.: McGraw-Hill Inc. 1979. XIII. – 567 p.

[4] Bear J., Bachmat Y. Introduction to modeling of transport phenomena in porous media / Dordrecht et al.: Kluwer. 1990. – 533 p.

[5] Bachmat Y and Bear J. Mathematical formulation of transport phenomena in porous media. Proc. Int. Symp. of IAHR on the Fundamentals of Transport Phenomena in Porous Media, Guelph, Canada. 1972. 174–197.

[6] Ilyushin A. A. Continuum Mechanics. - Moscow: Moscow State University. 1979. 288 p.

[7] Case V. M. Convective heat and mass transfer. - Moscow: Energiya. 1972. 448 p.

[8] Landau L. D., editor. Landau L. D. and Lifshitz E. M. Continuum mechanics - Moscow: Gostekhizdat. 1954. 795 p.

[9] Nigmatulin R. I. Fundamentals of the mechanics of heterogeneous environments. - Moscow: Nauka. 1978. 336 p.

[10] Nicholaevskij V. N. Mechanics of porous and fractured environments. - Moscow: Nedra. 1984. – 232 p.

[11] Nicholaevskij V. N, Basniev K. S., Gorbunov A. T., Zotov G. A. The mechanics of saturated porous layers - Moscow: Nedra. 1970. 336 p.

[12] Sedov L. I., Continuum Mechanics. - Moscow: Nauka. 1994. Vol. 1 and 2.

[13] Prakash A. Radial dispersion through adsorbing porous media. Proc. Am. Soc. civ. Engrs, 102 (HY3). 1976. 379 – 396.

[14] Barmin A. A., Garagash D. I. On the filtration of the solution in a porous layer taking into account the adsorption of impurities on the skeleton // Mechanics of liquids and gases. 1994. - № 4. 97-110.

[15] Bondarev E. A. Convective diffusion in porous layers, with taking into account the phenomenon of adsorption / Bondarev E. A., Nikolaev V. N. // PMTF, 1962. Number 5. 128 - 134.

[16] Zhemzhurov M. L., Serebrynij G. Z. Analytical model of radionuclide migration in porous layers // Journal of Engineering Physics. 2003. - T. 76. - № 6. 146 - 150.

[17] Zhemzhurov M. L., Serebrynij G. Z. Two-dimensional convective diffusion of radioactive impurities with taking into account the sorption in porous layers // Journal of Engineering Physics. 2008. - T. 81. - № 3. 417 - 420.

[18] Venetsianov E. V., Rubenstein R. N. Sorption dynamics of fluids. - Moscow: Nauka. 1983. 237 p.

[19] Philip J. R. Flow through porous media. Ann. Rev. Fluid Mechan. 1970. – 2. 177 – 204.

[20] Mikhaylov P. N., Filippov A. I. Asymptotic solution of the temperature field in a well with accout for the radial-velocity distribution // Journal of Engineering Physics and Thermophysics. – 2005. – V. 78. – № 4. 87 – 90.

[21] Mikhaylov P. N., Filippov A. I., Filippov K. A., Bagautdinov R, Potapov A. Temperature Field in Oil-Gas Beds Exposed to the Action of an Acid // Journal of Engineering Physics and Thermophysics. – 2005. – V. 78. – № 2. 256 – 271.

[22] Collins R. Fluid flows through porous materials. - Moscow: Mir 1964. 350.

[23] Lebedev A. V. Assessment of the balance of groundwater. - Moscow: Nedra. 1989. 178 p.

[24] Lukner L., Shestakov V. M. Modeling the migration of groundwater - Moscow:Nedra.1986. 209 p.

[25] Swing R. E. Simulation techniques for multicomponent flows // Commun. Appl. Numer. Meth. 1988. – V.4. – № 3. 335 – 342.

[26] Belitsky, A. S., Orlova E. I. Protection of underground water from radioactive contamination - Moscow: Medicine. 1969. - 209 p.

[27] Rybalchenko A. I., Pimenov M. K., Kostin P. P. et al., Deep burial of the radioactive waste, Moscow IzdAT. 1994. – 256 p.

[28] Sox M. D., Noskov M. D., Istomin A. D., Kessler A., Zubkov A. A. and Zakharova E. V. Modeling the distribution of radionuclides in the reservoir during deep burial of acidic liquid waste // Radiochemistry. 2007. - T. 49. - № 2. - 182 - 187.

[29] Larin V. K., Zubkov A. A., Kesler A. G. Modeling of the distribution of radionuclides in the reservoir during the deep burial of the acidic liquid waste. // Atomic energy. 2002. - T. 92. - № 6. 451 - 455.

[30] Kosareva I. M., Savushkina M. K., Arkhipova M. M., Wolin M., Kabakchi S. A., Egorov N. N., Rakow N. A., Kudryavtsev E. G. Temperature field in the deep disposal of liquid radioactive waste // Atomic Energy, 1998. - T. 85. - № 6. - 441 - 448.

[31] Kosareva I. M., Savushkina M. K., Arkhipova M. M., Wolin M., Kabakchi S. A., Egorov N. N., Rakow N. A., Kudryavtsev E. G. Temperature field in the deep disposal of liquid radioactive waste: modeling multi-step removal // Atomic Energy. 2000. - T. 89. - № 6. - 435 - 440.

[32] Kosarev I. M., Savushkina M. K. The temperature field in the deep disposal of liquid radioactive waste // Atomic Energy, 1998. - T. 85. - № 6. 441 - 448.

[33] Kosarev I. M., Savushkina M. K. The temperature field in the deep disposal of liquid radioactive waste: modeling of multi-stage disposal // Atomic energy. 2000. - T. 89. - № 6. 435 - 440.

[34] Rybalchenko A. I., Pimenov M. K., Kostin P. P. The deep disposal of liquid radioactive waste - Moscow IzdAT. 1994. 256 p.

[35] Chekalyuk E. B. Fundamentals piezometry of oil and gas deposits.- Kiev: GITL UkrSSR. 1965.-286 p.

[36] Mikhaylov P. N., Filippov A. I., Guenther D. A , Ivanov D. V. "Exact on the average" asymptotic solution of the problem of underground radioactive waste disposal / Journal of Kherson National Technical University. B. 2 (28). - Kherson: KNTU. 2007. 365 - 370.

[37] Mikhaylov P. N., Filippov A. I., Mickhaylichenko I. N., editor. Sabitov C. B. Field of concentration in the injection of fluid solutions of radioactive impurities in the deep layers / / Modern problems of physics and mathematics. Proceedings of the Russian Scientific Conference (16 - 18 September 2004, Sterlitamak) - Ufa: Guillem. 2004. 89 - 97.

[38] Gurov K. P. Phenomenological thermodynamics of irreversible processes. - Moscow: Nauka. 1978. 128 p.

[39] Mikhaylov P. N., Filippov A. I., Ivanov D. I. "Exact on the average" asymptotic solution to the problem of mass transfer during the underground disposal of liquid radioactive waste / Differential Equations and Related Topics: Proceedings of the International Conference (24 - 28 June 2008, Sterlitamak). - T. III. - Ufa: Guillem. 2008. 238 - 258.

[40] Mikhaylov P. N., Filippov A. I., Guenther D. A., Ivanov D. V. The asymptotic solution to the problem of the underground disposal of radioactive waste // Siberian Journal of Industrial Mathematics. 2008. - T. XI. - № 2 (34). 124 - 138.

[41] Mikhaylov P. N., Filippov A. I. The concept of "Exact on the average" asymptotic solution to the problem of the underground disposal of nuclear waste / SamDif 2007: Conference "Differential Equations and Their Applications", Samara, 29 - February 2, 2007 Abstracts. - Samara Universe groups. - 2007. 149 - 150.

[42] Mikhaylov P. N., Filippov A. I., Guenther D. A., Ivanov D. V. On the construction of asymptotic solutions to the problems of conjugation/ / Journal of Computational Mathematics and Mathematical Physics. 2008. - T. 48. - № 11. 2046 - 2057.

[43] Mikhaylov P. N., Filippov A. I., Mickhaylichenko I. N. Determination of the contamination zones in the underground disposal of solutions of radioactive dissolved substances // Bulletin of Kherson National Technical University. B. 2 (25). - Kherson: KSNTU. 2006. 508 - 511.

[44] Mikhaylov P. N., Filippov A. I., Fattakhov R. G., Ivanov D. V.. Garifullin R. N., Guenther D. A. Boundary layer solution to the problem of mass transport of radioactive contaminants // Eurasian integration processes in science, education and produc-

tion: Proceedings of the Russian Scientific Conference (Kumertau, 19-20 October 2006) - Ufa: Guillem. 2006. 177 - 186.

[45] Mikhaylov P. N., Filippov A. I., Ivanov D. A., Guenther D. A. Temperature and concentration fields in the deep disposal of radioactive multicomponent solutions // Modern science: research, ideas, results, and technology. № 1, 2009. Series: Actual problems of thermophysics and physical hydrodynamics. Special issue based on the 7th Conference 21 - 25 September 2009, Alushta. 75 - 76.

[46] Mikhaylov P. N., Filippov A. I., Guenther D. A. The calculation of interrelated fields of concentration and temperature of fluids in the injection of radioactive solutions into the porous layer // Review of Industrial and Applied Mathematics. 2007. - T. 14. - V. 4. 754 - 755.

[47] Filippov A. I., Mikhaylov P. N., Mickhaylichenko I. N. Field of concentration in the injection of aqueous solutions of radioactive impurities in the deep layers // Review of Industrial and Applied Mathematics. 2004. - T. 11. - V. 3. 595 - 596.

[48] Filippov A. I., Mikhailov P. N., Guenther D. A., Ivanov D. V. Fields of concentration of radioactive materials // Journal of Engineering Physics. 2008. - T. 81. - № 5 912 - 923.

[49] Filippov A. I, Mickhaylichenko I. N., Guenther D. A. Construction of the "exact on the average" of the asymptotic solution of the stationary problem of filtration of radioactive solutions // Proceedings of the Sterlitamak branch of Bashkortostan Academy of Sciences. A series of "Physical-mathematical and engineering sciences." B. 4. - Ufa: Guillem. 2006. 64 - 74.

[50] Filippov A. I., Mikhaylov P. N., Mickhaylichenko I. N., Krupinov A. G. The calculation of concentration fields in the underground disposal of solutions of radioactive dissolved substances // Ecological systems and devices. 2006. - № 5. 27 - 33.

[51] Ditkin V. A. and Prudnikov A. P. Reference guide to the operational calculation. - M.: High School, 1965. - 465 p.

Section 2

Advances in Numerical Analysis with Measurements

Chapter 10

Study of Effect of Temperature Radient on Solid Dissolution Process Under Action of Transverse Rotating Magnetic Field

Rafał Rakoczy, Marian Kordas and Stanisław Masiuk

Additional information is available at the end of the chapter

http://dx.doi.org/10.5772/51296

1. Introduction

The design, scale-up and optimization of industrial processes conducted in agitated systems require, among other, precise knowledge of the hydrodynamics, mass and heat transfer parameters and reaction kinetics. Literature data available indicate that the mass-transfer process is generally the rate-limiting step in many industrial applications. Because of the tremendous importance of mass-transfer in engineering practice, a very large number of studies have determined mass-transfer coefficients both empirically and theoretically. From the practical point of view, the agitated systems are usually employed to dissolve granular or powdered solids into a liquid solvent [3].

Transfer of the solute into the main body of the fluid occurs in the three ways, dependent upon the conditions. For an infinite stagnant fluid, transfer will be by the molecular diffusion augmented by the gradients of temperature and pressure. The natural convection currents are set up owing to the difference in density between the pure solvent and the solution. This difference in inducted flow helps to carry solute away from the interface. The third mode of transport is depended on the external effects. In this way, the forced convection closely resembles natural convection expect that the liquid flow is involved by using the external force.

One of the key aspects in the dynamic behaviour of the mass-transfer processes is the role of hydrodynamics. On a macroscopic scale, the improvement of hydrodynamic conditions can be achieved by using various techniques of mixing, vibration, rotation, pulsation and oscillation in addition to other techniques like the use of fluidization, turbulence promotes or magnetic and electric fields etc. The transverse rotating magnetic field (TRMF) is a versatile

option for enhancing several physical and chemical processes. Studies over the recent decades were focused on application of magnetic field (MF) in different areas of engineering processes [21, 22]. Static, rotating or alternating MFs might be used to augment the process intensity instead of mechanically mixing. The practical applications of TRMF are presented in the relevant literature [6, 16, 18, 23, 26, 27, 29].

Recently, TRMF are widely used to control different processes in the various engineering operations [2, 9, 10]. This kind of magnetic field induces a time-averaged azimuthal force, which drives the flow of the electrical conducting fluid in circumferential direction. According to available in technical literature, the mass-transfer during the solid dissolution to the surrounding liquid under the action of TRMF has been deliberated [21, 22]. These papers present literature survey for the applications of magnetic field (MF) and the magnetically assisted fluidization (MAF) in the mass transfer enhancement.

It should be noticed that the temperature gradient induces buoyancy-driven convective flow in the fluid. This temperature gradient has a significant practical interest to the mass transfer process. It is reported that the difference between the surface temperature of solid sample and the liquid temperature has strong influence on the dissolution process [1].

The main objective of the present study is to investigate the solid dissolution process that is induced under the action of TRMF and the gradient temperature between solid surface and liquid. According to the information available in technical literature, the usage of TRMF and gradient temperature is not theoretical and practical analyzed. The obtained experimental data are generalized by using the empirical dimensionless correlations.

2. Theoretical background

2.1. Equation of magnetic induction

The flow under the action of TRMF may be determined by taking into consideration the following magnetohydrodynamic Ohm law

$$\frac{1}{\mu_m} rot\,\bar{B} = \bar{J} \tag{1}$$

The current density ($\bar{J}$) and the total electric field current ($\bar{E}$) may be expressed as follows

$$\bar{J} = \sigma_e \left[\bar{E} + \left(\bar{w} \times \bar{B} \right) \right] \tag{2}$$

$$\bar{E} = -\bar{w} \times \bar{B} + \frac{rot\,\bar{B}}{\sigma_e \mu_m} \tag{3}$$

The general Eq.(3) may be rewritten as:

http://dx.doi.org/10.5772/51296

$$rot\,\overline{E} = -rot\left(\overline{w}\times\overline{B}\right) + \frac{rot\,rot\,\overline{B}}{\sigma_e \mu_m} \tag{4}$$

Taking into consideration the following expressions

$$\Delta\overline{B} = -rot\,rot\,\overline{B} + grad\,div\,\overline{B} \tag{5}$$

$$rot\,\overline{E} = -\frac{\partial\overline{B}}{\partial\tau} \tag{6}$$

$$div\,\overline{B} = 0 \tag{7}$$

we obtain from the Eq.(3) the well-known advection-diffusion type relation [8, 17]

$$\frac{\partial\overline{B}}{\partial\tau} = rot\left(\overline{w}\times\overline{B}\right) + \frac{\Delta\overline{B}}{\sigma_e\mu_m} \tag{8}$$

The above equation (8) is also called the induction equation and it characterizes the temporal evolution of the magnetic field where

$$\nu_m = \frac{1}{\sigma_e\mu_m} \tag{9}$$

is effective diffusion coefficient (magnetic viscosity or magnetic diffusivity).

Taking into accunt the above relation, Eq. (8) may be revritten in the following form

$$\frac{\partial\overline{B}}{\partial\tau} = rot\left(\overline{w}\times\overline{B}\right) + \nu_m\Delta\overline{B} \tag{10}$$

The term, $rot(\overline{w}\times\overline{B})$, in Eq.(8) dominates when the conductivity is large, and can be regarded as describing freezing of MF lines into the liquid. The term, $\nu_m\Delta\overline{B}$, in the B-field equation may be treated as a diffusion term. When the electrical conductivity, σ_e, is not too large, MF lines diffuse within the fluid.

Taking into account the below definitions of the dimensionless parameters

$$\overline{B}^* = \frac{\overline{B}}{B_0};\ \tau^* = \frac{\tau}{\tau_0};\ \overline{w}^* = \frac{\overline{w}}{w_0};\ l^* = \frac{l}{l_0};\ \nu_m^* = \frac{\nu_m}{\nu_{m_0}};\ rot^* = \frac{rot}{l_0^{-1}};\ \Delta^* = \frac{\Delta}{l_0^{-2}};\ \frac{\partial}{\partial\tau^*} = \frac{1}{\tau_0^{-1}}\frac{\partial}{\partial\tau} \tag{11}$$

we get the modified form of the relation (8)

$$\frac{B_0}{\tau_0}\left[\frac{\partial \overrightarrow{B}^*}{\partial \tau^*}\right] = \frac{w_0 B_0}{l_0}\left[rot^*\left(\overrightarrow{w}^* \times \overrightarrow{B}^*\right)\right] + \frac{\nu_{m_0} B_0}{l_0^2}\left[\Delta^* \overrightarrow{B}^*\right] \tag{12}$$

The above form of Eq. (8) may be used to examine the effect of liquid flow on the MF distribution. The non-dimensional forms of these equations may be scaled against the term $\left(\frac{\nu_{m_0} B_0}{l_0^2}\right)$. The dimensionless form of the equation (12) may be expressed by

$$\frac{l_0^2}{\nu_{m_0}\tau_0}\left[\frac{\partial \overrightarrow{B}^*}{\partial t^*}\right] = \frac{w_0 l_0}{\nu_{m_0}}\left[rot^*\left(\overrightarrow{w}^* \times \overrightarrow{B}^*\right)\right] + \left[\Delta^* \overrightarrow{B}^*\right] \tag{13}$$

This equation includes the following dimensionless groups

$$\mathrm{Fo_m} = \frac{\nu_{m_0}\tau_0}{l_0^2} \tag{14}$$

and

$$\mathrm{Re_m} = \frac{w_0 l_0}{\nu_{m_0}} \tag{15}$$

The magnetic Reynolds number (Re_m) is analogous to the traditional Reynolds number, describes the relative importance of advection and diffusion of the MF.

Taking into account the above definitions of the non-dimensional groups (Eqs (14) and (15)), we obtain the following general relationship of the magnetic induction equation

$$\frac{1}{\mathrm{Fo_m}}\left[\frac{\partial \overrightarrow{B}^*}{\partial \tau^*}\right] = \mathrm{Re_m}\left[rot^*\left(\overrightarrow{w}^* \times \overrightarrow{B}^*\right)\right] + \left[\Delta^* \overrightarrow{B}^*\right] \tag{16}$$

It should be noticed that the time of magnetic diffusion, τ_d, may defined as follows

$$\frac{1}{\mathrm{Fo_m}} \sim 1 \Rightarrow \tau_0 \sim \frac{l_0^2}{\nu_{m_0}} \Rightarrow \tau_d = \sigma_e \mu_m l_0^2 \tag{17}$$

Taking into account the following relation

http://dx.doi.org/10.5772/51296

$$rot\left(\overline{w}\times\overline{B}\right)\equiv\overline{B}\,grad\,\overline{w}-\overline{w}\,grad\,\overline{B}+\overline{w}\,div\,\overline{B}-\overline{B}\,div\,\overline{w} \tag{18}$$

we obtain the modified form of Eq. (8)

$$\overline{w}\,grad\,\overline{B}=\frac{\Delta\overline{B}}{\sigma_e\mu_m}\Rightarrow\overline{w}\,grad\,\overline{B}=\nu_m\Delta\overline{B} \tag{19}$$

The governing Eq.(19) may be rewritten in a symbolic shape which is useful in the case of the dimensionless analysis

$$\frac{w_0B_0}{l_0}\left[\overline{w}^*\,grad^*\,\overline{B}^*\right]=\frac{\nu_{m_0}B_0}{l_0^2}\left[\nu_m^*\Delta^*\,\overline{B}^*\right] \tag{20}$$

The above Eq.(20) admits the following relation

$$\frac{w_0B_0}{l_0}\sim\frac{\nu_{m_0}B_0}{l_0^2} \tag{21}$$

where $w_0\equiv\omega_{TRMF}l_0$ and$\Delta^*=\dfrac{\Delta}{l_0^{-2}}\Rightarrow\Delta^*=\dfrac{\Delta}{\delta_0^{-2}}$.

An important consequence of the above expression (Eq.(21)) is that the skin depth (or the penetration depth), δ, may be given as follows

$$\frac{w_0B_0}{l_0}\sim\frac{\nu_{m_0}B_0}{\delta_0^2}\Rightarrow\delta_0\sim\sqrt{\frac{\nu_ml_0}{w_0}}\Rightarrow\delta=\sqrt{\frac{\nu_m}{\omega_{WPM}}} \tag{22}$$

This parameter may be used to describe the well-known skin effect. From the practical point of view, this phenomenon is characterized by the so-called shielding parameter

$$S=\frac{\omega_{WPM}l_0^2}{\nu_m} \tag{23}$$

This dimensionless parameter see (Eq (23)) is usually applied characterize the interaction between the MF and the electrical conductivity of liquid. The condition $S\ll1$ means that MF is not changed by the conducting liquid. On the contrary, the condition $S\gg1$ describes the typical skin effect which means that MF can penetrate into the highly electrically conductive liquid.

2.2. Influence of transverse rotating magnetic field on solid dissolution process

Under forced convective conditions, the mathematical description of the solid dissolution process may be described by means of the differential equation of mass balance for the component *i*

$$\frac{\partial \rho_i}{\partial \tau} + div\left(\rho_i \overline{w_i}\right) = \Phi_i \tag{24}$$

where Φ_i is the mass flux of component *i* (the volumetric mass source of component *i*).

The flux density of component *i* $\left(\overline{J_i}\right)$ may be given by

$$\overline{J_i} = \rho_i \overline{w_i} \tag{25}$$

The diffusion flux density is described by means of the following expression

$$\overline{J_{dyf}} = \rho_i \, dif \, \overline{w_i} \Rightarrow \overline{J_{dyf}} = \rho_i \left(\overline{w_i} - \overline{w}\right) \tag{26}$$

The relation between $\overline{J_i}$ and $\overline{J_{dyf}}$ is defined as

$$\overline{J_i} = \overline{J_{dyf}} + \rho_i \overline{w} \Rightarrow \rho_i \overline{w_i} = \rho_i \left(\overline{w_i} - \overline{w}\right) + \rho_i \overline{w} \tag{27}$$

Including the relation (27) in equation (24) gives the following relationship for the mass balance of component *i*

$$\frac{\partial \rho_i}{\partial \tau} + div\left[\overline{J_{dyf}}\right] + div\left(\rho_i \overline{w}\right) = \Phi_i \tag{28}$$

Introducing the relation

$$div\left(\rho_i \overline{w}\right) = \rho_i \, div\left(\overline{w}\right) + \overline{w} \, grad\left(\rho_i\right) \tag{29}$$

in Eq.(28) gives the mass balance of component *i*

$$\frac{\partial \rho_i}{\partial \tau} + \overline{w} \, grad\left(\rho_i\right) + \rho_i \, div\left(\overline{w}\right) + div\left[\overline{J_{dyf}}\right] = \Phi_i \tag{30}$$

The concentration of component *i* may be expressed as follows

http://dx.doi.org/10.5772/51296

$$c_i = \frac{\rho_i}{\rho} \Rightarrow \rho_i = \rho c_i \tag{31}$$

Taking into account the above equation, we find the modified form of Eq.(30)

$$\frac{\partial(\rho c_i)}{\partial \tau} + \overline{w}\, grad(\rho c_i) + (\rho c_i)\, div\left(\overline{w}\right) + div\left[\overline{J_{dyf}}\right] = \Phi_i \tag{32}$$

Eq.(32) may be rewritten by

$$\frac{\partial(\rho c_i)}{\partial \tau} + \overline{w}\, grad(\rho c_i) = \rho \frac{\partial c_i}{\partial \tau} + \rho \overline{w}\, grad(c_i) + c_i \frac{\partial \rho}{\partial \tau} + c_i \overline{w}\, grad(\rho) \tag{33}$$

or

$$\rho \frac{\partial c_i}{\partial \tau} + \rho \overline{w}\, grad(c_i) + c_i \left[\frac{\partial \rho}{\partial \tau} + \overline{w}\, grad(\rho) + \rho\, div\left(\overline{w}\right) \right] + div\left[\overline{J_{dyf}}\right] = \Phi_i \tag{34}$$

The term in square brackets is so-called the continuity equation and this relation may be simplified in the following form

$$\frac{\partial \rho}{\partial \tau} + \overline{w}\, grad(\rho) + \rho\, div\left(\overline{w}\right) = 0 \Rightarrow \frac{d\rho}{d\tau} + div\left(\rho \overline{w}\right) = 0 \tag{35}$$

This leads to the final expression for the mass balance of component *i*:

$$\rho \frac{\partial c_i}{\partial \tau} + \rho \overline{w}\, grad(c_i) + div\left[\overline{J_{dyf}}\right] = \Phi_i \tag{36}$$

The total diffusion flux density $\left(\overline{J_{dyf}}\right)$ is expressed as a sum of elementary fluxes considering the concentration$\left(\overline{J}_i(c_i)\right)$, temperature$\left(\overline{J}_i(T)\right)$, thermodynamic pressure gradient$\left(\overline{J}_i(p)\right)$, and the additional force interactions $\overline{J}_i(\overline{F})$ (e.g. forced convection as a result of fluid mixing) in the following form

$$\overline{J_{dyf}} = \overline{J}_i(c_i) + \overline{J}_i(T) + \overline{J}_i(p) + \overline{J}_i\left(\overline{F}\right) \tag{37}$$

A more useful form of this equation may be obtained by introducing the proper coefficients as follows

$$\overline{J_{dyf}} = -\rho D_i \, grad(c_i) - \rho D_i k_t \, grad(\ln t) - \rho D_i k_p \, grad(\ln p) + \rho D_i k_{\bar{F}} \bar{F} \tag{38}$$

Under the action of TRMF the force $\bar{F}$ may be defined as the Lorenz magnetic force $\overline{F_{em}}$. This force is acting as the driving force for the liquid rotation and it may be described by

$$\overline{F_{em}} = \bar{J} \times \bar{B} \Rightarrow \overline{F_{em}} = \left[\sigma_e E + \sigma_e \left(\overline{w} \times \bar{B} \right) \right] \times \bar{B} \tag{39}$$

The above relation may be simplified as follows (the electric field vector $\bar{E}$ is omitted)

$$\overline{F_{em}} = \left(\sigma_e \left(\overline{w} \times \bar{B} \right) \right) \times \bar{B} \tag{40}$$

The related Lorenz force to the unit of liquid mass may be rewritten in the form

$$\overline{F_{em}} = \frac{1}{\rho} \left(\sigma_e \left(\overline{w} \times \bar{B} \right) \right) \times \bar{B} \tag{41}$$

Introducing the relation Eq.(41) in Eq.(38) gives the following relationship

$$\overline{J_{dyf}} = -\rho D_i \, grad(c_i) - \rho D_i k_t \, grad(\ln t) - \rho D_i k_p \, grad(\ln p) + D_i k_{\overline{F_{em}}} \left(\left(\sigma_e \left(\overline{w} \times \bar{B} \right) \right) \times \bar{B} \right) \tag{42}$$

Taking into account the above relation (Eq.(42)) we obtain the following general relationship for the mass balance of component *i*

$$\begin{aligned} &\frac{\partial c_i}{\partial \tau} + \overline{w} \, grad(c_i) + div\left[-D_i \, grad(c_i) - D_i k_t \, grad(\ln t) - D_i k_p \, grad(\ln p) \right] + \\ &+ div\left[\frac{D_i k_{\overline{F_{em}}}}{\rho} \left(\left(\sigma_e \left(\overline{w} \times \bar{B} \right) \right) \times \bar{B} \right) \right] = \frac{\Phi_i}{\rho} \end{aligned} \tag{43}$$

The obtained Eq.(43) suggests that this dependence may be simplified in the following form

$$\frac{\partial c_i}{\partial \tau} + \overline{w} \, grad(c_i) + div\left[-D_i \, grad(c_i) \right] + div\left[\frac{D_m}{\rho} \left(\left(\sigma_e \left(\overline{w} \times \bar{B} \right) \right) \times \bar{B} \right) \right] = \frac{\Phi_i}{\rho} \tag{44}$$

It should be noticed that the coefficient of magnetic diffusion D_m may be expressed as follows

$$D_m = D_i k_{\overline{F_{em}}} \tag{45}$$

http://dx.doi.org/10.5772/51296

This coefficient may be defined by means of the following expression

$$D_m = c_i \tau_d \Rightarrow D_m = c_i \sigma_e \mu_m l_0^2 \Rightarrow D_m = \frac{c_i l_0^2}{\nu_m} \tag{46}$$

Taking into consideration the above relation (Eq.(46)) we obtain the relationship

$$\frac{\partial c_i}{\partial \tau} + \overline{w}\, grad(c_i) + div\left[-D_i\, grad(c_i)\right] + div\left[\frac{c_i l_0^2}{\nu_m \rho}\left(\left(\sigma_e\left(\overline{w}\times\overline{B}\right)\right)\times\overline{B}\right)\right] = \frac{\Phi_i}{\rho} \tag{47}$$

The above relation (Eq.(47)) may be treated as the differential mathematical model of the solid dissolution process under the action of TRMF. The right side of this equation represents the source mass of component *i*

$$\Phi_i = -\frac{\beta_i dF_m}{dV}\left(c_i - c_r\right) \Rightarrow \Phi_i = -\left(\beta_i\right)_V \left(c_i - c_r\right) \Rightarrow \Phi_i = -\left(\beta_i\right)_V \widetilde{c_i} \Rightarrow \Phi_i = \left(\beta_i\right)_V \left(-\widetilde{c_i}\right) \tag{48}$$

where $\left(-\widetilde{c_i}\right)$ is the driving force for the solid dissolution process.

Introducing Eq.(48) in Eq.(47), gives the following relationship

$$\frac{\partial c_i}{\partial \tau} + \overline{w}\, grad(c_i) + div\left[-D_i\, grad(c_i)\right] + div\left[\frac{c_i l_0^2}{\nu_m \rho}\left(\left(\sigma_e\left(\overline{w}\times\overline{B}\right)\right)\times\overline{B}\right)\right] = -\frac{\left(\beta_i\right)_V \widetilde{c_i}}{\rho} \tag{49}$$

Taking into account the below definition of the dimensionless parameters

$$\begin{gathered} c_i^* = \frac{c_i}{c_{i_0}}; \widetilde{c_i}^* = \frac{\widetilde{c_i}}{c_{i_0}}; \overline{w}^* = \frac{\overline{w}}{w_0}; D_i^* = \frac{D_i}{D_{i_0}}; \tau^* = \frac{\tau}{\tau_0}; \mu_m^* = \frac{\mu_m}{\mu_{m_0}}; \\ \nu_m^* = \frac{\nu_m}{\nu_{m_0}}; \rho^* = \frac{\rho}{\rho_0}; \overline{B}^* = \frac{\overline{B}}{B_0}; \left[\left(\beta_i\right)_V\right]^* = \frac{\left(\beta_i\right)_V}{\left[\left(\beta_i\right)_V\right]_0} \\ div^* = \frac{div}{l_0^{-1}}; Div^* = \frac{Div}{l_0^{-1}}; grad^* = \frac{grad}{l_0^{-1}}; \end{gathered} \tag{50}$$

we obtain the governing Eq.(50) in a symbolic form

$$\begin{gathered} \frac{c_{i_0}}{\tau_0}\left[\frac{\partial c_i^*}{\partial \tau^*}\right] + \frac{c_{i_0} w_0}{l_0}\left[\overline{w}^*\, grad^*\left(c_i^*\right)\right] - \frac{D_{i_0} c_{i_0}}{l_0^2}\left[div^*\left[D_i^*\, grad^*\left(c_i^*\right)\right]\right] + \\ + \frac{c_{i_0}\sigma_{e_0} w_0 B_0^2 l_0}{\nu_{m_0}\rho_0}\left[div^*\left[\frac{c_i^*}{\nu_m^*\rho^*}\left(\left(\sigma_e^*\left(\overline{w}^*\times\overline{B}^*\right)\right)\times\overline{B}^*\right)\right]\right] = -\frac{\left[\left(\beta_i\right)_V\right]_0 c_{i_0}}{\rho_0}\left[\frac{\left[\left(\beta_i\right)_V\right]^* \widetilde{c_i}^*}{\rho^*}\right] \end{gathered} \tag{51}$$

The non-dimensional form of this equation may be scaled against the convective term $\left(\frac{c_{i_0} w_0}{l_0}\right)$. The dimensionless form of Eq.(51) may be given as follows

$$\frac{l_0}{\tau_0 w_0}\left[\frac{\partial c_i^*}{\partial \tau^*}\right]+\left[\overline{w}^*\, grad^*\left(c_i^*\right)\right]-\frac{D_{i_0}}{l_0 w_0}\left[div^*\left[D_i^*\, grad^*\left(c_i^*\right)\right]\right]+$$
$$+\frac{\sigma_{e_0} B_0^2 l_0^2}{\nu_{m_0}\rho_0}\left[div^*\left[\frac{c_i^*}{\nu_m^*\rho^*}\left(\left(\sigma_e^*\left(\overline{w}^*\times\overline{B}^*\right)\right)\times\overline{B}^*\right)\right]\right]=-\frac{\left[\left(\beta_i\right)_V\right]_0 l_0}{\rho_0 w_0}\left[\frac{\left[\left(\beta_i\right)_V\right]^*\widetilde{c}_i^*}{\rho^*}\right] \tag{52}$$

This relation includes the following dimensionless groups characterizing the dissolution process under the action of TRM

$$\frac{l_0}{\tau_0 w_0}\Rightarrow \mathrm{S}^{-1} \tag{53}$$

$$\frac{D_{i_0}}{l_0 w_0}\Rightarrow\left(\frac{\nu}{w_0 D}\right)\left(\frac{D_{i_0}}{\nu}\right)\Rightarrow \mathrm{Re}^{-1}\,\mathrm{Sc}_i^{-1}\Rightarrow \mathrm{Pe}_i^{-1} \tag{54}$$

$$\frac{\sigma_{e_0} B_0^2 l_0^2}{\nu_{m_0}\rho_0}\Rightarrow\left(\frac{\sigma_{e_0} B_0^2 l_0^2}{\nu\rho_0}\right)\left(\frac{\nu}{\nu_{m_0}}\right)\Rightarrow \mathrm{Q}\,\mathrm{Pr}_m\Rightarrow \mathrm{Ha}^2\,\mathrm{Pr}_m \tag{55}$$

$$\frac{\left[\left(\beta_i\right)_V\right]_0 l_0}{\rho_0 w_0}\Rightarrow\left(\frac{\left[\left(\beta_i\right)_V\right]_0 d_p^2}{\rho_0 D_{i_0}}\right)\left(\frac{\nu}{w_0 D}\right)\left(\frac{D_{i_0}}{\nu}\right)\left(\frac{D^2}{d_s^2}\right)\Rightarrow \mathrm{Sh}\,\mathrm{Sc}^{-1}\mathrm{Re}^{-1}\left(\frac{D^2}{d_s^2}\right) \tag{56}$$

Taking into account the proposed relations (53-56), we find the following dimensionless governing equation

$$\mathrm{S}^{-1}\left[\frac{\partial c_i^*}{\partial \tau^*}\right]+\left[\overline{w}^*\, grad^*\left(c_i^*\right)\right]-\mathrm{Pe}_i^{-1}\left[div^*\left[D_i^*\, grad^*\left(c_i^*\right)\right]\right]+$$
$$+\mathrm{Ha}^2\,\mathrm{Pr}_m\left[div^*\left[\frac{c_i^*}{\nu_m^*\rho^*}\left(\left(\sigma_e^*\left(\overline{w}^*\times\overline{B}^*\right)\right)\times\overline{B}^*\right)\right]\right]=-\mathrm{Sh}\,\mathrm{Sc}^{-1}\mathrm{Re}^{-1}\left(\frac{D^2}{d_s^2}\right)\left[\frac{\left[\left(\beta_i\right)_V\right]^*\widetilde{c}_i^*}{\rho^*}\right] \tag{57}$$

From the dimensionless form of Eq.(57) it follows that

$$\mathrm{Sh}\,\mathrm{Sc}^{-1}\mathrm{Re}^{-1}\left(\frac{D^2}{d_s^2}\right)\sim \mathrm{Ha}^2\,\mathrm{Pr}_m\Rightarrow \mathrm{Sh}\,\mathrm{Sc}^{-1}\sim \mathrm{Ha}^2\,\mathrm{Re}\,\mathrm{Pr}_m\left(\frac{d_s^2}{D^2}\right)\Rightarrow \mathrm{Sh}\,\mathrm{Sc}^{-1}\sim \mathrm{Ta}_m\mathrm{Pr}_m\left(\frac{d_s^2}{D^2}\right) \tag{58}$$

http://dx.doi.org/10.5772/51296

Under convective conditions a relationship for the mass-transfer similar to the relationships obtained for heat-transfer may be expected of the form [11]

$$\mathrm{Sh} = f\left(\mathrm{Re},\mathrm{Sc}\right) \tag{59}$$

The two principle dimensionless groups of relevance to mass-transfer are Sherwood and Schmidt numbers. The Sherwood number can be viewed as describing the ratio of convective to diffusive transport, and finds its counterpart in heat transfer in the form of the Nusselt number [3].

The Schmidt number is a ratio of physical parameters pertinent to the system. This dimensionless group corresponds to the Prandtl number used in heat-transfer. Moreover, this number provides a measure of the relative effectiveness of momentum and mass transport by diffusion.

Added to these two groups is the Reynolds number, which represents the ratio of convective-to-viscous momentum transport. This number determines the existence of laminar or turbulent conditions of fluid flow. For small values of the Reynolds number, viscous forces are sufficiently large relative to inertia forces. But, with increasing the Reynolds number, viscous effects become progressively less important relative to inertia effects.

Evidently, for Eq.(59) to be of practical use, it must be rendered quantitative. This may be done by assuming that the functional relation is in the following form [4, 13]

$$\mathrm{Sh} = a_1 \mathrm{Re}^{b_1} \mathrm{Sc}^{c_1} \tag{60}$$

The mass-transfer coefficients in the mixed systems can be correlated by the combination of Sherwood, Reynolds and Schmidt numbers. Using the proposed relation [60], it has been found possible to correlate a host of experimental data for a wide range of operations. The coefficients of relation [60] are determined from experiment. Under forced convection conditions the relation may be expressed as follows [7]

$$\mathrm{Sh} \sim \mathrm{Re}^{0.5} \mathrm{Sc}^{0.33} \tag{61}$$

The exponent upon of the Schmidt number is to be 0.33 [5, 12, 14, 19, 25] as there is some theoretical and experimental evidence for this value [24], although reported values vary from 0.56 [28] to 1.13 [15].

Mass transfer process under the TRMF conditions is very complicated and may be described by the non-dimensional Eq.(57). Use of the dimensionless Sherwood number as a function of the various non-dimensional parameters yields a description of liquid-side mass transfer, which is more general and useful. Taking into account that the magnetic Prandtl number

$\mathrm{Pr}_m = const$ (for water$\mathrm{Pr}_m = const$) and the ratio of diameters solid sample and diameter of container$\frac{d_s}{D} = idem$, the obtained relationship (see Eq.(58)) may be expressed as follows

$$\mathrm{Sh}\,\mathrm{Sc}^{-1} \sim \mathrm{Ta}_m \mathrm{Pr}_m \left(\frac{d_s^2}{D^2}\right) \Rightarrow \mathrm{Sh} = f\left(\mathrm{Ta}_m, \mathrm{Sc}\right) \tag{62}$$

Basing on the considerations given above, the correlations of mass transfer process under the TRMF action have the general form

$$\mathrm{Sh} = a_2 \mathrm{Ta}_m^{\,b_2} \mathrm{Sc}^{c_2} \tag{63}$$

2.3. Influence of temperature gradient on the solid dissolution controlled process

As mentioned above, the temperature gradient has strong influence on the solid dissolution process. The heat transfer from the sample to the ambient fluid may be modeled by means of the well-known Nusselt type equation.

$$\mathrm{Nu} = f\left(\mathrm{Re}, \mathrm{Pr}\right) \tag{64}$$

In the present report we consider the process dissolutions described by a similar but somewhat modified relationship between the dimensionless Sherwood number and the numbers which are defined the intensity of the magnetic effects in the tested experimental set-up with the TRMF generator. It should be assumed that the relationship for the heat transport under the TRMF conditions can be characterized in the following general form

$$\mathrm{Nu} = f\left(\mathrm{Ta}_m, \mathrm{Pr}\right) \tag{65}$$

In order to establish the effect of all important parameters on this process in the wide range of variables data we proposed the following general relationship.

$$\mathrm{Nu} = a_3 \mathrm{Ta}_m^{\,b_3}\, \mathrm{Pr}^{c_3} \tag{66}$$

The solid dissolution process under the action of TRMF and the gradient temperature between the solid surface and the liquid may be described by means of the following equations system

$$\begin{cases} \mathrm{Sh} = a_2 \mathrm{Ta}_m^{\,b_2} \mathrm{Sc}^{c_2} \\ \mathrm{Nu} = a_3 \mathrm{Ta}_m^{\,b_3}\, \mathrm{Pr}^{c_3} \end{cases} \tag{67}$$

http://dx.doi.org/10.5772/51296

From the above relation (Eq.(67)), the ratio of Sherwood and Nusselt numbers is given by

$$\frac{\mathrm{Sh}}{\mathrm{Nu}} = a_4 \mathrm{Ta}_m^{\,b_4} \left(\frac{\mathrm{Sc}}{\mathrm{Pr}}\right)^{c_4} \tag{68}$$

where $a_2 \neq a_3 \wedge\ a_4 = \dfrac{a_2}{a_3}$; $b_2 \neq b_3 \wedge\ b_4 = b_2 - b_3$ and $c_2 = c_3 \wedge\ c_4 = 0.33$.

In the relevant literature the ratio of the Schmidt and Prandtl numbers is called as the dimensionless Lewis number (the ratio of thermal diffusivity to mass diffusivity)

$$\mathrm{Le} = \left(\frac{\mathrm{Sc}}{\mathrm{Pr}}\right) \Rightarrow \mathrm{Le} = \left(\frac{\nu}{D_i}\right)\left(\frac{a}{\nu}\right) \Rightarrow \mathrm{Le} = \frac{a}{D_i} \tag{69}$$

According to Eq.(69) and the above assumptions, the ratio of Sherwood and Nusselt numbers is defined as follows

$$\frac{\mathrm{Sh}}{\mathrm{Nu}} = a_4 \mathrm{Ta}_m^{\,b_4} \mathrm{Le}^{0.33} \tag{70}$$

The enhancement effect of the solid dissolution process due to heat transfer process obtained from Eq.(70) is given by

$$\left(\frac{\beta_i d_s}{D_i}\right)\left(\frac{\lambda}{\alpha_s D}\right) = a_4 \mathrm{Ta}_m^{\,b_4} \mathrm{Le}^{0.33} \tag{71}$$

The ratio $\left(\dfrac{\beta_i}{\alpha_s}\right)$ may be defined by means of the following relationship

$$\left(\frac{\beta_i}{\alpha_s}\right) = a_4 \mathrm{Ta}_m^{\,b_4} \mathrm{Le}^{0.33} \left(\frac{D}{d_s}\right)\left(\frac{D_i}{\lambda}\right) \tag{72}$$

Introducing the thermal diffusivity $\left(a = \dfrac{\lambda}{c_p \rho} \Rightarrow \lambda = a c_p \rho\right)$ in Eq.(72), gives the relation

$$\left(\frac{\beta_i}{\alpha_s}\right) = a_4 \mathrm{Ta}_m^{\,b_4} \mathrm{Le}^{0.33} \left(\frac{D_i}{a}\right)\left(\frac{1}{c_p \rho}\right)\left(\frac{D}{d_s}\right) \Rightarrow \left(\frac{\beta_i}{\alpha_s}\right) = a_4 \mathrm{Ta}_m^{\,b_4} \mathrm{Le}^{0.33} \mathrm{Le}^{-1} \left(\frac{1}{c_p \rho}\right)\left(\frac{D}{d_s}\right) \tag{73}$$

Finally, form relation (73) it follows that

$$\left(\frac{\beta_i}{\alpha_s}\right) = a_4 \mathrm{Ta}_m^{\,b_4} \mathrm{Le}^{-0.66} \left(\frac{1}{c_p \rho}\right)\left(\frac{D}{d_s}\right) \tag{74}$$

3. Experimental details

3.1. Experimental set-up

All experimental measurements of mass-transfer process using the TRMF were carried out in a laboratory set-up including electromagnetic field generator. A schematic of the experimental apparatus is presented in figure 1.

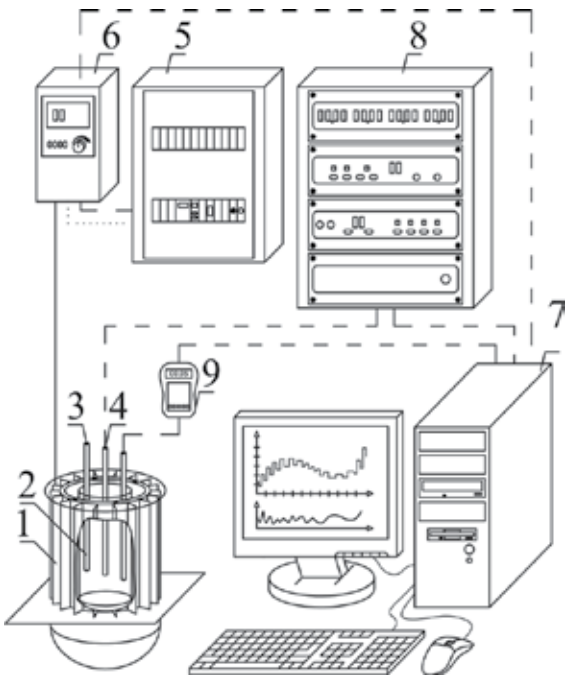

Figure 1. Sketch of experimental set-up: 1 - generator of rotating magnetic field, 2 - glass container, 3,4 - conductivity samples, 5 - electronic control box, 6 - a.c. transistorized inverter, 7 - personal computer, 8 - multifunctional electronic switch, 9 - Hall sample

This setup may be divided into: a generator of the rotating electromagnetic field (1), a glass container (2) with the conductivity samples (3-4), an electric control box (5) and an inverter (6) connected with multifunctional electronic switch (8) and a personal computer (7) loaded with special software. This software made possible the electromagnetic field rotation control, recording working parameters of the generator and various state parameters.

From preliminary tests of the experimental apparatus, the glass container is not influenced by the working parameters of the stator. The TRMF was generated by a modified 3-phase

http://dx.doi.org/10.5772/51296

stator of an induction squirrel-cage motor, parameters of which are in accordance with the Polish Standard PN-72/E-06000. The stator is supplied with a 50 Hz three-phase alternating current. The transistorized inverter (4) was used to change the frequency of the rotating magnetic field in the range of $f_{TRMF} = 1 - 50 Hz$. The stator of the electric machine, as the RMF generator is made up of a number of stampings with slots to carry the three phase winding. The number of pair poles per phase winding, p, is equal to 2. The windings are geometrically spaced 120 degrees apart. The stator and the liquid may be treated as apparent virtual electrical circuit of the closed flux of a magnetic induction. The stator windings are connected through the a.c. transistorized inverter to the power source. The generator produces an azimuthal electromagnetic force in the bulk of the TRMF reactor with the magnetic field lines rotating in the horizontal plane.

For the experimental measurements, MF is generated by coils located axially around of the cylindrical container. As mentioned above, this field is rotated around the container with the constant angular frequency,ω_{TRMF}. The TRMF strength is determined by measuring a magnetic induction. The values of the magnetic induction at different points inside the glass container are detected by using a Hall sample connected to the personal computer. The typical example of the dependence between the spatial distributions of magnetic induction and the various values of the alternating current frequency for the cross-section of container is given [20]. The obtained results in this paper suggest that the averaged values of magnetic induction may be analytically described by the following relation

$$\left[B_{TRMF}\right]_{avg} = 14.05\left[1 - \exp\left(-0.05 f_{TRMF}\right)\right] \tag{75}$$

3.2. Rock-salt sample

Two conductive samples connected to a multifunction computer meter were used to measuring and recording of the concentration of the achieve solution of the salt. The mass of the rock salt sample decreasing during the process of dissolution is determined by an electronic balance that connected with rocking double-arm lever. On the lever arm the sample was hanging, the other arm connected to the balance. In the present investigation the change in mass of solid body in a short time period of dissolution is very small and the mean area of dissolved cylinder of the rock salt may be used. Than the mean mass-transfer Raw rock-salt (>98% NaCl and rest traces quantitative of chloride of K, Ca, Mg and insoluble mineral impurities) cylinders were not fit directly for the experiments because their structure was not homogeneous (certain porosity). Basic requirement concerning the experiments was creating possibly homogeneous transport conditions of mass on whole interfacial surface, which was the active surface of the solid body. These requirements were met thanks to proper preparing of the sample, mounting it in the mixer and matching proper time of dissolving. As an evident effect were fast showing big pinholes on the surface of the dissolved sample as results of local non-homogeneous of material. Departure from the shape of a simple geometrical body made it impossible to take measurements of its area with sufficient precision. So it was necessary to put those samples through the process of so-called hardening. The turned

cylinders had been soaked in saturated brine solution for about 15 min and than dried in a room temperature. This process was repeated four times. To help mount the sample in the mixer, a thin copper thread was glued into the sample's axis. The processing was finished with additional smoothing of the surface with fine-grained abrasive paper. A sample prepared in this way had been keeping its shape during dissolving for about 30 min. The duration of a run was usually 30 sec. The rate of mass-transfer involved did not produce significant dimensional change in diameter of the cylinder. The time of a single dissolving cycle was chosen so that the measurement of mass loss could be made with sufficient accuracy and the decrease of dimensions would be relatively small (maximum about 0.5 mm).

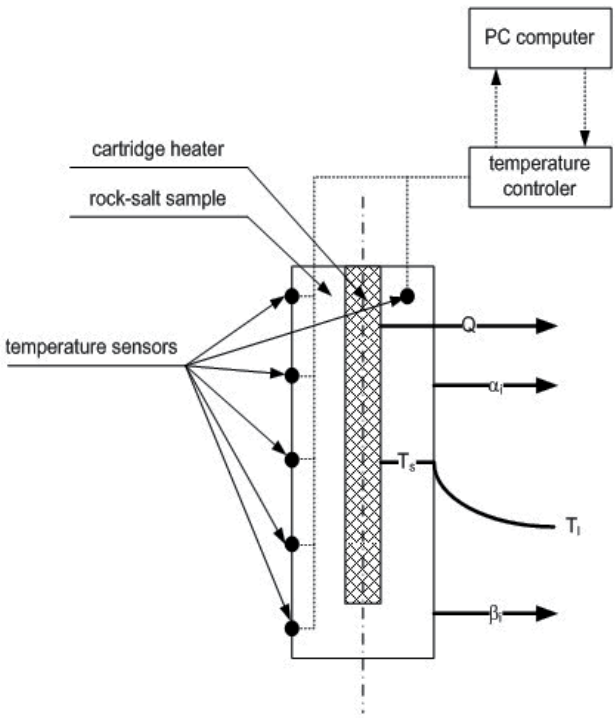

Figure 2. Sketch of rock-salt sample with the heating set-up

Before starting every experiment, a sample which height, diameter and mass had been known was mounted in a mixer under the free surface of the mixed liquid. The reciprocating plate agitator was started, the recording of concentration changes in time, the weight showing changes in sample's mass during the process of solution, and time measuring was started simultaneously. After finishing the cycle of dissolving, the agitator was stopped, and then the loss of mass had been read on electronic scale and concentration of NaCl (electrical conductivity) in the mixer as well. This connection is given by a calibration curve, showing the dependence of the relative mass concentration of NaCl on the electrical conductivity [21].

http://dx.doi.org/10.5772/51296

3.3. Rock-salt sample heated by means of the cartridge heater

In the case of this experimental investigations the gradient temperature between the surface and liquid was caused by using the cartridge heater (power ~1200W). This tubular device was inserted into drilled holes of rock-salt sample for heating. Moreover, the heating set-up was contained the temperature controller and sensors. The sensors for the temperature control was placed between the working surface of the sample and the heater. These sensors was also located on the surface of the solid sample. The sketch of rock-salt sample with the heating set-up is graphically presented in figure 2. The sample was kept at a constant temperature (65°C, 70°C or 80°C). The heat transfer from the sample to ambient fluid was realized for the various temperature (20°C, 40°C and 60°C). The system of temperature sensors was used to control the temperature of the water during the solid dissolution process.

3.4. Experimental calculation of mass transfer coefficient

The mass transfer coefficient under the action of TRMF may be calculated form the following equation

$$-\frac{dm_i}{d\tau} = \beta_i F_m \tilde{c_i} \Rightarrow \beta_i = \frac{1}{F_m\left(-\tilde{c_i}\right)}\frac{dm_i}{d\tau} \tag{76}$$

The above Eq.(76) cannot be integrated because the area of solid body, F_m, is changing in time of dissolving process. It should be noted that the change in mass of solid body in a short time period of dissolving is very small and the mean area of dissolved cylinder may be used. The relation between loss of mass, mean area of mass-transfer and the mean driving force of this process for the time of dissolving duration is approximately linear and then the mass-transfer coefficient may be calculated from the simple linear equation

$$\left[\beta_i\right]_{avg} = \frac{1}{\left[F_m\right]_{avg}\left[\tilde{c_i}\right]_{avg}}\frac{\left(-dif\, m_i\right)}{\left(dif\,\tau\right)} \tag{77}$$

The averaged surface F_m is defined as follows

$$\left[F_m\right]_{avg} = \pi\left[d_s\right]_{avg} h_s \tag{78}$$

The volumetric mass transfer coefficient $\left(\beta_i\right)_V$ in Eq.(48) is described by relation

$$\left(\beta_i\right)_V = \frac{\beta_{\alpha i} dF_m}{dV} \Rightarrow \left[\left(\beta_i\right)_V\right]_{avg} = \frac{\left[\beta_i\right]_{\alpha\tau}\left[F_m\right]_\tau}{V_l} \tag{79}$$

3.5. Experimental calculation of heat transfer coefficient

The heat transfer from the sample to liquid may by modelled by the following relationship

$$Q_s = Q_l \Rightarrow \alpha_s F_m \Delta T_1 = m_l c_{p_l} \Delta T_2 \tag{80}$$

This equation can be rewritten as

$$\alpha_s F_m \left(T_s - [T_l]_{t_2} \right) = m_l c_{p_l} \left([T_l]_{t_2} - [T_l]_{t_1} \right) \Rightarrow \alpha_s = \frac{m_l c_{p_l} \left([T_l]_{t_2} - [T_l]_{t_1} \right)}{F_m \left(T_s - [T_l]_{t_2} \right)} \tag{81}$$

and the averaged heat transfer coefficient is given as follows

$$[\alpha_s]_{avg} = \frac{m_l \left[c_{p_l} \right]_{avg} \left([T_l]_{t_2} - [T_l]_{t_1} \right)}{[F_m]_{avg} \left(T_s - [T_l]_{t_2} \right)} \tag{82}$$

The averaged coefficient of heat transfer $\left([\alpha_s]_{avg}\right)$ varies with the parameters of the TRMF mixing process and depends on the operating conditions and physical properties of the liquid.

4. Results and discussion

Under the TRMF conditions a relationship for the mass-transfer can be described in the general form$\mathrm{Sh} = f\left(Ta_m, Sc\right)$. The results of experiments suggest that the Sherwood number, the magnetic Taylor number and the Schmidt number may be defined as follows (see Eqs 53-56)

$$\mathrm{Sh} = \frac{\left[(\beta_i)_V \right]_0 d_p^2}{\rho_0 D_{i_0}} \Rightarrow \mathrm{Sh} = \frac{\left(\frac{[\beta_i]_{cr} [F_m]_{cr}}{V_l} \right) d_p^2}{\rho_l D_{i_l}} \tag{83}$$

$$\mathrm{Sc}_i = \frac{\nu}{D_{i_0}} \Rightarrow \mathrm{Sc}_i = \frac{\nu_l}{D_{i_l}} \tag{84}$$

http://dx.doi.org/10.5772/51296

$$\mathrm{Ta}_m = \mathrm{Ha}^2\,\mathrm{Re}_m \Rightarrow \mathrm{Ta}_m = \left(\frac{\sigma_{e_0} B_0^2 l_0^2}{\nu\,\rho_0}\right)\left(\frac{w_0 D}{\nu}\right) \Rightarrow \mathrm{Ta}_m = \left(\frac{\sigma_{e_l}\left(\left[B_{TRMF}\right]_{avg}\right)^2 D^2}{\nu_l\,\rho_l}\right)\left(\frac{\omega_{TRMF} D^2}{\nu_l}\right)$$
$$\Rightarrow \mathrm{Ta}_m = \frac{\omega_{TRMF}\left(\left[B_{TRMF}\right]_{avg}\right)^2 D^4 \sigma_{e_l}}{\nu_l^2\,\rho_l} \tag{85}$$

The TRMF Reynolds number $\left(\mathrm{Re}_m = \dfrac{\omega_{TRMF} D^2}{\nu_l}\right)$ with $\omega_{TRMF} = 2\pi f_{TRMF}$ as angular frequency of TRMF equal to angular field frequency of the field generated by the a current of frequency. The product $\omega_{TRMF} D$ plays the role of a rotational velocity. The above dimensionless groups (Eqs 83-85) were calculated with the physical properties in the temperature range 20-60°C (the liquid temperature).

The effect of dissolution process under the action of TRF can be described by using the variable $\mathrm{ShSc}^{-0.33}$ proportional to the term $a(Ta_m)^b$. The experimental results obtained in this work are graphically illustrated in $\log(\mathrm{ShSc}^{-0.33})$ versus $\log(a(Ta_m)^b)$ in figure 3. Moreover, the influence of the temperature gradient between the surface temperature of solid and the liquid temperature on the mass transfer coefficient is presented in this figure.

In order to establish the effect of all important parameters on the dissolution process in the analyzed set-up, we propose the following relationship to work out the experimental database

$$\frac{\mathrm{Sh}}{\mathrm{Sc}^{0.33}} = a\left(\mathrm{Ta}_m\right)^b \tag{86}$$

The presented results in figure 3 suggest that these points may be described by a unique monotonic function. The constants and exponents are computed by employing the Matlab software and the principle of least squares and the proposed relationships are collected in table 1.

Figure 4 shows the effect of the constant temperature of the surface of rock-salt sample and the variation of the liquid temperature on the Sherwood number.

temperature of surface of salt-rock sample	temperature of liquid		
	20°C	40°C	60°C
65°C	$\frac{\mathrm{Sh}}{\mathrm{Sc}^{0.33}} = 80.36\left(\mathrm{Ta}_m\right)^{0.148}$	$\frac{\mathrm{Sh}}{\mathrm{Sc}^{0.33}} = 79.71\left(\mathrm{Ta}_m\right)^{0.08}$	$\frac{\mathrm{Sh}}{\mathrm{Sc}^{0.33}} = 51.95\left(\mathrm{Ta}_m\right)^{0.06}$
70°C	$\frac{\mathrm{Sh}}{\mathrm{Sc}^{0.33}} = 85.54\left(\mathrm{Ta}_m\right)^{0.132}$	$\frac{\mathrm{Sh}}{\mathrm{Sc}^{0.33}} = 84.13\left(\mathrm{Ta}_m\right)^{0.05}$	$\frac{\mathrm{Sh}}{\mathrm{Sc}^{0.33}} = 67.52\left(\mathrm{Ta}_m\right)^{0.04}$
80°C	$\frac{\mathrm{Sh}}{\mathrm{Sc}^{0.33}} = 92.87\left(\mathrm{Ta}_m\right)^{0.09}$	$\frac{\mathrm{Sh}}{\mathrm{Sc}^{0.33}} = 92.85\left(\mathrm{Ta}_m\right)^{0.04}$	$\frac{\mathrm{Sh}}{\mathrm{Sc}^{0.33}} = 73.71\left(\mathrm{Ta}_m\right)^{0.02}$

Table 1. The developed relationships for the obtained experimental data

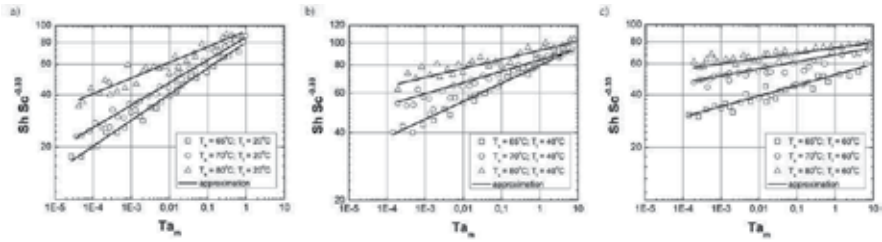

Figure 3. The graphical presentation of mass transfer data under the action of TRMF: a)T_s=var; T_l=20^oC, b) T_s=var; T_l=40$^oC$and c) T_s=var; T_l=60^oC

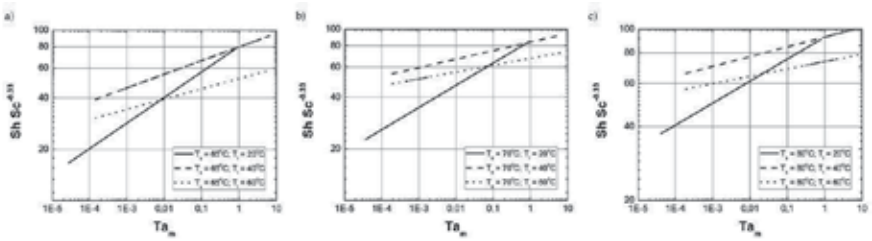

Figure 4. The comparison of obtained results: : a)T_s=65^oC; T_l=var, b) T_s=70^oC; T_l=varand c) T_s=80^oC; T_l=var

Figures 3 and 4 present a graphical form of the collected relations in table 1, as the full curves, correlated the experimental data very well with the percentage relative error±10%. Figure 5 gives an overview results in the form of the proposed analytical relationships for the experimental investigations (see table 1)

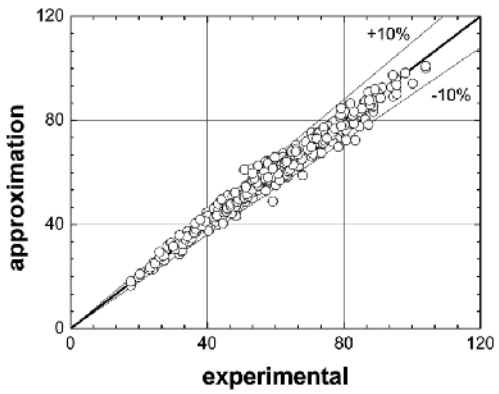

Figure 5. Dependence between experimental and predicted $\left(\frac{Sh}{Sc^{0.33}}\right)$ values

http://dx.doi.org/10.5772/51296

As can be clearly seen (see Figure 3) mass transfer rates expressed as $\left(\frac{Sh}{Sc^{0.33}}\right)$ increase with increasing the values of magnetic Taylor number. It is found that as the intensity of magnetic field increases, the velocity of liquid inside the cylindrical container increases. It may be concluded that the TRMF strongly influenced on the mass transfer process. It should be noticed that this process may be improved by means of the gradient temperature between the surface of rock-salt sample and the liquid. Figure 3 shows that Sherwood number increases with the increasing difference between the temperature of rock-salt surface and the liquid temperature. It is clear that the effect of TRMF on the dissolution process is also depended on the temperature gradient.

Comparison of the obtained results for the analyzed process is graphically presented in figure 4. This figure shows that for the given temperature of surface of rock-salt sample the mass transfer coefficients in tested set-up are strongly depended on the values of magnetic Taylor number. These plots also confirm that the gradient temperature has significant effect on the mass transfer process. Initially, the high mass transfer rates is achieved by the liquid temperature 40°C and 60°C. Further increase of the magnetic field intensity leads to even higher mass transfer rates for the liquid temperature is equal to 20°C. It should be noticed that the NaCl-cylinder was placed in the middle of container. When the TRMF rotated slowly the liquid was mixed near the wall of cylindrical container. When the TRMF rotated faster, the resulting liquid movement directly leads to an increase of the mass and heat transfer coefficients. This difference appears to be linked to the increase in the difference between the surface temperature of rock-salt sample and the liquid temperature associated with increasing the influence of TRMF. The high value of the exponents of magnetic Taylor number and the multiplicative coefficients seen in the relations given in table 1 agree with the existence of more intensive flow near the hot surface of the rock-salt sample promoted by the increase of the magnetic induction and the temperature of the cartridge heater.

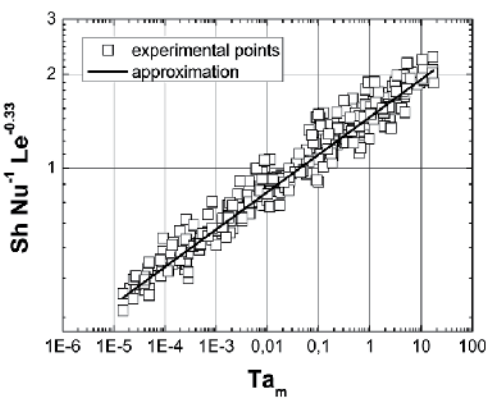

Figure 6. The graphical presentation of mass and heat transfer data at TRMF

The enhancement due to heat transfer process is modeled in terms given in Eq.(70). The graphical presentation of the calculated experimental points is presented in figure 6.

The constant a_4 and exponent b_4 in Eq.(70) are computed by using the principle of least square. Applying the software Matlab the analytical relationship may be obtained

$$\frac{\mathrm{Sh}}{\mathrm{Nu}} = 1.5\left(\mathrm{Ta}_m\right)^{0.12}\mathrm{Le}^{0.33} \tag{87}$$

where the ratio of the dimensionless Sherwood and Nusselt numbers is function of the adequate dimensionless groups. The fit of experimental data with Eq.(87) is given in figure 7. The averaged absolute relative error was estimated at 2.12%.

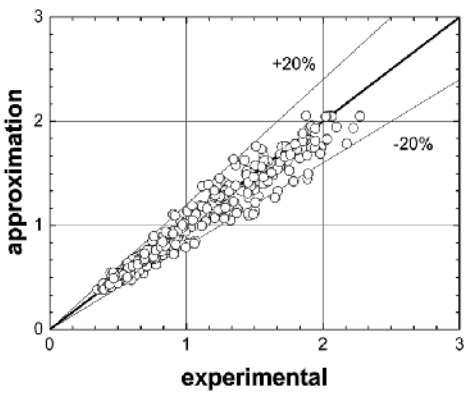

Figure 7. Comparison of model prediction (Eq.(87)) with experimental data

Figure 6 shows that the ratio of mass and heat transfer coefficients (via ratio of Sherwood and Nusselt numbers) increases with the magnetic Taylor number. This figure shows a strong increase in mass transfer process when the TRMF is applied. It was found that the intensification of this process is depended on the temperature gradient between the temperature of surface of salt-rock sample and the liquid temperature.

In order to evaluate the influence of the gradient temperature on the mass transfer under the action of TRMF, the comparison between the obtained database and the empirical correlation for the dissolution process under the TRMF is presented. For comparison these results with literature, it is recommended to correlate them under analogous form. The dissolution process under the action of TRMF is correlated by means of the equation [22]

$$\mathrm{Sh} = 2 + 22.5\left\{\mathrm{Ta}_m\right\}_x^{0.015}\mathrm{Sc}^{0.33}\left(\frac{x}{D}\right)^{0.33} \tag{88}$$

http://dx.doi.org/10.5772/51296

Taking into account that the dimensionless location of a NaCl-cylindrical sample $\left(\frac{x}{D}\right)$ is equal to 0.125 (the sample was located in the middle of cylindrical container) and the local Taylor number $\left(\{\mathrm{Ta}_m\}_x\right)$ is treated as the magnetic Taylor number(Ta_m), the Eq.(88) may be rewritten in the following form

$$\mathrm{Sh} = 2 + 11.3\{\mathrm{Ta}_m\}_x^{0.015}\,\mathrm{Sc}^{0.33} \Rightarrow \mathrm{Sh}_I = 2 + 11.3(\mathrm{Ta}_m)^{0.015}\,\mathrm{Sc}^{0.33} \tag{89}$$

As a matter of fact, Eq.(70) may be written by alternate equations as follows

$$\mathrm{Sh}_{II} = 1.5(\mathrm{Ta}_m)^{0.12}\,\mathrm{Le}^{0.33}\,\mathrm{Nu} \tag{90}$$

The comparison in this case may be realized by considering the calculated averaged values of the dimensionless Schmidt$([Sc]_{avg}=477)$, Lewis $([Le]_{avg}=74)$ and Nusselt $([Nu]_{avg}=102)$ numbers. For established averaged values of these dimensionless groups the Eqs (89-90) reduce to

$$\mathrm{Sh}_I = 2 + 86.5(\mathrm{Ta}_m)^{0.015} \tag{91}$$

$$\mathrm{Sh}_{II} = 616.3\,(\mathrm{Ta}_m)^{0.12} \tag{92}$$

The graphical comparison between Eq.(91) and Eq.(92) are illustrated in the plot in figure 8. This figure demonstrates that the dimensionless Sherwood number for the analyzed case (Sh_{II}) increases with increasing the magnetic Taylor number. It was found that as the intensity of TRMF increases, the influence of hydrodynamic conditions on the transport processes inside the cylindrical container increases. The obtained relationship (Eqs (91-92)) indicate that the transfer rates increase with Taylor number for case I $\mathrm{Sh}_I \sim (\mathrm{Ta}_m)^{0.015}$ and case II $\mathrm{Sh}_{II} \sim (Ta_m)^{0.12}$. The mass transfer data obtained for the additional transfer gradient is consequently higher than the data obtained for the mass transfer under the action of TRMF.

It can be observed that the enhancement of the mass transfer coefficients due to temperature gradient may be evaluated by applying the ratio$\left(\frac{\mathrm{Sh}_{II}}{\mathrm{Sh}_I}\right)$. In the present study $\left(\frac{\mathrm{Sh}_{II}}{\mathrm{Sh}_I}\right)$ becomes

$$\left(\frac{\mathrm{Sh}_{II}}{\mathrm{Sh}_I}\right) = \frac{616.3\,(\mathrm{Ta}_m)^{0.12}}{2 + 86.5(\mathrm{Ta}_m)^{0.015}} \Rightarrow \left(\frac{\mathrm{Sh}_{II}}{\mathrm{Sh}_I}\right) \approx 5\,(\mathrm{Ta}_m)^{0.105} \tag{93}$$

Figure 9 shows the obtained relation (see Eq.(93)) as the function of the magnetic Taylor number. It was found that as the intensity of TRMF has strong influence on the mass transfer rate. It is interesting to note that the enhancement of this process in the case of upper values of the magnetic Taylor number is increased for the supported process by using the cartrige heater.

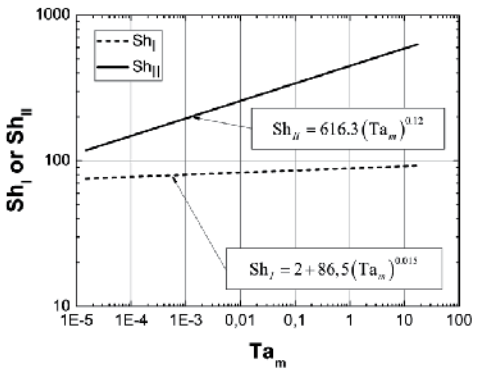

Figure 8. Comparison of obtained results (Sh_{II}) with literature data (Sh_I)

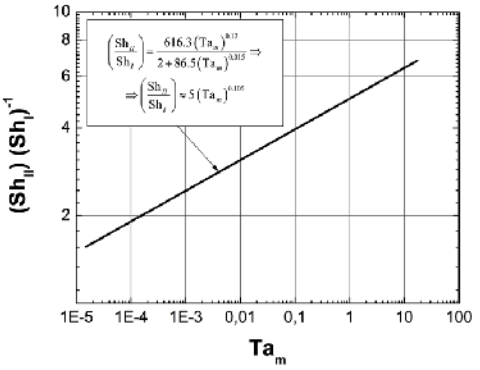

Figure 9. Graphical presentation of Eq.(93)

5. Conclusion

The present experimental study shows interestingfeatures cocncerning the effects of transverse rotating magnetic field (TRMF) on the mass transfer process. Inspecting the obtained measuremenst reveals the following conclusions:

http://dx.doi.org/10.5772/51296

1. The study of mass transfer process under the action of TRMF results is significant enhancement of the solid dissolution rate per localization of a NaCl-cylindrical sample. The mass transfer rate increases with an increase of a magnetic field level. It was found that the TRMF strongly influcnecd the mass transfer process.

2. It should be noticed that the novel approach to the mixing process presented and based on the application of TRMF to produce better hydrodynamic conditions in the case of the mass-transfer process. From practical point of view, the dissolution process of solid body is involved by using the turbulently agitated systems. In previous publications are not available data describing the mass-transfer operations of the dissolution process under the TRMF conditions and the temperature gradient. Moreover, the influence of the additional indirect heating on the mass-transfer was determined.

3. With the respect to the other very useful mass transfer equations given in the pertinent literature, the theoretical description of problem and the equations predicted in the present article is much more attractive because it generalizes the experimental data taking into consideration the various parameters, which defined the hydrodynamic state and the intensity of magnetic effects in the tested system (see chapter 2.2).

4. On the basis of the experimental investigations, the results were successfully correlated by using the general relationship [74]. The influence of the TRMF and the temperature gradient on this process may be also described using the non-dimensional parameters formulated on the base of fluid mechanics equations. These dimensionless numbers allow quantitative representation and characterization of the influence of hydrodynamic state under the TRMF conditions on the mass-transfer process. The dimensionless groups are used to establish the effect of TRMF on this operation in the form of the novel type dimensionless correlation [87].

5. In order to evaluate the influence of the gradient temperature on the mass transfer under the action of TRMF, the comparison between the obtained database and the empirical correlation for the dissolution process under the TRMF is presented. This coparsion is presented as the specific relation [93]. It can be observed that the enhancement of the mass transfer coefficients due to temperature has strong influence on the mass transfer rate (see Fig.8).

6. Nomenclature

$\tilde{B}$	magnetic induction	$kg \cdot A^{-1} \cdot s^{-2}$
c_i	concentration	$kg_i \cdot kg^{-1}$
c_p	specific heat capacity of liquid	$J \cdot kg^{-1} \cdot deg^{-1}$
d_s	sample diameter	m

D	diameter of container	m
D_i	diffusion coefficient	$m^2 \cdot s^{-1}$
D_m	magnetic diffusion	$m^2 \cdot s^{-1}$
$\bar{E}$	electric field	$V \cdot m^{-1}$
f_{TRMF}	frequency of electrical current (equal to frequency of TRMF)	s^{-1}
F_m	cylindrical surface of dissoluble sample	m^2
$\overline{F_{em}}$	Lorenz magnetic force	N
h_s	length of sample	m
l	characteristic dimension	m
$\bar{j}$	electrical current density vector	$A \cdot m^{-2}$
$\bar{J}_i$	flux density of component i	$kg_i \cdot m^{-3} \cdot s^{-1}$
$\overline{J_{dyf}}$	diffusion flux density	$kg_i \cdot m^{-3} \cdot s^{-1}$
k_p	relative coefficient of barodiffusion	$kg_i \cdot m^2 \cdot kg^{-1} \cdot N^{-1}$ $\left(kg_i \cdot m \cdot s^2 \cdot kg^{-2}\right)$
k_p	relative coefficient of thermodiffusion	$kg_i \cdot kg^{-1} \cdot \deg^{-1}$
$k_{\overline{F_{em}}}$	relative coefficient of diffusion resulting from additional forced interactions (e.g. magnetic field)	$kg_i \cdot m^{-1} \cdot N^{-1}$ $\left(kg_i \cdot s^2 \cdot m^{-2} \cdot kg^{-1}\right)$
m_i	mass of dissoluble NaCl sample	kg_{NaCl}
p	hydrodynamic pressure	$N \cdot m^{-2}$
Q_l	heat flow from liquid	W
Q_s	heat flow from sample	W
S	shielding parameter	-
T	temperature	deg
$[T_l]_{t_1}$	temperature of liquid at moment t_1	deg
$[T_l]_{t_2}$	temperature of liquid at moment t_2 (after time of dissolution process)	deg
T_s	temperature of sample	deg
V	volume of liquid	m^3
$\bar{w}$	velocity	$m \cdot s^{-1}$
$\bar{w}_i$	velocity of component i	$m \cdot s^{-1}$
x	distance (for localization of sample)	m

http://dx.doi.org/10.5772/51296

Table 2.

α_s	heat transfer coefficient	$W \cdot m^{-2} \cdot deg^{-1}$
β_i	mass transfer coefficient	$kg_i \cdot m^{-2} \cdot s^{-1}$
δ	skin depth	-
η	dynamic viscosity	$kg \cdot m^{-1} \cdot s^{-1}$
μ_m	magnetic permeability	$kg \cdot m \cdot A^{-2} \cdot s^{-2}$
λ	thermal conductivity of liquid	$W \cdot m^{-1} \cdot deg^{-1}$
ν	kinematic viscosity	$m^2 \cdot s^{-1}$
ν_m	magnetic viscosity	$m^2 \cdot s^{-1}$
ρ	density	$kg \cdot m^{-3}$
ρ_i	concentration of component i	$kg_i \cdot m^{-3}$
σ_e	electrical conductivity	$A^2 \cdot s^3 \cdot kg^{-1} \cdot m^{-3}$
τ	time dissolution or time	s
Φ_i	mass flux of component i	$kg_i \cdot m^{-3} \cdot s^{-1}$
ω_{TRMF}	angular velocity of transverse rotating magnetic field	$rad \cdot s^{-1}$

Greek letters

avg	averaged value
l	liquid
s	sample
0	reference value

Subscripts

AC	alternating current
MF	magnetic field
TRMF	transverse rotating magnetic field

Abbreviation

$Ha = B_0 l_0 \sqrt{\frac{\sigma_{e_0}}{\nu \rho_0}}$	Hartman number

$Le = \frac{a}{D_i}$	Lewis number
$Nu = \frac{[\alpha_s]_{avg} D}{\lambda}$	Nusselt number
$Pe_i = \frac{l_0 w_0}{D_{i_0}}$	mass Peclet number
$Pr_m = \frac{\nu}{\nu_{m_0}}$	magnetic Prandtl number
$Q = \frac{\sigma_{e_0} B_0^2 l_0^2}{\nu \rho_0}$	Chandrasekhar number
$\mathrm{Re} = \frac{w_0 D}{\nu}$	Reynols number
$S = \frac{\tau_0 w_0}{l_0}$	Strouhal number
$Sc_i = \frac{\nu}{D_{i_0}}$	Schmidt number
$\mathrm{Sh} = \frac{[(\beta_i)_V]_0 d_p^2}{\rho_0 D_{i_0}}$	Sherwood number

Dimensionless numbers

Acknowledgements

This work was supported by the Polish Ministry of Science and Higher Education from sources for science in the years 2012-2013 under Inventus Plus project

Author details

Rafał Rakoczy*, Marian Kordas and Stanisław Masiuk

*Address all correspondence to: rrakoczy@zut.edu.pl

Institute of Chemical Engineering and Environmental Protection Process, West Pomeranian University of Technology, Poland

http://dx.doi.org/10.5772/51296

References

[1] Aksielrud, G. A., & Mołczanow, A. D. (1981). *Dissolution process of solid bodies*, WNT Poland (in polish).

[2] Al-Qodah, Z., Al-Bisoul, M., & Al-Hassan, M. (2001). Hydro-thermal behavior of magnetically stabilized fluidized beds. *Powder Technology*, 115, 58-67.

[3] Basmadjian, D. (2004). *Mass transferPrinciples and applications* CRC Press LLC, USA.

[4] Bird, R. B., Stewart, W. E., & Lightfoot, E. N. (1966). *Transport phenomena*, Wiley, USA.

[5] Condoret, J. S., Riba, J. P., & Angelino, H. (1989). Mass transfer in a particle bed with oscillating flow. *Chemical Engineering Science*, 44(10), 2107-2111.

[6] Fraňa, K., Stiller, J., & Grundmann, R. (2006). Transitional and turbulent flows driven by a rotating magnetic field. *Magnetohydrodynamics*, 42, 187-197.

[7] Garner, F. H., & Suckling, R. D. (1958). Mass transfer form a soluble solid sphere. *AIChE Journal*, 4(1), 114-124.

[8] Guru, B. S., & Hiziroğlu, H. R. (2004). *Electromagnetic field theory fundamentals*, Cambridge University Press.

[9] Hristov, J. (2003). Magnetic field assisted fluidization- A unified approach. Part 3: Heat transfer in gas-solid fluidized beds- a critical re-evaluation of the results. [a], *Reviews in Chemical Engineering*, 19(3), 229-355.

[10] Hristov, J. (2003). Magnetic field assisted fluidization- A unified approach. Part 7: Mass Transfer: Chemical reactors, basic studies and practical implementations thereof. [b], *Reviews in Chemical Engineering*, 25(1-3), 1-254.

[11] Incropera, F. P., & De Witt, D. P. (1996). Fundamentals of heat and mass transfer. John Wiley & Sons Inc., USA.

[12] Jameson, G. J. (1964). Mass (or heat) transfer form an oscillating cylinder. *Chemical Engineering Science*, 19, 793-800.

[13] Kays, W. M., & Crawford, M. E. (1980). Convective heat and mass transfer. McGraw-Hill, USA.

[14] Lemcoff, N. O., & Jameson, G. J. (1975). Solid-liquid mass transfer in a resonant bubble contractor. *Chemical Engineering Science*, 30, 363-367.

[15] Lemlich, R., & Levy, M. R. (1961). The effect of vibration on natural convective mass transfer. *AIChE Journal*, 7, 240-241.

[16] Melle, S., Calderon, O. G., Fuller, G. G., & Rubio, M. A. (2002). Polarizable particle aggregation under rotating magnetic fields using scattering dichroism. *Journal of Colloid and Interface Science*, 247, 200-209.

[17] Möβner, R., & Gerbeth, G. (1999). Buoyant melt flows under the influence of steady and rotating magnetic fields. *Journal of Crystal Growth*, 197, 341-345.

[18] Nikrityuk, P. A., Eckert, K., & Grundmann, R. (2006). A numerical study of unidirectional solidification of a binary metal alloy under influence of a rotating magnetic field. *International Journal of Heat and Mass Transfer*, 49, 1501-1515.

[19] Noordsij, P., & Rotte, J. W. (1967). Mass transfer coefficients to a rotating and to a vibrating sphere. *Chemical Engineering Science*, 22, 1475-1481.

[20] Rakoczy, R., & Masiuk, S. (2009). Experimental study of bubble size distribution in a liquid column exposed to a rotating magnetic field. *Chemical Engineering and Processing: Process Intensification*, 48, 1229-1240.

[21] Rakoczy, R., & Masiuk, S. (2010). Influence of transverse rotating magnetic field on enhancement of solid dissolution process. *AIChE Journal*, 56, 1416-1433.

[22] Rakoczy, R. (2010). Enhancement of solid dissolution process under the influence of rotating magnetic field. *Chemical Engineering and Processing: Process intensification*, 49, 42-50.

[23] Spitzer, K. H. (1999). Application of rotating magnetic field in Czochralski crystal growth. *Crystal Growth and Characterization of Materials*, 38, 39-58.

[24] Sugano, Y., & Rutkowsky, D. A. (1968). Effect of transverse vibration upon the rate of mass transfer for horizontal cylinder. *Chemical Engineering Science*, 23, 707-716.

[25] Tojo, K., Miyanami, K., & Mitsui, H. (1981). Vibratory agitation in solid-liquid mixing. *Chemical Engineering Science*, 36, 279-284.

[26] Volz, M. P., & Mazuruk, K. (1999). Thermoconvective instability in a rotating magnetic field. *International Journal of Heat and Mass Transfer*, 42, 1037-1045.

[27] Walker, J. S., Volz, M. P., & Mazuruk, K. (2004). Rayleigh-Bénard instability in a vertical cylinder with a rotating magnetic field. *International Journal of Heat and Mass Transfer*, 47, 1877-1887.

[28] Wong, P. F. Y., Ko, N. W. M., & Yip, P. C. (1978). Mass transfer from large diameter vibrating cylinder. *Trans. Item*, 56, 214-216.

[29] Yang, M., Ma, N., Bliss, D. F., & Bryant, G. G. (2007). Melt motion during liquid-encapsulated Czochralski crystal growth in steady and rotating magnetic field. *International Journal of Heat and Mass Transfer*, 28, 768-776.

Chapter 11

Mass Transfer Over the Surface of Metal Nanostructures Initiated and Stopped by Illumination

T.A. Vartanyan, N.B. Leonov, S.G. Przhibel'skii and N.A. Toropov

Additional information is available at the end of the chapter

http://dx.doi.org/10.5772/51955

1. Introduction

Metal nanostructures play an increasing role in modern technologies. Being far from the thermodynamic equilibrium they are vulnerable to the influence of external agents. In particular, thermal stability of metal nanostructure is an issue in many applications. In this contribution we are going to discuss one counterintuitive way of stabilization of metal nanostructure, namely, illumination. It is generally agreed that illumination will destroy nanostructure if do not leave it intact. Nevertheless, we found that in some circumstances illumination may lead to tiny restructuring of the nanostructure surface that improves its thermal stability. This restructuring is not readily observable after illumination but lead to a pronounce effect after annealing. Illuminated nanostructures acquire immunity to the heating and change their structure much more slowly than the nanostructures that were not illuminated in advance. Moreover, the final state of the illuminated nanostructures after annealing differs considerable from that of unilluminated one being much more similar to its initial state. Taking into account close connection between the structure and the optical properties of the plasmonic metal nanostructures it is not surprising that after annealing illuminated and non-illuminated regions may be differentiated by eye.

More traditionally, illumination may initiate structural changes of the metal nanostructures. In particular, reshaping of metal nanoparticles that support plasmon excitation was studied by optical means. Resonance enhancement of the transformation rate was observed in our experiments on the arrays of alkali metal nanoparticles.

On the other hand, illumination can initiate structural transformations of the organic molecules adsorbed on the surface of metal nanostructures. In our experiments silver nanoparti-

cles were prepared by vacuum evaporation on a sapphire substrate. Cyanine dye molecules were spread over the silver nanoparticle arrays by spin-coating technique. The samples were characterized by scanning electron microscopy and optical spectroscopy. A significant increase of the dye photoinduced transformation rate was observed. Simultaneously, an enhanced absorption and fluorescence were observed.

The extinction spectrum of the hybrid material was rationalized as a result of mutual interactions between the plasmon oscillations localized in the metal nanoparticles and resonance absorption and refraction of dye molecules. Plasmon resonances are shifted due to the anomalous refraction of dye molecules. Depending on the spectral position of the dye absorption band relative to the inhomogeneously broadened plasmon band this shift may lead to considerable clarification of the sample at particular wavelengths that was observed experimentally. On the other hand, the absorption of dye molecules is enhanced due to the incident field amplification in the near field of metal nanoparticles. Even when the dye absorption band overlaps with the tail of the plasmon band of silver nanoparticles, 3 to 5 times enhancement of the dye absorption was obtained. Besides that a nearly 4-fold increase of cyanine dyes fluorescence intensity in the presence of metal nanoparticles was observed.

The photoinduced transformations of the dye molecules situated in the near field of the metal nanoparticles were studied. The rate of the transformations on the surface of metal nanoparticles was found to increase as compared to that on the surface of a dielectric substrate.

2. Illumination as a control over the surface mass transfer

Mass transfer over the solid surfaces is of crucial importance in many technological processes like vacuum vapor deposition, heterogeneous catalysis and many others. For example, when the granular metal films are grown via Volmer-Weber growth mode the atoms evaporated from the source first impinge on the surface and then diffuse over it. A nucleus of a metallic phase is formed by several atoms met together after a long way through the surface made separately by each of them. Then, the nucleus grows incorporating new atoms that first diffuse over the substrate and then climb up the existing flat metal cluster to form a 3D nanoparticle. All these processes being random, the resultant nanostructure is highly irregular. Figure 1 plots the optical extinction spectrum of silver granular film grown on a sapphire substrate. The broad band with a maximum at 420 nm shown as curve 1 is due to the absorption by surface plasmons localized in the silver nanoparticles. The width of this band is so large because there are nanoparticles of different shapes in the film. In particular, the red tail of the plasmon band is due to the flat pancake-like nanoparticles. These shapes are metastable and transform into more round shapes when heated. The band shifts in this case to the blue as a whole.

Illumination provides a means of much more delicate action upon the particle. Being irradiated by ruby laser the granular film changes in such a way that its extinction spectrum acquire the form shown in Figure 1 by curve 2. The shape of the extinction spectrum evidenced the light initiated mass transfer process over the surface of metal nanoparticles.

http://dx.doi.org/10.5772/51955

Indeed, one can notice that the number of flat particles that contribute to the red absorption is reduced while the number of the more round particles that contribute to the yellow absorption is increased. Thus, laser illumination may be used to the fine tuning of the shape distribution of metal nanoparticle. This possibility may be employed to obtain the values of the plasmon dephasing times [1,2].

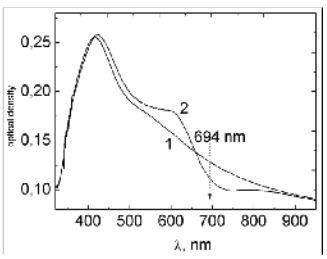

Figure 1. Light-induced mass transfer over the surface of silver nanoparticles. After illumination by three pulses of ruby laser with the fluence of 44 mJ/cm^2 the original extinction spectrum of the silver granular film on sapphire (1) transforms into (2). The observed changes in the extinction spectrum are due to the thermal diffusion of silver atoms over the surface of metal nanoparticles comprising the granular film.

The observed changes of the extinction spectrum are due to the contraction and reshaping of the nanoparticles in the course of the laser illumination. The sign variation of the optical density difference bears witness of an important role played by surface diffusion. Should evaporation be the sole consequence of the laser heating of the nanoparticles, one expects to observe only a dip centered at the laser frequency. Contrary to that, diffusion leads to the dip accompanied by a bump at a shorter wavelength, the laser frequency being in the midpoint between them. In reality both processes take place. A good fit to the experimental observations may be obtained with the formula that takes into account evaporation as well as diffusion. According to [3] the optical density difference $\Delta D$is a function of the normalized laser detuning

$$x = \frac{\omega - \Omega}{\Gamma}, \tag{1}$$

where Ω is the laser frequency, $\omega$is the frequency at which one observes the extinction difference and Γ is the dephasing rate of the plasmon resonance localized in the nanoparticles. This function reads as

$$\Delta D(x) = -A\frac{1}{1+x^2} + B\frac{x}{\left(1+x^2\right)^2}, \tag{2}$$

where A and B are the constants that define the relative contributions of the evaporation and diffusion processes, correspondently. Figure 2 plots the optical density difference ΔD ob-

tained experimentally as well as the theoretical curve computed according to Eqs. (1) and (2) with the following parameters A=0.013 and B=0.36. As B is much larger than A, one may conclude that it is the diffusion of silver atoms over the surface of silver nanoparticle that contributes most in the mechanism of the spectral hole burning while the contribution of evaporation is rather small.

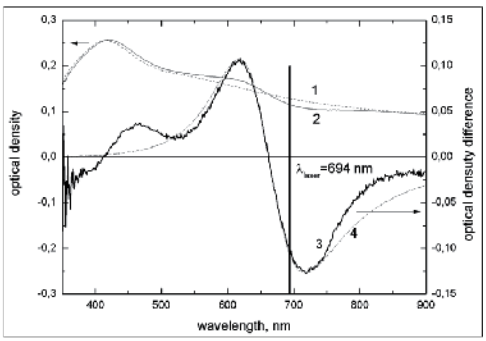

Figure 2. Optical density difference ΔD obtained experimentally (3) and the theoretical fit (4). Both curves are related to the right vertical axis. Two other curves related to the left vertical axis represent the optical density of the film before and after illumination.

To make a meaningful fit a slight shift of the laser frequency is required. As it was shown in [4], when the optical density of the film is considerable, as it is in our case, reflection is to be accounted for even though an individual particle absorb the light much stronger than scatter it. This additional contribution to the optical density of the film shifts the spectrum but does not affect the relative values of the diffusion and evaporation contributions.

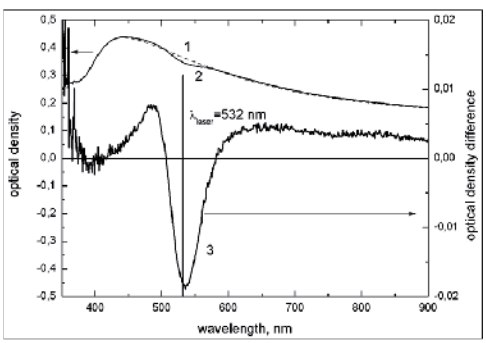

Figure 3. The original extinction spectrum of the silver granular film on sapphire (1) transforms into (2) after illumination by second harmonic of Nd:YAG laser. The optical density difference ΔDbefore and after illumination is given by curve (3). In this case contribution of the evaporation process is more pronounced than in the case of ruby laser illumination.

Figure 3 plots the hole burnt in the extinction spectrum of the silver granular film after illumination by the second harmonic of the Nd:YAG laser at 532 nm. Obviously, the dip follows

http://dx.doi.org/10.5772/51955

the laser frequency. On the other hand, relative contributions of the diffusion and evaporation processes in this case are different. Evaporation is much more evident in this case as compared with the case of ruby laser.

3. Initiation of the surface diffusion via a non-thermal laser action

Mass transfer described in the previous section was initiated by a crude force of a pulsed laser induced heating. More intriguing processes may be induced on the nanoparticle surface illuminated by cw lasers with low intensity. Heating is not operative in this case. Nevertheless, non thermal photo induced diffusion still causes the reshaping of metal nanoparticles. As the spectral position of the plasmon resonance is very sensitive to the particle shape, absorption spectroscopy may be employed to reveal this phenomenon. In the Figure 4 we present the results of the selective action of the low intensity cw diode laser on the ensemble of sodium nanoparticles on sapphire substrate. Due to the high reactivity of sodium this experiment was performed in a sealed glass cell with sapphire windows. Excitation of the surface plasmons localized in the sodium nanoparticles is responsible for the broad bell-shaped curve in the extinction spectrum. Illumination of the sodium granular film by a diode laser operating at the wavelength of 875 nm for 600 s with the power of 40mW produces tiny changes in the extinction spectrum. Although being small these changes are clearly visible in the differential spectrum also plotted in the Figure 4. Figure 5 and 6 plot the results of the similar experiments with lasers operating at the shorter wavelengths 852 nm and 810 nm. A striking feature of this experiments is that the laser action on the sodium nanoparticle shape is selective. Indeed, the zero crossing point of the differential spectrum is close to the laser wavelength and follows it as the laser wavelength changes. This may be clearly seen the Figure 7 where the position of the zero crossing point is plotted against the laser wavelength. At present we do not have a theoretical description of the spectral profile of the differential spectrum in this case. Nevertheless, one sees that general features are similar to the case of the heating induced reshaping. Non-thermally induced diffusion leads to the blue shift of the resonance frequencies of the plasmon resonances. Thus, the particles acquire more round shapes.

4. Inhibition of the surface diffusion by UV irradiation

Thin metal films on dielectric substrate are widely used in different applications ranging from microelectronics to heterogeneous catalysis. In most cases it is desirable that the structure preserves its properties for a long time. In particular, it is of practical importance to improve the thermal stability of the films. On the other hand, to reach such stability is not easy because the thin films are metastable. Thermal stability of the thin silver films is actively studied [5-7] because the agglomeration speeds up at the elevated temperature and leads to the undesirable changes in the film morphology as well as its chemical, electrical and optical properties.

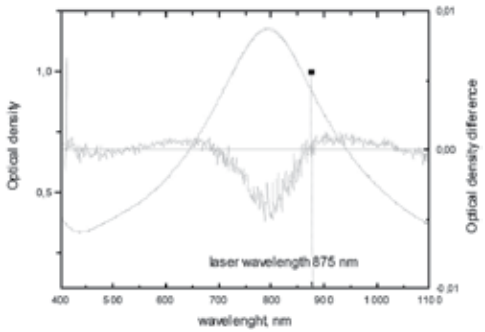

Figure 4. The broad bell-shaped curve represents the absorption band due to the surface plasmons localized in the sodium nanoparticles on the sapphire substrate. Tiny changes of the extinction spectrum after illumination for 600 s with 40mW cw diode laser at 875 nm are revealed by plotting the difference spectrum.

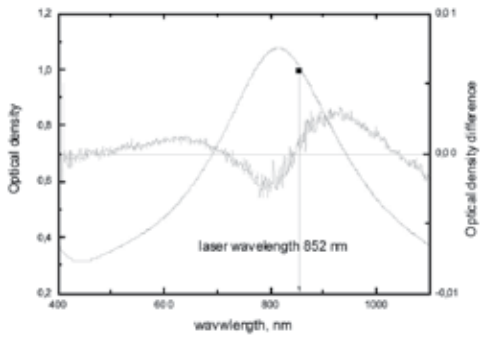

Figure 5. Same is Figure 4 with cw diode laser illumination at 852 nm.

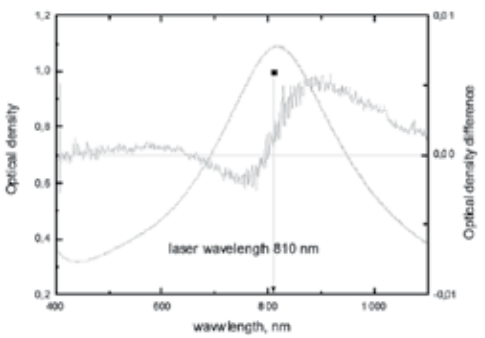

Figure 6. Same is Figure 4 with cw diode laser illumination at 810 nm.

http://dx.doi.org/10.5772/51955

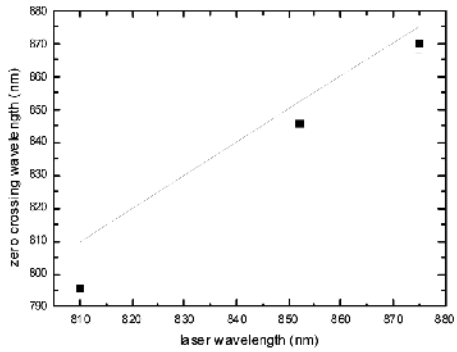

Figure 7. Selectivity of the laser action is made evident by the strong correlation between the position of the zero crossing point (squares) and laser wavelength. The straight light aids the eyes to see that this correspondence is not perfect.

Here we report on the new phenomenon of thin silver film stabilization under UV illumination. The illumination itself does not lead to any noticeable changes in the film appearance. At the same time, the illuminated films demonstrate enhanced stability against heating.

The films were obtained by thermal evaporation of silver on a sapphire substrate kept at the room temperature. The film prepared in vacuum was transferred into a glass cell with the sapphire windows. Then, the cell was evacuated and, finally, sealed off the vacuum system. UV radiation was produced by a mercury lamp. An optical filter was used to deliver radiation in the range from 300 to 400 nm. The intensity of UV illumination was set to 20 mW cm^{-2}. The duration of illumination was typically about 3 hours. To be on the safe side, only one half of the film was illuminated with the UV light. Another part of the film was used as a reference that undergoes just the same annealing procedures as the part, which was treated with the UV light.

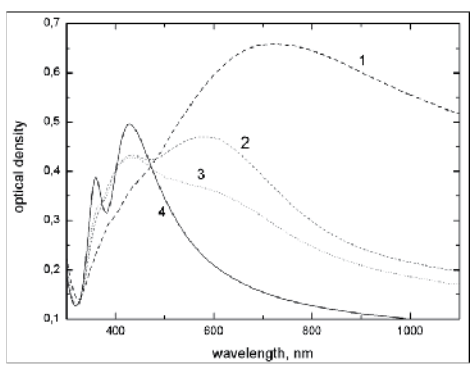

Figure 8. Extinction spectra of the thin silver films on sapphire: Extinction spectra of silver films on sapphire. Curve 1 was obtained after deposition and holding at room temperature for 3 hours. Curves 2 and 4 show the results obtained after annealing of the unirradiated film at 200°C for 5 and 30 minutes, respectively. Curve 3 shows the result obtained after annealing of the irradiated film at the same temperature for 30 minutes.

Figure 8 shows the results obtained in the course of annealing of the films. Just after the deposition the films undergo although very slight but noticeable changes. For this reason, the curve designated as 1 represents the extinction spectrum of the film that was hold at room temperature for 3 hour. This time required for the film to come into its metastable state that may be preserved for many days. Illumination with the UV radiation does not lead to any changes of the extinction spectrum. Hence, curve 1 represents the extinction spectra of the irradiated as well unirradiated film. In the course of annealing at 200°C the unirradated film passes through the states with the extinctions represented by curves 2 and 4. Curve 2 corresponds to annealing for 5 minutes and curve 4 corresponds to annealing for 30 minutes. Curve 3 corresponds to the annealing of the irradiated film for 30 minutes. Obviously, the annealing of the irradiated film proceeds much slowly than that of the unirradiated film. The final result of the annealing of the irradiated film is not so dramatic as that of unirradiated film.

Theses observations obtained via optical means were confirmed by scanning electron microscopy. Microphotographs are shown in Figure 9. After annealing of an unirradiated film its structure transforms into an array of well separated nearly spherical nanoparticles that may be seen in the image 4 of Figure 9. These changes are in accord with the blue shift and narrowing of the plasmon resonance represented by curve 4 in Figure 8. On the other hand, in image 3 of Figure 9 one finds much more in common with the image 1 of the initial film. This corresponds to the optical extinction spectrum 3 with a prolonged red tail resembling the red tail of the initial film 1.

It is to be mentioned that these results are representative in that sense that annealing at higher temperatures (up to 280°C) and for longer times (up to 3 hours) changes nor the morphology neither extinction spectra of the films.

Using of the UV light is essential for obtaining the described stabilization effect. We tried the irradiation at the wavelength of 440, 530 and 810 nm with the same intensity and duration of the irradiation and seen no effect of irradiation at this wavelengths on the films thermal stability.

5. Light induced transformations in the layers of organic molecules spread over the granular metal films

Cyanine dye molecules include a chain made of an odd number of methine groups bound together by alternating single and double bonds and two heteroaromatic rings at both ends of the chain. The structure of the cyanine dye molecules used in our experiments is shown in the Figure 10. Being adsorbed on the surface of a solid material, dye molecules form a layer with several preferable orientations of the long molecular axis relative to the surface normal. Heating and illumination are known to cause the reversible as well as irreversible mass transfer in the molecular layer that may be used for sensing and information recording applications [8,9]. It is tempting to study the possibility of enhancing these properties of the dye molecular layers by spreading them over the metal nanostructures. If the absorption

http://dx.doi.org/10.5772/51955

bands of the plasmon excitations in the metal nanostructure coincides or lies close to the absorption bands of the dye molecules one expects the mutual interaction between two resonances that may lead both to their enhancement as well as inhibition.

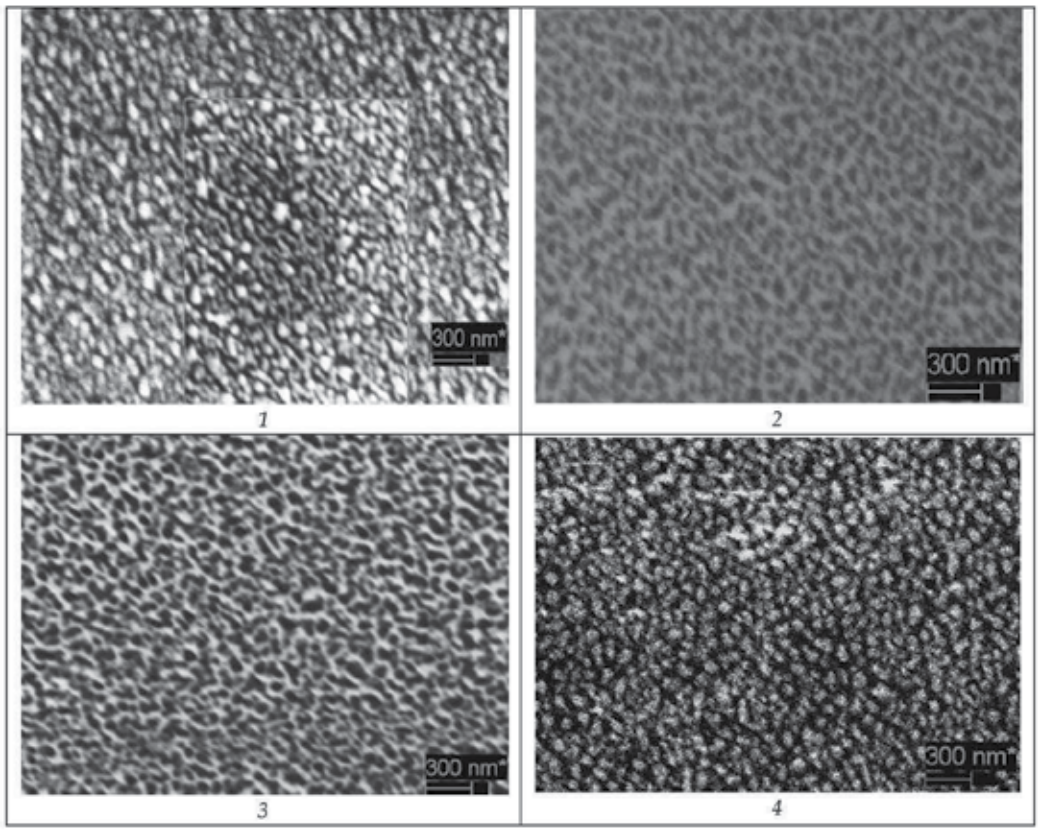

Figure 9. SEM images of silver films: Micrograph *1* represents the original unirradiated film. Micrographs *2* and *4* represent the results obtained after annealing of the unirradiated film at 200°C for 5 and 30 minutes, respectively. Micrograph 3 represents the result obtained after annealing of the irradiated film at the same temperature for 30 minutes.

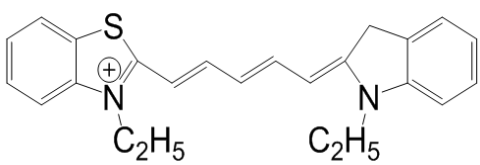

Figure 10. Structure of the cyanine dye molecule used in the experiments.

In our experiments silver nanoparticles were prepared by vacuum evaporation on a sapphire substrate. Cyanine dye molecules were spread over the silver nanoparticle arrays by

spin-coating technique. To achieve the homogeneity of the molecular layers the substrate spins with the rate of 4000 revolutions per minute. The dye layer thickness was set by the concentration of the solution used for spin coating. It was further checked by dissolution of the dye layer in the known quantity of solvent and determination of the dye concentration in it via optical means. The dye layer thickness in our experiments varied from 0.1 to 10 monolayers.

A special attention was paid to the stability of the granular metal film in the course of the dye deposition by spin coating technique. It was found that the as prepared granular metal film is not stable enough to ensure the reproducibility of the results. For this reason the granular metal films obtained via vacuum vapor deposition were suspended in ethanol overnight. After this treatment the optical density of the granular metal films reduces substantially due to the loss of the metal particles with low adhesion to the substrate. Those particles that remain on the surface after such treatment withstand many cycles of spin coating by dyes and subsequent rinsing in ethanol without noticeable changes in their morphology and optical properties.

Figure 11 plots the extinction spectrum of the dye molecular layer coated on the granular silver film on the sapphire substrate (curve 3). For comparison, extinction spectra of the dye molecular coated on the bare sapphire substrate (curve 1) and the granular silver film without dye (curve 2) are shown as well. The dye molecules contribution to the extinction of a hybrid material is revealed by the curve (4) that is the difference between (3) and (2). Clearly, the dye molecules absorbed much stronger when they are put in the vicinity of the silver nanoparticles as compared to the dye molecules on the bare sapphire substrate, the surface densities of the dye molecules being the same in both cases.

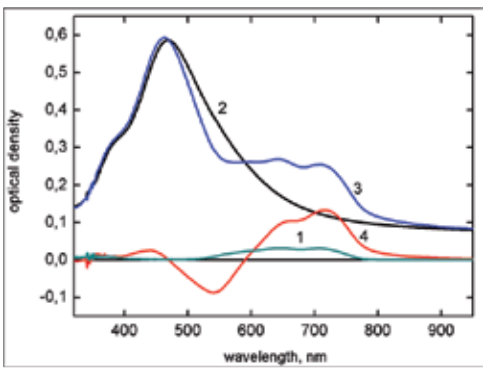

Figure 11. Extinction spectra of the dye layer on the sapphire substrate (1), the granular silver film on the sapphire substrate (2), and the dye layer coated over the granular silver film on the sapphire substrate. The curve (4) plots the difference between (3) and (2), i.e. the dye molecules contribution to the extinction of a hybrid material. Clearly, the dye molecules absorbed much stronger when they are put in the vicinity of the silver nanoparticles as compared to the dye molecules on the bare sapphire substrate, the surface densities of the dye molecules being the same in both cases.

The curve (4) in the Figure (11) demonstrates not only the fact that the absorption by dye molecules is enhanced in the vicinity of silver nanoparticles but also a more subtle effect of

http://dx.doi.org/10.5772/51955

the reduced absorption of silver nanoparticles being coated by dye molecules. This may be rationalized by considering the inhomogeneous broadening of the plasmon band and the anomalous dispersion associated with the absorption bands of the dye molecules. It is well known that the spectral position of the plasmon resonance depends on the refractive index of the surrounding material. Near the blue edge of the dye absorption band the anomalous dispersion leads to the low values of refractive index. Hence, the frequency of the plasmon resonance is expected to rise and its spectral position to shift in the blue direction. As in the spectral range under consideration the relative concentration of the nanoparticles rises with the rise of the resonance frequency, the above mentioned sift of the resonance frequencies of plasmon oscillations leads to the observed reduction of the hybrid material extinction. One can expect that the extinction maximum shifts as well. Such a shift indeed observed but it is rather small due to the damping of the plasmon resonance by interband transitions in silver.

The photoinduced transformations of the dye layers were observed under the action of the of the second harmonic of the Nd:YAG laser at the wavelength of 532 nm. Five pulses of 8 ns duration were delivered on the surface. The fluence was kept at the value of 8 mJ cm^{-2} to avoid burning of the spectral holes described above. First, the laser induced transformations were observed in the molecular layers on the bare sapphire substrate. Figure 12 plots the optical density of the dye layer before illumination (1) and after illumination (2). These changes may be interpreted as the departure of the molecules that form the aggregates from each other. In the extinction spectrum this process is seen as the reduction of absorption in the wings and the increase of absorption in the central part the band.

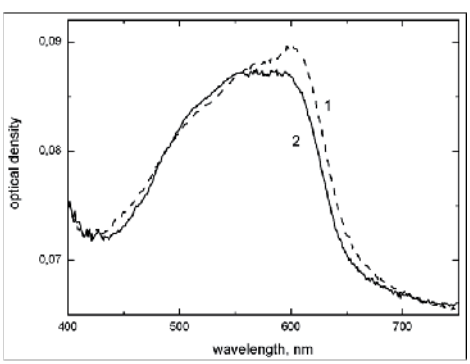

Figure 12. Optical density of the dye layer on the bare sapphire substrate before illumination (1) and after illumination (2).

The molecular movement under illumination in the case of the dye layer coated on the granular metal film is quite different. Figure 13 plots the optical density of the dye layer before illumination (1) and after illumination (2). To facilitate comparison with the case of the bare sapphire substrate absorption of the silver granular film was subtracted. One can easily see that even the sign of the laser induced is different from the case of dye layer on the bare sapphire substrate. As absorption in the wings rises one can conclude that the dye molecules moves to each other to produce the aggregated forms.

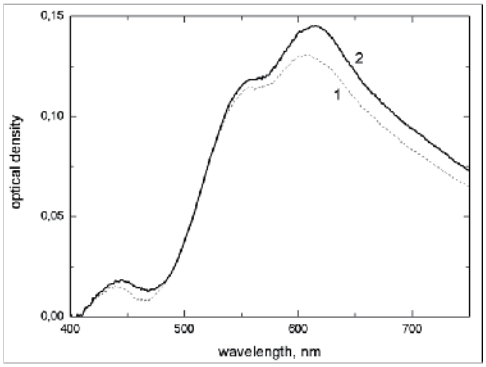

Figure 13. Optical density of the dye layer coated on the granular silver film on the sapphire substrate before illumination (1) and after illumination (2).

6. Conclusion

In this contribution we have presented experimental evidences that illumination is a convenient control of surface mass transport. This starts with the ordinary thermal action of light. In the case of granular metal films that consist of a collection of nanoparticles, this thermal action may be highly selective because the narrow band laser irradiation interacts strongly only with those particles that posses the plasmon resonance at the laser wavelength. Thus, although the diffraction limit avoids possibility to restrict the area of interaction tighter than a fraction of the wavelength, selectivity of the laser action is obtained in the spectral domain. Even the low intensity illumination may be used to initiate the mass transfer over the surface of metal nanoparticles. The selectivity of the laser action has been demonstrated in this case too.

An important issue of the thermal stability of thin metal films may be addressed with the ultraviolet irradiation. In this case we have shown that the granular silver film irradiated with UV light reduces its susceptibility to the thermal stress to a great extent.

Finally it was shown that the dye molecular movement initiated by illumination is quite different in the case of the dye molecules spread over the bare sapphire substrate and the granular metal film on the sapphire substrate.

Acknowledgments

This work was supported in part by Russian Foundation for Basic Research under grant #11-02-01020.

Author details

T.A. Vartanyan*, N.B. Leonov, S.G. Przhibel'skii and N.A. Toropov

St. Petersburg National Research University of Information Technology, Mechanics and Optics, St. Petersburg, Russian Federation

References

[1] Stietz, F., Bosbach, J., Wenzel, T., Vartanyan, T., Goldmann, A., & Träger, F. Decay Times of Surface Plasmon Excitation in Metal Nanoparticles by Persistent Spectral Hole Burning. Phys. Rev. Lett. (2000). , 84(24), 5644-5647.

[2] Bosbach, J., Hendrich, C., Stietz, F., Vartanyan, T., & Träger, F. Ultrafast dephasing of surface plasmon excitation in silver nanoparticles: Influence of particle size, shape, and chemical surrounding. Phys. Rev. Lett., (2002). , 257404 EOF.

[3] Vartanyan, T., Bosbach, J., Stietz, F., & Träger, F. Theory of spectral hole burning for the study of ultrafast electron dynamics in metal nanoparticles. Appl. Phys. B, (2001). , 73-391.

[4] Bonch-Bruevich, A. M., Vartanyan, T. A., Leonov, N. B., Przhibel'skii, S. G., & Khromov, V. V. Comparative Investigation of the Effect of Heat and Optical Radiation on the Structure of Island Metal Films by Optical Fluctuation Microscopy. Optics and Spectrosc., (2001). , 91(5), 779-785.

[5] Simrick N.J., Kilner J.A., Atkinson A., Thermal stability of silver thin films on zirconia substrates, Thin Solid Films,. (2012). 2012(520), 2855-2867.

[6] Kim H.C., Alford T.L., Allee D.R., Thickness dependence on the thermal stability of silver thin films, Appl.Phys. Lett, (2002). , 4287 EOF-4289 EOF.

[7] Lv J., Lai F., Lin L., Lin Y., Huang Z., Chen R., Thermal stability of Ag films in air prepared by thermal evaporation, Appl.Surf. Sci, (2007). , 2007(253), 7036-7040.

[8] Kaliteevskaya E.N., Krutyakova, V.P., Razumova, T.K., Thermally induced variations in the conformational compositionand spatial orientation of molecular components of a dicarbocyanine dye layer, Opt. and Spectr., (2006). , 300 EOF-306 EOF.

[9] Asnis, L. N., Kaliteevskaya, E. N., Krutyakova, V. P., Razumova, T. K., Tarnovskii, A. N., Tibilov, A. S., & Chizhov, S. A. (2008). , 6985, 6985A-08.

Chapter 12

Convective Mass Transfer in a Champagne Glass

Fabien Beaumont, Gérard Liger-Belair and
Guillaume Polidori

Additional information is available at the end of the chapter

http://dx.doi.org/10.5772/51956

1. Introduction

Legend has it that the Benedictine monk Dom Pierre Pérignon discovered the Champagne method for making sparkling wines more than 300 years ago. As it happens, a paper presented to the Royal Society in London described the Champagne production method in 1662, six years before Pérignon ever set foot in a monastery. In fact, Pérignon was first tasked with keeping bubbles out of wine, as the effervescence was seen as vulgar at the time. But then tastes changed and fizz became fashionable, so Pérignon's mandate was reversed; he went on to develop many advances in Champagne production, including ways to increase carbonation. In any case, the process was not regularly used in the Champagne region of France to produce sparkling wine until the 19th century. Since that time, Champagne has remained the wine of celebration, undoubtedly because of its bubbling behavior.

But what is the exact role of the bubbles? Is it just aesthetics? Do they contribute to only one aspect, or to many aspects, of the subjective final taste? We have been rigorously analyzing Champagne for more than a decade, using the physics of fluids in the service of wine in general and Champagne- tasting science in particular.

2. The Champagne method

Fine sparkling wines and Champagne result from a two-step fermentation process. After completion of the first alcoholic fermentation, some flat Champagne wine (called base wine) is bottled with a mixture of yeast and sugar. Consequently, a second fermentation starts inside the bottle as the yeast consumes the sugar, producing alcohol and a large amount of carbon dioxide (CO_2). This is why Champagne has a high concentration of CO_2 dissolved in

it about 10 grams per liter of fluid and the finished Champagne wine can be under as much as five or six atmospheres of pressure. As the bottle is opened, the gas gushes out in the form of tiny CO_2 bubbles. In order for the liquid to regain equilibrium once the cork is removed, it must release about five liters of CO_2 from a 0.75 liter bottle, or about six times its own volume. About 80 percent of this CO_2 is simply outgassed by direct diffusion, but the remaining 20 percent still equates to about 20 million bubbles per glass (a typical flute holds about 0.1 liter). For Champagne connoisseurs, smaller bubble size is also a measure of quality.For consumers and winemakers as well, the role usually ascribed to bubbles in Champagne tasting is to awaken the sight sense. Indeed, the image of Champagne is intrinsically linked to the bubbles that look like "chains of pearls" in the glass and create a cushion of foam on the surface. But beyond this visual aspect, the informed consumer recognizes effervescence as one of the main ways that flavor is imparted, because bursting CO_2 bubbles propel the aroma of sparkling wine into the drinker's nose and mouth (Figure 1).

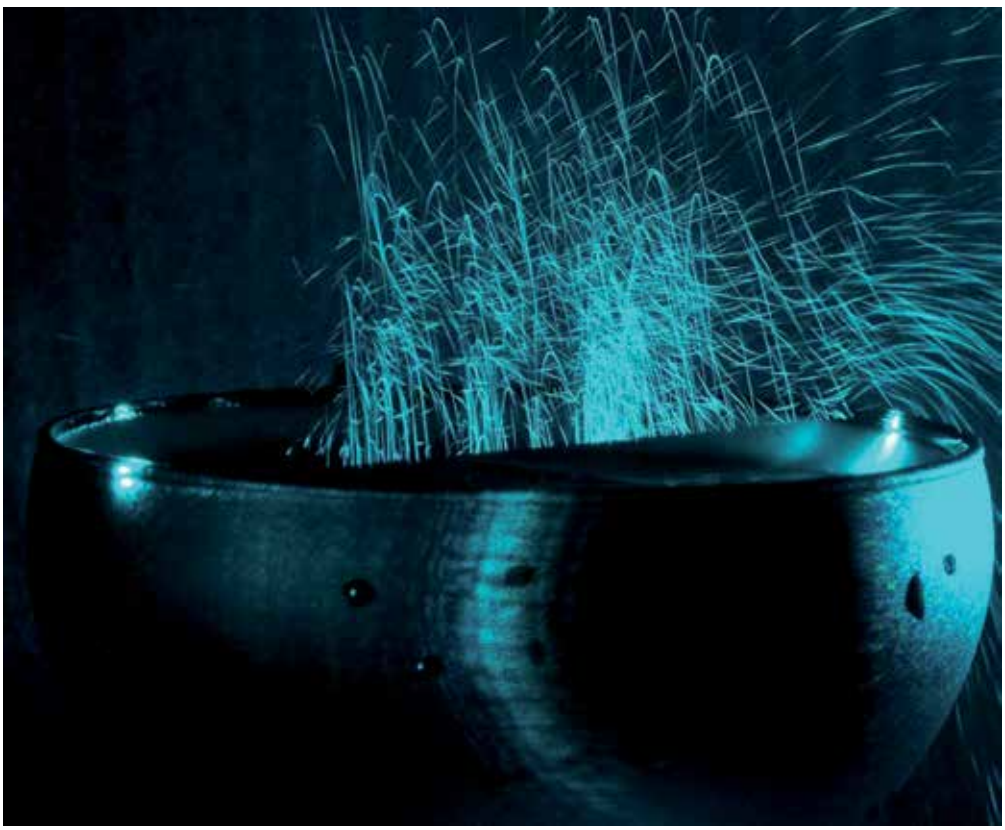

Figure 1. A glass of Champagne is a feast for all the senses; indeed it is sight and sound that make sparkling wines particularly special. Elegant bubble trains rise from nucleation sites suspended in the fluid *(right).* Bubbles reaching the top of the glass burst and produce a fog of droplets *(above).* The questions being explored by enologists include how the carbonation and effervescence induce fluid flow in, and affect the flavor of, the beverage. (All photographs are courtesy of the authors.)

http://dx.doi.org/10.5772/51956

One cannot understand the bubbling and aromatic exhalation events in champagne tasting, however, without studying the flow-mixing mechanisms inside the glass. Indeed, a key assumption is that a link of causality may exist between flow structures created in the wine due to bubble motion and the process of flavor exhalation [1]. But the consequences of the bubble behavior on the dynamics of the Champagne inside the glass and the CO_2 propelling process are still unknown. Quantifying the exhalation of flavors and aromas seems a considerable challenge, something that is difficult to control experimentally, but this constitutes the aim of our current work.

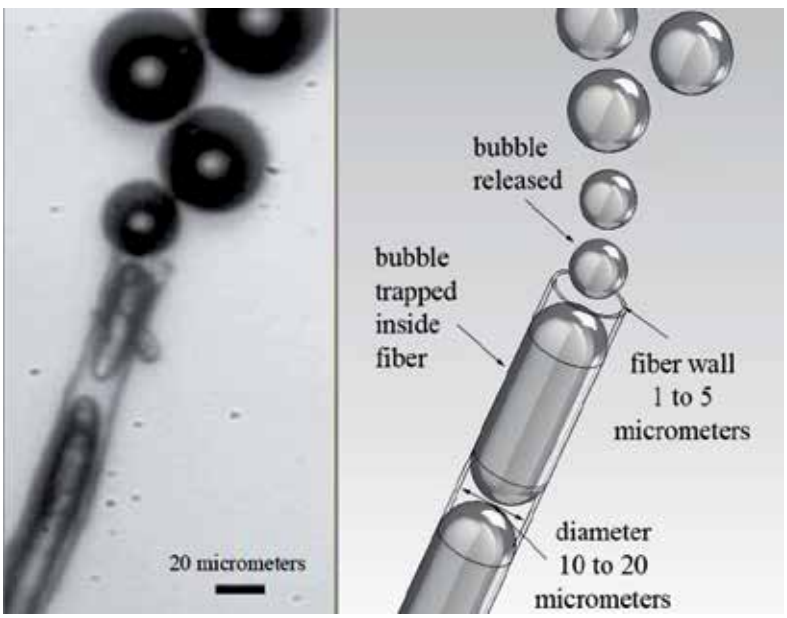

Figure 2. Bubbles in sparkling wines do not spring into existence unaided, but require a starting point. These nucleation sites take the form of microscopic cellulose fibers, from the air or a towel used to dry the glass, which trap air pockets as the glass is filled. Carbon dioxide from the wine diffuses into the gas pockets, producing bubbles like clockwork *(left).*

3. The birth of bubbles

The first step is to elucidate how bubbles themselves come into being. Generally speaking, two ways exist, and sometimes coexist, to generate bubble chains in Champagne glasses [2-6]. Natural effervescence depends on a random condition: the presence of tiny cellulose fibers deposited from the air or left over after wiping the glass with a towel, which cling to the glass due to electrostatic forces (Figure 2). These fibers are made of closely packed microfibrils, themselves consisting of long polymer chains composed mainly of glucose. Each fiber, about 100 micrometers long, develops an internal gas pocket as the glass is filled. Capillary action tries to pull the fluid inside the micro-channel of the fiber, but if the fiber is

completely submerged before it can be filled, it will hold onto its trapped air. Such gas trapping is aided when the fibers are long and thin, and when the liquid has a low surface tension and high viscosity. Champagne has a surface tension about 30 percent less than that of water, and a viscosity about 50 percent higher.

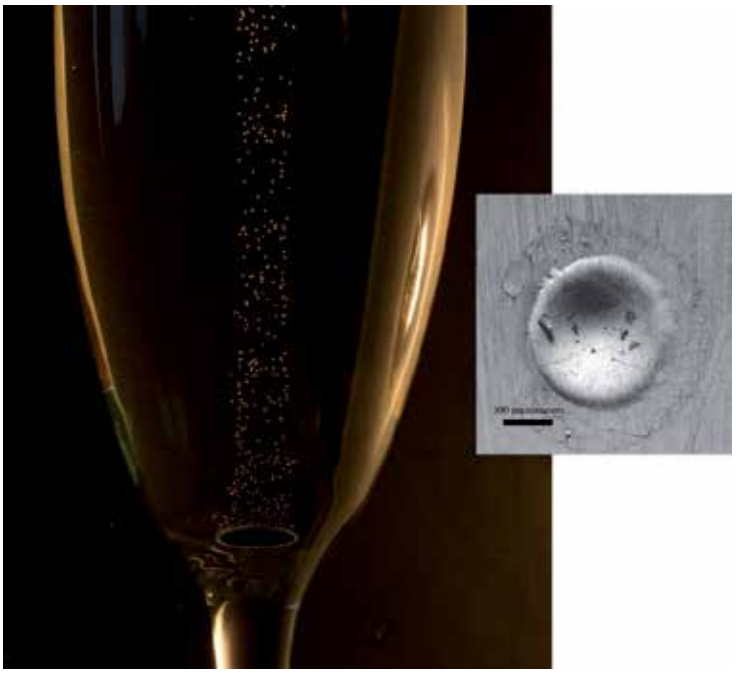

Figure 3. In order to study effervescence in Champagne and other sparkling wines, random bubble production must be replaced with controlled creation of bubble streams. The glass bottom is etched with a ring that provides nucleation sites for regular bubble trains *(left).* The ring consists of many small impact points *(right)* from a laser, one of which is shown above. Glasses etched with a single nucleation point were used in studies to see how a single stream of bubbles would induce motion in the surrounding fluid, and what shape that fluid motion would take.

These microfiber gas pockets act as nucleation sites for the formation of bubbles. To aggregate, CO_2 has to push through liquid molecules held together by van der Waals forces, which it would not have enough energy to do on its own. The gas pockets lower the energy barrier to bubble formation (as long as they are above a critical size of 2 micrometers in radius, because below that size the gas pressure inside the bubble is too high to permit CO_2 to diffuse inside). It should be noted that irregularities in the glass surface itself cannot act as nucleation sites such imperfections are far too small, unless larger micro scratches are purposely made. Once a bubble grows to a size of 10 to 50 micrometers, it is buoyant enough to detach from the fiber, and another one forms like clockwork; an average of 30 bubbles per second are released from each fiber. The bubbles expand from further diffusion of CO_2 into them as they rise, which increases their buoyancy and accelerates their speed of ascent [2, 5-6]. They usually max out at less than a millimeter in diameter over the course of their one- to five-second travel time up the length of a flute. Because natural nucleation is very random

http://dx.doi.org/10.5772/51956

and not easily controllable, another way to generate bubbles is to use a mechanical process that is perfectly reproducible from one filling to the next. Glassmakers use a laser to engrave artificial nucleation sites at the bottom of the glass; such modified glasses are commonly used by Champagne houses during tastings (Figure 3). To make the effervescence pattern pleasing to the eye, artisans use no fewer than 20 impacts to create a ring shape, which produces a regular column of rising bubbles [3-5, 7].

4. Fizz and flow

The displacement of an object in a quiescent fluid induces the motion of fluid layers in its vicinity. Champagne bubbles are no exception to this rule, acting like objects in motion, no matter whether the method used to produce them was random or artificial. Viscous effects make the lower part of a bubble a low-pressure area, which attracts fluid molecules around it and drags some fluid to the top surface, although the bubbles move about 10 times faster than the fluid (Figure 4). Consequently, bubbles and their neighboring liquid move as concurrent upward flows along the center line of the glass. Because the bubble generation from nucleation sites is continuous, and because a glass of Champagne is a confined vessel, this constant upward ascent of the fluid ineluctably induces a rotational flow as well [2-5, 7-8]. To get a precise idea of the role bubbles play in the fluid motion, we observed a Champagne flute with single nucleation site at the bottom (Figure 4). A bubble's geometric evolution is well studied in carbonated beverages. For example, we know that the bubble growth rate during vertical ascent reliably leads to an average diameter of about 500 micrometers for a 10 centimeter migration length in a flute. In fact, for such a liquid supersaturated with dissolved CO_2 gas molecules, empirical relationships reveal the bubble diameter to be proportional to the cube root of the vertical displacement. Another property of bubbles is that they can act as either rigid or flexible spheres as they rise, depending on the content of the fluid they are in, and rigid spheres experience more drag than flexible ones. Champagne bubbles do not act as rigid spheres, whereas bubbles in other fizzy fluids, such as beer, do. Beer contains a lot of proteins, which coat the outside of the bubbles as they ascend, preventing their deformation. Beer is also less carbonated than Champagne, so bubbles in it do not grow as quickly, making it easier for proteins to completely encircle them. But Champagne is a relatively low-protein fluid, so there are fewer surfactants to stick to the bubbles and slow them down as they ascend. In addition, Champagne's high carbonation makes bubbles grow rapidly on their upwards trip, creating ever more untainted surface area, in effect cleaning themselves of surfactants faster than new molecules can fill in the space. However, some surfactants are necessary to keep bubbles in linear streams with none; fluid flows would jostle the bubbles out of their orderly lines.

We carried out filling experiments at room temperature to avoid condensation on the glass surface, and allowed the filled glass to settle for a minute or so before taking measurements [2-5, 7-9]. Our visualization is based on a laser tomography technique, where a laser sheet 2 millimeters wide crosses the center line of the flute, imaging just this two- dimensional section of the glass using long-exposure photography. To avoid optical distortions by the

curved surface of the glass, this latter is partially immersed in a parallelepiped tank full of water (Figure 5) with a refractive index close to that of champagne (RI champagne 1.342 while RI pure water 1.332).

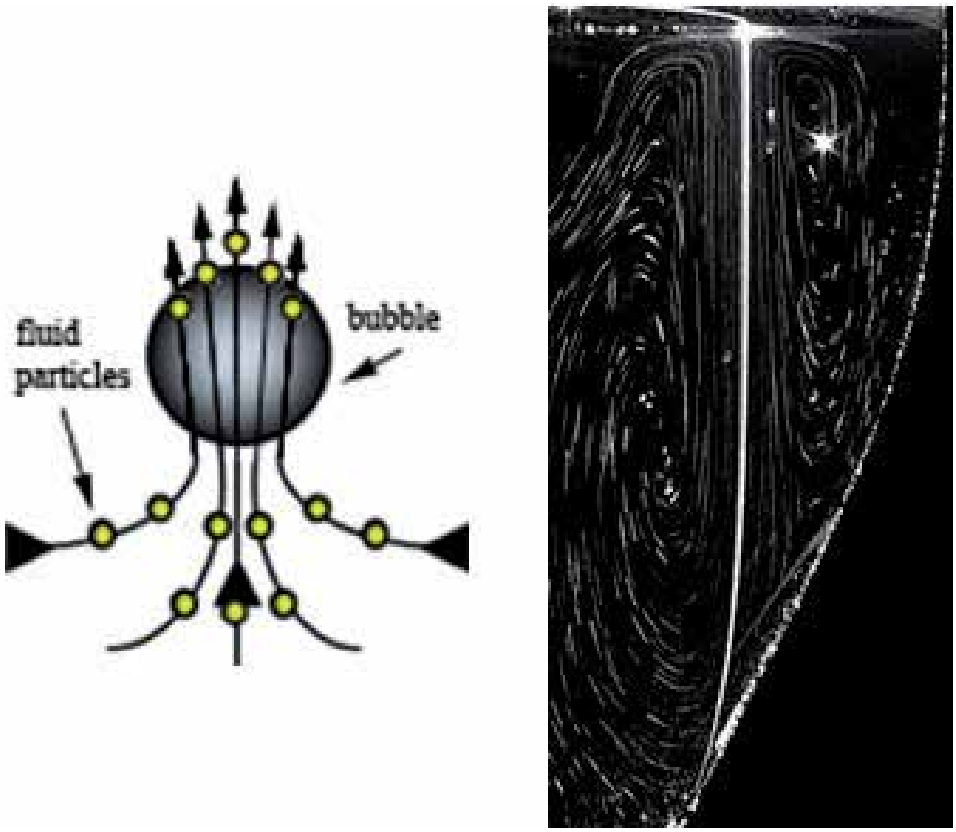

Figure 4. The fluid motion occurs because as the bubbles rise, they drag the fluid along in their wake (left). When seeded with tiny polymer particles and imaged in a time-lapse photo with a laser, the bubble stream appears as a white line, and the regular ring vortex of movement induced in the fluid from the bubble movement is clearly outlined by the particles (right).

We seeded the Champagne with Rilsan particles as tracers of fluid motion. These polymer particles are quasi-spherical in shape, with diameters ranging from 75 to 150 micrometers, and have a density (1.060) close to that of Champagne (0.998). The particles are neutrally buoyant and do not affect bubble production, but they are very reflective of laser light. It is amazing to see the amount of fluid that can be set in motion by viscous effects. In our resulting images, a central line corresponds to the bubble train path during the exposure time of the camera, and the fluid motion is characterized by a swirling vortex that is symmetrical on both sides of the bubble chain (Figure 6). The vortex-pair in the planar view of our image can be extrapolated to show a three-dimensional annular flow around the center line of bub-

http://dx.doi.org/10.5772/51956

bles (Figure 6). This means that a single fixed nuclear site on the glass surface can set the entire surrounding fluid into a small-scale ring vortex.

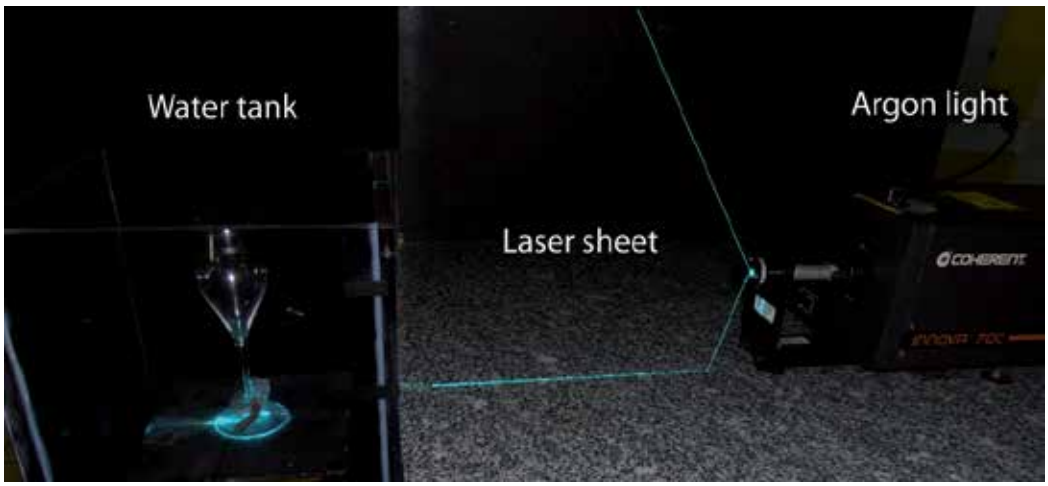

Figure 5. Experimental set-up

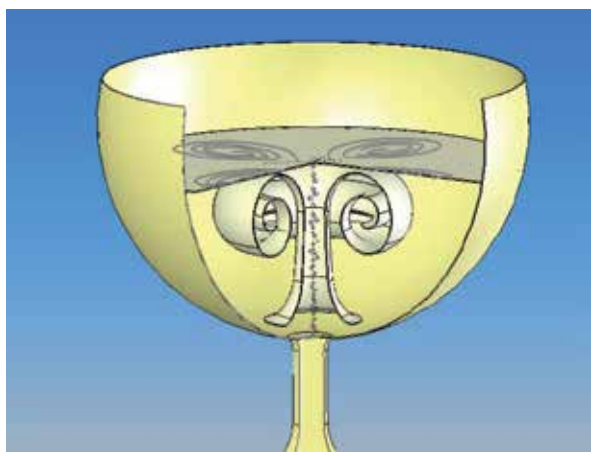

Figure 6. Illustration of the three-dimensional flow in an engraved coupe-glass (right).

5. Controlled mixing

Champagne-tasting science involves a number of very subjective judgments, often difficult to quantify. For example, there is an inherent compromise between the visual aspects of bubbly behavior and olfactory stimulation, as these two qualities appear to be at odds. Too

much nucleation will excite the sense of sight but cause the carbonation to quickly fizzle out, making for unpleasant tasting. On the contrary, poor nucleation will produce fewer bubbles in the glass, but more bubbles and aromas in the taster's nose and mouth, consequently enhancing the senses of smell and taste at the expense of sight. From the many experiments we have conducted with controlled effervescence, it seems that an ideal number of about 20 nucleation sites best satisfies this dilemma. Our laser visualizations of fluid flow have shown that a flute with an engraved circular crown reaches a steady state of fluid motion about 30 seconds after the glass is poured [2-5, 7-8]. The vortices do not swirl around and change shape, in contrast to those created in unetched glasses. The bubbles are highly reflective, allowing one to clearly observe the formation of a rising gas column along the vertical glass axis from the treated bottom up to the free surface of the beverage. Consequently, the driving force it imparts to the surrounding fluid generates two large counter-rotating vortices in the vertical lighted section (Figure 6-7). These cells are located outside the rising bubbles, close to the wall of the flute. Because this gas column acts like a continuous swirling-motion generator within the glass, the flow structure exhibits a quasi-steady two-dimensional behavior with a geometry that is symmetrical around the center line of the glass. It clearly appears in the case of an engraved flute that the whole domain of the liquid is homogeneously mixed (Figure 7, right). To complete our observations, we also studied the flow in an engraved traditional Champagne coupe, which is much wider but shallower than the flute. As in the flute, the rising CO_2 bubble column causes the main fluid to move inside the coupe. However, two distinctive steady-flow patterns, instead of one, appear in a glass of this shape. Like the flute, the coupe clearly exhibits a single swirling ring, whose cross section appears as two counter- rotating vortices close to the glass axis. What strongly differs from the motion in the flute is that this recirculation flow region does not occupy the whole volume of the glass. The periphery of the coupe is instead characterized by a zone of no motion. Thus, for a wide-rimmed glass, only about half of the liquid bulk participates in the Champagne mixing process. Nevertheless, in an engraved glass of either shape, the presence of a ring vortex is not time-dependent; it still forms in the coupe, despite the ascent time being about a third of that in the flute.

6. Infrared imaging technique used to visualize the flow of gaseous CO_2 desorbing from champagne

A visualization technique based on the Infrared (IR) thermography principle has been used to film the gaseous CO_2 fluxes outgassing from champagne (invisible in the visible light spectrum) [10]. The CO_2 absorptions observable by the IR camera are quite weak because this gas molecule has only a strong absorption peak in the detector bandwidth at 4.245 mm. Consequently, the best way to visualize the flow of gaseous CO_2 desorbing from champagne is to fit the IR video camera with a band-pass filter (centered on the CO_2 emission peak). The experimental device consists of a CEDIP middle waves Titanium HD560M IR video camera, coupled with a CO_2 filter (Ø 50.8 mm X 1 mm thick– Laser Components SAS). In comple-

http://dx.doi.org/10.5772/51956

ment, the technique involves an extended high-emissivity (0.97) blackbody (CI systems provided by POLYTEC PI), used at a controlled uniform temperature of 80°C, and placed approximately 30 cm behind the glass. The IR video camera was used at a 10 frames per second (fps) filming rate.

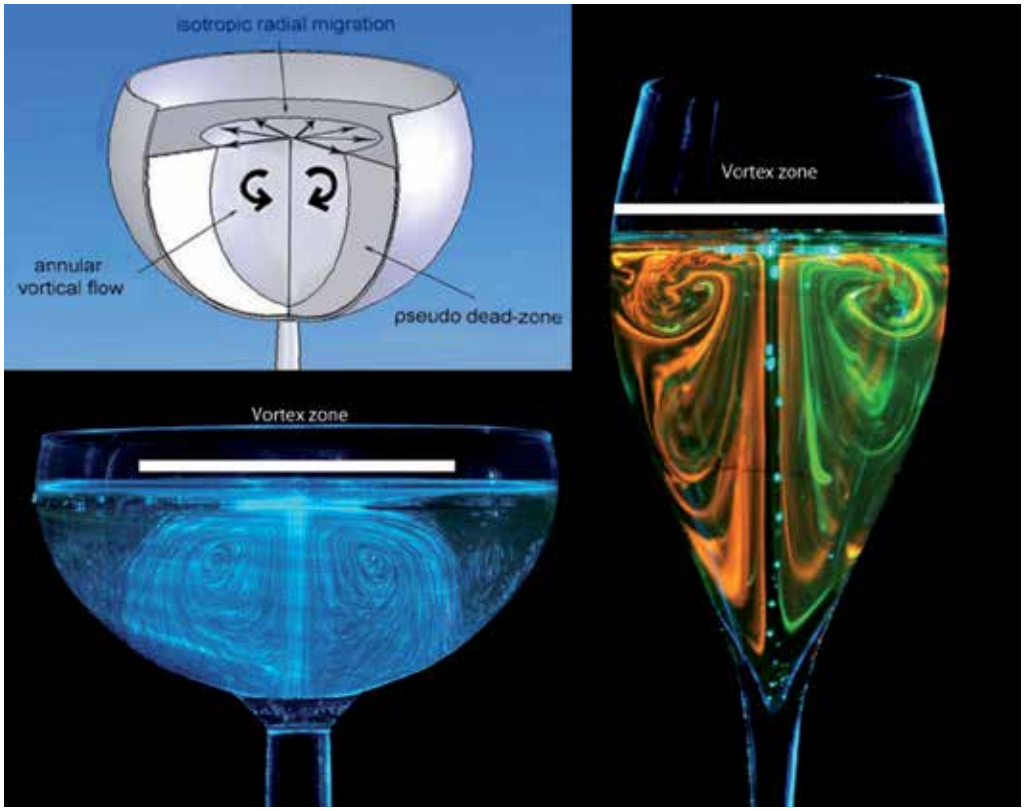

Figure 7. Glass shape and size have great influence on fluid flow and mixing in Champagne and sparkling wines. A flute imaged with fluorescent dye *(right)* shows that the resulting fluid vortex spans the entire width of the glass. A coupe glass, much shorter and wider, imaged with a laser and polymer particles, produces a similar vortex, but the vortex zone only extends across about half of the liquid *(bottom left).* A dead zone of no motion arises in the outer perimeter of the glass, and bubbles do not reach this area before bursting. A pseudo–dead zone beneath the liquid surface experiences only minimal movement and mixing *(top left).*

7. Results and discussion

7.1. Losses of dissolved CO2 during the service of champagne in each type of drinking vessel

As recently shown in a previous article, the pouring process is far from being inconsequential with regard to the concentration of CO_2 dissolved into the wine [11]. During the several

seconds of the pouring process, champagne undergoes highly turbulent and swirling flows. During this phase, champagne loses a very significant part of its initial content in dissolved CO_2. Gray scale infrared thermography time-sequences displayed in Figure 9 illustrate the progressive losses of dissolved CO_2 desorbing from the liquid phase into the form of a cloud of gaseous CO_2, whether champagne is poured in a flute or in a coupe. Clouds of gaseous CO_2 escaping from the liquid phase clearly appear. Consequently, at the beginning of the time series (i.e., at t=0, after the glass was poured with champagne and manually placed below the sampling valve of the chromatograph), champagne holds a level of dissolved CO_2 well below 11.6± 0.3 g L^{-1} (as chemically measured inside a bottle, after uncorking, but before pouring). In the present work, the initial bulk concentration of dissolved CO_2 after pouring, denoted c_i, was also chemically accessed by using carbonic anhydrase. To enable a statistical treatment, six successive CO_2 dissolved measurements were systematically done for each type of drinking vessel, after six successive pouring (from six distinct bottles). When served at 20°C,champagne was found to initially hold (at t=0, after pouring) a concentration of CO_2 dissolved molecules of $c_i^{flute} = 7.4 \pm 0.4$ g L^{-1} in the flute, and $c_i^{coupe} = 7.4 \pm 0.5$ g L^{-1} in the coupe (i.e., approximately 4 g L^{-1} less in both types of drinking vessel after pouring than inside the bottle, before pouring).

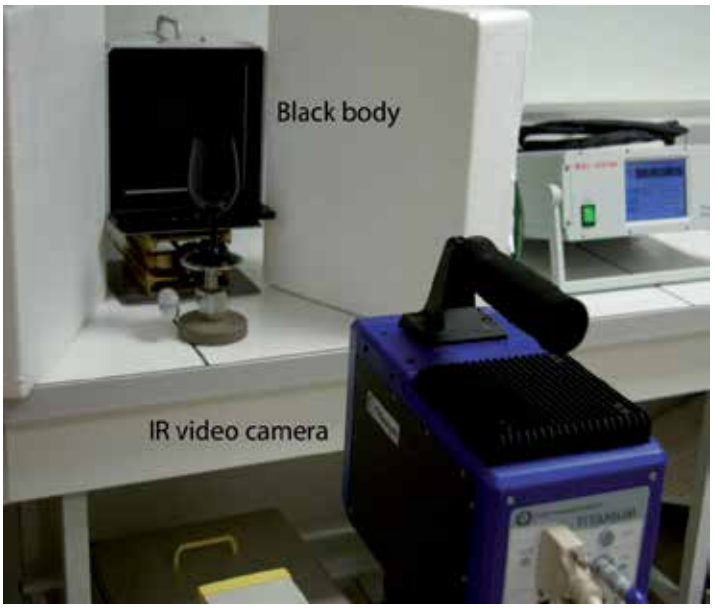

Figure 8. Experimental device

http://dx.doi.org/10.5772/51956

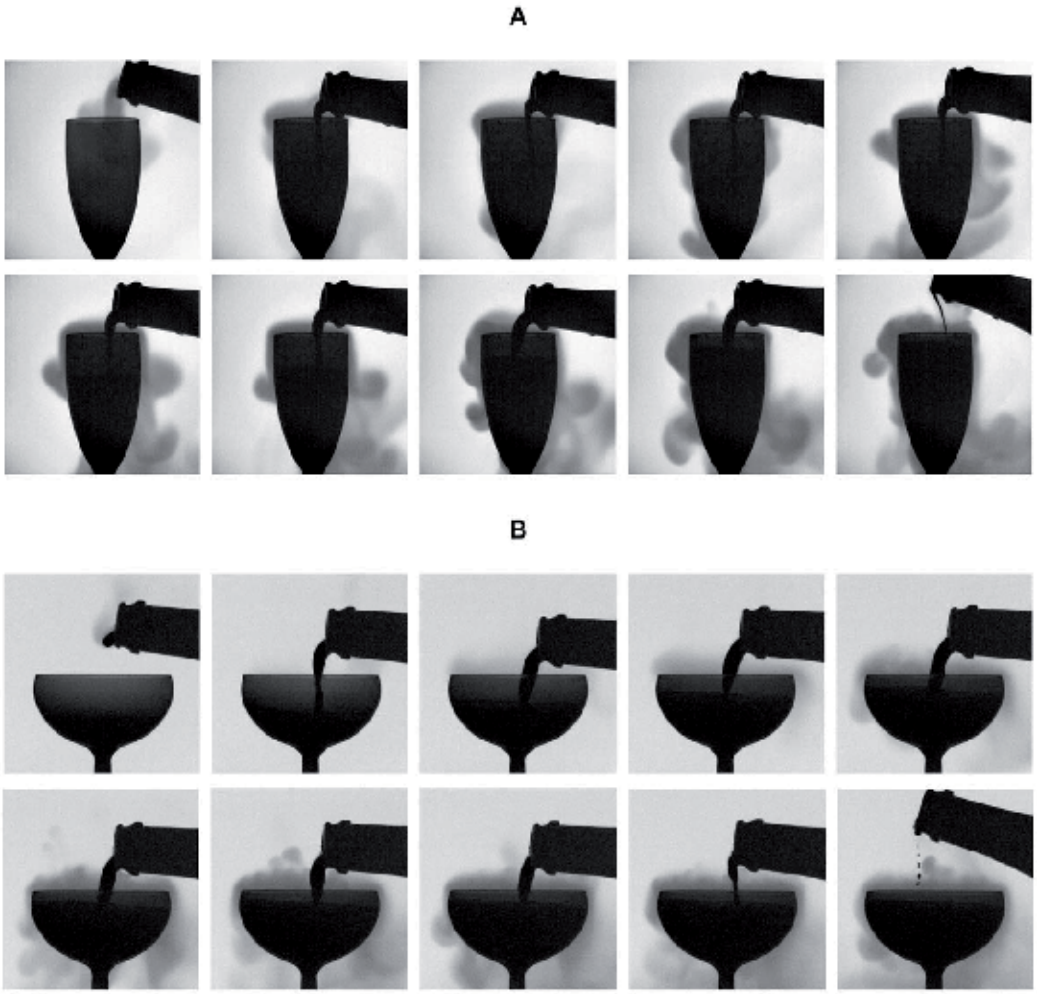

Figure 9. Infrared imaging of gaseous CO_2 desorbing when pouring champagne into both glass types. Gray scale time-sequences illustrating the pouring step as seen through the objective of the IR video camera – for a bottle stored at 20°C – whether champagne is served into the flute (a) or into the coupe (b).

7.2. Gaseous CO_2 and ethanol content found in the headspace above each type of drinking vessel

All along the first 15 minutes following pouring, concentrations of gaseous CO_2 found close to the edge of the flute are approximately between two and three times higher than those reached above the coupe. This observation is self-consistent with some recent data about volume fluxes of gaseous CO_2 measurements above glasses poured with champagne, including a flute and a coupe [11]. Fluxes of gaseous CO_2 per unit surface area offered to gas discharging are indeed significantly higher above the surface of the flute than above the surface of the coupe because the same total amount of dissolved CO_2 (<0.7 gram

for both glass types after pouring) has to be released by bubbles from a narrower surface, thus concentrating in turn more gaseous CO_2 in the headspace above the flute. Actually, due to higher concentrations of gaseous CO_2 above the flute than above the coupe, the smell of champagne, and especially its first nose, is always more irritating when champagne is served into a flute. It is indeed well-known that a sudden and abundant quantity of CO_2 (a strong trigeminal stimulus) may irritate the nose during the evaluation of aromas [12]. By using time-sequences provided through infrared imaging, the gaseous CO_2 desorbing from champagne and progressively invading the headspace above glasses was made visible in a false color scale (see Figure 10). Such an image processing analysis provides a better visualization of the relative differences in the CO_2 concentration field between both glass types, as shown in the thermography images displayed in Figure 11. Zones highly concentrated in gaseous CO_2 appear in black and dark blue, whereas zones slightly concentrated in gaseous CO_2 appear in red. The concentration of CO_2 found above the flute (close to the edge) is indeed always significantly higher than that found above the coupe. It can be noted for example, through infrared imaging, that the headspace (above the champagne surface, but below the glass edge) remains black during the first 3 min following pouring in case of the flute, whereas it progressively turns blue in case of the coupe.

Moreover, it is also worth noting from infrared imaging time-sequences that the cloud of gaseous CO_2 escaping from champagne tends to stagnate above the glass, or even tends to flow down from the edge of glasses by ''licking'' the glass walls (rather than diffuse isotropically around them). These observations conducted through infrared imaging betray the fact that gaseous CO_2 is approximately 1.5 times denser (ρ CO2 $\approx$ 1.8 g L^{-1} *at* 20 °C) than dry air is (ρ air $\approx$ 1.2 g L^{-1} *at* 20 °C), and therefore tends to naturally flow down.

7.3. Numerical modeling of bubble induced flow patterns in champagne glasses

A numerical modeling of flow dynamics induced by the effervescence in a glass of champagne has been carried out for the first time using the finite volume method by CFD (Computational Fluid Dynamics). In order to define source terms for flow regime and to reproduce accurately the nucleation process at the origin of effervescence, specific subroutines for the gaseous phase have been added to the main numerical model. These subroutines allow the modeling of bubbles behavior based on semi-empirical formulas relating to bubble diameter and velocity or mass transfer evolutions. So, the idea of this study is to develop a "universal" numerical modeling allowing the study of bubble-induced flow patterns due to effervescence, whatever the shape of the glass in order to quantify the role of the glass geometry on the mixing flow phenomena and induced aromas exhalation process. Details and development of the steps of modeling are presented in this paper, showing a good agreement between the results obtained by CFD simulations in a reference case of those from laser tomography and Particle Image Velocimetry experiments, validating the present model.

http://dx.doi.org/10.5772/51956

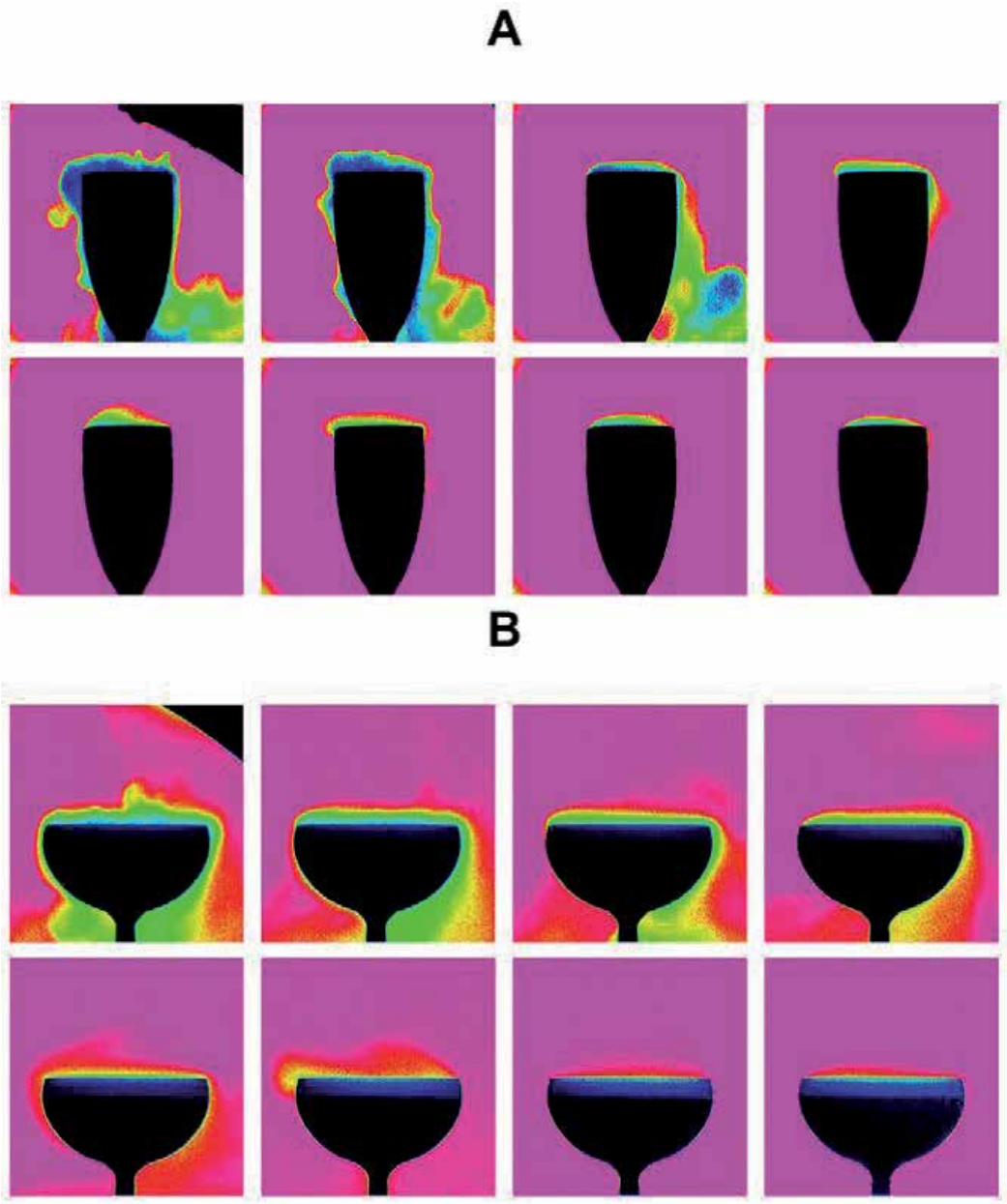

Figure 10. Infrared imaging of gaseous CO_2 desorbing from glasses filled with champagne. False color time-sequences illustrating champagne glasses as seen through the objective of the IR video camera, after the pouring step – for a bottle stored at 20°C –whether champagne is served into the flute (a) or into the coupe (b).Zones highly concentrated in gaseous CO_2 appear in black and dark blue, whereas zones slowly concentrated in gaseous CO_2 appear in red.

8. Geometry, equations and boundary conditions

8.1. Geometry and mesh generation

A traditional flute has been considered as a reference glass case. The glass geometry used in this study has been created from the real dimensions measured of the glass used for the experiments.

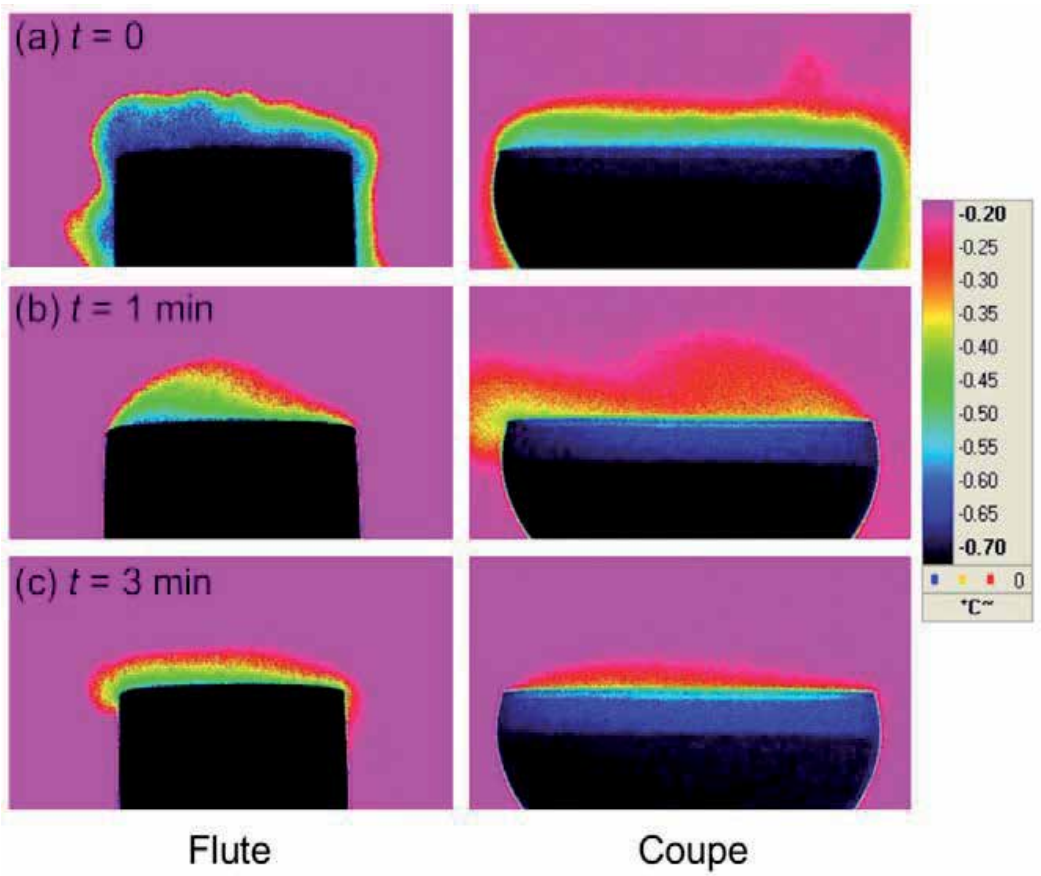

Figure 11. Close-up on gaseous CO_2 desorbing above both glass types. False color IR time-sequences showing close-up snapshots of CO_2 clouds desorbing above the flute and the coupe, respectively, immediately after pouring (a), 1 min after pouring (b), and 3 minutes after pouring (c); By using the color scale which provides a correspondence between the relative abundance of gaseous CO_2 and the temperature detected by the IR sensor of the camera after absorption by the gaseous headspace above glasses, it clearly appears that gaseous CO_2 is always more concentrated above the flute than above the coupe.

To ensure a continuous and perfectly controled process of effervescence, glassmakers usually consider circulary engraved glasses (figure 3). In such a way, as previously mentionned, the flow structure exhibits a quasi steady two dimensional behavior [2] (figures 6-7).

http://dx.doi.org/10.5772/51956

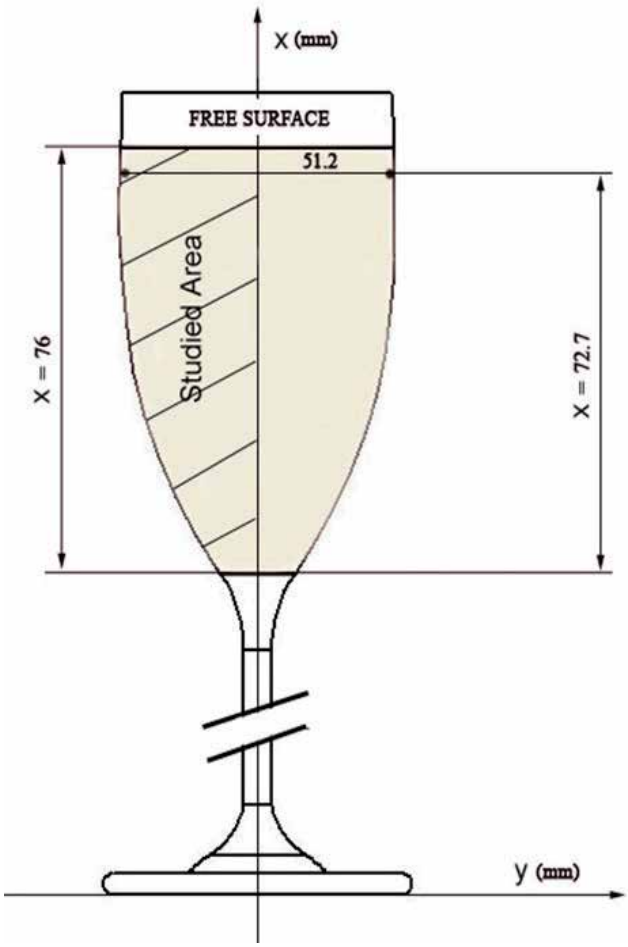

Figure 12. Champagne flute model.

In this situation, a 2D examination in the axis-symmetry plane can be considered as sufficient. For this purpose, only half of the studied area was drawn. The study area has a total height of 76 mm which corresponds to the fill level and its diameter is 51.2 mm at the liquid surface level (figure 12).

The ANSYS® Workbench Design Modeler software has been used to draw the geometry from the real size (scale 1:1) of the numerical study glass used as reference.

The mesh of the domain has been carried out using the ANSYS® Workbench meshing software. It consists in a two-dimensional mesh efficient in the case of simulations of axisymmetrical flow features. The body has been meshed with quadrilateral elements along the central part of the flow curvature, he is structured composed by square elements (L X L) but to follow the wall, the mesh is unstructured (figure 4).

8.2. Equations and numerical scheme

Because champagne is a wine in which as well gaseous as liquid phase are simultaneous present, the flows in a glass of champagne have been simulated numerically with a multi-phase model. The flow is supposed laminar [6,14] and governed by the volume finite equations. The liquid phase hydrodynamics are described with the continuity and momentum conservation equations for laminar flows:

Continuity equation:

The general form of the continuity equation can be written as:

$$\frac{\partial \rho}{\partial t} + \nabla \bullet (\varrho \vec{v}) = S_m \tag{1}$$

The source S_m is the mass added to the continuous phase from the dispersed second phase.

For 2D axisymmetric geometries, the continuity equation is given by:

$$\frac{\partial \rho}{\partial t} + \frac{\partial}{\partial x}(\rho v_x) + \frac{\partial}{\partial r}(\rho v_r) + \frac{\rho v_r}{r} = S_m \tag{2}$$

where x is the axial coordinate, r is the radial coordinate, v_x is the axial velocity and v_r is the radial velocity.

Conservation of momentum is described by:

$$\frac{\partial}{\partial t}(\varrho \vec{v}) + \nabla \bullet (\varrho \vec{v}\vec{v}) = -\nabla p + \rho \vec{g} + \vec{F} \tag{3}$$

where ϱ is the static pressure and $\rho \vec{g}$ and $\vec{F}$ are the gravitational body force and external body forces (forces that arise from interaction between the liquid phase and the dispersed one).

For 2D axisymmetric geometries, the axial and radial momentum conservation equations are given by:

$$\frac{\partial}{\partial t}(\rho v_x) + \frac{1}{r}\frac{\partial}{\partial x}(r\rho v_x v_x) + \frac{1}{r}\frac{\partial}{\partial r}(r\rho v_r v_x) = -\frac{\partial \rho}{\partial x} + F_x \tag{4}$$

and

$$\frac{\partial}{\partial t}(\rho v_r) + \frac{1}{r}\frac{\partial}{\partial x}(r\rho v_x v_r) + \frac{1}{r}\frac{\partial}{\partial r}(r\rho v_r v_r) = -\frac{\partial \rho}{\partial r} + F_r \tag{5}$$

where

http://dx.doi.org/10.5772/51956

$$\nabla \bullet \vec{v} = \frac{\partial v_x}{\partial x} + \frac{\partial v_r}{\partial r} + \frac{v_r}{r} \tag{6}$$

In this work, we hve used the Lagrangian-Eulerian approach which analyzes the liquid phase (primary phase) by the Eulerian method and the bubble phase (secondary phase) by Lagrangian assumption allowing the monitoring of bubbles life cycle.

The Euler-Lagrange approach is the basis of the lagrangian discrete phase model. The dispersed phase is solved by tracking the bubbles through the calculated flow domain while the fluid phase is treated continuously by solving the Navier-Stockes equations. Exchanges of momentum and mass are realized between the dispersed phase and the fluid one.

According to the lagrangian multiphase model, the volume fraction of the discrete phase (secondary phase) is quite small.

The bubbles trajectories are computed individually at each time step during the fluid phase calculation. This model is perfectly adapted for modeling the flows in a glass of champagne. In order to reproduce as closely as possible the principle of nucleation, subroutines have been used for the gaseous phase. These subroutines have been written based on physical laws that are taken from experimental results [5, 6].

The trajectory of a bubble is predicted by integrating the force balance in a Lagrangian reference frame.

During its rise in the liquid, a bubble is subjected to the action of several forces [14]:

The buoyancy:

$$F_B = \frac{4}{3}\pi R^3 \rho g \tag{7}$$

The drag force F_D which is related to the fluid flow around the bubble, when the bubble begins to move the fluid that is around it. The movement of the surrounding fluid leads to an additional force F_{MA} called "added mass" related to the variation in the amount of movement of liquid displaced:

$$F_{MA} = \frac{\rho d}{dt}(Vu) \tag{8}$$

The volume V of liquid entrained in the wake of the bubble is roughly equal to the half of the volume of the bubble. Thus:

$$F_{MA} = \frac{2}{3}\rho\pi\frac{d}{dt}(R^3 u) \tag{9}$$

The equation of motion can be written:

$$\frac{2}{3}\rho\pi R^3\left(\frac{dU}{dt}+\frac{3U}{R}\frac{dR}{dt}\right)=\frac{4}{3}\pi R^3\rho g - \frac{1}{2}C_D\rho U^2\pi R^2 \tag{10}$$

The force of added mass has been compared to the buoyancy along the path of the bubble to the surface. The force of added mass does not exceed 2-3% of the buoyancy, so it can be neglected in the remainder of the study. The equation of motion is finally reduced to a simple equality between the drag force and buoyancy.

In this case, the drag force F_D is defined as

$$F_D=\frac{1}{2}C_D\rho u^2\pi R^2 \tag{11}$$

where C_D is the drag coefficient. During ascent, surface active materials progressively accumulate at the rear part of the rising bubble, thus increasing the immobile area of the bubble surface.

Arising bubble rigidified by surfactants runs into more resistance than a bubble presenting a more flexible interface free from surface-active materials. The champagne bubbles showed therefore a behavior intermediate between that of a rigid and that a fluid sphere. To take into account the surfactants accumulation, the two following experimental drag coefficients laws, available in the range of intermediate Reynolds numbers (10^{-1} *to* 10^2) covered by champagne bubbles, have been used.

Magnaudet et al [14] have proposed a semi empirical relationship between the drag coefficient and the Reynolds number:

$$C_D=\frac{16}{Re}\left(1+0.15\sqrt{Re}\right) \qquad (Re<50) \tag{12}$$

This experimental determination of the drag coefficient for fluid spheres is available for Reynolds number less than 50.

Since the Reynolds number exceeds the limit of 50 for sufficiently long path, another empirical law has been used available for $Re>50$, determined by *Maxworthy et al* [14]

$$C_D=11.1Re^{-0.74} \qquad (1<Re<800) \tag{13}$$

Because bubbles do not exceed a critical diameter of 2 mm, they are spherical during their ascent. Moreover, the assumption that the bubbles do not coalesce or breakup has been considered.

The Reynolds number is defined by:

$$R_e=\frac{2\rho Ru}{\eta} \tag{14}$$

http://dx.doi.org/10.5772/51956

The density and the viscosity of the champagne wine for the liquid phase and the density and the viscosity of the carbon dioxide for the gaseous phase have been stored in the materials database (table 1).

The numerical simulations have been carried out with the ANSYS FLUENT® software using volume finite approach. The convergence criteria were based on the residuals resulting from the integration of the conservation equations over finite control-volumes. During the iterative calculation process, these residuals were constantly monitored and carefully scrutinized. For all simulations performed in this study, converged solutions were usually achieved with residuals as low as 10^{-5} (or less) for all the governing equations. To carry out numerical simulations on the dynamics of the fluid, a structured mesh, whose dimensions are 0.2 x 0.2 mm², has been chosen in the main central part of the domain where bubbles are present.

9. Boundary conditions

Models based on classical nucleation theory do not give a satisfactory approach of nucleation in the effervescent wines [13]. The idea has been to create routines to simulate the principle of nucleation and then compare the results with those obtained with experimental data [5, 6]. In order to simulate the bubbles growth, the bubbles velocity, the mass transfer between bubbles, the mass flow rate and the drag law, we have written User Defined Functions (UDF) in C language which defines source terms for the flow regime. The variation of bubbling frequency, which is a function of the CO_2 dissolved concentration, is made possible by changing the time step during the calculation.

The radius R(m) of champagne bubbles increase in time at a constant growth rate $k = \frac{dR}{dt}$, as bubbles rise toward the liquid surface. Thus, $R(t) = R_0 + kt$ where R_0 is the bubble radius as it detaches from the nucleation site.

The semi-empirical growth rate (k, μm/s) of bubbles rising in champagne was linked with some physicochemical properties of liquids as follows [5, 6]:

$$k = \frac{dR}{dt} \approx 0.63 \frac{R_\theta}{P_0} D_0^{\frac{2}{3}} (2\alpha\rho g / 9\eta)^{1/3} (C_L - k_H P_0) \tag{15}$$

The bubbles diameter depends on both the distance to the surface H (m) and the growth rate k (μm/s) which decreases over time. The law governing the change in radius R(m) of a bubble is [5, 6]:

$$R \approx 3\left(\frac{\eta}{2\alpha\rho g} kH\right)^{1/3} \tag{16}$$

Where α is a numerical coefficient that depends on the fluid in question, estimated to be 0.7 in the case of sparkling wines [5, 6].

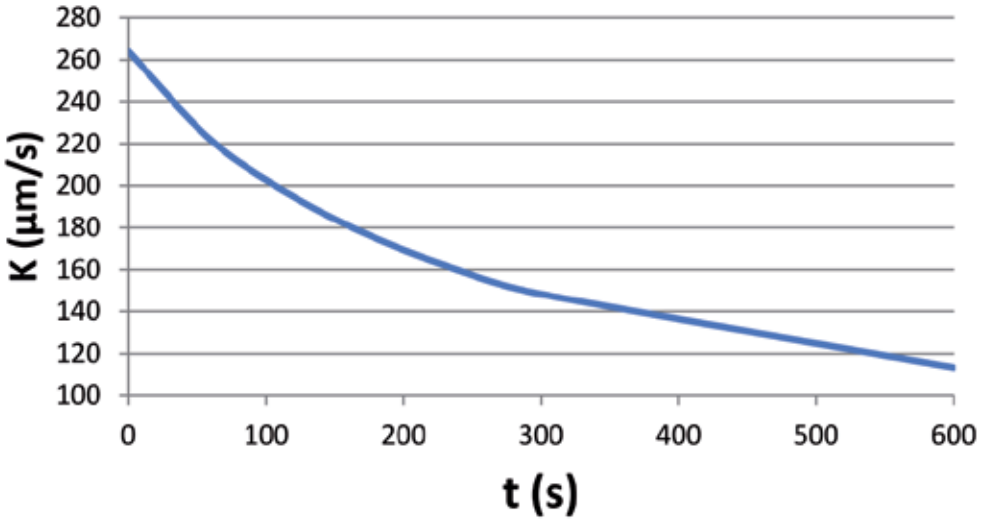

Figure 13. Evolution of the bubble growth rate according to time after pouring.

The bubbles velocity u(m/s) varies according to the following expression [6, 14]:

$$u \approx \frac{2\alpha\rho g}{9\eta} R^2 \tag{17}$$

This factor accounts the rigidity of the bubble and thus the braking effect due to the presence of surfactant molecules on the surface of bubbles. It will be smaller if the bubble is made rigid by a thick shield of surfactant molecules.

The mass flow rate Q_m (kg/s) is defined by:

$$Q_m = \frac{N}{t} \times \rho_p \times V_b \tag{18}$$

The CO_2 dissolved concentration C_L decreases continuously over time once the wine is poured into the glass. This parameter also varies with the temperature. In this study, we have used the champagne physicochemical parameters at 20° C corresponding to our reference temperature for the experiments (**Table 1**).

	Champagne (20°C)	Carbon dioxide (20°C)
Density (kg/m³)	998	1.7878
viscosity (kg/m/s)	0.00166	$1.37 \cdot 10^{-5}$
Surface tension (N/m)	0.0468	0

Table 1. Physicochemical parameters of Champagne and Carbon dioxide (from [14]).

http://dx.doi.org/10.5772/51956

10. Numerical results

The results obtained by numerical simulation have been compared with those from experiments using two flow visualization techniques to get both qualitative and quantitative viewpoints (figure 14) [2-5]. The laser tomography as a qualitative analysis method has been used to visualize the flow patterns and vertical structures induced by the continuous column of ascending bubbles in the reference flute poured with champagne. A comparison of the flow feature is presented in Figure 9. During the time-exposure of a camera, the liquid seeded with solid Rilsan particles [2-5, 7-8] and lighted by a planar laser sheet exhibits streamline patterns (figure 14b). Comparison between these experimental streamlines and the numerical ones (figure 14a) shows a good agreement, especially regarding to the location of the vortex cores in the investigated domain. The global flow features are satisfactory modeled with the CFD developed code.

To highlight a quantitative validation of the numerical modeling, velocity profiles as well velocity profiles as velocity iso-contour maps have been interested. The experimental data have been obtained by Particle Image Velocimetry measurements [15]. Figure 15 presents a comparison between the two experimental and CFD velocity profiles drawn for a 72.7mm X-location. The general trend is well reproduced as well for the X-velocity peak on the axis of symmetry as for the return flow characterized by negative velocity X-component values. Curve extrema are located at the same Y-location. Numerical results are in good accordance with those obtained by PIV measurement for the velocity profiles. Similar conclusions have been deduced for other X-locations (not presented here).

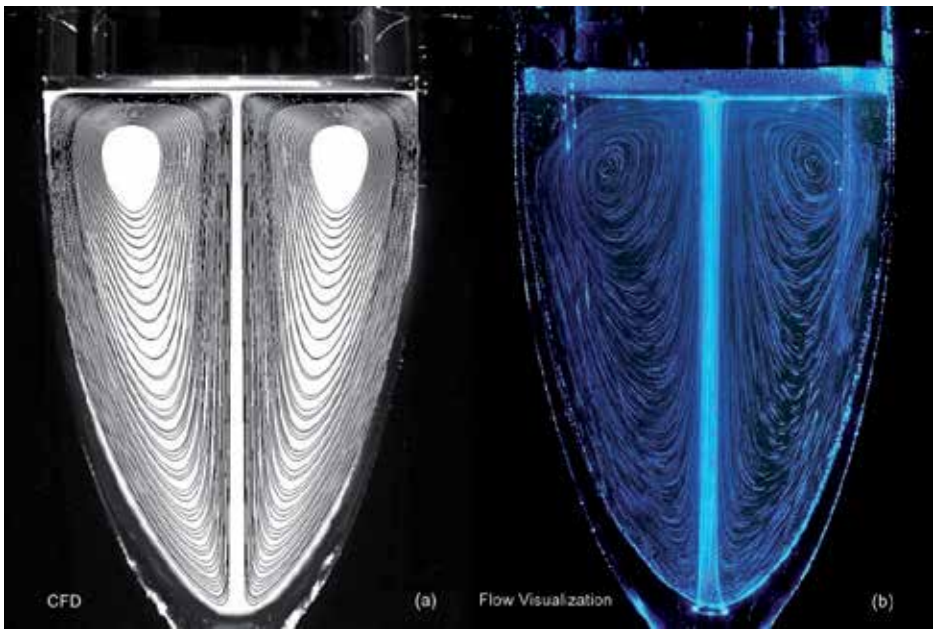

Figure 14. Streamlines obtained by CFD simulation (a) compared with classic flow visualization (b) at t = 5 minutes following the pouring process.

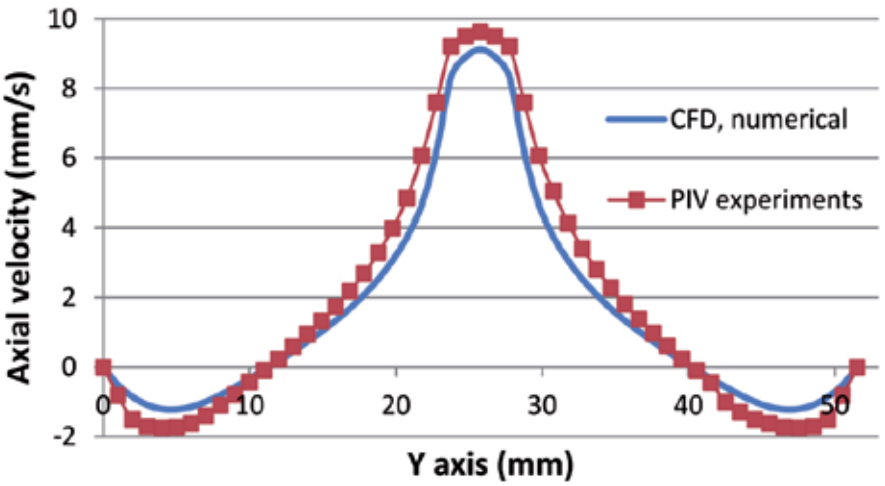

Figure 15. Axial velocity of liquid phase at t = 1 minute after pouring process and X = 72.7 mm, comparison between PIV measurement and CFD simulation.

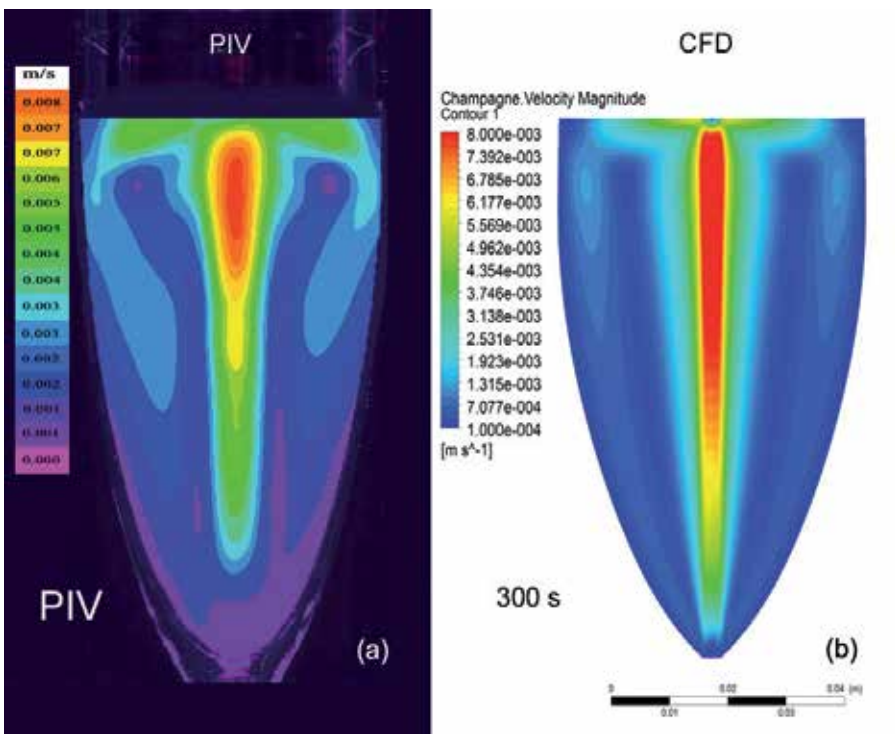

Figure 16. PIV measurements (a) compared with CFD simulation (b) at t = 5 minutes after pouring process, velocity magnitude of the liquid phase.

http://dx.doi.org/10.5772/51956

Velocity-magnitude maps are drawn in figure 16 for the two numerical and PIV-measurement approaches. A close agreement appears on the two maps. A same maximum velocity magnitude whose value is 8 mm/s is observed at the same location on the central part of the flow. Similar comments can be drawn concerning the vortex cores locations. Even if iso-contour curves differ a little bit, the trend is duplicated on these two maps and the estimated velocity is the same order of magnitude as those measured by experimental one.

Thus, one can conclude that the numerical simulation allows a satisfactory approach of the fluid dynamics.

11. Conclusion

A classical flow visualization technique was used in order to capture the fluid motion in traditional flutes and coupes poured with champagne. It was found that glasses engraved around their axis of symmetry produce a rising gas column along the vertical glass axis which induces, in turn, recirculating flow regions. In case of the classical engraved champagne flute, the whole domain of the liquid phase is homogeneously mixed, whereas in the case of the engraved champagne coupe, the recirculating flow region does not occupy the whole volume in the glass. In the engraved coupe, a "dead-zone" of no motion was identified which inhibits the formation of the collar at the glass edge. Because the kinetics of flavor and gas release also strongly depend on the velocity of the recirculating flows close to the interface, we therefore strongly believe that this paper brings objective elements and clues in order to better understand the role of glass shape and engravement conditions on the "olfactive" behavior of champagne and sparkling wines in a glass. To go further; a developed gaseous CO_2 visualization technique based on infrared imaging was performed. Those analytical results are self-consistent with sensory analysis of champagne and sparkling wines, since it is generally accepted that the smell of champagne, and especially its first nose, is always more irritating (because more concentrated in gaseous CO_2 which is a strong trigeminal stimulus) when champagne is served into a flute than when it is served into a coupe. In addition, a numerical modeling of flow dynamics induced by effervescence in a glass of champagne has been carried out for the first time in order to quantify the role of the glass geometry on the mixing flow phenomena and induced aromas exhalation process.

Appendix

C_D drag coefficient (dimensionless)

C_l lift coefficient (dimensionless)

C_L CO_2 dissolved concentration in the liquid (g/l)

D_0 diffusion coefficient of CO_2 molecules (m^2 / s)

F_D drag force

g acceleration due to gravity (m.s^{-2})

H liquid height (m)

k theoretical growth rate of bubbles (μm/s)

L characteristic dimension of a mesh element (mm)

N bubbling frequency (H_Z)

P_0 atmospheric pressure (atm)

Q_m mass flow rate (kg/s)

R bubble radius (m)

R_e Reynolds number (dimensionless)

u bubble velocity (m/s)

v liquid velocity (m/s)

V_b bubble volume (m^3)

R ideal gas constant (8.31 J/mol/K)

ρ liquid density (kg/m^3)

ρ_p density of CO2 (kg/m^3)

η dynamic viscosity (kg/m/s)

α numerical coefficient (dimensionless)

θ liquid temperature (°C)

λ molecular mean free path (m)

ϕ bubble diameter (m)

Author details

Fabien Beaumont[1], Gérard Liger-Belair[2] and Guillaume Polidori[1*]

1 GRESPI/Thermomécanique, Université de Reims, France

2 GSMA, UMR CNRS 7331, Université de Reims, France

http://dx.doi.org/10.5772/51956

References

[1] Liger Belair G., Cilindre C., Gougeon R.D., Lucio M., Gebefügi I., Jeandet P., Schmitt-Kopplin P., Unraveling different chemical fingerprints between a champagne wine and its aerosols, PNAS 2009, volume 106, n°39, 16545-16549.

[2] Polidori G., Jeandet P., Liger-Belair G., Bubbles and flow patterns in Champagne, American Scientist 2009, 97, 294.

[3] Liger Belair G., Religieux J.-B., Fohanno S., Vialatte M.-A., Jeandet P., Polidori G., Visualization of mixing phenomena in champagne glasses under various glass-shape and engravement conditions, J. Agric. Food Chem 2007, 55, 882.

[4] Polidori G., Beaumont F., Jeandet P., Liger Belair G., Artificial bubble nucleation in engraved champagne glasses, J. Visualization 2008, 11-4, 279.

[5] Liger Belair G., Polidori G., Jeandet P., Recent advances in the science of champagne bubbles, Chem. Soc. Rev. 2008, 37, 2490.

[6] Liger Belair G., Ann.Phys 2002. (Paris) 27, 1.

[7] Polidori G., Beaumont F., Jeandet P., Liger Belair G., Ring vortex scenario in engraved Champagne glasses, J. Visualization 2009, 12-3, 275.

[8] Polidori G., Beaumont F., Jeandet P., Liger Belair G., Visualization of swirling flows in champagne glasses, J. Visualization 2008, 11-3, 184.

[9] Liger Belair G., Beaumont F., Jeandet P.and Polidori G., Flow patterns of bubble nucleation sites (called fliers) freely floating in champagne glasses, Langmuir 2007, 23, 10976.

[10] Liger-Belair G, Bourget M, Villaume S, Jeandet P, Pron H, et al., On the losses of dissolved CO2 during champagne serving, J Agric Food Chem 2010, 58: 8768–8775.

[11] Liger-Belair, G., Villaume, S., Cilindre, C., Jeandet, P., CO2 volume fluxes outgassing from champagne glasses: The impact of champagne ageing, Analytica Chimica Acta 2010, 660, 29–34.

[12] Duteurtre B, Le Champagne: de la tradition à la science 2010. Paris: Lavoisier. 384 p.

[13] Herrmann E., Lihavainen H., Hyvärinen A.P., Riipinen I., Wilk M., Stratmann F., Kulmala M., Nucleation Simulations using the fluid dynamics software FLUENT using the Fine Particle Model FPM, The Journal of physical chemistry 2006, A 2006, 110, 12448-12455.

[14] Liger Belair G., Marchal R., Robillard B., Dambrouck T., Maujean A., Vignes-Adler M., Jeandet P., On the Velocity of Expanding Spherical Gas Bubbles Rising in Line in Supersaturated Hydroalcoholic Solutions: Application to Bubble Trains in Carbonated Beverages, Langmuir 2000, 16, 1889-1895.

[15] Liu Z., Zheng Y., Jia L., Zhang Q., Study of bubble induced flow structure using PIV , Chemical Engineering Science 2005, 60, 3537-3552.

Chapter 13

Lattice Boltzmann Modeling of the Gas Diffusion Layer of the Polymer Electrolyte Fuel Cell with the Aid of Air Permeability Measurements

Hironori Nakajima

Additional information is available at the end of the chapter

http://dx.doi.org/10.5772/56363

1. Introduction

Polymer electrolyte fuel cells (PEFCs, PEMFCs) with high efficiency and low environmental impact recently have attracted considerable interest. However, further improvement in performance and reliability is required to realize practical use of PEFCs as future power generation devices. To improve PEFC performance, an appropriate water balance between the water content and product water is a key technology. Loss of water content in the polymer electrolyte membrane decreases proton conductivity, thereby increasing the internal resistance of the cell. A PEFC basically consists of a membrane electrode assembly (MEA), gas diffusion layers (GDLs) and separators having flow fields with flow channels and ribs. The design parameters for the GDL, such as thickness, pore size distribution, and gas permeability play important roles in characterizing the gas flow and water management during PEFC operation[1]. In this chapter, 2D anisotropic modeling of a monolayer of the GDL substrate is carried out by comparing calculated and measured gas permeability with the lattice Boltzmann method (LBM)[2, 3] and through-plane/in-plane gas permeability measurements, respectively.

2. Lattice Boltzmann method

LBM is a numerical fluid dynamic simulation method that describes macroscopic fluid dynamic phenomena by analyzing the behavior of virtual particles of which fluid is regarded as aggregate. LBM gives simplified kinetic models that incorporate the essential physics of microscopic processes so that the macroscopic averaged properties obey the macroscopic Navier–Stokes equations. Because the conventional Navier–Stokes equation takes long time

to calculate and results in poor convergence in porous media, LBM has been developed to take advantage the simplicity of the algorithm and flexibity for complex geometries such as porous media[4]. It is therefore reasonable to apply LBM to fluid flows in the porous structure of the GDLs[5].

2.1. Governing equations

LBM analyzes flow by solving the lattice Boltzmann equation (LBE) that describes particle distribution function, which represents flow velocities of virtual particles. Macroscopic parameters such as the flow velocity and pressure are derived from the summation of the moment of the particle velocity.

In general, LBM uses a single relaxation time approximation by the Bhatnager, Gross, Krook (BGK) model[3, 6]. Equation 1 presents the Boltzmann equation with the BGK approximation

$$\frac{\partial f}{\partial t} + v\nabla f = -\frac{1}{\tau}(f - f^{\mathrm{eq}}) \tag{1}$$

where f represents the distribution function depending on space, x, velocity, v and time, t. f^{eq} is the local equilibrium distribution function, and τ is the relaxation time to local equilibrium. The discrete Boltzmann equation is thus

$$\frac{\partial f_\alpha}{\partial t} + v_\alpha \nabla f_\alpha = -\frac{1}{\tau}(f_\alpha - f_\alpha^{\mathrm{eq}}) \tag{2}$$

since v-space is discretized by a finite set of particle velocities, v_α and associated distribution function $f_\alpha(x, t)$.

Discretizing with δt and $x + e_\alpha \delta t$, Eq. 2 gives

$$f_\alpha(x + e_\alpha \delta t, t + \delta t) - f_\alpha(x, t) = -\frac{1}{\tau}(f_\alpha(x, t) - f_\alpha^{\mathrm{eq}}(x, t)) \tag{3}$$

The collision-streaming process of the LBM is calculated with the following equations.

$$\tilde{f}_\alpha(x, t) = f_\alpha(x, t) - \tfrac{1}{\tau}(f_\alpha(x, t) - f_\alpha^{\mathrm{eq}}(x, t)) \tag{4}$$

$$f_\alpha(x + e_\alpha \delta t, t + \delta t) = \tilde{f}_\alpha(x, t) \tag{5}$$

http://dx.doi.org/10.5772/56363

Here, $\tilde{f}_i$ is the distribution function after the streaming process. The collision process represents the process that the distribution function converges to the equilibrium state, while the streaming process is the process that the virtual particles move to the neighboring sites.

2-dimensional fluid calculation uses the 2D9V model. The virtual particle velocity vector is

$$e = C \begin{bmatrix} 1 & 0 \\ 0 & 1 \\ -1 & 0 \\ 0 & -1 \\ 1 & 1 \\ -1 & 1 \\ -1 & -1 \\ 1 & -1 \\ 0 & 0 \end{bmatrix} \begin{matrix} \alpha = 1 \\ \alpha = 2 \\ \alpha = 3 \\ \alpha = 4 \\ \alpha = 5 \\ \alpha = 6 \\ \alpha = 7 \\ \alpha = 8 \\ \alpha = 9 \end{matrix} \tag{6}$$

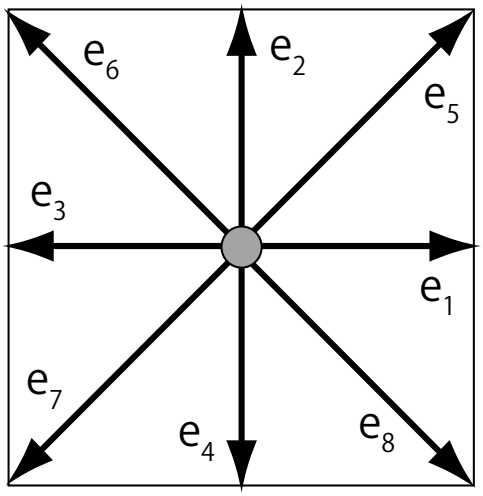

Figure 1. 2D9V velocity model.

where $C = \delta x / \delta t$ is velocity of a virtual particle.

The local distribution function for the 2D9V model is

$$f_\alpha^{\mathrm{eq}}(\rho, \boldsymbol{u}) = \varpi_\alpha \rho (1 + \frac{3}{C^2}(e_\alpha \cdot \boldsymbol{u}) + \frac{9}{2C^4}(e_\alpha \cdot \boldsymbol{u})^2 - \frac{3}{2C^2}\boldsymbol{u}^2) \tag{7}$$

where ρ is the density per node, $\boldsymbol{u} = \begin{bmatrix} u_x & u_y \end{bmatrix}^T$ is the fluid velocity, ϖ_α is the weighting function expressed as follows.

$$\omega_{1\sim4} = \frac{1}{9},\ \omega_{5\sim8} = \tfrac{1}{36},\ \omega_9 = \frac{4}{9} \tag{8}$$

The distribution function for each direction is

$$f_1^{\mathrm{eq}}(\rho, \boldsymbol{u}) = \frac{1}{9}\rho\left[1 + \frac{3u_x}{C} + \frac{9u_x^2}{2C^2} - \frac{3(u_x^2+u_y^2)}{2C^2}\right] \tag{9}$$

$$f_2^{\mathrm{eq}}(\rho, \boldsymbol{u}) = \frac{1}{9}\rho\left[1 + \frac{3u_y}{C} + \frac{9u_y^2}{2C^2} - \frac{3(u_x^2+u_y^2)}{2C^2}\right] \tag{10}$$

$$f_3^{\mathrm{eq}}(\rho, \boldsymbol{u}) = \frac{1}{9}\rho\left[1 - \frac{3u_x}{C} + \frac{9u_x^2}{2C^2} - \frac{3(u_x^2+u_y^2)}{2C^2}\right] \tag{11}$$

$$f_4^{\mathrm{eq}}(\rho, \boldsymbol{u}) = \frac{1}{9}\rho\left[1 - \frac{3u_y}{C} + \frac{9u_y^2}{2C^2} - \frac{3(u_x^2+u_y^2)}{2C^2}\right] \tag{12}$$

$$f_5^{\mathrm{eq}}(\rho, \boldsymbol{u}) = \frac{1}{36}\rho\left[1 + \frac{3(u_x+u_y)_x}{C} + \frac{9u(u_x+u_y)^2}{2C^2} - \frac{3(u_x^2+u_y^2)}{2C^2}\right] \tag{13}$$

$$f_6^{\mathrm{eq}}(\rho, \boldsymbol{u}) = \frac{1}{36}\rho\left[1 + \frac{3(u_x-u_y)}{C} + \frac{9u(u_x-u_y)^2}{2C^2} - \frac{3(u_x^2+u_y^2)}{2C^2}\right] \tag{14}$$

$$f_7^{\mathrm{eq}}(\rho, \boldsymbol{u}) = \frac{1}{36}\rho\left[1 - \frac{3(u_x+u_y)}{C} + \frac{9u(u_x+u_y)^2}{2C^2} - \frac{3(u_x^2+u_y^2)}{2C^2}\right] \tag{15}$$

$$f_8^{\mathrm{eq}}(\rho, \boldsymbol{u}) = \frac{1}{36}\rho\left[1 + \frac{3(u_x-u_y)}{C} + \frac{9u(u_x-u_y)^2}{2C^2} - \frac{3(u_x^2+u_y^2)}{2C^2}\right] \tag{16}$$

http://dx.doi.org/10.5772/56363

$$f_9^{\mathrm{eq}}(\rho, \boldsymbol{u}) = \frac{4}{9}\rho\left[1 - \frac{3(u_x^2 + u_y^2)}{2C^2}\right] \tag{17}$$

The density and macroscopic flow velocity at a node are defined by

$$\rho = \sum f_\alpha \tag{18}$$

$$\rho \boldsymbol{u} = \sum f_\alpha \mathbf{e}_\alpha \tag{19}$$

respectively.

Equations 6 and 19 give the velocity as follows.

$$u_x = C(f_1 + f_5 + f_8 - f_3 - f_6 - f_7)/\rho \tag{20}$$

$$u_y = C(f_2 + f_5 + f_6 - f_4 - f_7 - f_8)/\rho \tag{21}$$

In 2D9V model, the sound velocity C_s and the pressure p are

$$C_\mathrm{s} = \frac{C}{\sqrt{3}} \tag{22}$$

$$p = \rho C_\mathrm{s}^2 = \frac{1}{3}\rho C^2 \tag{23}$$

Kinetic viscosity is expressed as

$$\nu = (\tau - \frac{1}{2})C_\mathrm{s}^2 \delta t \tag{24}$$

2.2. Boundary conditions

LBM defines the velocity distribution function at boundary from the velocity and pressure to use the boundary condition. In general, the following bounce back boundary condition has been employed.

2.2.1. Half-way wall bounce-back boundary condition

Half-way wall bounce back boundary condition is no-slip boundary condition at a given solid surface as follows[2, 3].

$$f_1^{''}(x-\delta x,\, y) = \tilde{f_3}(x,\, y) \tag{25}$$

$$f_8^{''}(x-\delta x,\, y+\delta c) = \tilde{f_6}(x,\, y) \tag{26}$$

$$f_5^{''}(x-\delta x,\, y-\delta c) = \tilde{f_7}(x,\, y) \tag{27}$$

where $f_\alpha^{''}$ represents the distribution function after the streaming step. Since this boundary condition gives higher precision than the conventional bounce back boundary condition[3], it is employed in the present chapter.

2.2.2. Periodic boundary condition

For large area calculation, periodicity of the solution can be assumed. In this case, the periodic boundary condition is employed along the axis direction. The distribution function is

$$f_1^{''}(0,\, y) = \tilde{f_1}(Nx,\, y) \tag{28}$$

$$f_5^{''}(0,\, y) = \tilde{f_5}(Nx,\, y) \tag{29}$$

$$f_8^{''}(0,\, y) = \tilde{f_8}(Nx,\, y) \tag{30}$$

$$f_3^{''}(Nx,\, y) = \tilde{f_3}(0,\, y) \tag{31}$$

http://dx.doi.org/10.5772/56363

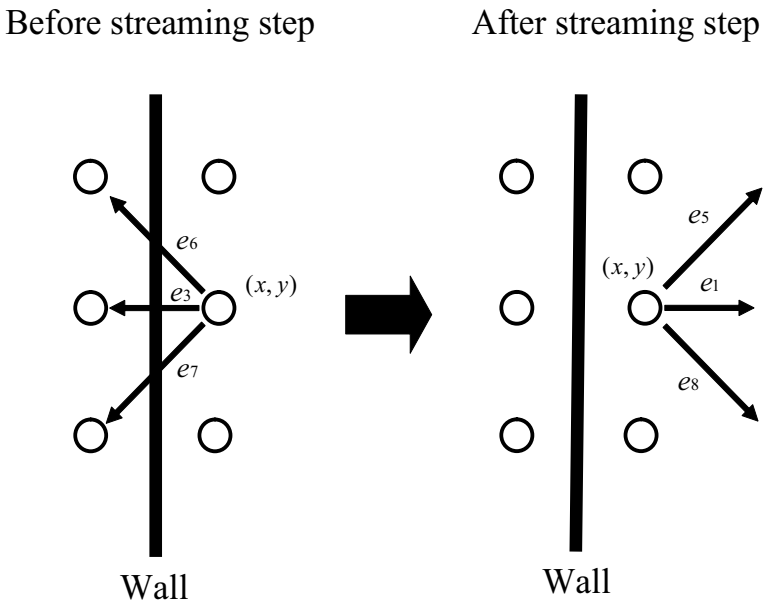

Figure 2. Half-way bounce-back boundary condition

$$f_6^{''}(Nx, y) = \tilde{f}_6(0, y) \tag{32}$$

$$f_7^{''}(Nx, y) = \tilde{f}_7(0, y) \tag{33}$$

where Nx is the maximum value of x.

2.2.3. Pressure difference boundary condition

The pressure difference boundary condition is applied to a case that there is pressure difference between inlet and outlet while the velocity distribution is the same at the inlet and outlet. The distribution functions at the inlet are assumed as follows[7].

$$f_1^{''}(0, y) = \tilde{f}_1(Nx, y) + D \tag{34}$$

$$f_5^{''}(0, y) = \tilde{f}_5(Nx, y) + \frac{1}{4}D \tag{35}$$

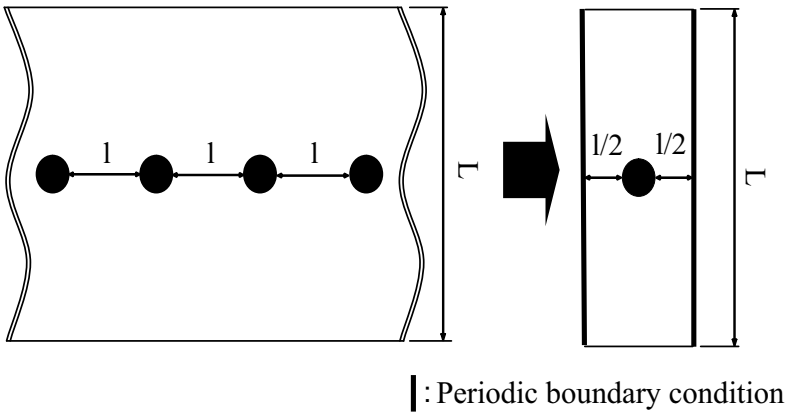

Figure 3. Periodic boundary condition.

$$f_8^{''}(0, y) = \tilde{f}_8(Nx, y) + \frac{1}{4}D \tag{36}$$

with

$$D = \frac{\Delta p}{C^2} - \frac{1}{3}\left[\tilde{f}_2(1, y) - \tilde{f}_2(Nx, y) + \tilde{f}_4(1, y) - \tilde{f}_4(Nx, y) + \tilde{f}_9(1, y) - \tilde{f}_9(Nx, y)\right] \tag{37}$$

while the distribution functions at the outlet are

$$f_3^{''}(Nx, y) = \tilde{f}_3(0, y) - D \tag{38}$$

$$f_6^{''}(Nx, y) = \tilde{f}_6(0, y) - \frac{1}{4}D \tag{39}$$

$$f_7^{''}(Nx, y) = \tilde{f}_7(0, y) - \frac{1}{4}D \tag{40}$$

http://dx.doi.org/10.5772/56363

2.2.4. Pressure and velocity boundary conditions

Pressure and velocity boundary conditions proposed by Zou and He[8] are also used for the calculation. The case for an inlet at $x = 0$ is considered for instance here. At the boundary, pressure, that is, ρ_{in}, and $u_y = 0$ are applied. Because f_2'', f_3'', f_4'', f_6'', f_7'', f_9'' after streaming step are known, u_x, f_1'', f_5'', f_8'' are derived as follows.

Equation 18 gives

$$f_1'' + f_5'' + f_8'' = \rho_{\text{in}} - (f_2'' + f_3'' + f_4'' + f_6'' + f_7'' + f_9'') \tag{41}$$

while Eqs. 20 and 21 lead to

$$C(f_1'' + f_5'' + f_8'') = \rho_{\text{in}} u_x + C(f_3'' + f_6'' + f_7'') \tag{42}$$

$$f_5'' - f_8'' = -f_2'' + f_4'' - f_6'' + f_7'' \tag{43}$$

Hence

$$u_x = C\left[1 - \frac{f_2'' + f_4'' + f_9'' + 2(f_3'' + f_6'' + f_7'')}{\rho_{\text{in}}}\right] \tag{44}$$

Then the deviation from the equilibrium shall be equal for the distribution function of $i = 1,3$ as follows to determine the remaining distribution functions.

$$f_1'' - f_1^{\text{eq}} = f_3'' - f_3^{\text{eq}} \tag{45}$$

Thus Eqs. 9 and 11 yield

$$f_1'' = f_3'' + \frac{2\rho u_x}{3C} \tag{46}$$

Eqs. 42, 43, and 46 give

$$f_5'' = f_7'' - \frac{f_2'' - f_4''}{2} + \frac{\rho u_x}{6C} \tag{47}$$

$$f_8'' = f_6'' - \frac{f_2'' - f_4''}{2} + \frac{\rho u_x}{6C} \tag{48}$$

Thereby u_x, f_1, f_5, f_8 are determined. On the other hand, the distribution function at the corner should be dealt with in other way. The case for the bottom of the inlet at $x = 0$, $y = 0$ is described here for instance. After the streaming step, f_3'', f_4'', f_7'', ρ_{in} is obtained. The no-slip boundary condition gives $u_x = 0$, $u_y = 0$. Thus f_1, f_2, f_5, f_6, f_8 can be determined as follows. Eq. 46 provides

$$f_1'' = f_3'' \tag{49}$$

In a similar manner,

$$f_2'' = f_4'' \tag{50}$$

Equations 18 and 47 yield

$$f_5'' = f_7'' \tag{51}$$

$$f_6'' = f_8'' = \frac{1}{2}\left[\rho_{\text{in}} - (f_1'' + f_2'' + f_3'' + f_4'' + f_5'' + f_7'' + f_9'')\right] + \tag{52}$$

From Eq. 44,

$$\rho = \frac{C}{C - u_x}\left[f_2'' + f_4'' + f_9'' + 2(f_3'' + f_6'' + f_7'')\right] \tag{53}$$

http://dx.doi.org/10.5772/56363

2.3. LBM binary mixtures with different molecular weights

In this section, LBM binary mixtures with different molecular weights (LBM-BMD) model proposed by Luo and Girimaji[9] and extended by McCracken and Abraham[10] is described. LMB-BMD model consists of LBM and the effect of diffusion. This model deals with two components A and B having different molecular weights. The model can analyze advective flow in addition to diffusion. i and j represent the functions, variables, and constants for the species A and B, respectively.

The equilibrium distribution function is

$$f_\alpha^i(x + e_\alpha^i \delta t,\, t + \delta t) - f_{\alpha i}^i(x,\, t) = \Omega_\alpha^{ii} + \Omega_\alpha^{ij} \tag{54}$$

where Ω_α^{ii} and Ω_α^{ij} are the following self-collision and cross-collision terms for A-A and A-B, respectively. Velocity vector is defined as the similar manner as LBM in the previous section.

$$\Omega_\alpha^{ii} = -\frac{1}{\tau^i}(f_\alpha^i(x,\, t) - f_\alpha^{i(0)}(x,\, t)) \tag{55}$$

$$\Omega_\alpha^{ij} = -\frac{1}{\tau_D^{ij}}\left(\frac{\rho_j}{\rho}\right)\frac{f_\alpha^{i(0)}}{(C_s^i)^2}(e_\alpha^i - \boldsymbol{u})(\boldsymbol{u}^i - \boldsymbol{u}^j) \tag{56}$$

where $\tau^i$and τ_D^{ij} are the relaxation times for the kinetic viscosity, ν^i, and diffusion coefficient, D^{ij}. The local equilibrium distribution function, $f_\alpha^{i(0)}$ is

$$f_\alpha^{i(0)} = \left[1 + \frac{3}{C^{i2}}(e_\alpha^i - \boldsymbol{u})(\boldsymbol{u}^i - \boldsymbol{u}^j)\right] f_\alpha^{i,\mathrm{eq}} \tag{57}$$

In a similar manner as the single component LBM in the previous section,

$$f_\alpha^{\mathrm{eq}}(\rho,\, \boldsymbol{u}) = \varpi_\alpha \rho^i \left(1 + \frac{3}{C^{i2}}(e_i \cdot \boldsymbol{u}) + \frac{9}{2C^{i4}}(e_i \cdot \boldsymbol{u})^2 - \frac{3}{2C^{i2}}\boldsymbol{u}^2\right) \tag{58}$$

$$f_1^{i(0)} = \left\{1 + \frac{3}{C^{i2}}\left[(C^i - u_x)u_{\mathrm{diff},x}^i - u_y u_{\mathrm{diff},y}^i\right]\right\} f_1^{i,\mathrm{eq}} \tag{59}$$

$$f_2^{i(0)} = \left\{1 + \frac{3}{C^{i2}}\left[(C^i - u_y)u^i_{\mathrm{diff},y} - u_x u^i_{\mathrm{diff},x}\right]\right\} f_2^{i,\mathrm{eq}} \tag{60}$$

$$f_3^{i(0)} = \left\{1 - \frac{3}{C^{i2}}\left[(C^i - u_x)u^i_{\mathrm{diff},x} + u_y u^i_{\mathrm{diff},y}\right]\right\} f_3^{i,\mathrm{eq}} \tag{61}$$

$$f_4^{i(0)} = \left\{1 - \frac{3}{C^{i2}}\left[(C^i + u_y)u^i_{\mathrm{diff},y} + u_x u^i_{\mathrm{diff},x}\right]\right\} f_4^{i,\mathrm{eq}} \tag{62}$$

$$f_5^{i(0)} = \left\{1 + \frac{3}{C^{i2}}\left[(C^i - u_x)u^i_{\mathrm{diff},x} + (C^i - u_y)u^i_{\mathrm{diff},y}\right]\right\} f_5^{i,\mathrm{eq}} \tag{63}$$

$$f_6^{i(0)} = \left\{1 + \frac{3}{C^{i2}}\left[(C^i - u_x)u^i_{\mathrm{diff},x} + (C^i - u_y)u^i_{\mathrm{diff},y}\right]\right\} f_6^{i,\mathrm{eq}} \tag{64}$$

$$f_7^{i(0)} = \left\{1 + \frac{3}{C^{i2}}\left[(C^i - u_x)u^i_{\mathrm{diff},x} - (C^i - u_y)u^i_{\mathrm{diff},y}\right]\right\} f_7^{i,\mathrm{eq}} \tag{65}$$

$$f_8^{i(0)} = \left\{1 + \frac{3}{C^{i2}}\left[(C^i - u_x)u^i_{\mathrm{diff},x} - (C^i + u_y)u^i_{\mathrm{diff},y}\right]\right\} f_8^{i,\mathrm{eq}} \tag{66}$$

$$f_9^{i(0)} = \left\{1 - \frac{3}{C^{i2}}\left[u_x u^i_{\mathrm{diff},x} + u_y u^i_{\mathrm{diff},y}\right]\right\} f_9^{i,\mathrm{eq}} \tag{67}$$

where $u^i_{\mathrm{diff},x}$ and $u^i_{\mathrm{diff},y}$ are x and y direction of $\boldsymbol{u}^i_{\mathrm{diff}} = \boldsymbol{u}^i - \boldsymbol{u}$

http://dx.doi.org/10.5772/56363

Collision terms are:

$$\Omega_1^{ij} = -\frac{3}{\tau_D^{ij}} \left(\frac{\rho^j}{\rho}\right) \frac{f_1^{i(0)}}{C^{i2}} \left[(C^i - u_x)u_x^{i-j} - u_y u_y^{i-j}\right] \tag{68}$$

$$\Omega_2^{ij} = -\frac{3}{\tau_D^{ij}} \left(\frac{\rho^j}{\rho}\right) \frac{f_2^{i(0)}}{C^{i2}} \left[(C^i - u_y)u_y^{i-j} - u_x u_x^{i-j}\right] \tag{69}$$

$$\Omega_3^{ij} = \frac{3}{\tau_D^{ij}} \left(\frac{\rho^j}{\rho}\right) \frac{f_3^{i(0)}}{C^{i2}} \left[(C^i + u_x)u_x^{i-j} + u_y u_y^{i-j}\right] \tag{70}$$

$$\Omega_4^{ij} = \frac{3}{\tau_D^{ij}} \left(\frac{\rho^j}{\rho}\right) \frac{f_3^{i(0)}}{C^{i2}} \left[(C^i + u_y)u_y^{i-j} + u_x u_x^{i-j}\right] \tag{71}$$

$$\Omega_5^{ij} = -\frac{3}{\tau_D^{ij}} \left(\frac{\rho^j}{\rho}\right) \frac{f_3^{i(0)}}{C^{i2}} \left[(C^i - u_x)u_x^{i-j} + (C^i - u_y)u_y^{i-j}\right] \tag{72}$$

$$\Omega_6^{ij} = -\frac{3}{\tau_D^{ij}} \left(\frac{\rho^j}{\rho}\right) \frac{f_3^{i(0)}}{C^{i2}} \left[(C^i - u_x)u_x^{i-j} + (C^i - u_y)u_y^{i-j}\right] \tag{73}$$

$$\Omega_7^{ij} = -\frac{3}{\tau_D^{ij}} \left(\frac{\rho^j}{\rho}\right) \frac{f_3^{i(0)}}{C^{i2}} \left[(C^i - u_x)u_x^{i-j} + (C^i - u_y)u_y^{i-j}\right] \tag{74}$$

$$\Omega_8^{ij} = -\frac{3}{\tau_D^{ij}} \left(\frac{\rho^j}{\rho}\right) \frac{f_3^{i(0)}}{C^{i2}} \left[(C^i - u_x)u_x^{i-j} + (C^i - u_y)u_y^{i-j}\right] \tag{75}$$

where

$$\boldsymbol{u}^{\boldsymbol{i-j}} = \begin{bmatrix} u_x^{i-j} \\ u_y^{i-j} \end{bmatrix} = \begin{bmatrix} u_x^i - u_x^j \\ u_y^i - u_y^j \end{bmatrix} \tag{76}$$

The density and flow velocity are derived by

$$\rho^i = \sum f_\alpha^i \tag{77}$$

$$\rho^i \boldsymbol{u}^{\boldsymbol{i}} = \sum f_\alpha^i \mathbf{e}_\alpha^i \tag{78}$$

The total density and mass averaged velocity are

$$\rho = \rho^i + \rho^j \tag{79}$$

$$\rho \boldsymbol{u} = \rho^i u^i + \rho^j u^j \tag{80}$$

Since the partial pressure is

$$p_i = \rho_i C_s^{i2} \tag{81}$$

total pressure is

$$p = \rho^i C_s^{i2} + \rho^j C_s^{j2} = \frac{1}{3}(\rho^i C_s^{i2} + \rho^j C_s^{j2}) \tag{82}$$

The relation between the sound velocities, C_s^i and C_s^j is

http://dx.doi.org/10.5772/56363

$$C_s^j = \sqrt{\frac{m^i}{m^j}} C_s^i \tag{83}$$

where $m^i > m^j$ are the molecular weights of A and B, respectively. The kinetic viscosity and diffusion coefficient have the following relations.

$$\nu^i = \frac{1}{3}(\tau^i - \frac{1}{2}) C_s^{i2} \delta t \tag{84}$$

$$D^{ij} = \frac{\rho p}{n^2 m^i m^j} \left(\tau_D^i - \frac{1}{2} \right) \tag{85}$$

where

$$n^i = \frac{\rho^i}{m^i} \ , \ n^j = \frac{\rho^j}{m^j} \tag{86}$$

$$n = n^i + n^j \tag{87}$$

2.4. Streaming step of species with different velocities

In LBM-BMD model, species A snd B have different velocities. During δt , the species A travel δx, while the species B travel $\sqrt{m^i/m^j}\delta x$. Since $\delta x = e_\alpha^i \delta t$, the species B have different streaming distance. So, the distribution function of B on the nodes should be determined from the interpolation of the distribution functions of surrounding particles. Although McCracken and Abraham proposed a second-order Lagrangian interpolation[10], and Joshi et. al proposed bi-linear interpolation[11], these interpolation methods seem not appropriate for porous structure despite their higher accuracy. Thus linear interpolation of fewer nodes is employed here. The case for $\alpha = 1$ is depicted in Fig. 4. After the streaming step, the distribution function at (x, y) is determined by the interpolation of the distribution functions at $(x - \delta x, y)$ and (x, y) before the streaming step.

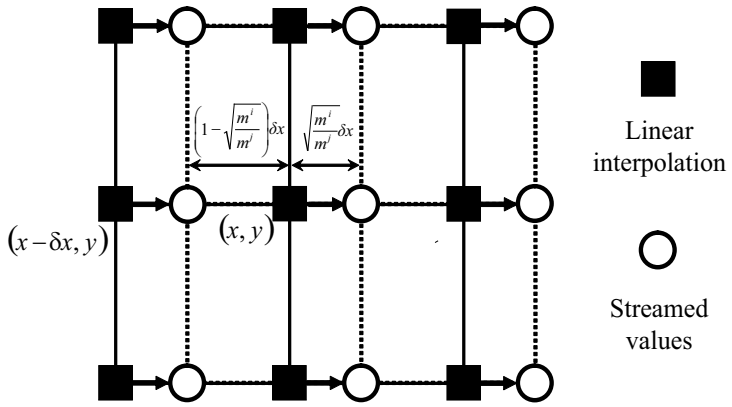

Figure 4. Streaming and interpolation for species B

$$f_1^{j''}(x, y) = \tilde{f}_1^j(x-\delta x, y) + \frac{x-\left[(x-\delta x)+\sqrt{\frac{m^i}{m^j}}\delta x\right]}{\left(\sqrt{\frac{m^i}{m^j}}\delta x\right)-\left[(x-\delta x)+\sqrt{\frac{m^i}{m^j}}\delta x\right]}\left[\tilde{f}_1^j(x, y)-\tilde{f}_1^j(x-\delta x, y)\right] \tag{88}$$

$$= \sqrt{\frac{m^i}{m^j}}\tilde{f}_1^j(x-\delta x, y) + \left(1-\sqrt{\frac{m^i}{m^j}}\right)\tilde{f}_1^j(x, y) \tag{89}$$

when $(x-\delta x, y)$ is an obstacle node, $\tilde{f}_1^j(x-\delta x, y) = \tilde{f}_3^j(x, y)$ can be applied.

$$f_1^{j''}(x, y) = \sqrt{\frac{m^i}{m^j}}\tilde{f}_3^j(x, y) + \left(1-\sqrt{\frac{m^i}{m^j}}\right)\tilde{f}_1^j(x, y) \tag{90}$$

3. GDL models

In the present research, 3D structure of the GDL is projected to 2D structure. So, the following models are created.

Model 1 Cross-section of the carbon fiber is simulated as a circle so that averaged number of the fiber in unit area is the same as that of the actual GDL.

http://dx.doi.org/10.5772/56363

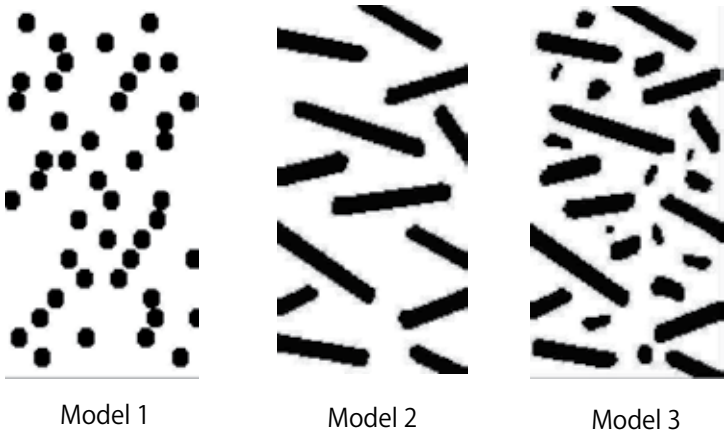

Figure 5. 2D anisotropic GDL models for the LBM.

Model 2 Fiber is simulated so that porosity is the same as the actual GDL.

Model 3 Fiber and its cross-section are simulated by so that porosity is the same as the actual GDL.

Figure 5 illustrates the GDL models. Through-plane and in-plane anisotropic Darcy coefficients are obtained by LBM employed to these GDL models. These Darcy coefficients are compared with those from the following permeability measurements so that an anisotropic GDL model which agrees the most with the measurements can be found. The GDL model found is then used for the LBM-BMD flow analysis in the GDL with the flow channels and ribs having actual PEFC flow field geomeory under actual operation condition.

The calculation in the present chapter was carried out with a personal computer having Intel Core2 Quad CPU Q6600 2.4GHz and 4GB memory on ASUS P5K motherboard. MatLab (MathWorks, Inc.) was used for the LBM and LBM-BMD calculations.

4. Experimental

Figure 6 shows a schematic diagram of GDL permeability measurement apparatus. GDL, which was a commercial carbon paper (SIGRACET GDL 24AA, SGL Carbon Inc.) with a thickness of 190 μm, was placed between two cylindrical plates. A soft O-ring was used for gas sealing between the plates. The force required to deform the O-ring was negligible compared with the compression force acting on the GDL. The compression force was controlled using a clamp screw and was measured with a load cell. For air permeability tests, the compression pressure was set at 1 MPa, as measured in a typical PEFC.

Fig. 7 presents geometries of the GDL used for the through-plane and in-plane permeability tests[12]. Volumetric air flow rates in through-plane direction, Qth, and in-plane direction, Qin, in the following equations were measured using a mass flow meter (KOFLOC). Pressure drop by the apparatus was compensated beforehand.

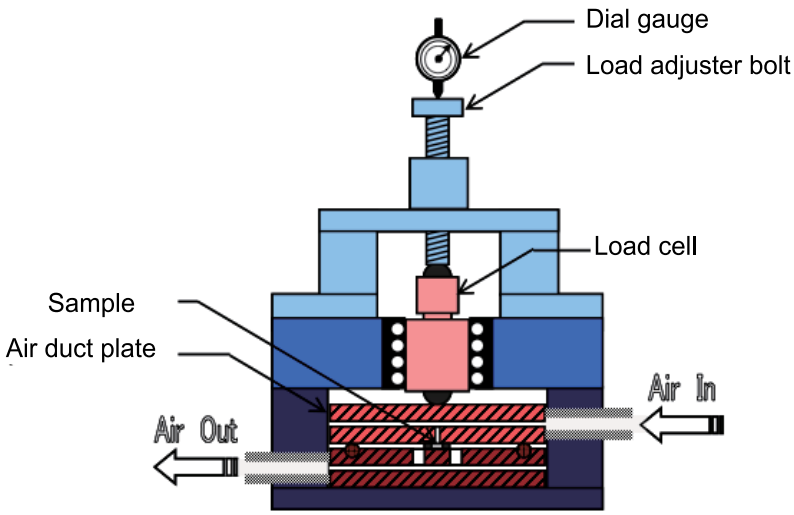

Figure 6. Apparatus for the permeability measurement.

$$Q_{\text{th}} = \frac{k}{\mu}\frac{p_{\text{i}} - p_{\text{o}}}{\delta}A = \frac{k}{\mu}\frac{p_{\text{i}} - p_{\text{o}}}{\delta}2\pi r^2 \tag{91}$$

$$Q_{\text{in}} = \frac{k}{\mu}\frac{p_{\text{i}} - p_{\text{o}}}{r_{\text{o}} - r_{\text{i}}}\frac{2\pi t(r_{\text{o}} - r_{\text{i}})}{\ln(r_{\text{o}}/r_{\text{i}})} \tag{92}$$

where k, μ, and r are the Darcy coefficient of the GDL, viscosity of air[13], and radius of the GDL, respectively. P_{i}, P_{O}, δ, and A are inlet and outlet air pressures, thickness of the GDL, and cross-sectional area of air flow, respectively. r_{i} and r_{O} are inner and outer radii of the GDL for the in-plane permeability measurement. The Darcy coefficients in through-plane and in-plane directions are thereby obtained from relations between the flow rates and the pressure difference.

5. Results and discussion

Figures 8 and 9 show the through-plane and in-plane Darcy coefficients obtained from the LBM calculation and permeability measurements. Darcy coefficients of the GDL model 3 agrees well with the experimental results in the cases of in-plane flow and through-plane flow below flow velocity of 1 ms^{-1}. Since the through-plane flow velocity is below 1 ms^{-1} in a cell in general, the model 3 shall be used for the LBM-BMD calculation for GDL under flow channels and a rib in an actual cell below.

http://dx.doi.org/10.5772/56363

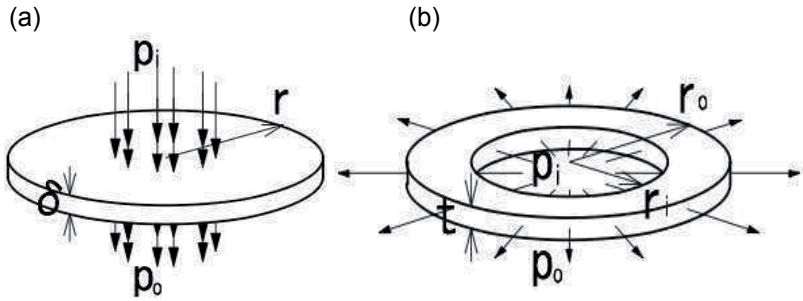

Figure 7. GDL geometries for the permeability measurements. (a)Through-plane (b)In-plane

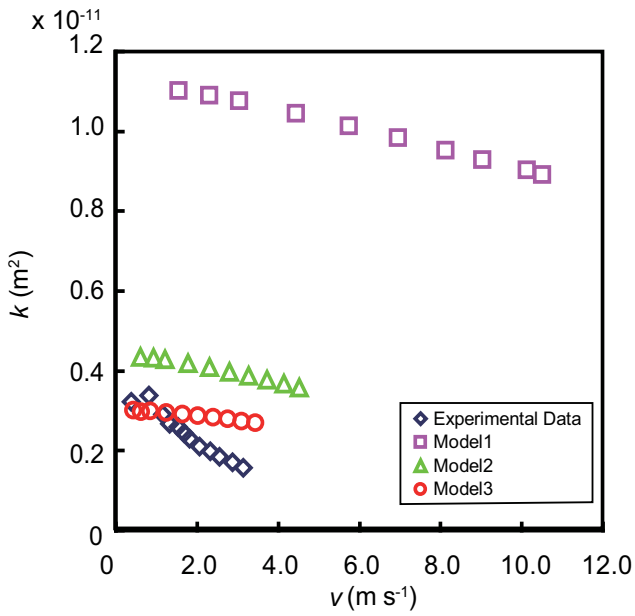

Figure 8. Darcy coefficients in through-plane direction.

Figure 10 illustrates a parallel-serpentine flow field in the cathode of a PEFC. Flow analyses for the GDL between the flow channels indicated in the blue and red circles. The pressure difference between the channels in the former part is rather smaller than the lattar. This comparison represents that between the parallel and serpentine flow fields.

The GDL is modeled with the flow channel and rib as presented in Fig. 11.

Cell temperature is 75°C and water vapor pressure shall be the saturation vapor pressure at 75 °C. Air utilization is 30%. Oxygen and nitrogen partial pressure is assumed to linearly change from the inlet to the outlet, yielding 1.60 and -0.81 kPa, respectively, between the flow channels in the red part at 1.0 A cm^{-2}. It is assumed that current distribution is uniform and there is no liquid water in the GDL to simplify the calculation. Thickness of the GDL, rib width, and channel width are 190 μm, 0.6 mm, and 0.5 mm, respectively. Viscosities of

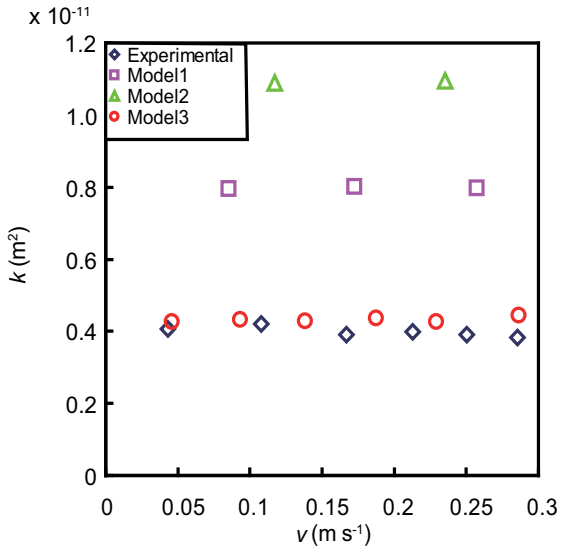

Figure 9. Darcy coefficients in in-plane direction.

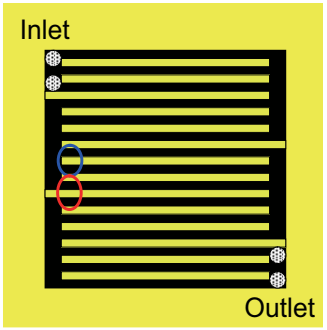

Figure 10. Serpentine flow field.

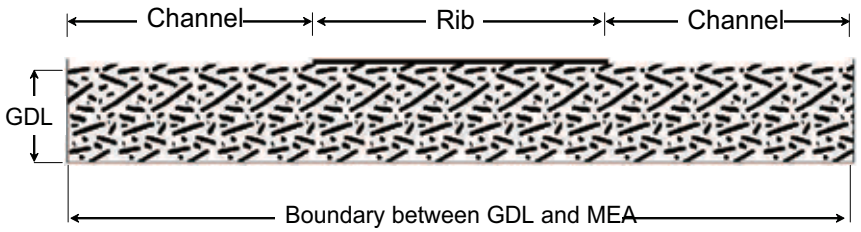

Figure 11. GDL model with the channels and rib of the PEFC.

http://dx.doi.org/10.5772/56363

nitrogen and oxygen of 20.00×10^{-6} and $23.26 \times \times 10^{-6}$ Pa·s, respectively[13], and binary diffusion coefficient for nitrogen-oxygen mixture of $2.59 \times 10^{-5} m^2 s^{-1}$[14] are used for the LBM-BMD calculation. Oxygen flow velocity distribution at 1.0 A cm^{-2} is presented in Fig. 12. Oxygen amount consumed by the electrochemical reaction is calculated with the Faraday's law.

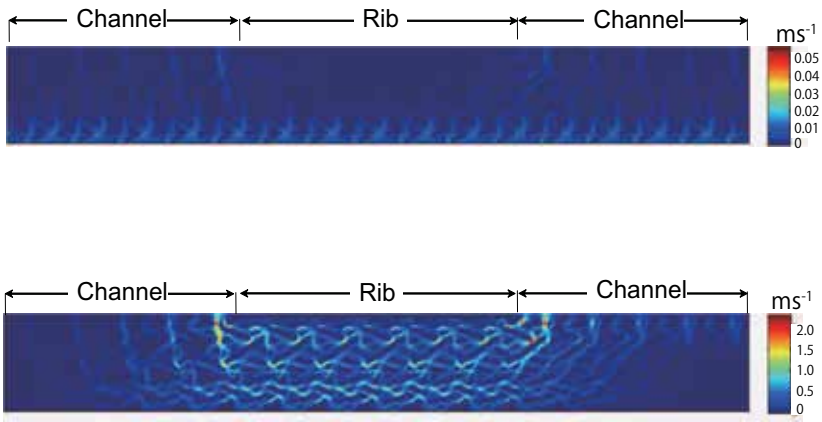

Figure 12. Oxygen flow velocity distributions in the GDLs (a) without pressure difference and (b) with pressure difference between the flow channels at 75 °C, 1.0 A cm^{-2}.

Figures 12(a) and (b) depict oxygen flow velocities for the GDLs without and with pressure differences between the flow channels, respectively. Oxygen is transported to the surface of the MEA mainly by diffusion in the case without the pressure differences since there is small forced convection thorough the GDL. On the other hand, oxygen flow velocity is rather larger under the rib in the case with pressure difference that leads to forced convection in the GDL. The forced convection also enhances the discharge of liquid and vapor product water in actual cells. The forced convection in the GDL by the pressure difference between flow channels plays a significant role on the exhaust of the product water and oxygen transport for the interdigitated flow field[15, 16].

6. Conclusion

In this chapter, an anisotropic 2D GDL model is proposed by comparisons of the through-plane and in-plane permeabilities between those obtained by LBM calculation and permeability measurements. The modeled carbon fiber structure agrees well with the actual GDL in terms of the permeability. Moreover, the difference of oxygen flow in GDLs with parallel and serpentine flow channels is visualized with the oxygen-nitrogen two components LBM-BMD calculations using the above anisotropic GDL model. This procedure can be used

to optimize the GDL porous structure, flow field patterns, and operation conditions of PEFCs. Liquid-gas two phase modeling[17, 18], modeling, modeling of microporous layers[19–21], and expansion to 3D modelings are future studies.

Acknowledgments

The author is grateful to a graduate student, Tomokazu KOBAYASHI (presently TOYOTA Motor Corp.) for considerable assistance with the modeling and calculation. The author also thank Associate Professor Kitahara and a graduate student, Teppei YASUKAWA (presently DENSO Corp.) for help with the permeability measurements. The author is indebted to Professor Konomi for valuable discussions.

Author details

Hironori Nakajima

Department of Mechanical Engineering at Kyushu University, Japan

References

[1] H. Nakajima, T. Konomi, and T. Kitahara. Direct water balance analysis on a polymer electrolyte fuel cell (PEFC): Effects of hydrophobic treatment and micro porous layer addition to the gas diffusion layer of a PEFC on its performance during a simulated start-up operation. *Journal of Power Sources*, 171:457–463, 2007.

[2] Dieter A. Wolf-Gladrow. *Lattice-Gas Cellular Automata and Lattice Boltzmann Models: An introduction*, volume 1725 of *Lecture Notes in Mathematics*. Springer, 2000.

[3] Sauro Succi. *The Lattice Boltzmann Equation for Fluid Dynamics and Beyond*. Oxford University Press, New York, 2001.

[4] M. Yoshino and T. Inamuro. Lattice boltzmann simulations for flow and heat/mass transfer problems in a three-dimensional porous structure. *International Journal for Numerical Methods in Fluids*, 43(2):183–198, 2003.

[5] J. Park and X. Li. Multi-phase micro-scale flow simulation in the electrodes of a PEM fuel cell by lattice Boltzmann method. *Journal of Power Sources*, 178(1):248 – 257, 2008.

[6] P. L. Bhatnagar, E. P. Gross, and M. Krook. A model for collision processes in gases. i. small amplitude processes in charged and neutral one-component systems. *Phys. Rev.*, 94:511–525, May 1954.

[7] Takaji Inamuro, Koji Maeba, and Fumimaru Ogino. Flow between parallel walls containing the lines of neutrally buoyant circular cylinders. *International Journal of Multiphase Flow*, 26(12):1981 – 2004, 2000.

[8] Qisu Zou and Xiaoyi He. On pressure and velocity boundary conditions for the lattice Boltzmann BGK model. *Physics of Fluids*, 9(6):1591–1598, 1997.

http://dx.doi.org/10.5772/56363

[9] Li-Shi Luo and Sharath S. Girimaji. Lattice Boltzmann model for binary mixtures. *Physical Review E*, 66:035301, Sep 2002.

[10] Michael E. McCracken and John Abraham. Lattice Boltzmann methods for binary mixtures with different molecular weights. *Physical Review E*, 71:046704, Apr 2005.

[11] Abhijit S Joshi, Aldo A Peracchio, Kyle N Grew, and Wilson K S Chiu. Lattice boltzmann method for continuum, multi-component mass diffusion in complex 2D geometries. *Journal of Physics D: Applied Physics*, 40(9):2961, 2007.

[12] Tatsumi Kitahara, Toshiaki Konomi, and Hironori Nakajima. Microporous layer coated gas diffusion layers for enhanced performance of polymer electrolyte fuel cells. *Journal of Power Sources*, 195(8):2202 – 2211, 2010.

[13] *JSME Data Book: Thermophysical Properties of Fluids*. The Japan Society of Mechanical Engineers, Tokyo, 1983.

[14] S. Oe. *Estimation Methods of Physical Property Constants for Designers (in Japanese)*. Nikkan Kogyo Shimbun, Tokyo, 1985.

[15] T. V. Nguyen. A gas distributor design for proton-exchange-membrane fuel cells. *Journal of the Electrochemical Society*, 143:L103–L105, 1996.

[16] D.L. Wood III, J.S. Yi, and T.V. Nguyen. Effect of direct liquid water injection and interdigitated flow field on the performance of proton exchange membrane fuel cells. *Electrochimica Acta*, 43(24):3795–3809, 1998.

[17] U. Pasaogullari and C.-Y. Wang. Two-phase transport and the role of micro-porous layer in polymer electrolyte fuel cells. *Electrochimica Acta*, 49(25):4359–4369, 2004.

[18] U. Pasaogullari and C.Y. Wang. Liquid water transport in gas diffusion layer of polymer electrolyte fuel cells. *Journal of the Electrochemical Society*, 151(3):A399–A406, 2004.

[19] Z. Qi and A. Kaufman. Improvement of water management by a microporous sublayer for PEM fuel cells. *Journal of Power Sources*, 109(1):38–46, 2002.

[20] A.Z. Weber and J. Newman. Effects of microporous layers in polymer electrolyte fuel cells. *Journal of the Electrochemical Society*, 152(4):A677–A688, 2005.

[21] Tatsumi Kitahara, Hironori Nakajima, and Kyohei Mori. Hydrophilic and hydrophobic double microporous layer coated gas diffusion layer for enhancing performance of polymer electrolyte fuel cells under no-humidification at the cathode. *Journal of Power Sources*, 199:29 – 36, 2012.

Chapter 14

General Aspects of Aqueous Sorption Process in Fixed Beds

M. A. S. D. Barros, P. A. Arroyo and E. A. Silva

Additional information is available at the end of the chapter

http://dx.doi.org/10.5772/51954

1. Introduction

Adsorption as well as ion exchange share many common features. Although such phenomena are distinct (ion exchange is a stoichiometric process) they can be generically denominated as sorption processes. Then, as already known, sorption is a well-established technology in chemical engineering.

The sorption ability of different sorbents is strongly dependent on the available surface area, polarity, contact time, pH and the degree of hydrophobic nature of the adsorbent and adsorbate (Suzuki, 1990). Therefore, the selection of the sorbent is the first step in such investigation. Studies should be firstly focused on batch systems in equilibrium and isotherms should be constructed.

Equilibrium condition is attained when the concentration of the solute remains constant, as a result of zero net transfer of solute sorbed and desorbed from sorbent surface. The equilibrium sorption isotherms describe these relationships between the equilibrium concentration of the sorbate in the solid and liquid phase at constant temperature. Experimental data may provide different isotherm shapes such as: Linear, Favorable, Strongly favorable, Irreversible and Unfavorable (McCabe et al., 2001) as shown in Figure 1.

The linear isotherm starts from the origin. Although it does not show a selectivity behavior, the sorbent related to this isotherm sometimes is chosen because the linear isotherm facilitates the column modeling, mainly when equilibrium data is added to the phenomenological dynamic model (Helferich, 1995).

Sorbents that provide isotherms with convex upward curvature are denominated as favorable and strongly favorable. These shapes are often selected for dynamic studies because they show the sorbent selectivity to the sorbate of interest. Nevertheless, they are not convenient

when regeneration is required because it may be related to an unfavorable isotherm and quite long mass-transfer zones in the bed (McCabe et al., 2001). Moreover, the famous Langmuir model provides good adjustments to strongly favorable isotherms as it forms a plateau that represents in many cases, the monolayer sorption. Here, it must be remembered that the equilibrium equation is used in the modeling of fixed bed.

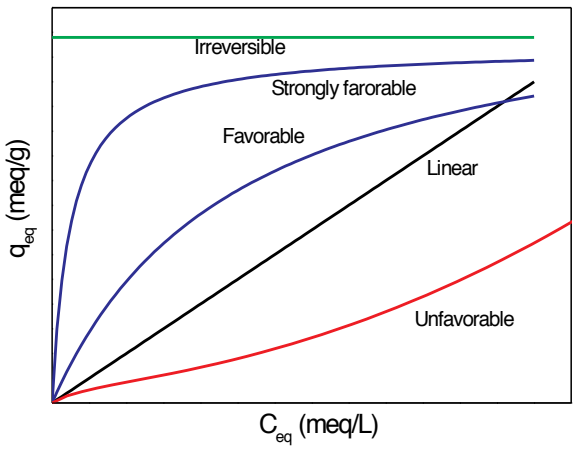

Figure 1. Adsorption isotherms

Finally, it may be emphasized that the Langmuir isotherm is derived assuming a uniform surface, which is many cases is not rigorously valid. This relation works fairly well, even with sorbents with high heterogeneity such as zeolites, clays or activated carbon.Here some aspects should be stressed. The first one is related to the model itself. Sometimes the Langmuir model represents the experimental data although it is known that are different sites involved in the sorption process such as the ones located in the supercages or in the sodalite cages of NaX zeolite (Barros et al., 2004). On the other hand, sorbent may have high heterogeneity and only one type of site is effective in the sorption process. Then, the experimental data may be fitted successfully to such model and the assumptions previously considered are still valid. This may be case of sorption of large molecules such as dyes.

The limiting case of the extremely favorable isotherm is the irreversible sorption represented by a horizontal line, that means a constant amount of sorbed compound. When the irreversible isotherm is obtained no regeneration is possible.

Designing of dynamic sorption processes also takes into account the multicomponent effluent. It means that studies of batch competitive systems should be relevant. Sorbents that have affinity to different sorbates may be less effective in removing the one of interest. It these cases, higher packed beds are required. The multicomponent equilibrium data are obtained considering the initial multicomponent solution. Many models have been proposed.

http://dx.doi.org/10.5772/51954

Some of them are derived from the single Langmuir model. As it happens with the single sorption, even when the ion exchange phenomenon is involved, release of the out-going ion is neglected (Misak 2000; Sprynskyy et al., 2006).

The Binary Langmuir Model assumes a homogeneous surface with respect to the energy of adsorption, no interaction between adsorbed species and that all adsorption sites are equally available to all adsorbed species The Noncompetitive Langmuir Model considers that the concentration of the sorbate of interest in the sorbent depends on the concentration of the respective specie in the fluid phase only. In this case, monocomponent Langmuir can be applied for each one of the species in solution (Sánchez et al., 1999). In both cases, the Binary Langmuir Model and the Noncompetitive Langmuir Model, as there is no competition to the same sites, no overshooting is observed in the breakthrough curve. Overshooting will be discussed later.

The Langmuir Type Model was developed to describe the noncompetitive inhibition during enzymatic kinetic studies. According to the adsorption point of view such model may be applied when a synergism effect is presented due to the existence of sites containing both species (Bailey and Ollis, 1986; Sánchez et al., 1999). It means that in the dynamic sorption more adsorption occurs than the one it was expected, and the uptake on the sorbate of interest is promoted by the presence of other sorbates. No overshooting is expected to occur in this system.

Jain and Snoeyink (1973) have proposed an adsorption model for binary mixtures based on the hypothesis that a part of adsorption occurs without competition. In other words it means that there is at least one type of sorption site where the sorbate of interest is preferentially retained with no competition. In other types of sites, competition occurs. Then, it may be supposed that a slightly overshooting curvature may be evidenced in the breakthrough curve.

Myers and Prausnitz (1965) developed the ideal adsorbed solution theory (IAST) based on the Gibbs adsorption isotherm. The IAST model has the main advantage to predict the equilibrium in multicomponent systems in microporousmaterials through the single isotherms only. However, although the model allows its application in many complex mixtures of solutes, the IAST model limits its use in the range of concentration where the single equilibrium data were obtained. It has been used to predict the sorption process in gas phase, mainly in diluted systems.

A non-predictive thermodynamic approach called RAST (Real Adsorbed Solution Theory) extends the IAST theory to more concentrated solutes using the corresponding activity coefficients.

Finally, when the ion exchange process is much more pronounced then the adsorption process, it may be applied the Ion Exchange Model taking into account the Mass Action Law. In typical ion exchangers such as zeolites this mode are applied with successful results.

After selecting the sorbent and investigating the sorption mechanism, the second step is the dynamic studies in the fixed bed system.

2. Dynamic studies in fixed bed systems

2.1. The breakthrough curve

Most ion-exchange operations, whether in laboratory or in plant-scale processes, are carried out in columns. A solution is passed through a bed of sorbent beads where its composition is changed by sorption. The composition of the effluent and its change with time depend on the properties of the sorbent (as already discussed), the composition of the feed, and the operating conditions (flow rate, temperature etc.). Plots of the ratio C/C_o (outlet sorbate concentration/sorbate feed concentration) versus time are denominated as breakthrough curves.

As the run stars, most of the mass transfer takes place near the inlet of the bed, where the fluid first contacts the sorbent. If the solid contains no sorbate at the start, the concentration in the fluid drops exponentially to zero before the end of the bed is reached. This concentration profile as well as the breakthrough curve is shown in Figure 1. As the run proceeds, the solid near the inlet is nearly saturated, and most of the mass transfer takes place further from the inlet. The concentration gradient is S shaped. The region where most of the change in concentration occurs is called the mass-transfer zone. This is the real behavior of mass transfer process in fixed beds. When the axial or radial mass transfer resistances are neglected sorption occurs homogeneously and this is the ideal case. In fact, mass transfer resistances can be minimized but not effectively eliminated. Comments about such phenomenon will be better detailed. The limits of the breakthrough curve are often taken as C/C_o values of 0.05 to 0.95, unless any other recommendation is fixed. They are related to the breakpoint (t_b, C_b) and saturation point (t_s, C_s), respectively. In most of cases C_s C_o. This is the case of wastewater treatment of highly toxic sorbates. When the concentration reaches the limiting permissible value, say, 1 ppm, it is considered the break point. The flow is stopped, the column is regenerated and the inlet concentration is redirected to a fresh sorbent bed.

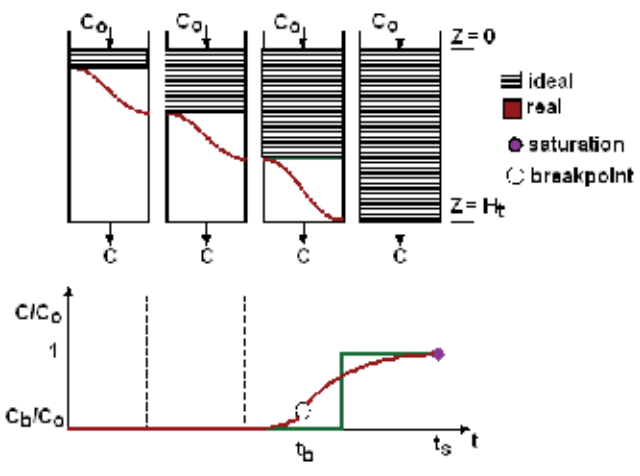

Figure 2. Breakthrough curve for the sorption process in fixed beds Co is the concentration of the inlet solution, C_b is the concentration of the breakthrough, t_b is the breakpoint time and t_s is the saturation time.

http://dx.doi.org/10.5772/51954

2.2. Mass transfer in fixed beds

In fixed-bed ion exchange, the concentration in the fluid phase and in the solid phase changes with time as well as with position in the bed. The transfer process is described by the overall volumetric coefficient ($K_c a$), obtained from a metal material balance in the column assuming irreversible sorption as proposed in McCabe et al. (2001):

$$K_c a = \frac{N . u_o}{H_t} \tag{1}$$

where N is the overall number of transfer units, H_t is the bed length and u_o is the superficial velocity of the fluid.

In fact, Eq. 1 can be used for modeling the breakthrough curves, if the batch isotherms can be considered as irreversible.

The overall number of transfer units may be obtained graphically by plotting C/C_o versus $N(\tau\text{-}1)$, where $N(\tau\text{-}1) = 1+\ln(C/C_o)$ (McCabe et al., 2001). Parameter τ is dimensionless time defined as

$$\tau = \frac{u_o C_o \left(t - \frac{\varepsilon}{u_o} H_t\right)}{\rho_p (1 - \varepsilon) W_{sat} H_t} \tag{2}$$

The term $\frac{\varepsilon}{u_o} H_t$ in Eq. 2 is the time required to displace fluid from external voids in the bed, which is normally negligible. The product is the total amount of metal fed per unit cross section of the bed up to time t and $\rho_p (1 - \varepsilon) W_{sat} H_t$ is the capacity of the bed, which is equal to the time equivalent to total stoichiometric capacity of the packed-bed tower (t_t).

The time equivalent to usable capacity of the bed (t_u) and the time equivalent to total stoichiometric capacity of the packed-bed tower (t_t) if the entire bed reaches equilibrium are provided by a mass balance in the column and they are easily determined by (Geankoplis 1993):

$$t_u = \int_0^{t_b} \left(1 - \frac{C}{C_o}\right) dt \tag{3}$$

$$t_t = \int_0^{\infty} \left(1 - \frac{C}{C_o}\right) dt \tag{4}$$

where t_b is the breakpoint time.

If time t is assumed to be the time equivalent to the usable capacity of the bed (t_u) up to t_b, parameter τ may be simplified to t_u/t_t.This ratio is the fraction of total bed capacity or length utilized to the breakpoint (Geankoplis, 1993). Hence, the length of unused bed (H_{UNB}) is the unused fraction times the total length (H_t).

$$H_{UNB} = \left(1 - \frac{t_u}{t_t}\right) H_t \tag{5}$$

H_{UNB} is assumed to be constant and, as a consequence, an important tool when scaling-up processes (McCabe et al., 2001). Unfortunately it is not always true. A constant mass-transfer zone is valid for ideal sorption systems associated with sorbates of small molecular diameter and simple structures (Walker and Weatherly, 1997). Changes in pH speciation through the column may also change the MTZ (Gazola et al., 2006). It probably happens because the rate at which the sorption zone travels through the bed decreases with bed height (Walker and Weatherly, 1997). Therefore, it may be concluded that the hypothesis of a constant length of mass transfer zone for the same feed concentration can be acceptable depending on the variation of the bed height and specific sorbates.

H_{UNB} represents the mass-transfer zone (MTZ). Small values of this parameter mean that the breakthrough curve is close to an ideal step with negligible mass-transfer resistance. Moreover, in the ideal condition, no axial dispersion would occur. The velocity profile would be analogous to the one observed in a Plug Flow Reactor and the ideal breakthrough curve would be the response to a positive-step test, called the Cumulative Distribution Function or F curve. In the ideal breakthrough curve H_{UNB} is zero. This condition is never reached although it is recommended to operate the column as close as possible. The closer the column is operated to the ideal condition, the more efficient is the mass transfer zone. Therefore, the ideal situation means $H_{UNB} = 0$. In experimentally effective situation $0 < H_{UNB} < H_t$. If $H_{UNB} > H_t$ in the very beginning of the run the sorbate is presented in the outlet solution, the sorption process is highly inefficient, mainly if the sorption unit has been used for wastewater treatment. An increase in H_t is recommended.

Besides the minimum MTZ, some other mass transfer parameters may be used to identify, quantitatively, the condition with the lowest resistances over the operational conditions investigated.

One of this parameter is the residence-time distribution (RTD). According to Fogler (2004), the RTD is determined experimentally by injecting a tracer in the column at some time t=0 and then measuring the outlet concentration as a function of time. In this case, the tracer is used to determine RTD in reactors and must be nonreactive, easily detectable, completely soluble to the mixture and more important: it should not adsorb on the walls or any other surface of the reactor. If the injection of a tracer is given as a step injection, the response is the F curve which shape is analogous to the breakthrough curve as seen in Figure 2. Then, it is possible to obtain the average residence time (t_{res}). Correlation between the F curve from the non-ideal concept and the sorption process in fixed beds can be done only in terms of the graphical shape. No more similarities are corrected.

The average residence time (t_{res}) of the fluid in the columnis estimated based on principles of probability as follows (Hill, 1977):

http://dx.doi.org/10.5772/51954

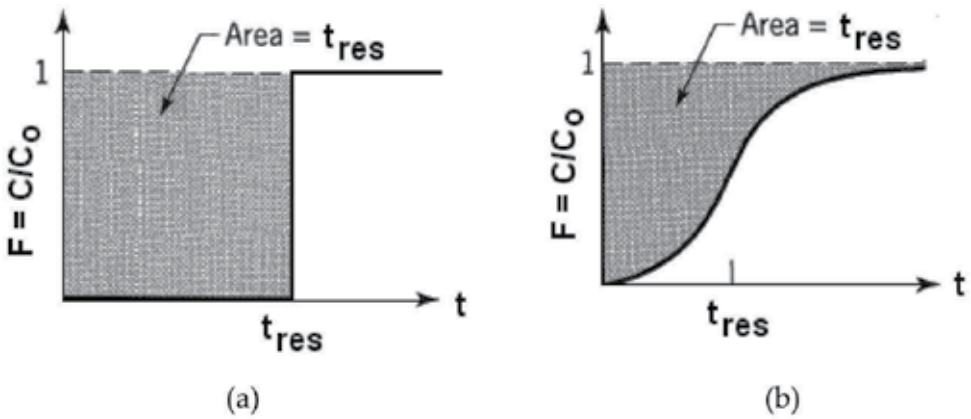

Figure 3. Breakthrough curves considering the F response of a step input: a) ideal situation (H_{UNB} = 0) ; b) real situation (H_{UNB}> 0).

$$t_{res} = \int_0^\infty t dF(t) \tag{6}$$

where F(t) is the weight fraction of the effluent of an age less than t, which is equivalent to C/C_o for breakthrough curves (Barros et al, 2003).

An indirect measure of how far from the optimum operational condition the column operates is expressed by the operational ratio (R) as (Barros et al., 2003)

$$R = \left| \frac{t_{res} - t_u}{t_u} \right| \tag{7}$$

Values of parameter R close to zero indicate that the operational conditions imposed are near the ideal condition, i.e., the optimal region of operation. Therefore, this difference may contribute to the selection of the best operational conditions in the column design.

With the average residence time it is also possible to evaluate the variance in the breakthrough curve (Hill, 1977), which is given by:

$$\sigma^2 = \int_0^\infty t^2 \left(\frac{F(t)}{dt} \right) - t_{res}^2 \tag{8}$$

The dimensionless variance should be calculated as

$$\sigma_\theta^2 = \frac{\sigma^2}{t_{res}^2} \tag{9}$$

Determination of this parameter is useful to estimate the axial dispersion in the packed bed. Values of dimensionless variance close to zero mean that the behavior of the velocity profile in packed beds is close ideal plug-flow with negligible axial dispersion.

Finally, through a mass balance it is possible to obtain the amount of sorbate retained up to the breakpoint time (U^{t_b}) and up to the saturation time (U^{t_s}).

$$U^{t_b} = t_u . f_R . C_o \tag{10}$$

$$U^{t_s} = t_t . f_R . C_o \tag{11}$$

where t_u and t_t are obtained through Eqs. 3 and 4, f_R is the flow rate and C_o is the inlet concentration.

2.3. Minimum mass transfer resistances in the fixed bed

Operate the fixed bed with minimum mass transfer resistances is quite advantageous. It maximizes the sorption process as more sorption sites are available to the dynamic process. Therefore, optimizing the operational conditions is highly recommended. It can be done investigating a range of particle diameters of the sorbent or different flow rates in the column. In some cases, temperature should be also investigated. It is expected to obtain higher amount of uptaken sorbate with increasing temperatures when chemisorption and/or ion exchange are presented as the more significant mechanism. Nevertheless, if the retention is due to physisorption phenomenon, an increase in temperature is disadvantageous.

The optimal operational condition is the one that minimizes, as close as possible, the film and particle resistances, that means to maximize the pore diffusion and the solid diffusion. Figure 3 gives an idea about the mass transfer mechanism in a fixed bed.

Therefore, when the film and particle resistances are minimized it is seen that:

The mass transfer zone, the operational ratio and the dimensionless variance are minimum;

The closer the system is of the optimal condition, the closer the breakpoint time is to the saturation time;

The sorbate uptake up to breakpoint time (U^{t_b}) and up to saturation time (U^{t_s}) are the maximum. It happens when there is at least a favorable isotherm;

In most of cases, a steep breakthrough curve is observed.

Figure 4 shows an example of breakthrough curves at different flow rates. It is seen that at 11 mL/min the breakthrough curve is almost a step curve. Table 1 presents the numerical data and it is total agreement with Figure 4. It means that at this flow rate the minimum mass transfer resistance was reached considering the range investigated.

http://dx.doi.org/10.5772/51954

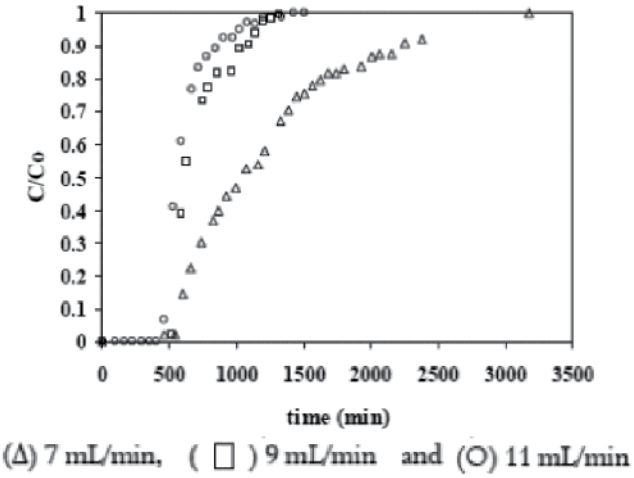

Figure 4. Breakthrough curves for Cr (III) uptake in NaA zeolite (Barros et al., 2002)

Flow rate (mL/min)	H_{UNB} (cm)	R	$\sigma_\theta^2 = \frac{\sigma^2}{t_{res}^2}$	$U_{Cr}^{t_b} \Big/ CEC_{bed}$
7.0	3.9	1.3	0.3	0.25
9.0	1.7	1.0	0.3	0.30
11.0	1.0	0.4	0.1	0.31

$U_{Cr}^{t_b} \Big/ CEC_{bed}$ = ratio of amount of Cr (III) retained up to the breakpoint and the cation exchange capacity of the zeolite in the bed.

Other examples can be found in Pereira et al. (2006).

Table 1. Mass-transfer parameters obtained for Cr(III) uptake in NaA zeolite packed bed (Barros et al., 2002)

2.4. Sorption in competing systems

When the feed solution is composed by different sorbates, the competition for the sorption sites may occur. Uptake of the sorbate of interest is well evidenced by the dynamic capacity of the column. Thus, the term $U_{i\text{-}mix}^{t_b}$ is defined as the amount of sorbate uptaken at t_b prior to the sorbate *i* breakpoint (Valdman et al., 2001).

The effect of competitive systems on the sorption process may be represented by the ratio of the uptake capacity for the sorbent *i* in multicomponent solution and in single solution, that is the removal ratio $\left(U_{i\text{-}mix}^{t_b} \Big/ U_{i\text{-}single}^{t_b} \right)$ -Mohan and Chander, (2001).

Thus if the removal ratio:

> 1: uptake is promoted by the presence of other sorbates;

=1: no interaction exists between the sorbates;

< 1: uptake is suppressed by the presence of other sorbates.

Therefore, the evaluation of the removal ratio at the time equivalent to usable capacity of the bed t_u for sorbate *i* may be useful to investigate the influence of different sorbates on the uptake of such sorbate (Barros et al., 2006).

Moreover, in the competing systems, sometimes the breakthrough curves for the competing sorbates may have values higher than one that is called overshooting. When the ion exchange phenomenon is dominant, it is also called sequential ion exchange (Barros et al., 2006). Figure 5 shows an example of a sequential ion exchange. The ion exchange preferentially occurs up to the occupation of all available sites. As the sorption proceeds, the competing sorbates are released at different running times with continued feed of the multicomponent solution. Potassium ions are smaller than the other ions. Then, they diffuse faster into the ion exchanger framework and are firstly retained. Calcium ions are larger and probably face some difficulties in diffusing as fast as the potassium ions. Nevertheless, once they diffuse, they are preferentially retained due to its higher charge, displacing the potassium ions. Finally, chromium ions are the largest ones with the highest charge. They diffuse slowly into the exchanger framework. They displace the calcium ions. The consequence of such process is the presence of two overshooting waves: one related to the release of potassium ions and another related to the release of the calcium ions. In this competing ion exchange process it is seen that $\left(U^{t_b}_{Cr\text{-}mix} \Big/ U^{t_b}_{Cr\text{-}single}\right)$ is 0.79, which means that there is a decrease of 21% in the chromium uptake. Probably the presence of potassium and mainly the presence of calcium ions suppressed the chromium uptake due to competition towards the exchanging sites located in the large cages of the zeolite NaY.

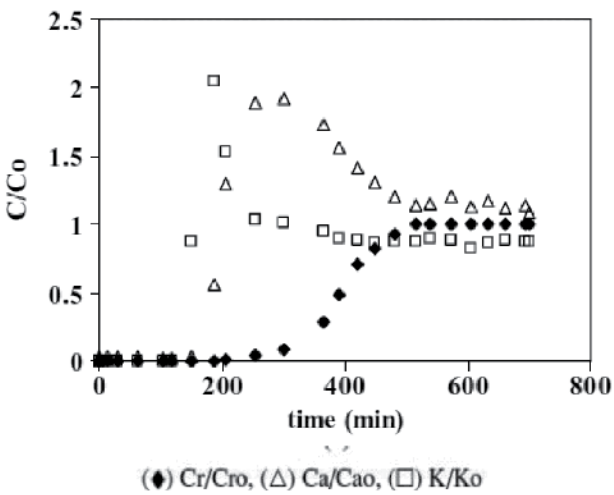

Figure 5. Breakthrough curves for competitive system Cr/Ca/K in NaY zeolite (Barros et al.,2006)

http://dx.doi.org/10.5772/51954

Overshooting may occur in different sorbents such as activated carbons (Mohan and Chander, 2001), biosorbents (Sağ et al., 2000) or even ion exchanger membranes (Labanda et al., 2011). It depends on the selectivity of the sorbent, the sorption mechanism (that can be seen through the isotherms) and on the operational conditions imposed. If the operational condition is the one that minimizes the mass transfer resistances of one sorbate is imposed, it is expected a pronounced overshooting when the optimal operational conditions of the other sorbates are different from the one of interest. When the optimal conditions are close, there should be some overshooting depending of the selectivity provided by the isotherms and the concentration of the sorbates, as shown in Figure 6.

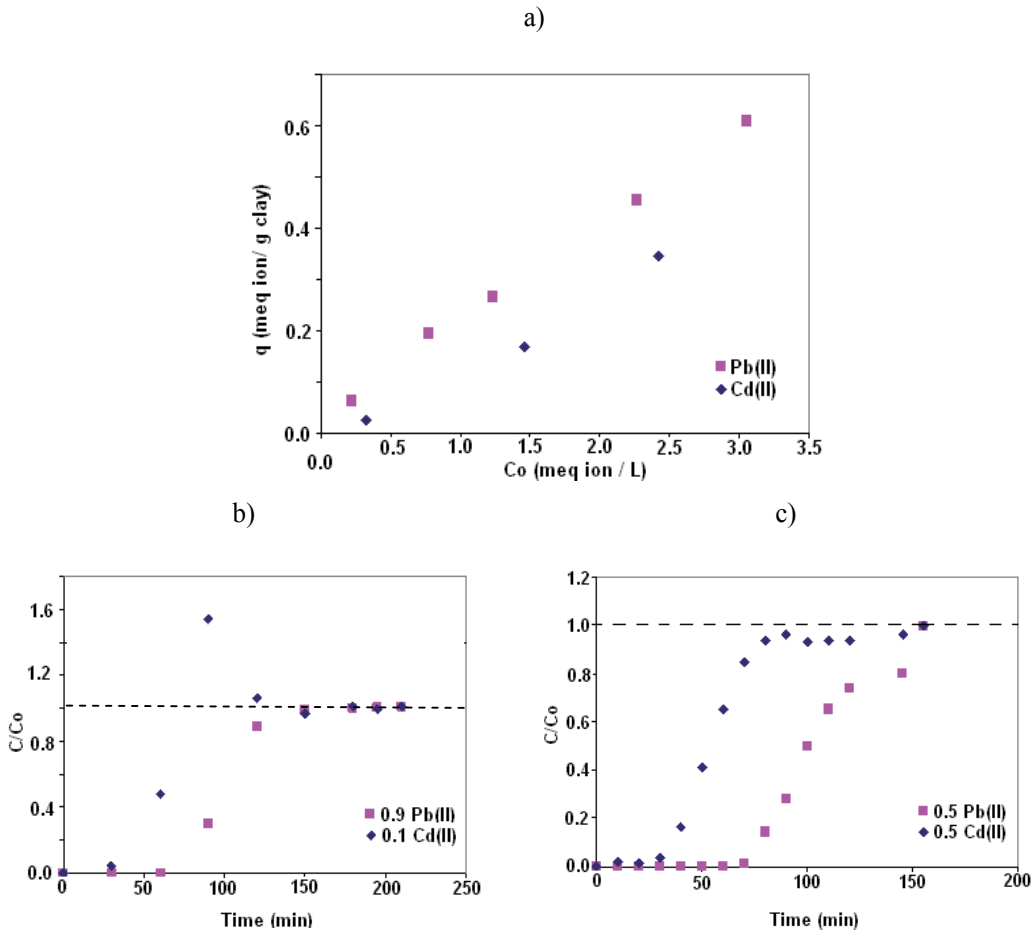

Figure 6. a) Dinamic isotherm (see item 2.5) of Pb (II)/Cd (II) in bentonite clay pretreated with calcium at 30 °C and 2 mL/min; b) breakthrough curve at 2 mL/min and total concentration of 3.0 meq/L, 90% Pb (II), 10% Cd (II); c) breakthrough curve at 2 mL/min and total concentration of 3.0 meq/L, 50% Pb (II), 50% Cd (II).

In Figure 6a it is seen the bicomponent dynamic isotherm of Cd (II) and Pb(II) ions in bentonite clay from Boa Vista-PB-Brazil. The clay sample was pretreated with calcium in order to obtain, as far as possible, a homoionic sample. The concept of dynamic isotherm will be discussed in section 2.5. In this system, the flow rate of 2 mL/min may be considered as the optimal condition that minimize the mass transfer resistances of both Cd(II) and Pb(II) uptake. It is seen that the clay sample has more affinity to lead ions, probably due to its electronegativity (Kang et al., 2004).

Figures 6b and 6c show the breakthrough curves for two different inlet percentages of cadmium and lead and the same total concentration of 3 meq/L. In the first case the inlet concentration was composed by 90% Pb (II), 10% Cd (II) (2.7 meq/L of Pb (II) and 0.3 meq/L of Cd (II). In the second case the composition was 50% for each ion, or 1.5 meq/L of Pb (II) and 1.5 meq/L of Cd (II). The overshooting is clearly observed in Figure 6b due to the higher selectivity to lead ions. When cadmium concentration was increased no overshooting was observed although, according to the breakpoint times, it is also seen the preference of lead as its breakpoint occurs later.

2.5. Dynamic isotherms

Most separation and purification processes that employ the sorption technology use continuous-flow columns. In order to understand and to model the dynamic process, a deep knowledge of the equilibrium in the fixed bed is essential. For the complete comprehension of the whole process, information about the equilibrium and the kinetics of the process should be combined with the mass balance. Kinetic investigations in a column are almost exclusively restricted to those processes of which the equilibria either can be represented by a linear or a Langmuir isotherm or satisfy the law of mass action. However, the results of this study of industrially applicable commercial products have shown that the above equilibria usually fail to fit the experimental results adequately. Furthermore, the customary procedures of determining the equilibria in batch systems are not, in general, applicable to all types of sorbents (Klamer and Van Krevelen, 1958).For example, the batch isotherm was not able to represent correctly, the breakthrough curve of Cr (III) sorption in NaX zeolite modeled by a phenomenological model. Such model will be discussed in section 2.6. Figure 7 presents the batch isotherm of Cr (III) in zeolite NaX and its use in a LDF model. It is clearly seen that it is totally inadequate.

The dynamic isotherm surged to better describe the sorption mechanisms involved in a dynamic process where kinetics and equilibrium acts simultaneously. In fixed beds, solution is fed continuously, and, at equilibrium, concentration and pH are equal to their respective feed values that do not occur in batch isotherms. Its procedure is based on the breakthrough data. Each run up to the saturation is related to one point of such data, that is, the amount of sorbate retained up to saturation plotted against the inlet concentration (Barros et al., 2004). The dynamic isotherm has the advantage of controlling the fluid-phase concentration. Results of the column dynamic simulations depend on the selection of an appropriate mathematical relation used to represent the equilibrium. Therefore, in order to model the dynamic

http://dx.doi.org/10.5772/51954

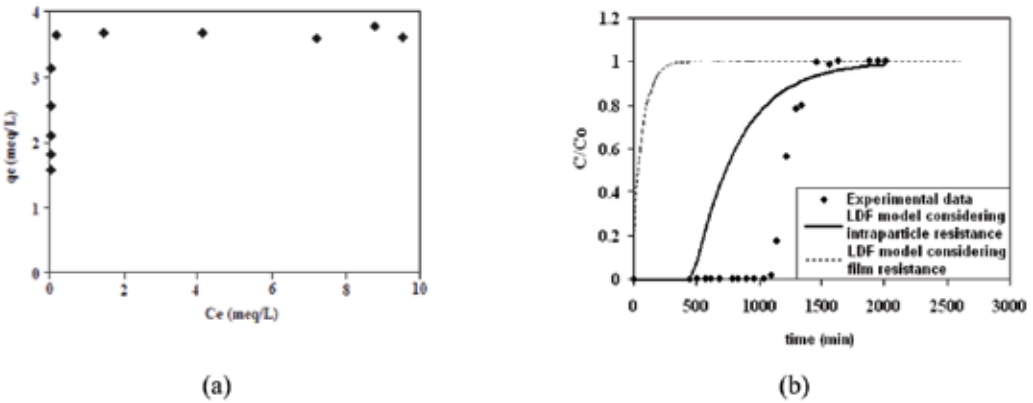

Figure 7. a) Batch isotherm of Cr (III) in zeolite NaX at 30 °C (Barros et al., 2004); b) Use of batch isotherm to model Cr (III) breakthrough data in NaX columns

sorption, dynamic isotherms should be considered instead of the frequently used batch isotherms as they better represent equilibrium in fixed bed (Barros et al., 2009).

The dynamic isotherm of Cr (III) in NaX is shown in Figure 8 at the optimal particle size and flow rate previously determined (Barros et al., 2004). Its shape is totally different, as one can see comparing Figures 8 and 7a.

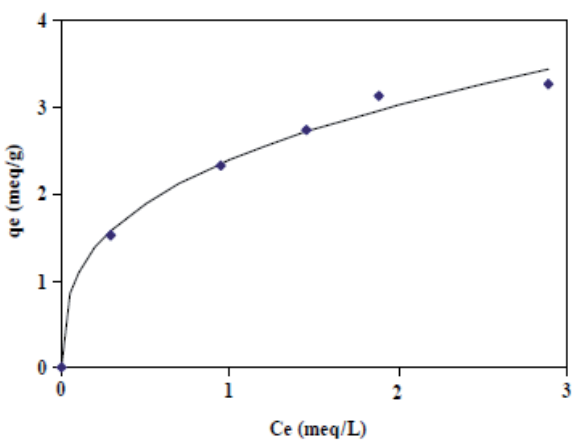

Figure 8. Dynamic isotherm of Cr (III) in zeolite NaX at 30 °C (Barros et al., 2004)

2.6. Modeling of the breakthrough curve

The phenomenological mathematical models are important tools in the design of sorption in fixed bed columns. The validation is done by experimental data obtained in laboratory scale. Mathematical models are useful for designing and optimizing purposes in industrial scale.

The effects of mass transfer in breakthrough curves are complex, mainly if the isotherms are expressed by non-linear mathematical equations. The concentration of the sorbate varies with the position and time. Therefore, the phenomenological model is represented by partial differential equations, which are difficult to be solved analytically.

Due to such complexity, the phenomenological mathematical models have many simplifications to make them feasible to obtain an analytical solution. Bohart and Adams (1920) developed one of the first mathematical models. The respective equation is given by Equation 12. This model was firstly used to describe the dynamic sorption of chlorine in columns packed with activated carbon and are still widely used by several researchers (Singh et al., 2012; Kumar et al., 2011; Rao et al., 2011; Trgo et al., 2011, Chu et al., 2011; Martin-Lara et al., 2010, Muhammad et al., 2010, Borba et al., 2008.). The model Bohart Adams considers that the limiting step of the mass transfer is controlled by the kinetics of sorption which is represented by a second-order reaction.

$$\frac{C_{out}}{C^F} = \begin{cases} 0 & t < t_F \\ \dfrac{1}{\left(e^A + e^{-B} - 1\right)e^B} & t > t_F \end{cases} \tag{12}$$

where: $A = \dfrac{L\ \beta}{u_0}$, $B = \dfrac{\left(-t u_0 + L\ \right)\beta}{\alpha u_0}$, $\alpha = \dfrac{\rho_{bed} q^*}{C^F \varepsilon}$, $\beta = k_a C^F \alpha$ and $t_F = \dfrac{L}{u_o}$

Bohart and Adams model presented only one adjustable parameter that is the rate constant k_a.The parameter q^*has been also reported as an adjustable parameter. However, its value can be determined is the saturation point of the breakthrough curves.

The model developed by Thomas (1944) has also analytical solution. The sorption rate is described by Langmuir adsorption kinetics. Both models, Thomas and Bohart and Adams consider negligible film and particle resistances as well as the dispersion within the column.

The Thomas mathematical model is obtained by mass balances of the sorbate in the fluid phase and in the solid phase. Such mass balances originate an equation that describe the equilibrium in the system. The mass balance in the fluid phase results in the following equation:

$$\frac{\partial C}{\partial t} + \rho_{bed} \frac{\left(1-\varepsilon\right)}{\varepsilon} \frac{\partial q}{\partial t} = -u_0 \frac{\partial C_j}{\partial z} + D_L \frac{\partial^2 C_j}{\partial z^2} \tag{13}$$

with the following initial and boundary conditions:

$$C(0,z) = 0 \tag{14}$$

In the inlet sample in the column ($z = 0$):

http://dx.doi.org/10.5772/51954

$$D_L \frac{\partial C}{\partial z} = u_0 \left(C(t,0) - C^F \right) \tag{15}$$

In the outlet sample in the column($z = L$):

$$\frac{\partial C}{\partial z} = 0 \tag{16}$$

A rigorous mathematical model that takes into account the variation of the concentration of the adsorbate within the particle is described by the Fick's second law. In these cases, solution of equations of the bed and the particle should be solved simultaneously, which increases the complexity and computational effort. One alternative for reducing the computational effort is to replace Fick's Law by the simplified kinetics equation. (Hsuen, 2000). The approach mostly used to replace the Fick's Law is the LDF model (Linear Driving Force). It applies the expression of the first order kinetics represented by Equation (17). Several authors have used such models with successful results for sorbents and biosorbents.

$$\frac{\partial q}{\partial t} = -K_S \left(q - q_{eq} \right) \tag{17}$$

In the adsorption models represented by Equation (17), it is assumed that the driving force for mass transfer is linear with the concentration of the sorbate in the solid. Moreover, it means the equilibrium condition at the interface between the local phase fluid, as illustrated in Figure 9. The equilibrium in the adsorption process is usually represented by adsorption isotherms, such as: Langmuir, Freundlich, Tóth, Sips. Figure 9 also illustrates the mechanism of the external mass transfer occurs around the surface of the particle. From the interface solid-fluid, the mass transfer occurs, which is represented by following equation:

$$-K_S \left(q - q^* \right) = \frac{K_F a \varepsilon}{\rho_{bed}} \left(C - C_{eq} \right) \tag{18}$$

The mathematical model that considers both mass transfer resistances (external and intraparticle) is called double resistance model. This model is composed by the set of Equations (13)-(18). When the mass transfer in predominantly intraparticle, that is$\left(C^{eq} \approx C\right)$, the equilibrium concentration of the sorbate in the solid is directly related to the concentration in bulk phase. In cases where the mass transfer resistance is in the film, that is $\left(C^{eq} \approx C\right)$, the rate of sorption can be expressed by the following below:

$$\frac{\partial q}{\partial t} = \frac{K_F a \varepsilon}{\rho_{bed}} \left(C - C_{eq} \right) \tag{19}$$

When the operational condition is experimentally optimized, the film and intraparticle resistances of the sorption processes (adsorption, ion exchange or adsorption + ion exchange) are minimized in the experimental range investigated. It means that the film thickness is the thinnest one and there is no significant steric resistance of the sorbate in the particle pores.

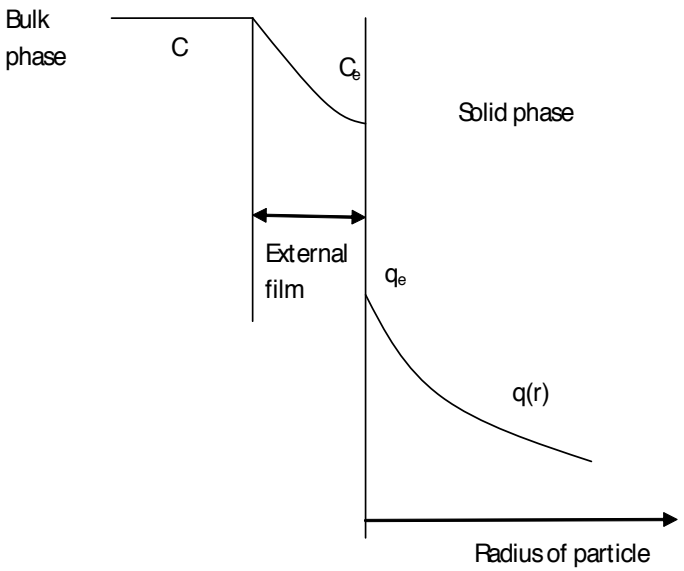

Figure 9. Mass transfer in adsorption process

Some parameters of the model can be calculated from the correlation, namely: axial dispersion coefficient (D_L) and external mass transfer coefficient. The relationship for calculating the axial dispersion is usually expressed from the dimensionless groups: Reynolds (Re), Peclet (Pe), Schmidt (Sc). Delgado (2006) presents several correlations for calculating of axial dispersion of gases and liquids in packed beds. There are many correlations for calculating external mass transfer coefficients in porous media, usually expressed in terms of Reynolds (Re_p), Schmidt and Sherwood (Sh_p). Wakao and Funazkri (1978) developed the following expression for $3 < Re_p < 2000$:

$$Sh_p = 1 + 1.1 \mathrm{Re}_p^{0.6} Sc^{1/3} \tag{20}$$

Where: $Sh_p = \frac{K_F d_p}{D}$, $\mathrm{Re}_p = \frac{u_0 d_p}{\nu}$, $Sc = \frac{\nu}{D}$

The mass transfer coefficient in the solid (K_S) is an adjustable parameter of the model obtained from the experimental breakthrough curves.

http://dx.doi.org/10.5772/51954

2.6.1. Examples of breakthrough modeling

Example 1 – Modeling of Breakthrough curves

Table 2 shows the experimental data of breakthrough curve of zinc in fixed bed columns using Na-Y zeolite as adsorbent obtained by Ostroski (2007) and Table 3 shows the operational conditions and bed parameters.

Time (min)	C_{out} / C^F
0.00	0.0000
22.00	0.0000
31.00	0.0000
55.00	0.0050
68.00	0.0156
74.00	0.1980
87.00	0.3564
93.00	0.5916
118.00	0.7721
136.00	0.8500
147.00	0.9248
180.00	0.9490
205.00	0.9655
230.00	0.9788
250.00	0.9874
260.00	0.9913
280.00	0.9963
307.00	1.0000

Table 2. Experimental data of zinc breakthrough curve

C^F - Feed concentration of adsorbate (meq / cm^3)	2.447x10^{-3}
L –Height of the bed (cm)	3.0
m_s - Weight of the adsorbent (g)	0.8
u_0 – Interstitial velocity (cm/min)	25.104
ε - Bed porosity	0.5
ρ_{bed} - Bed density (g / cm^3)	0.4192

Table 3. Operational conditions and bed parameters.

From these data it will be tested the Bohart and Adams and the LDF models that consider intraparticle resistance only. Both models have only one adjustable parameter: (k_a) for Bohart and Adams and (K_s) for LDF model.

Bohart and Adams model

From the experimental breakthrough curve it is calculated the capacity of the adsorbent (q^*), since the column experiments are carried outup to the complete exhaustion of the column (saturation point), ie, when the concentration of sorbate in the outlet of the column is equal to the feed concentration. From a mass balance in the column, one can obtain the following equation:

$$q^* = \frac{C^F \dot{Q}}{1000\, m_s} \int_0^{t_{END}} \left(1 - \frac{C_{out}}{C^F}\right) dt \tag{21}$$

Where:

q^*-Capacity of the adsorbent(meq/g);

C_{out}-Concentration of zinc in the outlet of the column (meq/L);

C^F-Feed concentration of zinc (meq/L);

$\dot{Q}$-Volumetric flow rate (cm^3/min);

t-time (min);

m_s-Weight of adsorbent (g).

The capacity of the adsorbent was calculated from the area determinate by term $\left(1 - \frac{C_{out}}{C^F}\right)$ calculate by experimental breakthrough curve, illustrated in Figure 10. The integral $\int_0^{t_{END}} \left(1 - \frac{C_{out}}{C^F}\right) dt = 102.78 \text{min}$, calculated by trapeze method.

$$q^* = \frac{C^F \dot{Q}}{1000\, m_s} \int_0^{t_{END}} \left(1 - \frac{C_{out}}{C^F}\right) dt = \left(\frac{2.447 \times 8}{1000 \times 0.8}\right) \times 102.78 = 2.515 \text{ meq/g}$$

$$\alpha = \frac{\rho_{bed} q^*}{C^F \varepsilon} = \left(\frac{0.4192 \times 2.515}{2.447 \times 10^{-3} \times 0.5}\right) = 861.7 \text{ meq/g}$$

$$\beta = k_a C_0 \alpha = k_a \times 861.7 \times 10^{-3} \times 2.447 = 2.1086\, k_a$$

$$A = \frac{L\ \beta}{u_0} = \frac{0.8 \times 2.1086 k_a}{25.104} = 67.20\, k_a$$

$$B = \frac{(-t u_0 + L\ )\beta}{\alpha\ u_0} = \frac{(-t \times 25.104 + 3) x 2.1086\, k_a}{861.7 \times 25.104} = 9.75 \times 10^{-5} \times (3 - t \times 25.104)\, k_a \text{ min}$$

http://dx.doi.org/10.5772/51954

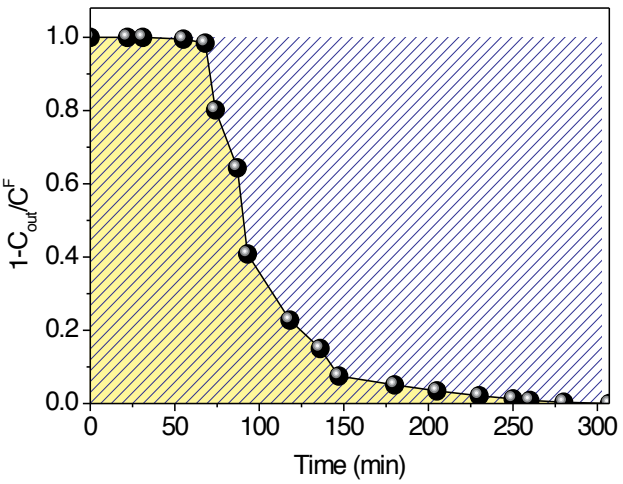

Figure 10. Area of curve $\left(1-\frac{C_{out}}{C^F}\right)$

Applying in the Equation (12), it follows that: $t_F = \frac{L}{u_o} = \frac{0.8}{25.104} = 0.03187$

The parameter (k_a) estimated from the experimental data of breakthrough curve and applied method for one-dimensional optimization golden search, minimizing the following objective function:

$$F = \sum_{j=1}^{n\_exp} \left(\left(\frac{C_{out}}{C^F} \right)_j^{EXP} - \left(\frac{C_{out}}{C^F} \right)_j^{EXP} \right)^2 \tag{22}$$

Where:

$F = \sum_{j=1}^{n\_exp} \left(\left(\frac{C_{out}}{C^F} \right)_j^{EXP} - \left(\frac{C_{out}}{C^F} \right)_j^{EXP} \right)^2$-Ratio of the concentrations in the outlet of the column and feed determined experimentally

$\left(\frac{C_{out}}{C^F} \right)_j^{EXP}$ -Ratio of the concentrations in the outlet of the column and feed determined by model

$\left(\frac{C_{out}}{C^F} \right)_j^{MOD}$ -Number of experimental data

The value of adjustable parameter k_a was 22.35 (meq / cm^3 min).

Intraparticle model

In this model considerate that the internal diffusion is controller the mass transfer, the LDF approximation was used to represent the diffusion, described by Equation (17). This model also has only one adjustable parameter (K_S). To solve the equations of the model is also necessary to define an equation for the isotherm and the coefficient of axial dispersion. The Langmuir isotherm, represented by Equation (23), was used in the simulation. The values of parameters used were as follows: D_L = 8.96x10^{-3} cm^2/min, q_{max} = 2.83 meq / g and b = 3.06 L / meq (Ostroski, 2007). The parameter coefficient of mass transfer from adjusted breakhtrough curve was:K_s = 0.0431x10^{-3} min^{-1}.

$$q_{eq} = \frac{q_{\max} b C_{eq}}{1 + b C_{eq}} \tag{23}$$

The phenomenological model can provide good results only if the equilibrium model used is appropriate to make this analysis. Its hould compare the values of the equilibrium concentrationsof the adsorbent predicted by the model, in this case calculated by Equation (21) and the experimental value obtained from Equation (23).

Adsorption capacity predicted by the model= $q_{eq} = \frac{q_{\max} b\, C_{eq}}{1 + b\, C_{eq}}$ =2.497 meq/g

Experimental adsorption capacity= 2.515 meq/g

In this case, the deviation between predicted adsorption capacity and experimental was 0.7%. It demonstrates that the equilibrium model is appropriated to use in the modeling of the column. When the deviation is high, it is not possible to achieve good adjustments for the breakthrough curves. In these cases, one must first search different isotherm models or theories (RAST –Real Adsorption Solution Theory, VSM - Vacancy Solution Model) to correlate the equilibrium data. In electrolytic systems it can used the Law of Action Mass.

When the parameters of model equilibrium are estimated from batch systems, the model accurately describes the behavior of the equilibrium curve. However, these values are different from the one obtained in the capacity of the column. Such behavior occurs generally for electrolyte systems. Several authors (Bajracharya and Vigneswaran 1990; Silva et al. 2002; Palma et al. 2003; Barros et al 2004; Izquierdo[a,b] et al., 2010) reported the differences between batch and column capacity of adsorption. In these cases for modeling the dynamic adsorption column fixed bed must perform the adjustment of the parameters from the equilibrium data obtained in fixed bed column at different feed concentration. See section 2.5.

To solve the partial differential equations (Eq. 13 and Eq.17) it was used the lines method, which transforms the partial differential equations in a system of ordinary differential equations by approximating the spatial derivatives by finite differences. Further details of the resolution method used can be found in Silva (2001). The results obtained with the LDF model (Numerical solution) and Adams Bohart (analytical solution) is shown in Figure (11).

http://dx.doi.org/10.5772/51954

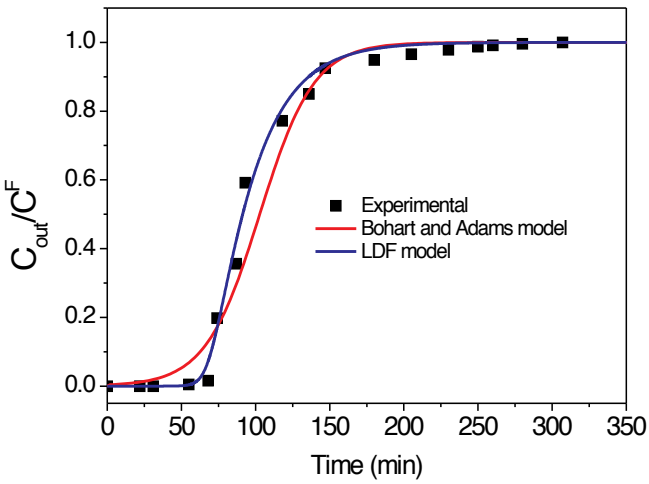

Figure 11. Zinc Breakthroughs curves

In this example, the model LDF described more accurately the behavior of zinc breakthrough curve due the consideration of mass transfer controlled by the intraparticle diffusion. It is more realistic than consideration that the kinetics is phase controller, which is the hypothesis of the Bohart and Adams model.

3. Final comments

Design of dynamic sorption is considered a simple process. Nevertheless, to reach higher and higher efficiencies is always a challenge.

Differences in packing procedures may provide quite different breakthrough behavior. Therefore, much attention should be paid to avoid channeling and bubbles of different fluid phase. Channeling promotes undesired dispersion in the bed keeping the system away from plug-flow behavior. Bubbles create additional mass transfer resistances and diminish the uptake efficiency. Much attention should be paid in the operational conditions imposed to the column. The ones that minimize the mass transfer resistances are always recommended.

Mathematical modeling of dynamic behavior with analytical solutions, such as: Bohart and Adams and Thomas considers that the limiting step is controlled by adsorption kinetics and can be applied only to monocomponent systems. The advantage of these models is that the estimation is simpler. Models with a numerical solution is more realistic because they take into account various aspects related to mass transfer (axial dispersion, external film diffusion and intraparticle diffusion) are more suitable for use in the design and optimization of

sorption processes in industrial scale. The phenomenological models are generated by mass balances of adsorbate in fluid and solid phase and require information of mass transfer mechanism and equilibrium. A prerequisite for phenomenological models is the theory and / or model used to represent the equilibrium of adsorption (isotherms, the law of mass action, RAST, VSM). Particularly in electrolyte systems, it is recommended that the equilibrium data are obtained in columns experiments on the basis of no pH correction. As already seen, the equilibrium conditions are different in batch and in dynamic systems. In the batch system, the counter ions are in solution, whereas in systems in a fixed bed column is loaded by the feed solution. The LDF model is an approximation to represent the intraparticle diffusion and has been shown to be efficient to describe the behavior of breakthrough curves for different systems (monocomponent and mixtures).

Nomenclature

a-Mass transfer area per unit bed volume (m^{-1})

$\frac{2.83 \times 3.06 \times 2.447}{1 + 3.06 \times 2.447}$-Concentration of the adsorbate in the fluid phase (mmol / L);

C-Feed concentration of the adsorbate in the fluid phase (mmol / L);

C^F-Equilibrium concentration of the adsorbate fluid phase (mmol / L);

C_{eq}-Particle diameter (m);

d_p-Molecular coefficient diffusion (m^2/min);

D-Axial dispersion coefficient (m^2/min);

D_L -Height of bed (m);

L -Mass transfer coefficient in the solid (min^{-1})

k_a-Kinetics parameters of Bohart and Adams model (L / mol min)

K_S-External film mass transfer coefficient (m/mim^{-1})

u_0-Interstitial velocity (m/min);

K_F-Coordinated in the axial direction (m);

z-Bed porosity;

ε-Bed density (g / L);

ρ_{bed}-Kinematic viscosity (m^2/min);

Author details

M. A. S. D. Barros[1], P. A. Arroyo[1] and E. A. Silva[2]

1 Department of Chemical Engineering, State University of Maringá, Maringá, Brazil

2 Department of Chemical Engineering, West Paraná State University, Jardim La Salle, Toledo, Brazil

References

[1] Bailey, J.E.,Ollis, D.F.:Biochemical engineering fundamentals. McGraw-Hill, New York, (1986).

[2] Bajracharya, K., Vigneswaran, S., Adsorption of cadmium and zinc in saturated soil columns: Mathematical models and experiments, Environmental Technology, 11, 9-24. 1990.

[3] Barros, M,A,S,D, Zola, A,S., Arroyo, P.A., Sousa-Aguiar, E.F., Tavares, C.R.G. Binary Ion Exchange of Metal Ions in Y and X Zeolites, Brazilian Journal of Chemical Engineering, 20, 4, 413-421, 2003.

[4] Barros, M.A.S.D., Silva, E.A., Arroyo, P.A., Tavares, C.R.G., Schneider, R.M., Suszek, M., Sousa-Aguiar, E.F., Removal of Cr(III) in the fixed bed column and batch reactors using as adsorbent zeolite NaX, Chemical Engineering Science, 59, 5959 – 5966, 2004.

[5] Barros, M.A.S.D., Zola, A.S, Tavares, C.R.G., Sousa-Aguiar, E.F. Chromium uptake from tricomponent solution in zeolite fixed bed, Adsorption, 12, 229-248, 2006.

[6] Barros, M.A.S.D., Zola, A.S., Arroyo, P.A., Sousa-Aguiar, E.F., Tavares, C.R.G.Equilibrium and dynamic ion exchange studies of Cr3+ on zeolites NaA and NaX, Acta Scientiarum, 24, 6, 1619-1625, 2002.

[7] Bohart, G. S., Adams, E. Q., Some aspects of the behavior of charcoal with respect to chlorine,Journal of the American Chemical Society, 42, 523-544, 1920.

[8] Borba, C. E., Silva, E.A., Fagundes-Klen, M. R., Kroumov, A. D., Guirardello, R. , Prediction of the copper (II) ions dynamic removal from a medium by using mathematical models with analytical solution,Journal of Hazardous Materials, 152 (1), 366-372, 2008.

[9] Chu, K. H., Kim, E. Y., Feng, X., Batch Kinetics of Metal Biosorption: Application of the Bohart-Adams Rate Law, Separation Science and Technology, 46 (10), 1591-1601, 2011.

[10] Comiti, J., Mauret, E., Renaud, M., Mass transfer in fixed beds: proposition of a generalizedcorrelation based on an energetic criterion, Chemical Engineering Science, 55, 5545-5554, 2000.

[11] Delgado, J.M.P.Q., A critical review of dispersion in packed bed, Heat Mass Transfer, 42, 279-310, 2006.

[12] Fogler, H.S., Elements of Chemical Reaction Engineering, 3rd ed., Prentice Hall, New Delhi- India, 2004.

[13] Gazola, F. C., Pereira, M.R., Barros, M.A.S.D, Silva, E.A, Arroyo, P.A. Removal of Cr3+ in fixed bed using zeolite NaY, Chemical Engineering Journal, 117, 253–261, 2006.

[14] Geankoplis, C.J., Transport Processes andUnit Operations, 3rd ed., PTR Prentice Hall, USA, 1993.

[15] Helferich, F.,Ion Exchange, Dover Publications Inc., New York, 1995.

[16] Hill, C.G.,An Introduction to Chemical Engineering Kinetics and Reactor Design, John Wiley & Sons, USA, 1977.

[17] Hsuen, H. K., An improved linear driving force approximation for intraparticle adsorption, Chemical Engineering Science, 55,3475-3480, 2000.

[18] Izquierdoa, M., Gabaldón, C., Marza, P., Álvarez-Hornos, F. J., Modeling of copper fixed-bed biosorption from wastewater by Posidonia oceanica, Bioresource Technology, 101, 510–517, 2010.

[19] Izquierdob, M., Gabaldón, C., Marzal, P., Sempere, F., Sorption of copper by a highly mineralized peat in batch and packed-bed systems, Journal of Chemical Technology and Biotechnology, 85, 165-172, 2010.

[20] Jain, J.S., Snoeyink, V.L.: Adsorption from biosolute systems on active carbon. J. Water Pollut. Control Fed. 45, 2463-2479 (1973).

[21] Kang, S. Y., Lee, J. U., Moon, S. H., Kim, K. W., 2004, Competitive adsorption characteristics of Co2+ Ni2+ and Cr3+ by IRN 77 cation exchange resin in synthesized wastewater, Chemosphere, v. 56, pp.141–147.

[22] KLamer, K, Van Krevelen, D. W., Studies on ion Exchange-I, Chem. Eng. Sci, 7, 4, 197-203, 1958.

[23] Klein, G., Tondeur, D., Vermeulen, T. Multicomponent ion exchange in fixed beds, Ind. Eng. Chem. Fundam., 6, 3, 339-351, 1967.

[24] Kratochvil, D., Volesky, B., Demopoulos, G. Optimizing Cu removal/recovery in a biosorption column, Wat. Res., .31, 9, 2327-2339, 1997.

[25] Kumar, J, Chatterjee, A., Schiewer, S., Biosorption of Cadmium(II) Ions by Citrus Peels in a Packed Bed Column: Effect of Process Parameters and Comparison of Different Breakthrough Curve Models,Clean-Soil Air Water, 39 (9),874-881, 2011.

[26] Labanda, J., Sabaté, J., Llorens, J., Experimental and modeling study of the adsorption of single and binary dye solutions with an ion-exchange membrane adsorber, Chemical Engineering Journal, 166, 536–543, 2011.

[27] Martin-Lara, M. A., Hernainz, F., Blazquez, G., Tenorio, G., Calero, M., Sorption of Cr (VI) onto Olive Stone in a Packed Bed Column: Prediction of Kinetic Parameters and Breakthrough Curves, Journal of Environmental Engineering-ASCE, 136 (12), 1389-1397, 2010.

[28] McCabe, W. L., Smith, J.C., and Harriot, P.Unit Operations of Chemical Engineering, McGraw-Hill International Ed., 6th ed., New York, USA, 2001.

[29] Misak, N.Z., Some aspects of the application of adsorption isotherms to ion exchange reactions. React. Funct. Polym., 43, 153-164 (2000).

[30] Mohan, D. and Chander, S., Single Component and Multi-component Adsorption of Metal Ions by Activated Carbons, Colloids and Surfaces A: Physicochemical and Engineering Aspects, 177, 2-3, 183-196, 2001.

[31] Muhamad, H., Doan, H., LOHI, A., Batch and continuous fixed-bed column biosorption of Cd2+ and Cu2+, Chemical Engineering Journal, 158 (3), 369-377, 2010.

[32] Myers, A. L.; Prausnitz, J. M.; Thermodynamics of mixed-gas adsorption; AIche Journal, 11, 1, 121-127, 1965.

[33] Ostroski, I. C., Borba, C. E., Silva, E. A., Arroyo, P. A., Guirardello, R., Barros, M. A.S.D. Mass Transfer Mechanism of Ion Exchange in Fixed Bed Columns, J. Chem. Eng. Data, 56, 375-382, 2011.

[34] Ostroski, I.C., Mechanism of removal of Iron(III) and Zinc(II) ontoZeolite Na-Y, In Portuguese, Master Thesis, UEM - State University of Maringá, Brazil, Chemical Engineering Department , 2007.

[35] Ostroski, I.C., Barros, M.A.S.D. , Silva, E. A., Dantas, J.H., Arroyo, P.A., Lima, O.C.M., A comparative study for the ion exchange of Fe(III) and Zn(II) on zeolite NaY, Journal of Hazardous Materials, 161 , 1404–1412, 2009.

[36] Palma, G; Freer, J; Baeza, J.; Removal of metal ions by modified Pinus radiata bark and tannins from water solutions, Water Research, 37, 4974-80, 2003.

[37] Pereira, M. R., Arroyo, P.A., Barros, M.A.S.D., Sanches, V.M., Silva, E.A., Fonseca, I. M., Lovera, R.G. Chromium adsorption in olive stone activated carbon, Adsorption, 12, 155–162, 2006.

[38] Perry, R. H., Perry's Chemical Engineers' Handbook, 7th. Ed.,Mc-Graw Hill, 1999.

[39] Rao, K. S., Anand, S., Venkateswarlu, P., Modeling the kinetics of Cd(II) adsorption on Syzygium cumini L leaf powder in a fixed bed mini column,Journal of Industrial and Engineering Chemistry, 17 (2), 174-181, 2011.

[40] Sağ, Y., I. Ataçoğlu, and T. Kutsal, Equilibrium Parameters for the Single and Multicomponent Biosorption of Cr(VI) and Fe(III) Ions on R. Arrhizus in a Packed Column, Hidrometallurgy, 55, 165–179, 2000.

[41] Sánchez, A., Ballester, A., Blásquez, M.L., González, F., Muñoz, J., Hammaini, A.: Biosorption of copper and zinc by cymodocea nodosa. FEMS Microbiol. Rev. 23 527-536 (1999).

[42] Silva, E.A., Biosorption of chromium(III) and copper (II) ions on seaweed Sargassum sp. in fixed bed columns. In Portuguese, Doctorate thesis, UNICAMP, University State of Campinas, Brazil,Faculty ofChemical Engineering,2001.

[43] Silva, E.A., Cossich, E.S., Tavares, C.R.G., Filho, L.C., Guirardello, R. Modeling of copper(II) biosorption by marine alga Sargassum sp. In fixed-bed column, Process Biochemistry, 38, 791-799, 2002.

[44] Singh, A., Kumar, D., Gaur, J. P., Continuous metal removal from solution and industrial effluents using Spirogyra biomass-packed column reactor,Water Research, 46 (3), 779-788, 2012.

[45] Sprynskyy, M., Buszewski, B., Terzyk, A.P., Namiesnik, K.: Study of the selection mechanism of heavy metal (Pb2+, Cu2+, Ni2+ and Cd2+) adsorption on clinoptolilite. J. Colloid Interface Sci. 304, 21-28 (2006).

[46] Suzuki, M. Adsorption Engineering, Elsevier Science Publishers B.V., 1990.

[47] Thomas, H.C., Heterogeneous ion exchange in a flowing system, Journal of the American Chemical Society, 66, 1664–1666, 1944.

[48] Trgo, M., Medvidovic, N. V., Peric, J., Application of mathematical empirical models to dynamic removal of lead on natural zeolite clinoptilolite in a fixed bed column, Indian Journal of Chemical Technology, 18 (2), 123-131, 2011.

[49] Valdman, E., Erijman, L., Pessoa, F.L.P. and Leite, S.G.F. Continuous Biosorption of Cu and Zn by Immobilized Waste Biomass Sargassum sp., Process Biochemistry, 36, 869-873, 2001.

[50] Walker, G.M., Weatherly, L.R. Adsorption of acid dyes on to granular activated carbon in fixed beds, Water Research, 31, 8, 2093–2101, 1997.

Chapter 15

Airlift Bioreactors: Hydrodynamics and Rheology Application to Secondary Metabolites Production

Ana María Mendoza Martínez and
Eleazar Máximo Escamilla Silva

Additional information is available at the end of the chapter

http://dx.doi.org/10.5772/53711

1. Introduction

The bubble column and airlift bioreactors are pneumatically agitated and often employed in bioprocesses where gas-liquid contact is important. The role of the gas is to provide contact with the liquid for mass transfer processes such as absorption or desorption and to provide energy through gas expansion or bubble buoyancy for liquid mixing. In these two pneumatically agitated reactors, gas is sparger usually through the bottom and the buoyancy of the ascending gas bubbles causes mixing. The main difference between these two pneumatically agitated reactors is in their fluid flow characteristics. The flow in the airlift is ordered and in a cyclic pattern like in a loop beginning from top through to bottom. The airlift differs from the bubble column by the introduction of inner draft tubes which improves circulation, whereas the bubble column is a simple tower. In the airlift, liquid recirculation occurs due to the four distinct sections; the riser, downcomer, gas separator and bottom or base. The bubble column is a simple vessel without any sectioning making the flow rather a complex one.

Some attractive features of the airlift are the low power consumption, simplicity in construction with no moving parts, high mass and heat transfer rates and uniform distribution of shear [1, 2].

The advantage of its low power consumption is of particular importance in effluent (e.g. wastewater) treatment where the product value is comparatively low. Therefore, operational cost (efficient use of energy) is greatly considered since corresponding applications are usually on a large scale. Homogenous shear is particularly important for biological processes that are shearing sensitive. In the conventional stirred tank, shear is greatest at the stirrer and decreases away from it to the walls of the vessel. This creates a gradient of shearing which can have

adverse effect on the morphology or sometimes can damage cells (e.g. animal and plant cells). The simple construction of the airlift without shafts makes it not only aesthetically pleasing to look at but also eliminates contamination associated with the conventional stirred tank which is a major drawback in the production of microorganism. A sterile environment is crucial for growing organisms especially in the bioprocesses since contamination reduces product quality, generates wastes, also more time and money are spent to restore the whole process.

In addition to the previously described, the development of new biotech products: drugs, vaccines, tissue culture, agrochemicals and specialty chemicals, biofuels and others have had a major breakthrough during the last decade. But engineering to scale these developments to the production phase is lagging far behind in advances in the efficient development of bioprocesses. Normally these processes are complicated because they are conducted in complex systems, three or four phases, microorganisms that are susceptible to large shear produced by stirring; require high airflow rates, and changes in rheology and morphology cultures through the time. The soul of a bioprocess is still the bioreactor, since it determines the success of a good separation and therefore the cost of the product. In this chapter we describe one of the most promising bioreactors for their processing qualities, good mixing, low shear, easy to operate with immobilized microorganisms, low consumption of energy, we are talking about the airlift bioreactors. In this context the parties will start from basic engineering bioreactors: mass balances, mass transfer, and modelling and to cover the hydrodynamics and rheology of the process. Finally we will present two cases of application on the production of Bikaverin (a new antibiotic), and L-lysine.

2. Hydrodynamic characteristic of airlift reactors

Fluid mixing is influenced by the mixing time and gas holdup which defines the fluid circulation and mass transfer properties. The fluid recirculation causes the difference in hydrostatic pressure and density due to partial or total gas disengagement at the gas separator (top clearance, *tt*). Studies have been documented during the last two decades with various correlations applicable for hydrodynamic parameters [3-5]. This implies that for a successful design, fundamental understanding of mixing parameters is important for industrial scale-up.

It is difficult to generalize the performance of the bioreactor according to the process for which the airlift will be employed. For example, in aerobic fermentation, oxygen is important for mass transfer and therefore, it is imperative to consider a design where there will be less disengagement of gas resulting in higher gas holdup for a higher mass transfer rate. In this case, the liquid circulation velocity is low because less gas is disengaged at the top resulting in a lower differential density. Furthermore, other processes require good mixing other than a high mass transfer rate. However, provision can be made by increasing the gas disengagement at the top to improve the liquid recirculation as in the case for anaerobic fermentation. Therefore, it is safe to conclude as have been confirmed [3, 6, 7] that, the geometry parameters such as the top clearance (*tt*), ratio of cross sectional area of the downcomer to the riser (*Ad*/*Ar*), bottom clearance (*tb*), the cross sectional areas of riser (*Ar*) and that of the downcomer

http://dx.doi.org/10.5772/53711

(*Ad*), draft tube internal diameter (*Dd*), and height of the column (*H*) and superficial gas velocity *(Ug*) have an influence on fluid hydrodynamics.

There is extensive information on the measurement of fluid hydrodynamics published with a handful of equations. However, most of them Gumery et al.: Characteristics of Macro-Mixing in Airlift Column Reactors 7 Published by The Berkeley Electronic Press, 2009 cannot be correlated due to the different medium (Newtonian versus non-Newtonian) used and various assumptions made. The different measuring techniques often used cannot discriminate diffusion and convection for mixing whiles others disturb process flow.

On the other hands the interconnections between the design variables, the operating variables, and the observable hydrodynamic variables in an airlift bioreactor are presented diagrammatically in Figure 4 as has been reported by [8]. The design variables are the reactor height, the riser-to-downcomer area ratio, the geometrical design of the gas separator, and the bottom clearance (C_b, the distance between the bottom of the reactor and the lower end of the draft tube, which is proportional to the free area for flow in the bottom and represents the resistance to flow in this part of the reactor). The main operating variables are primarily the gas input rate and, to a lesser extent, the top clearance (C_t, the distance between the upper part of the draft tube and the surface of the non-aerated liquid). These two independent variables set the conditions that determine the liquid velocity in the airlift bioreactor via the mutual influences of pressure drops and holdups, as shown in Figure 1 [9]. Viscosity is not shown in Figure 1 as an independent variable because in the case of gas–liquid mixtures, it is a function of the gas holdup (and of liquid velocity in the case of non-Newtonian liquids), and because in a real process, it will change with time due the changes in the composition of the liquid.

3. Flow configuration

3.1. Riser

In the riser, the gas and liquid flow upward, and the gas velocity is usually larger than that of the liquid. The only exception is homogeneous flow, in which case both phases flow at the same velocity. This can happen only with very small bubbles, in which case the free-rising velocity of the bubbles is negligible with respect to the liquid velocity. Although about a dozen different gas–liquid flow configurations have been developed [10], only two of them are of interest in airlift bioreactors [11, 12]:

1. Homogeneous bubbly flow regime in which the bubbles are relatively small and uniform in diameter and turbulence is low.
2. Churn-turbulent regime, in which a wide range of bubble sizes coexist within a very turbulent liquid.

The churn-turbulent regime can be produced from homogeneous bubbly flow by increasing the gas flow rate. Another way of obtaining a churn-turbulent flow zone is by starting from slug flow and increasing the liquid turbulence, by increasing either the flow rate or the

diameter of the reactor, as can be seen in Figure 5 [12]. The slug-flow configuration is important only as a situation to be avoided at all costs, because large bubbles bridging the entire tower cross-section offer very poor capacity for mass transfer.

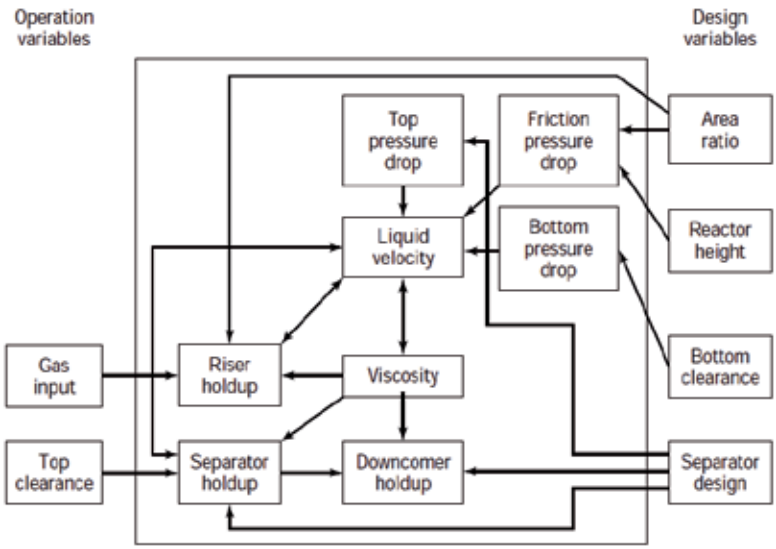

Figure 1. Interaction between geometric and fluid dynamic variables in an airlift bioreactor [9].

3.2. Downcomer

In the downcomer, the liquid flows downward and may carry bubbles down with it. For bubbles to be entrapped and flow downward, the liquid velocity must be greater than the free-rise velocity of the bubbles. At very low gas flow input, the liquid superficial velocity is low, practically all the bubbles disengage, and clear liquid circulates in the downcomer. As the gas input is increased, the liquid velocity becomes sufficiently high to entrap the smallest bubbles. Upon a further increase in liquid velocity larger bubbles are also entrapped. Under these conditions the presence of bubbles reduces the cross-section available for liquid flow, and the liquid velocity increases in this section.

Bubbles are thus entrapped and carried downward, until the number of bubbles in the cross-section decreases, the liquid velocity diminishes, and the drag forces are not sufficient to overcome the buoyancy. This feedback loop in the downcomer causes stratification of the bubbles, which is evident as a front of static bubbles, from which smaller bubbles occasionally escape downward and larger bubbles, produced by coalescence, escape upward. The bubble front descends, as the gas input to the system is increased, until the bubbles eventually reach the bottom and recirculate to the riser. When this point is reached, the bubble distribution in the downcomer becomes much more uniform. This is the most desirable flow configuration in the downcomer, unless a single pass of gas is required. The correct choice of cross-sectional area ratio of the riser to the downcomer will determine the type of flow.

http://dx.doi.org/10.5772/53711

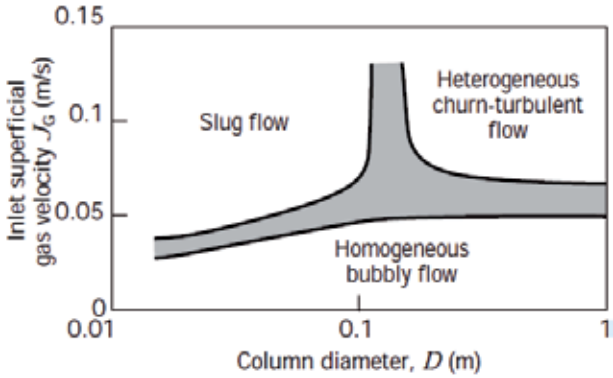

Figure 2. Map of flow configurations for gas–liquid concurrent flow in a vertical tube [12].

3.3. Gas separator

The gas separator is often overlooked in descriptions of experimental airlift bioreactor devices, although it has considerable influence on the fluid dynamics of the reactors. The geometric design of the gas separator will determine the extent of disengagement of the bubbles entering from the riser. In the case of complete disengagement, clear liquid will be the only phase entering the downcomer. In the general case, a certain fraction of the gas will be entrapped and recirculated. Fresh gas may also be entrapped from the headspace if the fluid is very turbulent near the interface. The extent of this entrapment influences strongly gas holdup and liquid velocity in the whole bioreactor.

It is quite common to enlarge the separator section to reduce the liquid velocity and to facilitate better disengagement of spent bubbles. Experiments have been reported in which the liquid level in the gas separator was high enough to be represented as two mixed vessels in series [13]. This point will be analysed further in the section devoted to mixing.

4. Gas holdup

Gas holdup is the volumetric fraction of the gas in the total volume of a gas–liquid–solid dispersion:

$$\varphi_1 = \frac{V_G}{V_L + V_G + V_S} \tag{1}$$

where the sub-indexes L, G, and S indicate liquid, gas, and solid, and *i* indicates the region in which the holdup is considered, that is, gas separator (s) the riser (r), the downcomer (d), or the total reactor (T).

The importance of the holdup is twofold: (a) the value of the holdup gives an indication of the potential for mass transfer, since for a given system a larger gas holdup indicates a larger gas–

liquid interfacial area; and (b) the difference in holdup between the riser and the downcomer generates the driving force for liquid circulation. It should be stressed, however, that when referring to gas holdup as the driving force for liquid circulation, only the total volume of the gas is relevant. This is not the case for mass transfer phenomena, in this case, the interfacial area is of paramount importance, and therefore some information on bubble size distribution is required for a complete understanding of the process.

Because gas holdup values vary within a reactor, average values, referring to the whole volume of the bioreactor, are usually reported. Values referring to a particular section, such as the riser or the downcomer, are much more valuable, since they provide a basis for determining liquid velocity and mixing. However, such values are less frequently reported.

The geometric design of the airlift bioreactor has a significant influence on the gas holdup. Changes in the ratio $\frac{A_d}{A_r}$, the cross-sectional areas of the downcomer and the riser, respectively, will change the liquid and gas residence time in each part of the reactor and hence their contributions to the overall holdup. Gas holdup increases with decreasing $\frac{A_d}{A_r}$, [14-17].

4.1. Gas holdup in internal airlift reactors

Correlations presented for internal-loop airlift bioreactors are shown in Table 1. These take into account liquid properties and geometric differences within a particular design. Most of the correlations take the form:

$$\varphi_r = a(J_G)^{\alpha}\left(\frac{A_d}{A_r}\right)^{\beta}(\mu_{ap})^{\gamma} \tag{2}$$

where φ_r is the gas holdup in the riser, J_G is the superficial gas velocity (gas volumetric flow rate per unit of cross sectional area), μ_{ap} is the effective viscosity of the liquid, and α, β, γ, and a are constants that depend on the geometry of the reactor and the properties of the liquid. The correlation can be used to predict the holdup in a system that is being designed or simulated as a function of the operating variables, the geometry of the system, or the liquid properties. Such correlations are effective for fitting data for the same type of reactor (e.g., a split-vessel reactor) with different area ratios or even different liquid viscosities, but they are mostly reactor-type specific.

The cyclic flow in the airlift bioreactor complicates the analysis of the system. The riser gas holdup depends strongly on the geometric configuration of the gas–liquid separator and the water level in the gas separator. This has been shown experimentally in a split-vessel rectangular airlift bioreactor [18], but the premise can essentially be extended to any internal loop airlift bioreactor. Analysis of the system revealed that these factors influence the gas disengagement and hence the gas recirculation in the downcomer. When this influence is taken into account and the holdup is plotted against the true gas superficial velocity, J_G, true, which is defined as the sum of the gas superficial velocity due to the freshly injected gas, Qin, and to the recirculated gas, Q_d, that is,

http://dx.doi.org/10.5772/53711

$$J_{G,\,true} = \left(\frac{Q_{in} + Q_d}{A_r}\right) \tag{3}$$

Then all the data for the different gas separators may be represented by a single relationship, such as equation 3. In other words, if the actual gas flow is known, the influence of gas recirculation (which depends on $\frac{A_d}{A_r}$, and the design of the gas separator) has been airlift bioreactor ready taken into account and does not need to be considered again. Nevertheless, this simple approach has a drawback in that the true gas superficial velocity is difficult to measure because the gas recirculation rate is usually not known. Thus, correlations that take into account all the variables, which may be easily measured, remain the option of choice. Table 1 shows most of the correlations of this type that have been proposed for the riser holdup in internal loop Airlift bioreactors. Comparison of a number of these correlations shows that there is reasonable agreement between the predictions of the different sources. Figure 1 can be used as an example of the actual state of-the-art in airlift bioreactor design. A number of correlations have been proposed, and three variables ($\frac{A_d}{A_r}$, l_{ap}, and J_G) have been tested by most researchers. The ranges in which these variables were studied vary from source to source.

In addition, some other variables (such as bottom clearance, top clearance or gas separator design, and surface tension) have been used by some authors but ignored by others. One example is the disengagement ratio defined by Siegel and Merchuk [19], which represents the mean horizontal path of a recirculating bubble relative to the external diameter and is equivalent to the parameter obtained by dimensional analysis [1] as:

$$M = \frac{D_S}{4D} \tag{4}$$

where D is the diameter of column and D_s the diameter of gas separator. If this parameter is not taken into account, then studies of the influence of the top clearance [13, 20] are incomplete and difficult to extrapolate to other designs.

The same can be said about the filling factor [21] given by the ratio of the gas separator volume to the total volume.

The foregoing discussion thus explains why all the correlations coincide for some ranges of these secondary variables while in other ranges they may diverge. In addition, in some cases the number of experiments may not have been sufficient to provide correlations or they may have been ill-balanced from the statistical point of view. The obvious solution to this problem lies in the collection of a large and detailed bank of reliable data that will constitute the basis for correlations with greater accuracy and validity. The safest procedure for the prediction of the gas holdup in an airlift bioreactor under design is to take data provided by researchers who have made the measurements in that particular type of reactor with the same physico-chemical properties of the system. If this option is not available, then correlation 9 in Table 1 [17], is recommended for prediction of the gas holdup in the riser.

Gas holdup in the downcomer is lower than that in the riser. The extent of this difference depends mainly on the design of the gas separator [22]. The downcomer gas holdup is linearly dependent on the riser holdup, as a consequence of the continuity of liquid flow in the reactor.

Many expressions of this type have been published [3]. At low gas flow rates, u_d is usually negligible, since most of the bubbles have enough time to disengage from the liquid in the gas separator. This usually happens at the low gas flow rates frequently used for animal cell cultures.

The gas holdup in the separator is very close to the mean gas holdup in the whole reactor [1] as long as the top clearance C_t is relatively small (one or two diameters). For larger top clearances, the behaviour of the gas separator begins to resemble that of a bubble column, and the overall performance of the reactor is influenced by this change.

In our laboratory we had some studies on the production of some secondary metabolites like phytohormones and protein hydrolysis, amino acid production, xanthophyll and new antibiotics. The next part of this chapter shows two cases were we try to show the applications of air lift bioreactors from various viewpoints, such as hydrodynamics, rheology and engineering aspects themselves. So to provide some useful engineering tools when these bioreactors takes to consideration:

5. Case 1: Hydrodynamics, mass transfer and rheological studies of Bikaverin production in an airlift bioreactor

5.1. Introduction

Antibiotics are small chemical agents (m.w. 600-800 Daltons) designed to eliminate harmful bacteria. They are produced from yeasts of fungi and bacteria. The first antibiotic discovered was penicillin in 1928/29 The first therapeutic application was in 1940 by Florey and Chain, during the Second World War when the need for antibiotics was increasing. Antibiotics belong to a group of substances called secondary metabolites. These substances appear to be unrelated to the main process of growth and reproduction. Good producers of secondary metabolites possess weak regulation of primary metabolism and visa-versa. Antibiotics are produced in limited substrate and oxygen conditions. They are produced to provide some protection against competing species in critical growth conditions. The starting points for antibiotic production are mainly amino acids and acetyl CoA with isoprene and shikimic acid also being involved. Antibiotic production commences at some point in differentiation often during sporulation. Process development consists essentially of modifying the metabolic system so that diversion of the material and biosynthesis are greatly increased. No cell growth or reproduction occurs during antibiotic production as the energy produced is being used to produce the antibiotic so that the cell can survive in the limited substrate.

After the discovery and first use of antibiotics the productivity and product concentration was increased by development of better strains or by improvement of the reaction conditions such

http://dx.doi.org/10.5772/53711

1	$\varphi_r = 0.44\ f_{G_r}^{0.841} \mu_{ap}^{-0.135}$ $\varphi_d = 0.297\ f_{G_r}^{0.935}$
2	$\varphi_r = 2.47\ f_{G_r}^{0.97}$
3	$\varphi_r = 0.465\ f^{0.65}\left(1 + \frac{A_d}{A_r}\right)^{-1.06} \mu_{ap}^{-0.103}$
4	$\varphi_r = 0.65\ f^{(0.603+0.078C_o)} \left(1 + \frac{A_d}{A_r}\right)^{-0.258}$ $\varphi_d = 0.46\varphi_r - 0.0244$
5	$\varphi_r = \left(0.491 - f_{G_r}^{0.706}\right) \left(\frac{A_d}{A_r}\right)^{-0.254} D_r \mu_{ap}^{-0.068}$
6	$\varphi_r = 0.16 \left(\frac{J_{Gr}}{J_{1r}}\right)^{0.57} \left(1 + \frac{A_d}{A_r}\right)$ $\varphi_d = 0.79\varphi_r - 0.057$
7	$\varphi_r = 0.364\ J_{Gr}$
8	$\frac{\varphi_r}{1 - \varphi_r} = \frac{J_{G_r}^{n+2/2(n+1)}}{2^{3n+1}\ {}^{n+2}\sqrt{2(n+1)\left(\frac{K}{\rho_1}\right)^{1/2(n+1)} g^n}\ {}^{2(n+1)}\sqrt{\left(1+\frac{A_d}{A_r}\right)^{3(n+2)/4(n+1)}}}$
9	$\frac{\varphi}{(1-\varphi)^4} = \frac{0.124\left(\frac{J_G \mu_1}{\sigma_1}\right)^{0.996}\left(\frac{\rho_1 \sigma_1^3}{g\mu_1^4}\right)^{0.294} \frac{D_r}{D}^{0.114}}{1 - 0.276\left(1 - e^{-0.0368 M_a}\right)}$
10	$\varphi_r = \frac{F_r}{0.415 + 4.27\left(\frac{J_{Gr} + J_{1r}}{\sqrt{g D_r}}\right)\left(\frac{g\rho_1 D^2}{\sigma_1}\right)^{-0.188} + 1.13 F_r^{1.22} M_o^{0.0386}\left(\frac{\Delta\rho}{\rho_1}\right)^{0.0386}}$
11	$\frac{\varphi}{(1-\varphi)^4} = 0.16 \left(\frac{J_{Gr}}{\sigma_1}\mu_1\right) M_o^{-0.283}\left(\frac{D_r}{D}\right)^{-0.222}\left(\frac{\rho_1}{\Delta\rho}\right)^{0.283} + \left(1 - 1.61\left(1 - e^{-0.00565 M_a}\right)\right)$
12	$\varphi_d = 4.51 \times 10^6 M_o^{0.115}\left(\frac{A_r}{A_d}\right)^{4.2} \varphi_r$ When $\varphi_r < 0.0133\left(\frac{A_d}{A_r}\right)^{-1.32}$ and $\varphi_d = 0.05 M_o^{-0.22}\left[\left(\frac{A_r}{A_d}\right)^{0.6} \varphi_r\right]^{0.31 M_o^{-0.0273}}$ When $\varphi_r > 0.0133\left(\frac{A_d}{A_r}\right)^{-1.32}$
13	$\varphi_r = 0.0057\left[(\mu_1 - \mu_w)^{2.75} - 161\frac{73.3 - \sigma}{79.3 - \sigma}\right] . f_{G_r}^{0.88}$
14	$\varphi_r = \frac{0.4 F_r}{1 + 0.4 F_r\left(1 + \frac{J_1}{J_{Gr}}\right)}$
15	$\varphi = 0.24 n^{-0.6} F_r^{0.84 - 0.14n} G_a$

Table 1. Gas Hold-Up in Internal-Loop airlift bioreactors

as substrates and process controls. There was also a change from surface cultures to batch stirred tank reactors with complex media. The next step was the introduction of the fed batch configuration, which extended the length of the production phase and avoided repression during high substrate levels.

For maximum yield we have to design a process that only minimally involves the primary metabolism.

The main function of a properly designed bioreactor is to provide a controlled environment in order to achieve optimal growth and/or product formation. In this review we will look at the bioreactor design and the factors that are available in producing high yields of antibiotics. In general bioreactor design, the growth kinetics of the microorganism plays a key role in determining the type of reactor. Factors include; yield coefficients and maintenance requirements, the exponential, stationary and lag phase kinetics, and the formation of growth and non-growth associated product production formation. Due to the constraints of the report, these factors are largely ignored and the main focus is on gaining knowledge on reactor configuration on the maximum yield of general antibiotics.

In our laboratory after work of ten years in research the optimal production of gibberellins we found that the *Gibberella fujkuroi* produce a potent antibiotic named Bikaverin. Bikaverin is a red pigment with specific anti-protozoal activity against *Leishmania brasiliensis* and anti-tumour activity. Additionally, bikaverin and its derivatives have a cytotoxic effect on in vitro proliferating cells of Erlich ascites carcinoma, Sarcoma 37 and leukaemia L-5178 and is a fermentation product of *Gibberella fujikuroi* or *Fusarium sp*. The formation of bikaverin precedes that of gibberellin [23] and both secondary metabolites are produced from the primary metabolite acetyl-CoA. Bikaverin is synthesized via the polyketide route while gibberellin is synthesized through the isoprenoid pathway [24].

The industrial production of these secondary metabolites is done with cultures of mycelia in liquid (submerged) or solid substrate fermentation. Models of mould growth and metabolic production based on characteristics of mycelial physiology are important to understand, design, and control those industrial fermentation processes [23, 25]. In other words these models enable us to obtain information in a practical way, facilitating fermentation analysis, and can be used to solve problems that may appear during the fermentation process.

5.2. Materials and methods

Microorganism and inoculum preparation *Gibberella fujikuroi* (Sawada) strain CDBB H-984 maintained on potato dextrose agar slants at 4 °C and sub-cultured every 2 months was used in the present work (Culture collection of the Department of Biotechnology and Bioengineering, CINVESTAV-IPN, Mexico). Fully developed mycelia materials from a slant were removed by adding an isotonic solution (0.9% NaCl). The removed mycelium was used to inoculate 300 ml of fresh culture medium contained in an Erlenmeyer flask. The flask was placed in a radial shaker (200 rev min^{-1}) for 38 h at 29 ± 1°C. Subsequent to this time; the contents of the flask were used to inoculate the culture medium contained in the airlift bioreactor. The culture medium employed for the inoculum preparation is reported by Escamilla [26].

http://dx.doi.org/10.5772/53711

5.3. Batch culture in the airlift bioreactor

An airlift bioreactor (Applikon, Netherlands, working volume, 3.5 l) was employed in the present work (Fig 3). It consists of two concentric tubes of 4.0 and 5.0 cm of internal diameter with a settler. The air enters the bioreactor through the inner tube. A jacket filled with water allowing temperature control surrounds the bioreactor. It is also equipped with sensors of pH and dissolved oxygen to control these variables. Moreover it allows feed or retiring material from the bioreactor employing peristaltic pumps.

During the fermentation period, the pH was controlled to 3.0, temperature to 29 °C and aeration rate to 1.6 volume of air by volume of media by minute (vvm). These conditions promoted Bikaverin production with the studied strain were optimized values [26]. About 30 ml subsamples were withdrawn from the bioreactor at different times and were used to perform rheological studies. Biomass concentration was quantified by the dry weight method.

Figure 3. Airlift bioreactor used for the process for Bikaverin production

5.4. Batch culture in the airlift bioreactor

Typical culture medium contained glucose (50 g l^{-1}), NH_4Cl (0.75 g l^{-1}) or NH_4NO_3 (1.08 g l^{-1}), KH_2PO_4 (5 g l^{-1}), $MgSO_4.7H_2O$ (1 g l^{-1}) and trace elements (2 ml l^{-1}). A stock solution of the trace elements used contained (g l^{-1}) 1.0 Fe SO_4. $7H_2O$, 0.15 $CuSO_4$. $5H_2O$ 1.0 $ZnSO_4$. $7H_2O$, 0.1 $MnSO_4$ $7H_2O$, 0.1 $NaMoO_4$, 3.0 EDTA (Na_2 salt) 1 l of distilled water, and hydrochloric acid sufficient to clarify the solution (Barrow et al. 1960). During the fermentation period, the pH was controlled to 3.0, temperature to 29 °C and aeration rate to 1.6 v/v/m. These conditions promoted Bikaverin production with the studied strain but they are not optimized values. About 30 ml subsamples were withdrawn from the bioreactor at different times and were used to perform rheological studies. Biomass concentration was quantified by the dry weight method.

5.5. Hydrodynamics and mass transfer studies

Gas holdup was determined in the actual culture medium using an inverted U-tube manometer as described by [27]. Liquid velocities in the riser were determined measuring the time required for the liquid to travel through the riser by means of a pulse of concentrated sulphuric acid using phenolphthalein as an indicator; the same was done for the downcomer.

The mixing time was calculated as the time required obtaining a pH variation within 5% of the final pH value. For doing this, pH variation was followed after injection of a pulse of a concentrated solution of ammonium hydroxide. The volumetric mass transfer coefficient was determined employing the gassing-out method as described elsewhere [28].

5.6. Rheological studies

Rheological studies of fermentation broth were performed in a rotational rheometer (Haake, Model CV20N) equipped with a helical impeller to perform torque measurements. This type of geometry is appropriate when dealing with complex fluids and the measurement methodology is reported by Brito [29]. Rheological results, like hydrodynamics and mass transfer, are given as the average of two replicates for each sample. All the experiments were carried out in triplicate and the results that are presented are an average.

5.7. Results and discussion

5.7.1. Gas holdup

The importance of gas holdup is multifold. The gas holdup determines the residence time of the gas in the liquid and, in combination with the bubble size, influences the gas–liquid interfacial area available for mass transfer. The gas holdup impacts upon the bioreactor design because the total design volume of the bioreactor for any range of operating conditions depends on the maximum gas holdup that must be accommodated [1]. Figure 4 shows the gas holdup (ε) variation with superficial gas velocity in the riser (v_{gr}).

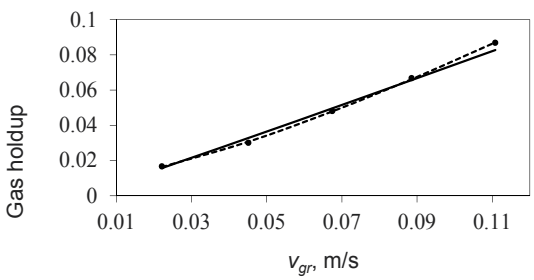

•Experimental data; — Equation 5;—Equation 14

Figure 4. Gas holdup variation with superficial gas velocity in the riser.

Experimental data were fitted to a correlation of the type of Eq. 5.

http://dx.doi.org/10.5772/53711

$$F = A v_{G_r}^{B} \tag{5}$$

Where F could be the gas holdup (ε), the liquid velocity in the riser (v_{lr}), liquid velocity in the downcomer (v_{ld}) or the volumetric mass transfer coefficient ($k_L a$). This type of correlation has been applied by many investigators (1, 30-33) and was derived empirically. [34] presented an analysis for Newtonian and non-Newtonian fluids where shows the theoretical basis of Eq. 5 (for the gas holdup case). He found that parameters A and B were dependent on the flow regime and on the flow behaviour index of the fluid.

Moreover, parameter A is dependent on the consistency index of the fluid, on the fluid densities and on the gravitational field. Equation 6 was obtained from fitting experimental data.

$$\varepsilon = 0.7980\ v_{gr}^{1.0303} \tag{6}$$

An increase in superficial gas velocity in the riser implies an increase in the quantity of gas present in the riser, that is, an increase of gas fraction in the riser [27, 32]. Chisti, [34] reports a correlation that calculates the value of *B* in Equation 5 (for gas holdup case). The obtained value employing this correlation is 1.2537. Gravilescu and Tudose [32] present a similar correlation, which predicts a value of 0.8434 for *B*. The *B* value obtained in the present work is between the *B* values obtained from these correlations that employ the flow behaviour index obtained from rheological studies. Shah [30] reported that *B* values in Equation 5 oscillate between 0.7 and 1.2.

5.7.2. Liquid velocity

The liquid circulation in airlift bioreactors originates from the difference in bulk densities of the fluids in the riser and the downcomer. The liquid velocity, while itself controlled by the gas holdups in the riser and the downcomer, in turn affects these holdups by either enhancing or reducing the velocity of bubble rise. In addition, liquid velocity affects turbulence, the fluid-reactor wall heat transfer coefficients, the gas-liquid mass transfer and the shear forces to which the microorganism are exposed. Figure 5 shows liquid velocities variation in the riser and the downcomer as a function of superficial gas velocity in the riser.

Liquid velocities in the riser (v_{lr}) and in the downcomer (v_{ld}) were fitted to correlations of the type of Equation 1 and Equations 7 and 8 were obtained.

$$v_{lr} = 1.3335\ v_{gr}^{0.3503} \tag{7}$$

$$v_{ld} = 0.8716\ v_{gr}^{0.2970} \tag{8}$$

Freitas and Teixeira [35] point out that *B* value in equation 7 must be close to 0.3333 for the liquid velocity in the riser since this value was theoretically derived by Kawase [36] and others. The *B* value obtained in the present work (0.3503) is only a little bit higher than 0.3333. Freitas

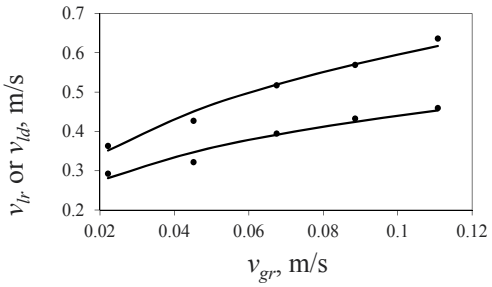

•Experimental data — Equation 7 or 8

Figure 5. Liquid velocities as a function of superficial gas velocity in the riser.

and Teixeira [35] also obtain that *B* value for the liquid velocity in the downcomer is less than *B* value for the liquid velocity in the riser which agrees with the results obtained in this work. Liquid velocities in the riser and in the downcomer increase with an increase in gas velocity in the riser due to an increase in the density difference of the fluids in the riser and the downcomer.

5.7.3. Mixing time

Mixing in airlift bioreactors may be considered to have two contributing components: backmixing due to recirculation and axial dispersion in the riser and downcomer due to turbulence and differential velocities of the gas and liquid phases [37](Ch. Mixing time is used as a basis for comparing various reactors as well as a parameter for scaling up [32]. Figure 6 shows the mixing time variation with the superficial gas velocity in the riser.

Once again, the mixing time variation was fitted to a correlation of the type of Equation 5 and Equation 8 was obtained.

$$t_m = 5.0684\ v_{gr}^{-0.3628} \tag{9}$$

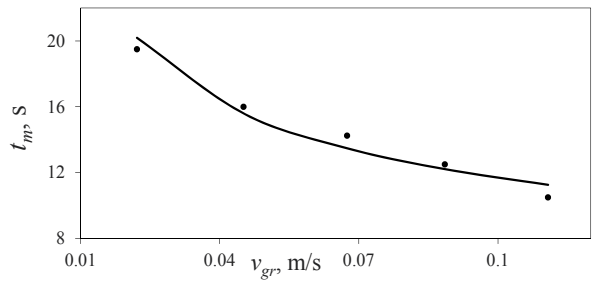

• Experimental data — Equation 5

Figure 6. Mixing time as a function of superficial gas velocity in the riser.

http://dx.doi.org/10.5772/53711

Choi *et al*., [37] report a *B* value in Equation 5 of –0.36 while Freitas and Teixeira [35] report a *B* value equal to –0.417. The *B* value obtained in this work is similar to the value reported by Choi *et al*., [37]. The mixing time decreases with an increase in superficial gas velocity in the riser since the fluid moves more often to the degassing zone where most of the mixing phenomenon takes place due to the ring vortices formed above the draught tube [35].

5.7.4. Volumetric mass transfer coefficient

One of the major reasons that oxygen transfer can play an important role in many biological processes is certainly the limited oxygen capacity of the fermentation broth due to the low solubility of oxygen. The volumetric mass transfer coefficient (k_La) is the parameter that characterizes gas-liquid oxygen transfer in bioreactors. One of the commonest employed scale-up criteria is constant k_La. The influences of various design (i.e., bioreactor type and geometry), system (i.e., fluid properties) and operation (i.e., liquid and gas velocities) variables on k_La must be evaluated so that design and operation are carried out to optimize k_La [37].

The value of the volumetric mass transfer coefficient determined for a microbial system can differ substantially from those obtained for the oxygen absorption in water or in simple aqueous solutions, i.e., in static systems with an invariable composition of the liquid media along the time. Hence k_La should be determined in bioreactors which involve the actual media and microbial population [38]. Figure 7 shows the volumetric mass transfer coefficient variation with the superficial gas velocity in the riser.

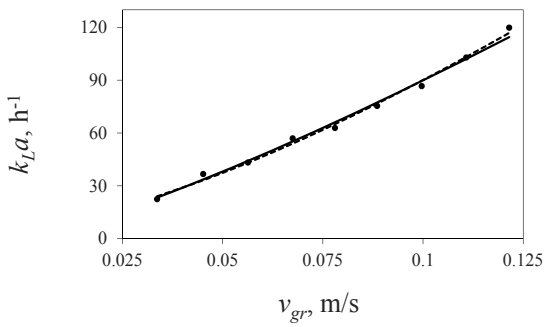

Figure 7. Effect of the superficial gas velocity in the riser on k_La.

Experimental data shown in Figure 7 were fitted to a correlation of the type of Equation 1 and Equation 6 was obtained.

$$k_La = 0.4337\ v_{gr}^{1.2398} \tag{10}$$

[39] report a *B* value in Equation 6 equal to 1.33 and Schügerl *et al*., [40] report a value of 1.58. The value of 1.2398, obtained in this work, is closed to these last values.

Volumetric mass transfer coefficient (k_La) increases with an increase in superficial gas velocity in the riser due to an increase in gas holdup which increases the available area for oxygen transfer. Moreover an increase in the superficial gas velocity in the riser increases the liquid velocity which decreases the thickness of the gas-liquid boundary layer decreasing the mass transfer resistance.

Figure 8 shows the evolution of k_La through fermentation course employing two different nitrogen sources. The k_La decreases in the first hours of fermentation and reaches a minimum value at about 24 hours. After this time the k_La starts to increase and after 48 hours of fermentation it reaches a more or less constant value which remains till the end of fermentation process. This behaviour is similar irrespective of the nitrogen source and will be discussed with the rheological results evidence.

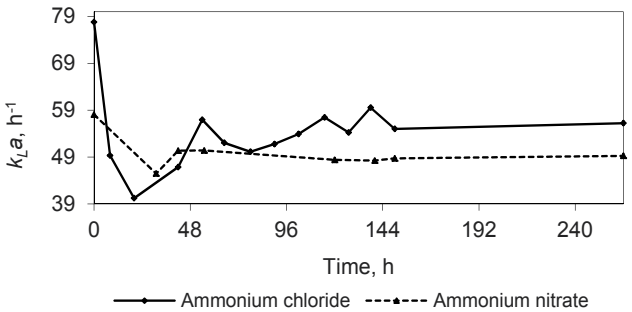

Figure 8. Sthe evolution of k_La through fermentation course employing two different nitrogen sources.

Figure 9 shows the relation between gas holdup and k_La. Mc Manamey and Wase [21] point out that the volumetric mass transfer coefficient is dependent on gas holdup in pneumatically agitated systems. The later was experimentally determined in bubble columns by Akita and Yoshida and other authors [30, 41, 42] they mention that this was expectable since both the volumetric mass transfer coefficient and the holdup present similar correlations with the superficial gas velocity. Mc Manamey and Wase [21] proposed a correlation similar to Equation 1 to relate volumetric mass transfer coefficient with gas holdup. Equation 7 presents the obtained result.

$$k_La = 0.2883\ \varepsilon^{0.9562} \tag{11}$$

Akita and Yoshida [41] and Prokop *et al*. [42] found that the exponent in Equation 7 oscillates between 0.8 and 1.1.

It is well known [16] that logarithmic scale plots of k_La vs. $\varepsilon/(1-\varepsilon)$ for any particular data set should have a unit slope according to Equation 8.

http://dx.doi.org/10.5772/53711

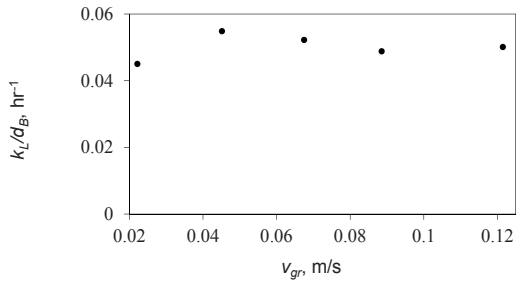

Figure 10. The k_L/d_B ratio as a function of superficial gas velocity.

$$\ln k_L a = \ln\left(6\frac{k_L}{d_B}\right) + \ln\frac{\varepsilon}{(1-\varepsilon)} \tag{12}$$

Where k_L is the mass transfer coefficient and d_B is the bubble diameter. Even though the latter is a generally known fact, few investigators determined these slopes for their data to ascertain the validity of their experimental results. Figure 10 shows this analysis for the experimental data of the present work obtaining a slope of 1.034. Chisti [16] shows the same analysis for two different data set and obtained slopes of 1.020 and 1.056.

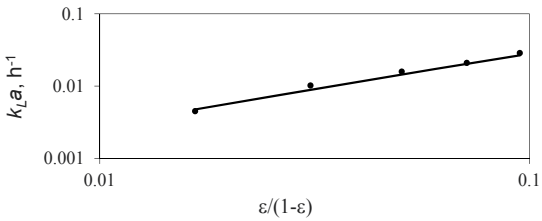

Figure 9. k_La vs. gas holdup in the airlift bioreactor, unit slope.

A rearrangement of Equation 8 leads to Equation 9 which results are shown in Figure 10

$$\frac{k_L}{d_B} = \frac{k_L a\left(1-\varepsilon\right)}{6\varepsilon} \tag{13}$$

The average value of k_L/d_B obtained in the present work is 0.050 s^{-1}. Chisti [27] performed a similar analysis for 97 data points obtained from several different reactors and found an average value of 0.053 s^{-1}. The foregoing observations have important scale-up implications. In large industrial fermenters the k_La determination is not only difficult, but there is uncertainty as to whether the measured results reflect the real k_La or not. The gas holdup measurements

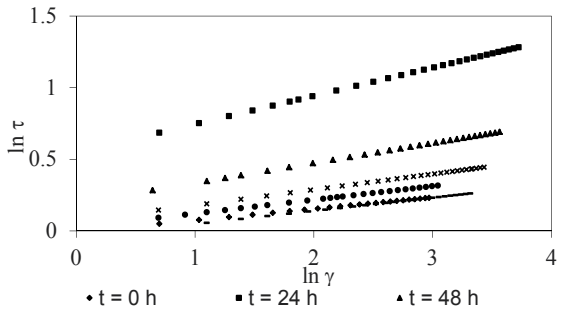

Figure 11. Typical rheogram employing impeller viscometer.

on these reactors are relatively easy to carry out, however. Thus, Equation 9 can help to estimate k_La in these reactors once holdup measurements have been made [1].

5.7.5. Rheology

Rheological parameters such as the flow index (n) and the consistency index (K) depend on such factors as the concentration of solids in the broth, the morphology (length, diameter, degree of branching, shape) of the particles, the growth conditions (flexibility of cell wall and particle), the microbial species and the osmotic pressure of the suspending liquid, among others possible factors.

For the case of mycelia cultures, as the biomass concentration increases the broth becomes more viscous and non-Newtonian; leading to substantial decreases in oxygen transfer rates. This effect is often important since for many aerobic processes involving viscous non-Newtonian broths oxygen supply is the limiting factor determining bioreactor productivity [43]. Apparent viscosity is a widely used design parameter which correlates mass transfer and hydrodynamic parameters for viscous non-Newtonian systems [44].

It is worth to mention that the present work uses impeller viscometer for performing rheological studies avoiding the use of other geometries, i.e., concentric tubes or cone and plate, overcoming associated problems with these geometries such sedimentation, solids compacting and jamming between measuring surfaces or pellet destruction [45].

Rheograms obtained for the fermentations employing different nitrogen source were fitted to Ostwald-de Waele model (power law) and in both cases a pseudoplastic behaviour for the fermentative medium was found. Figure 11 shows the results of consistency and flow indexes for these two fermentations where similar results were obtained.

During the first 24 hours of fermentation, medium viscosity increases due to exponential growth of mycelia (no lag phase is present) which causes a k_La decrease in Figure 9. After this time, the formation of pellets by the fungus starts to occur reflected in a decrease of medium viscosity and hence an increase in k_La value in Figure 10. After 72 hours of fermentation the medium viscosity was practically unchanged because the stationary growth phase is reached by the fungus reflected in practically constant values of medium viscosity and k_La. With the

http://dx.doi.org/10.5772/53711

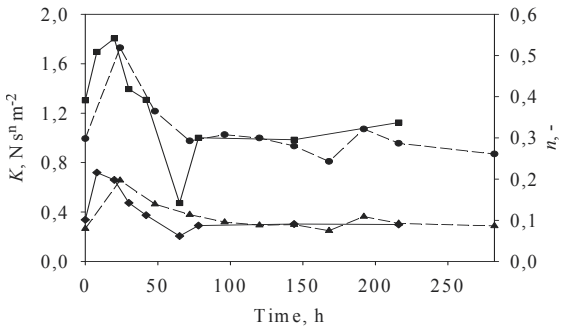

Figure 12. *K* and *n* through fermentation time in the airlift bioreactor.• *K* for ammonium nitrate ▲ *n* for ammonium nitrate ■ *K* for ammonium chloride ◆ *n* for ammonium chloride,

aid of rheological studies is possible to use correlations of the type of Equation 10 to relate holdup and volumetric mass transfer coefficient with fermentation medium viscosity [20, 31, 39, 44] to obtain Equations 12 and 13.

$$F = Av_{gr}^{B}\mu_{app}^{C} \tag{14}$$

$$k_L a = 0.0036\ v_{gr}^{0.3775}\mu_{app}^{-0.5488} \tag{15}$$

$$\varepsilon = 0.0072\ v_{gr}^{0.2381}\mu_{app}^{-0.5703} \tag{16}$$

Figures 2 and 6 show experimental data fitting for holdup and k_La, respectively. As it was expectable, Equations 12 and 13 present a better fit to experimental data than that obtained with the aid of Equations 2 and 3 due to the existence of an extra adjustable parameter.

As can be seen in Fig. 13, there is no lag phase and exponential growth of mycelia starts immediately and ceases during the first 24 h of fermentation. The later causes the medium viscosity to increase (K and n increase in Fig. 12), which causes a k_La decrease in Fig. 6. After 24 h of fermentation, the formation of pellets by the fungus starts to occur, reflected in a decrease of medium viscosity (K and n start to decrease in Fig. 12) and hence an increase in k_La value in Fig. 5. After 72 h of fermentation the medium viscosity was practically unchanged (K and n remain constant in Fig. 12) because the stationary growth phase is reached by the fungus reflected in practically constant values of medium viscosity and k_La. Also, after 72 h of fermentation, the pellet formation process by the fungus stops.

Figure 13 shows the correlation between consistency and flow indexes with biomass concentration. Experimental data were fitted to Eqs. 12 and 13 proposed in the present work. Optimized values for constants in Eqs. 12 and 13 are summarized in Table 1.

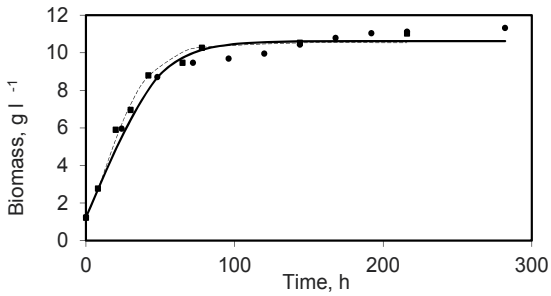

Figure 13. Growth kinetics employing ammonium chloride (◆) or ammonium nitrate (•) as nitrogen source.

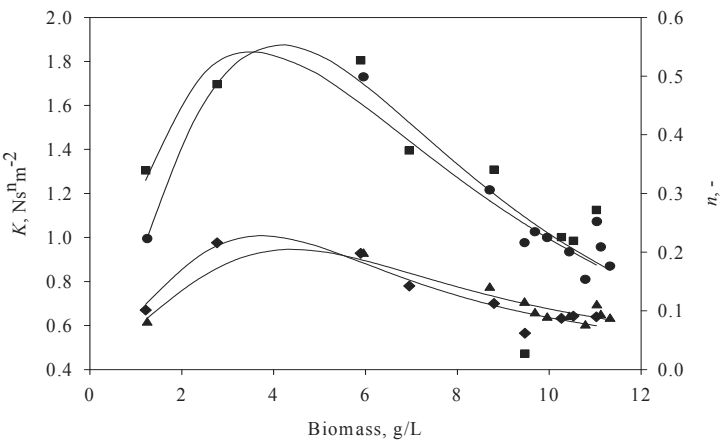

Figure 14. *K* and *n* as a function of biomass concentration in the airlift bioreactor. • *K* for ammonium nitrate ▲ *n* for ammonium nitrate ■ *K* for ammonium chloride ◆ *n* for ammonium chloride

$$K = \frac{c_1}{\left(1 + \frac{c_2}{x}\right) + \left(\frac{x}{c_3}\right)^2} \tag{17}$$

$$n = \frac{c_1}{\left(1 + \frac{c_2}{x}\right) + \left(\frac{x}{c_3}\right)^2} \tag{18}$$

With the aid of rheological studies is possible to use correlations of the type of Equation 14 to relate gas holdup and volumetric mass transfer coefficient with fermentation medium viscosity [20, 31, 39, 44] to obtain Equations 15 and 16.

http://dx.doi.org/10.5772/53711

$$F = A v_{gr}^{B} \mu_{app}^{C} \tag{19}$$

$$k_L a = 0.0036\ v_{gr}^{0.3775} \mu_{app}^{-0.5488} \tag{20}$$

$$\varepsilon = 0.0072\ v_{gr}^{0.2381} \mu_{app}^{-0.5703} \tag{21}$$

Figures 2 and 5 show experimental data fitting for gas holdup and $k_L a$, respectively. As it was expectable, Eqs. 15 and 16 present a better fit to experimental data than that obtained with the aid of Eqs. 2 and 3 due to the existence of an extra adjustable parameter.

5.8. Conclusions

In the present work preliminary hydrodynamics, mass transfer and rheological studies of Bikaverin production in an airlift bioreactor were achieved and basic correlations between gas holdup, liquid velocity in the riser, liquid velocity in the downcomer, mixing time and volumetric mass transfer coefficient with superficial gas velocity in the riser were obtained.

Adjustable parameters calculated for each variable were compared with literature reported values and a good agreement was obtained.

The gassing out method was successfully applied in determining volumetric mass transfer through fermentation time employing two different nitrogen sources. Irrespective of the nitrogen source the volumetric mass transfer behaviour was similar and it was explained in terms of the fungus growth and changes in its morphology, which affect the culture medium rheology.

Pellet formation by the fungus was used to explain the increase of $k_L a$ or the decrease of medium viscosity. In both fermentations, $k_L a$ decreases as exponential growth of the fungus occurs and reaches an asymptotic value once the stationary growth phase is reached. A helical impeller was employed successfully for rheological studies, avoiding problems of settling, jamming or pellet destruction, finding that the culture medium behaves as a pseudoplastic fluid. Rheological measurements were used to correlate gas holdup and $k_L a$ with apparent culture medium viscosity. Once again, for both fermentations, apparent viscosity increases as exponential growth of the fungus occurs and reaches an asymptotic value once the stationary growth phase is reached.

A satisfactory validation of experimental data for gas holdup and volumetric mass transfer coefficient was performed which allows the employment of these data in scale-up strategies.

6. Case 2: Studies on the kinetics, oxygen mass transfer and rheology in the l-lysine prodution by *Corynebaterium glutamicum*

6.1. Introduction

The industrial application of amino acids in broiler feed has a long history, from the late 1950's have been used to increase the efficiency of the food they eat these animals. Lysine is one of these amino acids to its importance as a feed additive for pigs and poultry, is that it increases the willingness of proteins, bone growth, ossification and stimulates cell division.

Lysine used as an additive for food, is imported because lysine production nationally not exist. The approximate amount of lysine produced worldwide is 550 000 tons per year and almost everything is produced by international companies. Only in the state of Guanajuato, the estimated demand of 300 tons of lysine [46], so that the implementation of appropriate technology for the production of this important amino acid, reduce production costs of animal feed feedlot to reduce imports and generate jobs in the country [47].

Lysine can be produced by chemical synthesis or by enzymatic or microbiological processes. Lysine for obtaining a chemical synthesis is expensive and inefficient process that also by this method are obtained racemic mixtures of D and L forms must then be processed to obtain the L-form which is biologically active. Microbiological fermentation processes are more efficient and direct methods to be based on the accumulation of amino acid that is excreted by the organism in culture media and / or fermentation containing high sugar concentrations and ammonium ions at neutral pH and under aerobic conditions in crops batches [48].

The most commonly used species for the production of lysine is the *Corynebaterium glutamicum* are employed although *Arthrobacter, Brevbibacterium, Microbacterium and Micrococuus.*

Traditionally, the production process of lysine by microbiological fermentation is carried out in stirred vessels, the characteristics of this type of reactor, sometimes, it is economically inconvenient. A better alternative to this configuration are the airlift reactors, the advantages are: low shear, high-speed transfer of oxygen and good mixing, implying a better mass transfer eliminating concentration gradients of either the medium components, avoiding sedimentation of the cells, thereby creating a more favourable environment for development and maintenance, increasing yields and production of lysine.

6.2. Methodology

Inoculum development. Inoculated to the reactor biomass was obtained from a pre-inoculum of ATCC 21253 in lyophilized strain *Corynebacterium glutamicum*.

Experiments in the bioreactor. The batch fermentations were carried out in a reactor airlift with a working volume of 3.4 litres at 30° C (Fig 15). Dissolved oxygen was monitored with a polarographic electrode. The pH of the culture pH was controlled at 7.0 by addition of a solution of 70% NH_4OH. The bioreactor has a condenser which minimizes the error by evaporation losses. The quantity of biomass was inoculated approximately 10% of the bioreactor working volume and sampled periodically.

http://dx.doi.org/10.5772/53711

Figure 15. Airlift bioreactor for L-Lysine production

6.3. Mass transfer

For the determination of K_La was used the gas elimination technique [49] and dynamic technique [28]. Measurements for the calculation of K_La by both methods were carried out at 30 ° C and pH 7.0, with a working volume of 3.4 litres of sterile fermentative medium.

Evaluation of the parameters α, β and m_s, the equations were solved using the Runge-Kutta 4th order and an adjustment of the experimental data by nonlinear regression using the GREG program.

The growth rate model is as follows

$$\frac{dX}{dt} = \mu X\left(1 - \frac{X}{L}\right) \tag{22}$$

Where μ is the specific growth rate and L is the maximum value that people can achieve.

The model of product formation rate where the rate of formation is related to the rate of growth:

$$\frac{dP}{dt} = \alpha \frac{dX}{dt} \tag{23}$$

Where α is a constant stoichiometric. In the case where the product is formed independently of the speed of growth:

$$\frac{dP}{dt} = \beta X \tag{24}$$

where β is a proportionality constant. The constant β is similar to the enzyme activity [28]

The substrate consumption model is represented by the following equation:

$$r_S = \frac{r_X}{Y'_{X/S}} + \frac{r_p}{Y'_{P/S}} + m_S X \tag{25}$$

6.4. Results and discussion

The results obtained with the gas elimination technique, allowed calculating the maximum oxygen transfer rate in the system, the dissolved oxygen conditions required.

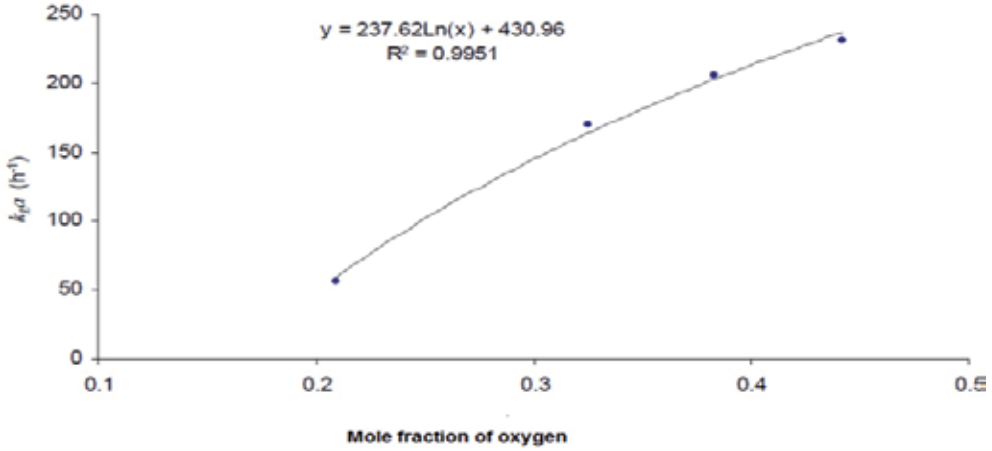

Figure 16. Adjusting $K_L a$ experimental values obtained by the technique of gas removal.

Finding no correlations suitable $K_L a$ experimental data obtained by the technique of gas phase were adjusted to a logarithmic trend line shown in Figure 16.

Figure 17, shows that the production of lysine started between 11 and 12 hours. From 21 up to 46 h the lysine production rate was kept constant (0.385 g / l of lysine h) and declined at 53 h the reduction in production rate was 22% approximately. The overall yield Y_P / S was 0.244 g of lysine / g glucose (at 53 h Y_P / S = 0.223 g lysine / g glucose).

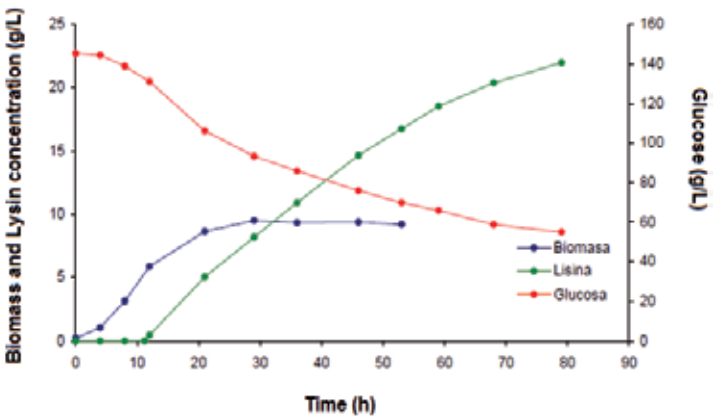

Figure 17. Kinetics of growth, production and consumption with initial glucose 145 g / l.

http://dx.doi.org/10.5772/53711

Parameter	102g/l glucose	145g/l glucose
μ	0.422	0.362
L	11.36	9.26
α	0.974	0.72
β	0.0405	0.0378
Y'X/S	0.42	0.38
Y'P/S	0.36	0.36
ms	–	0.0245

Table 2. Models parameter of growth, production, and lysine and glucose consumption.

In the experiment with 102 g / l initial glucose (Figure 17), lysine production started between 9 and 10 hours. From 22 up to 46 hours the lysine production rate was kept constant (0.475 g / l h of lysine), at 52 hours the reduction in production rate was only 8%. The overall yield Y_P / S was 0.247 g of lysine / g glucose.

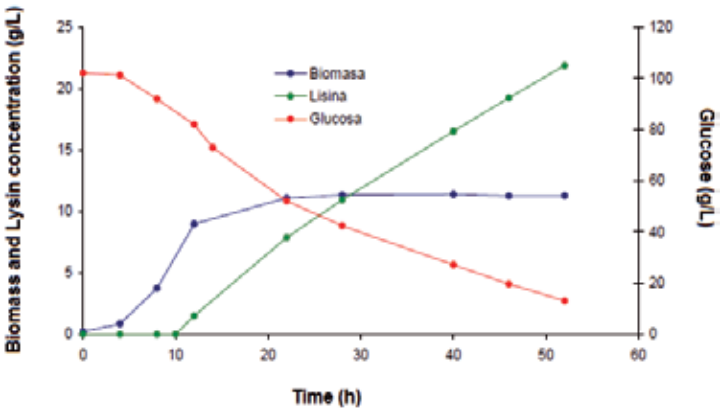

Figure 18. Kinetics of growth, production and consumption with initial glucose 102 g / l.

The model parameters of growth, production and consumption presented in equations [1] to [4] are presented in Table 2.

For evaluation of the parameters α, β and m_s. The equations were solved using the Runge-Kutta 4th order and an adjustment of the experimental data by nonlinear regression using the GREG program [50].

In evaluating the parameters α, β and m_s, the other parameters were kept constant and adjusting the experimental data was performed with the data obtained from 12 h until the end of the maintenance phase (phase to production rate constant).

In Figures 19 and 20 shows the experimental data and the values generated by equations (solid lines) and can be seen that models correctly predict the growth of the microorganism, product formation and substrate consumption from the beginning of the lysine production phase, until the end of the maintenance phase.

Initial Glucose (g/L)	$L - X_0$	μ	$Y_{X/Thr}$	q_{Thr}
145	9.04	0.362	30.1	0.0120
102	11.14	0.422	37.1	0.0114

Table 3. Results obtained from the specified speed of consumption of threonine to two different initial concentrations of glucose.

The rate of consumption of threonine is affected by the initial concentration of glucose due to the effect that the osmotic pressure produced in the cells.

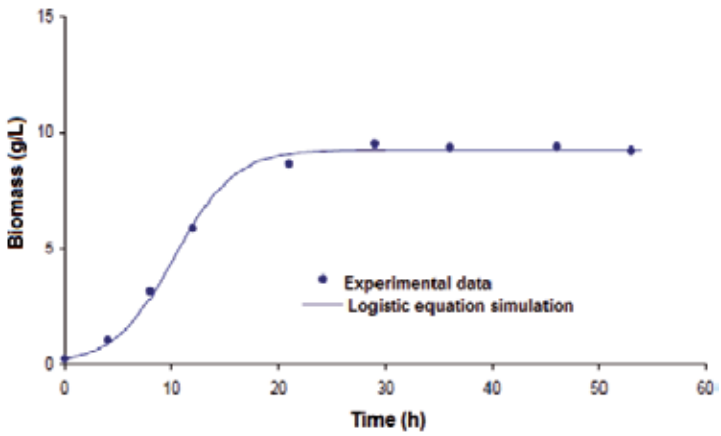

Figure 19. Setting the biomass data to the logistic model (glucose = 145 g/L)

Based on the data in Table 4, an experiment was conducted with airflow of 1 vvm and initial concentration of 150 g / l and 0.6 g / l glucose and L-threonine respectively (Figure 20). The dissolved oxygen began to decrease at approximately 2 h and reached a level below 5% saturation at approximately 20 hours. In Figure 20 it can be seen the effect of oxygen in the growth rate, until 8 h, $\mu = 0.250\ s^{-1}$with a saturation percentage of dissolved oxygen of 20% and 22 to 46, $\mu = 0.0135$, after the culture was oxygen limited.

Air flow (vvm)	ml of antifoam uptake (12 h)	liquid entrained by the air trapped in the condenser
0.5	<1	-
1.0	15	2.2
1.5	27.5	4.4
2.0	55.5	8.0
2.5	>75	11.2
3.0	-	16.8

Table 4. Exploratory experiments for found the optimal initial air flow in the airlift bioreactor.

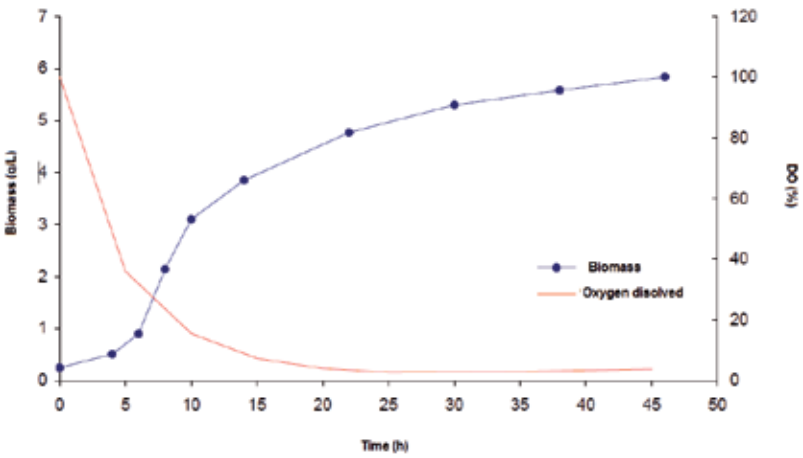

Figure 20. Oxygen limiting effect on the biomass formation.

6.5. Experimental determination of the volumetric coefficient of oxygen transfer

Determination of the solubility of oxygen in the fermentative culture. Because in the experiments with variable air flow was not possible to maintain the dissolved oxygen concentration required for the fermentation experiments was determined by enriching the airflow with oxygen. Were tested for solubility of oxygen in the fermentative culture with various concentrations of glucose, 100, 140 and 180 g / l were obtained the following results:

Glucose (g/l)	DO (%)	MgO_2/l
180	85.22	5.27
140	85.98	5.31
100	87.30	5.40

Table 5. Solubility of oxygen in the fermentative medium with different glucose concentrations.

The difference in concentration of dissolved oxygen concentration between the highest and lowest blood glucose was only 2.11% [51]. Therefore experiments to determine k_La is conducted in fermentative medium with 140 g / l glucose. One way to improve oxygen transfer in the fermentations is to increase the solubility by increasing the mole fraction of gas in the airflow. Based on this, we measured the concentration of dissolved oxygen in the bioreactor by varying the mole fraction of oxygen in the air flow. The results are presented in Table 6.

Oxygen flow rate (vvm)	Air flow rate (vvm)	Oxygen molar fraction	mmol O_2/l	mg O_2/l
0	3400	0.209	0.165	5.27
500	2900	0.325	0.255	8.15
750	2650	0.383	0.307	9.81
1000	2400	0.442	0.349	11.18
1500	1900	0.558	0.441	14.10

Table 6. Experimental results of the measurement of dissolved oxygen.

Experimental data of solubility of oxygen, according to Henry's Law can be adjusted to a straight line (Figure 21). These data were used in subsequent calculations.

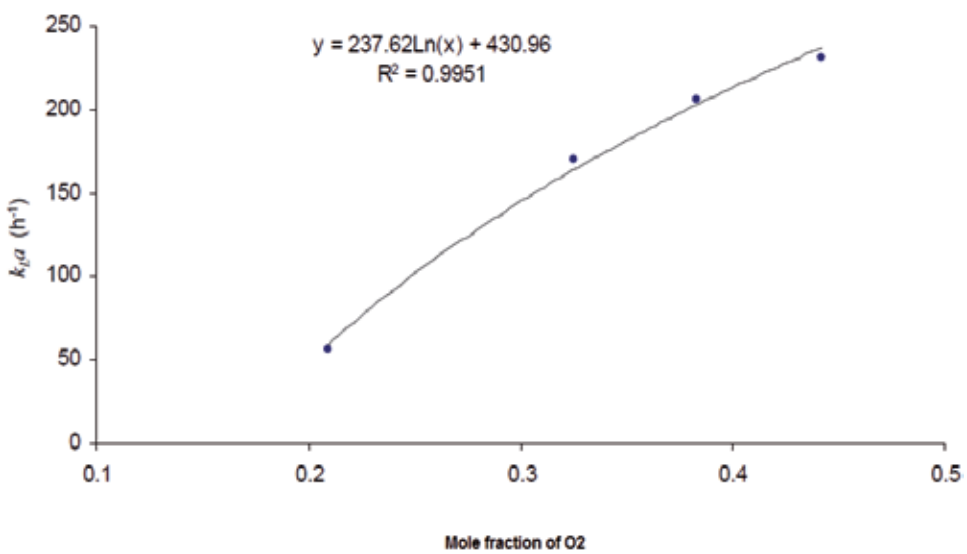

Figure 21. Adjusting k_La experimental values obtained by the technique of gas removal.

In 2003, Ensari and Lim [52] proposed a model in which incorporated the rate of oxygen consumption to describe the kinetics of fermentation of L-lysine and handled 0,266 mmolO_2 /

http://dx.doi.org/10.5772/53711

l as 100% saturation, 30% of this amount is equivalent mgO_2 to 2.55 / l. If we take the value of 2.55 mgO_2 / l, as the minimum value of dissolved oxygen should be maintained during the fermentation and used to calculate the oxygen transfer rate, as the mole fraction of oxygen increases in the air flow, the percentage of dissolved oxygen is reduced, due to the increase in the concentration gradient, which is the driving force for oxygen transfer.

Once the solubility data obtained at different levels of enrichment, we proceeded to calculate the values of the volumetric coefficient of oxygen transfer. K_La value is proportional to the increase in the molar fraction of oxygen in the air flow, this is because increasing the amount of oxygen in the flow, and the contact area is higher. The results obtained with the gas elimination technique, are shown in Table 7 and were useful because together with the values of solubility of oxygen, were used to calculate the maximum oxygen transfer rate in the system, the conditions of dissolved oxygen required.

Mole fraction of oxygen	k_La (h^{-1}]	Number of adjusted data	R^2
0.209	57	10	0.9977
0.209	56	10	0.9979
0.325	171	5	0.9958
0.325	169	5	0.9903
0.383	205	5	0.9921
0.383	208	5	0.9911
0.442	233	3	0.999
0.442	230	3	0.9975

Table 7. Experimental K_La data obtained by the technique of gassing out.

While gassing out method showed a good correlation decided to try the dynamic method to see if you got a better approximation.

6.6. Dynamic method

In Figure 22, shows the data obtained during the development of direct measurements were performed to calculate the volumetric coefficient of oxygen transfer. Data from the first phase of the experiment were used to measure the oxygen consumption rate in the second phase, the coefficient of volumetric oxygen transfer. In fermentation, the oxygen transfer rate can be calculated using the following equation:

$$\frac{dC_L}{dt} = K_L\, a\left(C_L^* - C_L\right) - Q_{O_2} X \tag{26}$$

Where, Q_{O2} is the specific rate of oxygen consumption, which can be defined as the specific growth rate between the yields of oxygen.

$$Q_{O_2} = \frac{\mu}{Y_{O_2}} \tag{27}$$

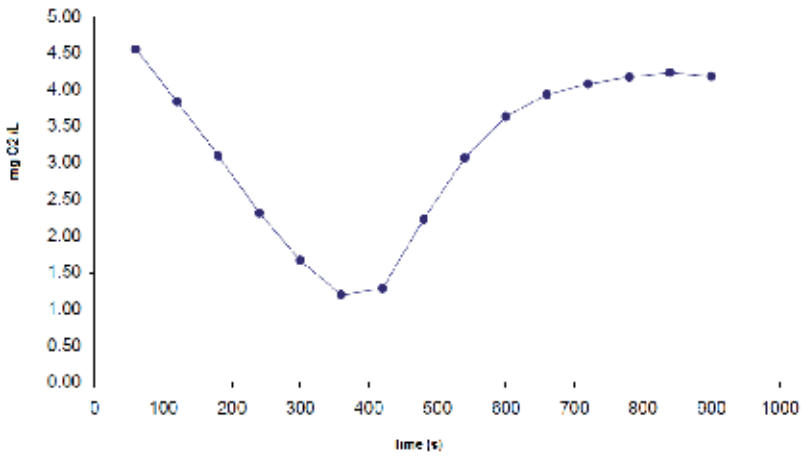

Figure 22. Typical response during the development of the dynamic technique of oxygen uptake

Q_{O2} value can be considered constant during the exponential phase of growth, since, during this stage, both the specific growth rate and yield of oxygen remained constant [25].

This dependency has been used by several authors [51, 53] for correlating the concentration of biomass and the rate of oxygen consumption by a constant parameter, at least during the exponential growth phase. For these experiments, we used a concentration we used a concentration of 140 g / l glucose and the flow of air not enriched with oxygen. The results of calculating the specific rate of oxygen consumption are shown in Table 8. The average value of Q_{O2}, was 159 mg O_2 / g of cells per h, with a standard deviation of 1,414. With this information it is possible to determine the amount of oxygen required for a given biomass concentration in a fermentation and establish the amount of oxygen to be provided shall in the airflow.

Molar fraction molar of Oxygen	$Q_{o2}X$	R^2	X (g cells)	Q_{O2} (mgO_2/g cell h)
0.209	0.01242	0.999	0.28	160
0.209	0.01443	0.997	0.33	158

Table 8. Calculation of the specific rate of oxygen consumption

To calculate the volumetric coefficient of oxygen transfer, we generated a graph (Figure 23) of dC / dt + $Q_{O2}X$ against C_L, where the slope of the line is -1/k_La and intercept and C_L. k_La value of the average between the two experiments was 53 with a standard deviation of 1.414 that show a good acceptation.

http://dx.doi.org/10.5772/53711

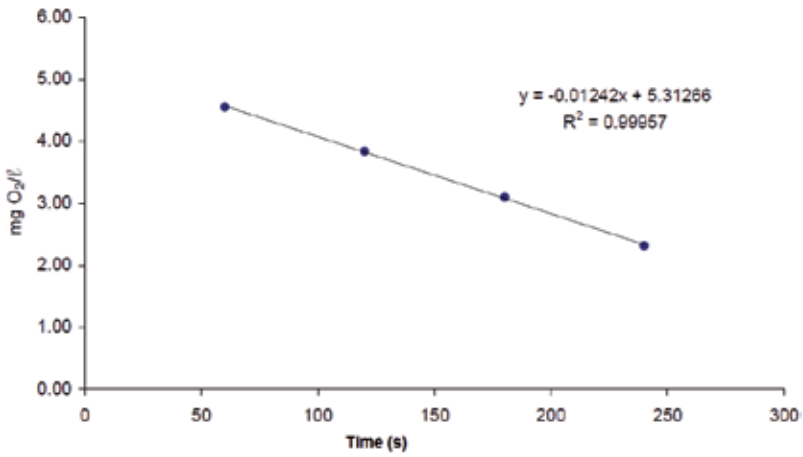

Figure 23. Calculation of the oxygen consumption rate using a direct method, the slope of the line is equal to-$Q_{O2}X$.

Comparing the values obtained with the technique k_La gas removal and direct measurement shows that the k_La value measured in the early hours of the fermentation is very similar to the calculated half fermentative bacteria free. Therefore, to calculate the oxygen transfer rate was determined considering constant since the viscosity during the fermentation does not vary significantly. The solubility of oxygen, may be affected if, therefore, the dissolved oxygen electrode was calibrated at the start of fermentation to a high saturation conditions chosen and the operation of the fermenter was held at the level of dissolved oxygen concentration corresponding.

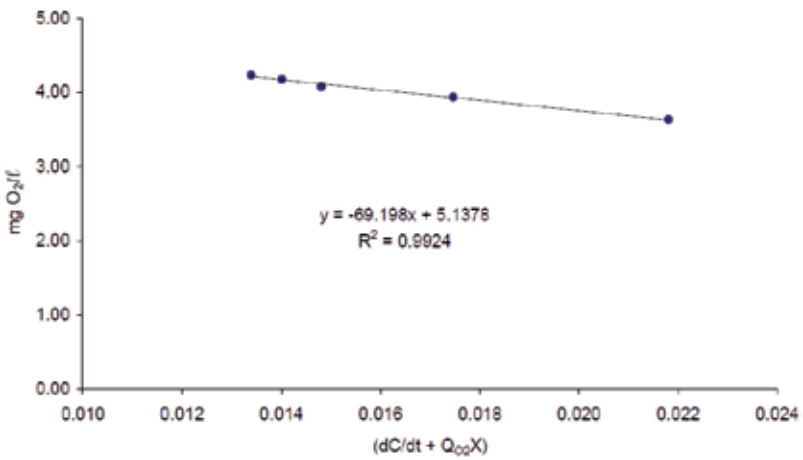

Figure 24. Calculating the volumetric coefficient of oxygen transfer, using a direct method, the slope of the line is equal to -1/k_La.

6.7. Oxygen enrichment experiments

In the case of the 21253 strain of *Corynebacterium glutamicum*, the course of the airlift fermentation in the bioreactor can be divided in 4 phases. The first phase is characterized by exponential growth of the organism (as long as there are no restrictions of any nutrient). The duration of this phase depends on the initial concentration of threonine in the fermentative medium. The depletion of threonine, the second phase begins. At this point lysine production begins, the dissolved oxygen concentration is increased (this implies a decrease in oxygen consumption at the maximum consumption of oxygen is given up to the point of exhaustion), the cell concentration continues to increase and eventually reaches a maximum of approximately 1.6 times the amount shown at the point of exhaustion of threonine 1.7 times [54].

The end of biomass production is due to the depletion of threonine [48] and begins the third phase, in which occurs the maintenance stage and the lysine production rate remains constant. In the fourth phase, the decrease in the production rate is remarkable, because it is not possible cell turnover by the lack of threonine, leucine and methionine, therefore, the biomass concentration decreases.

The yield of threonine should vary depending on the initial concentration of glucose due to growth inhibition that occurs in high concentrations. So far, in experiments with variable air flow, with an initial concentration average of 145 g / l of glucose values were $\mu = 0.331$ (h^{-1}) $Y_X / T_{hr} = 23.10$ (g biomass / g of threonine) and $q_{Thr} = 0.0143$ (g threonine / g biomass h) in the bioreactor airlift was obtained in a yield of 40.50 (g biomass / g of threonine). In both cases the oxygen limited the growth.

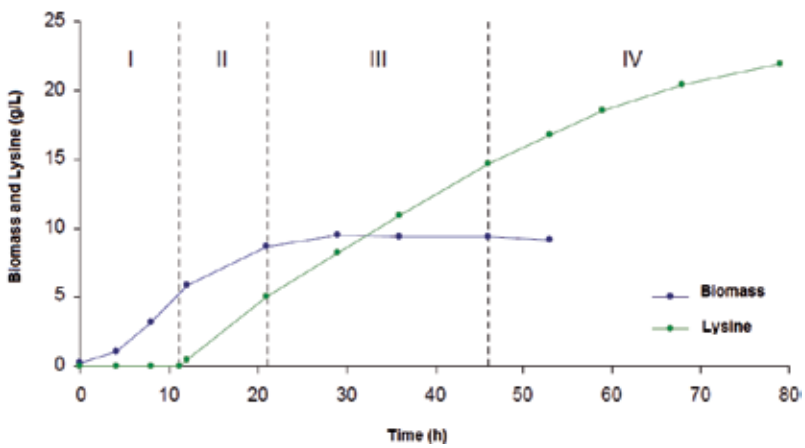

Figure 25. Stages in the lysine fermentation with *Corynebacterium glutamicum* ATCC 21253 in an airlift bioreactor.

To determine the parameters of the model without oxygen limitation were conducted two experiments with initial concentrations of 145 and 100 g / l glucose and 0.3 g / l of threonine. For fermentation with 145 g / l initial glucose, the maximum molar fraction of oxygen was 0.325 and 0.349 for fermentation with 102 g / l initial glucose. In Table 8 shows the final results of

http://dx.doi.org/10.5772/53711

the two fermentations. The kinetics of growth, product formation and substrate consumption can be observed in Figures 26 and 27.

Initial Glucose (g/l)	Biomass (g/l)	Lysine (g/l)	Residual glucose (g/l)	Process time(h)
145	9.26	21.96	55.0	79
102	11.36	21.9	13.2	52

Table 9. Final results of the fermentations with oxygen-enriched air at the same culture conditions.

The yield $Y_{X / Thr}$ between both experiments varied due to the inhibition caused by the initial concentration of glucose, for the experiment with 145 g / l initial glucose Y_X / T_{hr} = 30.13 (g biomass / g of threonine) and in which was used 102 g / l initial glucose was 37.1 (g biomass / g of threonine). This indicates that the amount of threonine to increase relative to the amount of glucose for an adequate quantity of biomass in each fermentation and minimize residual glucose concentrations.

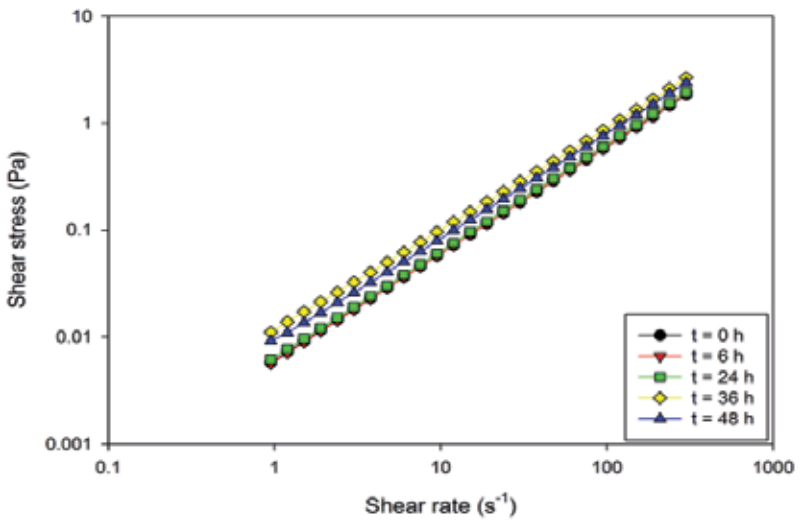

Figure 26. Rheological behaviour when the shear stress versus the shear stress change respect the times and with initial glucose concentration of 100 g / L.

6.8. Results of dynamic rheological behaviour of fermentation process

The model that best described the shear stress in function of the shear rate was

Biofluido behaviour in initial concentrations of 100 (Exp. 1), 140 (Exp. 2) and 180 g / l (Exp. 3) glucose and 1 vvm of air flow, presents different behaviour with respect to its apparent viscosity. Analyses were performed on a controlled stress rheometer with ARG2 type concentric cylinder geometry and with an observation range of 0.1 to 300 rps. The following figures

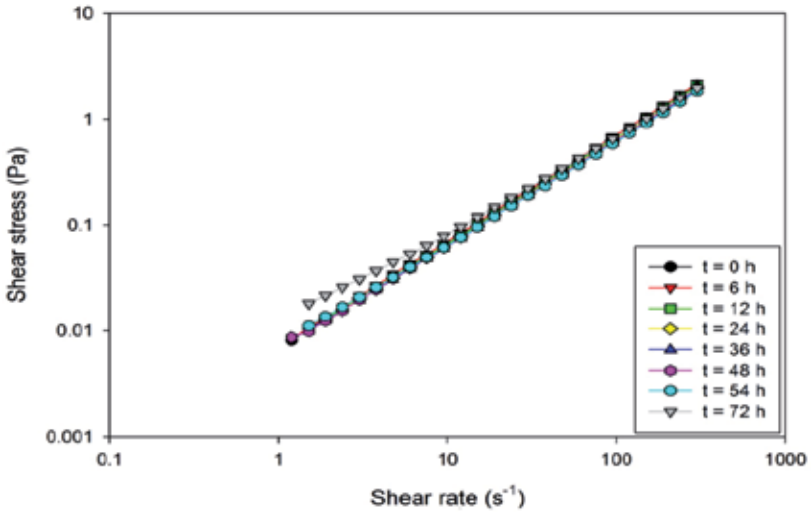

Figure 27. Rheological behaviour when the shear stress versus the shear stress change respect the times and with initial glucose concentration of 140 g / L.

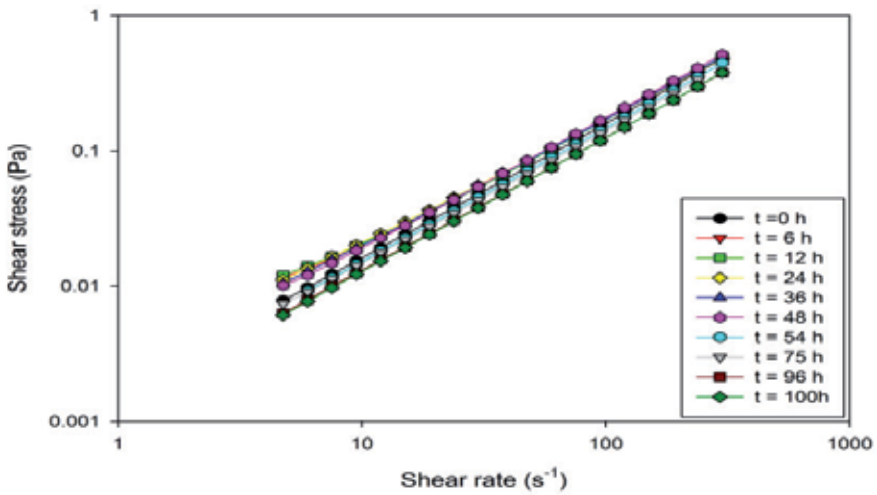

Figure 28. Rheological behaviour when the shear stress versus the shear stress change respect the times and with initial glucose concentration of 180 g / L.

show the behaviour of the shear stress on the shear rate and at different times to take sample of fermentation broth.

The rheological analysis was carried out both in increasing the shear rate and decreasing the same and no significant change was observed i.e. a curve passes over another, this being a feature of pseudoplastic fluids.

http://dx.doi.org/10.5772/53711

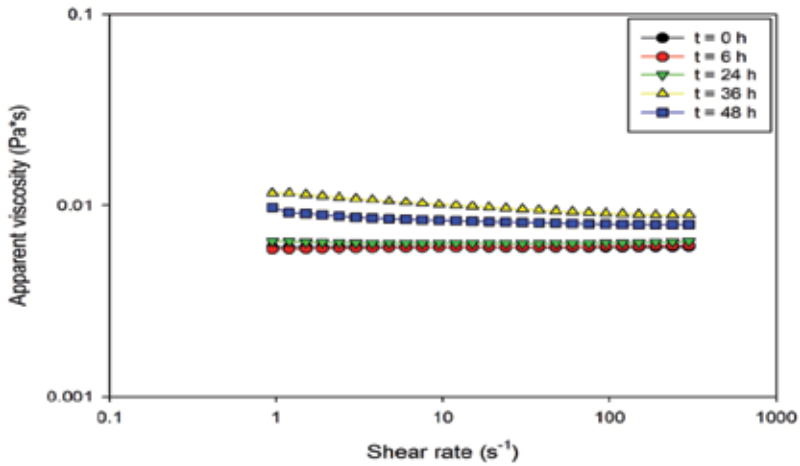

Figure 29. Apparent viscosity versus Shear rate at different times, with initial glucose 100 g / l.

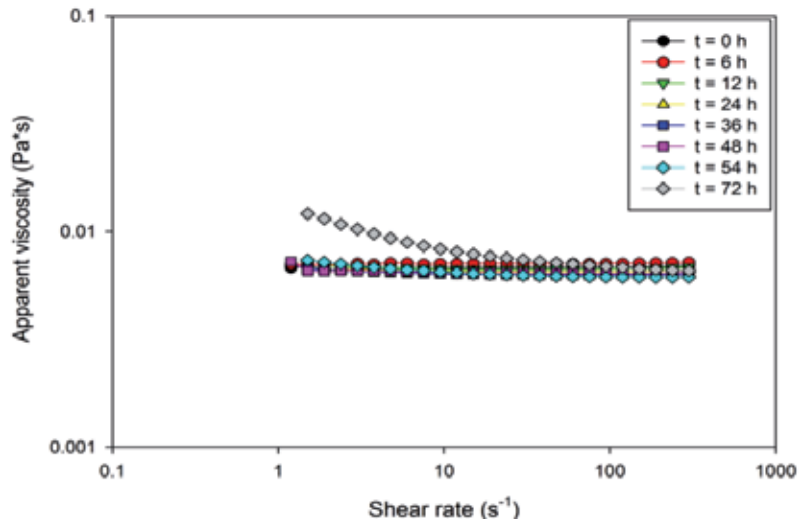

Figure 30. Apparent viscosity versus Shear rate at different times, with initial glucose 140 g / l.

It is evident that the maximum apparent viscosity is obtained between 24 and 36 hours the fermentation process, and subtly observed as the shear stress decreases with increasing the initial concentration of glucose in the medium (Figure 28) for the same shear rate.

The following graphs we can provide additional information to what occurs with respect to the apparent viscosity of the medium and in the same manner at different initial values of glucose.

Similarly one can conclude that the reduced carbon source leads to a decrease in apparent viscosity. The rheological parameters can be described in terms of the model of power law

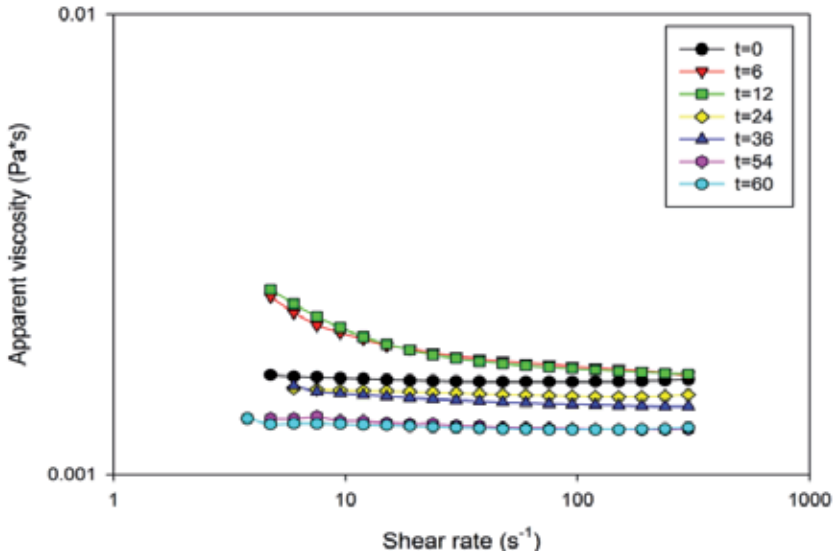

Figure 31. Apparent viscosity versus Shear rate at different times, with initial glucose 180 g / l.

fluids for pseudoplastic, which show a nonlinear relationship between shear stress (τ) and shear rate (γ).

$$\tau = k * \gamma^{n} \tag{28}$$

The constant k is a measure of the consistency of the fluid consistency index is called, and the exponent n is indicative of the deviation of the fluid flow about the behaviour and often called Newtonian behaviour index. For pseudoplastic fluids it holds that n <1, while n> 1 means a dilatant flow behaviour. The power law representing the Newtonian fluid when n = 1. To look more closely shown in the following tables the evolution of the flow rate and consistency index with respect to time and the initial glucose concentration.

Time (h)	K (Pa*s)	n
0	0.00509	1.0055
6	0.00580	1.0111
24	0.00599	1.0136
36	0.01010	0.9779
48	0.00827	0.9926

Table 10. Evolution of the flow and consistency index when were used the initial glucose 100 g / l.

http://dx.doi.org/10.5772/53711

Time (h)	K (Pa*s)	n
0	0.00640	1.0141
6	0.00682	1.0093
12	0.00320	1.0133
24	0.00625	1.0095
36	0.00620	1.0033
48	0.00626	1.0048
54	0.00638	0.9929
72	0.00864	0.9514

Table 11. Evolution of the flow and consistency index when were used the initial glucose 140 g / l.

Time (h)	K (Pa*s)	n
0	0.00157	1.0028
6	0.00209	0.9577
12	0.00202	0.9633
24	0.00227	0.9389
36	0.00212	0.9589
48	0.00199	0.9735
54	0.00152	0.9944
72	0.00149	0.9891
96	0.00133	0.9889
102	0.00126	0.9995

Table 12. Evolution of the flow and consistency indices when were used the initial glucose 180 g / l.

With these data it is easy to see how the cross breeding ground of a pseudoplastic to dilatant, if however it remains very close to the threshold of Newtonian behaviour.

Trying to interpret which may be the kinetic relationship with the following graphs are presented, which illustrates the behaviour of the indices of both flow and consistency.

Can be seen from the graph that during the growth phase of the microorganism fluid behaves as pseudoplastic and when it reaches the stationary phase changes dilatant. The interesting thing is that presented in this final stage the culture broth is such that can be separated easily from the microorganism and undesirable solids, providing the following extraction step of the lysine.

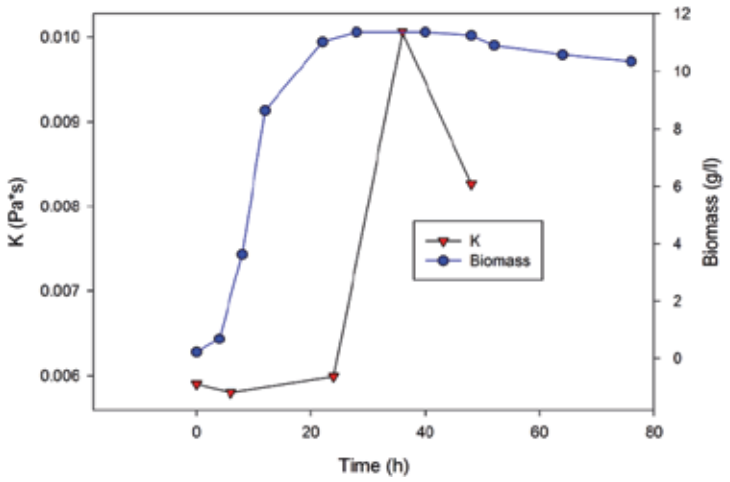

Figure 32. Behaviour consistency index (k) and biomass through fermentation time, using an initial glucose concentration of 100 g / l.

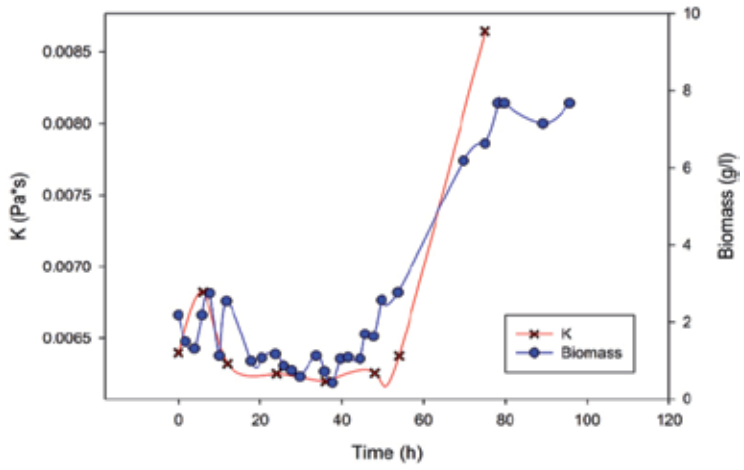

Figure 33. Behaviour consistency index (k) and biomass through fermentation time, using an initial glucose concentration of 140 g / l.

Shows the effect of glucose on the growth of the microorganism, presenting a catabolic repression, and which manifests itself in changing the rheology of the system. We can see that it is present a phase lag increased with increasing initial glucose concentration and the fluid is Newtonian behaviour.

When using the higher initial glucose concentration shows a higher apparent viscosity and thus shows the suppressive effect on growth of the microorganism, once decreases the concentration of glucose over time changes the rheological behaviour of the system, but with a low lysine production.

http://dx.doi.org/10.5772/53711

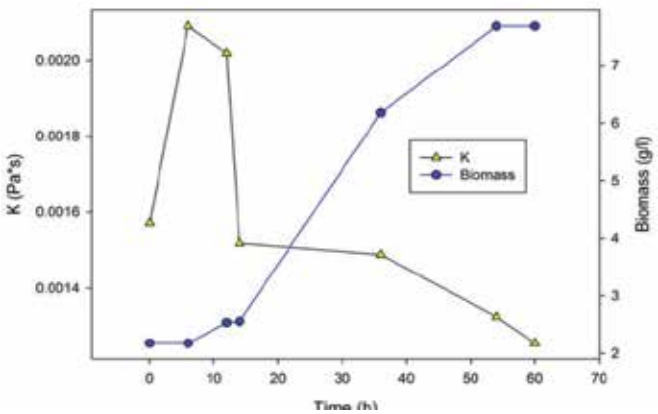

Figure 34. Behaviour consistency index (k) and biomass through fermentation time, using an initial glucose concentration of 180 g / l.

With this new information becomes more evident that the media has a high apparent viscosity at about 24 hours of fermentation, if this information is compared by the kinetics osmolality can be concluded to be due to agglomeration of biomass and the relative glucose in the medium.

Similarly one can conclude that the reduced carbon source leads to a decrease in apparent viscosity. The rheological parameters can be described in terms of the model of power law fluids for pseudoplastic, which show a nonlinear relationship between shear stress and shear rate.

7. Conclusions

Using the obtained relationships between amino acids were prepared culture media in which, L-threonine limits growth and the amino acids L-leucine and L-methionine is not present in excess, reducing the cost of these amino acid supplementation. The initial concentrations of threonine and glucose, affect the growth of the microorganism. The lack of threonine causes a cessation in growth and a subsequent decrease in biomass, while glucose depending on the initial concentration affects the specific growth rate and inhibits the formation of biomass. Thus the overall process yield is closely related to the initial concentrations of threonine and glucose airlift reactors in the oxygen transfer rate can be increased by increasing the air flow. In studies in the present study we observed that, the use of air flows greater than 1 vvm generate a large amount of foam, making it necessary to use defoamers, in decreasing the solubility of oxygen in the fermentative medium. To maintain adequate oxygenation, in combination with the advantages of the airlift bioreactor, resulted in a prolongation of the maintenance phase, whereby the lysine production rate was constant for a period of time greater than that reported in stirred tank bioreactors. In an airlift, using a minor amount of biomass can generate the same or greater amount of product, reducing the initial amount of amino acids, glucose and

ammonium sulfate. Growth models, product formation and substrate consumption correctly predict from the start of the production phase of lysine, to the end of phase constant production rate. It can therefore be used for the simulation of the process from the beginning of fermentation, until the end of the maintenance phase.

Author details

Ana María Mendoza Martínez[1] and Eleazar Máximo Escamilla Silva[2*]

*Address all correspondence to: eleazar@iqcelaya.itc.mx

1 Technological Institute of Madero City, Division of Graduate Studies and Research (ITCM), Madero, México

2 Chemical Departments, Technological Institute of Celaya, Celaya, México

References

[1] Chisti Y, Moo-Young, M. On the calculation of shear rate and apparent viscosity in airlift and bubble column bioreactors. Biotechnol Bioeng. 1989;34:1391-2.

[2] Merchuk JC, Ladwa, N., Cameron, A., Bulmer, M. and Pickett, A. Concentric-tube airlift reactors: Effects of geometrical design on performance. AIChE J. 1994;40:1105-17.

[3] Chisti Y. Pneumatically Agitated Bioreactors in Industrial and Environmental Bioprocessing: Hydrodynamics, Hydraulics and Transport Phenomena. American Society of Mechanical Engineers. 1998;51:33-112.

[4] Joshi J.B. RVV, Gharat S.D., Lee S.S.,. Sparged Loop Reactors. Canadian Journal of Chemical Engineering. 1990;68:705-41.

[5] Petersen E.E. MA. Hydrodynamic and Mass Transfer Characteristics of Three-Phase Gas-Lift Bioreactor Systems. Critical Review in Biotechnology. 2001;21:233-94.

[6] Merchuk JC, Ladwa N., Cameron A., Bulmer M., Pickett A.,. Concentric- Tube Airlift Reactors: Effects of Geometric Design on Performance. AIChE Journal. 1994;40:1105-17.

[7] Gravilescu M, Tudose, R.Z. Modelling mixing parameters in concentric-tube airlift bioreactors. Part I. Mixing time.. Bioprocess Eng,. 1999;20:423-8.

[8] Merchuk JC, Ladwa, N., Cameron, A., Bulmer, M., Pickett, A., Berzin, I. Liquid flow and mixing in concentric tube air-lift reactors. Chem Technol Biotech. 1996;66:172-82.

[9] Merchuk JC, Ladwa, N. Cameron, A. Bulmer, A., Pickett, M. and Berzin, I. Liquid flow and mixing in concentric tube air-lift reactors. Chem Technol Biotech. 1996;66:174-82.

[10] Barnea DT, Y. Fluid Mechanics. In: Cheremisinoff e, editor. Encyclopedia of Fluid Mechanics. Gulf, Houston, Tex., 1986. p. 403-91.

[11] Wallis GB, editor. One Dimensional Two-Phase Flow. New York, : McGraw-Hill; 1969.

[12] Wiswanathan K, editor. Flow Patterns in Bubble Columns. Gulf, Houston, Tex., 1969.

[13] Russell AB, Thomas, C.R., Lilly, M.D.. The influence of vessel height and top section size on the hydrodynamics characteristics of air lift fermenters. Biotechnol Bioeng,. 1994;43:69-76.

[14] Weiland P. Influence of draft tube diameter on operation behaviour of airlift loop reactors. Ger Chem Eng. 1984;7:374-85.

[15] Bello RAR, C.W., Moo-Young, M.. Prediction of the Volumetric Mass Transfer Coefficient in Pneumatic Contactors. Chem Eng Sci,. 1985;40:53-8.

[16] Chisti MY, Moo-Young, M. Airlift reactors: Characteristics, applications and design considerations. Chem Eng Commun,. 1987;60:195-242.

[17] Koide K, Horibe, K., Kawabata, H., Ito, S.,. Gas holdup and volumetric liquid-phase mass transfer coefficient in solid-suspended bubble column with draught tube. J Chem Eng Japan,. 1985;18:248-54.

[18] Merchuk JC, Bulmer, M. Ladwa, N.A., Pickett, M. and Cameron, A, editor. Bioreactor Fluid Dynamics London: Elsevier; 1988.

[19] Siegel MH, Robinson, C.W.,. Applications of airlift gas-liquid solid reactors in biotechnology. Chem Eng Sci 1992;47:3215-29.

[20] Halard B, Kawase, Y., Moo-Young, M.,. Mass transfer in a pilot plant scale airlift column with non-Newtonian fluids.. Ind Eng Chem Res,. 1989;28:243-5.

[21] Mc Manamey WJ, Wase, D.A.J.,. Relationship between the volumetric mass transfer coefficient and gas holdup in airlift fermentors.. Biotechnol Bioeng 1986;28:1446-8.

[22] Merchuk JC, Yunger, R.. The role of the gas—liquid separator of airlift reactors in the mixing process. Chem Eng Sci. 1990;45:2973-5.

[23] Escamilla S, E.M., Dendooven, L., Magaña, I.P., Parra, Saldivar, R., De la Torre, M.. Optimization of Gibberellic acid production by immobilized Gibberella fujikuroi mycelium in fluidized bioreactors. J Biotechnol,. 2000;76:147-55.

[24] Jones A, Pharis, R.P.,. Production of gibberellins and Bikaverin by cells of Gibberella fujikuroi immobilized in carrageenan.. J Ferment Technol,. 1987;65:717-22.

[25] Bailey JE, Ollis, D. F., editor. Transport phenomena in bioprocess systems, Design and analysis of biological reactors. Biochemical engineering fundamentals.. New York: Mc Graw-Hill, ; 1986.

[26] Escamilla S, E.S., Poggi, Varaldo, H., De la torre, Martínez, M., Sánchez, Cornejo, G., Dendooven, L. Selective production of Bikaverin in a fluidized biorreactor with immobilized Gibberella fujikuroi. World J of Microbiol Biotechnol 2001;17:469-74.

[27] Chisti MY, editor. Airlift bioreactor. London-New York: Elsevier Appl. Science, ; 1989.

[28] Quintero RR, editor. Ingeniería bioquímica, Teoría y aplicaciones.. México: Ed. Alambra. ; 1981.

[29] Brito-De la Fuente E, Nava, J.A., López, L.M., Medina, L, Ascanio, G., Tanguy, P.A. Process viscometry of complex fluids and suspensions with helical ribbon agitators. Can J Chem Eng,. 1998;76:689-95.

[30] Shah YT, Kelkar, B.G., Godbole, S.P., Deckwer, W.D.. Design parameters estimations for bubble column reactors.. AIChE J 1982;28:353-79.

[31] Godbole SP, Schumpe, A., Shah, T., Carr, N.L. Hydrodynamics and mass transfer in non-Newtonian solutions in a bubble column.. AIChE J,. 1984;30:213-20.

[32] Gavrilescu M. TRZ. Effects of Geometry on Gas Holdup. Bioprocess Engineering,. 1998;19:37-44.

[33] Abashar M.E. NU, Rouillard A.E., Judd R. Hydrodynamic flow regimes, gas holdup, and liquid circulation in airlift reactors. Ind Eng Chem Res,. 1998;37:1251-9.

[34] Chisti Y, Moo-Young, M. On the calculation of shear rate and apparent viscosity in airlift and bubble column bioreactors. Biotechnol Bioeng,. 1989;34:1391–2.

[35] Freitas C, Teixeira J.A. Hydrodynamic studies in an airlift reactor with an enlarged degassing zone. Bioprocess Engineering. 1998;18:267-79.

[36] Kawase Y. Liquid circulation in external-loop airlift bioreactors.. Biotechnol Bioeng 1989;35:540-6.

[37] Choi KH, Chisti, Y, Moo,Young, M.,. Comparative evaluation of hydrodynamic and gas–liquid mass transfer characteristics in bubble column and airlift slurry reactors. Biochem Eng J,. 1996;62:223-9.

[38] Tobajas M, García, Calvo, E.,. Comparison of experimental methods for determination of the volumetric mass transfer coefficient in fermentation processes. Heat Mass Transfer 2000;36:201-7.

[39] Barboza M, Zaiat M, Hokka, C.O.,. General relationship for volumetric oxygen transfer coefficient (kLa) prediction in tower bioreactors utilizing immobilized cells. Bioprocess Eng,. 2000;22:181-4.

[40] Schügerl KL, J. Oels, U. Bubble column bioreactors. Adv Biochem Eng. 1977;7:1-81.

[41] Akita K Y, F. Gas holdup and volumetric mass transfer coefficient in bubble columns. Effects of liquid properties. Ind Eng Chem Process Des Develop,. 1973;12:76-80.

[42] Prokop A, Janı´k, P., Sobotka, M., Krumphanzi, V.. Hydrodynamics, mass transfer, and yeast culture performance of a column bioreactor with ejector. Biotechnol Bioeng 1983;25:1140-60.

[43] Moo-Young M, Halard, B., Allen, D.G., Burrell, R., Kawase, Y.. Oxygen transfer to mycelial fermentation broths in an airlift fermentor.. Biotechnol Bioeng. 1987;30:746-53.

[44] Al-Masry W.A. DAR. Hydrodynamics and mass transfer studies in a pilot-plant air-lift reactor: non-Newtonian systems. Ind Eng Chem Res,. 1998;37:41-8.

[45] Metz B, Kossen, N.W.F., van Suijdam, J.C.,. The rheology of mould suspensions.. Adv Biochem Eng. 1979;11:103-56.

[46] (INEGI) INdEyG. Demanda de l-Lisina en el estado de Guanajuato. In: Estadistica, editor. Guanajuto2007.

[47] W. L, editor. Amino acids – technical production and use.1996.

[48] Toennies G. Role of aminoacids in postexponential growth.. J Bacteriol 1965;90:438-42.

[49] Van't Riet K. Review of measureing methods and results in nonviscous gas-liquid mass tranfer in stirred vessels. Ind Eng Chem Process Des Develop,. 1979;18:357-64.

[50] Keen RE, Spain, J.D., editor. Computer simulation in biology. Liss. USA: Wiley; 1992.

[51] Singh V. On-line measurements of oxygen uptake in cell culture usig the dynamic method.. Biotechnol Bioeng,. 1996;52:443-8.

[52] Ensari S, Lim, C. H.. Apparent effects of operational variables on the continuous culture of Corynebacterium lactofermentum.. Process Biochemistry 2003;38:1531-8.

[53] Pirt SJ, editor. Principles of microbe and cell cultivation.. London: Blackwell; 1975.

[54] Kiss RD. Metabolic activity control of the L-lisine fermentation by restrained growt fed-batch strategies. Cambridge, MA: M.I.T; 1991.

Chapter 16

Some Remarks on Modelling of Mass Transfer Kinetics During Rehydration of Dried Fruits and Vegetables

Krzysztof Górnicki, Agnieszka Kaleta, Radosław Winiczenko, Aneta Chojnacka and Monika Janaszek

Additional information is available at the end of the chapter

http://dx.doi.org/10.5772/54072

1. Introduction

Dehydration operations are important steps in the food processing industry. The basic objective in drying food products is the removal of water in the solids up to a certain level, at which microbial spoilage is minimized. The wide variety of dehydrated foods, which today are available to the consumer (dried fruits, dry mixes and soups, etc.) and the interesting concern for meeting quality specifications, emphasize the need for a thorough understanding of the operation [1].

Dehydrated products can be used in many processed or ready-to-eat foods in place of fresh foods due to several advantages such as convenience in transportation, storage, preparation and use. Dehydrated products need to be rehydrated before consumption or further processing [2]. Rehydration is a process of moistening dry material [3]. Rehydration is usually carried out by soaking the dry material in large amounts of water, although, instead of this, some authors have used air with high relative humidity, either statically or in a drying chamber with air circulation [4].

Three main processes take place simultaneously during rehydration: the imbibition of water into the dried material and the swelling and the leaching of solubles [5]. It is a very complex phenomenon that involves different physical mechanisms such as water imbibition, internal diffusion, convection at the surface and within large open pores, and relaxation of the solid

matrix. Capillary imbibition is very important during the early stages, leading to an almost instantaneous uptake of water. Tension effects between the liquid and the solid matrix may also be relevant [6]. In the rehydration process, two main crosscurrent mass fluxes are involved, a water flux from the rehydrating solution to the product, and a flux of solutes (sugars, acids, minerals, vitamins) from the food product to the solution, and the kinetics depends on the immersion medium [2,6,7].

Rehydration is influenced by several factors, grouped as intrinsic factors (product chemical composition, pre-drying treatment, drying techniques and conditions, post-drying procedure, etc.) and extrinsic factors (composition of immersion media, temperature, hydrodynamic conditions) [8]. Some of these factors induce changes in the structure and composition of the plant tissue, which results in the impairment of the reconstitution properties [9]. Therefore equilibrium moisture content at saturation does not reach the moisture content of the raw materials prior to dehydration, indicating that the dehydration procedure is irreversible [1]. Physical and chemical changes that take place during drying affect the quality of the dehydrated product, and by a simple addition of water, the properties of the raw material cannot be restored [10]. Rehydration cannot be simply treated as the reverse process to dehydration [11]. Hence, rehydration can be considered as a measure of the injuries to the material caused by drying and treatments preceding dehydration [12].

Rehydration characteristics are therefore employed as a parameter to determine quality [5]. Optimal reconstitution can be achieved by controlling the drying process and adjustment of the rehydration conditions [13]. The knowledge of the rehydration kinetics of dried products is important to optimise processes from a quality viewpoint since rehydration is a key quality aspect for those dried products that have to be reconstituted before their consumption [14]. The most important aspect of rehydration technology is the mathematical modelling of the rehydration process. Its purpose is to allow design engineers to choose the most suitable operating conditions. The principle of modelling is based on having a set of mathematical equations that can adequately describe the system. The solution of these equations must allow prediction of the process parameters as a function of time. Therefore the use of a simulation model is a valuable tool for prediction of performance of rehydration systems [15].

Many models have been investigated to predict migration of water in foods and, for example, relate moisture content to time. The models are theoretical, empirical, semi-empirical, exponential, and non-exponential ones, and despite the widespread use of computers and their associated softwares, empirical equations are still widely used in view of their simplicity and ease of computations [16]. Theoretical models, however, are based on the general theory of mass and heat transfer laws. They take into account fundamentals of the rehydration process and their parameters have physical meaning. Therefore, theoretical models can give an explanation of the phenomena occurring during rehydration. On the other hand however these models are more difficult in application compared to other mentioned models [15].

The aim of the present chapter was to discuss the suitability of rehydration models and indices for describing mass transfer kinetics during rehydration of dried fruits and vegetables.

http://dx.doi.org/10.5772/54072

2. Mathematical description of rehydration process

2.1. Rehydration indices

There is a large number of research reports in which authors measure the ability of dry material to rehydrate. Results of experiments are expressed in variable ways and quite often the same index is differently named. The most common index used to express rehydration of dry plant tissue is rehydration ratio defined as follows:

$$\text{Rehydration ratio (RR)} = \frac{\text{mass after rehydration}}{\text{mass before rehydration}} \tag{1}$$

Rehydration ratio was used to express the rehydration of the dried products such as carrots [17], mushrooms [18], pears [19], potatoes [20], and coriander leaves [21]. RR is sometimes named rehydration capacity [22,23]. To facilitate a mathematical description of the rehydration phenomenon, the experimental reconstitution data were correlated with time according to a second order polynomial relation [20,24]:

$$\text{RR} = \text{a}\,t^2 + \text{b}\,t + \text{c} \tag{2}$$

During rehydration together with water acquisition, soluble compounds can be leached. Observed increase in mass is a net result of those processes, and practically gives no information about the amount of absorbed water or the mass of lost solubles. Lewicki in [12] proposed three indices to estimate the rehydration characteristics of dried food. These are the water absorption capacity (WAC), the dry matter holding capacity (DHC), and the rehydration ability (RA).

The water absorption capacity gives information about the ability of the material to absorb water with respect to the water loss during dehydration and varies in the range $0 \le \text{WAC} \le 1$. The more the water absorption capacity is lost during dehydration the smaller the index. Water absorption capacity is defined by:

$$\text{WAC} = \frac{\text{mass of water absorbed during rehydration}}{\text{mass of water removed during drying}} \tag{3}$$

and can be calculated from the formula:

$$\text{WAC} = \frac{m_r(1-s_r) - m_d(1-s_d)}{m_o(1-s_o) - m_d(1-s_d)} \tag{4}$$

The dry matter holding capacity is a measurement of the ability of the material to retain soluble solids after rehydration and provides information on the extent of tissue damage and its

permeability to solutes. The more the tissue is damaged the smaller the index. The dry matter holding capacity varies in the range 0≤DHC≤1. The index is calculated by:

$$\mathrm{DHC} = \frac{m_r s_r}{m_d s_d} \tag{5}$$

The rehydration ability measures the ability of the dried product to rehydrate and shows the total damage of the tissue by drying and soaking processes. The index varies in the range 0≤RA≤1. The more the tissue is damaged the smaller is the index. The rehydration ability is given by:

$$\mathrm{RA} = \mathrm{WAC} \cdot \mathrm{DHC} \tag{6}$$

The indices proposed by Lewicki in [12] were employed to express the rehydration of the dried products such as apples [25,26], *Boletus edulis* mushrooms [4], chestnuts [5], and *Morchella esculenta* (morel) [14].

2.2. Mathematical models

The analysis of the rehydration kinetics can be very useful for optimizing process condition. Many theoretical and empirical approaches have been employed and in some cases empirical models were preferred because of their relative ease of use.

2.2.1. Empirical and semi-empirical models

Among the empirical models, the one proposed by Peleg in [27] is a two parameter, non-exponential equation to describe water transport from the surface to the interior of the solids. The model proposed by Peleg in [27] is as follows:

$$M = M_0 \pm \frac{\mathrm{t}}{\mathrm{A}_1 + \mathrm{A}_2 \mathrm{t}} \tag{7}$$

where A_1 is the Peleg rate constant (s) and A_2 is the Peleg capacity constant.

In Eq. (7) "±" becomes "+" if the process is absorption or adsorption and "–" if the process is drying or desorption.

The rate of sorption can be obtained from the first derivative of the Peleg equation:

$$\frac{\mathrm{dM}}{\mathrm{d}t} = \pm \frac{\mathrm{A}_1}{(\mathrm{A}_1 + \mathrm{A}_2 t)^2} \tag{8}$$

http://dx.doi.org/10.5772/54072

and at the very beginning (t=0):

$$\left.\frac{\mathrm{d}M}{\mathrm{d}t}\right|_{t=0} = \pm\frac{1}{\mathrm{A}_1} \tag{9}$$

If time of the process is long enough ($t\rightarrow\infty$), the equilibrium moisture content can be calculated by:

$$M_e = M_0 \pm \frac{1}{\mathrm{A}_2} \tag{10}$$

Linearization of Eq. (7) gives:

$$\frac{t}{M - M_0} = \pm(\mathrm{A}_1 + \mathrm{A}_2\, t) \tag{11}$$

allowing for the determination of A_1 and A_2 values by linear regression of experimental data.

Some of the authors correlated A_1 value by means of exponential equation according to an Arrhenius type relationship [4,5]:

$$\mathrm{A}_1 = \mathrm{A}_0 \exp(-\frac{\mathrm{E}_\mathrm{a}}{\mathrm{R}T}) \tag{12}$$

where A_0 is the constant.

The Peleg [27] model has been widely used due to its simplicity, and has been reported to adequately describe the rehydration of various dried products such as apples [28], bambara [29], candied mango [7], carrots [30], chickpea [31], red kidney beans [32], and wheat [33]. Bilbao-Sáinz et al. in [34] applied Peleg model to volume recovery data assuming the following form of equation:

$$V = V_0 + \frac{t}{\mathrm{A}_1 + \mathrm{A}_2\, t} \tag{13}$$

Marqes et al. in [35] modified the Peleg model obtaining the following form of equation:

$$\frac{m(t)}{m_d} = \left[\left(\frac{m}{m_d}\right)_{t\rightarrow\infty} - \frac{1}{\mathrm{A}_2}\right] + \frac{t}{\mathrm{A}_1 + \mathrm{A}_2\, t} \tag{14}$$

and applied it for modelling of dried tropical fruits rehydration.

Pilosof et al. in [36] proposed empirical, two parameter, non-exponential equation to describe kinetics of water uptake to food powders. The Pilosof-Boquet-Batholomai model [36] is as follows:

$$M = M_0 \pm \frac{A_3 t}{A_4 + t} \tag{15}$$

where A_3 and A_4 are constants.

If time of the process is long enough ($t \to \infty$), the equilibrium moisture content can be calculated by:

$$M_e = M_0 + A_3 \tag{16}$$

Linearization of Eq. (15) gives:

$$\frac{t}{M - M_0} = \frac{1}{A_3} t + \frac{A_4}{A_3} \tag{17}$$

It can be deducted from Eq. (11) (for absorption or adsorption) and (17) that $A_1=A_4/A_3$ and $A_2=1/A_3$.

The Pilosof-Boquet-Batholomai model [36] has been used by Sopade et al. in [16] for describing water absorption of wheat starch, whey protein concentrate, and whey protein isolate.

Singh and Kulshrestha in [37] proposed empirical, two parameter, non-exponential equation to describe kinetics of water sorption by soybean and pigeonpie grains. The model developed by Singh and Kulshrestha [37] is as follows:

$$M = M_0 \pm \frac{A_5 A_6 t}{A_6 t + 1} \tag{18}$$

where A_5 and A_6 are constants.

If time of the process is long enough ($t \to \infty$), the equilibrium moisture content can be calculated by:

$$M_e = M_0 + A_5 \tag{19}$$

Linearization of Eq. (18) gives:

http://dx.doi.org/10.5772/54072

$$\frac{t}{M - M_0} = \frac{1}{A_5} t + \frac{1}{A_5 A_6} \tag{20}$$

It can be deducted from Eq. (11) (for absorption or adsorption), (17) and (20) that $A_1=A_4/A_3=1/(A_5A_6)$, $A_2=1/A_3=1/A_5$ and therefore $A_3=A_5$ and $A_4=1/A_6$.

The Singh-Kulshrestha [37] model has been used in [16] for describing water absorption of wheat starch, whey protein concentrate, and whey protein isolate.

Wesołowski in [38] developed the following empirical, three parameter, exponential equation to describe rehydration of apples:

$$\frac{m(t)}{m_d} = A(B - e^{-Ct}) \tag{21}$$

where A, B, and C are constants.

For a long enough time, equilibrium value is given by:

$$\left(\frac{m(t)}{m_d}\right)_{t\to\infty} = A \cdot B \tag{22}$$

Equation (21) was also verified when mass has been replaced with moisture content [38,39].

The model proposed by Witrowa-Rajchert in [40] is as follows:

$$\frac{m(t)}{m_d} = A + B\left(1 - \frac{1}{1 + BCt}\right) \tag{23}$$

where A, B, and C are constants.

It is an empirical, three parameter, non-exponential model. For a long enough time, equilibrium value is given by:

$$\left(\frac{m(t)}{m_d}\right)_{t\to\infty} = A + B \tag{24}$$

Equation (23) was also verified for the increase of moisture content and volume. Discussed model has been applied for describing the rehydration of apples, carrots, parsleys, potatoes, and pumpkins [40,41].

The probabilistic Weibull model was described first by Dr. Walodi Weibull to represent the distribution of the breaking strength of materials and later to describe the behaviour of systems or events that have some degree of variability [14]. For drying and rehydration processes a two parameter, exponential equation based on the Weibull model is as follows:

$$\frac{M - M_0}{M_e - M_0} = 1 - \exp\left[-\left(\frac{t}{\alpha}\right)^{\beta}\right] \tag{25}$$

where α is the scale parameter (s) and β is the dimensionless shape parameter. The scale parameter α is a kinetic coefficient. It defines the rate of the moisture uptake process and represents the time needed to accomplish approximately 63% of the moisture uptake process. Different values of α lead to a very different curves: for instance, the higher its value, the slower the process at short times. The shape parameter is a behaviour index, which depends on the process mechanism [42]. Although the Weibull model is empirical one, it was demonstrated recently that the Weibull distribustion has a solid theoretical basis, stemming from physical principles [6].

The Weibull model was found to yield good results in the description of rehydration of a variety of dried foods such as *Boletus edulis* mushrooms [4], *Morchella esculenta* (morel) [14], oranges [43], and ready-to-eat breakfast cereal [42]. Cunha et al. in [44] correlated the scale parameter α value by means of exponential equation according to an Arrhenius type relationship (Eq. (12)).

Marques et al. in [35] modified the Weibull model obtaining the following form of equation:

$$\frac{m(t)}{m_d} = \left(\frac{m(t)}{m_d}\right)_{t\to\infty} + \left[1 - \left(\frac{m(t)}{m_d}\right)_{t\to\infty}\right]\exp\left[-\left(\frac{t}{d}\right)^{\beta}\right] \tag{26}$$

and applied it for modelling of dried tropical fruits rehydration.

Marabi et al. in [6] modified the Weibull model obtaining the following form of equation:

$$\frac{M - M_0}{M_e - M_0} = 1 - \exp\left[-\left(\frac{t}{\alpha'}\right)^{\beta}\right] \tag{27}$$

and

$$\alpha' = \frac{L^2}{D_{calc}} \tag{28}$$

http://dx.doi.org/10.5772/54072

$$D_{calc} = D_{eff} \cdot R_g \tag{29}$$

where R_g is the constant and is a characteristic of the geometry utilized. Marabi et al. in [6] applied Eq. (27) for modelling rehydration of carrots.

The rate of rehydration can be obtained from the semi-empirical first order kinetic model [45]:

$$\frac{dM}{dt} = -k(M - M_e) \tag{30}$$

At zero time M is equal M_0 the moisture content of the dry material, and Eq. (30) is integrated to give the following expression:

$$\frac{M - M_e}{M_0 - M_e} = \exp(-kt) \tag{31}$$

The Arrhenius equation (Eq. (12)) can be employed to describe the temperature dependence of rehydration rate constant k [45-47].

The first order kinetic model has been reported to adequately describe the rehydration of various dried products such as apples, potatoes, carrots, bananas, pepper, garlic, mushrooms, onion, leeks, peas, corn, pumpkins, and tomatoes [1], chickpeas [46], soybeans [47], and tamarind seeds [45].

Misra and Brooker in [48] developed the following empirical, exponential model

$$\frac{M - M_e}{M_0 - M_e} = \exp(-kt^n) \tag{32}$$

(where n is constant) and applied it for modelling the rewetting of dried corn. Equation (32) has been successfully used by Shatadal et al. in [49] to describe the rewetting of dried canola.

Mizuma et al. in [50] modified the first order kinetic model obtaining two form of equations:

$$\frac{dx}{dt} = k(1 - x)^n \tag{33}$$

and

$$\frac{dx}{dt} = k(1 - x)^n(x + a) \tag{34}$$

$$x = \frac{m(t) - m_d}{m_e - m_d} \tag{35}$$

(where a and n are constants) and applied them for modelling of water absorption rate of rice.

2.2.2. Theoretical models

Studies revealed that rehydration is a multifaceted mass transfer process, and uptake is governed by several mechanisms of liquid imbibition in porous media. Rehydration of dried plant tissues is a very complex phenomenon involving different transport mechanisms, including molecular diffusion, convection, hydraulic flow, and capillary flow. One or more mechanisms may occur simultaneously during water or other medium imbibition into a dry food sample [51].

Theoretical models take into account the process basic physical principles. Physically based modelling requires in depth process understanding. As evaluation of some physical properties and complex process interrelationships are very difficult to quantify, the efficiency of these models is typically limited to approximations [51].

Theoretical models describing water absorption in foods are mostly based on the diffusion of water through a porous medium, therefore they assume that liquid water sorption by plant tissue is a diffusion controlled process. If water transport is assumed to take place by diffusion, then the process of rehydration can be described using Fick's second law:

$$\frac{\partial M}{\partial t} = \nabla(D \nabla M) \tag{36}$$

In order to solve the differential equation (36) the following simplifying assumptions were adopted mostly in the literature:

- the initial moisture content in the solid is uniform (the initial condition):

$$M\big|_{t=0} = M_0 \tag{37}$$

- the water diffusion coefficient is constant,
- moisture gradient at the centre of the solid is zero,
- the sample geometry remains constant during the rehydration process,
- external resistance to heat and mass transfer is negligible, i.e. the sample surface attains saturation (equilibrium) moisture content instantaneously upon immersion in absorption media (the boundary condition of the first kind):

http://dx.doi.org/10.5772/54072

$$M\big|_A = M_e \tag{38}$$

- heat transfer is more rapid than mass transfer, so that the process can be assumed isothermal.

Biological materials before drying are cut into small pieces, mostly slices or cubes. They can also be spherical in shape. Therefore Eq. (36) applied to the description of the rehydration of dried material (with the simplifying assumptions mentioned above) takes the following form:

for an infinite plane (slices):

$$\frac{\partial M}{\partial t} = D\frac{\partial^2 M}{\partial x^2} \tag{39}$$

for a finite cylinder (slices):

$$\frac{\partial M}{\partial t} = D\left(\frac{\partial^2 M}{\partial r^2} + \frac{1}{r}\frac{\partial M}{\partial r} + \frac{\partial^2 M}{\partial z^2}\right) \qquad \left(t > 0; 0 < r < R_C;\ -h < z < +h\right) \tag{40}$$

for a cube:

$$\frac{\partial M}{\partial t} = D\left(\frac{\partial^2 M}{\partial x^2} + \frac{\partial^2 M}{\partial y^2} + \frac{\partial^2 M}{\partial z^2}\right) \qquad (t > 0;\ -R_c < x < +R_c;\ -R_c < y < +R_c;\ -R_c < z < +R_c) \tag{41}$$

for a sphere:

$$\frac{\partial M}{\partial t} = D\left(\frac{\partial^2 M}{\partial r^2} + \frac{2}{r}\frac{\partial M}{\partial r}\right) \qquad (t > 0;\ 0 < r < +R_c) \tag{42}$$

($t>0$; $0<r<+R_c$) The initial conditions (Eq. (37)) are following:

for an infinite plane

$$M(x,0) = M_0 = \text{const} \tag{43}$$

for a finite cylinder

$$M\left(r,z,0\right) = M_0 = \text{ const} \tag{44}$$

for a cube

$$M\left(x,y,z,0\right) = M_0 = \text{ const} \tag{45}$$

for a sphere

$$M\left(r,0\right) = M_0 = \text{ const} \tag{46}$$

The boundary conditions of the first kind (Eq. (38)) take the following form:

for an infinite plane

$$M\left(\pm R_c,t\right) = M_e = \text{ const} \tag{47}$$

for a finite cylinder

$$M\left(R_c,z,t\right) = M_e = \text{ const} \tag{48}$$

$$\frac{\partial M(0,z,t)}{\partial r} = 0,\ M\left(0,z,t\right) \neq \infty \tag{49}$$

$$M\left(r,h,t\right) = M_e = \text{ const} \tag{50}$$

$$\frac{\partial M(r,0,t)}{\partial z} = 0 \tag{51}$$

for a cube

$$M\left(\pm R_c,\ y,\ z,\ t\right) = M_e = \text{ const} \tag{52}$$

$$M\left(x,\ \pm R_c,\ z,\ t\right) = M_e = \text{ const} \tag{53}$$

$$M\left(x,\ y,\ \pm R_c,\ t\right) = M_e = \text{ const} \tag{54}$$

for a sphere

http://dx.doi.org/10.5772/54072

$$M\left(R_c,\ t\right) = M_e = \text{ const} \tag{55}$$

$$\frac{\partial M(0,t)}{\partial r} = 0 \tag{56}$$

An analytical solution of: (i) Eq. (39) at the initial and boundary conditions given by Eqs. (43) and (47), (ii) Eq. (40) at the initial and boundary conditions given by Eqs. (44) and (48)-(51), (iii) Eq. (41) at the initial and boundary conditions given by Eqs. (45) and (52)-(54), and (iv) Eq. (42) at the initial and boundary conditions given by Eqs. (46) and (55)-(56) with respect to mean moisture content as a function of time, take the following form [52]:

for an infinite plane

$$\frac{M(t)-M_e}{M_0-M_e} = \frac{8}{\pi^2}\sum_{\mathrm{n}=0}^{\infty}\frac{1}{(2\mathrm{n}+1)^2}\exp\left[-\frac{\pi^2(2\mathrm{n}+1)^2}{4}\cdot\frac{Dt}{R_c^2}\right] \tag{57}$$

for a finite cylinder

$$\frac{M(t)-M_e}{M_0-M_e} = \frac{32}{\pi^2}\sum_{\mathrm{n}=1}^{\infty}\frac{1}{\mu_{\mathrm{n}}^2}\exp\left(-\frac{\mu_{\mathrm{n}}^2 Dt}{R_c^2}\right)\sum_{\mathrm{m}=0}^{\infty}\frac{1}{(2\mathrm{m}+1)^2}\exp\left[-\frac{\pi^2(2\mathrm{m}+1)^2}{4}\cdot\frac{Dt}{h^2}\right] \tag{58}$$

where μ_{n} are the roots of the Bessel equation of the first kind of zero order

$$J_0\left(\mu_{\mathrm{n}}\right) = 0 \tag{59}$$

for a cube

$$\frac{M(t)-M_e}{M_0-M_e} = \frac{512}{\pi^6}\sum_{\mathrm{n}=0}^{\infty}\sum_{\mathrm{m}=0}^{\infty}\sum_{\mathrm{p}=0}^{\infty}\frac{1}{(2\mathrm{n}+1)(2\mathrm{m}+1)(2\mathrm{p}+1)}\exp\left\{-\frac{\pi^2}{4}\left[(2\mathrm{n}+1)^2+(2\mathrm{m}+1)^2+(2\mathrm{p}+1)^2\right]\frac{Dt}{R_c^2}\right\} \tag{60}$$

for a sphere

$$\frac{M(t)-M_e}{M_0-M_e} = \frac{6}{\pi^2}\sum_{\mathrm{n}=1}^{\infty}\frac{1}{\mathrm{n}^2}\exp\left(-\frac{\mathrm{n}^2\pi^2 Dt}{R_c^2}\right) \tag{61}$$

In order to take into account the necessary number of terms of the series, thirty terms are routinely used in the calculations [4,14], although Sanjuán et al. [11] stated that taking 6-7 terms

can be enough. The moisture diffusion coefficient *D*, also termed effective diffusivity, is an apparent value that comprises all the factors involved in the process. This coefficient is often assumed to be temperature-dependent according to an Arrhenius type relationship (Eq. (12)) [11,53,54]. Fick's equation was also solved considering that the effective diffusivity is moisture-dependent [4]. In that case, the diffusion model cannot be solved analytically. The finite element method (FEM) was used in order to identify the parameters. The relationship between the moisture diffusion coefficient and the moisture content considered was:

$$D = \exp\left(\mathrm{a} + \mathrm{b}\, M\right) \tag{62}$$

where a and b are the parameters.

Equation (57) has been reported to adequately describe the rehydration of slices of various dried products such as *Boletus edulis* mushrooms [4], broccoli stems [11], carrots [2,8], and *Morchella esculenta* (morel) [14]. Bilbao-Sáinz et al. in [34] stated that Fick's equation of diffusion (Eq. (58)) was not suitable to model the sorption data of apples (var. Granny Smith). Equation (61) was found to yield good results in the description of rehydration of dried amaranth grains [53], dried date palm fruits [54], and dried soybeans [47].

The mathematical model of rehydration developed by Górnicki in [55] is based on the general theory of mass and heat transfer laws. The model assumes that mass transfer in plant tissue is a diffusion controlled process. The model allows for determination of temperature distribution and concentration distribution of both dry matter and water in time and space inside rehydrated material. The developed model takes into account changeable boundary conditions and changes of material geometry. Six methods of determination of mass transfer coefficients were proposed. The proposed model has been reported to adequately describe the rehydration of slices and cubes both parsley and apples (var. Idared).

Few researches recently embarked on a new approach, which is motivated by the recognition that rehydration of dry food particulates could not be explained and/or modeled solely by a Fickian mechanism. Mechanisms, such as water imbibition, capillarity and flow in porous media, were suggested and are considered relevant for describing the ingress of water into the dried food particulates [51].

Lee et al. in [56] described the rehydration process of freeze-dried fruits (avocado, kiwi fruit, apple, banana, and potato) based on capillary movement of water in the fruit samples. The movement of water through the dried material was assumed to follow capillary motion as described by the Lucas-Washburn equation. The following assumptions were made: (i) the food structure may be simplified as to consist of multi-individual pores, (ii) one dimensional flow, (iii) steady state flow, (iv) fully developed flow, (v) Newtonian fluid with negligible inertia effects, and the following equation was obtained:

$$\frac{\mathrm{d}\, h(t)}{\mathrm{d}\, t} = \frac{k_1}{h(t)} - k_2 \tag{63}$$

http://dx.doi.org/10.5772/54072

where

$$k_1 = \frac{r\gamma \cos\Theta}{4\eta} \quad \text{and} \quad k_2 = \frac{r^2 g\rho}{8\eta} \tag{64}$$

Lee et al. in [56] stated that the parameter k_1 (m^2s^{-1}) will be the dominant factor of the initial rate of rehydration while the parameter k_2 ($m\ s^{-1}$) will become significant during the final state as rehydration approaches equilibrium.

Other researches started to apply the capillary imbibition theory to model the rehydration of foods. Weerts et al. in [57-59] utilized a capillary flow approach to model the temperature and anisotropy effects during the rehydration of tea leafs. Saguy et al. in [60] studied the kinetics of water uptake of freeze-dried carrots and stated that water imbibition followed the general Lucas-Washburn equation. Utilizing different liquid media highlighted, however, the need for model improvement overcoming several discrepancies mainly related to the utilization of a simple "effective" cylindrical capillary and a constant contact angle.

Consequently, due to the complexity of water transport into porous media, the need for further research necessary for the development of the theory and model for the application of capillary imbibition is emphasized [60]. Saguy et al. in [51] elaborated a list of recommended future studies in this field.

3. Discussion of some results of modelling of mass transfer kinetics during rehydration of dried apple cubes

The authors' own results of research are presented in this chapter.

Ligol variety apples used in this study were acquired in local market. The apples were washed in running tap water, hand peeled and the seeds were removed, and then cut into 10 mm cubes thickness using specially cutting machine. Samples were dried on the same day. The fluidized bed drying was carried out using the laboratory dryer constructed in the Department of Fundamental Engineering, Faculty of Production Engineering, Warsaw University of Life Sciences, Warsaw, Poland. The drying chamber consists of a column, which is a Plexiglas cylinder of 12 cm in diameter and 180 cm in height. Drying conditions were 60°C of temperature and 6 m s^{-1} of air velocity. Prior to placing the sample in the drying chamber, the system was run for about one hour to obtain steady conditions. Once the air temperature and fluidization velocity had stabilized, the sample was put into the fluidized bed dryer and the drying begins. Drying was continued until there was no weight change. Experiments were replicated three times. Dried apple cubes were stored in airtight glass containers after dehydration until they were used in the rehydration experiments.

The dried apple sample was rehydrated by immersion in distilled water at 20°C. The ratio of the volume of apple cubes to that of the medium (water) was maintained at 1:25. An initial

amount of 10 g of dried apples was used in each trial. The following measurements were replicated three times under laboratory conditions: (i) dry matter of solid changes of the examined samples during rehydration, (ii) volume changes of the examined samples during rehydration, (iii) mass changes of the examined samples during rehydration. Rehydration times were 10, 20, 30, 50, 60, 90, 120, 180, 240, 300 and 360 min. At these specified intervales, samples were carefully removed, blotted with paper towel to remove superficial water, and weighted. Dry matter of solid was determined according to AOAC standards [61]. The mass of samples during rehydration and dry matter of samples were weighted with the electronic scales WPE-300 (RADWAG, Radom, Poland). Maximum relative error was 0.1%. The volume changes of apple cubes during rehydration were measured by buoyancy method using petroleum benzine. Maximum relative error was 5%.

Plot for the variation in mass, dry matter of solid, and volume with time during rehydration are shown in Fig. 1, 2, and 3, respectively. It can be seen from Fig. 1 and 3 that moisture uptake increases with increasing rehydration time, and the rate is faster in the initial period of rehydration and decreased up to the saturation level. This initial period of high water uptake can be attributed to the capillaries and cavities near the surface filling up rapidly [4,62]. As water absorption proceeds, rehydration rates decline due to increased extraction rates of soluble materials [63]. Similar trends have been reported in the previous studies [24,28,64]. It can be observed from Fig. 2 that solute loss increases with increasing rehydration time, and the rate is faster in the initial period of rehydration and decreased up to the saturation level. The explanation of such a course of variation in dry matter of solid with time can be the following. There is an initial steep decrease in solid content because of a high rate of mass transfer (solid gradient). As the solute concentration equilibrated with the environment, the rate of change of solid dry matter is substantially reduced [16]. Similar findings have been noted in the previous studies [2,8,40,55].

The course of rehydration characteristics of apple cubes was described with the following models: the Peleg model (Eq. (7)) [27], the Pilosof-Boquet-Batholomai model (Eq. (15)) [36], the Singh-Kulshrestha model (Eq. (18)) [37], and Witrowa-Rajchert model (Eq.(23)) [40]. The mentioned models were applied for the description of the increase in mass and volume, and the decrease in dry matter of solid. Mass transfer kinetics during rehydration of apple cubes was also modelled using theoretical model based on Fick's second law (Eq. (60)). The variation of dry matter of solid with time and moisture content was described with this model. The goodness of fit of the tested models to the experimental data was evaluated with the determination coefficient (R^2), the root mean square error (RMSE), and reduced chi-square (χ^2). The higher the R^2 value, and lower the RMSE and χ^2 values, the better is the goodness of fit [15,28]. In this study, the regression analyses were done using the STATISTICA routine.

Coefficients of the chosen empirical models and the results of the statistical analyses are given in Table 1.

As can be seen from the statistical analysis results, generally high determination coefficient R^2 were observed for all considered empirical models. The values of RMSE and χ^2 are comparable for all models, although it can be noticed that Witrowa-Rajchert model [40] gave the lowest values of RMSE and χ^2. It turned out from the statistical analyses that the Witrowa-

http://dx.doi.org/10.5772/54072

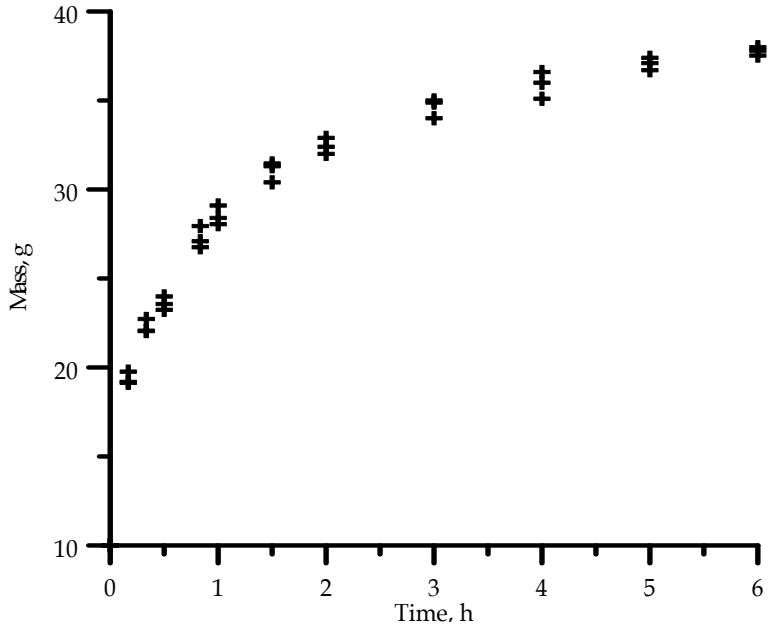

Figure 1. Variation in mass with time during rehydration of apple cubes immersed in distilled water at 20ºC

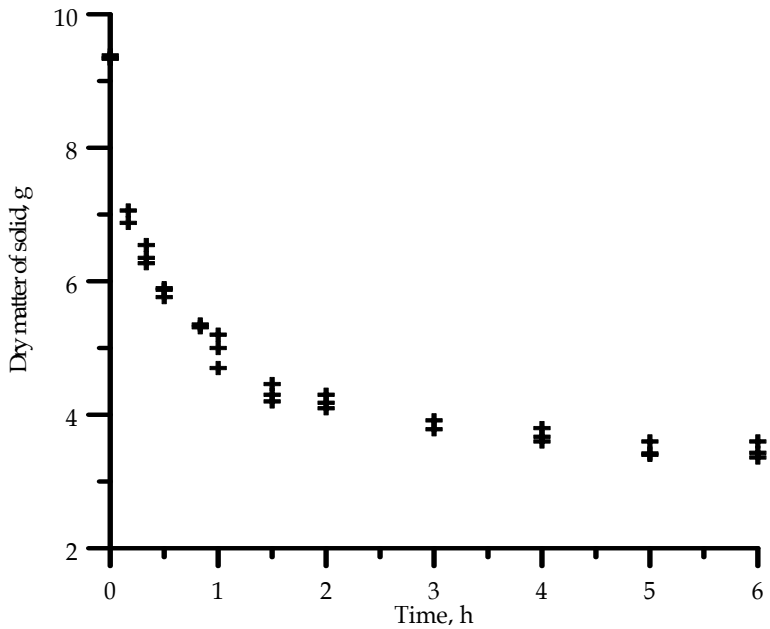

Figure 2. Variation in dry matter of solid with time during rehydration of apple cubes immersed in distilled water at 20ºC

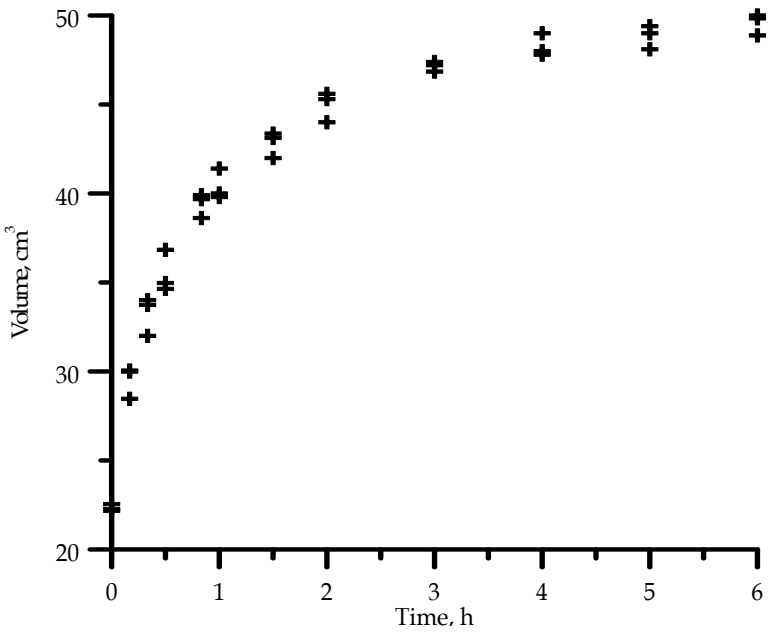

Figure 3. Variation in volume with time during rehydration of apple cubes immersed in distilled water at 20ºC

Rajchert model [40] can be considered as the most appropriate. Taking into account values of determination coefficient R^2 it can be, however, stated that all considered models may be assumed to represent the rehydration characteristics. The equilibrium mass and dry matter of solid obtained from the models are in good agreement with the experimental data but only Witrowa-Rajchert model [40] gave appropriate value of equilibrium volume.

Diffusion coefficients estimated from Fick's second law for a cube (Eq. (60)) and the results of the statistical analyses are given in Table 2. Diffusion coefficients are considered constant and because the cubes dimensions changed during the rehydration, four kinds of variables were identified: D/R_c^2, D_1 for R_c=10 mm, D_2 for mean dimension of cube according to time, and D_3 for mean dimension of cube according to moisture content. It can be noticed that diffusion model described the mass transfer kinetics during rehydration of dried apple cubes well. The determined values of D/R_c^2($1.37 \cdot 10^{-5}$ s^{-1} and $2.64 \cdot 10^{-5}$ s^{-1}) were found to be lower than the reported in the literature for mushrooms: $4.9 \cdot 10^{-4}$ s^{-1} and $7.9 \cdot 10^{-4}$ s^{-1} [4,14]. The determined values of mass diffusion coefficients was found to be between $2.78 \cdot 10^{-10}$ m^2s^{-1} and $6.60 \cdot 10^{-10}$ m^2s^{-1}. These values are within the general range of 10^{-12}-10^{-8} m^2s^{-1} (mostly about 10^{-10} m^2s^{-1}) for food materials [65,66].

The swelling of dried apple cubes during rehydration was also described using following formula:

$$\frac{V}{V_r} = \left(\frac{M}{M_r} \right)^n \tag{65}$$

http://dx.doi.org/10.5772/54072

Variable	Model name	Eq. no.	Model parameters	Equilibrium value	R^2	RMSE	χ^2
Mass	Peleg [27]	7	A_1=0.017407 A_2=0.034360	39.104	0.986810	0.970836	1.001431
	Pilosof-Boquet-Batholomai [36]	15	A_3=29.10352 A_4=0.506620	39.407	0.986810	0.986810	0.970836
	Singh-Kulshrestha [37]	18	A_5=29.10352 A_6=1.973866	39.104	0.986810	0.986810	0.970836
	Witrowa-Rajchert [40]	23	A=1.102427 B=2.838299 C=0.622424	39.407	0.987488	0.987488	0.867144
Dry matter of solid	Peleg [27]	7	A_1=-0.04470 A_2=-0.14997	3.332	0.985213	0.204884	0.044601
	Pilosof-Boquet-Batholomai [36]	15	A_3=-6.66822 A_4=0.298063	3.332	0.985213	0.204884	0.044601
	Singh-Kulshrestha [37]	18	A_5=-6.66679 A_6=3.358309	3.333	0.985177	0.204886	0.044602
	Witrowa-Rajchert [40]	23	A=0.932323 B=-0.614312 C=-4.268212	3.154	0.989715	0.168853	0.031271
Volume	Peleg [27]	7	A_1=0.020528 A_2=0.033683	39.689	0.992019	0.762512	0.617763
	Pilosof-Boquet-Batholomai [36]	15	A_3= 29.71020532 A_4= 0.611001699	39.710	0.992033	0.762450	0.617663
	Singh-Kulshrestha [37]	18	A_5=29.71820 A_6=1.634618	39.718	0.992039	0.762449	0.617660
	Witrowa-Rajchert [40]	23	A=1.018117 B=1.317555 C=1.191287	52.156	0.992155	0.740390	0.601227

Table 1. Coefficients of the chosen empirical models and the results of the statistical analyses

Variable	D/R_c^2	D_1	D_2	D_3	R^2	RMSE	χ^2
Dry matter of solid	$2.6407 \cdot 10^{-5}$	$6.6017 \cdot 10^{-10}$	$6.1702 \cdot 10^{-10}$	$5.3756 \cdot 10^{-10}$	0.985583	0.034884	0.000996
Moisture content	$1.3661 \cdot 10^{-5}$	$3.4153 \cdot 10^{-10}$	$3.1921 \cdot 10^{-10}$	$2.7811 \cdot 10^{-10}$	0.99637	0.057613	0.003265

Table 2. Diffusion coefficients ($m^2 s^{-1}$) estimated from the Fick's second law for a cube (Eq. (60)) and the results of the statistical analyses

Such a formula has been used in the literature for modelling drying shrinkage [67]. The model showed a very good fit to the experimental swelling data with a high value of the determination coefficient R^2=0.98920 and low values of root mean square error RMSE=0.01780 and reduced chi-square χ^2=0.00032. The estimated value of swelling coefficient n=0.293.

The coefficients shown in Table 1 were calculated by fitting experimental data to four chosen empirical models. As it was stated in chapter 2.2.1, the coefficients of the Peleg model, the Pilosof-Boquet-Batholomai model, and the Singh-Kulshrestha model are connected between themselves. Table 3 shows the model parameters estimated using these interdependences.

It turned out from the comparison of the results of calculations presented in Tables 1 and 3 that the values of coefficients determined using both methods are almost the same. It can be stated therefore that there is a similarity of these three considered models and their predictive abilities for rehydration of dried apple cubes are identical. The same results have been obtained by Sopade et al. in [16] for describing water absorption of wheat starch, whey protein concentrate, and whey protein isolate. Shittu et al. in [68] observed, however, differences in discussed models predictive ability for the hydration of African breadfruit seeds.

Variable	Model name	Equation no.	Coefficients estimated using coefficients from the following model	Model parameters
Mass	Peleg [27]	7	Pilosof-Boquet-Batholomai [36]	A_1=0.017407518 A_2=0.034360111
	Peleg [27]	7	Singh-Kulshrestha [37]	A_1=0.017407518 A_2=0.034360111
	Pilosof-Boquet-Batholomai [36]	15	Singh-Kulshrestha [37]	A_3=29.10351515 A_4=0.506619958
Dry matter of solid	Peleg [27]	7	Pilosof-Boquet-Batholomai [36]	A_1=-0.044699038 A_2=-0.149964985
	Peleg [27]	7	Singh-Kulshrestha [37]	A_1=-0.044664539 A_2=-0.149997317
	Pilosof-Boquet-Batholomai [36]	15	Singh-Kulshrestha [37]	A_3=-6.666785913 A_4=0.29776892
Volume	Peleg [27]	7	Pilosof-Boquet-Batholomai [36]	A_1=0.020565381 A_2=0.033658468
	Peleg [27]	7	Singh-Kulshrestha [37]	A_1=0.020585496 A_2=0.033649414
	Pilosof-Boquet-Batholomai [36]	15	Singh-Kulshrestha [37]	A_3=29.71819917 A_4=0.611763873

Table 3. Coefficients of the Peleg model [27], the Pilosof-Boquet-Batholomai model [36], and the Singh-Kulshrestha model [37] estimated using the interdependences between the coefficients

http://dx.doi.org/10.5772/54072

4. Conclusions

Four empirical and one theoretical models were investigated for their suitability to describe the mass transfer kinetics during rehydration of dried apple cubes. The determination coefficient, root mean square error, and reduced chi-square method were estimated for all models considered to compare their goodness of fit the experimental rehydration data. All models described the rehydration characteristics of dried apple cubes satisfactorily (R^2>0.9852). The empirical Witrowa-Rajchert model [40] and the theoretical model based on Fick's second law can be considered as the most appropriate. Theoretical models give an explanation of the phenomena occurring during rehydration but are difficult in application compared to empirical models. Therefore, if the description of rehydration curves is only needed it is better to apply empirical models. Such need occurs especially in food industry.

The determined values of mass diffusion coefficient was found to be between $2.78 \cdot 10^{-10}$ $m^2 s^{-1}$ and $6.60 \cdot 10^{-10}$ $m^2 s^{-1}$. These values are within the general range for food materials.

Acknowledgements

The authors are grateful for the financial support from research project No. N N313 780940 from the Polish National Science Centre.

Nomenclature

a, b - constants (Eq.(62))

A, B - constants (Eqs. (21), (22), (23), and (24))

A - surface area (m^2)

C - constant (Eqs. (21) and (23))

A_0 - constant (Eqs. (12))

A_1 -constant (Eqs. (7), (8), (9), (11), (12), (13), and (14))

A_2 - constant (Eqs. (7), (8), (10), (11), (13), and (14))

A_3 - constant (Eqs. (15), (16), and (17))

A_4 - constant (Eqs. (15), and (17))

A_5 - constant (Eqs. (18), (19), and (20))

A_6 - constant (Eqs. (18), and (20))

a - constant (Eq. (34)

a, b, c - equation coefficients (Eq. (2))

E_a - activation energy (J mol^{-1})

D - mass diffusion coefficient (effective diffusivity) (m^2s^{-1})

D_{calc} - calculated diffusion coefficient (m s^{-1})

D_{eff} - effective diffusion coefficient (m s^{-1})

g - gravitational constant (m s^{-2})

h - half of cylinder heigh, high of liquid rise (m)

k - rehydration rate constant (s^{-1})

k_1 - constant (Eq. (64)) (m^2s^{-1})

k_2 - constant (Eq. (64)) (m^2s^{-1})

L - characteristic dimension (m)

M - moisture content (dry basis)

M_e - equilibrium moisture content (dry basis)

m - mass kg

n - constant (Eqs. (32), (33), and (34))

n - swelling coefficient (Eq. (65))

r - mean pore radius (m)

r, x, y, z - coordinates (m)

R - universal gas constant (J K^{-1} mol^{-1})

R_c - half of plane or cube thickness, cylinder radius, sphere radius (m)

R_g - constant in Eq.(29)

RMSE - root mean square error

R^2 - coefficient of determination

s - dry matter content (kg d.m. kg^{-1})

T - temperature (K)

t - time (s)

x - water absorption ratio (Eqs. (33), (34), (35))

V - volume (m^3)

α - constant (Eqs. (25) and (26))

α' - constant (Eqs. (27) and (28))

http://dx.doi.org/10.5772/54072

β - constant (Eqs. (25), (26), and (27))

γ - surface tension (N m^{-1})

η - fluid viscosity (Pa s)

θ - advancing liquid constant angle (rad)

ρ - liquid density (kg m^{-3})

χ^2 - reduced chi-square

Subscripts

0 - initial

A - outer surface of body

d - dried

o - before drying

r - rehydrated

Author details

Krzysztof Górnicki, Agnieszka Kaleta, Radosław Winiczenko, Aneta Chojnacka and Monika Janaszek

Faculty of Production Engineering, Warsaw University of Life Sciences, Poland

References

[1] Krokida MK, Marinos-Kouris D. Rehydration Kinetics of Dehydrated Products. Journal of Food Engineering 2003;57(1) 1-7, ISSN 0260-8774.

[2] Nayak CA, Suguna K, Rastogi NK. Combined Effect of Gamma-Irradiation and Osmotic Treatment on Mass Transfer During Rehydration of Carrots. Journal of Food Engineering 2006;74(1) 134-142, ISSN 0260-8774.

[3] Femenia A, Bestard MJ, Sanjuán N, Rosselló C, Mulet A. Effect of Rehydration Temperature on the Cell Wall Components of Broccoli (Brassica oleracea L. Var. italica) Plant Tissues. Journal of Food Engineering 2000;46(3) 157-163, ISSN 0260-87774.

[4] García-Pascual P, Sanjuán N, Bon J, Carreres JE, Mulet A. Rehydration Process of Boletus edulis Mushroom: Characteristics and Modelling. Journal of the Science of Food and Agriculture 2005;85(8) 1397-1404, ISSN 0022-5142.

[5] Moreira R, Chenlo F, Chaguri L, Fernandes C. Water Absorption, Texture, and Color Kinetics of Air-Dried Chestnuts During Rehydration. Journal of Food Engineering 2008;86(4) 584-594, ISSN 0260-8774.

[6] Marabi A, Livings S, Jacobson M, Saguy IS. Normalized Weibull Distribution for Modeling Rehydration of Food Particulates. European Food Research and Technology 2003;217(4) 312-318, ISSN 1438-2385.

[7] Giraldo G, Vázquez R, Martín-Esparza ME, Chiralt A. Rehydration Kinetics and Soluble Solids Lixiviation of Candied Mango Fruit as Affected by Sucrose Concentration. Journal of Food Engineering 2006;77(4) 825-834, ISSN 0260-8774.

[8] Rastogi NK, Nayak CA, Raghavarao KSMS. Influence of Osmotic Pre-Treatments on Rehydration Characteristics of Carrots. Journal of Food Engineering 2004;65(2) pp. 287-292, ISSN 0260-8774.

[9] Taiwo KA, Angarsbach A, Knorr D. Rehydration Studies on Pretreated and Osmotically Dehydrated Apple Slices. Journal of Food Science 2002;67(2) 842-847, ISSN 1750-3841.

[10] Krokida MK, Marolis ZB. Structural Properties of Dehydrated Products During Rehydration. International Journal of Food Science and Technology 2001;36(5) 529-538, ISSN 0950-5423.

[11] Sanjuán N, Simal S, Bon J, Mulet A. Modelling of Broccoli Stems Rehydration Process. Journal of Food Engineering 1999;42(1) 27-31, ISSN 0260-8774.

[12] Lewicki PP. Some Remarks on Rehydration of Dried Foods. Journal of Food Engineering 1998;36(1) 81-87, ISSN 0260-8774.

[13] Marabi A, Thieme U, Jacobson M, Saguy IS. Influence of Drying Method and Rehydration Time on Sensory Evaluation of Rehydrated Carrot Particulates. Journal of Food Engineering 2006;72(3) 211-217, ISSN 0260-8774.

[14] Garcia-Pascual P, Sanjuán N, Melis R, Mulet A. Morchella esculenta (morel) Rehydration Process Modelling. Journal of Food Engineering 2006;72(4) 346-353, ISSN 0260-8774.

[15] Kaleta A, Górnicki K. Some Remarks on Evaluation of Drying Models of Red Beet Particles. Energy Conversion and Management 2010;51(12) pp. 2967-2978, ISSN 0196-8904.

[16] Sopade PA, Xun PY, Halley PJ, Hardin M. Equivalence of the Peleg, Pilosof and Singh-Kulshrestha Models for Water Absorption in Food. Journal of Food Engineering 2007;78(2) 730-734, ISSN 0260-8774.

[17] Wang J, Xi YS. Drying Characteristics and Drying Quality of Carrot Using a Two-Stage Microwave Process. Journal of Food Engineering 2005;68(4) 505-511, ISSN 0260-8774.

[18] Giri SK, Prasad S. Drying Kinetics and Rehydration Characteristics of Micrwave-Vacuum and Convective Hot-Air Dried Mushrooms. Journal of Food Engineering 2007;78(2) 512-521, ISSN 0260-8774.

[19] Komes D, Lovrić T, Kovačević-Ganić K. Aroma of Dehydrated Pear Products. LWT 2007;40(9) 1578-1586, ISSN 0023-6438.

[20] McMinn WAM, Magee TRA. Physical Characteristics of Dehydrated Potatoes – Part II. Journal of Food Engineering 1997;33(1-2) 49-55, ISSN 0260-8774.

[21] Kaur P, Kumar A, Arora S, Ghuman BS. Quality of Dried Coriander Leaves as Affected by Pretreatments and Method of Drying. European Food Research and Technology 2006; 223(2) 189-194, ISSN 1438-2385.

[22] Doymaz I. Air-Drying Characteristics of Tomatoes. Journal of Food Engineering 2007;78(4) 1291-1297, ISSN 0260-8774.

[23] Prothon F, Ahrné LM, Funebo T, Kidman S, Langton M, Sjőholm I. Effects of Combined Osmotic and Microwave Dehydration of Apple on Texture, Microstructure and Rehydration Characteristics. Lebensm. Wiss. u.- Technol.2001;34(2) 95-101, ISSN 0023-6438.

[24] Jambrak AR, Mason TJ, Paniwnyk L, Lelas V. Accelerated Drying of Button Mushrooms, Brussels Sprouts and Cauliflower by Applying Power Ultrasound and Its Rehydration Properties. Journal of Food Engineering 2007;81(1) 88-97, ISSN 0260-8774.

[25] Atarés L, Chiralt A, González-Martínez C. Effect of Solute on Osmotic Dehydration and Rehydration of Vacuum Impregnated Apple Cylinders (cv. Granny Smith). Journal of Food Engineering 2008;89(1) 49-56, ISSN 0260-8774.

[26] Atarés L, Chiralt A, González-Martínez C. Effect of the Impregnated Solute on Air Drying and Rehydration of Apple Slices (cv. Granny Smith). Journal of Food Engineering 2009; 91(2) 305-310, ISSN 0260-8774.

[27] Peleg M. An Empirical Model for the Description of Moisture Sorption Curves. Journal of Food Science 1988;53(4) 1216-1219, ISSN 1750-3841.

[28] Deng Y, Zhao Y. Effect of Pulsed Vacuum and Ultrasound Osmopretreatments on Glass Transition Temperature, Texture, Microstructure and Calcium Penetration of Dried Apples (Fuji). LWT- Food Science and Technology 2008;41(9) 1575-1585, ISSN 0023-6438.

[29] Jideani VA, Mpotokwana SM. Modeling of Water Absorption of Bostwana Bambara Varieties Using Peleg's Equation. Journal of Food Engineering 2009;92(2) 182-188, ISSN 0260-8774.

[30] Markowski M, Zielińska M. Kinetics of Water Absorption and Soluble-Solid Loss of Hot-Air Dried Carrots During Rehydration. International Journal of Food Science and Technology 2011;46(6) 1122-1128, ISSN 0950-5423.

[31] Turhan M, Sayar S, Gunasekaran S. Application of Peleg Model to Study Water Absorption in Chickpea During Soaking. Journal of Food Engineering 2002;53(2) 153-159, ISSN 0260-8774.

[32] Abu-Ghannam N, McKenna B. The Application of Peleg's Equation to Model Water Absorption During the Soaking of Red Kidney Beans (Phaseolus Vulgaris L.). Journal of Food Engineering 1997;32(4) 391-401, ISSN 0260-8774.

[33] Maskan M. Effect of Processing on Hydration Kinetics of Three Wheat Products of the Same Variety. Journal of Food Engineering 2002;52(4) 337-341, ISSN 0260-8774.

[34] Bilbao-Sáinz C, Andrés A, Fito P. Hydration Kinetics of Dried Apple as Affected by Drying Conditions. Journal of Food Engineering 2005;68(3) 369-376, ISSN 0260-8774.

[35] Marques LG, Prado MM, Freire JT. Rehydration Characteristics of Freeze-Dried Tropical Fruits. LWT-Food Science and Technology 2009;42 1232-1237, ISSN 0023-6438.

[36] Pilosof AMR, Boquet R, Batholomai GB. Kinetics of Water Uptake to Food Powders. Journal of Food Science 1985;50(1) 278-282, ISSN 1750-3841.

[37] Singh BPN, Kulshrestha SP. Kinetics of Water Sorption by Soybean and Pigeonpea Grains. Journal of Food Science 1987;52(6) 1538-1541, ISSN 1750-3841.

[38] Wesołowski A. Badanie Suszenia Jabłek Promieniami Podczerwonymi (Investigation on Apple Drying Infrared Radiation). PhD thesis. Warsaw University of Life Sciences, Warsaw, Poland (in Polish); 2000.

[39] Kaleta A, Górnicki K, Kościkiewicz A. Wpływ Parametrów suszenia pod Obniżonym Ciśnieniem na Kinetykę Rehydratacji Suszu z Korzenia Pietruszki (Influence of Vacuum Drying Parameters on Kinetics of Rehyration of Dried Parsley Root). Inżynieria Rolnicza 2006;10 3(78), 69-77, ISSN 1429-7264.29-7264

[40] Witrowa-Rajchert D. Rehydracja Jako Wskaźnik Zmian Zachodzących w Tkance Roślinnej w Czasie Suszenia (Rehydration as an Index of Changes Occurring in Plant Tissue During Drying), Fundacja "Rozwój SGGW", ISBN 83-87660-95-7, Warszawa, Poland (in Polish); 1999.

[41] Kaleta A, Górnicki K. Effect of Initial Processing Methods Used in Conventional Drying Process on the Rate of Getting Equilibrium State in Rehydrated Dried Parsley Root. Annals of Warsaw Agricultural University-SGGW, Agriculture (Agricultural Engineering) 2006;49 9-13, ISSN 1898-6730.

[42] Machado MF, Oliveira FAR, Cunha LM. Effect of Milk Fat and Total Solids Concentration on the Kinetics of Moisture Uptake by Ready-to-Eat Breakfast Cereal. International Journal of Food Science and Technology 1999;34(1) 47-57, ISSN 0950-5423.

[43] Ruiz-Diaz GR, Martínez-Monzó J, Chiralt A. Modelling of Dehydration-Rehydration of Orange Slices in Combined Microwave/Air Drying. Innovative Food Science and Emerging Technologies 2003;4(2) 203-209, ISSN 1466-8564.

[44] Cunha LM, Oliveira FAR, Oliveira JC. Optimal Experimental Desing for Estimating the Kinetic Parameters of Process Described by the Weibull Probability Distribution Function. Journal of Food Engineering 1998;37(2) 175-191, ISSN 0260-8774.

[45] Bhattacharya S, Bal S, Mukherjee RK, Bhattacharya S. Kinetics of Tamarind Seed Hydration. Journal of Food Engineering 1997;33(1-2) 129-138, ISSN 0260-8774.

[46] Gowen A, Abu-Ghannam N, Frias J, Oliveira J. Modelling of Water Absorption Process in Chickpeas (Cicer arietinum L.) – The Effect of Blanching Pre-Treatment on Water Intake and Texture Kinetics. Journal of Food Engineering 2007;78(3) 810-819, ISSN 0260-8774.

[47] Gowen A, Abu-Ghannam N, Frias J, Oliveira J. Influence of Pre-Blanching on the Water Absorption Kinetics of Soybeans. Journal of Food Engineering 2007;78(3) 965-971, ISSN 0260-8774.

[48] Misra MK, Brooker DB. Thin-Layer Drying and Rewetting Equations for Shelled Yellow Corn. Transactions of the ASAE 1980;23(5) 1254-1260, ISSN 0001-2351.

[49] Shatadal P, Jayas DS., White NDG. Thin-Layer Rewetting Characteristics of Canola. Transactions of the ASAE 1990;33(3) 871-876, ISSN 0001-2351

[50] Mizuma T, Tomita A, Kitaoka A, Kiyokawa Y, Wakai Y. Water-Absorption Rate Equation of Rice for Brewing Sake. Journal of Bioscience and Bioengineering 2007;103(1) 60-65, ISSN 1389-1723.

[51] Saguy I S, Marabi A, Wallach R. New Approach to Model Rehydration of Dry Food Particulates Utilizing Principles of Liquid Transport in Porous Media. Trends in Food Science and Technology 2005;16(10) 495-506, ISSN 0924-2244.

[52] Crank J. Mathematics of Diffusion, 2nd ed., Clarendon Press, ISBN 0198534116, Oxford, UK; 1975.

[53] Calzetta Resio AN, Aguerre RJ, Suárez C. Study of Some Factors Affecting Water Absorption by Amaranth Grain During Soaking. Journal of Food Engineering 2003;60(4) 391-396, ISSN 0260-8774.

[54] Falade KO, Abbo ES. Air-Drying and Rehydration Characteristics of Date Palm (Phoenix dactylifera L.) Fruits. Journal of Food Engineering 2007;79(2) 724-730, ISSN 0260-8774.

[55] Górnicki K. Modelowanie Procesu Rehydratacji Wybranych Warzyw i Owoców (Modelling of Selected Vegetables and Fruits Rehydration Process), Wydawnictwo SGGW, ISBN 978-83-7583-325-6, Warszawa, Poland (in Polish); 2011.

[56] Lee KT, Farid M, Nguang SK. The Mathematical Modelling of the Rehydration Characteristics of Fruits. Journal of Food Engineering 2006;72(1) 16-23, ISSN 0260-8774.

[57] Weerts AH, Lian G, Martin DR. Modeling Rehydration of Porous Biomaterials: Anisotropy Effects. Journal of Food Science 2003;68(3) 937-942, ISSN 1750-3841.

[58] Weerts AH, Lian G, Martin DR. Modeling the Hydration of Foodstuffs: Temperature Effects. AIChE Journal 2003;49(5) 1334-1339, ISSN 1547-5905.

[59] Weerts AH, Martin DR, Lian G, Melrose JR. Modelling the Hydration of Foodstuffs. Simulation Modelling Practice and Theory 2005;13(2) 119-128, ISSN 1569-190X.

[60] Saguy IS, Marabi A, Wallach R. Liquid Imbibition During Rehydration of Dry Porous Foods. Innovative Food Science and Emerging Technologies 2005;6(1) 37-43, ISSN 1466-8564.

[61] AOAC Official Methods of Analysis. Arlington, VA: Association of Official Analytical Chemists (No. 934.06); 2003.

[62] Cunningham SE, McMinn WAM, Magee TRA, Richardson PS. Effect of Processing Conditions on the Water Absorption and Texture Kinetics of Potato. Journal of Food Engineering 2008;84(2) 214-223, ISSN 0260-8774.

[63] Abu-Ghannam N, McKenna B. Hydration Kinetics of Red Kidney Beans (Phaseolus vulgaris L.). Journal of Food Science 1997;62(3) 520-523, ISSN 1750-3841.

[64] Planinić M, Velić D, Tomas S, Bilić M, Bucić A. Modelling of Drying and Rehydration of Carrots Using Peleg's Model. European Food Research and Technology 2005;221(3-4) 446-451, ISSN 1438-2385.

[65] Doulia D, Tzia K, Gekas V. A Knowledge Base for the Apparent Mass Diffusion Coefficient (DEFF) of Foods. International Journal of Food Properties 2000;3(1) 1-14, ISSN 1532-2386.

[66] Maroulis ZB, Saravacos GD, Panagiotou NM, Krokida MK. Moisture Diffusivity Data Compilation for Foodstuffs: Effect of Material Moisture Content and Temperature. International Journal of Food Properties 2001;4(2) 225-237, ISSN 1532-2386.

[67] Górnicki K, Kaleta A. Modelling Convection Drying of Blanched Parsley Root Slices. Biosystems Engineering 2007;97(1) 51-59, ISSN 1537-5110.

[68] Shittu TA, Awonorin SO, Raji AO. Evaluating Some Empirical Models for Predicting Water Absorption in African Breadfruit (Treculia Africana) Seeds. International Journal of Food Properties 2004;7(3) 585-602, ISSN 1532-2386.

Chapter 17

Subcritical Water Extraction

A. Haghighi Asl and M. Khajenoori

Additional information is available at the end of the chapter

http://dx.doi.org/10.5772/54993

1. Introduction

Extraction always involves a chemical mass transfer from one phase to another. The principles of extraction are used to advantage in everyday life, for example in making juices, coffee and others. To reduce the use of organic solvent and improve the extraction methods of constituents of plant materials, new methods such as microwave assisted extraction (MAE), supercritical fluid extraction (SFE), accelerated solvent extraction (ASE) or pressurized liquid extraction (PLE) and subcritical water extraction (SWE), also called superheated water extraction or pressurized hot water extraction (PHWE), have been introduced [1-3].

SWE is a new and powerful technique at temperatures between 100 and 374°C and pressure high enough to maintain the liquid state (Fig.1) [4]. Unique properties of water are namely its disproportionately high boiling point for its mass, a high dielectric constant and high polarity [4]. As the temperature rises, there is a marked and systematic decrease in permittivity, an increase in the diffusion rate and a decrease in the viscosity and surface tension. In consequence, more polar target materials with high solubility in water at ambient conditions are extracted most efficiently at lower temperatures, whereas moderately polar and non-polar targets require a less polar medium induced by elevated temperature [5].

Based on the research works published in the recent years, it has been shown that the SWE is cleaner, faster and cheaper than the conventional extraction methods. The essential oil of *Z. multiflora* was extracted by SWE and compared with two conventional methods, including hydrodistillation and Soxhlet extraction [7]. The total extraction yields found for the total essential oil of *Z. multiflora* were 2.58, 1.51 and 2.21% (w/w) based on the dry weight for SWE, hydrodistillation and Soxhlet extraction, respectively.

The comparison among the amount of thymol and carvacrol (milligram per gram dried sample) by SWE, hydrodistillation and Soxhlet extraction is shown in Table 1 [7]. The amount of valuable oxygenated components in the SWE method is significantly higher than hydro-

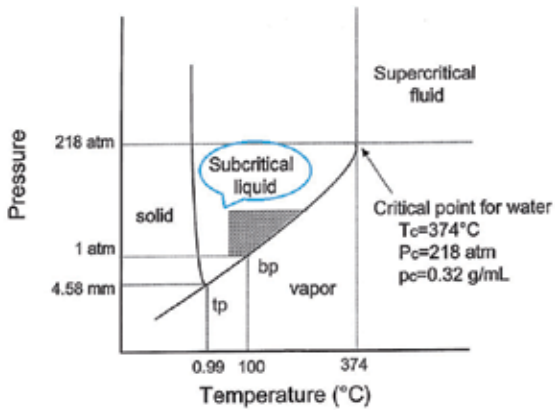

Figure 1. Phase diagram of water as a function of temperature and pressure (Cross-hatched area indicates the preferred region (SWE)) [4].

Components	SWE*	Hydrodistillation†	Soxhlet extraction‡	RI§
Thymol	9.25 (4.77%)**	4.38 (2.97%)	0.94 (2.78%)	1,232
Carvacrol	11.51 (4.33%)	4.06 (3.31%)	1.39 (2.83%)	1,242

Sample weight = 4 g; particle size = 0.5 mm; flow rate = 2 mL/min; temperature = 150C; pressure = 20 bar; and extraction time = 150 min.

* Extraction time = 150 min.

** Relative SD percent.

† Extraction time = 180 min.

‡ Extraction time = 210 min.

§ Retention indices (RI) on the DB-5 column.

* Extraction time = 150 min.

** Relative SD percent.

1' Extraction time = 180 min.

i Extraction time = 210 min.

§ Retention indices (RI) on the DB-5 column.

Table 1. The amount of Thymol and carvacrol (mg/g dried sample) of the essential oil of *Z.multiflora*, extracted by SWE, hydrodistillation and Soxhlet extraction [7].

distillation and Soxhlet extraction. As hexane is a nonpolar solvent, non-oxygenated components are enhanced compared to subcritical water. On the other hand, in general, non-oxygenated components present lower vapor pressures compared to oxygenated components, and in this sense, its content in hydrodistillated extracts are increased. Because of the significant presence of the oxygenated components, the final extract using the SWE method was relatively better and more valuable.

http://dx.doi.org/10.5772/54993

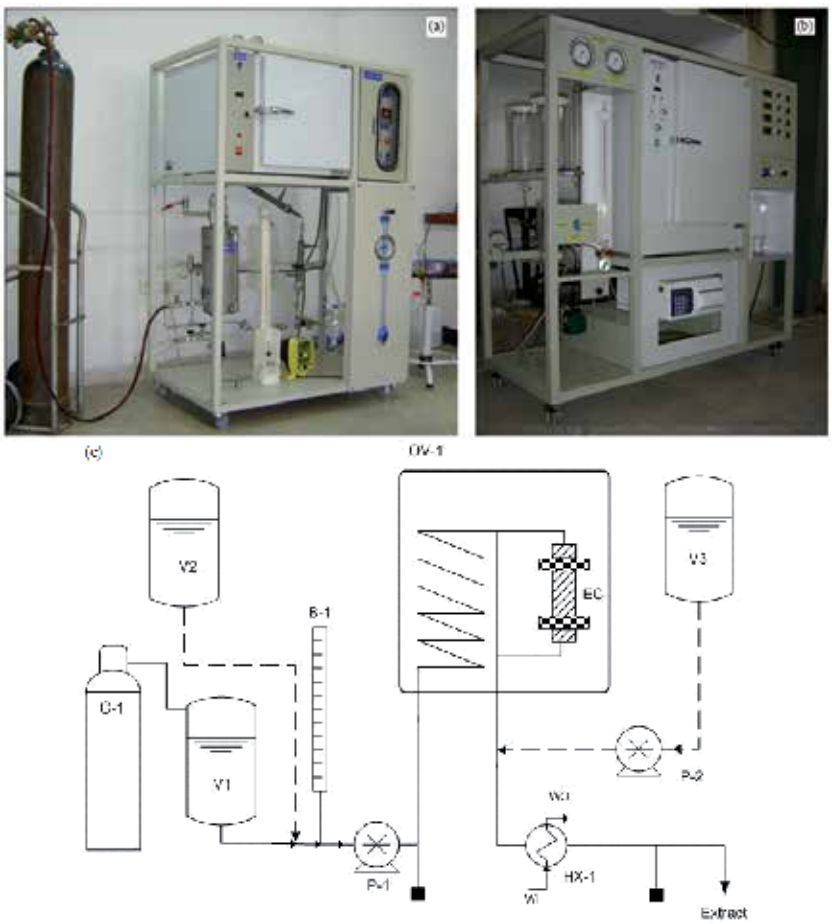

Figure 2. (a) and (b) pictures of first and second generated systems respectively and (c) Schematic diagram of SWE system, B-1: Burette, C-1: Nitrogen cylinder, EC: Extraction cell, HX-1: Heat Exchanger, OV-1: Oven, P-1, 2: Pumps, V-1: Water tank, V-2: Solvent tank, V-3: Rinsing solvent tank, WI: Water inlet, WO: Water outlet.

2. Equipment of subcritical water extraction

No commercial SWE equipment is available, but the apparatus is easy to construct in the laboratory. SWE is performed in batch or continue systems but continue system is current. In this system, extraction bed is fixed and flow direction is usually up to down for easily cleaning of analytes. Already, we worked SWE of *Z. multiflora* with first generated system (Iranian Research Organization for Science and Technology [IROST], Tehran, Iran) [7] (Fig. 2(a)). After it, laboratory-built apparatus of SWE equipment was designed by studying of different systems and have advantages versus first generation (Semnan University, Semnan, Iran) (Fig. 2(b)).

The second generated system is presented in Fig. 2(c). The main parts of a dynamic SWE unit are the following: three tanks, two pumps, extraction vessel, oven for the heating of the

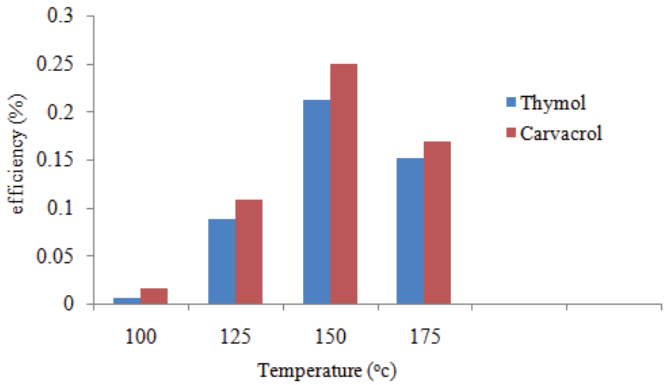

Figure 3. Effect of temperature on the main essential oil components SWE of *Z. multiflora*. Operating conditions: sample weight=4.0 g; flow rate=2 mL/min; particle size=0.50 mm; pressure=20 bar; and extraction time=60 min.

extraction vessel, heat Exchanger for cooling of exteract, pressure restrictor and sample collection system. One of the pumps is employed for pumping the water (and extract) and another pump is employed for flushing the tubings. Also, one of tank is employed for organic solvent that is as a main solvent or co-solvent. A pressure restrictor is needed to maintain the appropriate pressure in the equipment. It was constructed of stainless steel.

3. Effective parameters in subcritical water extraction

3.1. Effect of temperature

One of the most important parameters affecting SWE efficiencies is the extraction temperature. As the temperature rises, there is a marked and systematic decrease in permittivity, an increase in the diffusion rate and a decrease in the viscosity and surface tension. SWE must be carried out at the highest permitted temperature. It should be mentioned that increasing the extraction temperature above a certain value gives rise to the degradation of the essential oil components. The maximum permitted extraction temperature must be obtained experimentally for different plant materials. Regarding the extraction of essential oils, it has been shown that temperatures between 125 and 175°C will be the best condition. The extraction temperature for *Z. multiflora* was optimized in order to maximize the efficiency of thymol and carvacrol (structural isomers) as key components (more than 72%) [7]. Its influence was studied between 100 and 175°C, and the mean particle size, flow rate, extraction time and pressure were selected to be 0.5 mm, 2 ml/min, 60 min and 20 bar pressure, respectively (Fig. 3).

It was seen that the efficiency of thymol and carvacrol increased generally with increase in temperature up to 150°C. At 175°C, it decreased, and an extract with a burning smell was produced. It may be the result of degradation of some of the constituents at higher temperatures. Because of the highest efficiency of thymol and carvacrol essential oil at 150°C and the

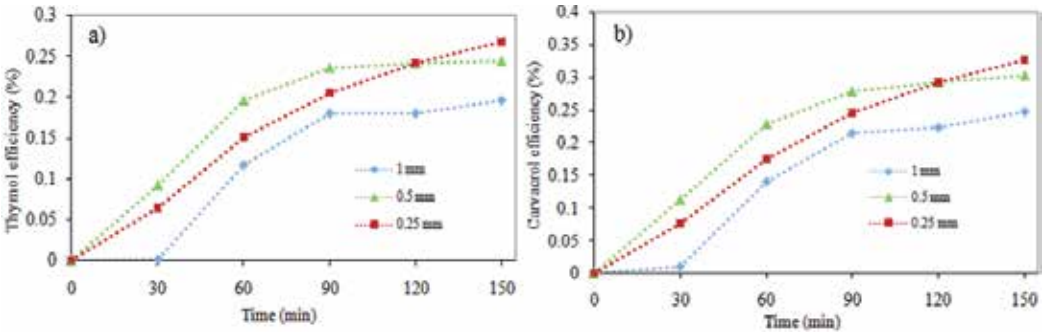

Figure 4. Effect of particle size on the efficiency of a) thymol and b) carvacrol SWE of *Z.multiflora.* Operating conditions: sample weight = 4.0g; flow rate = 2 ml/min; temperature = 150°C; and pressure = 20 bar [7].

disagreeable odor of the extract at higher temperatures, further experiments were carried out at this temperature.

3.2. Effect of particle size

The effect of the mean particle size on the efficiency of thymol and carvacrol at 150°C temperature, 2ml/min flow rate, 20 bar pressure and 150 min extraction time is shown in Fig. 4 [7]. The mean ground leaf particles were selected to be 0.25, 0.5 and 1.0 mm. The final amount of thymol and carvacrol extracted from 0.5-mm-size particles was near to 0.25-mm particles. It shows that, at least in the selected range of mean particle sizes (0.25-0.5 mm), the extraction process may not be controlled by the mass transfer of thymol and carvacrol. It was expected that the rate of the 0.25-mm-size particles was more than the 0.5-mm-size particles, but it did not happen.

A possible explanation for this observation could be that the particles were close fitting at initial times, and the extraction was done slowly. After the expired time, the close fitting particles opened from each other, and at final extraction value of the 0.25-mm-size particles was more than the 0.5-mm-size particles. Regarding the larger 1.0-mm-size particles, the efficiency is substantially lower. It shows that the process may be controlled by the mass transfer of thymol and carvacrol for larger particle sizes.

To prevent the probable vaporization of the essential oils during the grinding of the leaves and also to make the work of the filters easier, for further experiments, the best value of mean particle size was selected as 0.50 mm.

3.3. Effect of flow rate

The effect of water flow rate on the efficiency of thymol and carvacrol at 150°C temperature, 0.5-mm-particle size, 20 bar pressure and 150 min extraction time is shown in Fig. 5 [7]. The water flow rate was studied at 1, 2 and 4 ml/min. As can be seen, the rate of the essential oil extraction was faster at the higher flow rate. The rate is slower at 2 ml/min and even slower at 1 ml/min. It is in accordance with previous works [8, 9]. It means that the mass transfer of the

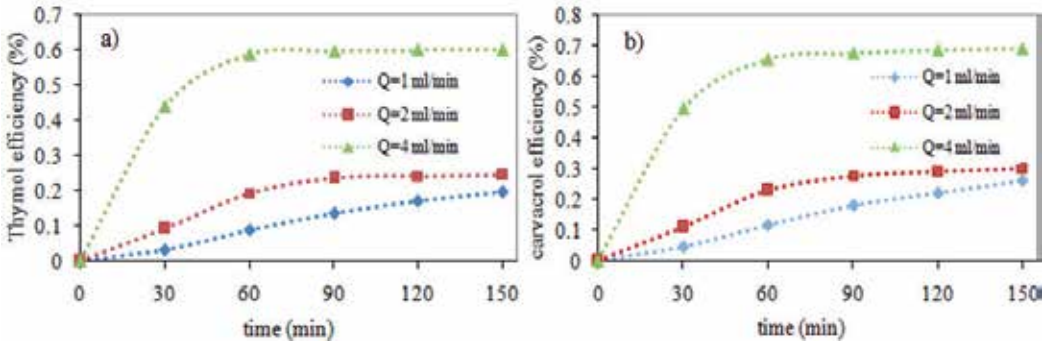

Figure 5. Effect of flow rate on the efficiency of a) thymol and b) carvacrol SWE of *Z. multiflora.* Operating conditions: sample weight = 4.0g; particle size= 0.5 mm; temperature = 150°C; and pressure = 20 bar [7].

thymol and carvacrol components from the surface of the solid phase into the water phase regulated most of the extraction process. Increase in flow rate resulted in increase in superficial velocity, and thus, quicker mass transfer [10]. The main disadvantage of applying higher water flow rates is increasing the extract volume and consequently, lower concentration of the final extracts. In practice, the best flow rate must be selected considering two important factors, including the extraction time and the final extract concentration. It is clear that a shorter extraction time and more concentrated extracts are desirable. To prevent a slower extraction rate and longer extraction times, despite the larger amount of the final extracts, a flow rate of 2 ml/min was selected as the optimum value.

While temperature, particle size and flow rate extraction are the main parameters affecting SWE, type of analyte, extraction vessel characteristics and use of modifiers and additives are also important. Although matrix and other effects play a role, many of these are less critical in SWE than in SFE because of the harsh extraction conditions (high temperature) typical in SWE, particularly for non-polar analytes.

4. Extraction mechanism

The SWE process can be proposed to have six sequential steps: (1) rapid fluid entry; (2) desorption of solutes from matrix active sites; (3) diffusion of solutes through organic materials; (4) diffusion of solutes through static fluid in porous materials; (5) diffusion of solutes through layer of stagnant fluid outside particles; and (6) elution of solutes by the flowing bulk of fluid (Fig. 6).

As we know, the extraction rate is limited by the slowest of these three steps. The effect of step (1) is typically small and often neglected. Although the diffusion of the dissolved solute within the solid is usually the rate limiting step for most botanicals, partitioning of solute between the solid matrix and solvent have been reported as the rate-limiting mechanism for SWE of essential oil from savory [10].

http://dx.doi.org/10.5772/54993

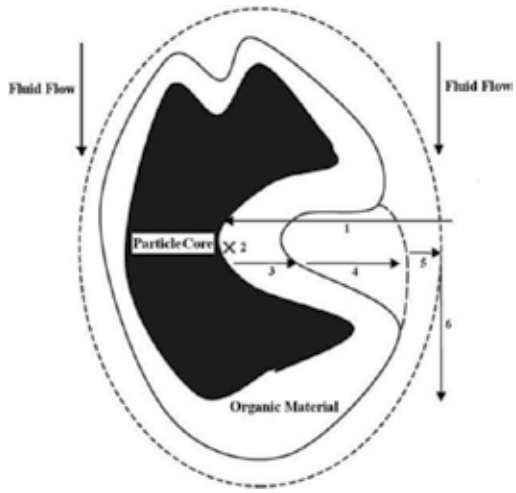

Figure 6. Proposed schematic presentation of the extraction steps in SWE.

The plots the amount of compound extracted versus solvent flow rates and versus solvent volume can determine the relative importance of these steps. For example, if the rate of extraction is controlled by intra-particle diffusion or kinetic desorption, the increase in bulk fluid flow rate would have little effect on extraction rate. On the other hand, if the extraction is controlled by external film transfer diffusion, extraction rates increase with solvent flow rate. In the case where the extraction rate is controlled by thermodynamic partitioning, doubling the bulk fluid flow rate would double the extraction rate, while the curves of extraction efficiency versus the volume of water passed for all flow rates would overlap. In one of our previous work, four proposed models have been applied to describe the extraction mechanisms obtained with SWE of *Z. multiflora* essential oil. These were included (1) partitioning coefficient model, (2) one-site (3) two-site desorption models and (4) thermodynamic partition with external mass transfer model [11]. In other studying unsteady state mass balance of the solute in solid and subcritical water phases (two-phase model) was investigated [12]. Also Computational Fluid Dynamics (CFD) modeling of extraction was considered [13].

5. Modeling of SWE

5.1. Thermodynamic model (Partitioning coefficient (K_D) model)

Partitioning coefficient model, adopted from Kubatova et al. [10], describes the extraction process that is controlled by partitioning of solute between matrix and solvent similar to elution of solute from a partition chromatography column. For extraction, this type of behavior occurs when the initial solute concentration in the plant matrix is small. This model assumes that the initial desorption step and the subsequent fluid-matrix partitioning is rapid. Here the thermodynamics partitioning coefficient, K_D, is defined as:

$$K_D = \frac{Concentration\ of\ \ solute\ in\ the\ matrix}{Concentration\ of\ \ solute\ in\ the\ extraction\ \ fluid}\ ;at\ equilibrium \quad (1)$$

Hence the Extraction with subcritical water can be fitted using this simple thermodynamic model. The mass of analyte in each unit mass of extraction fluid and the mass of analyte remaining in the matrix at that period in the entire extraction time is based on the K_D value determined for each compound. The thermodynamic elution of analytes from matrix was the prevailing mechanism in SWE as evidenced by the fact that extraction rate increased proportionally with the subcritical water flow rate. Therefore, if the K_D model applies to a certain extraction, the shape of an extraction curve would be defined by:

$$\frac{M_b}{M_i} = \frac{\left(1 - \frac{M_a}{M_i}\right)}{\left(\frac{K_D m}{(V_b - V_a)\rho} + 1\right)} + \frac{M_a}{M_i} \quad (2)$$

M_a: cumulative mass of the analyte extracted after certain amount of volume V_a (mg/g dry sample)

M_b: cumulative mass of the analyte extracted after certain amount of volume V_b (mg/g dry sample)

M_i: total initial mass of analyte in the matrix (mg/g dry sample)

M_b/M_i and M_a/M_i: cumulative fraction of the analyte extracted by the fluid of the volume V_b and V_a (ml)

K_D: distribution coefficient; concentration in matrix/concentration in fluid

ϱ: density of extraction fluid at given condition (mg/ml)

e: exponential function

m: mass of the extracted sample (mg dry sample).

The model eq. (1) and the experimental data for *Z. multiflora* from all volumetric flow rate, were used to determine the K_D value by minimizing the errors between the measured data and the K_D model using Matlab curve fitting solver. The values of K_D are shown in Table 2 for different flow rates [11]. It was demonstrated that individual essential oil compounds have a range of K_D values from ~4 to ~250 [10].

Flow rate/ ml·min^{-1}	K_D	
	Thymol	Carvacrol
1	80	70
2	80	70
4	2	2

Table 2. K_D values of partitioning coefficient model for different volumetric flow rates [11].

http://dx.doi.org/10.5772/54993

5.2. Mass transfer models

5.2.1. Diffusion model

Mass transfer can be defined as the migration of a substance through a mixture under the influence of a concentration gradient in order to reach chemical equilibrium. The diffusion coefficient (D_e) is the main parameter in Fick's law, and application of this mathematical model to solid foods during solid-liquid extraction is a common way to calculate the effective diffusion coefficient (Crank, 1975 [14]). However, Gekas (1992) noted, values of D_e can vary by several orders of magnitude for the same material which may be due to structural changes in the food material during different stages of the process [15]. Therefore, it is important to keep a constant particle size as breakage of cell wall or grinding can reduce the particle size and hence decrease the distance for solute to travel from inside to surface of particle.

Fick derived a general conservation equation for one-dimensional non-steady state diffusion when the concentration within the diffusion volume changes with respect to time, known as Fick's second law (Cussler, 1984; Mantell et al., 2002) [16, 17]:

$$\frac{\partial C}{\partial t} = D_e \frac{\partial^2 C}{\partial r^2}$$

With the initial condition:

$$C_{(t=0)} = C_o \qquad \text{a}$$

And boundary conditions:

$$\frac{\partial C}{\partial r}_{(r=0)} = 0 \qquad \text{b}$$

$$C_{(r=R)} = 0 \qquad \text{c}$$

(3)

Where C is the solute concentration (mg/ml) at any location in the particle at time t (s); C_o is the initial solute concentration (mg/ml); D_e is the effective diffusion coefficient (m^2/s) assuming that D_e is constant with the concentration; t is extraction time (s); r is the radial distance from the centre of a spherical particle (m); R is radius of spherical particle (m).

Various solutions of Fick's second law have been presented for the diffusion of a compound during solid-liquid extraction depending on the shape of the particle. An approximate numerical solution to Fick's second law (eq. 2) for a spherical particle was given by Crank (1975) and Cussler (1984):

$$\frac{M_t}{M_\infty} = 1 - \frac{6}{\pi^2} \sum_{n=1}^{\infty} \frac{1}{n^2} \exp\left[\frac{-D_e n^2 \pi^2 t}{R^2}\right] \tag{4}$$

Where M_t: total amount of solute (mg/g) removed from particle after time t, M_∞: maximum amount (mg/g) of solute extracted after infinite time. M_t/M_∞: ratio of total migration to the

maximum migration concentration, R: average radius of an extractable particle. When time becomes large, the limiting form of Eq. 3 becomes:

$$1 - \frac{M_t}{M_\infty} = \frac{6}{\pi^2} \exp\left[\frac{-D_e \pi^2 t}{R^2}\right] \quad (5)$$

To determine the effective diffusion coefficient values two methods were used. The first method was a linear (graphical) solution in which D_e was determined from the slope of the ln $(1-M_t/M_\infty)$ vs. time plot (Dibert et al., 1989) [18]. Thus, eq. 4 can be solved by taking the natural logarithm of both sides. It shows that the time to reach a given solute content will be directly proportional to the square of the particle radius and inversely proportional to D_e:

$$ln\left[1 - \frac{M_t}{M_\infty}\right] = \ln\frac{6}{\pi^2} - \frac{-D_e \pi^2 t}{R^2} \quad (6)$$

Where slope $= \frac{\pi^2 D_e}{R^2}$.

The second method of solution used involved nonlinear regression with effective diffusivity (D_e) as a fitting parameter. In this method, the effective diffusivity D_e was estimated from eq. 4 using a Microsoft Excel Solver program. The program minimizes the mean square of deviations between the experimental and predicted $\ln(1-M_t/M_\infty)$ values (Tutuncu and Labuza, 1996) [19]. The first 10 terms of the series solution are taken into consideration by the program as the solution to the series becomes stable after 10 terms (n=10).

Most researchers in this area have adopted diffusion models based on solutions to Fick's second law for various defined geometrical shapes of the solid given in Crank method, usually based on infinite or semi-infinite geometries of a slab (plane sheet), a cylinder or a sphere. For example, a slab can be used to describe an apple slice or a sheet of herring muscle; a sphere for the description of coffee beans or particles of cheese curd, and a cylinder for the description of cucumber pickles. There is considerable variation in the solutions adopted by various researchers. The starting point for modeling a particular diffusion process is to consider the shape of the solid and the nature of the process itself: uptake of solute into the food, leaching of solute from the food or diffusion of solute through the food, and the experimental conditions in terms of initial and equilibrium solute concentrations.

The solution models usually consider a uniform initial solute concentration throughout the food, no resistance to mass transfer in the diffusion medium and no chemical reaction; but vary for a particular geometry depending on the solute concentrations at the surface of the solid, the volume of the solution (and therefore the relative change in solute concentration in the external solvent), and the time period of the experiment. A representative selection of solutions is given in Table 3. For example, Bressan et al. investigated solute diffusional loss from coffee beans and cottage cheese curd, respectively [20]; they chose solution models to Fick's second law from Crank which assumed the geometry of the solids approximate to that of infinite spheres. However, the former researchers considered a system in which the solute

concentration in the external solvent remains effectively constant and zero throughout the extraction. This can be the case for large infinite solvent volumes and small solute solid concentrations. The latter group of researchers considered a process where the concentration of the solute in the surrounding medium changes significantly. This can be the case for small solvent volumes and high solid phase solute concentrations in the case of leaching, and high external solvent concentrations in the case of solute uptake processes; and consequently adopted a different model.

5.2.2. One-site kinetic desorption model

One-site kinetic desorption model describes the extractions that are controlled by intra-particle diffusion. This occurs when the flow of fluid is fast enough for the concentration of a particular solute to be well below its thermodynamically controlled limit. The one-site kinetic model was derived based on the mass transfer model that is analogous to the hot ball heat transfer model [29, 30]. The assumptions are that the compound is initially uniformly distributed within the matrix and that, as soon as extraction begins, the concentration of compound at the matrix surfaces is zero (corresponding to no solubility limitation). For a spherical matrix of uniform size, the solution for the ratio of the mass, M_r, of the compound that remains in the matrix sphere after extraction time, t, to that of the initial mass of extractable compound, M_i is given as:

$$\frac{M_r}{M_i} = \frac{6}{\pi^2}\sum_{n=1}^{\infty}\frac{1}{n^2}\exp(-D_e n^2\pi^2 t / r^2) \tag{7}$$

In which n is an integer and D_e is the effective diffusion coefficient of the compound in the material of the sphere (m^2/s).

Diffusion process	Diffusion equation	Experimental measurements	**Calculation Diffusivity**
proteins Diffusion though a potato disk [21]	$M_t = \frac{5D_eC_{L\ 1}t}{a} + \frac{2aS}{\pi^2} =$ $1 - \sum_{n=1}^{\infty}\left(C_{L\ 1}\cos(n\pi)exp\left[\frac{-D_e n^2 t}{a^2}\right]\right)$	Protein concentration on the source side initially; at intervals on receiving side	Fitting the experimental values for M_t to the equation by non-linear regression
Analytes diffusion though an apple disk [22]	$M_t = \frac{XAD_e(C - C_L)}{2a}$ A simple lumped parameter equation model	soluble analytes content in the limited volume of solvent	A single effective diffusivity was calculated for each set of data directly from the formula
Analytes diffusion though cheese curd [19]	$\frac{M_t}{M_\infty} = 1 - \sum_{n=1}^{\infty}\frac{6a(1+a)}{9+9a+q_n^2a^2}exp\frac{-D_eq_n^2t}{2a}$:	Samples of solvent surrounding curd	Experimental data fitted to the equation model

Diffusion process	Diffusion equation	Experimental measurements	**Calculation Diffusivity**
	Solution of Fick's 2nd law for solute loss or uptake for sphere geometry but for finite volume of solvent with attainment of equilibrium	withdrawn at intervals	
Analytes diffusion though carrot cylinders [23]	$E = \frac{C - C_L}{C_i - C_L} =$ $1 - \frac{4}{\pi^{\frac{1}{2}}}\left(\frac{D_e t}{a^2}\right)^{1/2} - \frac{D_e t}{a^2} - \frac{1}{3\pi^{\frac{1}{2}}}\left(\frac{D_e t}{a^2}\right)^{3/2}$: Solution of Fick's 2nd law for solute loss or uptake for an infinite cylinder for short time periods. Authors then modify values to apply to finite cylinder	Carrot samples withdrawn for analysis at intervals	Dimensionless time values calculated for each data point using equation, linear regression of Fourier relationship yields D_e
Analytes diffusion though potato tissue [24]	$\frac{M_t}{M_i} = \frac{8}{\pi^2}\sum_{n=0}^{\infty}\frac{1}{(2n+1)^2} exp\frac{-D_e(2n+1)^2}{a^2}\pi^2 t$: Solution of Fick's 2nd law similar to flow through a membrane	Samples of solvent surrounding slices withdrawn and assayed at intervals, material balance used to calculate M_i and M_t	Equation model modified by omitting terms n"/>0 and natural logarithms, by non-linear regression of $ln\ M_i/M_t$ against t
Analytes and pectic substances diffusion though apple tissue [25]	$E = \frac{C - C_L}{C_i - C_L} = \frac{M_t}{M_i} =$ $\frac{8}{\pi^2}\sum_{n=0}^{\infty}\frac{1}{(2n+1)^2} exp\left[-(2n+1)^2\left(\frac{D_e t}{a^2}\right)\frac{\pi^2}{2}\right]$: Solution of Fick's 2nd law for diffusion from an infinite slab developed by Newman [59]	Apple slices withdrawn for analysis at intervals	A series of dimensionless time values found for data using Newman's tables. D_e calculated by linear regression of Fourier relationship
Analytes diffusion though apple tissue [26]	$E = \frac{M_t}{M_i} = \frac{512}{\pi^6} exp\left[-\frac{\pi^2 D_e}{4(a^2 + b^2 + c^2)}\right]t$: Equation model adopted considers diffusion in a slab in three planes.	Apple slices withdrawn for analysis at intervals	Modification of equation model by natural logarithms enables regression of lnE against t give slope with D_e term
Salt and acetic acid diffusion though herring [27]	$\frac{M_t}{M_\infty} = 1 - \sum_{n=0}^{\infty}\frac{8}{(2n+1)^2\pi^2} exp\left[\frac{-D_e(2n+1)^2\pi^2 t}{4a^2}\right]$: Solution of Fick's 2nd law for diffusion from/or uptake by infinite solution.	Fish withdrawn for analysis at intervals	Experimental data fitted to equation model by successive approximations
Analytes diffusion though potato tissue [28]	$\frac{M_t}{M_\infty} = \frac{V_L\ C_{Li} - V_L\ C_L}{V_L\ C_{Li} - V_L\ C_\infty} =$ $1 - \sum_{n=1}^{\infty}\frac{2\alpha(1+\alpha)}{1+\alpha+\alpha^2 n^2} exp\frac{-D_e n^2 t}{a^2}$:	Initial solute content of potato strip and solute contents of solvent	Minimizing the residuals between experimental data and theoretical

Diffusion process	Diffusion equation	Experimental measurements	**Calculation Diffusivity**
	Solution of Fick's 2nd law for diffusion from/or uptake by an infinite slab for uptake from a solution of finite volume. $\frac{M_t}{M_\infty} = 1 - \sum_{n=0}^{\infty} \frac{8}{(2n+1)^2\pi^2} exp\left[\frac{-D_e(2n+1)^2\pi^2 t}{4a^2}\right]$: Solution of Fick's 2nd law for diffusion from/or uptake by infinite slab.	surrounding strip at intervals	values for M_t/M_∞ obtained from the appropriate equation models

Table 3. Diffusion phenomena.

The curve for the above solution tends to become linear at longer times (generally after $t > 0.5\ t_c$), and $\ln (M_r/M_i)$ is given approximately by:

$$Ln(M_r / M_i) = -0.4977 - t / t_0 \tag{8}$$

Where t_c (min) is a characteristic time quantity, defined as:

$$t_c = r^2 / \pi^2 D_e \tag{9}$$

An alternative form of eq. 7, or so called a one-site kinetic desorption model, can be written for the ratio of mass of analyte removed after time *t* to the initial mass, M_i, as given by:

$$\frac{M_t}{M_i} = 1 - e^{-kt} \tag{10}$$

In which M_t is the mass of the analyte removed by the extraction fluid after time t (mg/g dry sample), M_i is the total initial mass of analyte in the matrix (mg/g dry sample), M_t/M_i is the fraction of the solute extracted after time t, and k is a first order rate constant describing the extraction (min^{-1}).

Matlab curve fitting solver was used to determine the desorption rate constant, k, from the data for all flow rates. The values for *Z. multiflora* SWE are show in Table 4 [11]. As mentioned, the kinetic desorption model does not include a factor describing extraction flow rate, k should be the same value for all flow rates if the model is said to fit the experimental data. However, this was not the case (Table 4, the average error 3%-17%). The kinetic desorption rate increased for the volumetric flow rate of 1 to 4 ml/min. This indicated that the kinetic desorption model may not be suitable for describing the data at different flow rates of *Z. multiflora*.

5.2.3. Two-site kinetic desorption model

Two-site kinetic model is a simple modification of the one-site kinetic desorption model that describes extraction which occurs from the "fast" and "slow" part [10]. In such case, a certain

Flow rate/ ml·min^{-1}	k/min^{-1}	
	Thymol	Carvacrol
1	0.0025	0.0028
2	0.0042	0.0039
4	0.0157	0.0157

Table 4. Values of k for one-site kinetic desorption model for different volumetric flow rates [7].

fraction (F) of the analyte desorbs at a fast rate defined by k_1, and the remaining fraction (1-F) desorbs at a slower rate defined by k_2. The model has the following form:

$$\frac{M_t}{M_i} = 1 - \left[Fe^{-k_1 t} \right] - \left[(1-F)e^{-k_2 t} \right] \tag{11}$$

The two site kinetic model does not include solvent volume, but relies solely on extraction time. Therefore, doubling the extractant flow rate should have little effect on the extraction efficiency when plotted as a function of time. On the contrary, the thermodynamic model is only dependent on the volume of extractant used. Therefore, the extraction rate can be varied by changing the flow rate. Hence, the mechanism of thermodynamic elution and diffusion kinetics can be compared simply by changing the flow rate in SWE. If the concentration of bioactive compounds in the extract increases proportionally with an increase in flow rate at given extraction time when the solute concentration is plotted versus extraction time, the extraction mechanism can be explained by the thermodynamic model. However, if an increase in flow rate has no significant effect on the extraction of the bioactive compounds, with the other extraction parameters being kept constant, the extraction mechanism can be modeled by the two site kinetic model [10, 31]. The mechanism of control and hence the model valid for SWE may be different depending on the raw material, the target analyte and extraction conditions.

For the two-site kinetic desorption model, the values of k_1 and k_2 were determined by fitting the experimental data with the two-site kinetic desorption models by minimizing the errors between the data and the model results. In the two-site model, the extraction rate should not be dependent on the flow rate. The k_1 and k_2 values for *Z. multiflora* SWE shown in Tables 5 and 6 demonstrated that the extraction rates were not completely independent of flow rate (the average error 11%-20%).

5.2.4. Thermodynamic partition with external mass transfer resistance model

This model describes extraction which is controlled by external mass transfer whose rate is described by resistance type model of the following form:

Flow rate/ml·min^{-1}	k_1/min^{-1}	k_2/min^{-1}	Mole fraction F
1	0.0088	0.0015	0.21
2	0.0152	0.0026	0.28
4	0.0770	0.0083	0.27

Table 5. k_1 and k_2 values of two-site kinetic desorption model for thymol at different flow rates [11].

Flow rate/ml·min^{-1}	k_1/min^{-1}	k_2/min^{-1}	Mole fraction F
1	0.0101	0.0017	0.21
2	0.0747	0.0088	0.42
4	0.0469	0.0082	0.27

Table 6. k_1 and k_2 values of two-site kinetic desorption model for carvacrol at different flow rates [11].

$$\frac{\partial C_s}{\partial t} = -k_e a_p \left[\left(C_s / K_D \right) - C \right] \tag{12}$$

in which C is the fluid phase concentration (mol/m^3), C_s is the solid phase concentration (mol/m^3), k_e is the external mass transfer coefficient (m/min) and a_p is specific surface area of particles (m^2/m^3) [32]. If the concentration of the solute in the bulk fluid is assumed small and the solute concentration in the liquid at the surface of solid matrix is described by partitioning equilibrium, K_D, the solution of eq. 11 for the solute concentration in the solid matrix, C_s, becomes:

$$C_s = C_0 - \exp(-k_e a_p t / K_D) \tag{13}$$

eq. 11 can be rewritten as the ratio of the mass of diffusing solute leaving the sample to the initial mass of solute in the sample, M_t/M_i, as given by the following equation.

$$M_t = 1 - M_i \exp(-k_e a_p t / K_D) \tag{14}$$

Because a_p is difficult to be measured accurately, a_p and k_e are usually determined together as $k_e a_p$, which is called overall volumetric mass transfer coefficient. The factors that influence the value of $k_e a_p$ include the water flow rate through the extractor and the size and shape of plant sample.

The values for the model parameters, K_D and $k_e a_p$ in eq. (9) determined by Matlab curve fitting solver from the experimental data obtained at 150°C are summarized for *Z. multiflora* SWE in

Tables 7 and 8 for different mass flow rates (Q, mg min^{-1}) [11]. Linear regresion of the plot between $ln(k_e a_p)$ and lnQ gives the following correlation for $k_e a_p$ and Q:

$$\text{for thymol:} \quad k_e a_p = 6.5748\, Q_m^{0.2078} \tag{15}$$

$$\text{for carvacrol:} \quad k_e a_p = 0.1605\, Q_m^{0.6017} \tag{16}$$

Flow rate/ $ml \cdot min^{-1}$	Mass flow rate Q_m/$mg \cdot min^{-1}$	Parameter K_D	Parameter $k_e a_p$/min^{-1}
1	938	80	26.700
2	1876	80	32.7975
4	3752	2	1.300

Table 7. Parameters K_D and $k_e a_p$ for external mass transfer model of SWE of thymol [11].

Flow rate/ $ml \cdot min^{-1}$	Mass flow rate/$mg \cdot min^{-1}$	Parameter K_D	Parameter $k_e a_p$/min^{-1}
1	938	70	8.92
2	1876	70	62.013
4	3752	2	20.54

Table 8. Parameters K_D and $k_e a_p$ for external mass transfer model of SWE of carvacrol [11].

To quantitatively compare the extraction models, the mean percentage errors between the experimental data and the models were considered. Based on the result in fitting from experimental data, the K_D model was generally suitable for the description of extraction over all the volumetric flow rates tested. On the other hand, one-site and two-site kinetic desorption models describe the extraction data reasonably at lower volumetric flow rates. Of all the models considered, however, the thermodynamic partition with external mass transfer model could best describe the experimental data.

5.2.5. Two-phase model

A mathematical model can be developed to predict optimal operating parameters for SWE in a packed-bed extractor. Three important steps consist of diffusion of solutes through particles, diffusion and convection of solutes through layer of stagnant fluid outside particles and elution of solutes by the flowing bulk of fluid are assumed. Unsteady state mass balance of the solute in solid and subcritical water phases led to two partial differential equations. The model can be solved numerically using a linear equilibrium relationship. The model parameters were mass transfer coefficient, axial dispersion coefficient, and intraparticle diffusivity. The last

parameter was selected to be the model tuning parameter. The two other parameters were predicted applying existing experimental correlations.

5.2.5.1. Model description

The more precise method is based on differential mass balances along the extraction bed. A two-phase model comprising solid and subcritical water phases can be used. Extraction vessel is considered to be a cylinder filled by mono-sized spherical solid particles. The overall scheme of system was like Fig. 7.

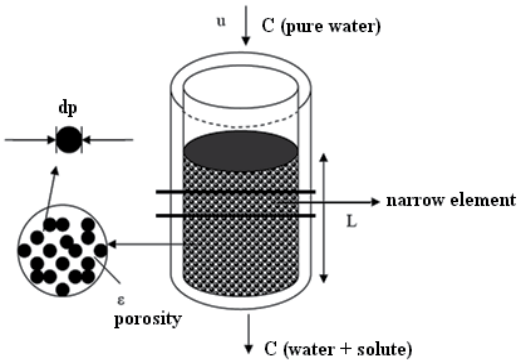

Figure 7. Characteristic dimensions and geometry of the packed bed SWE vessel.

The major assumptions used to describe the SWE process for deriving the essential oils extraction model were:

1. Packed bed extractor was isothermal and isobaric,
2. The physical properties of subcritical water were constant,
3. The hydrodynamics of a fluid bed was described by the dispersed plug-flow model,
4. The radial concentration gradient in the bulk fluid phase was assumed to be negligible,
5. The volume fraction of bed was not influenced by the weight loss of plant during the extraction,
6. The essential oil was assumed as a single component.

Under these assumptions, the differential mass balance equation for any component in the particle and bulk liquid phase and associated initial and boundary conditions can be written as following dimensionless forms:

- Solid phase:

$$\frac{\partial C_p}{\partial \tau} = \frac{2}{Pe_p}\frac{L}{R}\left(\frac{\partial^2 C_p}{\partial Y^2} + \frac{2}{Y}\frac{\partial C_p}{\partial Y}\right) \tag{17}$$

$$\tau = 0 \qquad C_p = C_{p0} \tag{18}$$

$$Y = 0 \qquad \frac{\partial C_p}{\partial Y} = 0 \tag{19}$$

$$Y = 1 \quad \frac{\partial C_p}{\partial Y} = Sh\left(C_f - C_{fp}\right) \tag{20}$$

- Subcritical water phase

$$\frac{\partial C_f}{\partial \tau} = \frac{1}{Pe_b}\frac{\partial^2 C_f}{\partial X^2} - \frac{\partial C_f}{\partial X} - \frac{6(1-\varepsilon)L}{\varepsilon R}\frac{Bi}{Pe_p}\left(C_f - C_{fp}\right) \tag{21}$$

$$\tau = 0 \qquad C_f = 0 \tag{22}$$

$$X = 0 \qquad C_f - \frac{1}{Pe_b}\frac{\partial C_f}{\partial X} = 0 \tag{23}$$

$$X = 1 \quad \frac{\partial C_f}{\partial X} = 0 \tag{24}$$

Eqs. (17) and (21) may be solved using a linear equilibrium relationship between concentrations in the solid phase and SW phase at the interface, as follows [33]:

$$C_{fp} = k_p C_p\big|_{Y=1} \tag{25}$$

Where C_{fp} is the solute concentration in the fluid phase at the particle surface, $C_p|_{Y=1}$ is the solute concentration in the solid phase at equilibrium with the fluid phase and k_p is the volumetric partition coefficient of the solute between the solid and the fluid phase. Therefore, there are three eqs. (17), (21) and (25) which can be solved, simultaneously, for three unknowns C_p, C_f and C_{fp}.

The finite difference equations are a set of simultaneous linear algebraic equations must be solved for implicit method to obtain the concentration distribution at any time. In both cases, tridiagonal systems arise which are conveniently solved at each time step by the Thomas algorithm [34]. A computer code was written using MATLAB simulation software.

5.2.5.2. Parameter identification and correlations

The possible control of mass transfer was assayed by estimating the diffusion coefficient in the liquid. We can use the correlation proposed by Wilke and Chang (1955) to estimate this coefficient [35]:

$$D_{AB} = \frac{7.4*10^{-8}}{\mu V_A^{0.6}}(\varphi M_2)^{0.5} T \tag{26}$$

http://dx.doi.org/10.5772/54993

Where φ is 2.26 for water and 1.5 for ethanol and V_A was estimated by the Tyn Calus equation:

$$V_A = 0.285\ (V_c)^{1.048} \tag{27}$$

Where V_c is the estimated by the method of Joback and Reid (1987), with the aid of Molecular Modeling Plus software (Norgwyn Montgomery Software, USA) [36]. The axial dispersion coefficient in the supercritical phase was approximated as follows [37] and it may be used for the subcritical phase:

$$D_L = \frac{u\ d_p}{\varepsilon\ Pe_{pd}} \tag{28}$$

Where the average void volume fraction of the fixed bed was ε = 0.4 and:

$$Pe_{pd} = 1.634\ Re^{0.265}\ Sc^{-0.919} \tag{29}$$

Intraparticle diffusivity of the essential oils in the solid phase, D_m, was selected to be the tuning parameter of the model. Mass transfer between liquids and beds of spheres, k_f, can be represented by Wilson and Geankoplis in two cases [38]:

$$\varepsilon\ j_D = 0.0016 < Re < 55, \quad 165 < Sc < 70600 \tag{30}$$

$$\varepsilon\ j_D = \frac{0.25}{Re^{0.31}} 55 < Re < 1500, \quad 165 < Sc < 10690 \tag{31}$$

$$k_f = \frac{J_D\ U_o}{Sc^{2/3}} \tag{32}$$

Density of water at high pressures and temperatures from 273 to 473 K was assumed to be the density of saturated water (kg). It was calculated as follows [39]:

$$\rho = 858.03 + 1.2128\ T - 0.0025\ T^2 \tag{33}$$

Where ϱ is density (kg/m^3) and T is temperature (K). The water viscosity at temperatures from 300 to 450 K was calculated by the following equation:

$$\mu = \exp\left(-10.2 + \frac{280970}{T^2}\right) \tag{34}$$

Where μ is the viscosity (Pa.s) and T is temperature (K). Viscosity of water was supposed to be independent of pressure. The model was verified successfully using the SWE data for *Z.multiflora* leaves at 20 bar and 150°C. The optimum value of 2×10^{-12} m^2/s was obtained for the intraparticle diffusivity [12].

5.2.6. CFD model

There is no scientific literature about the application of CFD modeling approach in the SWE processes. In our previous work, we have tried to do CFD modeling of essential oils of *Z. multiflora* leaves [13].

In CFD modeling in packed bed reactor, there are two cases. In first one, when the reactor to particle diameter ratio is less than10, it is needed to build the exact geometry and the location of the particles and solving the governing equations in meshes and can see the field of flow between particles inside reactor. But in another one, when the reactor to particle diameter ratio is higher than10, this system is defined as porous media. For modeling of these reactors, the Navier-stocks with one additional term, which is contained viscous force and inertia loss, in porous media is solved.

In this work, because of the reactor to particle diameter ratio is higher than10; the system can define as porous media. The momentum equation is defined as:

$$\frac{\partial}{\partial t}\left(\varepsilon\rho\vec{v}\right)+\nabla.\left(\varepsilon\rho\vec{V}\vec{V}\right)=-\varepsilon\nabla P+\nabla.\left(\varepsilon\tau\right)=\left(-\frac{\mu}{\beta}\vec{V}+\frac{1}{2}C\rho\left|\vec{V}\right|\vec{V}\right) \tag{35}$$

Where $\frac{\partial}{\partial t}(\varepsilon\rho\vec{v})+\nabla.(\varepsilon\rho\vec{V}\vec{V})=-\varepsilon\nabla P+\nabla.(\varepsilon\tau)=\left(-\frac{\mu}{\beta}\vec{V}+\frac{1}{2}C\rho\mid\vec{V}\mid\vec{V}\right)$ and C and β coefficient can define as:

$$\beta=\frac{d_P^2\varepsilon^3}{150\left(1-\varepsilon\right)^2} \tag{36}$$

$$C=\frac{3.5\left(1-\varepsilon\right)}{d_P\varepsilon^3} \tag{37}$$

In this work the porosity of bed is 0.4, so we have following value for C and β coefficients.

$$C=54687.5 \quad 1/m \tag{38}$$

$$\beta=0.23*10^{-10}\,1/m^2 \tag{39}$$

The energy equation is defined as:

$$\frac{\partial}{\partial t}\left(\varepsilon\rho_f E_f+\left(1-\varepsilon\right)\rho_s E_s\right)+\nabla.\left(\vec{V}\left(\rho_f E_f+P\right)\right)=\nabla.\left[\hat{K}\nabla T+\left(\tau.\vec{V}\right)\right]+S \tag{40}$$

http://dx.doi.org/10.5772/54993

Where the Effective thermal diffusion coefficient is defined as:

$$\hat{K} = \varepsilon \hat{K}_f + (1-\varepsilon)\hat{K}_s \tag{41}$$

The spices transfer equation is defined as:

$$\frac{\partial c_i}{\partial t} + \frac{\partial}{\partial x}\left(-D_x \frac{\partial c_i}{\partial x}\right) + \frac{\partial}{\partial x}\left(-D_x \frac{\partial c_i}{\partial x}\right) = \frac{D_y}{y}\frac{\partial c_i}{\partial y} - \frac{u}{\varepsilon}\frac{\partial c_i}{\partial x} - \frac{u}{\varepsilon}\frac{\partial c_i}{\partial y} + S \tag{42}$$

S is source term. Comparing the default of spices transfer equation with spices transfer equation of this system can define the $\frac{\partial c_i}{\partial t} + \frac{\partial}{\partial x}\left(-D_x \frac{\partial c_i}{\partial x}\right) + \frac{\partial}{\partial x}\left(-D_x \frac{\partial c_i}{\partial x}\right) = \frac{D_y}{y}\frac{\partial c_i}{\partial y} - \frac{u}{\varepsilon}\frac{\partial c_i}{\partial x} - \frac{u}{\varepsilon}\frac{\partial c_i}{\partial y} + S$ as the source term of this work.

C_{fs} was the concentration of Thymol & Carvacrol in the fluid face at the particle surface and was defined as:

$$c_{fs} = k_p c_{ss} \tag{43}$$

and

$$c_{ss} = 0.8\, c_0 \exp(-0.0005\, t) \tag{44}$$

In such works, the Reynolds number is defined as:

$$\mathrm{Re}_d = \frac{\rho \bar{U}_p \bar{d}_p}{\mu} \tag{45}$$

$\mathrm{Re}_d = \frac{\rho \bar{U}_p \bar{d}_p}{\mu}$ is mean characteristic length of porous and $\bar{d}_p$ is mean velocity based on porous. Based on this Reynolds number, it can be seen four regimes:

Re_d<1 Darcy regime or creeping flow

1<Re_d<150 inertia regime

150<Re_d<300 unsteady laminar flow regime

Re_d>300 unsteady Turbulent flow regime

The superficial velocity in this packed bed is defined as dividing flow rate by cross section.

Dividing superficial velocity by porosity, real velocity can calculate.

$$U = \frac{Q}{A} \tag{46}$$

$$\bar{U}_p = \frac{U}{\varepsilon} \tag{47}$$

and for calculating D_p

$$\bar{D}_p = \frac{6}{A_0} \tag{48}$$

In this work the mean particle diameter was 0.6 mm.

$$A_0 = \frac{A}{V} = \frac{4\pi r^2}{\frac{4}{3}\pi r^3} \tag{49}$$

In this work the Reynolds number is 0.2, so there is laminar flow in this system.

The material of system was mixture of Thymol & Carvacrol and water. The inlet flow was contained water with mole fraction 1 and the outer flow was consisted of water and Thymol & Carvacrol [13]. The packed bed had 103 mm height and the diameter of bed was 16 mm. The uniform mesh was used for this domain.

The governing equations are solved by a finite volume method. At main grid points placed in the center of the control volume, volume fraction, density and spices fraction are stored. The conservation equations are integrated in space and time. This integration is performed using first order upwind differencing in space and fully implicit in time. For a first-order upwind solution, the value at the center of a cell is assumed to be an average throughout the cell. The SIMPLE algorithm is used to relate the velocity and pressure equations.

The simulation geometry is shown in Fig.8. The 2D calculation domain is divided into 22*146 grid nodes, in the radial and axial directions, respectively. The grid and mesh size are chosen to be uniform in the two directions. The inlet of system was pure water and the outlet of system was extracted Thymol & Carvacrol.

The extraction values versus time for 150^{o}C were shown in Fig. 9. It can be seen, the extraction values were increased as exponentially. After 60 min, the change of extraction values with time was very little.

http://dx.doi.org/10.5772/54993

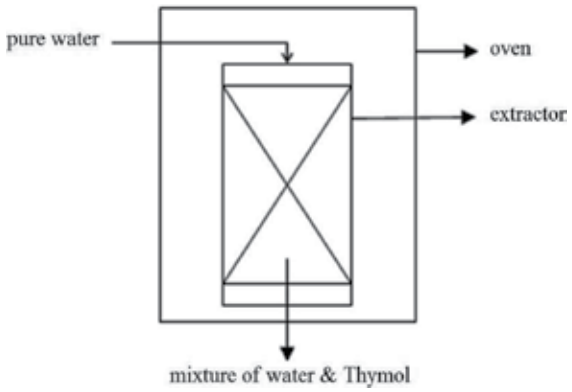

Figure 8. The Schematic of extractor [13].

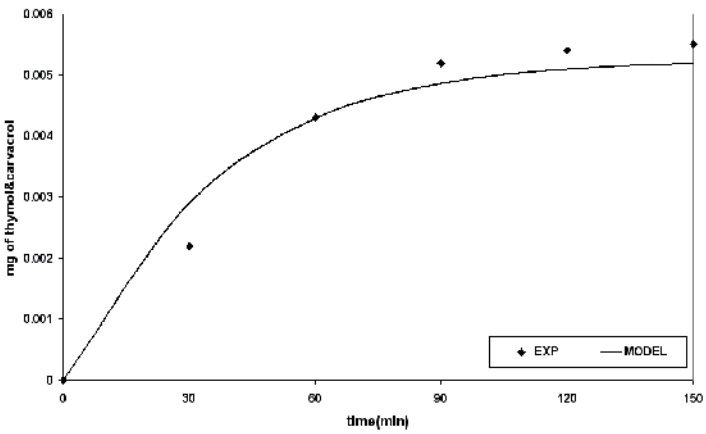

Figure 9. Extraction values versus time for 150°C [13].

In order to investigate the applicability of the CFD model, the theoretical results are compared with experimental measurements obtained at optimum conditions (20 bars, 150°C, and 2 ml/min). Fig. 9 shows that the modeling extraction values profile is increasing rapidly in the period of 0-60 min and thereafter in the second region (60-120 min) the slope reduces until reaches a constant trend in the third period of 120-150 min. In the first region, because of high Thymol & Carvacrol concentrations in the *Z. multiflora* leaves and therefore, high mass transfer driving force, high desorption rate of Thymol & Carvacrol from solid matrix occurs.

6. Conclusion

It was tried to give overall view about subcritical water extraction. Effective parameters, mechanism and modeling of extraction were surveyed. Overall by considering mean average

errors of models, a mathematical model base on the combination of partition coefficient (*K*D) and external mass transfer gave a good description of subcritical water extraction of *Z. multiflora*, while the kinetic model reasonably described the extraction behavior at lower flow rates [11].

On the other side, model was developed by introducing differential mass balances using two phase model, and applying a linear equilibrium relationship. Because of considering the effect of variation of the concentration profile in the SW phase, it seems that the proposed model is more significant from the physical point of view.

The Last model was CFD modeling of extraction from *Z. multiflora* leaves using subcritical water. It was concluded that CFD is poised to remain at the forefront of cutting edge research in the sciences of fluid dynamics and mass transfer. Also, the emergence of CFD as a practical tool in modern engineering practice is steadily attracting much interest and appeal. The results of CFD model have been agreed well with experimental data. As shown, along of extractor, Thymol was extracted and was in outflow.

Notations

specific surface, m^2/m^3 ($=\frac{3}{R_p}$)	a or a_p
Biot number ($=\frac{k_f R_p}{D_m}$)	Bi
solute concentration in the solid phase, $kmol/m^3$	C
solute concentration in the SW phase, $kmol/m^3$	C_f
solute concentration in the fluid phase at the particle surface, $kmol/m^3$	C_{fp}
solute concentration in the solid phase, $kmol/m^3$ ($\frac{C_p}{C_{po}}$)	C_p
initial solute concentration in the solid phase, $kmol/m^3$	C_{po}
diffusivity of solute (A) in liquid (B), m^2/s	D_{AB}
effective diffusion coefficient (m^2/s)	D_e
axial dispersion coefficient, m^2/s	D_L
diffusivity in the solid, m^2/s	D_m
particle diameter, m	d_p
exponential function	e
a certain fraction of the analyte desorbs at a fast rate by k_1	F
remaining fraction desorbs at a slower rate by k_2	$(1-F_1)$
thermodynamics partitioning coefficient	K_D
external mass transfer coefficient (m/min)	k_e

mass transfer between liquids and beds of spheres	k_f
volumetric partition coefficient of the solute between the solid and the fluid phase	k_p
cumulative mass of analyte extracted after certain amount of volume V_a (mg/g dry sample)	M_a
cumulative mass of the analyte extracted after certain amount of volume V_b (mg/g dry sample)	M_b
total initial mass of analyte in the matrix (mg/g dry sample)	M_i
cumulative fraction of the analyte extracted by the fluid of the volume V_b and V_a (ml)	M_b/M_i and M_a/M_i
total amount of solute (mg/g) removed from particle after time t	M_t
maximum amount (mg/g) of solute extracted after infinite time	M_∞
ratio of total migration to the maximum migration concentration	M_t/M_∞
mass of the extracted sample (mg dry sample)	m
Peclet number of the bed ($= \frac{u_o L}{D_L \varepsilon}$)	Pe_b
Peclet number of the solid ($= \frac{u d_p}{D_m \varepsilon}$)	Pe_p
average radius of an extractable particle	R
Reynolds number ($= \frac{2 R u \rho}{\mu}$)	Re
Schmidt number ($= \frac{\mu \rho}{D_{AB}}$)	Sc
Sherwood number ($= \frac{2 kf R}{D_{eff}}$)	Sh
Stanton number ($\frac{L (1 - \varepsilon) k_f a}{u}$)	St
Temperature, K	T
superficial SW fluid velocity, m/s	u
molar volume of the solute at its normal boiling point, cm^3/mol	V_A
critical volume, cm^3/mol	V_c
dimensionless axial coordinate along the bed, z/L	X
dimensionless radius ($= \frac{r}{R}$)	Y

Greek symbols

ε	void volume fraction
μ	viscosity, Pa.s
ρ	density, kg/m^3
φ	association factor for the solvent

τ	dimensionless time ($=\frac{u\,t}{L\,\varepsilon}$)

Acknowledgements

This research was supported by Semnan University. The authors would like to thanks the Office of Brilliant Talents at the Semnan University for financial support.

Author details

A. Haghighi Asl and M. Khajenoori

School of Chemical Gas and Petroleum Engineering, Semnan University, Semnan, I.R., Iran

References

[1] C.W. Huie, "A review of modern sample-preparation techniques for the extraction and analysis of medicinal plants," Anal. Bioanal. Chem. 373 (2002) 23-30.

[2] B. Zygmunt, J. Namiesnik, "Preparation of samples of plant material for chromatographic analysis," J. Chromatogr. Sci. 41 (2003) 109-116.

[3] E.S. Ong, "Extraction methods and chemical standardization of botanicals and herbal preparations," J. Chromatogr. B 812 (2004) 23-33.

[4] King, et al., US Patent 7,208,181, B1, 2007.

[5] R. M., Smith, "Superheated water: The ultimate green solvent for separation science", Anal. Bioanal. Chem., 385(3), 419 (2006).

[6] D. J., Miller, S. B., Hawthorne, "Solubility of liquid organics of environmental interest in subcritical (hot/liquid) water from 298 K to 473 K", J. Chem. Eng. Data, 45, 78 (2000).

[7] M. Khajenoori, A. Haghighi Asl, and F. Hormozi, M. H. Eikani and H. Noori. "Subcritical Water Extraction of *Zataria Multiflora Boiss.*", *Journal of Food Process Engineering*, 32, (2009) 804–816.

[8] M.H., Eikani, F., Golmohammad and S., Roshanzamir, "Subcritical water extraction of essential oils from coriander seeds (*Coriandrum sativum Mill.*)", J. Food Eng. 80 (2) (2007a) 735-740.

[9] M.H., Eikani, F., Golmohammad, S., Roshanzamir and M. Mirza, "Extraction of volatile oil from cumin (*Cuminum cyminum L.*) with superheated water", J. Food Process Eng., 30 (2) (2007b) 255-266.

[10] A., Kubatova, B., Jansen, J.F., Vaudoisot, S. B., Hawthorne, "Thermodynamic and kinetic models for the extraction of essential oil from savory and polycyclic aromatic hydrocarbons from soil with hot (subcritical) water and supercritical CO_2", J. Chromatography A., 975(1), (2002) 175-188.

[11] M. Khajenoori, A. Haghighi Asl, and F. Hormozi, "Proposed Models for Subcritical Water Extraction of Essential Oils", Chinese Journal of Chemical Engineering, Vol. 17, No. 3, (2009) 359-365.

[12] M. Khajenoori, A. Haghighi Asl, and M. H. Eikani "Modeling of Superheated Water Extraction of Essential Oils". Submitted in "13th Iranian National Chemical Engineering Congress & 1st International Regional Chemical and Petroleum Engineering Kermanshah, Iran, 25-28 October, 2010".

[13] M. Khajenoori, E. Omidbakhsh, F. Hormozi, and A. Haghighi Asl, "CFD modeling of subcritical water extraction". the 6th International chemical Engineering Congress (IChEC), Kish Island, Iran, 16-20 November 2009.

[14] J., Crank,. "The mathematics of Diffusion". Oxford, England: Clarendon Press. (1975) pp. 150-175.

[15] V., Gekas, "Transport phenomena of foods and biological material". Boca Raton, FL. CRC Press., (1992) pp. 156-178.

[16] E. L., Cussler, "Diffusion: Mass Transfer in Fluid Systems". Cambridge University Press. Cambridge, UK., (1984) pp. 146-177.

[17] C., Mantell, M., Rodriguez, and E. Martinez de la Ossa, "Semi-batch extraction of anthocyanins from red grape pomace in packed beds: experimental results and process modeling", Chem. Eng. Sci., 57 (2002). 3831-3838.

[18] Dibert, K., Cros, E., and Andrieu, J. Solvent extraction of oil and chlorogenic acid from green coffee. Part II. Kinetic data. J. Food Eng., 10, (1989) 199-214.

[19] Tutuncu, M. A., and labuza, T.P.. Effect of geometry on the effective moisture transfer diffusion coefficient. J. Food Eng. 30: (1996) 433-447.

[20] J.A. Bressan, P.A. Carroad, R.L. Merson, W.L. Dunkley, Temperature dependence of effective diffusion coefficient for total solids during washing of cheese curd. J. Food Sci, 46 (1958) 9.

[21] E.S.A., Biekman, C., Van Dijk, "Measurement of the apparent diffusion coefficient of proteins in potato tissue", Presented at DLOA grotechnological Research Institute, The Netherlands, (1992).

[22] C.R., Binkley, RC., Wiley, "Chemical and physical treatment effects on solid–liquid extraction of apple tissue", J. Food Sci., 46 (1981) 729-732.

[23] NS., Kincal, F., Kaymak, "Modeling dry matter losses from carrots during blanching", J. Food Process Eng., 9 (1987) 201–211.

[24] I., Lamberg, 'Transport phenomena in potato tissue". Ph.D. thesis, University of Lund, Lund, Sweden; (1990).

[25] G.C., Leach, DL., Pyle, K., Niranjan, 'Effective diffusivity of total solids and pectic substances from apple tissue", Int. J. Food Sci. Technol., 29 (1995) 687–897.

[26] A., Lenart, PP., Lewicki, J., Dziuda, "Changes in the diffusional properties of apple tissue during technological processing". In: Spiess WEL, Schubert H., editors. Engineering and food, vol.1: Physical properties and process control. London: Elsevier Applied Science; (1989) pp. 531-540.

[27] G., Rodger, R., Hastings, C., Cryne, J., Bailey, "Diffusion properties of salt and acetic acid into herring and their subsequent effect on the muscle tissue". J. Food Sci., 49 (1984) 714-732.

[28] P., Tomasula, MF., Kozempel, "Diffusion coefficients of glucose, potassium, and magnesium in Maine Russet Burbank and Maine Katahdin potatoes from 45 to 90°C", J. Food Sci. 54 (4) (1989) 985–999.

[29] H.G., Schwartzberg, R.Y., Chao, "Solute diffusivities in leaching process", Food Technol., 36, (1982) 73-86.

[30] D.D., Gertenbach, "Solid-liquid extraction technologies for manufacturing nutraceuticals", Shi, J., Mazza, G., Maguer, M.L., eds., Functional Foods: Biochemical and Processing Aspects (Vol.2), CRC Press, Boca Raton, Flordia (2002).

[31] J.E., Cacace, G., Mazza, "Pressurized low polarity water extraction of lignans from whole flaxseed", J. Food. Eng., 77 (2006) 1087-1095.

[32] Th., Anekpankul, M., Goto, M., Sasaki, P., Pavasant, A., Shotipruk, "Extraction of anti-cancer damnacathal from roots of *Morinda citrifolia* by subcritical water", Sep. Purif. Technol., 55 (2007) 343-349.

[33] E., Reverchon, "Mathematical modeling of supercritical extraction of sage oil," A.I.Ch.E. Journal, 42 (1996).1765-1771.

[34] Y. Jaluria, "Computer Methods for Engineering". Allyn and Bacon, Newton, MA, U.S.A. (1988).

[35] C. R. Wilke, P. Chang, "Correlation of diffusion coefficients in dilute Solutions", AICHE Journal, 1 (1955) 264-270.

[36] K. Joback, R. Reid, "Estimation of pure component properties from group contributions", Chemical Eng. Commun., 57 (1987) 233-243.

[37] C. S. Tan and D. C. Liou, "Axial dispersion of Supercritical carbon dioxide in packed beds," Ind. Eng. Chem. Res., 28 (1989) 1246-1250.

[38] J. R. Welty, C. E. Wicks, R. E. Wilson, "Fundamentals of Momentum, Heat, and Mass Transfer", 3rd ed., John Wiley & Sons, New York, (1984).

[39] R. Perry, D. W. Green, J. O. Maloney, "Perry Chemical Engineers Handbook," 5rd ed. McGraw-Hill, New York (1984).

Chapter 18

Mass Transfer: Impact of Intrinsic Kinetics on the Environment

Engr Owabor

Additional information is available at the end of the chapter

http://dx.doi.org/10.5772/55990

1. Introduction

Emerging trends in environmental engineering and biosystem analysis indicate that a clean, safe and healthy ecosystem is still possible regardless of the increased quest for technology and industrialization by a dynamic society where the fuel requirements of the energy sector and the chemical and petrochemical needs of the chemical and allied industries are greatly dependent on the petroleum industry in which the downstream sector is a key player. These needs range from the feedstock requirements of the chemical industries, polymeric industrial sector, the solvent sector, the cosmetics industries etc. The concern over industrial and technological expansion, energy utilization, waste generation from domestic and industrial sources viz a viz their attendant negative effects on the environment cannot be overemphasized.

This chapter is intended to expose the reader to the role of mass transfer on the topical issue of environmental remediation. This is against the backdrop of the interrelationship between mass transfer and the major processes such as biological, chemical and phyto-oxidation acting during the removal of toxic substances from the environment and the dependence of these processes on the availability of these substances which over time compromise the integrity of the environment. Research reports advanced in this chapter is aimed at highlighting the crucial need to very seriously exploit the principles of mass transfer in addressing the critical issue of environmental degradation. The underlying mechanisms involved in the removal process and the systematic protocol developed for accelerated clean up are incorporated.

Basically, mass transfer is one of the important three transport operations commonly encountered and employed in chemical transformations. It has been described fundamentally, as the movement of the components of a mixture from one point to another as a result of observed

differences in concentration [1]. The material transfer is usually in the direction of decreasing concentration gradient.

The concept of mass transfer is very important in the fields of engineering (particularly Chemical Engineering) and sciences in general where it is applied for physical processes. From the standpoint of chemical engineering, mass transfer is of prime significance because most of the unit operations involving separation of mixtures into their component parts employ mass transfer operation. The relevance of mass transfer operations is continuously a subject of discourse as specifically, there is hardly any chemical process which does not require a preliminary purification of raw materials or final separation of desired products from by-products. In essence it can be described as the process that determines the rate at which separation will occur. Issues relating the removal of certain materials from fluid streams typically by adsorption are important industrial applications of the mass transfer operation.

The challenges of maintaining a clean environment stem primarily from the increasing pollution of waters and land by heavy metals that are difficult to decompose biologically and organic compounds which are persistent, recalcitrant and ubiquitous. This is because these substances resist the self-purification capabilities of the rivers as well as decomposition in conventional wastewater treatment plant. Consequently, conventional mechanical-biological purification no longer suffices. It thus becomes imperative to supplement an additional stage of processing and this improvement has been augmented by adsorption; an innovative treatment method based on the principle of diffusion (a mechanism of mass transfer). Literature reports have shown that the mechanism of the process of material transfer is by diffusion and this is dependent to a large extent on the physical characteristics and attributes of the mass been considered for transfer. The transfer process which is dependent on concentration gradient is basically of two types; molecular diffusion and convective transfer. While the former is known to be involved with movement of a material between two points i.e from a high to low area of concentration, the latter relates to the flow of liquids around a solid surface in forced convection motion. Interestingly, the two transfer types are governed by Fick's first law of diffusion under the condition of unchanging concentration gradient with the passage of time. However, Fick's second law becomes applicable under unsteady-state diffusion. The principles of Fick's laws which suggest that the rate of diffusion is a linear function of the solute concentration gradient has continuously been affirmed by research results involving material transport. In general, mass transfer cannot really be separated from adsorption and desorption processes as the transport of materials from one phase to another is principally by the mechanism of diffusion. Sorption is the primary process in the evaluation of availability while mass transfer is the mechanism of movement from the fluid phase to the surface of the soil particle. Various isotherm correlations have been used to describe the surface adsorption of the solutes and their subsequent desorption from the soil surface [1]. The sorption of contaminant tends to separate the direct contact between microorganisms, adsorbents and contaminants, which is necessary for biodegradation detoxification to occur. The practical effect of the adsorption and desorption rate, is that it controls the overall reaction rate. The transport (mobility) of contaminant solute therefore is significantly dependent on two possible scenarios: fast sorption/desorption and slow sorption/ desorption.

http://dx.doi.org/10.5772/55990

Development of surface modified activated carbon from low cost and readily available natural materials and agricultural wastes have been advanced for the generation of activated carbon with far superior adsorption capacity for the treatment of contaminated water. The removal of pollutants from aqueous waste stream by adsorption in fixed beds has therefore progressively become an important treatment process and a subject of many excellent research works.

Laboratory and field studies results abound to demonstrate the applications of mass transfer in the management of the environment in terms of pollution monitoring and control. The intrinsic kinetics of the mass transfer process has through systematic and sustained researches become a relevant area of interest which provides information on availability, mobility and toxicity as a function of the measured concentration and the mechanism of sequestration of the solutes in the containing system.

2. Applications of mass transfer in water treatment technology

The demand for clean water for fishing activities, recreation etc and its non-ready availability has caused considerable attention to be focused towards recovery and re-use of waste waters. In water treatment procedures where the process of adsorption has been effectively engaged, the use of adsorbent materials has served as the solid surface onto which molecules of the adsorbates such as organic compounds, heavy metals, attach themselves. The removal of contaminant solutes from the environment has not been effectively accomplished by traditional methods. Hence it has now become universally recognized that adsorption technology provides a feasible and effective method for the removal of pollutants from polluted water resources and waste waters. Activated carbons are the most commonly used adsorbent in the adsorption process due to their high adsorption capacity, high surface area and high degree of surface reactivity. Adsorbents have been sourced variously from refinery residue, coal but mostly from agricultural waste materials such as coconut shell, soya bean, cotton seed, walnut and rice hulls, melon husk, orange peels etc.

The effectiveness of low density adsorbents dried (ground ripe and unripe orange peels) in the removal organics typified using naphthalene and pyrene from an aqueous stream has been extensively studied [2]. The influence of the variation in process conditions such as concentration, adsorbent dosage, agitation time and particle size, pH, and initial solute concentration were analyzed to highlight the contributions of mass transfer in the treatment of contaminated water. Under the operating conditions specified above, laboratory and experimental results showed that the removal efficiency defined by adsorption capacity increased with an increase in adsorbent dosage, contact time and initial solute concentration but decreased with an increase in the particle size. This experimental result clearly demonstrates that the transfer of any organic compound under consideration from one point to another is a linear function of the operating variables which positively improve the reliability of the process.

Following the same adsorption principle for mass transfer, the removal of mono and polycyclic aromatic hydrocarbons (PAHs) from bulk fluid stream onto adsorbents from periwinkle and coconut shell (PSC) also provides an alternative technology for effective mass transfer process in

the reduction of pollutant level of waste water. Naphthalene, phenanthrene and anthracene were used as the representative PAHs and the effluent stream was simulated refinery wastewater.

The result for the characterization of the refinery effluent before and after treatment with periwinkle shell activated carbon showed that the total suspended solids (TSS) reduced from an initial value of 53 mg/l to 2 mg/l after treatment.

Further insights into the role of adsorption on the contaminated water has revealed that the biochemical and chemical oxygen demand of the wastewater reduced drastically from an initial value to specifications recommended by the environmental protection agency (EPA) using activated carbon from materials such as periwinkle shell [3]. As contact time increased, percentage removal of the organic and inorganic contaminants present in the wastewater also increased. From the bench scale results [3], the total dissolved solids and total hydrocarbon content of the wastewater treated with activated periwinkle shell carbon reduced significantly. A maximum percentage removal of 78.5% was achieved. The clarity of the effluent water was observed to be greatly improved after the first hour of treatment where the turbidity dropped from 66 NTU to 6 NTU. Again the percentage turbidity increased with contact time until 100% removal was achieved following complete clarity.

The result showed comparatively, that the treated effluent water had maximum percentage reduction of approximately 83.26%, 91.19% (BOD, COD) for periwinkle shell carbon (PSC) and commercial activated carbon (CAC) respectively. The periwinkle shell carbon displayed the capacity to reduce the turbidity of the water contaminated with organic compounds via transfer of the contaminant solute from the bulk wastewater where their concentration is high to the external surface of the activated periwinkle shell carbon acting as the adsorbent.

In the development of alternative fixed filter bed for water treatment, the application of the mass transfer process by adsorption has also been shown to be feasible by examining the influence of modified clay on the rates of adsorption. The modifiers used were inorganic and organic acids, bases and salts. The results obtained showed that equilibrium adsorption of naphthalene i.e the transfer of naphthalene molecules from the bulk solution was attained at a faster rate using modified clay when compared with the unmodified clay. Amongst the modified clay used for the study, acids were found to be most suitable for the modification purpose [4].

This is attributable to the fact that the solutes in the acid medium had higher diffusive mobility defined by their dispersion coefficient/diffusivity as shown in Table 1 and higher influence on the physicochemical properties (porosity, surface area, bulk and particle density).

Overall, results from this study affirm that sediment modification directly affects the availability of the contaminant chemicals.

3. Applications in soil remediation

In soil remediation, the availability of the contaminant is of prime significance and it is commonly approached from the premise that chemicals are immediately accessible for

Modifying agents	D_{AB} (cm^2/s)
HCl	4.88×10^{-6}
H_2SO_4	4.5×10^{-6}
HNO_3	4.33×10^{-6}
H_3PO_4	2.97×10^{-6}
KOH	5.15×10^{-7}
NaOH	4.36×10^{-7}

*Adapted from Oladele, A.O. (2012). M.Eng. Thesis. University of Benin, Nigeria.

Table 1. Parameter estimation for naphthalene diffusivity in modified-clay sediment*

microbial uptake only when in aqueous solution. The rationale behind this premise is that the small pore spaces internal to aggregates of soil and sediment particles exclude microbes, such that compounds that are dissolved or sorbed within these immobile-water domains must first be transported to the external aqueous phase (i.e., bulk aqueous phase) before they can be metabolized [5]. This premise is supported by several laboratory studies that have found biodegradation to occur only, or predominantly, in the bulk aqueous phase [6], [7]. A variety of factors, including physical characteristics of the sorbent (e.g., particle shapes, sizes, and internal porosities), chemical properties of the sorbates and sorbents, and biological factors (e.g., microbial abundance and affinity for the contaminant) influence availability.

In a study conducted [8], the experimental data from a soil microcosm was analyzed using the method of temporal moments (MOM) which interprets solute transport with linear equilibrium sorption and first order degradation and the analytical solutions of a transport model CXTFIT version 2.0. This was with a view to estimating the transport parameters (pore-water velocity, V and dispersion coefficient, D) using non-reactive solute and the degradation parameters (retardation factor R and first order degradation rate λ) of the contaminant PAHs.

A dimensionless parameter called the retardation factor was used to represent bioavailability (i.e the accessibility of a chemical for assimilation and possible toxicity). This parameter increased with increasing solute hydrophobicity.

The result from the study is summarized in Table 2 and it showed that naphthalene had the lowest retardation factor with a corresponding higher degradation rate constant. The observed trend is similar and comparable to previous estimates from the Michaelis-Menten kinetics. The finding from this study can be attributed to the aqueous solubility, diffusivity and mobility of each contaminant solute.

PAHs	R			λ (per day)		
	MOM	CXTFIT	ε	MOM	CXTFIT	E
Naphthalene	25.77	20.23	0.21	3.54	4.22	-0.19
Anthracene	41.62	28.43	0.32	1.21	2.05	-0.69
Pyrene	35.66	25.89	0.27	2.25	3.26	-0.45

*Adapted from Owabor, C.N. (2007) PhD Thesis, University of Lagos, Nigeria.

Table 2. Comparison of the Degradation and Transport parameters for the Contaminant PAHs*

In general, the result is significant as it affirms that the biodegradation of the contaminant organic compound or specifically PAHs is a function of their bioavailability.

Studies have led researchers to conclude that some microorganisms are capable of degrading compounds directly from the sorbed phase. Also, for many studies where solid-phase degradation was reported, biodegradation rates were nonetheless observed to decrease with contaminant soil-water contact time. Access to contaminants is increasingly inhibited as solutes migrate deeper into submicron pores of impermeable sorption domains in soil/ sediment-water environments. From the foregoing, if solutes are degraded in the mobile aqueous phase, it then becomes pertinent to state that the rates of remediation will be reduced by sorption and/or diffusion into impermeable regions, with the overall rate controlled by the slowest process of desorption or biotransformation. For example, in batch systems where the solids have a large sorption capacity, only a small fraction of the contaminant mass may be present in the bulk water. Evolving experimental reports is thus emphasizing that sorbate *diffusion* is often the limiting step, particularly in systems involving contaminants with large organic-carbon partition coefficients (k_{OC}) and large fine-pored aggregates with high organic matter content.

Studies on mass transfer effects for the evaluation of bioavailability and biodegradation parameters of contaminant solutes in aqueous solid/sediment matrix applicable for biodegradation of the environmentally persistent and recalcitrant chemicals have been extensively investigated using models [7], [9] which incorporates a two-site sorption/desorption kinetics.

The applications of mass transfer by diffusion in multi-component mixtures were carried out by comparing the adsorption and desorption behavior of polycyclic aromatic hydrocarbons and benzene, toluene, ethylbenzene and xylene (BTEX) in sand and clay sediments fractions. Using equilibrium time as a basis for argument, research result showed that the contaminants in sand attained equilibrium faster than in the clay sediment for both sorption and desorption studies as a result of the higher permeability of sand sediment. The desorption equilibrium time in both sediment types was found to be slower than adsorption an indication that it may be the limiting step in the event of mineralization.

The adsorption and desorption kinetics of naphthalene using calcined and modified clay soil fractions at ambient temperature has also been investigated to demonstrate the role of mass

http://dx.doi.org/10.5772/55990

transfer in the removal of toxic chemicals from soil. Result of the batch experiments showed that adsorption equilibrium was attained at 24, 28 and 32 hours for modified, calcined and untreated soils; while the desorption equilibrium occurred at 46 hours for modified and 52 hours for calcined and untreated soils. Following the equilibrium time, the percentage of an initial 100mg/l of naphthalene in the slurry phase system unadsorbed was 30%, 32% and 35% for the calcined, modified and untreated soils respectively; while 12.3%, 11.2% and 9.5% of the adsorbed naphthalene resisted desorption by the calcined, modified and untreated samples respectively at equilibrium. The mass transfer rate was estimated using the Lagergren equation and found to be 0.12 mg/g.hr, 0.11mg/g.hr and 0.08mg/g.hr during adsorption while the desorption rate (k_{des}) were 0.06mg/g.hr, 0.05mg/g.hr and 0.07mg/g.hr for calcined, modified and untreated soil respectively. The results clearly confirm that the rate of adsorption and desorption of naphthalene differ among soil types and this directly affects its effective removal from the soil. Studies on the dynamic behavior of the adsorption of naphthalene onto natural clay with various modifying agents have shown that adsorption increased to a large extent with increasing surface area and porosity of the modified clay. The results using acids, bases and salts showed that equilibrium adsorption of naphthalene from the bulk solution were attained at a faster rate using inorganic acids. Further investigations revealed that of all the acids used, the diffusivity of naphthalene was highest in the HCl-modified clay which had the largest surface area and porosity.

Comparing this result with the data from the desorption study showed that while adsorption was inversely proportional to the pH of the medium, desorption was directly proportional. The implication of the retention time obtained from the equilibrium study is significant as it provides the bench mark for the interplay between sorption and degradation for transport and transformation of contaminant solutes within the soil matrix.

The adsorption and desorption kinetics of naphthalene, anthracene, and pyrene in a soil slurry reactor at ambient conditions was also investigated with a view to ascertaining the mechanisms controlling the retention and release rates of the compounds in the soil matrix. A stirred-flow method was employed to perform the experiments [10].

Analysis of the results of the batch adsorption/desorption kinetics and equilibria indicated that the desorption rate was slower than the adsorption rate. The cumulative extent of desorption for the tested chemicals (naphthalene, anthracene and pyrene) suggested that the desorption step was also the rate limiting for biodegradation. This may not be unrelated to the fact that diffusion in the pores may have been retarded by surface adsorption effects on soil organic carbon. The observed resultant effect was the lowering of the aqueous phase concentration of the contaminant PAHs which renders them not readily available to the microorganisms. The biodegradation will thus in the long run be controlled by the slow desorptive and diffusive mass transfer into biologically active areas. The extent of partitioning for the polycyclic aromatic hydrocarbons tested was found to be dependent on their solubility and diffusivity in the aqueous phase see Table 3. Experimental results from this study affirm that diffusivity/diffusion coefficient is a property dependent on the physical properties of a system as well as the molecularity, structural configuration and angularity of the solute [8].

Properties	Naphthalene	Anthracene	Pyrene
Molecular formula	$C_{10}H_8$	$C_{14}H_{10}$	$C_{16}H_{10}$
Molecular weight (g/mol)	128	178	202
Density (g/cm^3)	1.14	1.099	1.271
Melting point (^{o}C)	80.5	217.5	145-148
Boiling point (^{o}C)	218	340	404
Aqueous solubility (g/m^3)	0.93	0.07	0.14

*Adapted from Zander et al., (1993), Perry's Handbook of Chemical Engineers' (1998) and Oleszczuk and Baran, (2003).

Table 3. Some properties of investigated PAHs*

Overall, discussion of the subject under consideration indicates that mass transfer is assessed by the rate of adsorption/desorption and it must be emphasized that this is both the measured concentration of the solute with time and the mechanism of distributing the solutes into surfaces and pores of individual adsorbent medium. The successful predictions of the fate and transport of solutes in the environment is hinged on the availability of accurate transport parameters.

Solute transport with linear equilibrium therefore must as a matter of necessity be accounted for and be accommodated as an integral component of the mineralization of toxic chemicals.

Author details

Engr Owabor*

Address all correspondence to: owabor4you@yahoo.com

Department of Chemical Engineering, University of Benin, Benin City, Nigeria

References

[1] Treybal, R. E. (1981). Mass-Transfer Operations. , 19-23.

[2] Owabor, C. N, & Audu, J. E. (2010). Studies on the Adsorption of Naphthalene and Pyrene from aqueous medium using ripe orange peels as Adsorbent" Global Journal of Pure and Applied Sciences. , 16(1)

[3] Owabor, C. N, & Owhiri, E. (2011). Utilization of periwinkle shell carbon in the removal of polycyclic aromatic hydrocarbons from refinery wastewater." Journal of the Nigerian Society of Chemical Engineers, , 26

[4] Owabor, C. N, Ono, U. M, & Isuekevbo, A. (2012). Enhanced sorption of Naphthalene onto a Modified Clay Adsorbent: Effect of Acid, Base and Salt modifications of clay on sorption kinetics." Advances in Chemical Engineering and Science, , 2(3)

[5] Ehlers, J L, & Luthy, G R. (2003). Contaminant bioavailability in soil and sediment. Environmental Science and Technology, 37: 295A-302A.

[6] Bengtsson, G, & Carlsson, C. (2001). Degradation of dissolved and sorbed 2,4-dichlorophenol in soil columns by suspended and sorbed bacteria. Biodegradation, , 12(6), 419-32.

[7] Owabor, C. N, Ogbeide, S. E, & Susu, A. A. (2010). Degradation of polycyclic aromatic hydrocarbons: Model simulation for bioavailability and biodegradation". Canadian Journal of Chemical Engineering. , 88(2)

[8] Owabor, C. N. (2007). PhD Thesis, University of Lagos, Nigeria.

[9] Haws, N. W, Ball, P. W, & Bouwer, E. J. (2006). Modeling and interpreting bioavailability of organic contaminant mixtures in subsurface environments". J. of Contaminant Hydrology , 82, 255-292.

[10] Owabor, C. N, Ogbeide, S. E, & Susu, A. A. (2010). Adsorption and Desorption kinetics of Naphthalene, Anthracene and Pyrene in soil matrix". Petroleum Science and Technology. , 28(5)

[11] Oladele, A. O. Thesis. University of Benin, Nigeria.

[12] Zander et al(1993). Physical. and chemical properties of polycyclic aromatic hydrocarbons. Handbook of Polycyclic Aromatic Hydrocarbons. Marcel Dekker, Inc., New York, , 1-26.

[13] Perry, R. H, & Green, D. W. (1998). Perry's Chemical Engineers Handbook, 7th Edition. McGraw-Hill Inc.

[14] Oleszczuk and Baran(2003). Degradation of individual polycyclic aromatic hydrocarbons (PAHs) in soil polluted with aircraft fuel." Polish J. Environ. Studies, , 12, 431-437.

Chapter 19

Coordinated and Integrated Geomorphologic Analysis of Mass Transfers in Cold Climate Environments – The SEDIBUD (Sediment Budgets in Cold Environments) Programme

Achim A. Beylich

Additional information is available at the end of the chapter

http://dx.doi.org/10.5772/54725

1. Introduction

General background

Geomorphologic processes, responsible for transferring sediments and effecting landform change, are highly dependent on climate, and it is anticipated that climate change will have a major impact on the behaviour of Earth surface systems. Research on sedimentary fluxes from source to sink in a variety of different climatic environments is represented by a substantial body of literature. Studies on source-to-sink fluxes generally refer to the development of sediment budgets. A sediment budget is an accounting of the sources and disposition of sediment as it travels from its point of origin to its eventual exit from a defined landscape unit like a drainage basin, e.g. [1]. Accordingly, the development of a sediment budget necessitates the identification of processes of erosion, transport and deposition within a defined area, and their rates and controls [1, 2, 3]. The fundamental concept underpinning source-to-sink sediment flux and sediment budget studies is the basic sediment mass balance equation:

$I = O +- \Delta S$

Where inputs (I) equal outputs (O) plus changes in net storage of sediment (ΔS). Source-to-sink studies permit quantification of the transport and storage of sediment in a system. A thorough understanding of the current sediment production and flux regime within a system is fundamental to predict likely effects of changes to the system, whether climatic induced or human-influenced. Source-to-sink sediment flux and sediment budget research therefore enables the prediction of changes to erosion and sedimentation rates, knowledge of where

sediment will be deposited, how long it will be stored and how much sediment will be remobilised [1, 3, 4].

Sediment sources

Sediments are eroded and mobilised in source areas. Sediment sources are diverse and subject to variation in response to climate change. Global warming leads to the loss of glacial ice, which in turn increases slope instability caused by glacial de-buttressing, and flooding from glacial and moraine-dammed lakes [5, 6]. All these processes redistribute sediments and operate at different rates as a result of change to the system. Glaciers and ice sheets exert strong controls on the supply of sediments. For example, Knight et al. [7] identify the basal ice layer of a section of the Greenland ice sheet as the dominant source of sediment production. There is, however, only limited knowledge of debris fluxes from ice sheets and glaciers and its variability. The main mechanisms of sediment production in source areas can be described in terms of contemporary environmental conditions. However, in order to fully understand sediment supply a longer-term perspective is needed. Over the Quaternary, glacier fluctuations have had profound influences in depositing extensive mantles of sediments. More-widely, periglacial activity has altered the landscape under non-glacial cold climate conditions. The obvious imprint of this legacy is often reflected in contemporary sediment transfer rates where pre-existing deposits are eroded by present-day processes [6, 8].

Sediment transfers

Sediment transfers move eroded sediments from their source area to an area of temporal storage or long-term deposition in sinks. Rates of sediment transfer are not only conditioned by competence of geomorphic processes but also by the availability of sediment for transport. Accordingly, in assessing sediment transfer we need to quantify the forces, which drive transport processes but equally account for the factors, which control sediment supply [8]. Glacial fluxes are arguably the most significant processes for contemporary sediment flux [9]. Small-scale process studies very often focus on sedimentary fluxes from areas of weathering and erosion to areas of storage within defined landscape units like drainage basins, whereas large-scale sediment systems couple headwaters to oceanic sinks. For example, Gordeev [10], applying models developed by Morehead et al. [11], estimates the increase in sediment load in Arctic rivers in response to a rise in surface temperature of the drainage basins. Based on this model, increases in river discharge lead to an increase in the sediment flux of the six largest Arctic rivers, predicted to range from 30% to 122% by the year 2100.

Sediment stores / sinks

The identification of storage elements and sinks is critical to the effective study and understanding of source-to-sink sedimentary fluxes [1]. The setting of a particular drainage basin defines the boundary conditions for storage within that landscape unit. Within a defined landscape unit like a drainage basin, the slope and valley infill elements constitute the key storage units and storage volumes are important for addressing time-dependent sediment budget dynamics. Dating of storage in sedimentary source-to-sink flux studies is applied to determine or estimate the ages and chronology of the storage components within the system. An understanding of the nature of primary stores, secondary stores and the potential storage capacities of different types of drainage basins is important along with knowledge of sediment

http://dx.doi.org/10.5772/54725

residence times. Of growing importance is the development of innovative field methods, such as geophysical techniques for estimating sediment storage volumes [12, 13, 14]. Within large-scale sediment systems oceanic sinks are most important and provide the opportunity to estimate rates of sediment production and delivery at long-term temporal as well as continental spatial scales [15, 16].

2. The I.A.G. / A.I.G. SEDIBUD programme

Amplified climate change and ecological sensitivity of polar and cold environments has been highlighted as a key global environmental issue [17]. Projected climate change in cold regions is expected to alter melt season duration and intensity, along with the number of extreme rainfall events, total annual precipitation and the balance between snowfall and rainfall. Similarly, changes to the thermal balance are expected to reduce the extent of permafrost and seasonal ground frost and increase active layer and thaw depths. These effects will undoubtedly change surface environments in cold environments and alter the fluxes of sediments, nutrients and solutes, but the absence of data and analysis to understand the sensitivity of the surface environment are acute in cold climate environments.

The *SEDIBUD (Sediment Budgets in Cold Environments)* Programme of the International Association of Geomorphologists (I.A.G./A.I.G.) was formed in 2005 to address this identified key knowledge gap [18, 19]. SEDIBUD currently has about 400 members worldwide and the Steering Committee of this international programme is composed of ten scientists from eight different countries:

- Achim A. Beylich (*Chair*) (Norway)
- Armelle Decaulne (*Secretary*) (France)
- John C. Dixon (USA)
- Scott F. Lamoureux (*Vice-Chair*) (Canada)
- John F. Orwin (Canada)
- Jan-Christoph Otto (Austria)
- Irina Overeem (USA)
- Þorsteinn Sæmundsson (Iceland)
- Jeff Warburton (UK)
- Zbigniew Zwolinski (Poland)

The central research question of this global group of scientists is to

---

Assess and model the contemporary sedimentary fluxes in cold climates, with emphasis on both particulate and dissolved components.

Initially formed as European Science Foundation (ESF) Network SEDIFLUX (2004-2006) [20, 21], SEDIBUD has further expanded to a global group of researchers with in total 44 field research sites (SEDIBUD Key Test Sites) located in polar and alpine regions in the northern and southern hemisphere, see [22]. Research carried out at each site varies by programme, logistics and available resources, but typically represents interdisciplinary collaborations of geomorphologists, hydrologists, ecologists, permafrost scientists and glaciologists. SEDIBUD has developed a key set of primary surface process monitoring and research data requirements to incorporate results from these diverse projects and allow coordinated quantitative analysis across the programme. SEDIBUD Key Test Sites provide data on annual climate conditions, total discharge and particulate and dissolved fluxes as well as information on other relevant surface processes. A number of selected SEDIBUD Key Test Sites is providing high-resolution data on climate conditions, runoff and sedimentary fluxes, which in addition to the annual data contribute to the SEDIBUD Metadata Database which is currently developed. To support these coordinated efforts, the SEDIFLUX Manual [3] has been produced to establish common methods and data standards [18, 19]. In addition, a framework paper for characterizing fluvial sediment fluxes from source to sink in cold environments has been published by the group [23].

Comparable datasets from different SEDIBUD Key Test Sites are analysed to address key research questions of the SEDIBUD Programme as defined in the SEDIBUD Working Group Objective [24].

3. Compiled annual data from defined SEDIBUD key test sites

Table 1 compiles key parameters of four selected SEDIBUD research field sites (Figures 1 and 2) as examples.

SEDIBUD Key Test Site Catchment	Geographical coordinates	Area (km^2)	Elevation range (m); Topographic relief (m)	Mean annual air temperature in °C	Annual precipitation (mm)	Lithology
Hrafndalur (Iceland)	65°28`N, 13°42`W	7	6 – 731; 725	3.6	1719	Rhyolites
Austdalur (Iceland)	65°16`N, 13°48`W	23	0 – 1028; 1028	3.6	1431	Basalt
Latnjavagge (Sweden)	68°20`N, 18°30E	9	950 – 1440; 490	-2.0	852	Mica-garnet schists
Kidisjoki (Finland)	69°47`N, 27°05`E	18	75 – 365; 290	-2.0	415	Gneisses and granulites

Table 1. Key parameters of four selected catchment geo-systems (SEDIBUD Key Test Sites) in Eastern Iceland, Swedish Lapland and Finnish Lapland.

http://dx.doi.org/10.5772/54725

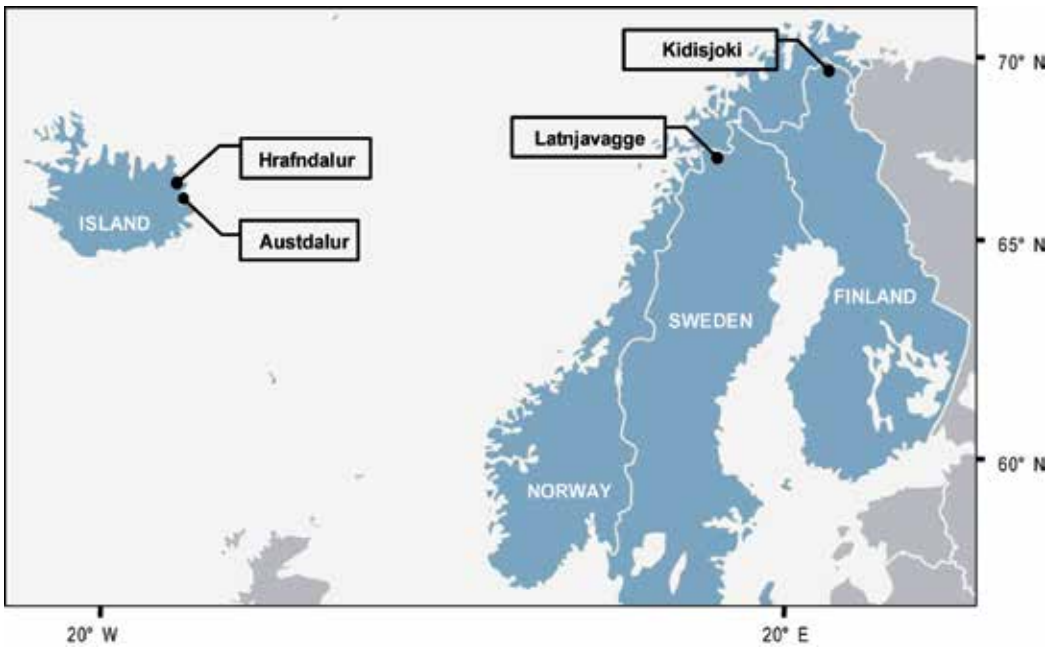

Figure 1. Location of the four selected SEDIBUD Key Test Sites Hrafndalur (Iceland), Austdalur (Iceland), Latnjavagge (Sweden) and Kidisjoki (Finland)

The generation and compilation of directly comparable data sets from the defined SEDIBUD Key Test Sites in the SEDIBUD Metadata Database is the basis for modelling effects of climate change on sedimentary fluxes and yields in cold climate environments by using space-for-time substitution [3, 18-21].

Annual data (as required from defined SEDIBUD Key Test Sites) from the four examples Hrafndalur (Iceland) [25, 26, 27], Austdalur (Iceland) [26, 27], Latnjavagge (Sweden) [25, 26, 28] and Kidisjoki (Finland) [25, 26] are compiled in Table 2. Time series of these mean annual data are published in [25-28].

4. Direct comparison and major controls of annual mass transfers within the four selected catchment geo-systems

On the basis of geomorphic process rates which were calculated for the Hrafndalur, Austdalur, Latnjavagge and Kidisjoki drainage basins after longer-term field studies (several years of process monitoring, mapping and observation) [26], the absolute and the relative importance of present-day denudative surface processes in the entire catchments was estimated by the quantification of the mass transfers caused by the different denudative surface processes. To allow direct comparison of the different denudative processes, all mass transfers are shown as tonnes multiplied by meter per year (t m yr^{-1}), i.e. as the product of the annually transferred mass and the corresponding transport distance, see [26, 29-31].

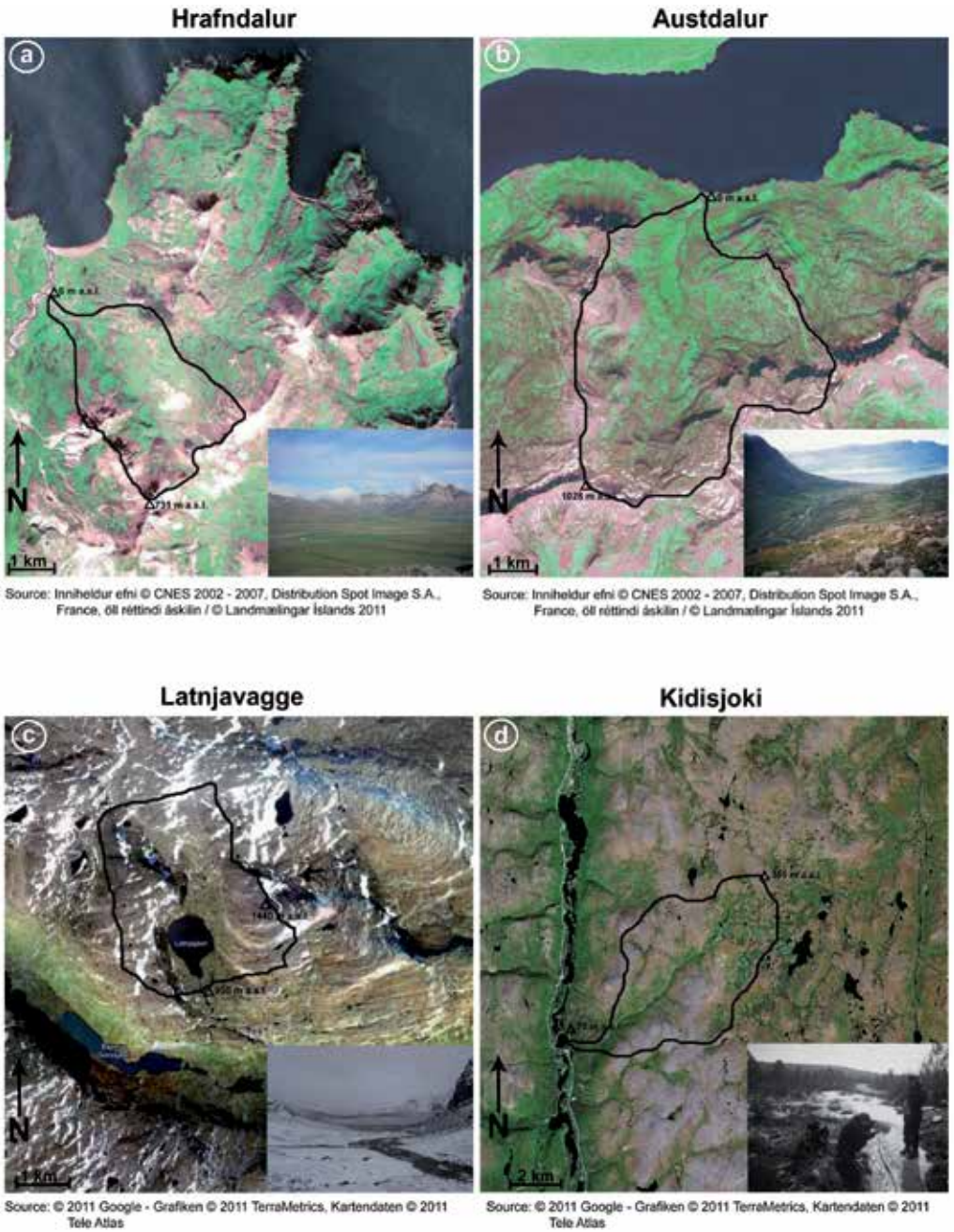

Figure 2. Views of the four selected SEDIBUD Key Test Sites Hrafndalur (Eastern Iceland), Austdalur (Eastern Iceland), Latnjavagge (Swedish Lapland) and Kidisjoki (Finnish Lapland)

http://dx.doi.org/10.5772/54725

Name of SEDIBUD Key Test Site: Hrafndalur (Iceland) Principal Investigator: Achim A. Beylich	**Period of investigations (years): 2002 - 2010 (Hydrological Year (HY) or Calender Year (CY); Published Data (PD) or Unpublished Data (UPD))**
Mean annual temperature (ºC):	3.6
Total annual precipitation [mm]:	1719
Total annual runoff [mm]:	1344
Annual suspended sediment yield [t km^{-2}]:	19
Annual solute yield (atmospherically corrected) [t km^{-2}]:	29
Name of SEDIBUD Key Test Site: Austdalur (Iceland) Principal Investigator: Achim A. Beylich	**Period of investigations (years): 1996 - 2010 (Hydrological Year (HY) or Calender Year (CY); Published Data (PD) or Unpublished Data (UPD))**
Mean annual temperature (ºC):	3.6
Total annual precipitation [mm]:	1431
Total annual runoff [mm]:	1130
Annual suspended sediment yield [t km^{-2}]:	42
Annual solute yield (atmospherically corrected) [t km^{-2}]:	8
Name of SEDIBUD Key Test Site: Latnjavagge (Sweden) Principal Investigator: Achim A. Beylich	**Period of investigations (years): 2000 - 2010 (Hydrological Year (HY) or Calender Year (CY); Published Data (PD) or Unpublished Data (UPD))**
Mean annual temperature (ºC):	-2.0
Total annual precipitation [mm]:	852
Total annual runoff [mm]:	717
Annual suspended sediment yield [t km^{-2}]:	2.4
Annual solute yield (atmospherically corrected) [t km^{-2}]:	4.9
Name of SEDIBUD Key Test Site: Kidisjoki (Finland) Principal Investigator: Achim A. Beylich	**Period of investigations (years): 2002 - 2010 (Hydrological Year (HY) or Calender Year (CY); Published Data (PD) or Unpublished Data (UPD))**
Mean annual temperature (ºC):	-2.0
Total annual precipitation [mm]:	415
Total annual runoff [mm]:	324
Annual suspended sediment yield [t km^{-2}]:	0.3
Annual solute yield (atmospherically corrected) [t km^{-2}]:	3.1

Table 2. Compiled annual data from four selected SEDIBUD Key Test Sites

As based on these quantitative investigations, in all selected study areas in sub-Arctic oceanic eastern Iceland, Arctic oceanic Swedish Lapland and sub-Arctic oceanic Finnish Lapland the intensity of contemporary denudative surface processes and mass transfers caused by these geomorphic processes is altogether rather low.

A direct comparison of the annual mass transfers within the four investigated drainage basins (Figure 3) summarises that there are differences between process intensities and the relative importance of different denudative processes within the study areas in Eastern Iceland, Swedish Lapland and Finnish Lapland.

The major controls of the detected differences are (see Figure 3):

i. *Hydro-climate and connected runoff:*

The higher annual precipitation along with the larger number of extreme rainfall events and the higher frequency of snowmelt and rainfall generated peak runoff events in eastern Iceland as compared to Swedish Lapland and Finnish Lapland leads to higher mass transfers (Figure 3). All four study areas are located in oceanic cold regions and projected climate change is expected to alter melt season duration and intensity, along with an increased number of extreme rainfall events, total annual precipitation and the balance between snowfall and rainfall. In addition, changes in the thermal balance are expected to reduce the extent of permafrost and seasonal ground frost and increase active layer depths [17]. Looking at the existing differences between Hrafndalur / Austdalur (eastern Iceland), Latnjavagge (Swedish Lapland) and Kidisjoki (Finnish Lapland) it seems obvious that the projected changes in climate will cause significant changes of mass transfers.

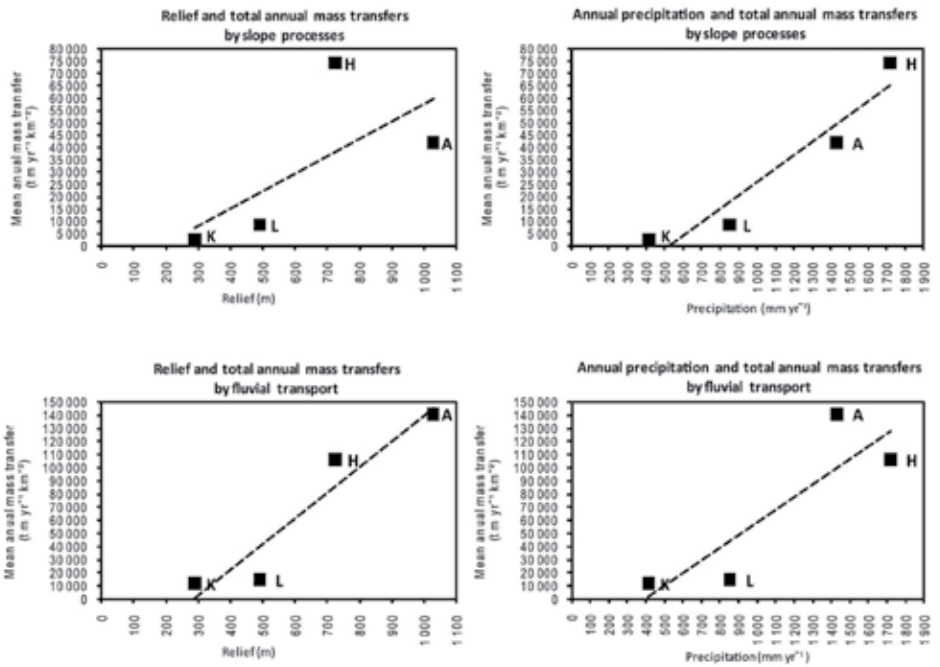

http://dx.doi.org/10.5772/54725

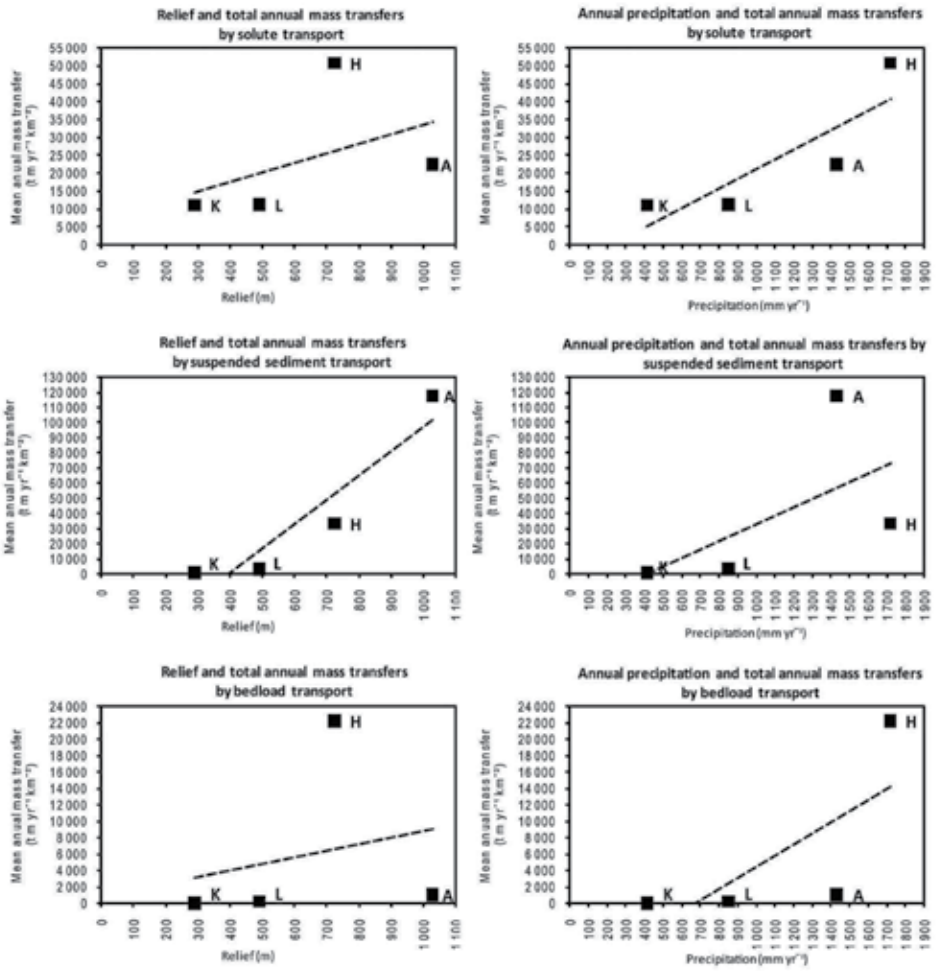

Figure 3. Statistical correlations between topographic relief and annual precipitation and annual mass transfers by slope processes and fluvial transport (fluvial solute transport, fluvial suspended sediment transport, fluvial bedload transport) for the four selected SEDIBUD Key Test Sites Hrafndalur (H), Austdalur (A), Latnjavagge (L) and Kidisjoki (K)

ii. *Topographic relief:*

The greater steepness of the Icelandic drainage basins leads to larger mass transfers here as compared to Latnjavagge and especially to Kidisjoki (Figure 3).

iii. *Lithology:*

The low resistance of the rhyolites in Hrafndalur causes especially high weathering rates and connected mass transfers in this drainage basin (see Figure 3). Due to the lower resistance of the rhyolites as compared to the basalts found in Austdalur Postglacial modification of the glacially formed relief is clearly further advanced in Hrafndalur as compared to Austdalur.

iv. *Vegetation cover (with vegetation cover being partly modified by human activity):*

The significant disturbance of the vegetation cover by direct human impacts in Hrafndalur / Austdalur (eastern Iceland) causes higher mass transfers by slope wash here whereas restricted sediment availability is a major reason for lower mass transfers in Latnjavagge (Swedish Lapland) and Kidisjoki (Finnish Lapland).

5. Conclusions

As a result, hydro-climate and topographic relief, followed by lithology and vegetation cover (with vegetation cover being partly modified by human activity), are the main controls of the mass transfers modifying the investigated sub-Arctic / Arctic landscapes, see also [32]. More studies to the present one, carried out within the SEDIBUD Programme with unified geomorphologic field methods [3, 21, 33, 34] in environments having different climatic, vegetation, human impact, topographic, lithological / geological and/or tectonic features will help to gain improved understanding of the internal differentiation of different global cold climate environments, see e.g. [21, 33, 35, 36]. Furthermore, additional information on the control mechanisms of processes, the role of extreme geomorphic events for longer-term mass transfers and sediment budgets, the general intensity of geomorphic processes and mass transfers, and the relative importance of different processes for slope and valley formation and relief development under different environmental conditions can be collected. Direct comparisons of SEDIBUD Key Test Sites (catchment geo-systems) and the application of the Ergodic principle of space-for-time substitution will improve the possibilities to model relief development as well as possible effects of projected climate change in cold climate environments.

Acknowledgements

The author would like to thank the SEDIBUD Steering Committee Members and numerous SEDIBUD Members for fruitful discussions and numerous valuable inputs.

Author details

Achim A. Beylich

Address all correspondence to: achim.beylich@ngu.no

Geological Survey of Norway (NGU), Geo-Environment Division, Trondheim, Norway

http://dx.doi.org/10.5772/54725

References

[1] Reid L.M., Dunne T. Rapid evaluation of sediment budgets. Catena 1996.

[2] Slaymaker O. Research developments in the hydrological sciences in Canada (1995-1998): Surface water – quantity, quality and ecology. Hydrological Processes 2000; 14 1539-1550.

[3] Beylich A.A., Warburton, J. editors. Analysis of source-to-sink fluxes and sediment budgets in changing high-latitude and high-altitude cold environments. SEDIFLUX Manual. NGU Report 2007.053.

[4] Gurnell A.M., Clark M.J. editors. Glacio-fluvial sediment transfer: An Alpine perspective. Chichester: Wiley; 1987.

[5] Evans S.G., Clague J.J. Recent climate change and catastrophic geomorphic processes in mountain environments. Geomorphology 1994; 10 107-128.

[6] Ballantyne C.K. Paraglacial geomorphology. Quaternary Science Reviews 2002; 21 1935-2017.

[7] Knight P.G., Waller R.I., Patterson C.J., Jones A.P., Robinson Z.P. Discharge of debris from ice at the margin of the Greenland ice sheet. Journal of Glaciology 2002; 48 192-198.

[8] Warburton J. Sediment budgets and rates of sediment transfer across cold environments in Europe: a commentary. Geografiska Annaler 2007; 89A(1) 95-100.

[9] Harbor J., Warburton J. Glaciation and denudation rates. Nature 1992; 356 751.

[10] Gordeev V.V. Fluvial sediment flux to the Arctic Ocean. Geomorphology 2006; 80 94-104.

[11] Morehead M.D., Syvitski J.P., Hutton E.W., Peckham S.D. Modeling the temporal variability in the flux of sediment from ungauged river basins. Global and Planetary Change 2003; 39 95-110.

[12] Schrott L., Hufschmidt G., Hankammer M., Hoffmann T., Dikau R. Spatial distribution of sediment storage types and quantification of valley fill deposits in an alpine basin, Reintal, Bavarian Alps, Germany. Geomorphology 2003; 55 45-63.

[13] Sass O. Spatial patterns of rockfall intensity in the northern Alps. Zeitschrift für Geomorphologie N.F. 2005; Suppl. 138 51-65.

[14] Hansen L., Beylich A.A., Burki V., Eilertsen R., Fredin O., Larsen E., Lyså A., Nesje A., Stalsberg K., Tønnesen J.-F. Stratigraphic architecture and infill history of a deglaciated bedrock valley based on georadar, seismic profiling and drilling. Sedimentology 2009; 56 1751-1773.

[15] Rise L., Ottesen D., Berg K., Lundin E. Large-scale development of the mid-Norwegian margin during the last 3 million years. Marine and Petroleum Geology 2005; 22 33-44.

[16] Dowdeswell J.A., Ottesen D., Rise L. Flow switching and large-scale deposition by ice streams draining former ice sheets. Geology 2006; 34 313-316.

[17] ACIA, Impacts of a warming Arctic: Arctic Climate Impact Assessment. ACIA Overview Report. Cambridge University Press; 2004.

[18] Beylich A.A. Quantitative studies on sediment fluxes and sediment budgets in changing cold environments – potential and expected benefit of coordinated data exchange and the unification of methods. Landform Analysis 2007; 5 9-10.

[19] Beylich A.A., Lamoureux S.F., Decaulne A. Coordinated quantitative studies on sediment fluxes and sediment budgets in changing cold environments examples from three SEDIBUD key test sites in Canada, Iceland and Norway. Landform Analysis 2007; 5 11-12.

[20] Beylich A.A., Etienne S., Etzelmüller B., Gordeev V.V., Käyhkö J., Rachold V., Russell A.J., Schmidt K.-H., Sæmundsson Th., Tweed F.S., Warburton J. Sedimentary Source-to-Sink-Fluxes in Cold Environments – Information on the European Science Foundation (ESF) Network SEDIFLUX. Zeitschrift für Geomorphologie N.F. 2005; Suppl. 138 229-234.

[21] Beylich A.A., Etienne S., Etzelmüller B., Gordeev V.V., Käyhkö J., Rachold V., Russell A.J., Schmidt K.-H., Sæmundsson Th., Tweed F.S., Warburton J. The European Science Foundation (ESF) Network SEDIFLUX – An introduction and overview. Geomorphology 2006; 80(1-2) 3-7.

[22] Beylich A.A., Decaulne A., Dixon J.C., Lamoureux S.F., Orwin J.F., Otto J.-Ch., Overeem I., Sæmundsson Th., Warburton J., Zwolinski Z. The global Sediment Budgets in Cold Environments (SEDIBUD) Programme: Coordinated studies of sedimentary fluxes and budgets in changing cold environments. Zeitschrift für Geomorphologie 2012; 56(1) 3-8.

[23] Orwin J.F., Lamoureux S.F., Warburton J., Beylich A.A. A framework for characterizing fluvial sediment fluxes from source to sink in cold environments. Geografiska Annaler 2010; 92A(2) 155-176.

[24] International association of Geomorphologists (I.A.G. / A.I.G.): SEDIBUD Website. http://www.geomorph.org/wg/wgsb.html (accessed 9 June 2012).

[25] Beylich A.A. Chemical and mechanical fluvial denudation in cold environments – Comparison of denudation rates from three catchments in sub-Arctic Eastern Iceland, sub-Arctic Finnish Lapland and Arctic Swedish Lapland. Jökull 2009; 59 19-32.

[26] Beylich A.A. Mass transfers, sediment budgets and relief development in cold environments: Results of long-term geomorphologic drainage basin studies in Iceland,

Swedish Lapland and Finnish Lapland. Zeitschrift für Geomorphologie 2011; 55(2) 145-174.

[27] Beylich A.A., Kneisel Ch. Sediment budget and relief development in Hrafndalur, sub-Arctic oceanic Eastern Iceland. Arctic, Antarctic and Alpine Research 2009; 41(1) 3-17.

[28] Beylich A.A., Mass transfers, sediment budget and relief development in the Latnjavagge catchment, Arctic oceanic Swedish Lapland. Zeitschrift für Geomorphologie N.F. 2008; 52(1) 149-197.

[29] Jäckli H. Gegenwartsgeologie des Bündnerischen Rheingebietes. Beitrag zur Geologischen Karte der Schweiz. Geotechnische Serie 1957; 36.

[30] Rapp A. Recent development of mountain slopes in Kärkevagge and surroundings, Northern Scandinavia. Geografiska Annaler 1960; 42 71-200.

[31] Barsch D. Studien zur gegenwärtigen Geomorphodynamik im Bereich der Oobloyah Bay, N-Ellesmere Island, N.W.T., Kanada. Heidelberger Geographische Arbeiten 1981; 69 123-161.

[32] Slaymaker O., Spencer T., Dadson S. Landscape and landscape-scale processes as the unfilled niche in the global environmental change debate: an introduction. In: Slaymaker O., Spencer T., Embleton-Hamann C. (eds.) Geomorphology and Global Environmental Change. Cambridge University Press; 2009. p1-36.

[33] Beylich A.A., Lamoureux S.F., Decaulne A. The global I.A.G./A.I.G. SEDIBUD (Sediment Budgets in Cold Environments) programme: Introduction and overview. Norwegian Journal of Geography 2008; 62(2) 50-51.

[34] Beylich A.A., Lamoureux S.F., Decaulne A. Developing frameworks for studies on sedimentary fluxes and budgets in changing cold environments. Quaestiones Geographicae 2011; 30(1) 5-18.

[35] Barsch D. Geomorphologische Untersuchungen zum periglazialen Milieu polarer Geosysteme. Zeitschrift für Geomorphologie N.F. 1984; Suppl. 50 107-116.

[36] Barsch D. Forschungen in Polargebieten. Heidelberger Geowissenschaftliche Abhandlungen 1986; 6 33-50.

Edited by Hironori Nakajima

Our knowledge of mass transfer processes has been extended and applied to various fields of science and engineering including industrial processes in recent years. Since mass transfer is primordial phenomenon, it plays a key role in the scientific researches and fields of mechanical, energy, environmental, materials, bio, and chemical engineering. In this book, energetic authors especially provide advances in scientific findings and technologies, and develop new theoretical models concerning mass transfer for sustainable energy and environment. This book brings valuable references for research engineers working in the variety of mass transfer sciences and related fields. Since the constitutive topics cover the advances in broad research areas, the topics will be mutually stimulus and informative not only to research engineers, but also to university professors and students.

ISBN 978-953-51-6356-5

Photo by openflower / iStock

IntechOpen